

Understanding the design principles of organic sensitizers for highly efficient dye sensitized solar cells

Présentée le 4 juin 2021

Faculté des sciences de base
Laboratoire de photonique et interfaces
Programme doctoral en chimie et génie chimique

pour l'obtention du grade de Docteur ès Sciences

par

Marko STOJANOVIC

Acceptée sur proposition du jury

Prof. R. Beck, président du jury
Prof. M. Graetzel, Dr S. M. Zakeeruddin, directeurs de thèse
Prof. J. Delcamp, rapporteur
Prof. C. Barolo, rapporteuse
Dr J. H. Yum, rapporteur

Abstract

The conversion of solar to electrical power has presented itself as a solution to meet the growing energy demand and replace our current fossil fuel dependence, which causes dramatic damages to the environment. At the heart of this challenge lies the performance optimization of photovoltaic (PV) technologies, but also rendering their manufacture cost-effective. Dye sensitized solar cells (DSSCs) have attracted significant attention over the past decades because of their low-cost, facile manufacturing processes and wide range of very peculiar applications. Notably, DSSCs can power portable electronic devices under low ambient light or be used as semi-transparent cells for building integrated photovoltaics (BIPV). These attractive features are the consequence of the device's unique architecture. A layer of mesoporous titanium dioxide (TiO_2) is coated with a colored light absorber in contact with a redox active electrolyte, squeezed between a counter electrode.

Dye design is an important step in developing high efficiency devices as each of the dye structural features will influence its opto-electrochemical properties. Modern era dyes are constructed according to the Donor- π -Acceptor (D- π -A) pattern, where the donor would be an electron rich moiety and the acceptor an electron poor one. The D- π -A pattern was improved over the years, by adding an auxiliary electron accepting unit between the donor and the π -bridge to yield the new D-A- π -A pattern.

The aim of this thesis was to understand the principles that dictate the design of efficient sensitizers. The efforts were focused on organic dyes combined with the newly developed high photo-voltage $\text{Cu}(\text{II/I})$ based electrolyte.

Initially, it is focused on expanding the library of available building blocks, by implementing an electron acceptor, benzothienothiophenedione (BTD), into D-A- π -A dyes. The resulting dyes produced power conversion efficiencies of 5 % under AM1.5G with the $[\text{Cu}(\text{tmby})_2]^{+2/+1}$ (tmby=4,4',6,6'-tetramethyl-2,2'-bipyridine) electrolyte. Thorough investigation of their molecular structure revealed that these new sensitizers were impaired by strong intermolecular aggregation.

The next step, was dedicated to a structural study of dyes including an indacenodithiophene (IDT) π bridging unit. The structural as well as electronic properties of the terminal acceptor were altered in order to understand the effects of these the latter in full devices with the $\text{Cu}(\text{II/I})$ electrolyte. It was found that for D-A- π -A dyes, the terminal A had to be at least as strongly withdrawing as the primary A in order to not impair the LUMO level distribution and ultimately the performances.

Following up, the challenging symmetrical diketopyrrolopyrrole (DPP) building block was successfully implemented in $\text{Cu}(\text{II/I})$ based DSSCs. Three dyes, each including either a thiophene, furan or phenyl π -linker, were synthesized. An impressive open-circuit potential of 970 mV associated to a PCE of 7.67 % under standard AM1.5G conditions was achieved by the phenyl linker containing dye. Detailed investigation via DFT calculations and time resolved spectroscopy revealed that the phenyl linker performed better because of its six-membered ring feature, compared to the other two five-membered linkers. Furthermore, the substitution of thiophene to furan was found to be deleterious for the dye performances.

Then, a dithienopyrrole (DTP) π bridge was implemented in D-A- π -A dyes. Two primary acceptors were used: benzo-thiadiazole and benzo-oxadiazole. The first dye produced a short-circuit current density of $16.43 \text{ mA}\cdot\text{cm}^{-2}$, which constitutes a record for copper based DSSC. Its associated PCE was 12.4 % under AM1.5G, whereas the other dye produced a PCE of 10.8 % under similar conditions. This difference originated from a much longer electron lifetime measured in devices fabricated with the benzo-thiadiazole dye. Careful analysis of the dyes' optimized geometries indicated that the substitution of benzo-oxadiazole for benzo-thiadiazole was improving the steric bulk around the electron donating unit. This was speculated to help repelling the Cu(II) species at the dye/electrolyte, thus increasing the electron lifetime.

In the following chapter, a new dye format was explored. The structure was reduced to a simple D-A pattern where a series of electron acceptors were screened. Their synthesis was simplified to a single one-pot, two steps procedure in order to demonstrate their easy up scaling for production. In devices fabricated with the $[\text{Cu}(\text{tmby})_2]^{+2/+1}$ redox couple, each dye achieved impressive photo-voltages above 1 V. Their performances were promising for such simple dye structure with the highest PCE (6.96 %) achieved by the dye including a benzo-oxadiazole/ethnynyl benzoic acid moiety under AM1.5G. The difference in performances was attributed to disparities in their spectral response, that were limiting the photo-current generation.

In the last chapter, the new D-A concept was further improved by a simple synthetic modification of the aliphatic chains on electron donating unit. A two-fold increase from hexyl to dodecyl revealed to achieve an impressive photo-voltage of 1.24 V and a PCE of 8 % with the $[\text{Cu}(\text{tmby})_2]^{+2/+1}$ redox couple under AM1.5G. This champion sensitizer was applied as co-sensitizer along with another strong-absorbing organic dye to yield a record PCE of 13.5 % under AM1.5G with the Cu(II/I) electrolyte. Analysis of the PV performances revealed that the longer alkyl chains helped inducing an ideality factor near unity in these devices, thus implying a linear recombination mechanism between electron located in the conduction band and the Cu(II) species.

Keywords: Photovoltaic · Dye Sensitized Solar Cells · Organic Dyes · Copper Electrolyte · Dye Design · Organic Synthesis

Résumé

La conversion de l'énergie solaire en énergie électrique représente la solution la plus viable pour arriver à remplacer notre dépendance aux énergies fossiles qui causent d'important dommages à l'environnement. Pour arriver à cette transition, il est impératif d'augmenter les performances des technologies photovoltaïques existantes ainsi que de réduire leurs coûts de production. Les cellules solaires à colorants (CSCs) possèdent de nombreux d'avantages, notamment leur procédé de fabrication facile et les possibilités de champs d'applications. Les CSCs peuvent être utilisé pour alimenter des appareils électroniques portables, à des intensités d'illuminations faibles ou encore elles peuvent être utilisées comme cellules solaires semi-transparentes et être intégrées a des façades vitrées. Ces avantages, découlent de l'architecture très particulières des cellules solaires : une couche d'oxyde de titane (TiO_2), recouverte d'un colorant, est en contact avec un électrolyte redox actif et une contre électrode.

La structure du colorant joue un rôle important dans le développement de cellules solaires à haut rendement. En effet, chaque élément constituant la structure fondamentale du colorant va influencer ses propriétés opto-électrochimiques. Les colorants modernes sont synthétisés selon le modèle électron donneur- π - électron accepteur (D- π -A). Ce modèle a été raffiné au fil des années grâce à l'ajout d'un groupe électron accepteur supplémentaire : D-A- π -A.

Le but de cette thèse a été la compréhension des principes qui régissent le design de colorants pouvant produire de hauts rendements. Les efforts ont été concentrés autour de colorants organiques qui ont été utilisées avec un électrolyte redox actif à base de Cu(II/I) .

Dans le premier chapitre, un nouveau groupe électron accepteur a été utilisé pour construire des nouveaux colorants D-A- π -A. Ces derniers ont produit un rendement d'environ 5 % dans les conditions d'illumination AM1.5G avec le complexe de cuivre $[\text{Cu}(\text{tmby})_2]^{+2/+1}$ (tmby=4,4',6,6'-tetramethyl-2,2'-bipyridine). Il a été découvert que ces colorants formaient des agrégats, qui étaient néfastes pour leurs performances.

Suite à cela, le groupe π -liant nommé indacenodithiophene (IDT) a été utilisé pour synthétisé trois nouveaux colorants D-A- π -A, à fin effets électroniques et géométriques induits par trois différents accepteurs terminaux sur les performances photovoltaïques de cellules solaires fabriquées avec l'électrolyte à base de Cu(II/I) . Il fut conclu que pour avoir une orbitale LUMO correctement positionnée, l'accepteur terminal devait posséder un pouvoir électro-attracteur plus fort que l'accepteur secondaire.

Dans le chapitre suivant, de nouveaux colorants ont été construits avec la variante symétrique du groupe nommé Diketopyrrolopyrrole (DPP). Ces nouvelles molécules ont été intégrés avec succès dans des CSC à base d'électrolyte au cuivre. Chaque colorant comportait un segment π -liant différent : phényle, furane ou thiophène. Le colorant qui contenait le groupe phényle a produit un rendement de 7.67 % ainsi qu'une tension de 970 mV dans les conditions AM1.5G. Les simulations effectuées par DFT combinées avec les mesures de spectroscopie transitoire ont indiqué que le groupe phényle offrait une meilleure conformation géométrique que les deux autres groupes.

Dans le chapitre 5, le groupe π -liant dithienopyrrole (DTP) a été utilisé pour la première fois dans des colorants D-A- π -A.

Deux groupes accepteurs ont été utilisés : un benzo-thiadiazole et un benzo-oxadiazole. Le colorant à base de benzo-thiadiazole a produit une densité de courant à court-circuit de $16.43 \text{ mA}\cdot\text{cm}^{-2}$ ce qui constitue un record pour une cellule contenant un électrolyte au cuivre. Il a été révélé que la substitution du benzo-thiadiazole pour le benzo-oxadiazole réduisait le volume du groupe électro-donneur ce qui engendrait une diminution du temps de vie des électrons libres.

Un nouvel format de colorant, a été développé dans le chapitre suivant. La structure de la molécule a été réduite à un simple motif D-A. Cinq différents groupes électro-accepteurs ont été étudiés pour évaluer la pertinence de ce modèle. De plus, la synthèse de ces colorants a été réduite à une procédure unique constituée de deux étapes. Dans des cellules solaires fabriquées avec l'électrolyte $[\text{Cu}(\text{tmby})_2]^{+2/+1}$, tous les colorants ont produits d'impressionnantes tensions supérieures à 1 V. Le plus haut rendement (6.96 %) a été produit par le colorant contenant un groupe benzo-oxadiazole et une liaison triple. Les différentes performances de ces colorants étaient dues à leurs différents spectres d'absorption.

Dans le chapitre final, le modèle D-A a été étoffé en modifiant la longueur des chaînes alkyles sur le groupe électro-donneur. Les chaînes hexyles ont été remplacées par des chaînes dodécyles ce qui a permis de produire une tension de 1.24 V associée à un rendement de 8 % dans les conditions AM1.5G avec l'électrolyte au cuivre. Le colorant champion, a été utilisé comme co-colorant avec un analogue possédant un spectre d'absorption plus étendu. Ce système a produit un rendement record de 13.5 % dans les conditions précédentes. Après analyse des cellules solaires, il a été découvert que l'élongation des chaînes alkyles avait aussi changé le mécanisme de recombinaison des électrons.

Mots-clés : Photovoltaïque · cellules solaires à colorant · colorant organique · électrolyte au cuivre · Design de colorants · Synthèse organique

List of abbreviations

ADEKA-1	(Z)-(1-(5'''-(9-ethyl-9H-carbazol-3-yl)-3',3'',3''',4-tetrahexyl-[2,2':5',2'':5'',2'''-quaterthiophen]-5-yl)-3-oxo-3-((4-(trimethoxysilyl)phenyl)amino)prop-1-en-2-yl)
APPI	Atmospheric pressure ionization
BA	Benzoic acid
BINAP	2,2'-bis(diphenylphosphino)-1,1'-binaphthyl
BO	Benzo-oxadiazole
Bpin ₂	Bis(pinacolato)diboron
bpy	2,2'-bipyridine
bpy-pz	6-(1H-pyrazol-1-yl)-2,2'-bipyridine
BT	Benzo-thiadiazole
BTd	5,7-bis(2-ethylhexyl)-4H,8H-benzo[1,2-c:4,5-c'] dithiophene-4,8-dione
BTz	Benzo-triazole
C101	Ruthenate(2-), [[2,2'-bipyridine]-4,4'-dicarboxylato(2-)-κN1,κN1'] [4,4'-bis(5-hexyl-2-thienyl)-2,2'-bipyridine-κN1,κN1']bis(thiocyanato-κN)-, hydrogen (1:2), (OC-6-32)-
C102	Ruthenate(2-), [[2,2'-bipyridine]-4,4'-dicarboxylato(2-)-κN1,κN1'] [4,4'-bis(5-hexyl-2-furanyl)-2,2'-bipyridine-κN1,κN1']bis(thiocyanato-κN)-, hydrogen (1:2), (OC-6-32)-
C205	(E)-3-(7'-(4-(bis(9,9-dimethyl-9H-fluoren-2-yl)amino)phenyl)-2,2',3,3'-tetrahydro-[5,5'-bithieno[3,4-b][1,4]dioxin]-7-yl)-2-cyanoacrylic acid
C218	(E)-3-(6-(4-(bis(4-(hexyloxy)phenyl)amino)phenyl)-4,4-dihexyl-4H-cyclopenta[2,1-b:3,4-b']dithiophen-2-yl)-2-cyanoacrylic acid
C219	(E)-3-(6-(7-(4-(bis(4-((2-ethylhexyl)oxy)phenyl)amino)phenyl)-2,3-dihydrothieno[3,4-b][1,4]dioxin-5-yl)-4,4-dihexyl-4H-silolo[3,2-b:4,5-b']dithiophen-2-yl)-2-cyanoacrylic acid
CN	Coordination number
CPDT	Cyclo-penta-dithienyl
D(E)	Density of state distribution
D149	5-[[4-[4-(2,2-Diphenylethenyl)phenyl]-1,2,3,3a,4,8b-hexahydrocyclopent[b]indol-7-yl]methylene]-2-(3-ethyl-4-oxo-2-thioxo-5-thiazolidinylidene)-4-oxo-3-thiazolidineacetic acid
D205	5-[[4-[4-(2,2-Diphenylethenyl)phenyl]-1,2,3,3a,4,8b-hexahydrocyclopent[b]indol-7-yl]methylene]-2-(3-octyl-4-oxo-2-thioxo-5-thiazolidinylidene)-4-oxo-3-thiazolidineacetic acid
D21L6	(E)-3-(5'-(4-(bis(4-(hexyloxy)phenyl)amino)phenyl)-[2,2'-bithiophen]-5-yl)-2-cyanoacrylic acid
D35	(E)-3-(5-(4-(bis(2',4'-dibutoxy-[1,1'-biphenyl]-4-yl)amino)phenyl)thiophen-2-yl)-2-cyanoacrylic acid
dmby	6,6'-dimethyl-2,2'-bipyridine
DMF	N,N'-dimethylformamide
dmp	2,9-dimethyl-1,10-phenanthroline
DPP	Diketopyrrolopyrrole
DPP13	(E)-3-(5-(4-(4-(5-(4-(bis(4-(hexyloxy)phenyl)amino)phenyl)thiophen-2-yl)-2,5-bis(2-ethylhexyl)-3,6-dioxo-2,3,5,6-tetrahydropyrrolo[3,4-c]pyrrol-1-yl)phenyl)furan-2-yl)-2-cyanoacrylic acid
DPP14	(E)-3-(5-(4-(2,5-bis(2-ethylhexyl)-3,6-dioxo-4-(5-(4-(p-tolyl)-1,2,3,3a,4,8b-hexahydrocyclopenta[b]indol-7-yl)thiophen-2-yl)-2,3,5,6-tetrahydropyrrolo[3,4-c]pyrrol-1-yl)phenyl)furan-2-yl)-2-cyanoacrylic acid
DPP15	(E)-3-(5-(4-(4-(5-(4-(2',4'-bis(hexyloxy)-[1,1'-biphenyl]-4-yl)-1,2,3,3a,4,8b-hexahydrocyclopenta[b]indol-7-yl)thiophen-2-yl)-2,5-bis(2-ethylhexyl)-3,6-dioxo-2,3,5,6-tetrahydropyrrolo[3,4-c]pyrrol-1-yl)phenyl)furan-2-yl)-2-cyanoacrylic acid
DPP17	(E)-3-(5-(4-(4-(5-(4-(4-(2,2-bis(2',4'-bis(hexyloxy)-[1,1'-biphenyl]-4-yl)vinyl)phenyl)-1,2,3,3a,4,8b-hexahydrocyclopenta[b]indol-7-yl)thiophen-2-yl)-2,5-bis(2-ethylhexyl)-3,6-dioxo-2,3,5,6-tetrahydropyrrolo[3,4-c]pyrrol-1-yl)phenyl)furan-2-yl)-2-cyanoacrylic acid
DTP	Dithieno-pyrrole
EBA	4-ethynyl-benzoic acid
Et	Ethyl
HexEt	2-ethyl-hexyl
HY63	(E)-3-(6-(7-(4-(bis(2',4'-bis(hexyloxy)-[1,1'-biphenyl]-4-yl)amino)phenyl)benzo[c][1,2,5]thiadiazol-4-yl)-4,4-dihexyl-4H-cyclopenta[2,1-b:3,4-b']dithiophen-2-yl)-2-cyanoacrylic acid
HY64	(E)-3-(6-(13-(4-(bis(2',4'-bis(hexyloxy)-[1,1'-biphenyl]-4-yl)amino)phenyl)dibenzo[a,c]phenazin-10-yl)-4,4-dihexyl-4H-cyclopenta[2,1-b:3,4-b']dithiophen-2-yl)-2-cyanoacrylic acid
IDT	4,4,9,9-tetrakis(4-hexylphenyl)-4,9-dihydro-s-indaceno[1,2-b:5,6-b']dithiophene

iPr	Iso-propyl
JF419	(E)-3-(6-(4-(bis(5,7-bis(hexyloxy)-9,9-dimethyl-9H-fluoren-2-yl)amino)phenyl)-4,4-dihexyl-4H-cyclopenta[2,1-b:3,4-b']dithiophen-2-yl)-2-cyanoacrylic acid
JK-318	3-(5'-(4-(3,6-Bis(4-(hexyloxy)phenyl)-9H-carbazol-9-yl)phenyl)-2,2'-bithiophen-5-yl)-2-cyanoacrylic acid
JK-319	3-(5-(6-(3,6-Bis(4-(hexyloxy)phenyl)-9H-carbazol-9-yl)-4,4-dimethyl-4H-indeno[1,2-b]thiophen-2-yl)thiophen-2-yl)-2-cyanoacrylic acid
JK-320	3-(5-(6-(3,6-Bis(2,4-bis(hexyloxy)phenyl)-9H-carbazol-9-yl)-4,4-dimethyl-4H-indeno[1,2-b]thiophen-2-yl)thiophen-2-yl)-2-cyanoacrylic acid
L349	4-(7-(7-(4-(bis(2',4'-bis(octyloxy)-[1,1'-biphenyl]-4-yl)amino)phenyl)-4,4,9,9-tetrakis(4-hexylphenyl)-4,9-dihydro-s-indaceno[1,2-b:5,6-b']dithiophen-2-yl)-5,6-difluorobenzo[c][1,2,5]thiadiazol-4-yl)benzoic acid
L350	4-(7-(7-(4-(bis(2',4'-bis(octyloxy)-[1,1'-biphenyl]-4-yl)amino)phenyl)-4,4,9,9-tetrakis(4-hexylphenyl)-4,9-dihydro-s-indaceno[1,2-b:5,6-b']dithiophen-2-yl)benzo[c][1,2,5]thiadiazol-4-yl)benzoic acid
L351	4-(7-(7-(4-(bis(2',4'-bis(octyloxy)-[1,1'-biphenyl]-4-yl)amino)phenyl)-4,4,9,9-tetrakis(4-hexylphenyl)-4,9-dihydro-s-indaceno[1,2-b:5,6-b']dithiophen-2-yl)benzo[c][1,2,5]oxadiazol-4-yl)benzoic acid
LEG4	3-{6-[4-[bis(2',4'-dibutyloxybiphenyl-4-yl)amino]-phenyl]-4,4-dihexyl-cyclopenta-[2,1-b:3,4-b']dithiophene-2-yl}-2-cyanoacrylic acid
LP225	(E)-3-(6-(4-(bis(2',4'-bis(hexyloxy)-[1,1'-biphenyl]-4-yl)amino)phenyl)-4-(tridecan-7-yl)-4H-dithieno[3,2-b:2',3'-d]pyrrol-2-yl)-2-cyanoacrylic acid
LP227	(E)-3-(6-(4-(bis(5,7-bis(hexyloxy)-9,9-dimethyl-9H-fluoren-2-yl)amino)phenyl)-4-(tridecan-7-yl)-4H-dithieno[3,2-b:2',3'-d]pyrrol-2-yl)-2-cyanoacrylic acid
Me	Methyl
MK-14	2-Cyano-3-[5''-[9-ethyl-3-(4-(n-hexyloxy)phenyl)-9H-carbazol-6-yl]-3',3'',4-tri-n-hexyl-[2,2',5',2'']terthiophen-5-yl]acrylic acid
MK-16	2-Cyano-3-[5''-(9-ethyl-3-(4-(n-hexyloxy)phenyl)-9H-carbazol-6-yl)-3',3'',3''',4-tetra-n-hexyl-[2,2',5',2'',5'',2''']quaterthiophenyl-5-yl]acrylic acid
MK-2	2-Cyano-3-[5'''-(9-ethyl-9H-carbazol-3-yl)-3',3'',3''',4-tetra-n-hexyl-[2,2',5',2'',5'',2''']quaterthiophen-5-yl]acrylic acid
N3	Cis-bis(isothiocyanato)bis(2,2'-bipyridyl-4,4'-dicarboxylato)ruthenium(II)
N719	cis-diisothiocyanato-bis(2,2'-bipyridyl-4,4'-dicarboxylato)ruthenium(II) bis(tetrabutylammonium)
N749	Tris(N,N,N-tributyl-1-butanaminium)[[2,2''6',2''-terpyridine]-4,4',4''-tricarboxylato(3-)-N1,N1',N1'']tris(thiocyanato-N)hydrogen ruthenate
NBS	N-bromosuccinimide
nBu	n-butyl
OctBu	2-butyl-octyl
Ox	Oxidizing agent
P(o-Tol) ₃	Tris(o-tolyl)phosphine
PCE	Power conversion efficiency
Pd(dba) ₂	Bis(dibenzylideneacetone)palladium(0)
Pd ₂ (dba) ₃	Tris(dibenzylideneacetone)dipalladium(0)
PEDOT	poly(3,4-ethylenedioxythiophene)
Ph	Phenyl
phen	1,10-Phenanthroline
PPh ₃	Triphenylphosphine
TA-St-CA	(E)-2-cyano-3-(4-((E)-4-(diphenylamino)styryl)phenyl)acrylic acid
TBP	4-tert-butylpyridine
tBu	Tert-butyl
TFSl	bis(trifluoromethanesulfonyl)imide
Th	Thiophene
THF	Tetrahydrofuran
tmby	6,6',4,4'-tetramethyl-2,2'-bipyridine
WS-70	(E)-3-(6-(8-(4-(bis(2',4'-bis(hexyloxy)-[1,1'-biphenyl]-4-yl)amino)phenyl)-2,3-diphenylquinoxalin-5-yl)-4,4-dihexyl-4H-cyclopenta[2,1-b:3,4-b']dithiophen-2-yl)-2-cyanoacrylic acid
WS-72	(E)-3-(6-(8-(4-(bis(2',4'-bis(hexyloxy)-[1,1'-biphenyl]-4-yl)amino)phenyl)-2,3-bis(4-(hexyloxy)phenyl)quinoxalin-5-yl)-4,4-dihexyl-4H-cyclopenta[2,1-b:3,4-b']dithiophen-2-yl)-2-cyanoacrylic acid
XPhos	2-Dicyclohexylphosphino-2',4',6'-triisopropylbiphenyl

List of abbreviations

XY1	(E)-3-(4-(6-(7-(4-(bis(2',4'-bis((2-ethylhexyl)oxy)-[1,1'-biphenyl]-4-yl)amino)phenyl)benzo[c][1,2,5]thiadiazol-4-yl)-4,4-bis(2-ethylhexyl)-4H-cyclopenta[2,1-b:3,4-b']dithiophen-2-yl)phenyl)-2-cyanoacrylic acid
XY1b	(E)-3-(4-(6-(7-(4-(bis(2',4'-dibutoxy-[1,1'-biphenyl]-4-yl)amino)phenyl)benzo[c][1,2,5]thiadiazol-4-yl)-4,4-bis(2-ethylhexyl)-4H-cyclopenta[2,1-b:3,4-b']dithiophen-2-yl)phenyl)-2-cyanoacrylic acid
XY2	(E)-3-(5-(6-(7-(4-(bis(2',4'-bis((2-ethylhexyl)oxy)-[1,1'-biphenyl]-4-yl)amino)phenyl)benzo[c][1,2,5]thiadiazol-4-yl)-4,4-bis(2-ethylhexyl)-4H-cyclopenta[2,1-b:3,4-b']dithiophen-2-yl)thiophen-2-yl)-2-cyanoacrylic acid
XY3	(E)-3-(5-(7-(6-(4-(bis(2',4'-bis((2-ethylhexyl)oxy)-[1,1'-biphenyl]-4-yl)amino)phenyl)-4,4-bis(2-ethylhexyl)-4H-cyclopenta[2,1-b:3,4-b']dithiophen-2-yl)benzo[c][1,2,5]thiadiazol-4-yl)thiophen-2-yl)-2-cyanoacrylic acid
Y123	3-{6-{4-[bis(2',4'-dibutyloxybiphenyl-4-yl)amino-]phenyl}-4,4-dihexyl-cyclopenta-[2,1-b:3,4-b']dithiophene-2-yl}-2-cyanoacrylic acid
YD2-o-C8	[5,15-bis(2,6-dioctoxyphenyl)-10-(bis(4-hexylphenyl)amino)-20-(4-carboxyphenyl ethynyl)porphyrinato] Zinc(II)
Z907	cis-Bis(isothiocyanato)(2,2'-bipyridyl-4,4'-dicarboxylato)(4,4'-di-nonyl-2'-bipyridyl)ruthenium(II)

Table of contents

Abstract	iii
Résumé	v
List of abbreviations	viii
Table of contents	xi
Chapter 1 : Introduction.....	1
1.1 Energy challenges of the XXIst century.....	1
1.2 Perspective of solar energy	3
1.3 Prospect of photovoltaic technology.....	5
1.3.1 Working principle of a Solar cell	5
1.3.2 Existing solar cell technologies.....	8
1.3.3 Losses and efficiency limits in solar cells	10
1.4 Dye sensitized solar cells	13
1.4.1 Working principle and structure	13
1.4.2 Components of a dye sensitized solar cell	20
1.4.3 Characterization techniques for dye sensitized solar cells.	37
1.4.4 Motivations and outline of the thesis	39
Chapter 2 : Implementing benzothienothiophenedione as electron accepting unit in D-A-π-A dyes.....	41
2.1 Introduction	41
2.2 Results and discussion	42
2.3 Conclusion.....	51
Chapter 3 : A structural study of D-A-π-A dyes, constructed with an indacenodithiophene π-bridge.	52
3.1 Introduction.....	52
3.2 Results and Discussion	54
3.3 Conclusion.....	63
Chapter 4 : Synthesis and study of organic dyes containing a symmetrical Diketopyrrolopyrrole chromophore/acceptor for efficient Cu(II/I) based dye sensitized solar cells.	64
4.1 Introduction	64
4.2 Results and discussion	66
4.3 Conclusion.....	74
Chapter 5 : From benzo-thiadiazole to benzo-oxadiazole: the effect of atom substitution on the photovoltaic performances of two D-A-π-A dyes containing a dithienopyrrole π-bridge.	75
5.1 Introduction.....	75
5.2 Results and discussion	76
5.3 Conclusion.....	83

Chapter 6 : Simple D-A dyes synthesized in a one pot method enable high photo voltage.	84
6.1 Introduction	84
6.2 Results and discussion	85
6.3 Conclusion.....	93
 Chapter 7 : Rational molecular design of a simple dye enables record photo-voltage and power conversion efficiencies, through alteration of electron recombination mechanism.	94
7.1 Introduction.....	94
7.2 Results and discussion.....	95
7.3 Conclusion.....	100
 Conclusion	101
 Supporting information	102
7.4 Supporting information to Chapter 2.....	105
7.5 Supporting information to Chapter 3.....	118
7.6 Supporting information to Chapter 4.....	136
7.7 Supporting information to Chapter 5.....	156
7.8 Supporting information to Chapter 6.....	171
7.9 Supporting information to Chapter 7.....	190
 References	199
 Acknowledgements	211
 Curriculum Vitae	212

Chapter 1 : Introduction

1.1 Energy challenges of the XXlst century

The industrial revolution marked an important transition in human history by considerably improving the world's population living standard. One of the main turning point was the development of coal based steam powered engines as well as the discovery of the first commercial oil well in 1859 in Titusville, Pennsylvania by Edwin L. Drake⁴. It was only 26 years later that Carl Benz developed the first internal combustion engine (ICE) powering an automobile⁵. He was followed by its American fellow Henry Ford only about 20 years later⁶. These historical events led to dramatic changes and shaped our modern human society but at the cost of important environmental problems.

The technology based on ICEs relies on a chemical reaction called combustion that takes place within the motors and produce mechanical work as well as side products such as carbon monoxide (CO) and carbon dioxide (CO₂). These molecules are naturally present in earth's atmosphere along with other gases such as nitrous oxide (N₂O), methane (CH₄) and water vapor (H₂O)⁷. Initially, they all contributed to establish a warm and prosperous climate on earth's surface, helping the development of life.

However, the industrial revolution that occurred in 1760 significantly increased the amount of these gases in earth's atmosphere, causing global warming through the so-called greenhouse effect. These greenhouse gases act as thermal insulators by retaining the radiations emitted from earth ultimately causing an increase in the global temperature, which ultimately leads to catastrophic consequences for humanity⁸. Moreover, the development of electrical science in the early 19th century, new tools and ways of living were established which resulted in an increased electricity consumption and demand⁹.

As a direct result of modernization and better living conditions, the 20th century witnessed a rapid growth of population.

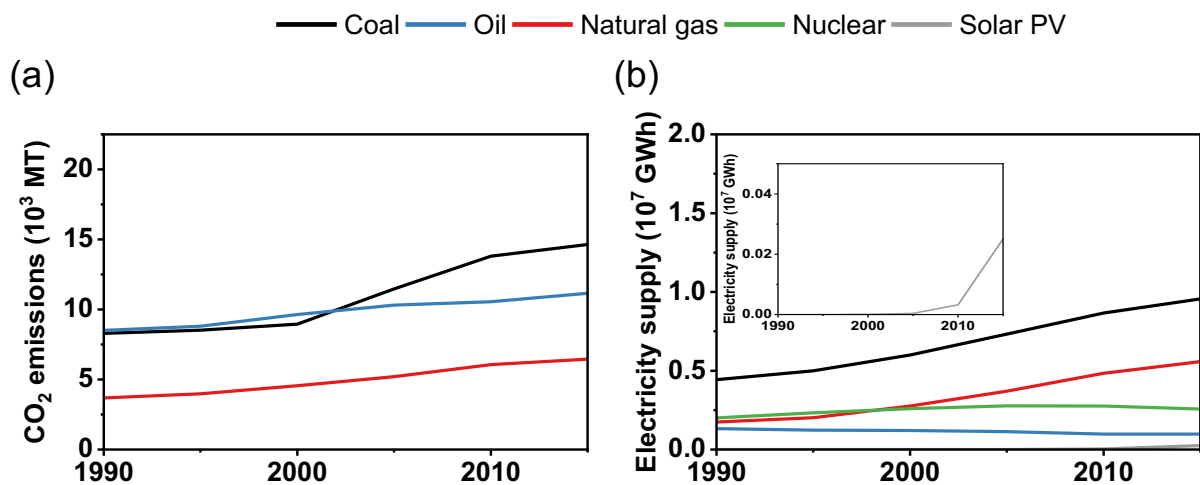


Figure 1.1. (a) Carbon dioxide emissions by energy source from 1990 to 2015. (b) Main sources of electricity production worldwide from 1990 to 2015. The Graphs were constructed with data obtained from the International Energy Association (IEA)^{12,13}.

The first solutions to this increasing energy demand were found in fossil fuels, nuclear combustibles and coal.

They rapidly established themselves over the centuries, up to this day, with only a small fraction of the production coming from photovoltaics (PV), within the last 10 years (see Figure 1.1b).

Fossil and nuclear based energy production successfully managed to meet the rapid demand but several inherent issues were identified along the process. For example, nuclear technology needs important efforts and costs in terms of waste processing as well as raises serious concerns regarding its toxicity. In addition to that, the nuclear catastrophes that occurred throughout the last 60 years, showed that nuclear based energy production can raise serious questions about the safety of this technology^{10,11}. Over the last 15 years, the increase of CO₂ emission in the atmosphere mainly originated from coal-based electricity production, followed by oil and natural gas, as described by Figure 1.1a.

Table 1.1. *Electricity consumption projection growth of Europe, China, India and USA over 20 years. The data was obtained from the IEA¹⁴.*

	Electricity consumption [TWh]	
	2020	2040
Europe	3	3
China	7	11
India	1	4
USA	4	5
Total:	15	23

In 2020, the international energy agency (IEA) estimated that the total amount of electricity consumption of India, China, USA and Europe was equal to 15 TWh. As summarized on Table 1.1, the IEA projected that by 2040, the total consumption of these locations will be approximately 8 TWh higher than in 2020, corresponding to a total amount of 23 TWh. These numbers rose serious concerns and highlighted the urgent need to develop technologies that could meet this demand without harming the planet's and earth's population health.

1.2 Perspective of solar energy

Solar based energy is among the most promising candidates for replacing humanity's addiction to fossil fuels and the underlying treat of nuclear technology. The sun's surface can be approximated by a black body radiating at a temperature of 5800 K^{15,16}. In this case, its spectral irradiance can be modeled by Plank's black body radiation law described by equation (1.1) also represented and by the grey area in Figure 1.2a.

$$F(\lambda) = \frac{2\pi hc^2}{\lambda^5 \left(\exp\left(\frac{hc}{k_B \lambda T}\right) - 1 \right)} \quad (1.1)$$

Where $h = 6.63 \cdot 10^{-34} \text{ J} \cdot \text{s}^{-1}$, $c = 2.99 \cdot 10^8 \text{ m} \cdot \text{s}^{-1}$ and $k_B = 1.38 \cdot 10^{-23} \text{ m}^2 \cdot \text{kg} \cdot \text{s}^{-2} \cdot \text{K}^{-1}$. Equation (1.1) describes the distribution of power density that resides in each wavelength of an emitting black body at a given temperature.

Furthermore, Boltzmann's law can be derived from Plank's law by integrating over the whole surface of a spherical emitting body and wavelength spectra. This latter estimates the total power per surface area emitted by the surface of the sun at a given temperature:

$$I(T) = \sigma T^4 \quad (1.2)$$

Where $\sigma = 5.67 \cdot 10^{-8} \text{ W} \cdot \text{m}^{-2} \cdot \text{K}^{-4}$, is a constant. Using the upper equation, the sun surface is found to deliver an energy flux of $I(5800\text{K}) = 64.10 \text{ MW} \cdot \text{m}^{-2}$. Once the flux described by Equation (1.2) has traveled through space and reached the earth, its intensity diminished to a new value called the solar constant (I_{SC})¹⁷⁻¹⁹ which corresponds to an irradiance of $I_{SC} = 1.367 \text{ kW} \cdot \text{m}^{-2}$. From there, the I_{SC} has to travel through the atmosphere to reach the surface. This will furtherly reduce its irradiance by 30 % due to scattering of the photons and absorption by atmospheric gases²⁰. Additionally, the interaction with the atmosphere and most specifically, the light's path length within this media will affect its intensity. This effect is quantified using the concept of Air mass (AM), that depends on the angle from the zenith position of the incoming flux, represented by θ ²¹:

$$AM = \frac{1}{\cos(\theta) + 0.51(96.08 - \theta)^{-1.64}} \quad (1.3)$$

Hence, AM1 will correspond to a perfectly vertical alignment of $\theta = 0^\circ$, and AM1.5 to a zenithal angle of $\theta \approx 48.2^\circ$. The irradiation intensity will also depend on whether the total radiation, that is diffuse and direct, is considered (denoted by the letter G) or only direct radiation (noted by the letter D). For the global condition, all the aforementioned atmospheric path length as well as zenithal angle effects are taken into account by the following expression²²:

$$I_G = 1.1 I_{SC} 0.7^{AM^{0.68}} \quad (1.4)$$

When these corrections are applied to the solar constant value I_{SC} , they yield to a surface irradiance of $I_{AM1.5G} = 1035.94 \text{ W} \cdot \text{m}^{-2}$ under AM1.5G conditions, that is, the standard value used for measuring solar cells efficiencies. Consistently, the integration of the measured AM1.5G spectral irradiance (black line) displayed in Figure 1.2a, yields to a similar irradiance of $I_{AM1.5G} = 1000.36 \text{ W} \cdot \text{m}^{-2}$, represented by the dotted line.

The spectral photon flux distribution ($\phi(\lambda)$) of the sun under the AM1.5G conditions, is divided into three wavelength ranges: the ultra violet (UV) that spans from approximately 100 nm to 380 nm, the visible light from 380 nm to 700 nm and the infrared (IR) from 700 nm to 1 mm. In terms of proportions, the UV portion hold 3 % of the total photon flux, the visible part 44 % and the IR 55 %. Additionally, several valleys can be observed in Figure 1.2b. These gaps correspond to absorption bands of the different atmospheric gases: ozone absorbing strongly in the UV region, carbon dioxide absorbing in the middle and far infrared part and water vapor strongly absorbing in the near IR.

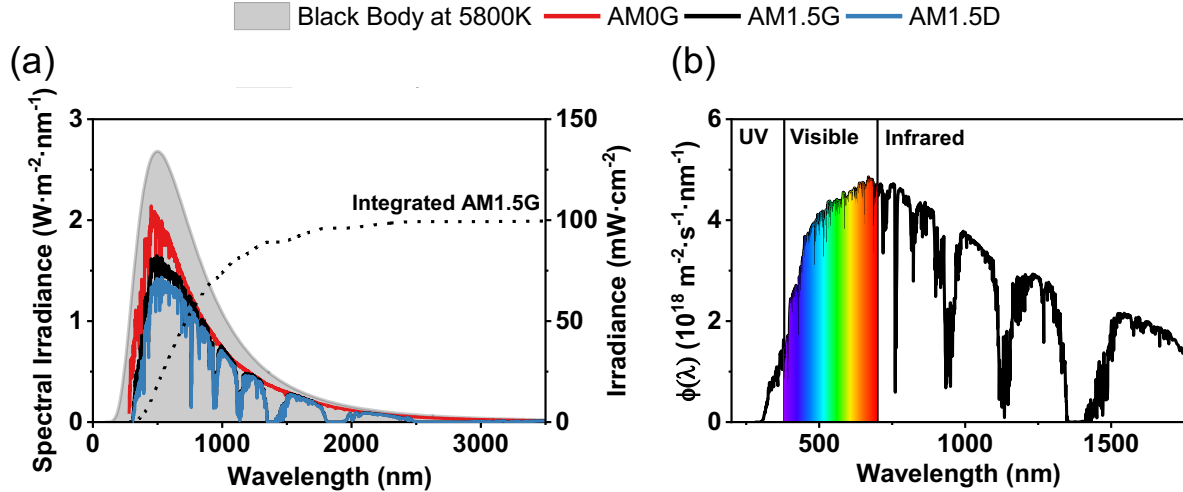


Figure 1.2. (a) Irradiance of the Sun at AM0 (outside the atmosphere), AM1.5G (after passing through the atmosphere with total radiation), AM1.5D (after passing through the atmosphere with only direct radiation) and the black body radiation approximation from Planck's equation (grey area). The absorption band of the atmospheric gases can be noticed between the AM0G and the other two curves (AM1.5G and AM1.5D). (b) Spectral photon flux under AM1.5G distribution over the wavelengths. The graphs were constructed with data obtained from National Renewable Energy Laboratory (NREL)²³.

1.3 Prospect of photovoltaic technology

1.3.1 Working principle of a Solar cell

The French physicist Edmond Becquerel was the first to report the photovoltaic effect in 1839²⁴. Fundamentally, converting the energy carried by photons into electrical work requires the formation of an interface between two materials. In conventional solar cells, two doped semiconductors are forming this interface called a junction. Semiconductors are a class of materials which exhibit conductive properties under certain conditions, as an example the room temperature conductivity of a semiconductor ranges between 10^{-4} to $10^4 \Omega^{-1} \cdot \text{m}^{-1}$. As a comparison, insulators show conductivities of $10^{-8} \Omega^{-1} \cdot \text{m}^{-1}$. Typical semiconducting materials include silicon (Si), germanium (Ge) or the gallium arsenide binary mixture (GaAs)²⁵. Their conductivity can be improved through a procedure called doping where impurities are introduced into the material.

The nature of the dopant will determine the doping type: a p-doping consists in introducing a free hole whereas n-doping, introduces a free electron in the atomic structure of the semiconductor²⁶. For example, Silicon based semiconductors are n-doped using phosphorus (P) atoms and p-doped using boron (B) atoms.

In terms of energy levels, an undoped or intrinsic semiconductor has an equal number of holes and electrons, which establishes its Fermi level (E_F) exactly halfway between its valence band (VB) and the conduction band (CB). The introduction of a p-dopant will create an accepting energy level close to the valence band, hence lowering its Fermi level ($E_{F,p}$), compared to the undoped case. On the other hand, introducing a n-dopant will create a donating energy level close to the conduction band, ultimately raising its Fermi level ($E_{F,n}$). The doping process and the corresponding movements of the energy levels are illustrated in Figure 1.3a.

When a n-type semiconductor is brought in contact with a p-type semiconductor to form a p-n junction, their fermi level will equilibrate. This process involves diffusion of the excess of electrons in the n-type semiconductor to the p-type material and diffusion of the excess of holes in the opposite direction, causing a bending of the respective valance and conduction bands of each material²⁷. This spatial zone where electrons and hole have migrated is called depletion region (see Figure 1.3b). This movement of charge leads to the formation of an internal electric field within the depletion region as well as a built-in potential (V_B). A scheme of the charges distributions is represented in Figure 1.3c.

The carrier transport takes place via two main processes, within the depletion region: drift and diffusion. The latter will be caused by a localized gradient of carrier concentration. In the n-type semiconductor side, the concentration of electron will decrease across the depletion region, causing the diffusion of electrons towards the edge of the depletion region, whereas the opposite phenomena will occur for the holes.

The drifting current, resulting from the internal electric field, will push the electron towards the n-side and the holes towards the p-side, that is in the opposite direction to the diffusion current. At equilibrium, the net current will be null implying that the diffusion will be canceled out by the drifting.

Applying an external voltage (V) to the p-n junction will disturb the equilibrium state. A forward bias, where the p-side is connected to the positive side of the voltage supply and the n-side to the negative end, will induce a reduction of the built in voltage V_B as well as the internal electric field ultimately shrinking the depletion region²⁸.

In this case, the drifting motion of carriers will therefore be suppressed thus allowing charges to flow, ultimately generating a current. In the opposite case, when a reverse bias is applied, V_B will increase along with the depletion region and, by extension, the internal electric field, preventing charges to flow. Consequently, a current can only be allowed to flow in one direction. Such an electrical element is called a semiconductor diode.

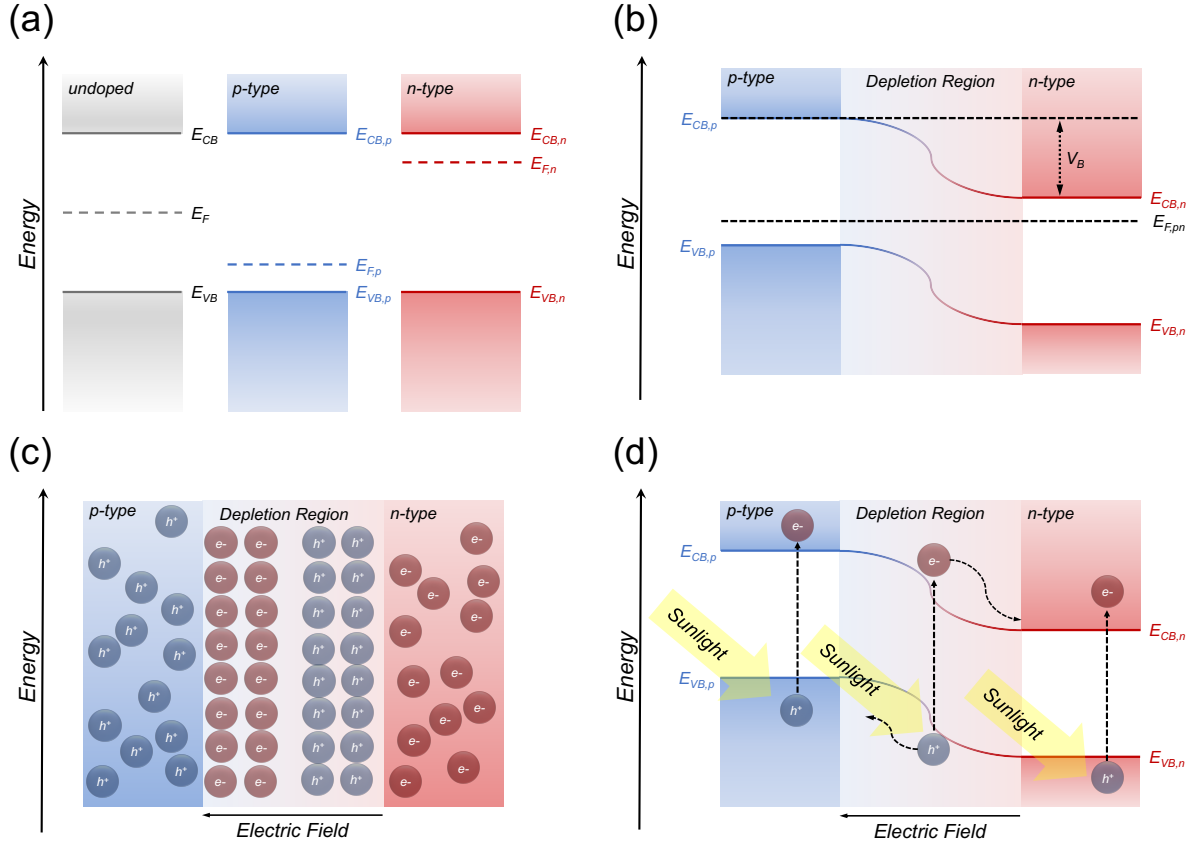


Figure 1.3. (a) Schematic representation of energy levels in undoped (left), p-doped (middle) and n-doped (right) semiconductors, with their corresponding Fermi levels. (b) Formation of a p-n junction with the depletion zone and band bending resulting from the Fermi levels adjustment. (c) Schematic representation of electrons and holes distribution in a p-n junction and the resulting internal electric field. (d) Schematic representation of a p-n junction operation principle under illumination.

Under illumination, the semiconductor diode will behave differently as explained in the illustration in Figure 1.3d. The energy provided by a photon (E_{ph}) depends on its wavelength λ according to Planck-Einstein equation :

$$E_{ph} = \frac{hc}{\lambda} \quad (1.5)$$

If the energy of the photon determined by (1.5) is superior or equal to the band gap energy (E_g), defined as the difference between the valence and conduction band energies, an electron hole pair will be generated.

Now, if the pair is produced within the depletion region, the two opposed charges will be separated by the internal electric field and migrate into the bulk of their respective material: the holes will travel to the p side and the electrons on the n-side. On the other hand, if the charges are generated outside the depletion region, they will either recombine with each other or diffuse to the depletion region and separate (see Figure 1.3d).

Additionally, if the two ends are short circuited, an electrical current will be measured. By contrast, if the two ends are left in an open circuit state under illumination, the photo-generated electrons, will accumulate on the n-side and holes will accumulate on the p-side²⁹.

The behavior of an ideal solar cell connected to a voltage supply under dark is very similar to a simple semiconductor diode. When the applied bias is null, a saturation current (J_0) flows through the cell in the opposition direction, as a result of carrier diffusion^{30,31}. As explained in the previous paragraphs, when a forward bias ($V_b > 0$) is applied to the device, the current is expected to increase. On the contrary, when a reverse bias ($V_b < 0$) is applied, little to no variation is expected to be noticed. The variation of current under dark is described by the equation (1.6):

$$J(V) = J_0 \left(\exp\left(\frac{qV}{k_B T}\right) - 1 \right) \quad (1.6)$$

When the solar cell is illuminated a photocurrent can be under short-circuit conditions (J_{SC}), i.e. at $V = 0$. The short circuit current density will not be influenced by the applied voltage, but only by the illumination intensity of the solar cell and rate of charge photogeneration³². In this case, equation (1.6) has to be modified to take into account this condition:

$$J(V) = J_{SC} - J_0 \left(\exp\left(\frac{qV}{k_B T}\right) - 1 \right) \quad (1.7)$$

As explained earlier, when the solar cell is maintained under open circuit conditions, the corresponding voltage (V_{OC}) can be extracted from equation (1.7) under the assumption that no net current is flowing through the device i.e. $J(V) = 0$. Theoretically, this value will be the maximum output voltage produced by the device and is estimated in the following way:

$$V_{OC} = \frac{k_B T}{q} \ln\left(\frac{J_{SC}}{J_0} - 1\right) \quad (1.8)$$

The equivalent circuit of a non-ideal solar cell is displayed in Figure 1.4a. Two additional elements have to be taken into account: a series resistance (R_{series}) that is responsible for electrical losses at the contacts and a shunt resistance (R_{shunt}) that is associated with a leakage current (J_{shunt})³³⁻³⁵. In addition to those two elements the non-ideality of the voltage dependence has to be accounted for by an ideality factor (m)^{36,37}. Thus, equation (1.7) can be modified to take into account all these resistive elements. This new expression becomes the so-called solar cell equation:

$$J(V) = J_{SC} - J_0 \left(\exp\left(\frac{q(V + JAR_{series})}{mk_B T}\right) - 1 \right) - \frac{V + JAR_{series}}{R_{shunt}} \quad (1.9)$$

Where A is the active area of the solar cell. From the above equation, it can be deduced that to minimize losses, a very low series resistance and a very high shunt resistance are preferred^{38,39}. The typical shape of a current density-voltage (J - V) plot, described by equation (1.9), is displayed in Figure 1.4b.

As mentioned earlier, the open circuit potential and short circuit current respectively give the maximum theoretical voltage and current density produced by the cell, but none of these conditions can be realistically reached when a load is connected to the external circuit.

The fill factor (FF) is defined as the ratio of the maximum power point (P_{\max}) described by the maximum measured voltage (V_{\max}) and current density (J_{\max}) over the product of the V_{OC} and J_{SC} (equation (1.10)). The FF helps evaluating how far the experimental solar cell performances are from the theoretical maximum values, in terms of potential and current density. This parameter can also be used to assess the resistive losses of the solar cell. A high FF will be synonym of high R_{shunt} and low R_{series} as well as very little losses and vice versa⁴⁰.

$$FF = \frac{V_{\max} J_{\max}}{V_{OC} J_{SC}} = \frac{P_{\max}}{V_{OC} J_{SC}} \quad (1.10)$$

Graphically it can be represented by the ratio of the red over the blue rectangle depicted in Figure 1.4b, with the ideal lossless case being the perfect overlap of the two rectangles.

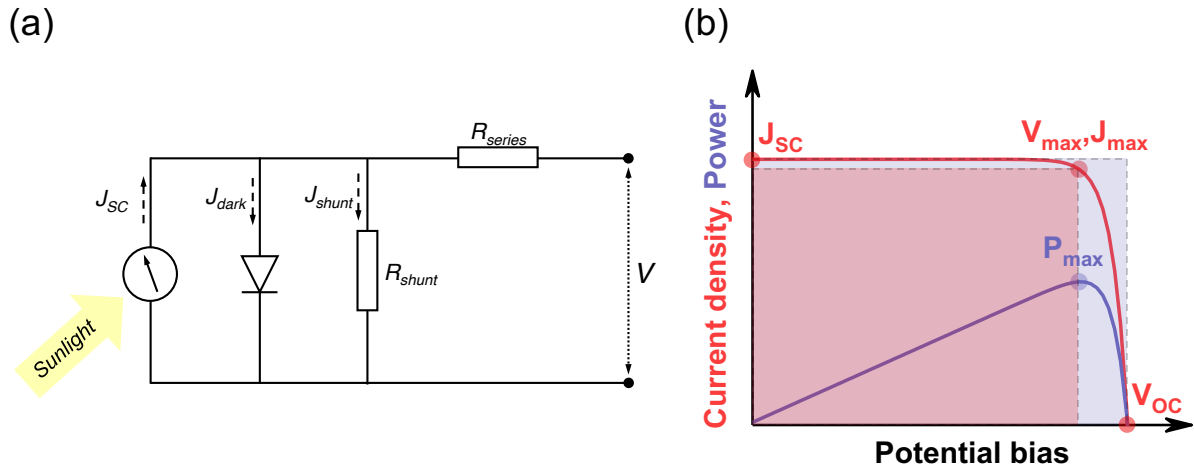


Figure 1.4. (a) Equivalent circuit of a solar cell under illumination, with all the other electrical elements: generated photocurrent J_{SC} , dark current (J_{dark}), shunt leakage current (J_{shunt}), series resistance (R_{series}) and shunt resistance (R_{shunt}). (b) Graphical representation of a J-V curve. The important parameters are highlighted. The fill factor (FF) represents the ratio of the area of the red rectangle over the blue rectangle.

Since the solar cell is a device converting solar energy into electrical work, there is a need to evaluate the maximum power output (P_{\max}) produced by the cell, with respect to the power input provided by the sun irradiance or any illumination source (P_{In}). The ratio of these two quantities defines the power conversion efficiency (PCE or η) of the solar cell:

$$PCE = \frac{P_{\max}}{P_{In}} \cdot 100 = \frac{V_{OC} J_{SC} FF}{P_{In}} \cdot 100 \quad (1.11)$$

1.3.2 Existing solar cell technologies

To compare solar cells efficiencies, standard test conditions (STC) have been established. As mentioned in paragraph 1.2, the terrestrial conditions has been set to AM1.5G^{41,42} with a solar irradiance of $I_{AM1.5G} = 1000.36 \text{ W} \cdot \text{m}^{-2}$, and temperature of 25°C . The ongoing evolution of various PV technologies has been summarized by the national renewable energy laboratory (NREL) in the so called “best research-cell efficiencies” chart, displayed in Figure 1.5.

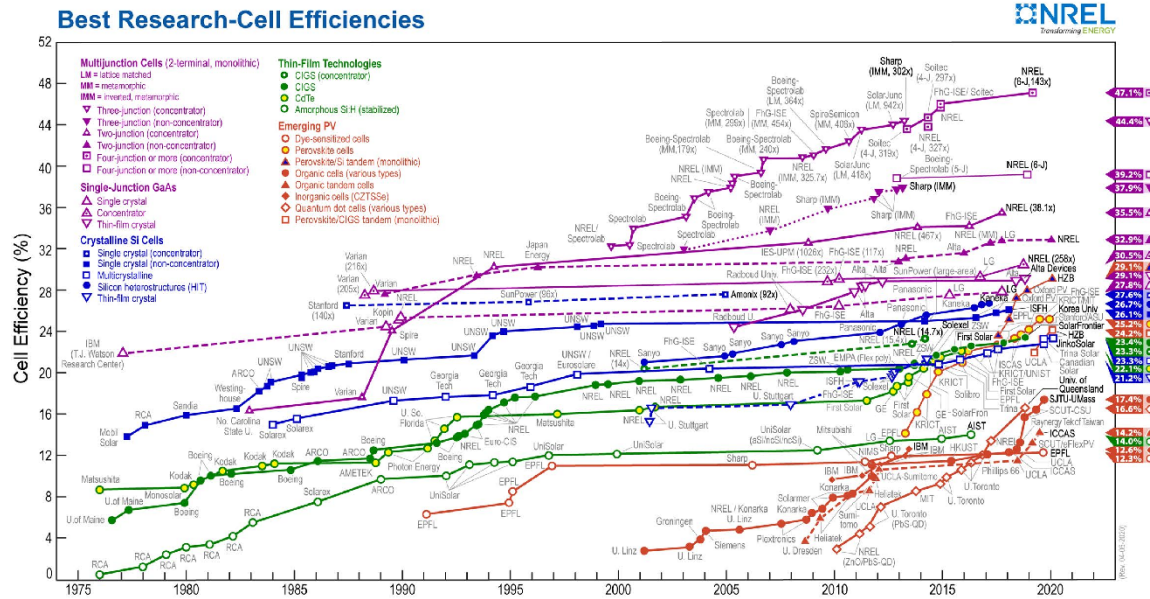


Figure 1.5. Certified solar cell efficiencies by the national renewable energy laboratory (NREL)⁴².

The first generation of solar cells is the most mature in terms of technologies and materials. It comprises crystalline silicon (c-Si), multicrystalline silicon (mc-Si) and gallium arsenide (GaAs) single junction devices. Silicon based solar cells hold around 90 % of the photovoltaic market share. This impressive popularity is due to the many advantages that c-Si cells have against other materials used to fabricate solar cells, specially the high earth-abundance of silicon as well as good stability and efficiencies of the modules.

The band gaps of these materials typically lie around 1.1 eV for c-Si and mc-Si based devices and 1.42 eV for GaAs^{43,44}. Crystalline Si solar cells can demonstrate efficiencies up to 26 %^a, with high current densities and fill factors⁴⁵. GaAs cells have similar efficiencies but compared to c-Si cells, they offer a much higher V_{OC} of 1.13 V as well as similarly high fill factors but at higher cost due to the lower abundance of gallium and arsenide compared to silicon⁴⁶.

The second generation of single junction solar cells comprises thin film devices that helps overcoming the energy intensive production cost of the Si and low abundance of the GaAs systems of the previous generation⁴⁷. These devices are fabricated using materials such as copper indium gallium selenide (CIGS), amorphous Silicon (a-Si) and gallium indium phosphide (GaInP).

The average band gaps of these semiconductors are: 1.13 eV (CIGS), 1.7 eV (a-Si) and 1.81 eV (GaInP). CIGS cells are able to deliver a power conversion above 20 %⁴⁸ with a record set at 23.35 %⁴⁹. Comparably to GaAs cells, GaInP devices present very few voltages losses and due to the high energy band gap of the semiconductor $E_g=1.81$ eV, it enables a V_{OC} of 1.47 V and a PCE near 20 %⁵⁰. Amorphous silicon, presents all the advantages of silicon technology but without the large costs inherent to the high crystallinity required for mc-Si or c-Si cells. As a tradeoff, a-Si cells offer very low efficiencies, with laboratory cells grade cells producing PCEs lying around 11 %^{51,52}.

^aFor the sake of comparison, all the efficiencies cited in the following paragraphs were measured under simulated AM1.5 G $I_{AM1.5G}=1000.36 \text{ W}\cdot\text{m}^{-2}$ conditions unless stated otherwise.

The third generation of solar cells, was inspired from the easy deposition techniques provided by the second generation but with the aim to use more earth-abundant, non-toxic materials in order to enable up-scaling⁵³. Third generation solar cells have different device architectures compared to the other two, which helps them achieving high efficiencies. Most of these systems are still not as mature as the first and second generation and are still being studied and developed at the laboratory scale, with only few close to being commercialized^{54,55}.

The most promising third generation systems are Dye Sensitized Solar Cells (DSSCs), Perovskites Solar Cells (PSCs) and Organic solar cells or Organic Photovoltaics (OPVs). The DSSC category will be furtherly developed in the up-coming paragraphs. The highest certified PCE for a DSSC was 12.3 % with an 1.85 eV band gap dye⁵⁶. Inspired from the DSSC architecture, hybrid organic lead halide perovskite cells use a light absorbing layer made of a lead halide anion and an organic cation. The holes are extracted via a hole conducting layer or hole transporting layer (HTL) to a gold counter electrode. The optimum band gap lies around 1.6 eV with an associated certified PCE of 25.2 %⁵⁷.

Organic photovoltaics have been the largest growing sector in the last decades and most promising in terms of low cost earth abundant materials and roll to roll printing. They mimic the principle of the p-n junctions by using electron accepting and electron donating layers blend as active materials. These layers are made of either organic polymers or single molecules. The recent progresses in materials design and synthesis have allowed PCEs as high as 17.6 % to be certified⁵⁸.

1.3.3 Losses and efficiency limits in solar cells

There are two main sources of energy losses in solar cells: extrinsic and intrinsic. The first refers to losses that can be theoretically bypassed and hence not taken into account when discussing fundamental limits, they include examples such as series resistance and recombination losses. Intrinsic losses are inherent to the solar cell physics and cannot be avoided, despite an ideal cell design and optimization of the materials.

There are five main sources of intrinsic losses^{59–61}. The first was briefly mentioned in paragraph 1.2. and concerns the light management of the device. When light interacts with the photo-absorber in a solar cell, only the photons of an energy above E_g will be absorbed and converted into an electron-hole pair. This implies that all the photons that do not meet this criteria will be transmitted by the device and lost. Furthermore, the photons with energies greater than the bandgap will generate so called hot-carriers, i.e. electron-hole pair of high energy.

This excess of energy will be lost through thermalization as these hot carriers relax to the edge of the conduction band. This relaxation process represents a supplementary source of losses, that impairs the efficiencies of solar cells. The third intrinsic loss arises from Kirchhoff's law which states that a body at an equilibrium temperature, has its absorptivity equal to its emissivity⁶².

These emission losses can be estimated using a generalized Plank equation⁶³:

$$F(E, T, \mu, \Omega) = \frac{2\Omega E^2}{c^2 h^3 \left(\exp\left(\frac{E - \mu}{k_B T}\right) - 1 \right)} \quad (1.12)$$

Where μ is the chemical potential and Ω , the solid angle of the emitting surface. The next source of losses originates from the heat flow taking place between the sun and the atmosphere and is accordingly named Carnot loss. Similarly, to a Carnot engine, work has to be lost in order to respect the energy balance. In this case, the Carnot engine would be the solar cell. In terms of performances these losses impair the V_{OC} . The final contribution to results from the anisotropic redistribution of the emitted photons, with respect to the absorbed flux. This phenomenon is of entropic nature and called Boltzmann loss.

The contribution of each of these losses will vary depending on E_g , hence the optimum bandgap was estimated to be lying between 1 eV and 2 eV⁶⁴. Generally, the Carnot and emission losses are relatively low due to the modest temperature at which the cells operate. For example, narrow bandgap solar cells mainly suffer from thermalization and Boltzmann losses, whereas wide bandgap devices will fail to harvest enough photons.

A case study is provided in the table below⁵⁹, where a solar cell of $E_g = 1.31$ eV is mainly impaired by photon and thermalization losses of respectively 25 and 30 %. Several solutions are being explored as ways to improve the PCE. Examples include multijunction solar cells, which would help reduce photon losses, or multi-exciton solar cells and hot carrier solar cells that concerns thermalization losses⁶⁵.

Table 1.2. *Estimated PCE and losses efficiencies for a device with $E_g = 1.31$ eV.*

	PCE	Photons loss	Thermalization	Boltzmann	Carnot	Emission
η [%]	33	25	30	9	2	1

The theoretical maximum PCE of a single p-n junction as function of the semiconductor bandgap, has been estimated by Shockley and Queisser in 1961⁶⁶, along with the limits of other parameters such as V_{OC} , FF and J_{SC} ^{67,68}. Figure 1.6 shows the Shockley Queisser (SQ) limit of all the aforementioned photovoltaic parameters (FF, V_{OC} and J_{SC}) calculated using the blackbody radiation model at 6000 K as irradiance source. Additionally, examples of current solar cell technologies have been added to the plots, three per solar cell generation with the following color code: black dots correspond to first generation, red dots correspond to second generation and blue dots correspond to third generation.

As mentioned in the upper paragraph, the maximum theoretical PCE (see Figure 1.6a), was found to be 33.7 % corresponding to a bandgap energy of 1.34 eV. GaAs, GaInP and c-Si are among the technologies that are the closest to reach their theoretical limits. Recently, PSCs have caught up this trio with a recent report of a PCE reaching 25 %.

As depicted in Figure 1.6b, GaAs, GaInP and c-Si are also slowly reaching the theoretical FF limit, with impressive values of 86.7 % (GaAs), 90.2 % (GaInP) and 84.9 % (c-Si).

The open circuit potential of a p-n junction solar cell is defined as the difference between quasi Fermi levels of respectively the p-type and n-type semiconductor. The dashed line showed in Figure 1.6c shows the theoretical value of the V_{OC} , that should be equal at first to E_g . However, there are several recombination mechanisms that take place within the device and a more realistic limit is represented by the solid line.

Ga based PV materials (GaAs and GaInP) showed impressive values reaching the theoretical limit. PSCs are also catching up with impressive reported voltages of 1.2 V. The theoretical J_{SC} values (Figure 1.6d) are also slowly reaching theoretical limits for most of the examples of solar cell generations, helped by the impressive improvements of the absorbing layer^{69,70}. Dye sensitized solar cells are still below the 50 % SQ limit threshold which is mainly due to remaining important losses in V_{OC} and FF.

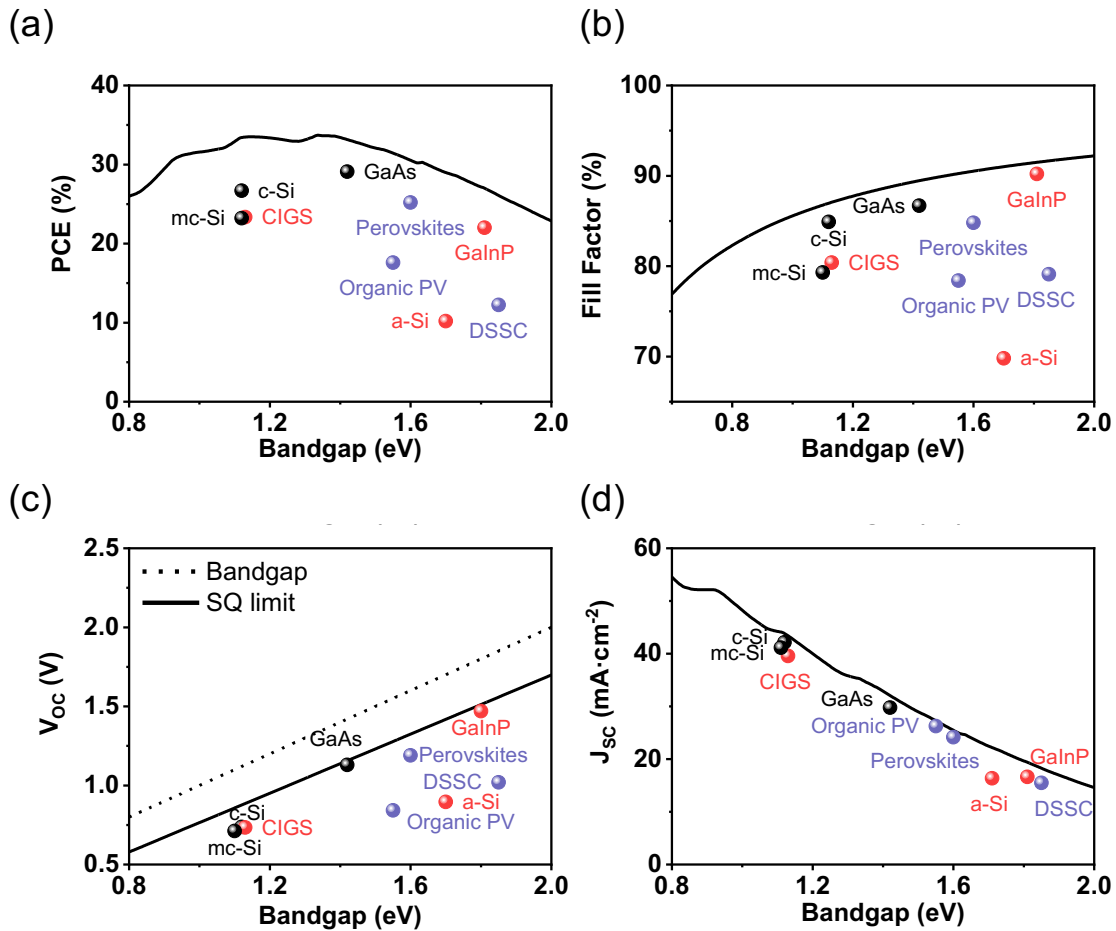


Figure 1.6. Maximum PCE (a), FF (b), J_{SC} (c) and V_{OC} (d) as function of E_g . (b) Maximum fill factor as function of the semiconductor bandgap. The reported values for each respective solar cell generation were obtained from this reference⁵⁶. The black spheres indicate first generation solar cells, the red spheres indicate second generation solar cell and the blue spheres indicate third generation solar cell. All the values reported were measured under simulated sunlight AM1.5G with the standard irradiance of $I_{AM1.5G} = 1000.36 \text{ W} \cdot \text{m}^{-2}$.

1.4 Dye sensitized solar cells

1.4.1 Working principle and structure

The cross section of a typical liquid dye sensitized solar cell is represented in Figure 1.7. Transparent glass coated with a conductive layer serves as substrate for both the counter and working electrode. The working electrode (WE) is fabricated by depositing a compact TiO_2 blocking layer, that will help to prevent deleterious electron recombination. The active mesoporous layer is then screen-printed on top. It can vary in size of the nanoparticles or thickness and both of these parameters will influence the device performances. The dye is chemically adsorbed onto the semiconductor by dipping the bare WE in a dye bath. The counter electrode (CE) is fabricated by deposition of an electroactive catalyst, on another piece of transparent conductive glass. Finally, the two electrodes are assembled with a sealant and filled under a slight vacuum with a solution of electrolyte through a hole drilled on the CE side.

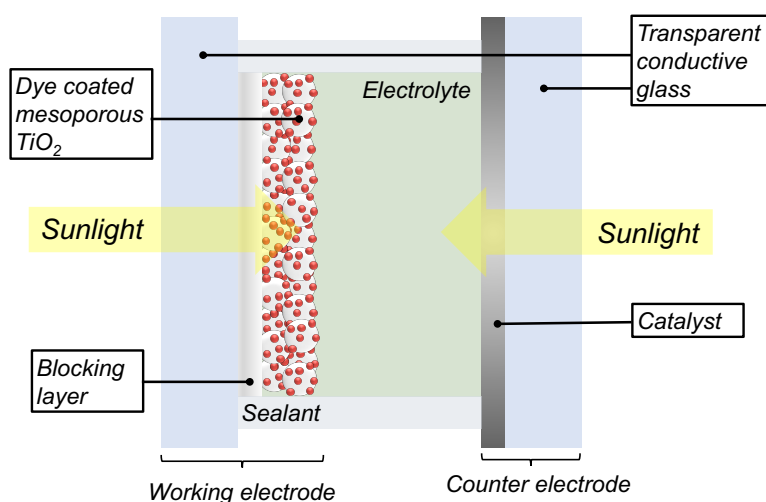


Figure 1.7. Cross sectional representation of a liquid dye sensitized solar cells.

1.4.1.1 Working principle

The operational mechanism (see Figure 1.8) starts with sunlight illuminating the cell and interacting with the dye, adsorbed the TiO_2 surface. The energy contained in the incident light will promote an electron from the high occupied molecular orbital (HOMO) or ground state redox potential of the dye ($E_{S^+/S}$) to the Lowest unoccupied molecular orbital (LUMO) or excited state redox potential of the dye ($E_{S^+/S}^*$)^b(1). The electron is subsequently injected into the TiO_2 conduction band (2) and the dye gets oxidized. Then, the injected electron diffuses in the semiconductor to the back contact (3) and through the external circuit (4) up to the counter electrode where it will be recaptured by the oxidizing agent (Ox) (5). The reducing agent (Red) will travel to the semiconductor interface and regenerate the neutral dye to complete the circuit (6). The overall mechanism is summarized in Figure 1.8.

^bTwo relative scales are used to described the energy levels of dye molecules: the absolute scale in eV vs. vacuum and the electrochemical scale, vs. a reference electrode, in this case the normal hydrogen electrode (NHE). To avoid confusion, the absolute scale will be associated with HOMO and LUMO levels whereas the electrochemical scale will be used when mentioning the ground state and excited state potentials of the dye.

Compared to the state of the art p-n junctions, DSSCs possess a layered architecture with several interfaces through which the electron has to cross. In addition to that, each component of the device has a predefined role within the overall operational mechanism: the dye has to generate the electron-hole pair, the TiO_2 collects the electrons whereas the redox electrolyte collects the holes. In comparison to a classical p-n junction, where the charge generation and transport occur within the same material. The design of DSSCs allows for a more precise tuning of the device performances through alteration of each layer⁷¹.

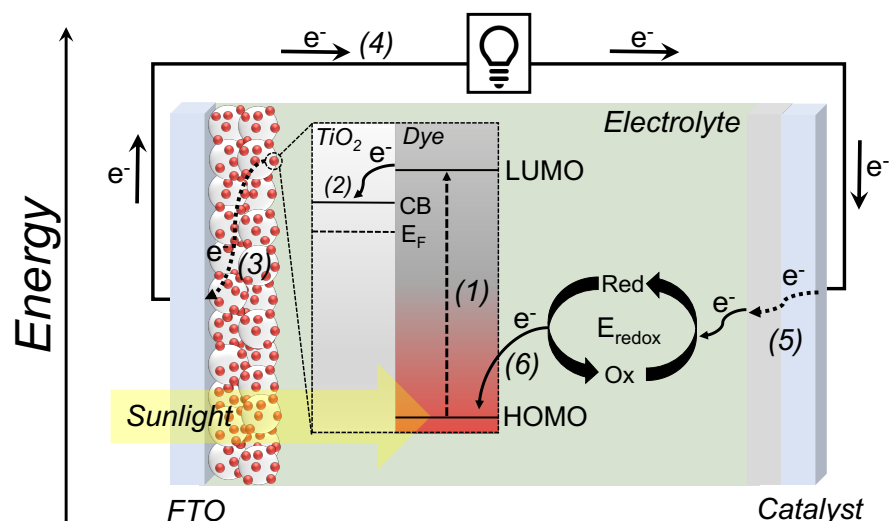


Figure 1.8. Operational mechanism of a DSSC under illumination. (1) photo-excitation of the dye. (2) electron injection of the dye LUMO level into the conduction band of the TiO_2 . (3) Diffusion of the electron to the FTO. (4) Travel in the back-circuit. (5) Reduction of the oxidizing species at the counter electrode. (6) dye cation reduction by the reducing agent.

1.4.1.2 Electron transfer in dye sensitized solar cells

As explained in the previous paragraph, a DSSC under illumination functions through a series of electron transfers (ET) between several interfaces. It is commonly accepted that these electron transfers occur according to Marcus's theory for electron transfer^{72–74}. The Marcus theory describes single electron transfer between a donating state (D) and an accepting state (A), i.e. in electrochemical terms, a reducing and oxidizing agent.

As represented in Figure 1.9a to d, the energy profiles of D and A are parabolic curves, function of nuclear coordinates. The intersection point between the two parabolas corresponds to the reaction intermediate. The over electron transfer reaction is described by three thermodynamical quantities, namely, the activation energy (ΔG^\ddagger), the reaction driving force or free energy (ΔG°) and the reorganizational energy (λ). Formally, ΔG^\ddagger is defined as the energy difference between the ground state of D and the intersection of the energy surfaces, ΔG° is the energy difference between D and A and λ corresponds to the energy required to bring the reactant to the nuclear coordinate of the product (q_p) which accounts for geometrical and structural rearrangement of both the donor itself but its surroundings, such as the solvent^{75,76}.

From this model, the parabolic curves can be used to mathematically derive the relation between the driving force ΔG° , λ and ΔG^\ddagger :

$$\Delta G^\ddagger = \frac{(\lambda + \Delta G^\circ)^2}{4\lambda} \quad (1.13)$$

The expression for the rate of electron transfer (k_{ET}) function of the reaction's free energy $k_{ET}(\Delta G^\circ)$ is derived using the activation energy equation (1.13 and transition state theory).

$$k_{ET} = k^0 \exp\left(-\frac{\Delta G^\ddagger}{k_B T}\right) = k^0 \exp\left(-\frac{(\lambda + \Delta G^\circ)^2}{4\lambda k_B T}\right) \quad (1.14)$$

Where k^0 is a pre-exponential factor. The upper equation describes the rate of electron transfer dependence on the driving force of the reaction as well as the reorganizational energy. Due to the parabolic nature of equation (1.13), $k_{ET}(\Delta G^\circ)$ will display three different regimes exist. The first case is pictured in Figure 1.9a. Here, ΔG^\ddagger is positive and λ is superior to ΔG° in this situation, an increase of $-\Delta G^\circ$ increases the reaction rate by reducing the activation energy until it reaches the conditions described by Figure 1.9b, where $\Delta G^\ddagger \approx 0$. At this point, the system becomes activation-less and $-\Delta G^\circ$ and λ are almost similar. Afterwards, ΔG^\ddagger will become positive again as $-\Delta G^\circ$ increases and becomes larger than λ (Figure 1.9c), causing the reaction to slow down. The regions where the reaction rate increases with $-\Delta G^\circ$ is called the Normal region or Marcus normal region, whereas the opposite region is called the Inverted region or Marcus inverted region⁷⁷. Hence, k_{ET} is expected to reach a maximum in the activation less case as represented in Figure 1.9d.

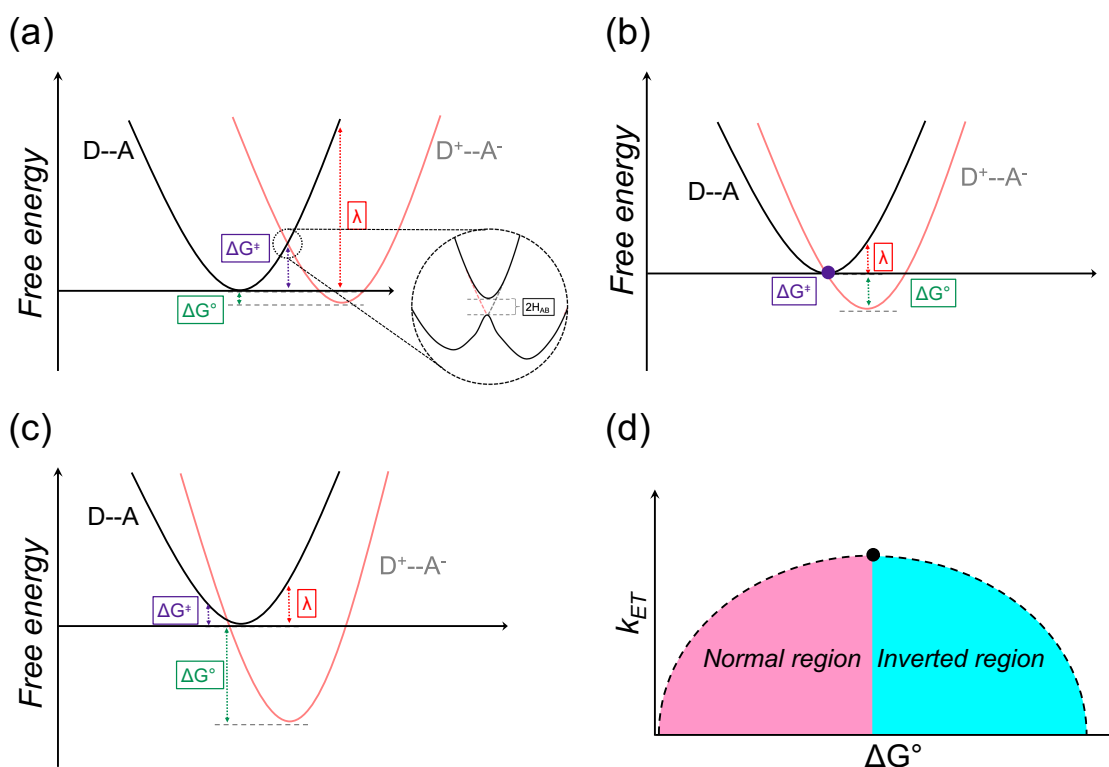


Figure 1.9. (a) Marcus normal region, where $\Delta G^\ddagger > 0$ and $-\Delta G^\circ < \lambda$, in this case the reaction rate k_{ET} increased with increasing driving force. (b) $\Delta G^\ddagger \approx 0$ and $-\Delta G^\circ = \lambda$, the reaction is activation less and k_{ET} is at its maximum. (c) Marcus inverted region where $\Delta G^\ddagger > 0$ again and $-\Delta G^\circ > \lambda$ and k_{ET} decreases. (d) Representation of the reaction rate dependence to the driving force.

A more accurate description of the phenomena can be provided if the electronic coupling between the acceptor and donor states is taken into account. This coupling is represented in Figure 1.9a by the quantity $2H_{AB}$. Furthermore, when $2H_{AB}$ is large, indicated by a strong coupling between the pair, the electron transfer will be labeled as adiabatic whereas for a weak coupling, the system will be called non-adiabatic, which is the one occurring in DSSCs.

The effect of the coupling is accounted for in a modified version of equation (1.14)^{78–80}:

$$k_{ET} = \frac{H_{AB}^0 \exp(-\beta(r-r_0))}{\sqrt{4\pi\lambda k_B T}} \exp\left(-\frac{(\lambda + \Delta G^\circ)^2}{4\lambda k_B T}\right) \quad (1.15)$$

The term $H_{AB}^0 \exp(-\beta(r-r_0))$ describes the electronic coupling between the two states, where H_{AB}^0 is the coupling at Van der Waals distance, β is a parameter expressing the energy barrier height that the electron has to tunnel through, and r the distance between the two states^{81,82}.

The interfacial electron transfer between the excited dye (S^*) and the conduction band of the TiO_2 is more accurately described using the Gerischer description of states along with Marcus theory^{83,84}. As depicted on see Figure 1.10, the Gerischer energy states are not represented as discrete levels but as a gaussian distribution function. This model accounts for effects such as interaction with the solvent or neighboring molecules. The expression for the Gaussian energy distribution($W(E)$) of a species i in the Gerischer model is defined as the following:

$$W_i(E) = \frac{1}{\sqrt{4\pi\lambda k_B T}} \exp\left(-\frac{(E+E_i^0)^2}{4\lambda k_B T}\right) \quad (1.16)$$

Where E_i^0 is the most probable energy state of the species, i.e. the maximum of $W(E)$ function.

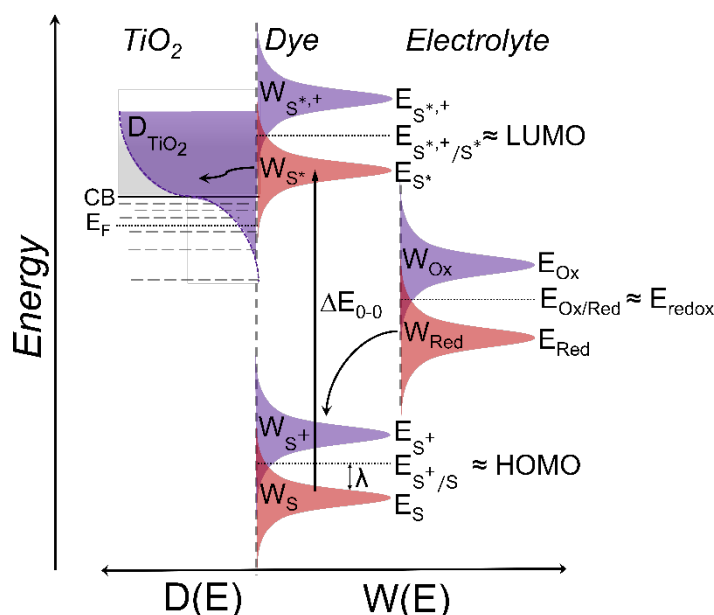


Figure 1.10. Representation of electron injection/dye regeneration according to the Marcus-Gerischer model, where the donor and acceptors are represented by Gaussian distribution functions.

In a DSSC, the acceptors and donors will vary depending on the electron transfer that is taking place. For example, there is an interfacial electron transfer between the excited state of the dye (S^*) and the conduction band of the semiconductor but also between the electron in the conduction band and the oxidizing agent in solution or the oxidized dye or between the reducing agent in solution and the dye cation. For the electron injection, the accepting partner will be the TiO_2 density of state (DOS), while the donating state will be the photoexcited dye $S^*(W_{S^*}(E))$. The rate of electron injection (k_{inj}) can therefore be estimated by integration over all the energy levels of $D_{\text{TiO}_2}(E)$, $W_{S^*}(E)$ and a transmission frequency term $\kappa(E)$ that accounts for the coupling between the two states^{85–87}:

$$k_{inj} = \int \kappa(E) D_{\text{TiO}_2}(E) W_{S^*}(E) dE \quad (1.17)$$

1.4.1.3 Photocurrent generation

Six fundamental steps constitute the overall cascade of electron transfers leading to the production of a photocurrent⁷³ (see Figure 1.8 and paragraph 1.4.1.1). The process is initiated by the energy contained in a photon by the sensitizer (S), anchored on the TiO_2 surface. Similar to the p-n junctions, the underlying conditions for this process to happen is that the energy of the photon has to be equal or greater than the energy band gap of the dye. If this condition is met, then the sensitizer will be promoted to an excited state (S^*) according to:



Subsequently, the injection of an electron from the excited dye (S^*), into the conduction band of the TiO_2 takes place. The injection rate (k_{inj}) will affect the generated photo current and will depend on the injection driving force (ΔG_{inj}) that is defined as the difference between the LUMO level of the dye and the conduction band edge (CBE) of the TiO_2 (see Figure 1.11a). This step will produce a dye cation (S^+) and a free electron ($e^-_{\text{CB-TiO}_2}$).



The location of the TiO_2 conduction band edge (CBE) is ambiguous since its value will be influenced by its surrounding media, and notably the surface electric field. This latter will depend on several elements such as the dye dipole moment or surface adsorption of various additives. However, it is commonly accepted that the CBE fluctuates between -0.7 and -0.5 V vs. NHE^{86,88–90}.

The charge injection efficiency (η_{inj}) is used to assess the charge injection step between the TiO_2 and the dye. Thus, η_{inj} is defined as the ratio of the injection rate, over the sum of the injection (k_{inj}) and deactivation rates (k_d)⁹¹.

$$\eta_{inj} = \frac{k_{inj}}{k_{inj} + k_{dec}} \quad (1.20)$$

The deactivation constant k_d , corresponds to the backward reaction described by equation (1.18 and accounts for the radiative and non-radiative decays of the dye. This process can either occur intramolecularly for a dye with a short live excited state or by intermolecular quenching of strongly aggregated dyes on the film surface^{92,93}.

Hence efficient electron injection requires sensitizers with long lived excited states, low intermolecular stacking and well-adjusted energy level. The average emission lifetime strongly fluctuates depending on the sample but for a dye adsorbed on a semiconductor, in contact with the redox active electrolyte, the lifetimes lie between ns and sub-ns^{94,95}.

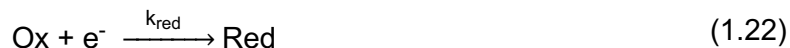
On the other hand, the electron injection occurs at much faster rate with typical values lying between femtoseconds and picoseconds time scales. It is worth mentioning that aggregation induced quenching can be reduced by using additives in the dye solution. These molecules act as co-adsorbent that will bind to the TiO₂ surface and break dye aggregates^{96,97}.

Following the injection step, electrons will diffuse in the TiO₂ bulk up to the back contact via trap-states, which are energy levels located close (shallow trap states) or relatively further away (deep trap states) from the TiO₂ CBE. These energy states are mostly located at the surface or grain boundaries of the titania particles^{98–100}. The charge collection efficiency (η_{coll}) is commonly used to describe this process and is defined as following¹⁰¹:

$$\eta_{\text{coll}} = \frac{1}{1 + \frac{\tau_{\text{TR}}}{\tau_n}} \quad (1.21)$$

Where τ_{TR} and τ_n are respectively the transport time and lifetime of electrons in the semiconductor. The transport time will mainly be affected by the film quality, that is its trap state distribution as well as light intensity^{102,103}. The electron lifetime will reflect the intensity of recombination reactions taking place between free electrons in the semiconductor with various acceptors present in the cell^{104,105}. Short transport times and long lifetimes are necessary to obtain a high charge collection efficiency.

Once electrons travel through and the back contact and reach the counter electrode, they will be transferred to the oxidizing agent (Ox) via an electroactive catalytic layer deposited on the conductive transparent glass, according to:



This step will depend on the nature of the redox active electrolyte and the material used as catalyst. The newly reduced species (Red) will travel to the dye/TiO₂ interface by diffusion through the electrolyte medium.

Finally, the photo-oxidized dye (S⁺) will be reduced by Red to regenerate the initial sensitizer S and the oxidizing agent.



This is a key step in the operation of the solar cell and its rate (k_{reg}) will depend on the regeneration driving force (ΔG_{reg}). As it can be seen in Figure 1.11a, it is defined as the difference between the HOMO level or ground state oxidation potential and the redox potential of the electrolyte (E_{redox})^{94,106}.

Similar to the injection and collection efficiencies, presented on equations (1.20) and (1.21), the regeneration efficiency (η_{reg}) is defined as:

$$\eta_{\text{reg}} = \frac{k_{\text{reg}}}{k_{\text{reg}} + k_{\text{recD}}} \quad (1.24)$$

Where k_{recD} represents the recombination rate between the oxidized dye (S^+) and an electron in the conduction band. It was found that a η_{reg} of at least 95% should be achieved in order to not impair photo-current generation^{94,107,108}, i.e., k_{reg} should be much higher than k_{recD} . Typically values of dye regeneration by redox electrolyte lie around the microseconds timescale¹⁰⁹.

1.4.1.4 Recombination reactions

The steps described by equations (1.19) to (1.23) correspond to the sequences of electron transfers that participate to the forward generation of photocurrent. However, other deleterious ET occur in parallel. They are called back reactions or recombination reactions because they impair the generation of current and compete with the back reactions on different timescales. As represented on see Figure 1.11b, most of the recombination reactions occur between an electron in the metal oxide and an acceptor (k_{recE} and k_{recD}). However, it is worth mentioning that they can also occur also between an acceptor and an electron in the conductive substrate, which is sometimes exposed to the electrolyte. This being said, this recombination pathway can be neglected if a layer of blocking material is deposited on the substrate¹¹⁰.

A free electron percolating in the conduction band can recombine either with the electrolyte (k_{recE}) or with the photo-oxidized dye (k_{recD}). The latter scenario is described by:



However, if the regeneration step described on equation (1.23) is fast enough to intercept the hole, the dye cation will be efficiently regenerated and the recombination reaction outlined on (1.25) can be neglected. The driving force for this recombination pathway is approximately equal to the difference between the energy of the TiO_2 conduction band edge and the ground state oxidation potential of the dye or HOMO level (ΔG_{recD})⁸².

The second and most prominent recombination reaction takes place between an electron in the TiO_2 and the oxidizing agent (Ox) in the electrolyte. Similar to the dye cation recombination pathway, the driving force for this reaction (ΔG_{recE}) is approximated by the difference between the energy of the TiO_2 conduction band edge and the redox potential of the electrolyte (E_{redox})¹⁰⁶.



The rate of recombination with the electrolyte (k_{recE}) can be effectively reduced by judicious dye design, more specifically by increasing the distance between the acceptor and the donor states^{86,107}.

The last deleterious deactivation pathway is the quenching of the dye excited state through radiative or non-radiative decay:



As it was explained in the previous paragraphs, the quenching mechanism can occur via an inter or intramolecular route. The former will be more important if the dye forms aggregates at the interface while the latter will depend on the dye structure^{94,111}.

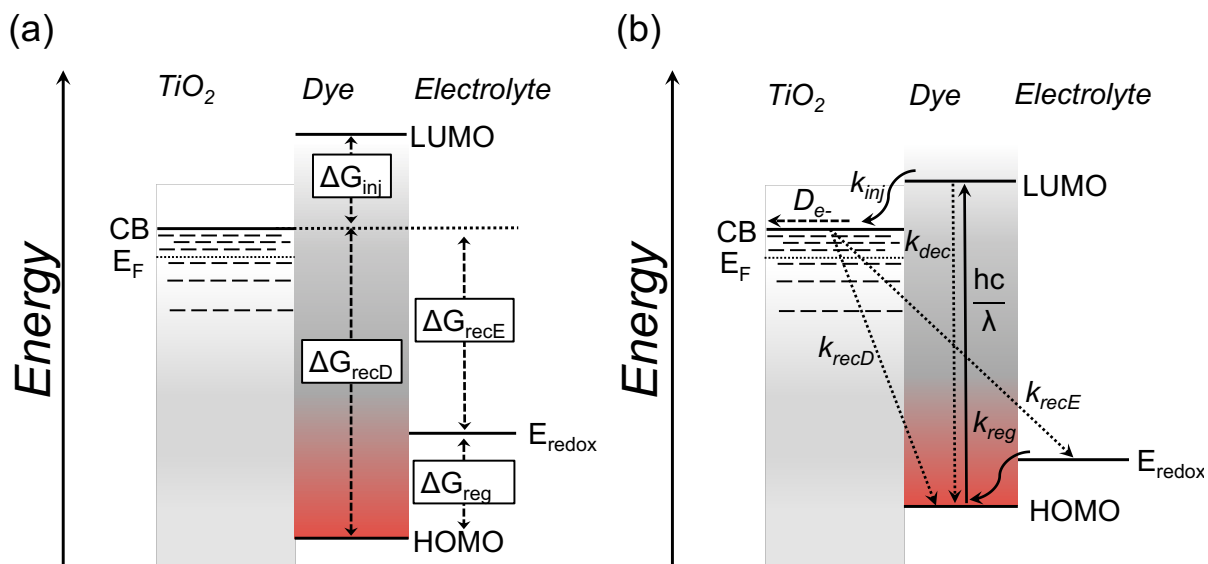


Figure 1.11. (a) Energy diagram representing the different driving forces dictating the performances of a DSSC. (b) Energy diagram representing the different kinetics of both back electron recombination and photocurrent generation.

1.4.2 Components of a dye sensitized solar cell

1.4.2.1 Transparent conductive glass

The transparent conductive glass acts as principal substrate for the fabrication of the electrodes. It consists in a piece of glass coated with a transparent conductive oxide (TCO) that will collect the current generated by the device. Two main materials are used as conductive layer: tin doped indium oxide (ITO) and fluoride doped tin oxide (FTO). ITO offers an excellent transparency in the visible region as well as high conductivity¹¹². Its alternative, FTO provides less conductivity and sheet transparency but is cheaper and more resistant to high temperatures, which is a crucial feature considering the 450°C sintering of mesoporous TiO₂ layer during the fabrication of the working electrode¹¹³.

1.4.2.2 Mesoporous semiconducting metal oxide

The state of the art DSSC employs titania (TiO₂) as semiconducting mesoporous metal oxide which is a very attractive material because of its non-toxicity, low price and abundance. The most encountered polymorphs of titania are rutile and anatase. The latter is usually preferred for device fabrication due to its better chemical stability and higher photocatalytic activity.

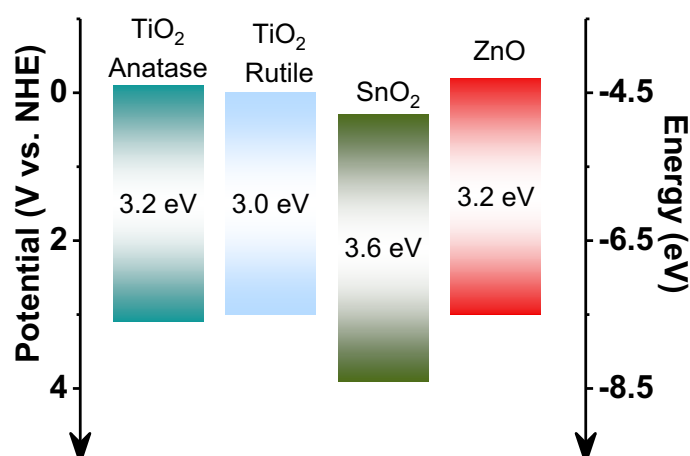


Figure 1.12. Band edges of semiconducting metal oxides for dye sensitized solar cells¹²⁷.

Furthermore, as seen in Figure 1.12, anatase offers a higher band gap (3.2 eV) compared to rutile (3.0 eV) because of its higher conduction band edge but also better morphological properties that enables higher performances^{114,115}.

The metal oxide layer is a key component of the DSSC as it will be hosting all the important electron transport, diffusion and recombination events^{116,117}, in this regard its particle size and thickness of the active layer will have to be optimized in order to fabricate a highly efficient cell¹¹⁸. The mesoporous feature of titania yields a very high internal surface area which allows a significant dye absorption, which is a key element in the high efficiencies recorded for DSSCs¹¹⁹.

The typical composition of a TiO₂ layer consist in 3 to 10 μm thick transparent layer composed of with a particle size distribution of 10 to 30 nm and a porosity ranging between 50-60%⁷³. Additionally, the light harvesting properties of the film can be enhanced using a scattering layer made of particle with larger size^{119,120}. This being said, anatase possess a series of drawbacks, notably its reactivity towards ultraviolet light. This polymorph can absorb light bellow approximately 388 nm which can induce photodegradation of the organic dye¹¹⁸.

Alternatively, two other semiconducting metal oxides can be used as substitutes for titania: tin(IV) oxide (SnO₂) and zinc(II) oxide (ZnO). SnO₂ solves the photostability issue due to its large band gap of 3.6 eV (see Figure 1.12). It also possesses a much higher electron mobility compared to TiO₂: 100 to 200 $\text{cm}^2 \cdot \text{V}^{-1} \cdot \text{s}^{-1}$ versus 0.1 to 1 $\text{cm}^2 \cdot \text{V}^{-1} \cdot \text{s}^{-1}$, which improves electron transport to the TCO and the back contact^{119,121}. Tin(IV) oxide also benefits from a conduction band edge 300 mV lower than anatase, that usually impairs the photovoltage produced by the device but improves the electron injection of dyes having a low lying excited state, by increasing ΔG_{inj} .

However, the better charge transport properties of SnO₂ also increase the probability of electron recombination with electrolyte acceptor or with oxidized dyes, ultimately leading to poorer performances for tin(IV)oxide based DSSCs¹²². This issue can however be slightly overcome by using insulating layers of other metal oxides or by structuring the mesoporous SnO₂ which helps controlling the trap states density^{123,124}.

Zinc(II) oxide (ZnO) presents itself as an attractive substitute for titania, because of their very similar band edges and band gap (see Figure 1.12) and higher electron mobility^{119,125}, which would in theory not impair the photovoltaic performances of devices. In addition to that, ZnO benefits from fewer trap states which would then reduce recombination losses with the redox active electrolyte¹²⁶. However, the use of ZnO working electrode in DSSC efficiencies still remains low. It was found that the protons coming from the acidic anchoring group of the dyes are able to dissolve the metal oxide creating Zn^{+2} /dye aggregates¹¹⁷.

1.4.2.3 Panchromatic light absorbing sensitizer

The sensitizer is at the heart of the dye sensitized solar cells. It is the element that will convert the energy contained in photons into charges. Hence there are several requirements that a dye has to fulfill in order to be performant^{73,128,129}.

- The dye absorption spectrum should overlap as closely as possible with the solar spectral photon flux showed in Figure 1.2b in paragraph 1.2, or any other light source, in order to maximize the current generation.
- The absorption of the dye should be strong, characterized by high molar extinction coefficients, which helps reducing the thickness of the titania films and electron transport issues.
- To be able to attach itself to the TiO_2 , the dye should possess at least one anchoring group in the form of an acidic unit, for example: carboxylic or phosphoric acids.
- To ensure high performances of the device, the dye should display well aligned HOMO and LUMO levels, with respect to E_{redox} and the TiO_2 CBE. This is a key feature as it will affect the photocurrent output.
- The sensitizer should demonstrate sufficient photostability and strong anchoring onto the TiO_2 surface.
- The structure of the dye should be design to minimize intermolecular aggregation of the molecules at the semiconductor surface in order to reduce self-quenching mechanisms and improve the performances.
- The dye should be easily accessible through few synthetic steps that would involve non-toxic, earth-abundant and cheap materials.

Meeting all these requirements is a challenging task, which emphasizes the importance of developing and studying new sensitizers. However, most of these points can be addressed through judiciously choosing the building blocks that will constitute the dye backbone.

The first reported high efficiency DSSC used a trimeric ruthenium based organometallic complex as sensitizer^{130–132}. The device sensitized with this dye produced a PCE of 7% under standard AM1.5G illumination^c. Ruthenium metal centers are mostly stable in an octahedral coordinated geometry. This class of sensitizers were found to be very attractive because of their promising light absorbing properties originating from a strong metal to ligand charge transfer (MLCT), vibronic transition in the visible spectrum.

Furthermore, the position of the MLCT can be tuned by modification of the electronic properties of the ligands bound to the ruthenium metal center. These ligands were derivatives from 2,2'-bipyridines, because of their strong bidentate coordinating abilities via the lone pair of the two nitrogen atoms. Quantum chemical calculations performed on a series of Ru-dyes indicated that the HOMO and LUMO states were respectively located on the t_{2g} orbital of the Ru center and π^* of the bipyridine¹³³, helping the rational design of the ligands.

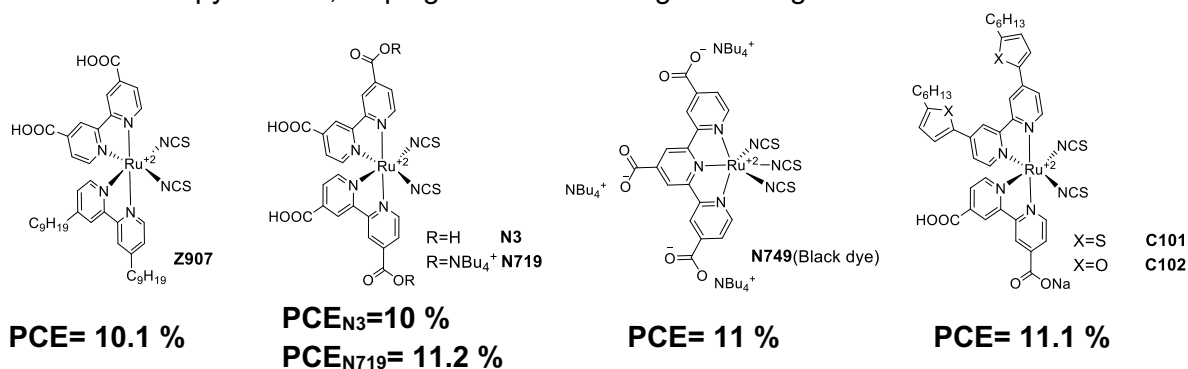


Figure 1.13. Molecular structures of octahedral ruthenium based organometallic complexes used as sensitizers in the early DSSC systems. The efficiency values correspond to an illumination of AM1.5G with the iodide/triiodide electrolyte.

Since the breakthrough in 1991, notable attention and efforts have been invested in developing organometallic Ru-based sensitizers. As a result, the dye coded **N3** (see Figure 1.13) managed to reach the symbolic bar of 10 % PCE under standard illumination¹³⁴. Its structure consisted in two 2,2'-bipyridine ligands functionalized with carboxylic acid groups at the 4,4' position to act as anchoring groups. The two remaining coordinating sites were occupied by thiocyanates anions.

Later on, **N719** was developed to overcome the issues resulting from the protonation of the TiO_2 surface by the carboxylic acid groups of **N3**. The modification consisted in substitution of the carboxylic acid protons for n-tetrabutyl ammonium cations (see Figure 1.13). As a result, **N719** produced higher photovoltages compared to its cousin **N3**, which lead to an improved PCE of 11.2% compared to the 10% reported for **N3**¹³⁵. The spectral properties of Ru dyes were pushed further with the synthesis of **N749** (Figure 1.13), also known as black dye. This sensitizer displayed impressive light harvesting abilities through the visible region and up to 920 nm¹³⁶. The initial PCE of the black dye was 10.4% under standard illumination, but extensive device optimization yielded an impressive certified PCE of 11.1% that was not improved for many years¹³⁷.

^cThe efficiencies reported in the following paragraph refer to devices fabricated with the iodide/triiodide (I^-/I_3^-) redox couple if not stated otherwise.

A more robust version of the **N3** dye was developed with the incorporation of hydrophobic alkyl chains on the 4,4' position of one of the two bipyridine ligands^{138,139}. This elegant synthetic modification allowed **Z907** (see Figure 1.13) to show unprecedented stability towards humidity with a PCE of 7.2% under standard AM1.5G conditions and with a 3-methoxypropionitrile (MPN) based electrolyte. This value was improved by nano-structuring of the TiO₂ electrode in devices containing acetonitrile based electrolyte. Under these conditions, **Z907** was able to produce an impressive 10.1 % PCE¹⁴⁰.

Despite the encouraging performances demonstrated by Ru-based sensitizers, several drawbacks remained. Their light absorption was strongly limited by low extinction coefficients with typical values lying around $10^4 \text{ M}^{-1} \cdot \text{cm}^{-1}$. This resulted in the necessity of using thick films of 10 μm thickness in order to obtain sufficient light harvesting^{71,72,141}.

Strategies aiming at improving the absorption consisted in grafting 5 membered heterocycles functionalized with a pending alkyl chain, on the 4,4' position of one of the two bipyridine ligands. The two dyes coded **C101** and **C102** (see Figure 1.13), respectively functionalized a 5-hexylthiophen-2-yl and 5-hexylfuran-2-yl, displayed ϵ values of $17.5 \times 10^3 \text{ M}^{-1} \cdot \text{cm}^{-1}$ and $16.8 \times 10^3 \text{ M}^{-1} \cdot \text{cm}^{-1}$ respectively, which was a slight improvement compared to the references **N719** ($14.2 \times 10^3 \text{ M}^{-1} \cdot \text{cm}^{-1}$) and **Z907** ($12.2 \times 10^3 \text{ M}^{-1} \cdot \text{cm}^{-1}$)¹⁴².

The former paragraph has presented the main drawbacks resulting from Ru-based sensitizers. To overcome these latter, efforts have been put into developing fully metal free organic dyes. These compounds have several advantages over their ruthenium analogues, notably, the absence of the rare earth metals which lowers the toxicity and cost of the compounds but also enhanced light harvesting properties.

High efficiency organic sensitizers are typically constructed following a particular electronic pattern. It consists in an electron donating moiety (D) attached to a π -conjugated linker that connects this donor part to an electron accepting unity (A). The backbone of the dye is usually fully π conjugated network that can be decorated with heteroatoms to tune the spectral response of the dye. The electron acceptor, also possesses an anchoring group in the form of a carboxylic acid, that will allow a firm attachment to the TiO₂.

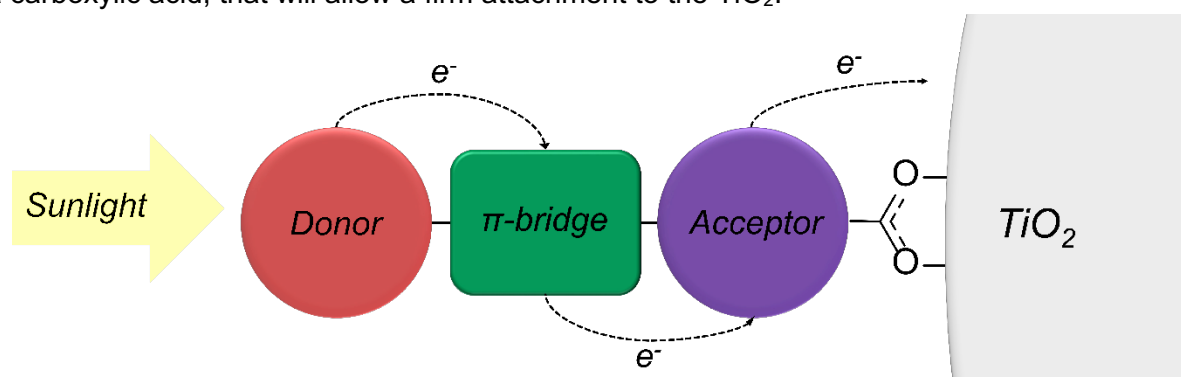


Figure 1.14. Representation of the charge transfer directionality present in a D- π -A organic dye. The arrangement of building blocks, from strongly electron donating to strongly electron withdrawing helps the charge separation process.

This peculiar arrangement creates a directionality in the charge transfer as upon interaction with light, the electron will flow from the electron donating moiety (D) cross the π -bridge to reach the electron acceptor (A) that is attached to the semiconductor surface hence facilitating the electron injection as illustrated in Figure 1.14.

The donor-acceptor model has been inspired from the field of organic solar cells, where it is commonly used to design efficient materials^{143–147}.

As described in the previous paragraphs, when a dye interacts with light, the photon will be absorbed if its wavelength λ is equal or superior to its bandgap (E_g). The energy contained in the photon will be used to transfer an electron from a singlet ground state (S_0) to an higher energy state (S_1)¹⁴⁸, as depicted in Figure 1.15. The electron will then relax to the lowest excited state conformation (q_{ES}) via thermalization. This absence of electron will create a vacant site with a positive charge called a hole¹⁴⁹. This loosely bound electron-hole pair is called an exciton. In aromatic molecules with large π conjugated systems, the excitons are called Frenkel excitons and possess binding energy typically ranging from 0.1 to 1 eV because of their high permittivity constant^{150–152}. The exciton binding energy (EBE) usually depends on geometrical features of the molecule such as its size but also its effective conjugation length, inversely proportional to its EBE^{153–155}. As an example, the dyes coded **JK-45** and **JK-46**, showed EBE of respectively 0.21 eV and 0.19 eV, with the sole difference being the additional fused benzothiophene unit present in **JK-46**, which increases its conjugation length (see Figure 1.16)^{156,157}. Additionally, a long effective conjugation will help stabilizing the ground and excited state, ultimately shifting the dye absorption onset towards longer wavelength¹⁵⁸. Furthermore, the π conjugated network of organic dyes is necessary as it allows them to have broad and intense optical transition, because of the strong coupling of the ground and excited states^{148,159}. This results in a strong charge transfer (CT) peak in the visible region, typically observed when measuring absorption spectra of organic D- π -A dyes.

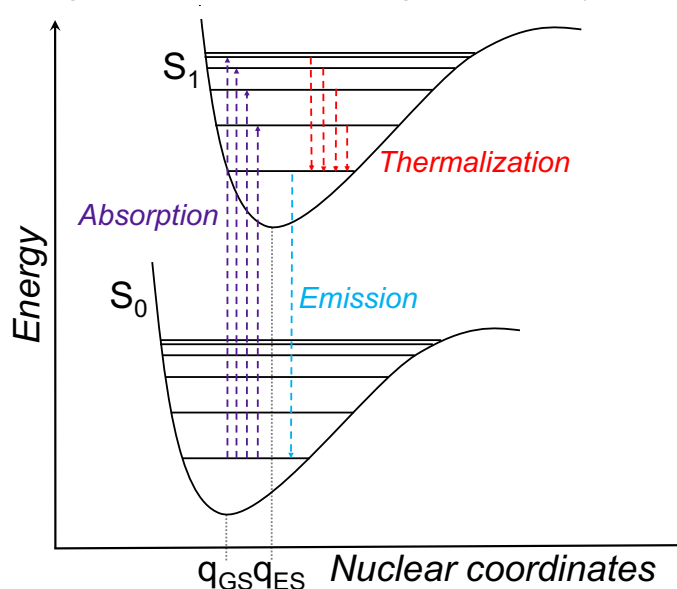


Figure 1.15. Representation of the vibronic transition occurring in an organic dye, upon light absorption. An electron located in a ground state S_0 is promoted to an excited state S_1 . After thermalization, the electron reaches an equilibrium state q_{ES} . Then the electron relaxes to its initial equilibrium state q_{GS} , in the ground state, through radiative or non-radiative emission.

The implementation of an electron donor and acceptor, also offers the advantage of creating a better spatial separation of the ground and excited states. More specifically, the HOMO level, will be mainly located on the most electron donating part and the LUMO level on the most electron accepting. This elegant strategy allows to independently fine tune these two distinct energy states that play an important role in the dye performance.

The electron donor usually contains a nitrogen atom attached to diverse, aromatic or aliphatic groups, that can be further decorated with other heteroatoms such as sulfur or oxygen. These latter will mainly serve as auxiliary source of electron donation. The three mostly encountered donor building blocks are derivatives of triphenylamines (TPA), carbazole (Cz) and indoline (Ind).

Indoline based dyes showed the earliest promising performances, with PCEs rapidly toping the state of the art Ru-dyes presented in the earlier paragraphs. The dyes coded **D149** and **D205** produced PCEs of respectively 8 and 7.18 % under AM1.5G¹⁶⁰. After further optimization of the films, these dyes were able to increase their PCEs up to 9 %, with the standard iodide/triiodide couple^{161,162}. Indoline donors are usually much more efficiently shift absorption spectra to longer wavelength due to their strong electron donation. This effect is attributed to the planarity originating from the fused aliphatic cycles as well as their σ -donation³. In addition to that, they can easily be functionalized at the nitrogen atom with a variety of groups that can not only improve their spectral response but reduce deleterious recombination reactions. This is illustrated in Figure 1.16, by comparing the dye coded **DPP13** with **DPP14**, **DPP15** and **DPP17**. The bulkiness and electron donating gradually increases from a TPA donor (**DPP13**) to a N-p-tolyl-indoline (**DPP14**) followed by a more elaborated N-2',4'-bis(hexyloxy)-[1,1'-biphenyl]-4-yl (**DPP15**) and finally 4-(2,2-bis(2',4'-bis(hexyloxy)-[1,1'-biphenyl]-4-yl) vinyl)phenyl (**DPP17**). The corresponding PCEs of these dyes were consistently increasing with the size of the electron donors with values of 8.97 (**DPP13**), 8.23 (**DPP14**), 9.81 (**DPP15**) and 10.1 % (**DPP17**), under AM1.5G with the $[\text{Co}(\text{bpy})_3]^{+3/+2}$ (bpy=2,2'-bipyridine) electrolyte.

Carbazole presents a similar structure to indoline, with its two benzene rings directly connected on one side by a C-C bond and bridged by a nitrogen atom on the other. Similar to the indoline donors, the presence of the nitrogen atom enables further functionalization. The carbazole donor can be connected to the π -bridge through either its nitrogen atom, or it's C3 position. The earliest reports of efficient carbazole dye came with the MK series (see Figure 1.16)¹⁶³. They consist in an oligo-alkyl thiophene π -bridge, with a carbazole donor connected at its C3 position, bearing an ethyl chain on the nitrogen atom and a cyanoacrylic acid electron accepting anchoring group. **MK-2** managed to produce a PCE of 8.3 % with the iodide/triiodide electrolyte under standard AM1.5G¹⁶⁴.

Carbazole donors possess the ability to carry an additional electron donating fragment attached at their C6 position, examples of this functionalization are shown in the dyes **MK-14** and **MK-16** that have a supplementary p-hexyloxyphenyl unit (Figure 1.16). It allows **MK-14** to generate a PCE of 8.1 % under standard conditions of illumination and I^-/I_3^- electrolyte by notably improving the devices' electron lifetime¹⁶⁵. It is worthy to mention that the carbazole based dye **ADEKA-1** along with the dye coded **LEG4** produced one of the highest PCEs reported of 14 %, with a cobalt based redox electrolyte $[\text{Co}(\text{phen})_3(\text{II/II})]$ (phen=1,10-phenanthroline) and under AM1.5G.

As mentioned previously, the other way to connect a carbazole building block to the π -bridge is through its nitrogen atom. This configuration is very similar to a triphenylamine the only difference being the C4a-C4b bond. This feature ultimately gives supplementary rigidity making the donor core more planar, hence better electron donating but at the cost of more intramolecular stacking^{166,167}. Examples of such structures are shown in the dyes coded **JK-318**, **JK-319** and **JK-320** (Figure 1.16). The best performing dye was **JK-320** with efficiencies of 6.66 and 5.88% with respectively I^-/I_3^- and $[Co(bpy)_3]^{+3/+2}$ under AM1.5G. **JK-320** benefits from the stronger donating strength of the two ortho and para n-hexyloxy units installed on its donor.

The most encountered electron donating unit is the triphenylamine due to its versatility¹⁶⁸. Its structure consists in a nitrogen atom, connected to three aromatic units that in most of the cases are phenyl rings. The donor is usually connected to the π -bridge via one of the phenyl or directly via its nitrogen atom, which usually enhances the donating strength. The two remaining rings are usually decorated with supplementary aromatic units used to enhance the electron donation but also repel the electrolyte more efficiently. As an example, **TA-St-CA**, possess a simple TPA donor, without any supplementary unit. It was one of the first reports of a fully organic dyes able to produce a PCE of 9.1 %, very close to **N719** (10.1 %) under AM1.5G and I^-/I_3^- electrolyte¹⁶⁹. As mentioned earlier, the TPA donor can be subsequently decorated with alkoxy chains to shift the spectral response to longer wavelength and increase its steric hindrance. Such example of functionalization can be found on the dye coded **C219**. This latter was decorated with two 2-ethyl-hexyloxy groups at the para position of two phenyl rings of the TPA. **C219** reached a PCE of 7.6 % with the iodide/triiodide electrolyte and standard illumination conditions. The devices fabricated with **C219** slightly outperformed the reference **Z907** (7.2 %), with similar ionic liquid based electrolyte¹⁷⁰.

Two of the phenyl rings can also be substituted for 9,9-dimethylfluorene-2-yl units. These latter provide more bulkiness and electron donation to the sensitizer. As an example, the dye **C205** achieved a PCE of 7.6 % and displayed remarkable stability with the triiodide/iodide electrolyte and under AM1.5G¹⁷¹. A new class of electron donating building blocks was created with the implementation of o,p-dialkoxyphenyl units on the TPA core. This structural modification provided a stronger electron donation as well as more efficient protection of the semiconductor/electrolyte interface towards electron recombination¹⁷². This building block was popularized with **D35**, that carried o,p-di-n-butyloxyphenyl units and produced a PCE of 6 % under standard illumination conditions with the I^-/I_3^- electrolyte¹⁷³. More development followed with the LEG series (Figure 1.16) and notably **LEG4** that was able to deliver a PCE of 6.8 % under standard illumination conditions with the $[Co(bpy)_3]^{+3/+2}$ electrolyte¹⁷⁴. This value was pushed to 8.8% under the same conditions, but with substitution of the n-butyloxy chains of **LEG4** for n-hexyloxy chains in **Y123**¹⁷⁵.

The role of the π -bridge is to efficiently transfer the charges from the donor to the acceptor. This is commonly achieved by using a strongly π -conjugated building blocks that provides good electronic communication. The light harvesting properties of the dye are also strongly dependent on the nature of the π -bridge, as it will directly affect the effective conjugation length of the molecule. The simplest aromatic π -unit that exists is the phenyl ring. However, it displays a higher resonance stabilization energy (RSE). The regular arrangement of C-sp² of the phenyl unit yields a high lying excited states compared to other heterocycles such as thiophene, pyrrole or furan¹⁷⁶. These latter possess heteroatoms (S, N and O) that disrupt the aromaticity of the ring by inclusion of their lone pair of electron in their p non-bonding orbital¹⁷⁷.

As a result, the dye benefits from the lower RSE of the heterocycles. **D35** is an example of a dye bearing a simple thienyl π -bridge. The spectral response can be shifted to longer wavelength by using a series of oligothiophene as seen with in the MK dyes. Furthermore, the molar extinction coefficient can be drastically improved if the π -bridge is fused. This helps assuring a good planarity of the backbone and improves the electronic coupling, charge delocalization and aromaticity. For example, the dye **C218** which uses a 4,4-dihexyl-4H-cyclopenta[2,1-b:3,4-b'] dithiophene (CPDT) bridge.

This π -bridge showed a maximum molar extinction coefficient of $62.7 \times 10^3 \text{ M}^{-1} \cdot \text{cm}^{-1}$ which is more than two fold higher than its analogue **D21L6**, constructed with a unfused CPDT¹⁷⁸ with a value of $33.8 \times 10^3 \text{ M}^{-1} \cdot \text{cm}^{-1}$. For this reason, 4H-cyclopenta[2,1-b:3,4-b'] dithiophene gained popularity as a building block. Other variations of this latter include the substitution of the tetrahedral sp^3 carbon by a heteroatom such as nitrogen^{179,180} or silicon, as seen in dyes **LP225**, **LP227** and **C219**.

Further improvement can be implement by using chromophores as π -bridges. This method usually yields strongly absorbing and very colorful sensitizers. This D-C-A sub-group can be regarded as variation of D- π -A dyes. Two examples of π chromophores will be discussed: zinc-porphyrins (ZnP) and diketopyrrolopyrroles (DPP).

Zinc porphyrins are an attractive class of building blocks because of their intense spectral transition called Soret band and Q bands that are the results of π - π^* transition within the conjugated network of the porphyrin ring¹⁸¹. This ultimately yield dyes with high molar extinction coefficients¹⁸² in the range of $10^5 \text{ M}^{-1} \cdot \text{cm}^{-1}$ with an attractive green color. **YD2-o-C8** and **SM315** are two examples of D- π -A dyes bearing porphyrin rings as π -bridge. They are both potent sensitizers which enables the fabrication of devices with PCEs close to 13% under standard illumination conditions with $[\text{Co}(\text{bpy})_3]^{+3/+2}$ electrolyte^{183,184}.

The second building block, DPP, has found a wide variety of applications ranging from pigment in car paints to building block in OPV polymers. Structurally, they have an ambiguous behavior as they can also be regarded as electron accepting building block due to the presence of the two strongly withdrawing lactam groups^{185,186}. This core can therefore be considered as a chromophore/acceptor unit. When implemented in D- π -A dyes, DPP enables high molar extinction coefficient ($\sim 10^4 \text{ M}^{-1} \cdot \text{cm}^{-1}$) associated to strong optical transitions in the visible part of the spectrum and very attractive blue colors^{187–190}. As examples, the performances of DPP dyes, **DPP13**, **DPP14**, **DPP15** and **DPP17** have been discussed in the earlier paragraph.

The electron accepting moiety is at the other extremity of the dye and comprises the anchoring group. The most frequently encountered acceptor is the cyanoacrylic acid unit¹⁹¹. This fonctionnal group helps locating the dye LUMO level close to the titania surface due to the particularly strong electron withdrawing character of the nitrile. Cyano acrylic acids represent the most elementary acceptor/anchoring unit. However, due to its structural simplicity, it is hard to tune the electron accepting strength. An alternative can be found in derivatives of benzoic acid. These latter can be attached to other aromatic units that have electron withdrawing properties, which enables a more straightforward tuning of their properties. The most encountered building blocks used for this purpose are poly-aromatic cycles with imine bonds. They possess a strong electron deficient nature that can be used to pull electronic density inwards^{192–194}. The most popular building block encountered is benzothiadiazole (BT), because of its low cost and simplicity. It consists in a six membered ring fused to a five membered ring. The five membered ring has two imine bonds and a bridged by a sulfur atom¹⁹⁵.

Several synthetic modifications can be performed to tune the electron accepting strength of BT and notably substituting the central sulfur atom with other heteroatom such as oxygen or an alkylated nitrogen^{196–198}. Further tuning can also be achieved through six membered ring, where the carbon atoms can be substituted increase the electron accepting strength¹⁹⁹.

The dyes coded **L349**, **L350** and **L351** are examples of such synthetic modifications, where the structural alteration of the electron accepting groups induces a stabilization of the LUMO level. These three dyes respectively produced PCEs of 9.2 % (**L349**), 11.2 % (**L350**) and 9.1 % (**L351**) with $[\text{Cu}(\text{tmby})_2]^{+2/+1}$ (tmby=4,4',6,6'-tetramethyl-2,2'-bipyridine) as redox active electrolyte and under AM1.5G²⁰⁰. Furthermore, the additional benzene spacer presents between the electron acceptor and the anchoring group was also found to be beneficial for charge injection. It was found strong acceptors located too close to the TiO_2 surface could act as electron-traps, that can recapture injected electrons. In this regard, the additional phenyl spacer was found to help by adopting a twisted geometry in the excited state thus breaking the electronic conjugation of the dye and prevent the electron recapture²⁰¹. This effect was observed with **GY21** and **GY50**. As seen in Figure 1.16, their sole difference resides in a phenyl spacer located between the BT unit and the carboxylic acid. However, in terms of performances under standard illumination conditions with $[\text{Co}(\text{bpy})_3]^{+3/+2}$, **GY50** was able to yield a PCE of 13 % which was an enormous improvement compared to the 2.51 % of **GY21**²⁰². Similar effects were found with a BT acceptor and cyanoacrylic acid anchoring group²⁰¹.

The D- π -A pattern was furtherly improved by addition of a supplementary electron accepting unit between the donor and the π -bridge. This novel D-A- π -A motif, was found to improve stability as well as allow a more fine tuning of the energy levels helping to improve the spectral response^{2,203–205}. Notable examples of such dyes can be seen with the XY series²⁰⁶. A supplementary BT unit was installed between the electron donor and the CPDT π -bridge that was connected to either a phenyl (**XY1**) or a thiophene (**XY2**) cyanoacrylic acid anchoring group. As a third structure, the BT unit was moved between the CPDT bridge and the thiophene-cyanoacrylic acid anchoring group (**XY3**). These dyes were used in solid state DSSCs and obtained PCEs of 6.69 % (**XY1**), 6.89 % (**XY2**) and 5.50 % (**XY3**) under AM1.5G. The better performances of **XY2** were attributed to its broader spectral response associated with a high molar extinction coefficient of $6.66 \times 10^4 \text{ M}^{-1} \cdot \text{cm}^{-1}$.

In liquid DSSCs, **XY1b** a cousin of **XY1**, only differing by n-butyloxy chains on the donor instead of 2-ethyl-hexyloxy, can produce PCEs close to 10 % under standard illumination and with the $[\text{Cu}(\text{tmby})_2]^{+2/+1}$ redox couple^{207,208}. Simpler but efficient dyes were developed by modification of the **LEG4** and **Y123** structures. The strategy consisted in inserting electron accepting units between the electron donor and the CPDT core. Such examples can be observed in the dyes **HY63**, **HY64**, **WS70** and **WS72**. The first dye (**HY63**) consists in **Y123** with an additional BT unit whereas **HY64** bears a more conjugated and rigid dibenzo[a,c]phenazine core. Compared to **Y123**, the HY dyes they show lower LUMO levels, due to the additional electron acceptor, and high molar extinction coefficients lying around $10^4 \text{ M}^{-1} \cdot \text{cm}^{-1}$. In devices they respectively produced PCEs of 10.3% and 12.5% with $\text{Cu}(\text{II/I})$ electrolyte and under AM1.5G²⁰⁹. The WS series uses derivatives of 2,3-diphenylquinoxaline (**WS70**) and 2,3-bis (4-(hexyloxy) phenyl) quinoxaline (**WS72**) as auxiliary acceptor. These dyes were also compared to **Y123** in cells fabricated with $[\text{Cu}(\text{tmby})_2]^{+2/+1}$. Under AM1.5G the WS dyes showed PCEs of 11 % (**WS70**) and 11.6 % (**WS72**) which were both higher than **Y123** (10.3%)²¹⁰.

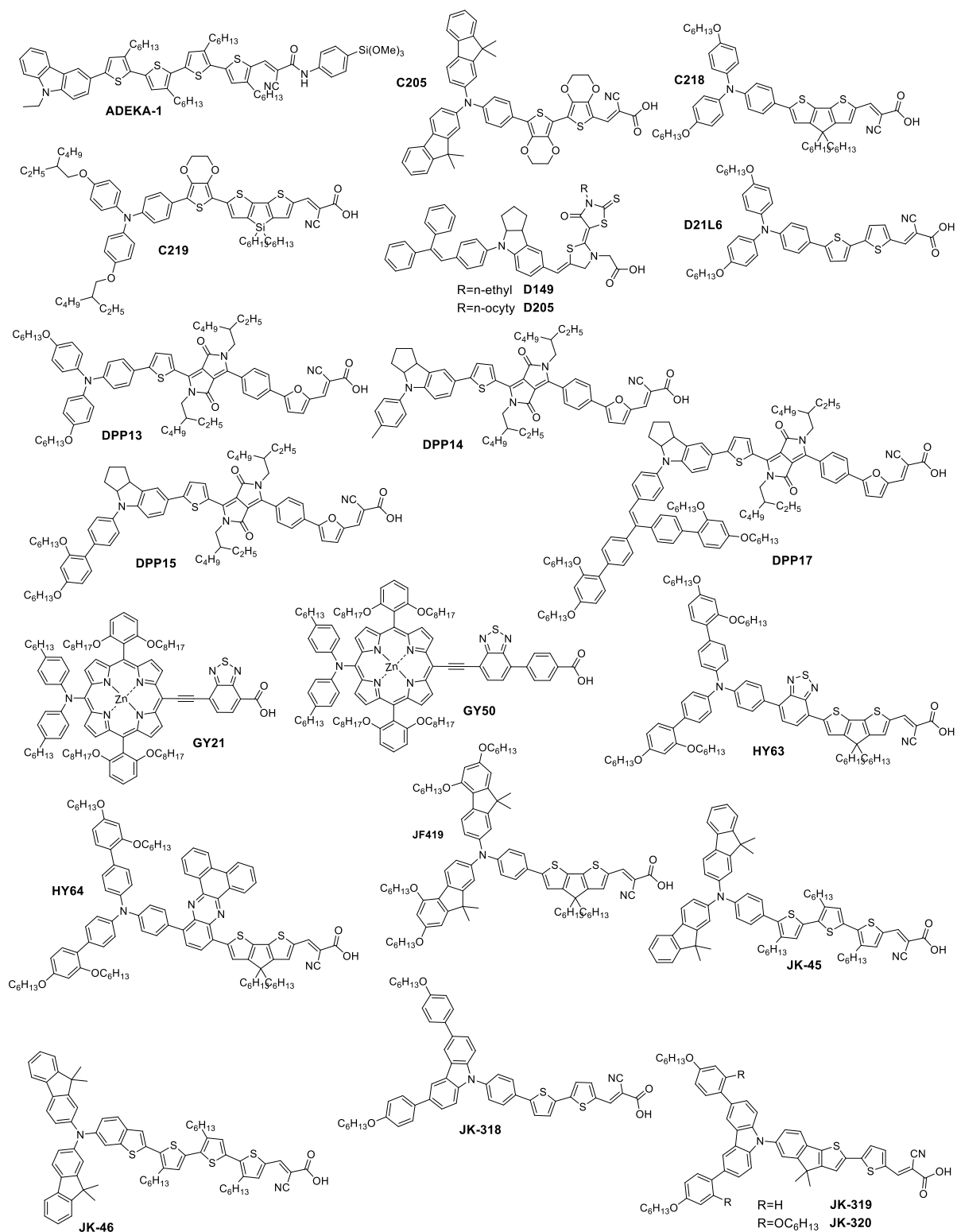


Figure 1.16. Molecular structure of organic $D-\pi-A$ and $D-A-\pi-A$ dyes.

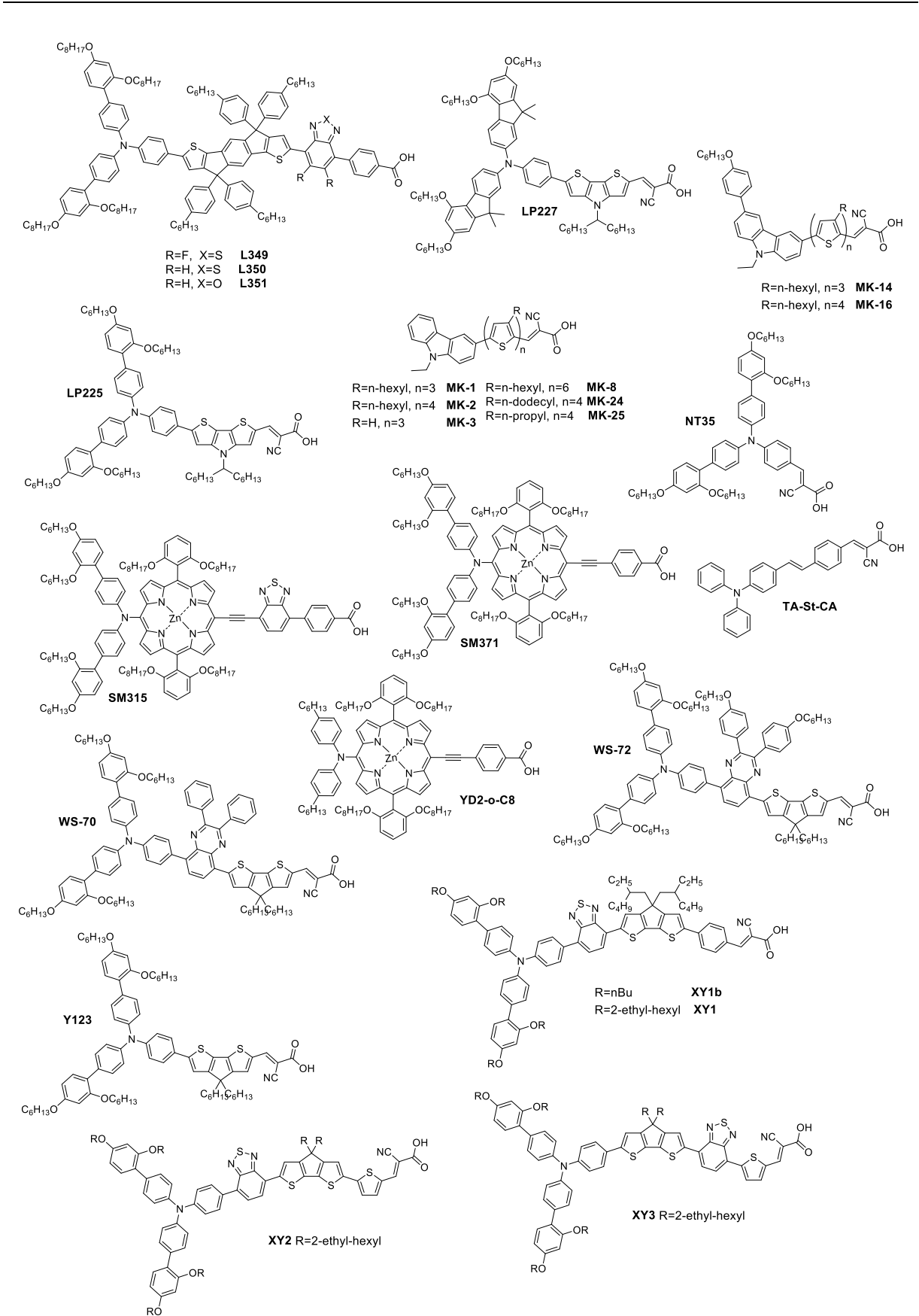


Figure 1.16. (Cont.). *Figure 1.16 Continued.*

As mentioned earlier, the electron donor (D) will mainly be responsible for defining the HOMO level or ground state oxidation potential of the dye ($E_{S^+/S}$). When the electron richness or the planarity of the donor increases, which translates into a reduced dye oxidation potential. This effect can be observed experimentally, by comparing the HOMO levels of three dyes: **Y123**, **C218** and **JF419**, represented in Figure 1.17. Comparing **Y123** and **JF419** shows the influence of rigidifying the donor going from the first dye to the second, with the help of dimethylfluorene units. As a result, the HOMO level shifts from 1.01 (**Y123**) to a less positive 0.85 V vs. NHE (**JF419**). **Y123** and **C218** have similar HOMO levels which can be explained by the biphenyl rings of the bulky donor. These latter display a more twisted conformation due to the steric clash between the two six-membered rings. Ultimately, this hinders a stronger donation from the two hexyloxy groups on the bulky donor²¹¹.

The π -bridge increases the effective conjugation length of the molecule. As a result, the molar extinction is improved along with a shift of the spectral response to longer wavelength, originating from a further stabilization of the LUMO and HOMO levels. An alternative strategy consists in implementing heteroatoms, such as N, S or Si, within the core of the π -bridge. This will reduce the π -bridge's resonance stabilization energy and yield to an energetically more accessible excited state. To achieve a high degree of charge delocalization a very planar structure is preferred. However, a dye that is too planar will easily form deleterious aggregates upon absorption on the TiO_2 film. To prevent such effect, it is necessary to install bulky alkyl chains on the π -bridged that will help break the aggregates.

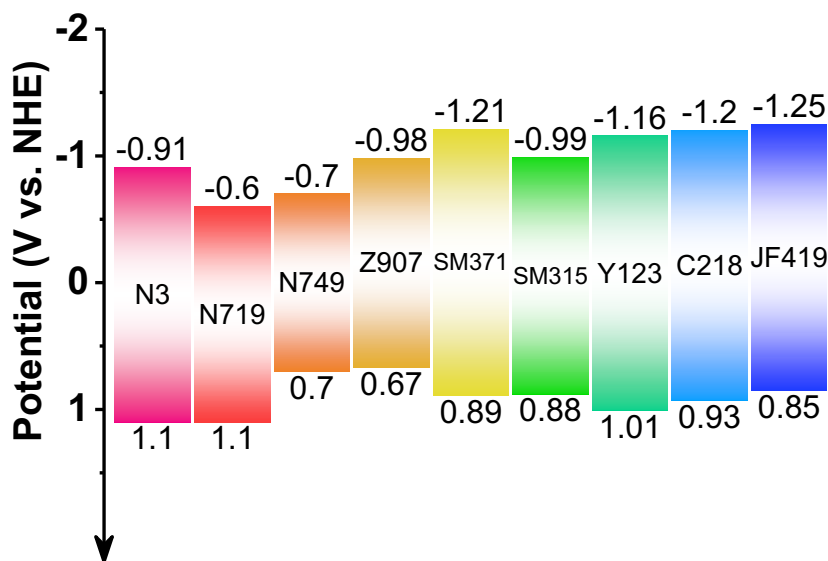


Figure 1.17. Selected examples of organic dyes' energy levels obtained from electrochemical measurements. The ruthenium dyes were added for comparison^{183,211–214}.

The electron acceptor was found to be defining the LUMO level or dye excited state redox potential (E_{S^+/S^*}). In this regard, if the electron accepting or deficiency increases the electrochemical potential will follow, because of the stronger ability to extract an electron, i.e., oxidize. Experimentally, this effect can be observed by comparing the energy levels of ZnP dyes **SM371** and **SM315** (Figure 1.17). The additional BT unit present on **SM315** induces a stabilization of the LUMO level by 220 mV²¹². A subtler tuning can also be achieved by substitution of the heteroatom as it was demonstrated with the **L350** and **L351** dyes.

It is important to mention that tuning the dyes' opto-electrochemical properties is not the result of one unique contribution. For example, adding a supplementary acceptor not only helps reducing the energy of the LUMO level but will also result in an increased effective conjugation length, that will also alter the dyes' energy levels.

1.4.2.4 Redox active electrolyte and additives

As it was explained in paragraph 1.4.1.1, the redox active electrolyte plays a key role in the operation of the device. It will dictate certain important kinetic parameters such as the dye regeneration rate. Furthermore it will also determine the energy output of the device, as the open circuit voltage of a DSSC is defined by the difference between the fermi level of the TiO_2 (E_F) and the redox potential of the redox electrolyte (E_{redox})²¹⁵.

$$V_{\text{OC}} = \frac{E_{\text{CBE}}}{q} - \beta \frac{k_B T}{q} \ln \left(\frac{n_e}{N_{\text{CB}}} \right) - \frac{E_{\text{redox}}}{q} \quad (1.28)$$

Where E_{CBE} is the TiO_2 conduction band edge energy, β is a factor that equals unity for a perfect defect free semiconductor. Additionally, N_{CB} is the number of energy states in the TiO_2 and n_e is the number of electrons in TiO_2 . Equation (1.28) emphasizes that optimizing the device performances and especially the maximum voltage output can be achieved by careful choice of the redox electrolyte.

One of the early redox couple used in DSSCs is triiodide/iodide (I_3^-/I^-)^{216,217}. Its redox potential lies around 0.35 V vs. NHE and the electrochemical reduction of I_3^- to I^- is a two electron process described by the following chemical equation:



The main advantage of the triiodide/iodide redox couple lie in the readily fast regeneration rates²¹⁸, high solubility in organic solvents and fast diffusion²¹⁹. However, one of its main shortcomings is its low redox potential value that causes important energy losses. For example, **N3** has a ground state oxidation potential of 1.1 V vs. NHE (see Figure 1.17) which implies that the driving force losses would be of approximately 0.7 V with the triiodide/iodide redox couple.

The main reason for such important internal losses comes from the complicated redox reaction described by equation (1.29), that involves a kinetically demanding two electrons transfer^{220,221}. In addition to these important potential losses, I_3^-/I^- shows a strong absorption in the visible spectrum while also dissolving counter electrode materials²²². In spite of all the aforementioned drawbacks and limitations, the I_3^-/I^- redox has been widely used and established as a reference in the DSSC research field.

Transition metal organometallic complexes were considered as viable alternative to I_3^-/I^- . They offered much simpler one-electron transfer that would follow the Marcus type transfer mechanism, described earlier in paragraph 1.4.1.2. Their other main advantage resides in the ability to tune their electrochemical, optical and physical properties through structural modification of the ligands coordinating the metal center.

At first, cobalt complexes were employed as redox mediators in DSSCs. These compounds usually exist in the Co(III)/Co(II) oxidation states. They respectively display d^7 and d^6 electronic configuration states²²³. Cobalt complexes adopt octahedral geometry with a coordination of CN = 6, for both oxidation states²²⁴. Additionally, they follow the high spin/low spin distribution described by the ligand field theory^{225,226}.

Cobalt coordination complexes have much simpler and faster electron transfer kinetics²²⁷ as well as low molar extinction coefficients in the order of $10^2 \text{ M}^{-1}\cdot\text{cm}^{-1}$, which is a drastic improvement compared to the values of $5.6 \times 10^4 \text{ M}^{-1}\cdot\text{cm}^{-1}$ recorded for the iodide couple²²⁸. They also have the advantage of being completely inert towards counter electrode materials²²⁹. The drawbacks associated with the use of Co-complexes redox mediators originated at first from their rather bulky size causing higher diffusion coefficient compared to I_3^-/I^- ²³⁰, their cationic nature that will favor recombination with negatively charged electrons, poor electrochemical activity at Pt counter electrodes²³¹ as well as energy losses due to spin transition upon electron transfer to the dye²³².

The most commonly used cobalt complexes in high efficiency devices are derived from nitrogen based polycyclic aromatics ligands. These latter coordinate the cobalt ion through the lone pair of the nitrogen atoms in a bidentate or tridentate mode, as shown in Figure 1.18. Although the most impressive results of cobalt based DSSCs have been achieved with organic dyes, such as the ones described in section 1.4.2.3, it is worth mentioning that the highest PCE obtained with a Ru-dye and $[\text{Co}(\text{bpy})_3]^{+3/+2}$ was 6.5 % under standard AM1.5G conditions²³³.

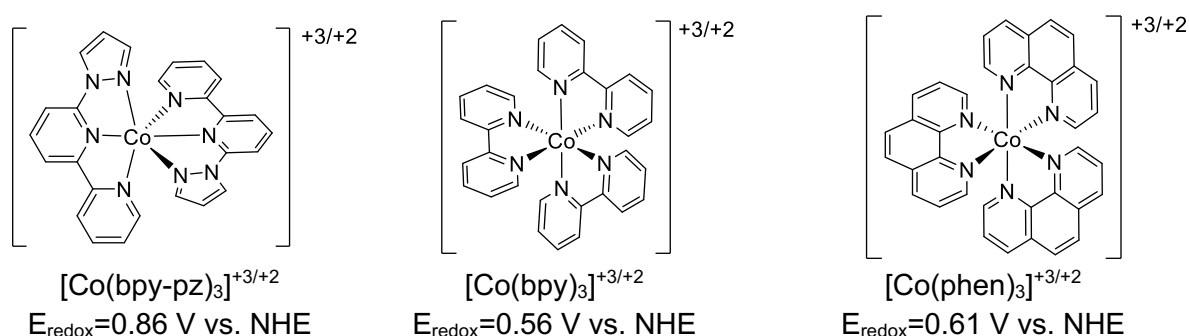


Figure 1.18. Molecular structure of the cobalt organometallic complexes as well as their redox potential versus normal hydrogen electrode (NHE).

It was rapidly observed that the redox potentials of Co-complexes could be tuned by simple modification of the ligand or by the nature of the ligand itself, i.e. changing a bidentate for a tridentate. As showed in Figure 1.18²³⁴, values as positive as 0.86 V vs. NHE for the $[\text{Co}(\text{bpy-pz})_3]^{+3/+2}$ redox couple. Low driving forces ranging between 0.2 and 0.4 eV were found to be enough to regenerate organic dyes efficiently²³⁵. It was found that bulky cobalt complexes were helping reduce electron recombination, at the cost of slower diffusion coefficients. This issue was solved by implementing repelling aliphatic chains on the electron donating part of the organic dye which allowed to use much smaller complexes such as $[\text{Co}(\text{bpy})_3]^{+3/+2}$ while retaining high electron lifetime^{183,236}. In addition to that, development of new electrode materials such as electrodeposited PEDOT (poly(3,4-ethylenedioxythiophene) or graphene based counter electrode, solved the problems related to poor electrochemical activities of the cobalt complexes and improved fill factors^{237–240}.

Cobalt based DSSCs caught up rapidly with the efficiencies superior to 10 % that were measured for the systems with triiodide/iodide. Notable examples comprise, the porphyrin dyes **YD2-o-C8**, **SM315** and **SM371**, that produced PCE over 10 % with the $[\text{Co}(\text{bpy})_3]^{+3/+2}$ redox couple^{183,212}, as well as the PCE of 14.3 % reported with the $[\text{Co}(\text{phen})_3]^{+3/+2}$ (phen=1,10-Phenanthroline) complex and **ADEKA-1/LEG4** combination²⁴¹. Among the many advantages provided by cobalt based redox active electrolyte, the improvement of the V_{OC} was the most striking. The symbolical value of 1 V was reached several times, notably with $[\text{Co}(\text{phen})_3]^{+3/+2}$ and the **ADEKA-1/LEG4** dye mixture but also with **Y123** alone and $[\text{Co}(\text{bpy-pz})_2]^{+3/+2}$ (bpy-pz=6-(1H-pyrazol-1-yl)-2,2'-bipyridine)²⁴².

The second group of organometallic complexes, considered as alternative to the triiodide/iodide redox active electrolyte was based on copper metal centers. These complexes usually exist in the Cu(I) or Cu(II) oxidation number, which gives them respectively, a d^{10} and a d^9 electronic configuration, much less prone to high spin or low spin fluctuations²²³. As opposed to cobalt complexes, the geometry of copper complexes varies upon the oxidation state. Cu(I) usually adopts a strongly distorted tetrahedral geometry with a coordination number of CN = 4, whereas its oxidized form, has geometries fluctuating between either CN = 5, associated to a distorted trigonal pyramidal geometry or CN=6, corresponding to a distorted octahedral configuration^{243,244}. Similar to cobalt complexes, Cu complexes offer fast outer sphere single electron transfer²⁴⁵ with the possibility to tune their electrochemical, optical and physical properties through alteration of the ligands^{246–248}.

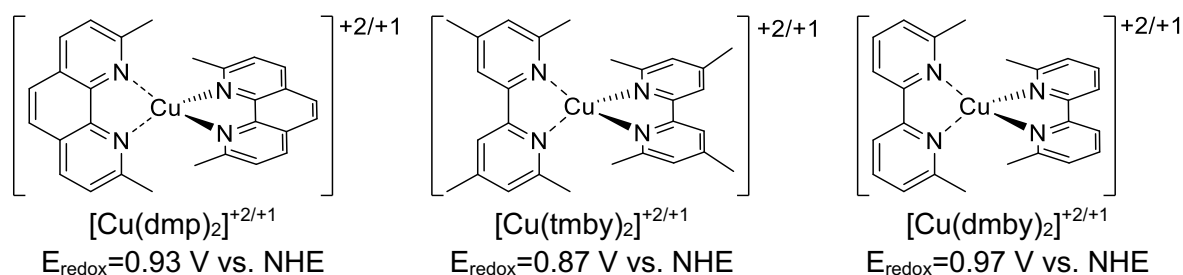


Figure 1.19. Molecular structure of the copper organometallic complexes with their redox potential versus normal hydrogen electrode (NHE).

The most commonly used ligand framework with copper based coordination complexes in DSSCs are derived from the 6,6'-dimethyl-2,2'-bipyridine structure. Three ligands turned out to be the more promising candidates for constructing stable and efficient complexes: 6,6'-dimethyl-2,2'-bipyridine (dmby), 6,6',4',4'-tetramethyl-2,2'-bipyridine (tmby) and 2,9-dimethyl-1,10-phenanthroline (dmp). The structures of the corresponding complexes are represented in Figure 1.19, with their respective E_{redox} values, that were found to be even more positive than the Co-complexes reported in Figure 1.18. These ligands coordinate the Cu(I) center in a bidentate mode leading to a strongly distorted but stable tetrahedral geometry. On the other hand, these Cu(II) complexes display a distorted trigonal bipyramidal structure with the fifth coordination site being occupied by a counter anion in the solid state or a solvent molecule in solution. DFT calculations highlighted that the two methyl groups at the 6,6' positions were found to help stabilize the geometry of the Cu(I)^{249–251}.

The first example of redox-active copper coordination complexes in DSSCs electrolyte were reported with the metal free organic dye coded **C218**, that produce a PCE of 7 % under standard AM1.5G with the $[\text{Cu}(\text{phen})_2]^{+2/+1}$ redox couple²⁵².

Further studies revealed that , $[\text{Cu}(\text{dmby})_2]^{+2/+1}$, $[\text{Cu}(\text{tmby})_2]^{+2/+1}$ and $[\text{Cu}(\text{phen})_2]^{+2/+1}$ could regenerate dyes efficiently with a ΔG_{reg} of only 0.1 eV reducing even furtherly the overpotential losses²⁵³. Notably, the three complexes presented in Figure 1.19, were used in DSSCs along with **Y123** and achieved PCEs of 10 % with photovoltages reaching 1.1 V, while retaining fast dye cation reduction rates lying between 2 and 3 μs ^{254,255}. It is worth mentioning that $[\text{Cu}(\text{tmby})_2]^{+2/+1}$ was used to fabricate DSSCs producing PCEs up to 28.9 % with **XY1b**²⁰⁸ and up to 31.8% with a co-sensitized **XY1b/Y123**²⁵⁶ system, both under $318.2 \mu\text{W}\cdot\text{cm}^{-2}$ (1000 lux).

This result highlighted the promising opportunities for indoor light to electricity conversion. Interestingly, it was discovered that dried up cells, fabricated with the $[\text{Cu}(\text{tmby})_2]^{+2/+1}$ electrolyte would still be functional. These so called “zombie cells” were found to be producing PCEs around 11 % with **Y123**. It was speculated that upon evaporation of the solvent, a solid hole transporting layer formed, allowing efficient charge transport to take place²⁵⁷.

The main issues that were highlighted with the use of copper complexes as redox mediators in DSSCs, not encountered with cobalt complexes, is the sensitivity to the 4-tertbutyl-pyridine (TBP) additive. More specifically, the presence of TBP in the electrolyte solution can induce a substitution of the ligands coordinating the Cu metal center and alter its mass transport as well as electrochemical properties^{258–260}.

The electrolyte of a liquid DSSC usually contains two types of compounds: the redox active electrolyte that was just discussed, whose role is to regenerate the dye and participate to the overall electron transfers cascade and the second, some additives that do not perform electron transfers but influence the device performances. Notably, these additives will be used to alter the conduction band edge level of TiO_2 ^{73,261,262}. Two different types of additives are used to either lower or lift the CBE. Cations such as Li^+ , Na^+ or Mg^{+2} , are used to lower the CBE of the semiconductor. This band shift is attributed to an intercalation of these cations into the TiO_2 matrix, which stabilizes trap states.

The lowered the conduction band edge would then increase the injection driving force and ultimately the current^{263–265} but at the cost of a lower V_{OC} . This being said, for anionic electrolytes such as I_3^-/I^- , it was found that cations could improve photovoltages through electrostatic shielding of electrons in the TiO_2 which would lead to reduced recombination rate and improved electron diffusion length²⁶⁶.

An upward shift of the CBE can be achieved by using additives possessing coordinating nitrogen atoms^{267,268} and particularly derivatives of pyridine functionalized at the 4 position, such as the previously mentioned TBP^{269,270}. The induced CBE shift is attributed to a coordination of the nitrogen lone pair to the TiO_2 that would fill the trap states while at the same time not only repelling the electron acceptors in the electrolyte from the surface but also a desorption of cations or protons^{271,272}. Ultimately, it would result in improved electron lifetimes and V_{OC} . Contrarily to the Li^+ effect, an upward shift of the CBE leads to a decreased injection driving force and as explained in earlier paragraphs, photocurrent. Electrolyte solution usually contain both cations and bases which renders their exact mechanism of action ambiguous. TBP can form complexes with Li^+ cations, therefore when both of them are present in the electrolyte their effect should cancel each other, however it appeared that when used together improvements of V_{OC} and charge injection efficiency could be observed^{273,274}.

1.4.2.5 Counter electrode

In the sequence of electron transfers occurring in an operating DSSC, the counter electrode (CE) has the task to regenerate the oxidized redox active electrolyte as pictured in Figure 1.8. The conductive glass substrate has a very high charge transfer resistance ($\sim 10^6 \Omega \cdot \text{cm}^{-2}$) hence it is necessary to use an auxiliary material that will allow a smoother electron transfer¹⁰⁶. There are certain criteria that CE materials have to meet in order to be efficient. First it needs to have a good electrochemical activity towards the selected redox electrolyte, as discussed in the previous paragraph. For example, Pt based electrodes were found to be very efficient with the iodide/triiodide couple but performed poorly with cobalt and copper complexes.

The catalytic activity is usually characterized by the counter electrode charge resistance $R_{\text{CT,CE}}$. High values will be synonym of poor activity and will translate into important resistive losses^{275,276}. The CE should also exhibit high chemical, thermal and electrochemical stability in order to not limit the device lifetime. Due to the particular architecture of a DSSC and the possibility of back illumination, the material should also demonstrate a high transmittance. Additionally, the CE should be made of a cheap, earth abundant and non-toxic material in order to facilitate manufacturing processes.

Platinum CE were among the first to be developed. This popularity was attributed to their high thermal and chemical stabilities, as well as the low $R_{\text{CT,CE}}$ measured with the iodide/triiodide redox couple^{277,278}. Thermal decomposition of platinum chloride salts enabled low Pt-loading of $3 \mu\text{g} \cdot \text{cm}^{-2}$ to be achieved with a transmittance of almost 70%²⁷⁹. The main drawback of Pt CE was related to the inherent low abundance correlated to the high price of Pt.

The emergence of organometallic complexes as efficient redox mediators for DSSCs pushed for the development of new CE materials, when it was found that they had a very low catalytic activities towards Pt counter electrodes²³⁷. Two types of materials were popularized: carbonaceous electrodes and electrodeposited organic polymers. Carbon based CE have attractive features such as good conductivity, high surface area as well as extremely low costs due to the high abundance of carbon²⁸⁰. Additionally, some of these electrode materials possess very low $R_{\text{CT,CE}}$ close to $1 \Omega \cdot \text{cm}^{-2}$ with high surface area^{281–283}.

Electrodeposition of conducting polymer from monomeric solutions was also very popularized notably because of the low cost of materials and easy deposition techniques. The most commonly used conducting polymer for CE is made of poly (3,4-ethylenedioxythiophene) (PEDOT). This material can be deposited on conducting glass as well as flexible substrate from aqueous micellar solutions of the 3,4-ethylenedioxythiophene monomer²⁸⁴. These polymers usually display low of $0.2 \Omega \cdot \text{cm}^{-2}$ for very thin films and short deposition time²⁴⁰.

1.4.3 Characterization techniques for dye sensitized solar cells.

1.4.3.1 Current density potential curves

Current density potential measurements allow to evaluate the efficiency of the device. A dye sensitized solar cell behaves similarly to a p-n junction, hence the diode equation (1.9) can be used to describe the current density-voltage dependence of a DSSC.

This also implies that the equivalent circuit model presented in Figure 1.4a is valid^{94,285}. Current density potential or J-V curves are measured by connecting the device in forward bias and measuring the current density response from a high resistance point (V_{OC}) to a nearly non-existing resistance (J_{SC}), by changing the applied voltage.

This measurement is usually repeated at different light intensities, commonly 10, 50 and 100 % of AM1.5G. The resulting graph is represented in Figure 1.4b. The photovoltaic parameters, J_{SC} , V_{OC} , P_{max} , and FF are subsequently extracted from the J-V curve and the power input (P_{in}) is measured using a calibrated reference Si-cell^{286,287}. These values are then combined according to equations (1.10) and (1.11) and the PCE of the device can be calculated.

1.4.3.2 Incident photon to current conversion efficiency

Conceptually, the incident photon to current conversion efficiency (IPCE) represents the percentage of converted electron per incident photon, at a certain wavelength^{94,106,288}, i.e., it is the ratio of the measured monochromatic short circuit current $J_{SC}(\lambda)$, over the monochromatic photon flux times the elementary charge $q\phi(\lambda)$.

$$IPCE(\lambda) = \frac{J_{SC}(\lambda)}{q\phi(\lambda)} \quad (1.30)$$

Fundamentally, the IPCE will depend on four parameters, the light harvesting efficiency $LHE(\lambda)$ and the regeneration, injection and collection efficiencies^{106,289}. The three latter have been introduced and explained in paragraph 1.4.1.3.

$$IPCE(\lambda) = LHE(\lambda)\eta_{reg}(\lambda)\eta_{inj}(\lambda)\eta_{coll}(\lambda) \quad (1.31)$$

The light harvesting efficiency is representing the film's absorption properties and is related to the dye. More specifically, it relates to the film absorbance $A(\lambda)$ in the following way:

$$LHE(\lambda) = 1 - 10^{-A(\lambda)} = 1 - 10^{-1000 \cdot \Gamma \cdot \epsilon(\lambda)} \quad (1.32)$$

Under the assumption that the dye molar extinction coefficient $\epsilon(\lambda)$ does not vary significantly between the solvated and adsorbed states, the film absorbance $A(\lambda)$ can be used to estimate Γ which is the dye loading in $\text{mol} \cdot \text{cm}^{-2}$ from light absorption measurements of sensitized TiO_2 films²⁹⁰.

The IPCE is usually measured using a split monochromatic light beam, that illuminates the DSSC and a Si solar cell detector to measure the incoming irradiance. The DSSC is short circuited under a bias light is added to mimic operating conditions.

Usually, the reliability of the IPCE measurement can be assessed by integrating the product of the measured IPCE times the AM1.5G solar photon flux (see Figure 1.2b) over the whole electromagnetic spectrum. This value is called integrated current (J_{Int}):

$$J_{Int} = q \int_{UV}^{IR} IPCE(\lambda) \phi_{AM1.5G}(\lambda) d\lambda \quad (1.33)$$

The obtained value should correspond to the short circuit current density measured under AM1.5G conditions. However, dye sensitized solar cells can suffer from mass transport limitations under higher illumination intensities. that will impair the generated photocurrent. Therefore, it is commonly accepted that J_{Int} density can be a slightly higher than the short circuit current density.

1.4.4 Motivations and outline of the thesis

As explained in chapter 1, the development of new materials is a bottleneck in order to push performances of DSSCs and helping both the commercialization as well as the widespread use of this technology. Among these materials, the sensitizer holds an important place in the solar cell and greatly influences the device power conversion efficiency. Nowadays, most of the high efficiency devices are fabricated by applying an organic dye composed according to the D- π -A/D-A- π -A pattern. This concept offers a first guidance and solid ground for the development of new sensitizers. Intensive research efforts have provided us the reason for the success of these dye systems (see paragraph 1.4.2.3). However, still we need further investigation to define clear dye design principles.

This work was conceived with the aim of establishing these design principles and refine the work previous achievements in the field of dye development. In this regard, each chapter has been constructed with a systematic approach that involves three phases.

1. Synthesis of the dyes followed by optical, electrochemical and also quantum mechanical characterization of the molecules.
2. Evaluation of the dyes' performances in full lab-scale devices, using state of the art J-V and IPCE measurements.
3. Further investigation of the dye's performances by means of several in-situ and ex-situ techniques.

In this regard, chapter 2 focuses on the implementation of a new electron acceptor building block, benzothienothiophenedione (BTD), in D-A- π -A dyes. This work aims to provide a methodical procedure for an efficient screening of new core materials for dye design.

It was found that BTD offered better performances when combined with the more planar linker thiophene but at the cost of stronger dye aggregation, compared to the phenyl linker. In devices, the new sensitizers offered PCEs around 5 % under AM1.5G and with the $[\text{Cu}(\text{tmby})_2]^{+2/+1}$ redox couple. Time resolved spectroscopy and small light modulation techniques revealed that these sensitizers suffered from intermolecular aggregation.

In chapter 3, three new D-A- π -A dyes, including an indacenodithiophene π -bridge were studied. The terminal acceptor was altered while the D-A- π segment was kept constant to allow a relevant comparison. Three terminal acceptors units were screened: benzoic acid, benzo-thiadiazole benzoic acid and phenyl cyanoacrylic acid.

A PCE of 5.6 % was measured for devices fabricated with the benzo-thiadiazole benzoic acid unit and the $\text{Cu}(\text{II/I})$ redox electrolyte under AM1.5G. Quantum mechanical investigations revealed that in the case of the benzoic acid dye, its LUMO level was inadequately positioned on the primary acceptor, a benzo-thiadiazole unit, which would explain its poor performance of almost 3 %. This study highlighted the importance of carefully choosing the relative electron withdrawing strengths of both acceptors in D-A- π -A dye. More precisely, the terminal acceptor has to be stronger than the primary in order to not impair the dye performances.

The next chapter studied the challenging symmetrical diketopyrrolopyrrole (DPP) building block. In this regard, three D-A- π -A dyes were synthesized, including either a thiophene, furan or phenyl linking unit.

Surprisingly, the phenyl-based dye, MS17, was found to be the best performing dye with an impressive V_{OC} of 970 mV, corresponding to a PCE of 7.67% in devices fabricated with $[Cu(tmby)_2]^{+2/+1}$ and under AM1.5G. These results constitute an unprecedented performance for a symmetrical DPP dye with a Cu(II/I) redox electrolyte. The PCE achieved by MS17 was found to be two folds higher than its furan and thiophene analogue. DFT calculations highlighted that the phenyl ring in MS17 reduced the planarity of the dye. Ultimately, it would result in a weaker dye aggregation and improved electron injection efficiency and electron lifetime. Interestingly, the furan ring induced significant structural distortions, which translated into a more distorted conformation of the corresponding dye compared to the thiophene analogue. This effect was ascribed to a smaller atomic radius of the oxygen atom that would contract the five-membered furan ring and reduce the steric interactions of its neighboring units.

Chapter 5 focused on D-A- π -A dyes constructed with a dithienopyrrole π -linker. This latter offers more synthetically accessible alternative to the popular cyclopentadithienyl. Two primary acceptors were screened: benzo-thiadiazole (MS9) and benzo-oxadiazole (MS20), with the aim of probing the effect of this delicate atom substitution. In devices under AM1.5G, MS9 produced a record J_{SC} of $16.43 \text{ mA}\cdot\text{cm}^{-2}$ for a $[Cu(tmby)_2]^{+2/+1}$ based device. The associated PCE was impressively high with a value of 12.5 %. MS20 offered a lower PCE of 10.8 %. The origin of this difference was found to be a shorter electron lifetime measured in MS20 based devices. Extensive analysis of DFT calculations indicated that MS20 possess a less distorted conformation than MS9, especially around the electron donating unit. This difference was ascribed to a smaller atomic radius of oxygen compared to sulfur, that would decrease the steric hindrance around the electron donor, ultimately impairing its Cu(II) repelling abilities.

In chapter 6, the dye structure was reduced to a minimal D-A pattern. Three different acceptors were tested, each including either a benzo-thiadiazole, benzo-oxadiazole and benzo-triazole combined with a simple benzoic acid or 4-ethynyl benzoic acid anchoring group. Furthermore, a short synthetic route was developed, which consisted in a one-pot, two steps method that allows a fast and easy synthesis of the dye. In spite of their very simple structure, each dye produced above 1 V open-circuit voltages with the $[Cu(tmby)_2]^{+2/+1}$ electrolyte and under AM1.5G. The differences in PV performances for these dyes mainly originated from their different photo-current, dictated by the position of their LUMO level as well as their spectral response. However, a very promising PCE of 6.9 % was achieved for the two dyes including the benzo-oxadiazole units.

Finally, chapter 7 pushed the D-A dye concept further by optimizing the chain length of the electron donor. More precisely, the donor size was increased by two folds, from hexyl (MS4) to dodecyl (MS5), in a dye based on the benzo-thiadiazole benzoic acid core. Gratifyingly, MS5 offered a record V_{OC} of 1.24 V corresponding to a PCE of 8 % with the $[Cu(tmby)_2]^{+2/+1}$ electrolyte and under AM1.5G. This latter was co-sensitized with a narrow-band gap absorber, XY1b, to produce a recorded PCE of 13.5 % under similar device conditions.

Further investigation of the device based on MS5 revealed an ideality factor near to unity, which is very uncommon for a DSSC. This indicates that for MS5 based devices, recombination of electron with the Cu(II) species occurs mainly via conduction band electrons.

Chapter 2 : Implementing benzothienothiophenedione as electron accepting unit in D-A- π -A dyes.

Contributions:

In this chapter, I designed, synthesized and characterized the dyes, measured TRPL and small light modulation spectra. Jean-David Decoppet fabricated the devices, samples for TAS and TRPL as well as measured JV curves and IPCEs of the devices. Ma Wei and Jing Fu performed the computational calculations and Etienne Socie measured the TAS.

2.1 Introduction

In this first chapter, we implemented for the first time an electron accepting building block named 5,7-bis(2-ethylhexyl)-4H,8H-benzo[1,2-c:4,5-c'] dithiophene-4,8-dione (BTD) in D-A- π -A dyes. This electron acceptor was used to synthesize efficient wide band gap polymers for fullerene free organic solar cells^{291–295}. This building block also presents several attractive features that could benefit organic dyes for DSSC applications.

Firstly, a fully conjugated and planar structure that ensures an efficient electronic communication throughout the molecule. Then, BTD contains two, strongly withdrawing carbonyl groups and finally, two branched aliphatic sidechains that could provide good solubility and can reduce dye aggregation. We combined this BTD unit with the strong electron donor, N-(2',4'-alkoxy-[1,1'-biphenyl]-4-yl)-2',4'-alkoxy-N-phenyl-[1,1'-biphenyl]-4-amine. This core is commonly encountered in modern organic sensitizers because of its high electron donation but also its ability to efficiently prevent recombination of free electrons with the electrolyte^{172,184,211,296}. Along with the new BTD acceptor, two different alkoxy chains were screened: n-dodecyloxy (C12) and n-hexyl (C6), as well as two distinctive π -bridges: phenyl (Ph) and thiophene (Th). A similar cyanoacrylic acid anchoring group was employed. All together, we combined these building blocks and synthesized three new dyes coded: **MS1** (C12/Ph), **MS2** (C6/Th) and **MS3** (C12/Th) (see Figure 2.1a).

The new dyes were firstly synthesized and their energy levels characterized experimentally as well as by means of density functional theory (DFT). Then, liquid state dye sensitized solar cells were fabricated using the new sensitizers and the redox active copper electrolyte $[\text{Cu}(\text{tmby})_2]^{+2/+1}$ (tmby=4,4',6,6'-tetramethyl-2,2'-bipyridine). In a second step, time resolved spectrometry as well as small light modulation techniques were applied in order to study the effects of the building blocks and the BTD unit, on the measured photovoltaic performances.

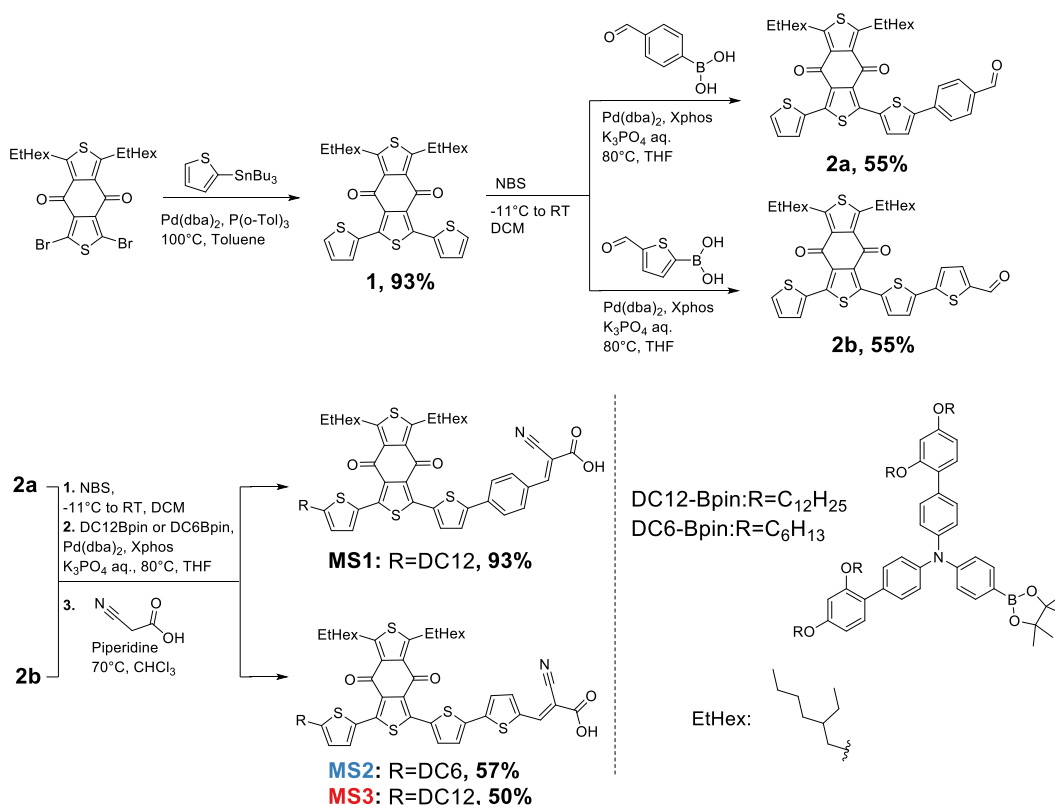
2.2 Results and discussion

The detailed synthesis of **MS1**, **MS2** and **MS3** was summarized on Scheme 2.1. Briefly, the procedure started with a Stille coupling between the commercially available dibrominated BTB building block and 2-tributyl-stannyl thiophene, to yield the desired product **1** in a satisfying yield of 93%.

This compound was then brominated by 1 equivalent of N-bromosuccinimide and subsequently submitted to a Suzuki coupling, with either 4-formylphenylboronic acid or 5-formylthiophen-2-ylboronic acid, to yield compounds **2a** (Ph) and **2b** (Th).

These two latter were submitted to a second bromination/Suzuki coupling sequence to attach the electron donating unit. **2a** was functionalized with 1 equivalent of N- (2',4'-dodecyloxy-[1,1'-biphenyl]-4-yl)-2',4'-dodecyloxy-N-phenyl-[1,1'-biphenyl]-4-amine whereas **2b** was split into two portions that were reacted with either N- (2',4'-dodecyloxy-[1,1'-biphenyl]-4-yl)-2',4'-dodecyloxy-N-phenyl-[1,1'-biphenyl]-4-amine or N- (2',4'-hexyloxy-[1,1'-biphenyl]-4-yl)-2',4'-hexyloxy-N-phenyl-[1,1'-biphenyl]-4-amine.

Finally, the obtained aldehydes intermediates were directly reacted with an excess of cyanoacrylic acid under the Knoevenagel condensation conditions to yield the final dyes **MS1**, **MS2** and **MS3** (see Figure 2.1a).



Scheme 2.1. Synthetic route for **MS1**, **MS2** and **MS3**.

Figure 2.1b and c show the absorption spectra of the three dyes in diluted THF solution and adsorbed on the surface of a 2.2 μm thick transparent TiO_2 film. Two distinct peaks can be observed in Figure 2.1b.

The first maximum, located around 340 nm, is assigned to the π - π^* transition while the second peak corresponds to the intramolecular charge transfer (CT). From Figure 2.1b, it can be seen that the wavelength of the π - π^* transition, was not affected by the structural modification. On the other hand, the position of the CT peak is red shifted in the following order **MS1** < **MS2**, **MS3**. This results indicates that the thiophene unit, present in **MS2** and **MS3**, induces a 15 nm red shift of $\lambda_{\text{max,CT}}$ compared to the dye containing the phenyl unit (**MS1**).

The dyes' molar absorptions were found to be very high, with values above $2 \times 10^4 \text{ M}^{-1} \cdot \text{cm}^{-1}$ for all dyes. The steady state emission spectra (see Figure 0.1b) of the dyes was recorded from diluted THF solutions. It was observed that the emission maxima followed the same trend as the absorption wavelengths $\lambda_{\text{max,CT}}$.

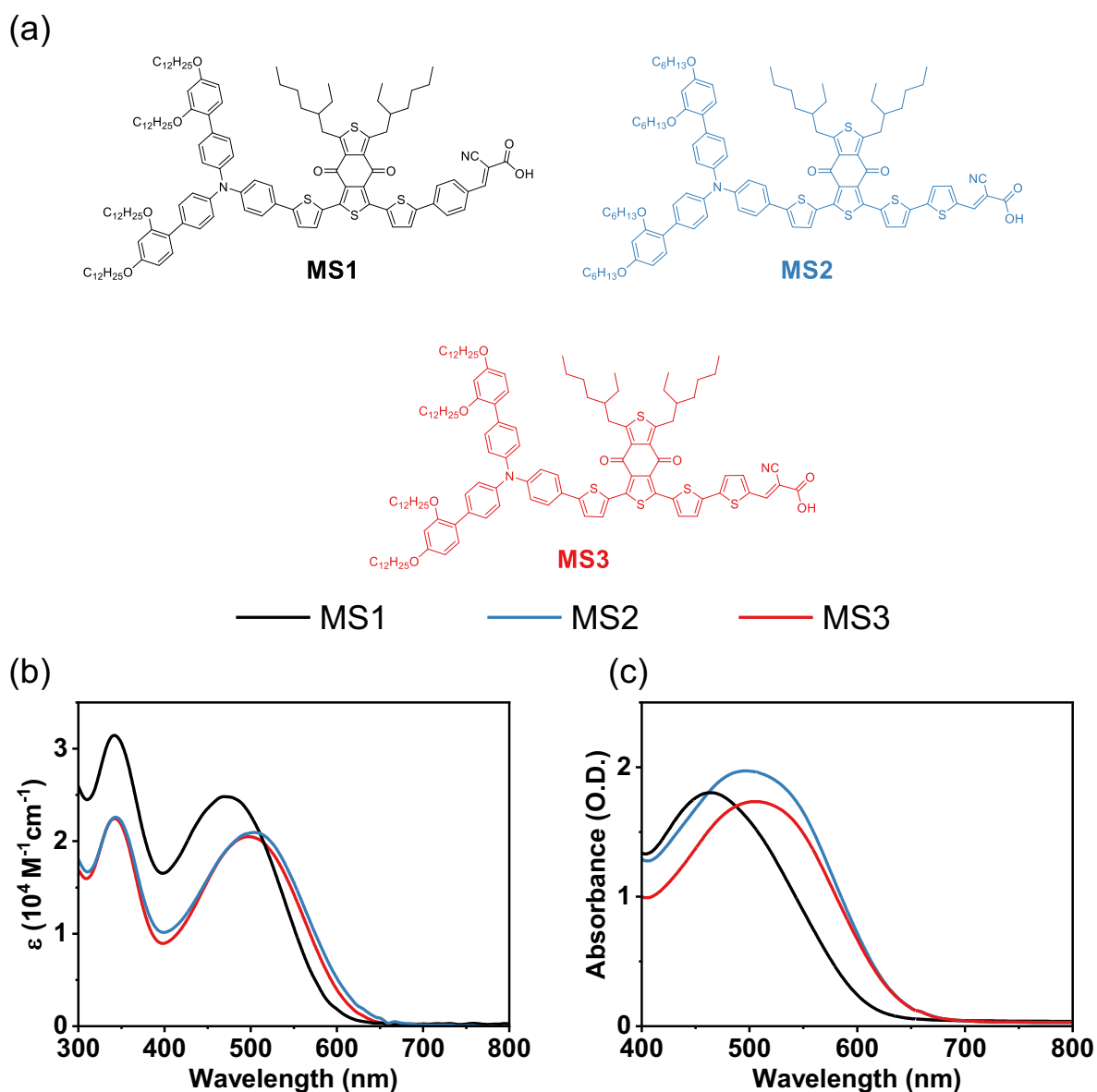


Figure 2.1. (a) Chemical structures of the new BTB based dyes **MS1**, **MS2** and **MS3**. (b) Absorption spectra measured from diluted THF solutions (c) 2.2 μm thick TiO_2 sensitized with **MS1**, **MS2** and **MS3**.

The Stoke shifts of **MS1**, **MS2** and **MS3** were found to be very similar with values of respectively 156, 149 and 153 nm. This suggests that the chemical nature of the π birthing unit does not induce significant geometries changes between the dyes' ground and excited states. The absorption spectra of sensitized titania films (Figure 2.1c) was measured and the trend in $\lambda_{\text{abs,max}}$ was found to be consistent with the solution experiments in Figure 2.1b.

Table 2.1. Optical and electrochemical properties of MS1, MS2 and MS3.

	λ_{onset}^a [nm]	$\lambda_{\text{max,CT}}(\epsilon)^a$ [nm($10^4 \text{ M}^{-1} \cdot \text{cm}^{-1}$)]	$\lambda_{\text{PL,max}}^{a,*}$ [nm]	$\lambda_{\text{abs,max}}^b$ [nm]	E_{HOMO}^c [V vs. NHE]	E_{LUMO}^d [V vs. NHE]	E_g^e [eV]
MS1	579	486(2.5)	625	473	1.01	-1.14	2.15
MS2	600	501(2.0)	724	497	1.06	-1.01	2.07
MS3	600	499(2.0)	736	501	1.07	-1.00	2.07

^aObtained from diluted THF solutions. ^bObtained from measurement 2.2 μm thick TiO_2 films sensitized with the dyes. ^cEstimated from the onset of the oxidation potential of the dyes adsorbed on TiO_2 measured using cyclic voltammetry, with Ferrocene as internal standard and subsequently converted to NHE by adding 0.624 V to the value²⁹⁹. ^dObtained from $E_{\text{HOMO}} - E_g$. ^eEstimated using: $E_g: 1242/\lambda_{\text{onset}}$. *Samples excited at 500 nm.

The dyes' HOMO/LUMO levels were obtained from cyclic voltammetry (CV) measurements of titania electrodes sensitized with each respective dyes (see Figure 0.2). As reported on Table 2.1, all dyes were found to have very similar E_{HOMO} lying around 1 V vs. NHE. This value should ensure a sufficient driving force for dye regeneration by the $[\text{Cu}(\text{tmbpy})_2]^{+2/+1}$ complex.

Furthermore, the similar E_{HOMO} values indicate no particular influence of the aromatic cycle on the oxidation potential of the dye. This result is in according with what was expected, as the HOMO level is defined by the chemical structure of the electron donating moiety. The LUMO levels, were estimated by subtracting E_g to the E_{HOMO} .

It was observed that the two thiophene based dyes (**MS2** and **MS3**), possess similar LUMO levels, both downwardly shifted by 100 mV, compared to **MS1**, which explains the red-shifted $\lambda_{\text{max,CT}}$. This result can be ascribed to the thiophene aromatic unit that possess a lower resonance stabilization energy than phenyl.

Furthermore, this five membered thiophene ring provides more planarity, which increase the dyes' effective conjugation length, compared to the phenyl ring^{297,298}. The LUMO levels of these dyes is located lower than the conduction band of TiO_2 (-0.5 V vs. NHE)¹⁰⁶, which should provide enough driving force for the electron injection process²⁰⁹.

To fully understand the electronic and optical disparities between **MS1**, **MS2** and **MS3**, their HOMO/LUMO frontier orbitals were calculated using density functional theory (DFT) (Figure 2.2). The results showed almost identical distributions of the HOMO and LUMO wave functions regardless of the π -bridge.

More specifically, the HOMO orbitals were mainly localized on the N - (2',4'-alkoxy-[1,1'-biphenyl]-4-yl) -2',4'-alkoxy -N-phenyl -[1,1'-biphenyl] -4-amine donor whereas the LUMO orbitals were spreading from the π -linker up to the cyanoacrylic acid acceptor moiety (see Figure 2.2). This adequate position of the wave-functions should guarantee a rapid charge transfer transition.

Consequently, HOMO-LUMO photo-excitation should issue an efficient electron transfer from the donor to TiO_2 substrate via the anchoring cyanoacrylic acid group. Finally, it should be noticed that the BTD unit only slightly participates in the delocalization of the orbitals.

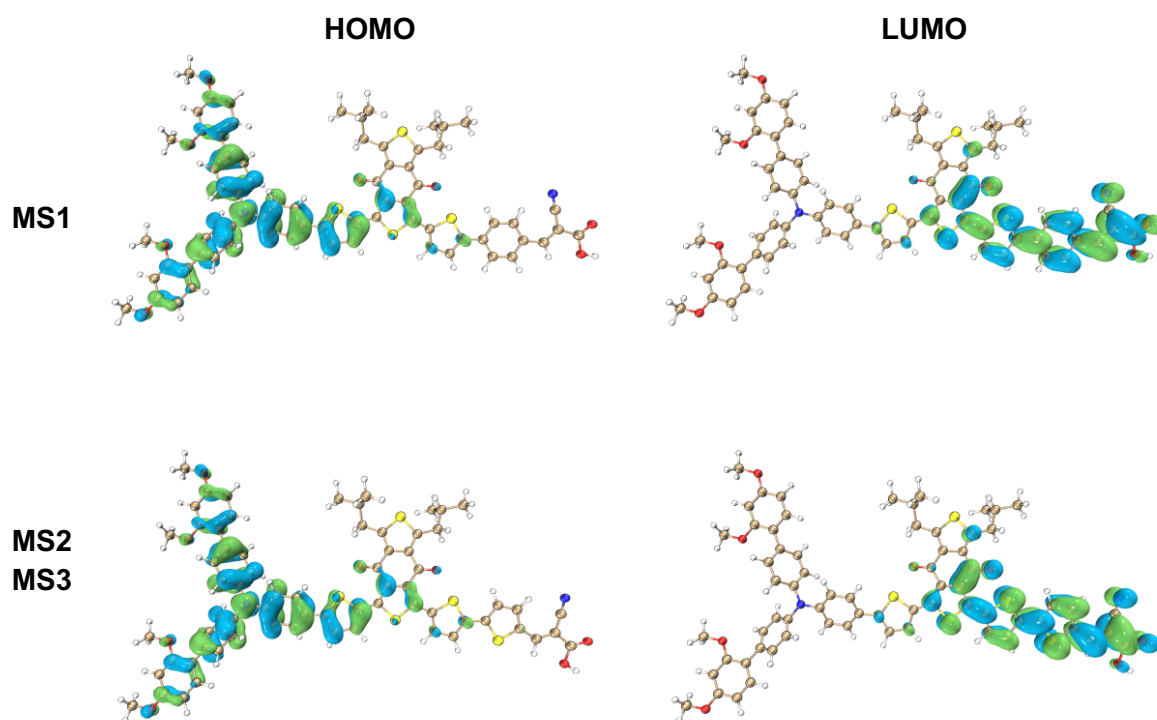


Figure 2.2. Distribution of the molecular orbitals obtained using the B3PW91 functional and 6-31G(d,p) basis sets.

The equilibrium geometries of the dyes' ground (S_0) and first excited state (S_1) were calculated using the CAM-B3LYP functional and 6-31G(d,p) basis sets (see Figure 2.3). The results highlighted marked structural differences between the 6 membered phenyl versus the 5 membered thiophene unit. More precisely, the ground state geometry of **MS1** displayed an angle of 2.91° between the thiophene adjacent to BTD and the phenyl ring.

On the other hand, the S_0 state of **MS2/MS3** showed almost perfect planarity at the same angle with a value of 0.26° . The configurations of the excited state displayed similar structures except for the angle between the phenyl ring of the electron donating unit and the thiophene adjacent to BTD.

It was observed that this angle was more twisted in **MS2/MS3** than in **MS1** with values of respectively 11.18° vs. 6.58° . More generally, the dyes' ground states have more twisted geometries than their respective excited-states.

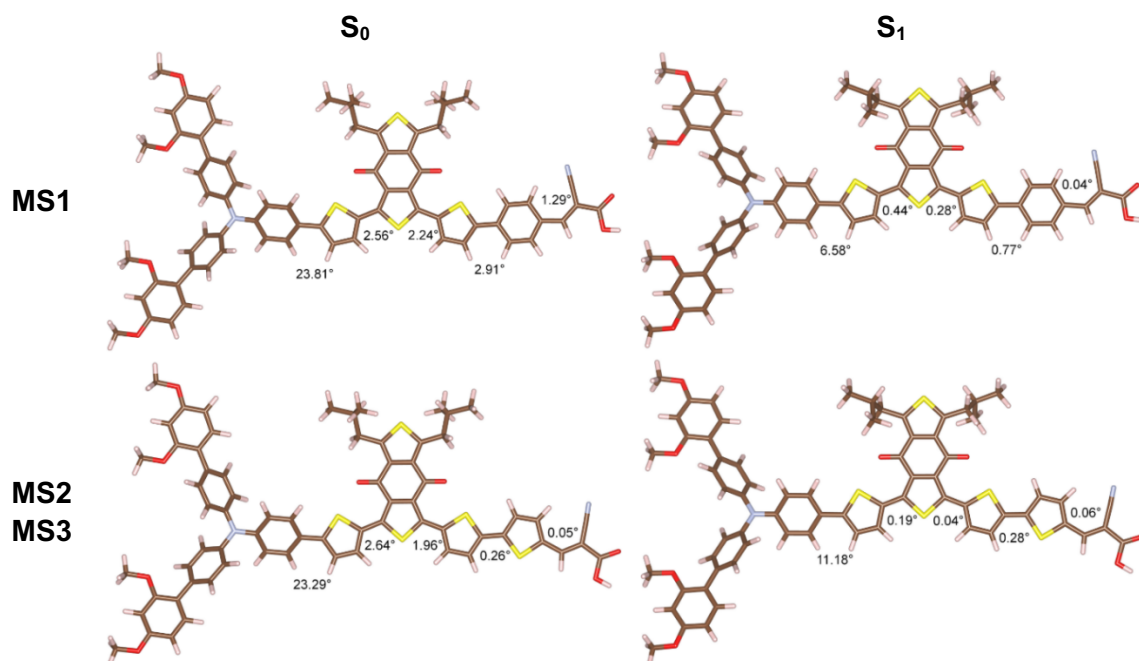


Figure 2.3. Geometry optimized structures of the ground state (S_0) and the first excited state (S_1) of MS1, MS2 and MS3 with the corresponding dihedral angles, determined using the CAM-B3LYP functional and 6-31G(d,p) basis sets.

The performances of **MS1**, **MS2** and **MS3** were evaluated under AM1.5G irradiation ($100 \text{ mW}\cdot\text{cm}^{-2}$) in devices fabricated with $[\text{Cu}(\text{tmby})_2]^{+2/+1}$. Table 2.2 shows the summarized photovoltaic parameters for each dye. The effect of the bridging unit can be observed by comparing the performances of **MS1** with **MS3**, which both possess similar chain length on the electron donor.

These two dyes showed similar photocurrent values close to $7.5 \text{ mA}\cdot\text{cm}^{-2}$, despite the 15 nm red-shifted absorption of **MS3**. Interestingly, different photo voltages were measured for **MS1** (910 mV) and **MS3** (859 mV). Shortening the chains on the electron donating moiety (**MS2** vs. **MS3**) seems to improve the current by almost $2 \text{ mA}\cdot\text{cm}^{-2}$. The photo voltage is also improved by roughly 30 mV, which is very surprising as longer alkyl chains on the electron donating unit are expected to slow the recombination rate of free electrons with the electrolyte and improve the photovoltage³⁰⁰. Comparatively, the PCEs follow the order **MS2** > **MS3** > **MS1**.

Table 2.2. Detailed PV performances measured under AM1.5G ($100 \text{ mW}\cdot\text{cm}^{-2}$).

	J_{sc} [$\text{mA}\cdot\text{cm}^{-2}$]	V_{oc} [mV]	FF [%]	PCE ^a [%]
MS1	7.4(8±1)	910(880±31)	68(69±3)	4.57(5±1)
MS2	9.3(9.2±0.3)	883(890±12)	65(66±4)	5.36(5.5±0.6)
MS3	7.7(7.4±0.3)	859(860±23)	76(69±4)	5.03(4.4±0.5)

^aParenthesis values were averaged over 4 cells.

Figure 2.4b shows the incident photo to current conversion efficiency (IPCE) of the corresponding cells, highlighting the more red shifted spectral response of **MS2** and **MS3**. As predicted by their short circuit current densities, **MS1** ($7.4 \text{ mA}\cdot\text{cm}^{-2}$) and **MS3** ($7.7 \text{ mA}\cdot\text{cm}^{-2}$) show IPCE maxima in the visible light region fluctuating between 40-50%, which is roughly 10% lower than **MS2** ($9.3 \text{ mA}\cdot\text{cm}^{-2}$).

Surprisingly, **MS1** and **MS3** were found to have similar J_{SC} values, despite the more red-shifted absorption onset displayed by **MS3**. However, it can be seen in Figure 2.4b that the broader spectral response of **MS3**, is impaired by IPCE values roughly 10% lower than **MS1** between 350 and 500 nm.

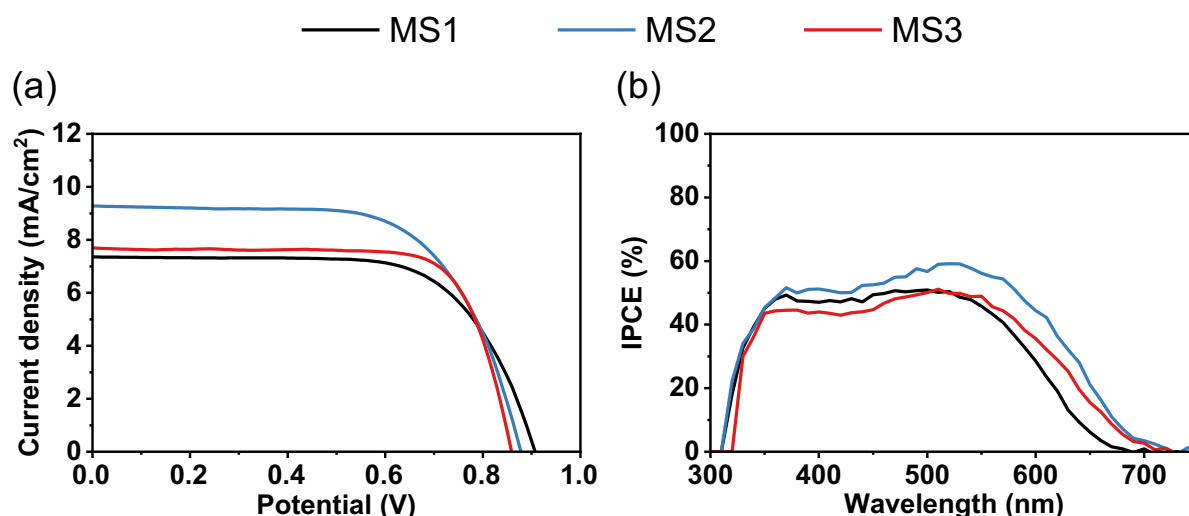


Figure 2.4. (a) J - V curves of cells measured under AM1.5G. (b) IPCE spectra of the cells.

The dyes' PV performances were further investigated by mean of transient absorption spectroscopy (TAS) and time resolved photoluminescence (TRPL).

Figure 2.5a, b and c show the results of TAS measurements performed on half devices sensitized with each of the three new dyes containing either an inert electrolyte or the copper-based redox couple. The ΔA traces of dye cations produced during charge injection from the excited state into the conduction band of TiO_2 was monitored.

The lifetimes corresponding to each decay curves are presented in Table 2.3. Conceptually, τ_{inert} represents the lifetime of the dye cation (D^+) recombining with the injected electron, whereas $\tau_{\text{Cu(II/I)}}$ is the reciprocal of the rate constant of the interception of D^+ by the redox active electrolyte.

Table 2.3. Lifetimes and η_{reg} obtained from TAS.

	τ_{inert} [μs]	$\tau_{\text{Cu(II/I)}}$ [μs]	η_{reg}^a [%]
MS1	178	9.2	95.1
MS2	48	7.9	85.9
MS3	35	7.6	82.2

^aThe regeneration efficiency was calculated using: $\eta_{i,\text{reg}} = k_{i,\text{Cu(II/I)}} / (k_{i,\text{inert}} + k_{i,\text{Cu(II/I)}})$, with $k_{i,\text{Cu(II/I)}} = 1 / \tau_{i,\text{Cu(II/I)}}$, $k_{i,\text{inert}} = 1 / \tau_{i,\text{inert}}$, $i = \text{MS1, MS2 or MS3}$.

The lifetimes of ΔA decays obtained from the fittings, show that the dye cations containing thiophene units (**MS2** and **MS3**) possessed shorter τ_{inert} than their phenyl analogue by more than 3 folds (see Table 2.3). As highlighted by DFT calculations, **MS2** and **MS3** showed more planarity in the S_0 state, compared to **MS1**. Hence, the trend in τ_{inert} could be the result of a more pronounced formation of dye aggregates in the case of **MS2** and **MS3**.

These aggregates could then accelerate the rate of electron recapture^{201,202}. On the contrary, $\tau_{\text{Cu(II/I)}}$ was not as drastically affected as τ_{inert} by the nature of the bridging unit with values of 9.2, 7.9 and 7.6 μs for respectively **MS1**, **MS2** and **MS3**. Interestingly, it was observed that the donor's aliphatic chains length (**MS2** vs. **MS3**) does not impair the dye regeneration time. Overall, the regeneration efficiencies were high with yields exceeding 80% for all dyes. This result is consistent with the adequately positioned E_{HOMO} levels estimated from CV measurements of the dyes adsorbed on titania films.

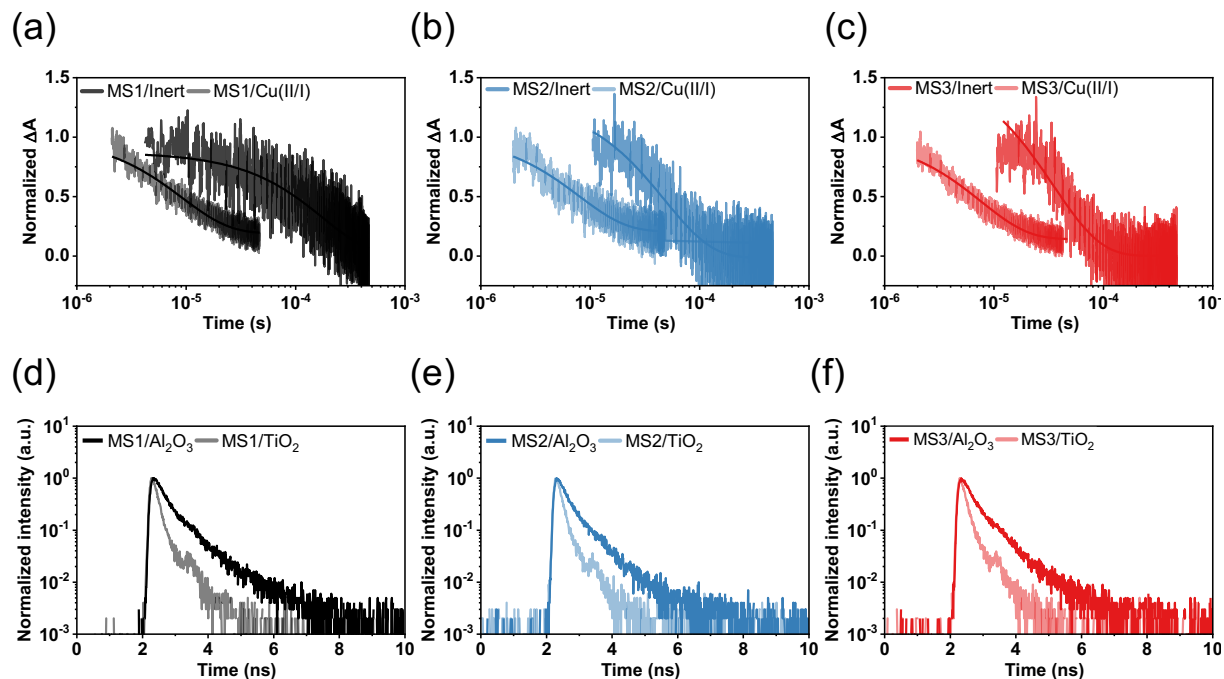


Figure 2.5. (a-c) Time-evolution of the dye oxidized state absorbance monitored at $\lambda_{\text{Probe}} = 820 \text{ nm}$ upon pulsed laser excitation at $\lambda_{\text{Pump}} = 500 \text{ nm}$ of half-devices composed of $4 \mu\text{m}$ thick TiO_2 layers sensitized with MS1 (a), MS2 (b) and MS3 (c), in contact with an inert electrolyte or a redox-active electrolyte containing the $[\text{Cu}(\text{tmby})_2]^{+2/+1}$ couple. The solid lines represent the monoexponential fittings. The laser fluence for the inert electrolyte samples was set to $2.2 \mu\text{J}\cdot\text{cm}^{-2}$ and subsequently increased to $0.6 \text{ mJ}\cdot\text{cm}^{-2}$ for the samples containing the copper electrolyte. (d-f) TRPL decays of half-cells composed of $4 \mu\text{m}$ thick TiO_2 or Al_2O_3 layers dyed by MS1 (d), MS2 (e) or MS3 (f), in contact with an inert or a redox-active electrolyte based on the $[\text{Cu}(\text{tmby})_2]^{+2/+1}$ redox couple ($\lambda_{\text{Pump}}=520 \text{ nm}$, $\lambda_{\text{Probe}}=750 \text{ nm}$).

TRPL was used to investigate the electron injection dynamics of the dyes^{301,302}. Each dye was absorbed on either $4 \mu\text{m}$ thick TiO_2 or $4 \mu\text{m}$ Al_2O_3 film and mounted in half devices. To mimic the operating conditions, the cells were injected with an electrolyte used in full cells, containing the copper electrolyte and its additives.

The decay curves are presented in Figure 2.5d, e and f. Every dye shows a faster decay upon switching from the alumina layers to the titania.

Alumina has a higher conduction band than TiO_2 , thus preventing electron injection electron injection and only allowing the excited state quenching⁹⁴. Once adsorbed on TiO_2 , the decay is accelerated due to the injection of the electron into the conduction band. The decay curves were fitted by a bi-exponential model convoluted with the instrument response function (IRF) and the extracted lifetimes averaged according to their respective amplitudes before being presented in the table below.

All the average lifetimes were found to be strikingly short lifetimes, within the order of the sub-nanosecond, regardless of the substrate (see Table 2.4). When adsorbed on Al_2O_3 , the dyes displayed $\tau_{\text{av}}(\text{A})$ lying around 0.5 ns whereas on TiO_2 , they showed $\tau_{\text{av}}(\text{T})$ lying around 100 ps. Overall, the η_{inj} of **MS1**, **MS2** and **MS3** were found to lie above 70%. It was speculated that these short lived excited state might result from the formation of dye aggregates.

Table 2.4. Averaged lifetimes on Al_2O_3 ($\tau(\text{A})_{\text{av}}$), TiO_2 ($\tau(\text{T})_{\text{av}}$) and η_{inj} obtained from TRPL.

	$\tau_{\text{av}}(\text{A})$ [ps]	$\tau_{\text{av}}(\text{T})$ [ps]	$\eta_{\text{inj}}^{\text{a}}$ [%]
MS1	450	105	77
MS2	360	93	74
MS3	410	108	74

^aThe injection efficiency was estimated using: $\eta_{\text{i, inj}} = 1 - \tau(\text{T})_{\text{i, av}} / \tau(\text{A})_{\text{i, av}}$, with $I = \text{MS1, MS2 or MS3}$.

In the next stage, transport time (τ_{TR}), charge extraction (Q_{OC}) and electron lifetimes (τ_{n}) measurements were performed on devices fabricated with the three new dyes to further explain the trends observed in the PV performances (see Table 2.2). As seen in Figure 2.6a τ_{TR} was found to be similar for all the dyes. Furthermore, Figure 2.6b indicate a downward shift of the titania conduction band edge (CBE) due to lower states distribution³⁰³ in the order: **MS2>MS3>MS1**. It is commonly accepted that shifts in the TiO_2 CBE are depending on the amount of dye adsorbed on TiO_2 (N), its dipole moment (μ) and orientation with respect to the normal of the surface (θ)^{304,305}:

$$\Delta\text{CBE} = \frac{N \cdot \mu \cdot \cos(\theta)}{\epsilon_r \cdot \epsilon_0} \quad (2.1)$$

The total dipole moment (μ) of the dyes were found to be 15.96 and 18.84 Debye for respectively **MS1** and **MS2/MS3**, which rules out this factor as the main reason for the observed CBE shifts. The dye loadings' were found to be, 33.7 (**MS1**), 44.1 (**MS2**) and 38.3 $\text{nmol} \cdot \text{cm}^{-2} \cdot \mu\text{m}^{-1}$ (**MS3**), which also cannot explain the lines' relative positions in Figure 2.6b. **MS2** presents the most downwardly shifted CBE despite having the highest loading (44. 1 $\text{nmol} \cdot \text{cm}^{-2} \cdot \mu\text{m}^{-1}$).

The last parameter is the tilt angle between the dye and the normal vector of the TiO_2 surface. From Figure 2.6b and equation (2.1), we can speculate that **MS2** presents the most tilted adsorption geometry, followed by **MS3** and finally **MS1**. This result suggests that the thiophene based dyes (**MS2** and **MS3**) could suffer from more important dye aggregation.

The electron lifetime estimates of the relative recombination rate between injected electrons and the $[\text{Cu}(\text{tmby})_2]^{+2}$ species. Figure 2.6c shows that τ_{n} follows the order **MS1 > MS2 > MS3**, which is similar to the trend observed with the open circuit voltages in Table 2.2: **MS1 > MS2 > MS3**.

Considering the behaviors observed Figure 2.6b and c, the photo voltage difference between **MS1** (910 mV) and **MS2** (883 mV) seems to originate from lower CBE of **MS2** based devices. Compared to the other dyes, **MS3** (859 mV), seems to suffer from short electron lifetimes as well as a low lying CBE. More generally, the faster charge recombination with the electrolyte, could also result from inhomogeneous dye coverage of the TiO_2 surface caused by the formation of localized dye aggregates.

Ultimately, these aggregates could leave areas of the mesoporous network exposed to the electrolyte, thus facilitating the recombination of free electrons with $[\text{Cu}(\text{tmby})_2]^{+2}$.

The order in the charge collection efficiency (Figure 2.6d) was found to be similar as the one observed in Figure 2.4b: **MS2** > **MS1** > **MS3**. As described by equation (1.31 and paragraph 1.4.3.2, the IPCE depends on the light harvesting (LHE), regeneration (η_{reg}), injection (η_{inj}) and collection efficiencies (η_{coll})^{106,289}. The LHE was found to be readily high, with values close to unity for **MS1**, **MS2** and **MS3** (see Figure 0.35c).

This result combined with the definition of IPCE seems to indicate that the PV performances of BTD dyes are mainly limited by their η_{coll} and η_{inj} . More precisely, we suspect fast recombination of the injected electron with the Cu(II) species present in the electrolyte and important self-quenching of the dye excited state to be the main causes.

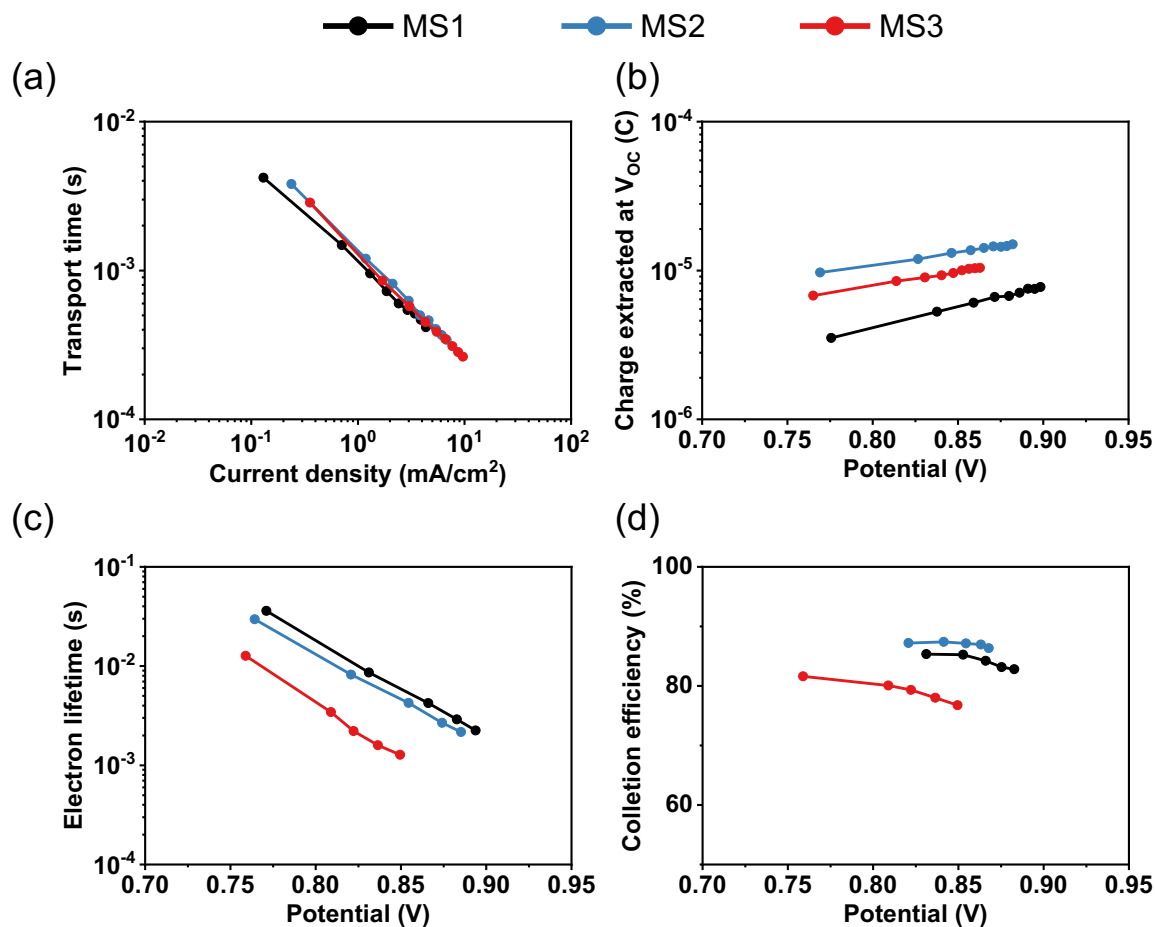


Figure 2.6. (a) Transport time as function of current density, (b) Extracted charge at open circuit potential, (c) Electron lifetime and open circuit potential and charge collection efficiency as function of potential. The charge collection efficiency (η_{coll}) was estimated from the electron lifetime (τ_n) and the transport time (τ_{TR}) using the following equation: $\eta_{\text{coll}} = 1/(1 + \tau_{\text{TR}}/\tau_n)$.

2.3 Conclusion

In summary, we reported the first ever synthesis of three new D-A- π -A dyes containing a 5,7-bis(2-ethylhexyl)-4H,8H-benzo[1,2-c:4,5-c'] dithiophene-4,8-dione (BTD) unit as electron acceptor. To optimize the structure, the π bridging and donor units were varied.

These dyes produced a PCE of 5 % under AM1.5G conditions with the $\text{Cu}(\text{tmby})_2^{+2/+1}$ electrolyte. The three dyes were studied by means of time resolved spectroscopy in order to investigate the origins of their different performances. Small light modulation techniques, revealed that all dyes suffered from important recombination between free electrons and the $\text{Cu}(\text{II})$ species, which impaired their photovoltages and photocurrents.

It was hypothesized that the high recombination rate with the electrolyte, might result from an inhomogeneous dye coverage of the titania surface, leaving areas of bare semiconductor exposed to the electrolyte. This insufficient insulation of the surface could originate from the formation of dye aggregates, triggered by the dyes' flat geometries. Furthermore, it was speculated that the deleterious planarity of the dyes could be caused by the flat BTD unit.

Chapter 3 : A structural study of D-A- π -A dyes, constructed with an indacenodithiophene π -bridge.

Contributions:

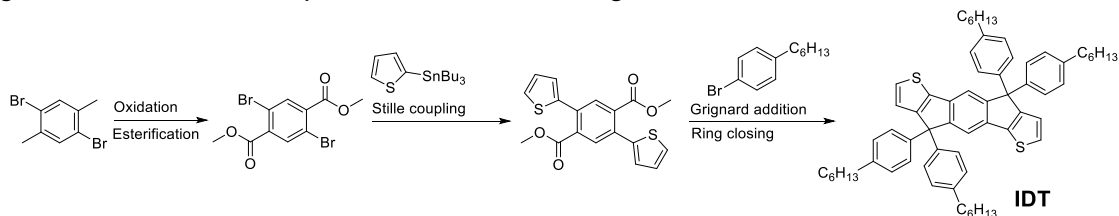
In this chapter, I have designed, synthesized, characterized the dyes and measured TRPL. Natalie Flores Diaz fabricated the devices, samples for TRPL and TAS, measured the small light modulation spectra as well as JV curves and IPCEs of the devices. Dr. Yameng Ren provided the dye solution conditions. Ma Wei and Jing Fu performed the computational calculations and Etienne Socie measured the TAS.

3.1 Introduction

Modern organic dyes rely on a Donor- π -Acceptor (D- π -A) pattern. This concept was extended further by addition of an auxiliary electron accepting unit, between the donor and the π -bridge. These new D-A- π -A dyes displayed a better stability and broader spectral response than their D- π -A analogues¹⁻³. Indacenodithiophene (IDT) is a compound commonly encountered in the field of organic photovoltaics, where it is used as potent building block for Donor-Acceptor polymer solar cells^{306,307}.

It possesses several attractive structural features that could benefit organic dyes for DSSC applications. Notably, IDT displays a rigid conjugated backbone that comprises a phenyl ring linked to two adjacent thiophene units. These units are interconnected via a two C_{sp^2} - C_{sp^2} bonds on one side and two bridging sp^3 on the other. These latter can be used to install various aliphatic units. An example of IDT-derivative can be seen on Scheme 3.1, with 4,4,9,9-tetrakis(4-hexylphenyl)-4,9-dihydro-s-indaceno[1,2-b:5,6-b']dithiophene (IDT).

This latter is accessed via a procedure that starts with the commercially available 1,4-dibromo-2,5-dimethylbenzene. This latter is firstly oxidized to the corresponding di-acid and subsequently esterified. At this point, the adjacent aromatic units, in this case thiophene units, can be installed via Pd-catalyzed cross-coupling. The molecule is finalized by a sequential Grignard addition of the aliphatic units followed ring closure under acidic conditions.



Scheme 3.1. Synthetic route to IDT.

In dye sensitized solar cells, IDT has only been used in D- π -A dyes^{308,309}. In this regard, we report a structural study and synthesis of three new IDT dyes, coded **MS6**, **MS7** and **MS8** synthesized following the D-A- π -A pattern. For comparative purposes the electron donating unit was chosen to be a N-(2',4'-bis(alkoxy)-[1,1'-biphenyl]-4-yl)-2',4'-bis(dodecyloxy)-N-phenyl-[1,1'-biphenyl]-4-amine unit because of its strong electron donating character as well as bulkiness.

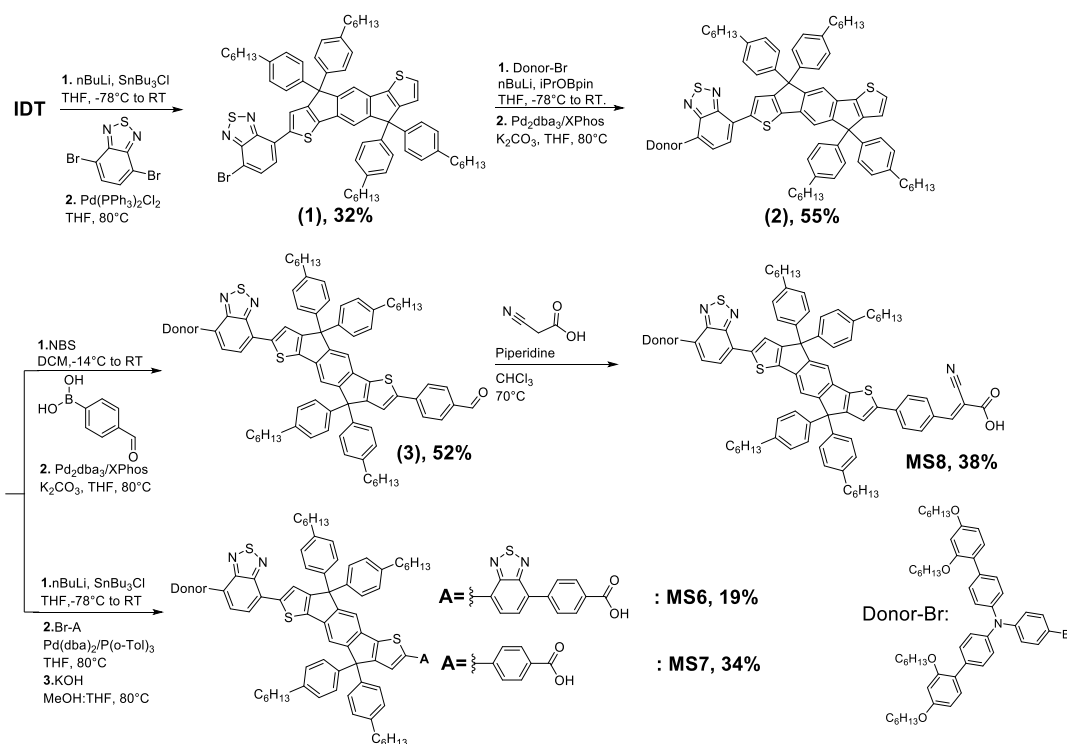
This donor was connected via a benzo-thiadiazole acceptor unit to the IDT. We screened three different electron acceptor/anchoring units: 4-(benzo-thiadiazol-4-yl) benzoic acid (**MS6**), benzoic acid (**MS7**) and phenyl cyanoacrylic acid (**MS8**). We studied the effect of the structural and electronic differences of these latter on the optoelectronic properties as well as devices performances of the resulting dyes. Furthermore, we investigated the results using time resolved spectroscopy as well as small light modulation techniques. The obtained results were compared to a well-known dye, **XY1b**.

3.2 Results and Discussion

The route to IDT core and detailed procedure can be found in the appendix. The synthesis of the new dyes (See Scheme 3.2) started with a Stille cross coupling between the IDT unit, functionalized in-situ with tri-butyl-stannyl at the thiophene α -position, and 4,7-dibromo-benzo-thiadiazole in order to install the first acceptor.

Then, the electron donating unit, (N-(2',4'-bis(alkoxy) -[1,1'-biphenyl]-4-yl) -2',4'-bis(dodecyloxy)-N-phenyl - [1,1'-biphenyl] - 4-amine) was converted into a pinacol ester and subsequently reacted with (1) under Suzuki cross coupling conditions catalyzed by the $\text{Pd}_2(\text{dba})_3/\text{Xphos}$ catalytic.

This corresponding product was portioned and submitted to two different protocols. The first, consisted in a N-bromo-succinimide mediated bromination of (2) followed by a Suzuki coupling, under the same conditions as mentioned before. This reaction yielded the aldehyde (3), that was reacted with cyanoacrylic acid, according to the Knoevenagel protocol, to obtain **MS8**. The second portion of (2), was reacted with n-butyl lithium and quenched with tri-butyl-tin chloride prior to a Still coupling with either of the two different acceptors ethyl esters precursors. Finally, the two dyes (**MS6** and **MS7**) were hydrolyzed to generate the free carboxylic acids.



Scheme 3.2. Synthetic route to **MS6**, **MS7** and **MS8**.

Figure 3.1b and c show the dyes' absorption profiles in THF solution and adsorbed on mesoporous TiO_2 . Figure 3.1b displays the presence of a very blue-shifted peak located around 330 nm, commonly attributed to the π - π^* transition. A second intense maxima can be observed, attributed to the intramolecular charge transfer (CT) transition. By comparing the dyes' profiles, $\lambda_{\text{max,CT}}$ and $\epsilon(\lambda)$, seem to be consistently increasing with the electron accepting strength : **MS7**, **MS8** < **MS6**, **XY1b**.

Additionally, implementation of an extra BT unit (**MS6** vs. **MS7**) induces a 24 nm red-shift of $\lambda_{\text{max,CT}}$. Interestingly, the substitution of a carboxylic acid for a cyanoacrylic acid does not seem to impact the absorption profiles (**MS8** vs. **MS7**). The photo-luminescence spectra of the dyes dissolved in THF (see Figure 0.15b) revealed similar $\lambda_{\text{PL,max}}$. Figure 3.1c shows the absorbance of sensitized TiO_2 films, where same trends as the solutions measurements were observed.

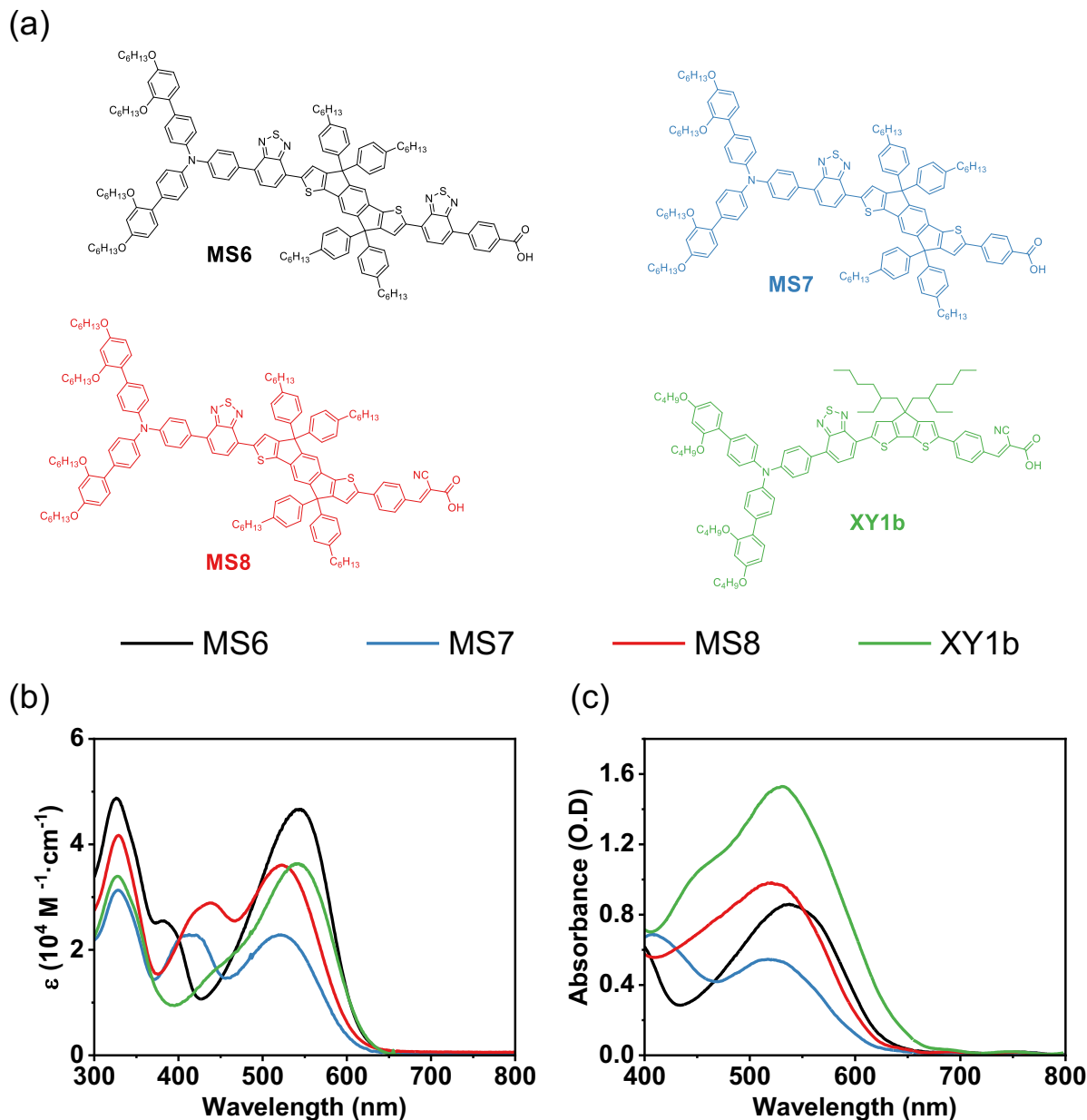


Figure 3.1. (a) Molecular structures of the dyes. Absorption spectra of the dyes in diluted THF solution (b) and adsorbed on 2.2 μm thick transparent TiO_2 films.

Cyclic voltammetry of sensitized TiO_2 electrodes was used to estimate the dyes' E_{HOMO} (see Figure 0.16). The values were similar for all the IDT dyes with figures lying around 1.1V vs. NHE. Compared to the other dyes, **XY1b** was found to have a HOMO level upwardly shifted by 0.1 V. The dyes' E_{LUMO} were found to be -0.85 (**MS6**), -0.93 (**MS7**), -0.92 (**MS8**) and -1.00 V vs. NHE (**XY1b**).

A difference of almost 100 mV can be observed between the BT containing IDT dye (**MS6**) and the two containing simple phenyl moieties (**MS7** and **MS8**). This difference reflects the stronger electron affinity of the BT unit but also a longer effective conjugation length. These features would ultimately further stabilize the LUMO level of **MS6** compared to **MS7** and **MS8**. A E_{LUMO} of -1 V vs. NHE was found for the reference dye **XY1b**. This value is almost 200 mV higher than **MS6** and 100 mV higher than **MS7** and **MS8**. This peculiar difference could be ascribed to the effective conjugation length of the IDT dyes compared to the smaller CPDT based **XY1b**.

Table 3.1. Optical and electrochemical properties of **MS6**, **M7**, **MS8** and **XY1b**.

	λ_{onset}^a [nm]	$\lambda_{\text{max,CT}}(\epsilon)^a$ [nm($10^4 \text{ M}^{-1} \cdot \text{cm}^{-1}$)]	$\lambda_{\text{PL,max}}^{a,*}$ [nm]	$\lambda_{\text{abs,max}}^b$ [nm]	E_{HOMO}^c [V vs. NHE]	E_{LUMO}^d [V vs. NHE]	E_g^e [eV]
MS6	616	543(4.6)	669	538	1.10	-0.85	2.03
MS7	609	519(2.8)	670	522	1.11	-0.93	2.04
MS8	603	523(3.6)	672	521	1.14	-0.92	2.06
XY1b	619	542(3.6)	676	531	1.01	-1.00	2.01

^aObtained from diluted THF solutions. ^bObtained from measurement 2.2 μm thick TiO_2 films sensitized with the dyes, ^cEstimated from the onset of the oxidation potential of the dyes adsorbed on TiO_2 measured using cyclic voltammetry, with Ferrocene as internal standard and subsequently converted to NHE by adding 0.624 V to the value²⁹⁹. ^dObtained from $E_{\text{HOMO}} - E_g$. ^eEstimated using: $E_g: 1242/\lambda_{\text{onset}}$. *Samples excited at 500 nm.

The wave functions of the dyes frontier molecular orbitals, determined by density functional theory (DFT), were represented in Figure 3.2. By comparing dyes' HOMO wave functions, it can be noticed that they are delocalized over the D-A- π segments, for **MS6**, **MS7** and **XY1b**. In the case of **MS8**, the HOMO wave function only extends up the first thiophene of the IDT bridge. The LUMO wave functions showed more marked differences than the HOMO levels. **MS6** displayed frontier orbitals mainly located on the acceptor/anchoring, with a pronounced feature on the benzo-thiadiazole unit.

By contrast, **MS7** possessed orbitals distributed on the benzothiadiazole adjacent to the donor. This inadequately positioned LUMO wave function could impair the coupling between the sensitizer excited state and the TiO_2 ^{74,108}. Furthermore, this result indicates that the benzothiadiazole unit is overpowering the electron accepting ability of the benzoic acid. **MS8** and **XY1b** presented similarly located in the vicinity of the anchoring group, the cyano-acrylic moieties bearing most of the LUMO character.

Considering these results, it seems that the acceptors/anchoring units based on cyano acrylic acids provide a more adequate placement of LUMO wave functions, compared to the benzoic acid derivatives. Finally, the comparison between **XY1b** and **MS8** highlights the difference between IDT and cyclo-penta-dithienyl (CPDT).

As observed in Figure 3.2, in CPDT provided a better delocalization of the LUMO level over the π -bridge compared to IDT. This effect might originate from the differences in aromaticity as well as geometries between the phenyl and thiophene rings.

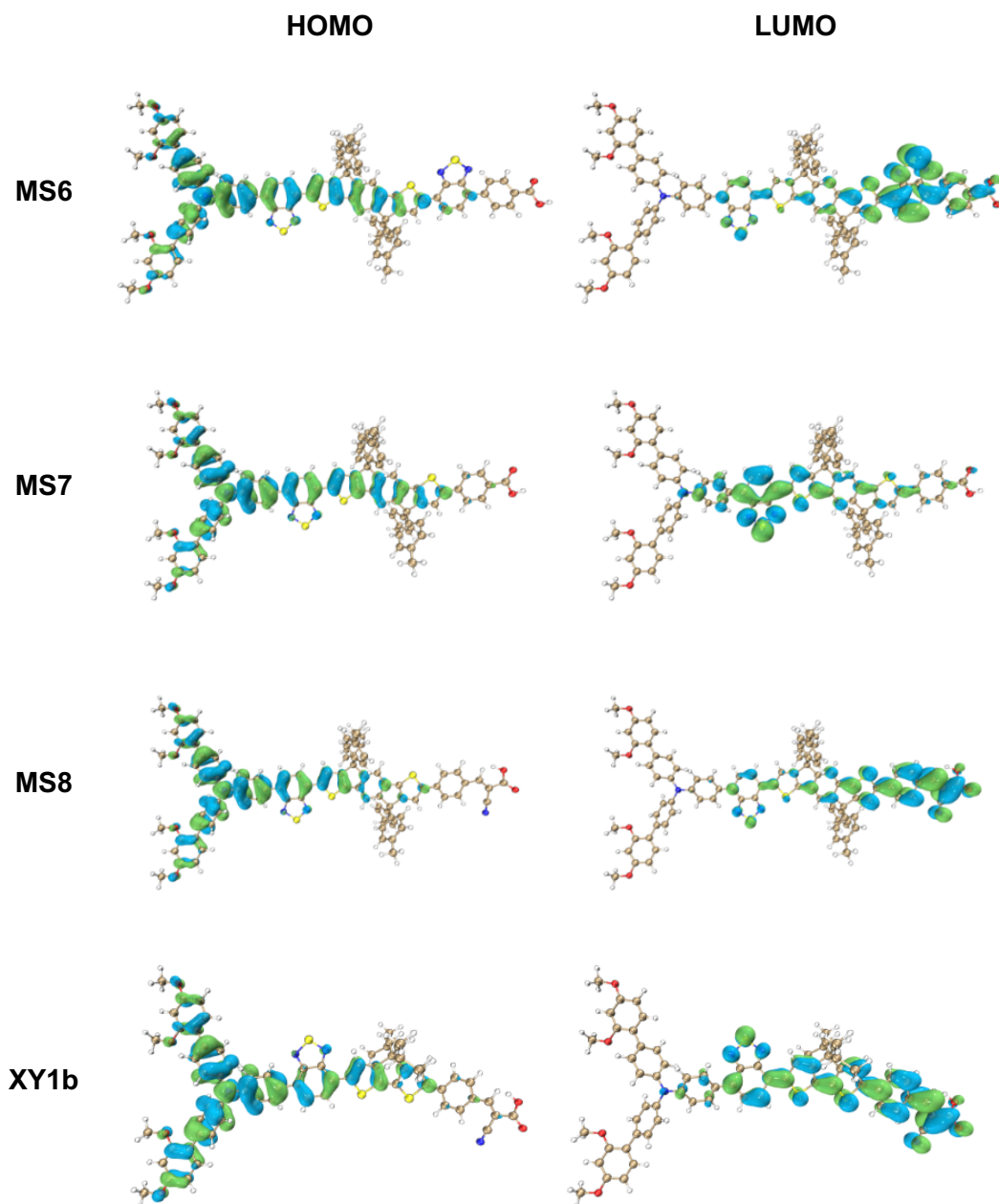


Figure 3.2. Distribution of the molecular orbitals obtained using the B3PW91 functional and 6-31G(d,p) basis sets.

The geometries of the ground and excited states were determined by means of DFT calculations (see Figure 3.3).

As expected, no differences in both states were observed for the angle between the phenyl ring of the donor and the BT acceptor. Similar values lying around 30 (S_0) and 16° (S_1) were found for all dyes. No differences either were found between the dihedral angles around the BT/ π -bridge bond: a slight twist of 8° (S_0) and values close to 0° (S_1) regardless of the sensitizer.

These findings indicate that IDT does not induce more distortion of the molecular structure than CPDT. As expected, the major conformational differences rose along the π -bridge/acceptor bond, that was varied.

MS6 possess a dihedral angle (7.38°) almost twice as twisted as its analogues **MS7** (3.33°) and **MS8** (2.62°), as well as the reference dye **XY1b** (4.33°). This difference can be attributed to the bulkier BT unit installed in **MS6**.

For the same bond angle, the excited states of **MS7** and **MS8** adopted a very distorted geometry with values of respectively 24.68 and 19.76° . On the other hand, **MS6** displayed a very similar dihedral angle than its ground state for the π -bridge/acceptor bond (8.96°).

Compared to the other dyes, **MS6** possess an additional phenyl ring between its carboxylic acid anchoring group and the BT unit. The dihedral angle corresponding to this axis remains almost unchanged upon transition to the excited state, with values lying around 33° .

To furtherly investigate the electronic effect of the acceptors on the dyes, their total dipole moment was calculated. The two dyes containing cyano-acrylic acid moieties (**MS8** and **XY1b**) were found to have dipole moments almost twice as high as **MS6** and **MS7**, with values of respectively 20.73 and 19.28 versus 12.38 and 11.53 D. This result highlights the stronger electron deficiency of the cyano-acrylic acid.

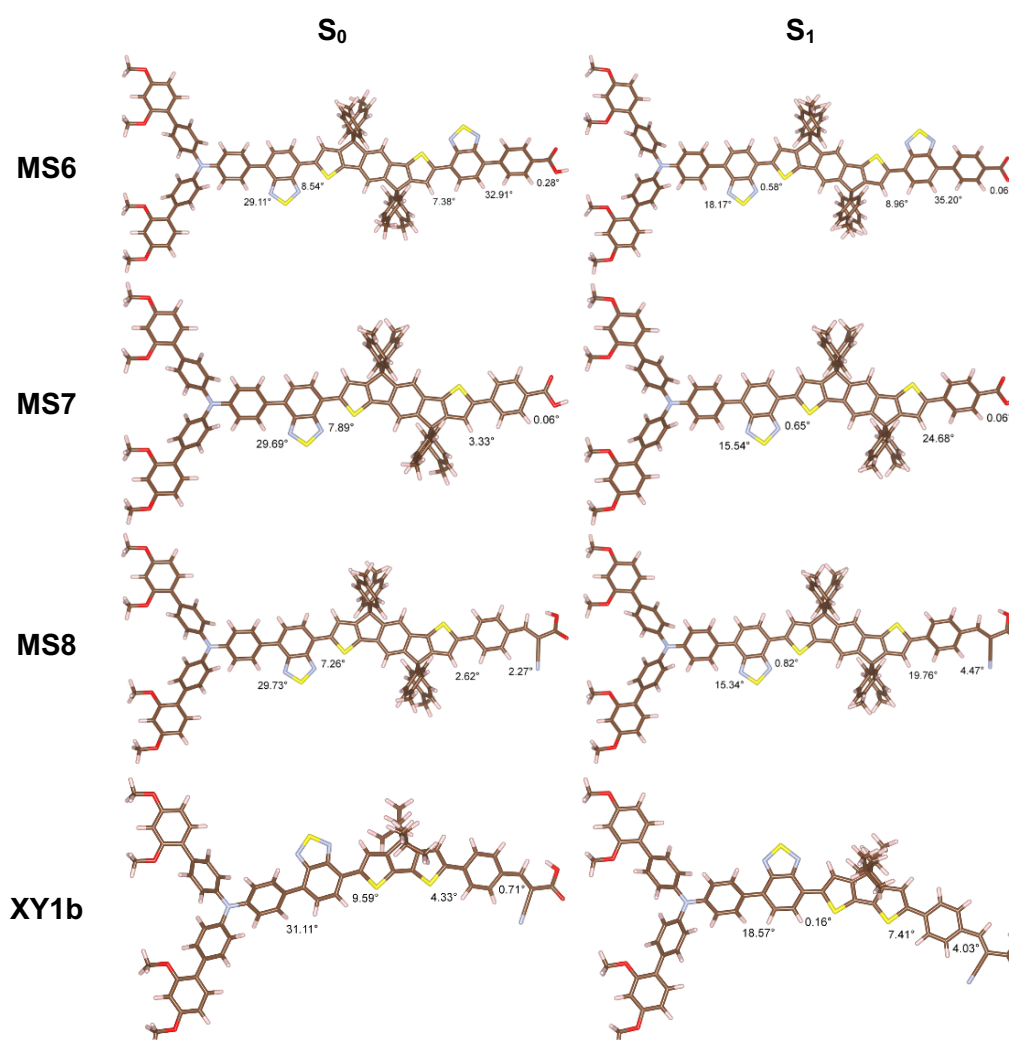


Figure 3.3. Geometry optimized structures of the ground state and the first excited state (S_1) of **MS17**, **MS18** and **MS19** with the corresponding dihedral angles between each plan using the CAM-B3LYP functional and 6-31G(d,p) basis sets.

MS6, **MS7** and **MS8** were tested in devices fabricated with the $[\text{Cu}(\text{tmby})_2]^{+2/+1}$ redox couple and compared with the reference dye, **XY1b**.

The current density-potential(J-V) curve and photovoltaic parameters were reported on respectively Figure 3.4a and Table 3.2. The short circuit current densities (J_{SC}) were found to be close for **MS6** ($7.49 \text{ mA}\cdot\text{cm}^{-2}$) and **MS8** ($6.82 \text{ mA}\cdot\text{cm}^{-2}$), whereas **MS7** produced a J_{SC} of $3.57 \text{ mA}\cdot\text{cm}^{-2}$.

Table 3.2. Detailed PV performances measured under AM1.5G ($100 \text{ mW}\cdot\text{cm}^{-2}$)

	J_{SC} [$\text{mA}\cdot\text{cm}^{-2}$]	V_{OC} [mV]	FF [%]	PCE ^a [%]
MS6	7.49(7.6±0.1)	955(950±18)	78(78±1)	5.6(5.5±0.1)
MS7	3.57(3.1±0.6)	861(870±10)	82(83±1)	2.5(2.3±0.3)
MS8	6.82(6.6±0.2)	912(950±26)	78(79±2)	4.8(5.1±0.3)
XY1b	13.81(13.5±0.4)	1003(980±14)	76(77±1)	10.8(10.4±0.5)

^aValues averaged over four cells.

This strikingly figure, might originate from the inadequate orbital coupling highlighted by the DFT calculations. The open-circuit voltages followed the trend of current densities, with the highest V_{OC} (955 mV), produced by **MS6**. Overall, the power output obtained by **MS6** and **MS8** were respectively 5.6% and 4.8 % under similar device conditions and illumination.

The reference devices, fabricated with **XY1b**, obtained a much higher PCE (11%) notably attributed to higher J_{SC} ($13.81 \text{ mA}\cdot\text{cm}^{-2}$) and V_{OC} (1.0 V). As expected, the corresponding devices' IPCEs, represented in Figure 3.4b, were consistent with the trends in J_{SC} and PCEs obtained from the J-V measurements.

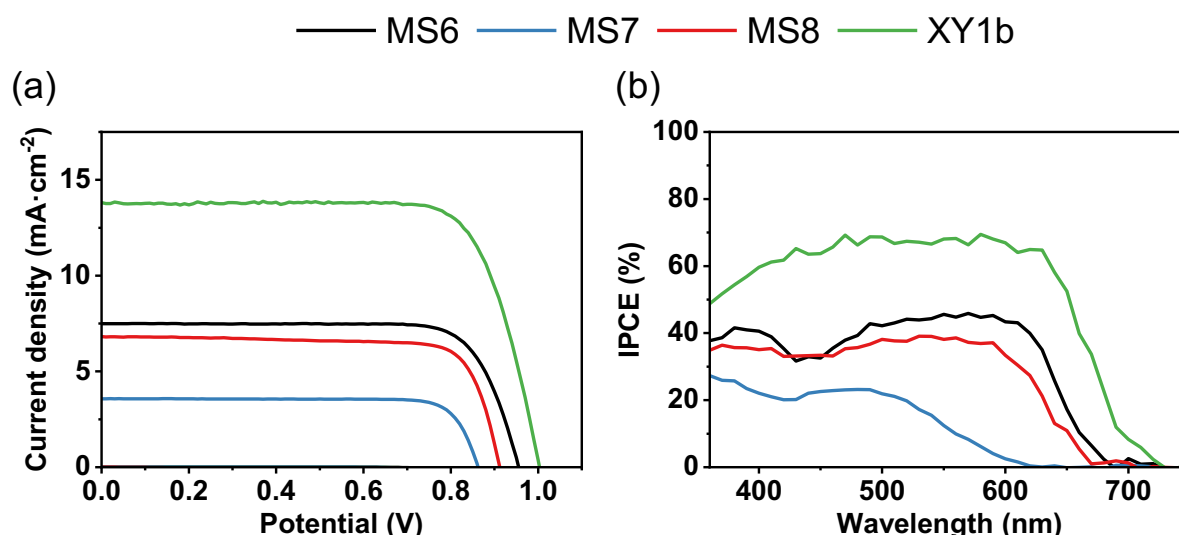


Figure 3.4. (a) J-V curves of cells measured under AM1.5G. (b) IPCE spectra of the cells.

To explain the differences in PV performances, the dyes regeneration efficiencies were determined using TAS. The decay profiles of the samples and associated lifetimes presented in Figure 3.5 (a-d) and reported on Table 3.3.

Strikingly, **MS7** showed a τ_{Inert} of 326 μs , which probably originates from a slow electron injection in the titania conduction band. As observed from the DFT calculations, the LUMO wave function of **MS7** was found to be located far away from the anchoring unit. **MS6** and **MS8** displayed τ_{Inert} roughly three times shorter than **MS7**, with values of respectively 90 and 118 μs . Interestingly, the decay of **XY1b**⁺ (59 μs), was found to be shorter than all IDT dyes and especially its analogue **MS8** (118 μs).

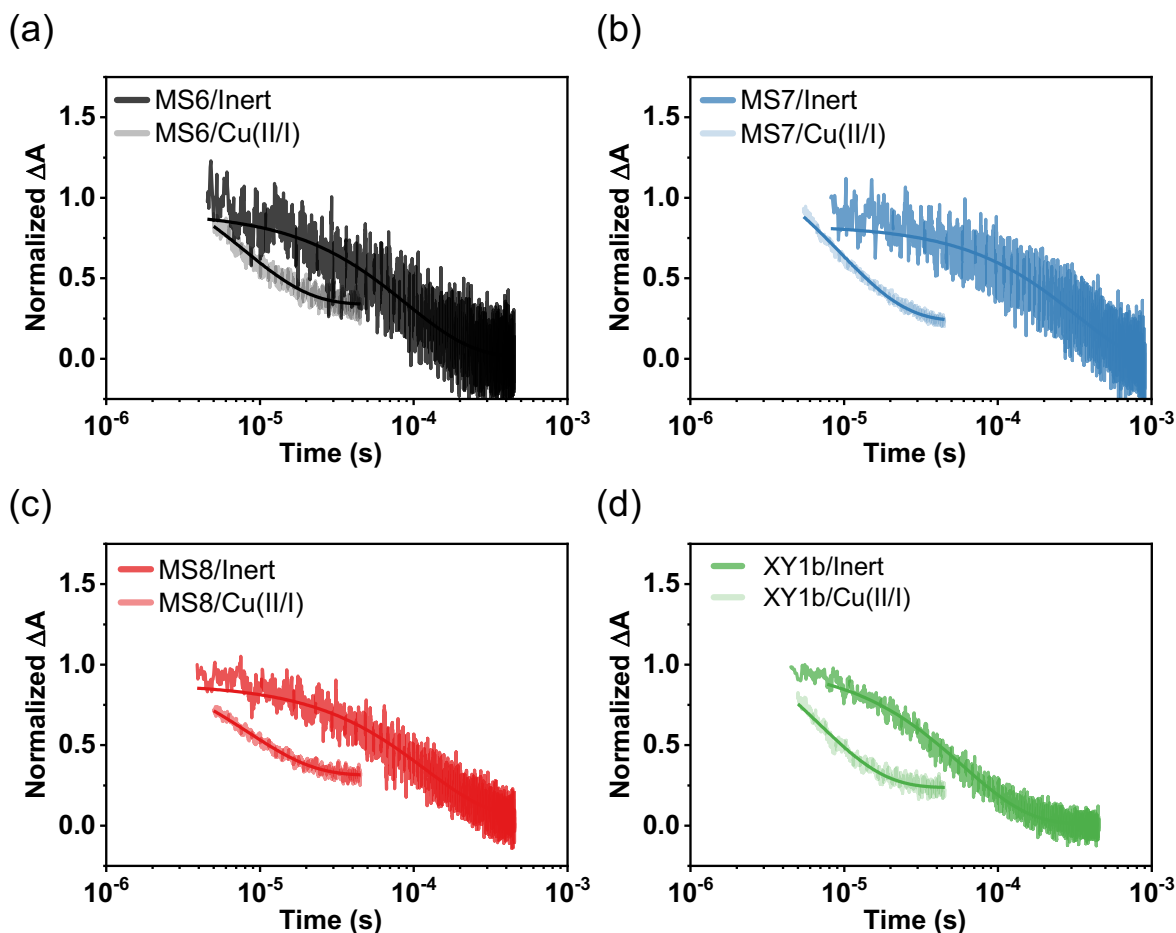


Figure 3.5. Time-evolution of the dye oxidized state absorbance monitored at $\lambda_{\text{Probe}} = 820 \text{ nm}$ upon pulsed laser excitation at $\lambda_{\text{Pump}} = 500 \text{ nm}$ of half-devices composed of $4 \mu\text{m}$ thick TiO_2 layers sensitized with **MS6** (a), **MS7** (b), **MS8** (c) and **XY1b**(d), in contact with an inert electrolyte or a redox-active electrolyte containing $[\text{Cu}(\text{tmbpy})_2]^{+2/+1}$. The solid lines represent the monoexponential fittings. The laser fluence for the inert samples was set to $2.2 \mu\text{J}\cdot\text{cm}^{-2}$ and subsequently increased to $0.6 \text{ mJ}\cdot\text{cm}^{-2}$ for the samples containing the copper electrolyte.

This result could indicate a faster and thus more efficiency electron transfer between **XY1b** and the TiO_2 . Table 3.3 shows that the dye cation regeneration is fast for most all sensitizers with $\tau_{\text{Cu(II/I)}}$ values below 10 μs . Overall, the regeneration efficiencies were all found to be lie close to 90 %.

Table 3.3. Lifetimes and η_{reg} obtained from TAS.

	τ_{inert} [μ s]	$\tau_{Cu(II/I)}$ [μ s]	η_{reg}^a [%]
MS6	90	8	94
MS7	326	9.5	96
MS8	118	8.4	95
XY1b	59	6.9	89

^aThe regeneration efficiency was calculated using: $\eta_{i,reg} = k_{i,Cu(II/I)} / (k_{i,inert} + k_{i,Cu(II/I)})$, with $k_i = 1 / \tau_{i,Cu(II/I)}$, $k_{i,inert} = 1 / \tau_{i,inert}$, $i = MS6, MS7, MS8$ or $XY1b$.

The dyes' electron injection efficiencies of the dyes were estimating using time resolved photoluminescence (TRPL)^{301,310}. The time-evolution of the PL signal was plotted in Figure 3.6 (a-d) and the estimated lifetimes reported on Table 3.4. It was found that all dyes present similar $\tau_{AV}(A)$ values, i.e., within the nanosecond regime.

The $\tau_{AV}(T)$ values were in the sub-nanosecond region, with an average value of 0.7 ns for **MS6**, **MS7** and **MS8**. Interestingly, the $\tau_{AV}(T)$ of **XY1b** was almost twice smaller (0.4 ns) which translated into a far superior η_{inj} of 70 %. The trend of η_{inj} follows the photon-conversion intensities reported in Figure 3.4b: **XY1b** > **MS6**, **MS8** > **MS7** and seem to explain the observed differences in IPCEs.

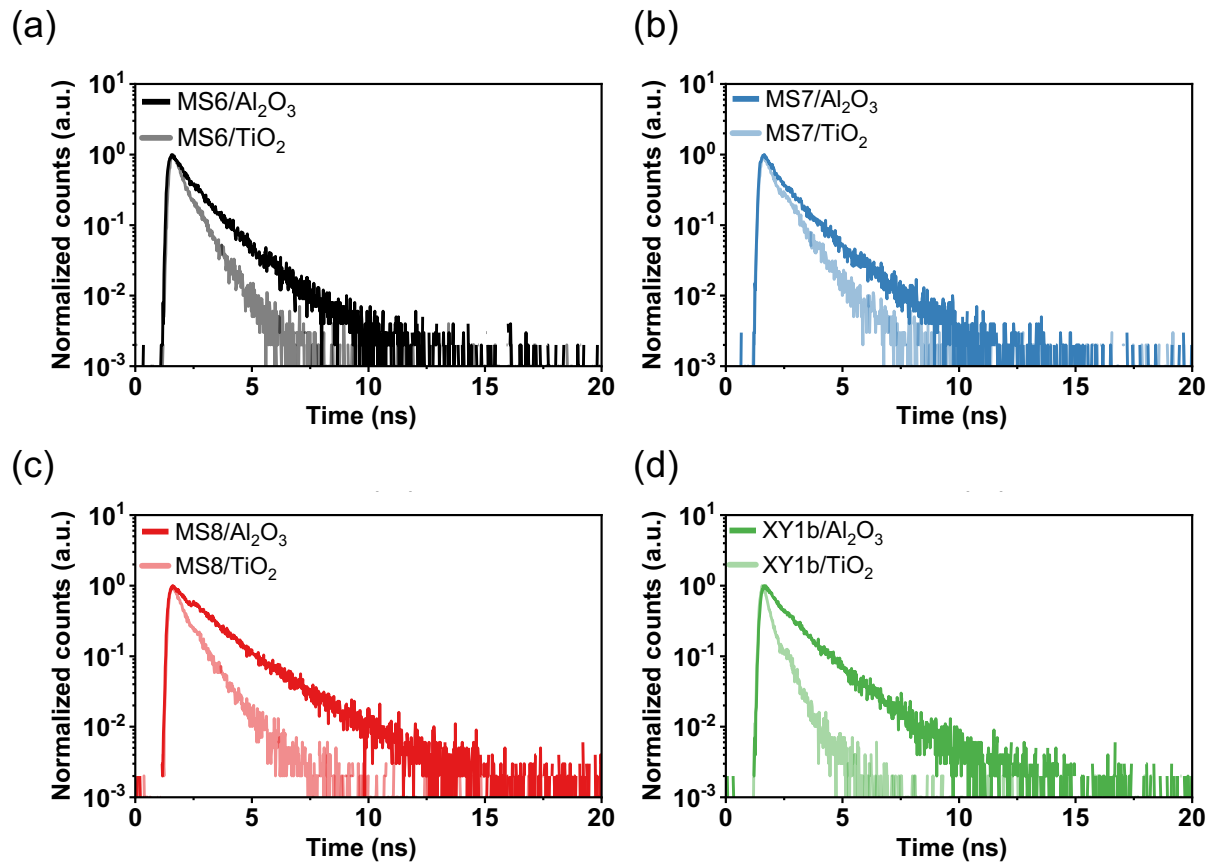


Figure 3.6. TRPL decays of half-cells composed of 4 μ m thick TiO_2 or Al_2O_3 layers dyed by MS6 (a), MS7 (b), MS8(c) or XY1b (d) and filled with the redox-active electrolyte containing $[Cu(tmbpy)_2]^{+2/+1}$. ($\lambda_{Pump}=520$ nm, $\lambda_{Probe}=750$ nm).

Table 3.4. Averaged lifetimes on Al_2O_3 ($\tau(\text{A})_{\text{av}}$), TiO_2 ($\tau(\text{T})_{\text{av}}$) and η_{inj} obtained from TRPL.

	$\tau_{\text{AV}}(\text{A})$ [ns]	$\tau_{\text{AV}}(\text{T})$ [ns]	$\eta_{\text{inj}}^{\text{a}}$ [%]
MS6	1.1	0.6	45
MS7	1.1	0.7	35
MS8	1.6	0.7	59
XY1b	1.2	0.4	70

^aThe injection efficiency was estimated using: $\eta_{i,\text{inj}} = 1 - \tau(\text{T})_{i,\text{av}} / \tau(\text{A})_{i,\text{av}}$, with $i = \text{MS6}, \text{MS7}, \text{MS8}$ or XY1b .

Several factor can impair the interfacial electron transfer of the dye. As mentioned before, a poor coupling between the sensitizer and the TiO_2 substrate could result in sluggish electron transfer, but an insufficient driving force for electron injection (ΔG_{inj}) could also impair the process. In this case, **MS7** and **MS8** were found to have similar LUMO level of approximately -0.92 V vs. NHE, and by extent identical driving force. On the other hand, their electron injection efficiencies were found to be drastically different with 35 (**MS7**) and 59% (**MS8**).

This result seems to indicate that the poor injection abilities of **MS7** is solely limited by the misplacement of its LUMO wavefunction. Compared to **XY1b**, the other two dyes, **MS6** and **MS7**, seem to suffer from lower $-\Delta G_{\text{inj}}$. Their LUMO level was found to be respectively 0.15 (**MS6**) and 0.1 V (**MS8**) below **XY1b** (-0.1 V vs. NHE).

In the last stage, the V_{OC} differences were investigated via electron lifetime (τ_n) and charge extraction measurements (Q_{OC}). The results were presented in Figure 3.7a and b.

The lifetimes of photo-injected electrons followed the trend: **MS7** < **MS6**, **MS8** < **XY1b**, which seems to explain the disparities in V_{OC} . To explain the observed tendencies in τ_n , the dye coverage was measured: 9.16 (**MS6**), 10.91 (**MS7**), 12.49 (**MS8**) and 19.74 $\text{nmol}\cdot\text{cm}^{-2}\cdot\mu\text{m}^{-1}$ (**XY1b**). From these results, it seems that the longer τ_n obtained with **XY1b** is due to a higher dye loading. **XY1b** possesses a smaller CPDT π -linker, that reduces their bulkiness and ultimately allows a higher adsorption on the titania surface. Charge extraction measurements (Figure 3.7b) indicated conduction band edge position for all dyes. Hence confirming that the measured open-circuit voltages were solely limited by electrons lifetimes.

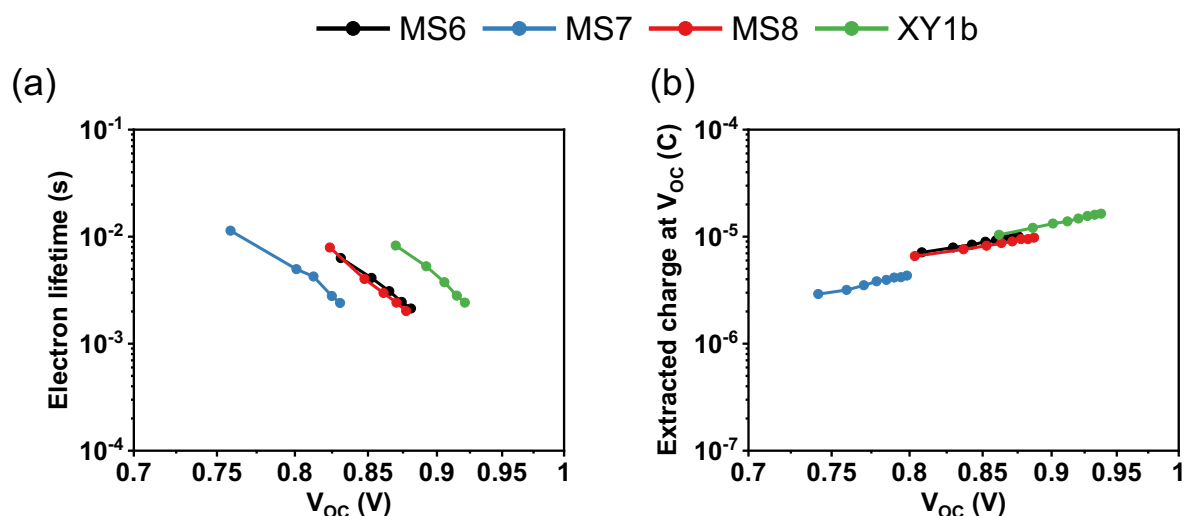


Figure 3.7. (a) Electron lifetime and (b) Extracted charge at open circuit potential of the devices fabricated with the $[\text{Cu}(\text{tmby})_2]^{+2/+1}$.

3.3 Conclusion

To conclude, three new D-A- π -A dyes bearing an IDT π -bridge were synthesized. It was found from DFT calculations that the dye with the weakest benzoic acid acceptor (**MS7**), possessed a LUMO level not adequately located.

Additionally, it was found that the cyanoacrylic acid terminal acceptor doubled the total dipole moment of the dyes, compared to the single benzoic acid (**MS7**) and the benzo-thiadiazole-benzoic acid (**MS6**) units.

In devices with the $[\text{Cu}(\text{tmby})_2]^{+2/+1}$ redox electrolyte, **MS6** and **MS8** produced PCEs twice as low as the reference dye **XY1b**. These values were found to be limited by the electron injection step, where **XY1b** out-performed all dyes.

As highlighted by TAS and TRPL, **MS7** was impaired by its inadequately localized LUMO wave function, whereas the other two dyes, suffered from insufficient electron injection driving force. The high photo-voltage recorded for **XY1b** based devices, resulted from longer electron lifetime, compared to the other dyes.

These observations were correlated with significantly higher dye loading found in **XY1b** sensitized films, explained by the bigger size of the IDT-based dyes. This study highlighted that as general design rule, the terminal accepting unit of D-A- π -A dyes should be the most electron deficient in order to obtain well localized orbitals. If this condition is not met, the interfacial electron injection step will be greatly impaired.

Chapter 4 : Synthesis and study of organic dyes containing a symmetrical Diketopyrrolopyrrole chromophore/acceptor for efficient Cu(II/I) based dye sensitized solar cells.

Contributions:

In this chapter, I designed, synthesized and characterized the dyes, measured TRPL and small light modulation spectra. Natalie Flores Diaz fabricated the devices, samples for TAS, measured the small light modulation spectra as well as JV curves and IPCEs of the devices. Ma Wei and Jing Fu performed the computational calculations and Etienne Socie measured the TAS and Jean-David Decoppet fabricated the samples for TRPL.

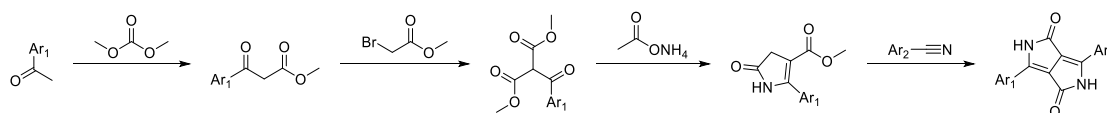
4.1 Introduction

To improve the spectral response of D- π -A a highly conjugated chromophore (C) can be used as π -linker. Most notable examples of such D-C-A dyes are based on zinc-porphyrin units that usually yield green-colored sensitizers^{184,311}.

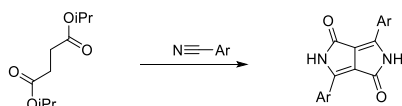
Another popular chromophore is Diketopyrrolopyrrole (DPP). This class of compounds is often found in the pigments industry, thanks to their strong and vivid colors¹⁸⁵ or as electron acceptors in donor-acceptor polymer solar cells^{312,313}. In sensitizers, this building block allows the synthesis of light absorbers with colors ranging from purple to blue^{188,314}. To broaden its spectral response and allow easier functionalization, the DPP core is flanked with two aromatic units.

As seen on Scheme 4.1, these aromatic units can be similar (symmetrical) or different (asymmetrical). Each configuration possesses unique advantages and drawbacks. The symmetrical DPP is accessible through a one-step reaction, starting from cheap and commercially available reagents whereas its asymmetrical analogue, will require four steps³¹⁵. In terms of performances, the asymmetrical DPP offers PCEs ranging between 7 to 10%^{189,316,317} depending on the electrolyte used, whereas the symmetric DPP has efficiencies lying around 4 or 5%^{190,318,319}. The better performances of the asymmetrical DPPs are due its phenyl aromatic unit that reduces the planarity of the molecule. This feature will ultimately yield a higher LUMO level compared to its symmetrical analogue. Furthermore, the symmetry of the DPP stabilized the energy levels to a greater extent than its analogue.

Asymmetrical DPP:



Symmetrical DPP:



Scheme 4.1. Synthetic route to asymmetrical and symmetrical DPP.

Recent developments in the DSSC field, highlighted the promising potential of organometallic complexes as redox active electrolyte²²⁴. Cobalt and copper based coordination complexes were found to be enable better performances due to lower potential losses. Rapidly, open circuit potentials of more than 1V were reached, with the redox couple $[\text{Cu}(\text{tmby})_2]^{+2/+1}$ (tmby=4,4',6,6'-tetramethyl-2,2'pyridine) and a series of new organic dyes^{200,209,320,321}.

In this regard, three new DPP-dyes coded **MS17**, **MS18** and **MS19** were synthesized to be tested with $[\text{Cu}(\text{tmby})_2]^{+2/+1}$. The electron donating unit was N-(2',4'-bis(hexyloxy)-[1,1'-biphenyl]-4-yl)-2',4'-bis(hexyloxy)-N-phenyl-[1,1'-biphenyl]-4-amine, that proved to be well compatible with the copper electrolyte. To reduce the number of synthetic step, the challenging symmetrical DPP unit was chosen as chromophore/acceptor. These dyes were terminated with three different linking units: phenyl, thiophene and furan combined with a cyanoacrylic acid anchoring/acceptor unit. The phenyl dye (**MS17**) was used as a reference and compared to the thiophene (**MS18**) and furan (**MS19**) (see Figure 4.1a). Phenyl linkers usually provides less stabilization of the energy levels due to their lower planarity and high resonance stabilization energy (RSE)³²².

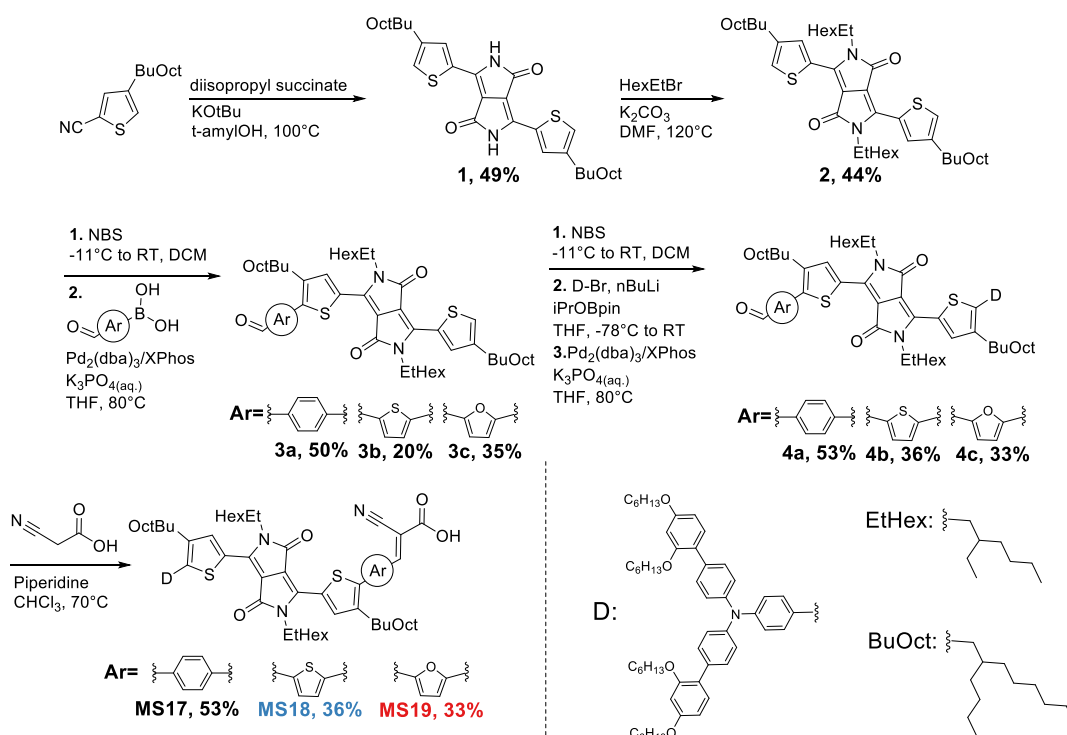
On the other hand, furans and thiophenes, are smaller and more planar five membered rings. They have reduced resonance stabilization energy due to the presence of oxygen and sulfur atoms. In addition to that, oxygen has a higher electronegativity and smaller size than sulfur.

4.2 Results and discussion

The synthetic route to **MS17**, **MS18** and **MS19** was represented on Scheme 4.2. In summary, the DPP core was obtained by reacting 4-(2-butyloctyl) thiophene-2-carbonitrile with bis-diisopropyl succinate ester along with a bulky alkoxide base.

The resulting DPP building block as N-alkylated with 2-ethyl-hexyl-bromide and K_2CO_3 . The resulting product, **2**, was then reacted with one equivalent of N-bromosuccinimide (NBS) subsequently followed by a Suzuki coupling with three different aromatic formyl boronic acids. The cross coupling reaction was catalyzed by $Pd_2(dba)_3$ and Xphos along with aqueous K_3PO_4 .

Afterwards, the electron donating unit was installed by reacting the commercial N-(2',4'-bis(hexyloxy)-[1,1'-biphenyl]-4-yl) – N - (4-bromophenyl) -2',4'-bis(hexyloxy) -[1,1'-biphenyl]-4-amine precursor with n-butyl lithium followed by quenching with 2-Isopropoxy-4,4,5,5-tetramethyl-1,3,2-dioxaborolane to generate the pinacol boronic ester in-situ. This mixture was then reacted under the aforementioned Suzuki conditions, with either of **3a**, **3b** or **3c** obtained from bromination with NBS. Finally, the aldehydes precursors, **4a**, **4b** and **4c**, were converted into the corresponding cyanoacrylic acids by refluxing in chloroform, with excess cyanoacetic acid and piperidine.

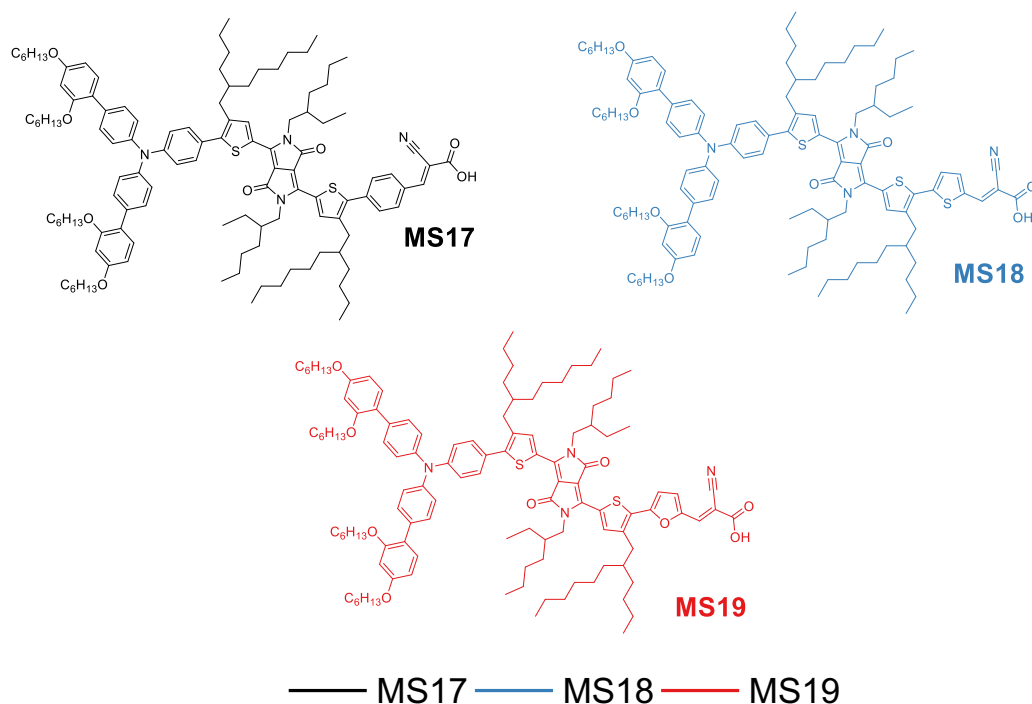


Scheme 4.2. Synthetic route to **MS17**, **MS18** and **MS19**.

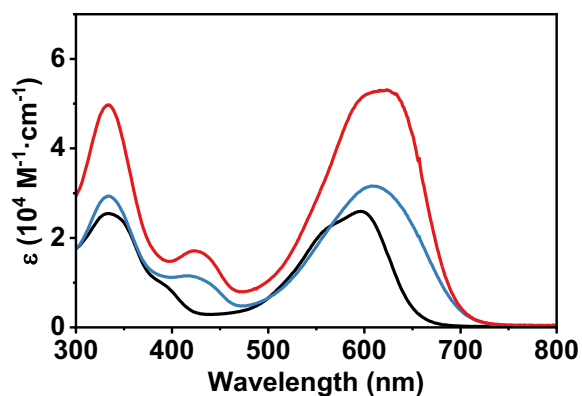
Figure 4.1b shows the molar absorptivity of the dyes dissolved in THF solutions. Two main peaks can be observed for all dyes. The highest in energy, lying slightly below 350 nm, is attributed to a π - π^* transition and seems to remain unaffected by the nature of the π -bridges. The second transition corresponds to the intramolecular charge transfer (CT).

This maxima ($\lambda_{\text{max,CT}}$) gradually shifts to longer wavelengths following the trend **MS17** < **MS18** < **MS19**. This tendency could be ascribed to the increased planarity of the five membered rings dyes (**MS18** and **MS19**). These latter would possess a longer effective conjugation compared to the more twisted **MS17**. In addition to this geometrical feature, furan and thiophene possess lower resonance stabilization energy than the phenyl ring by roughly 300 meV¹⁴⁶.

(a)



(b)



(c)

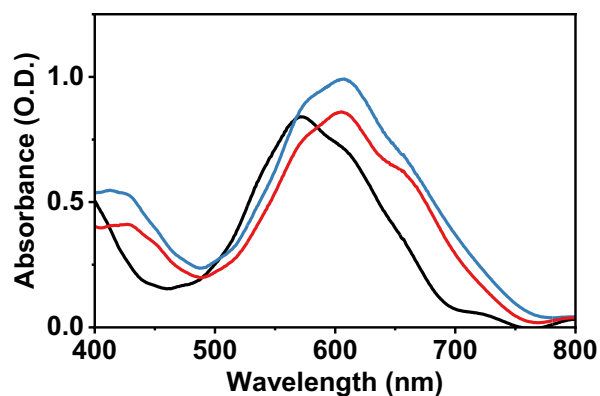


Figure 4.1. (a) Molecular structures of the DPP-based sensitizers **MS17**, **MS18** and **MS19**. (b) Molar absorptivity of the three dyes dissolved in THF. (c) Absorbance of 2.2 μm thick TiO_2 films sensitized with the three dyes.

The Stoke shifts of the dyes were estimated using $\lambda_{\text{max,CT}}$ and emission maxima ($\lambda_{\text{PL,max}}$) obtained from solution measurements. The shifts values were very close between the dyes with 79 (**MS17**), 81 (**MS18**) and 78 nm (**MS19**). This result indicates that the altered π -bridges do not induce significant geometrical distortions upon excitation to the ground state.

Cyclic voltammetry (see Figure 0.36) was used to estimate the E_{HOMO} levels of the dyes and It was found that all dyes possessed similar E_{HOMO} close to 1 V vs. NHE. The aromatic units were found to alter the dyes' E_{LUMO} levels where **MS17** showed a value of -0.89 V vs NHE, which is 120 mV higher than its other two analogues, **MS18** (-0.77 V vs. NHE) and **MS19** (-0.78 V vs. NHE).

Table 4.1. Optical and electrochemical properties of MS17, MS18 and MS19.

	$\lambda_{\text{onset}}^{\text{a}}$ [nm]	$\lambda_{\text{max,CT}}(\epsilon)^{\text{a}}$ [nm($10^4 \text{ M}^{-1} \cdot \text{cm}^{-1}$)]	$\lambda_{\text{PL,max}}^{\text{a,*}}$ [nm]	$\lambda_{\text{abs,max}}^{\text{b}}$ [nm]	$E_{\text{HOMO}}^{\text{c}}$ [V vs. NHE]	$E_{\text{LUMO}}^{\text{d}}$ [V vs. NHE]	E_{g}^{e} [eV]
MS17	654	597(2.5)	676	571	1.01	-0.89	1.90
MS18	702	607(3.2)	688	608	1.00	-0.77	1.77
MS19	692	623(5.3)	701	605	1.01	-0.78	1.79

^aObtained from diluted THF solutions. ^bObtained from measurement 2.2 μm thick TiO_2 films sensitized with the dyes, ^cEstimated from the onset of the oxidation potential of the dyes adsorbed on TiO_2 measured using cyclic voltammetry, with Ferrocene as internal standard and subsequently converted to NHE by adding 0.624 V to the value²⁹⁹. ^dObtained from $E_{\text{HOMO}} - E_{\text{g}}$. ^eEstimated using: E_{g} : $1242/\lambda_{\text{onset}}$. *Samples excited at 500 nm.

The optical and electronic properties of the new DPP dyes were investigated using density functional theory (DFT).

The molecular orbitals (MO) wave functions (see Figure 4.2) indicated that the aromatic units did not impact the distribution of HOMO and LUMO levels over the molecules.

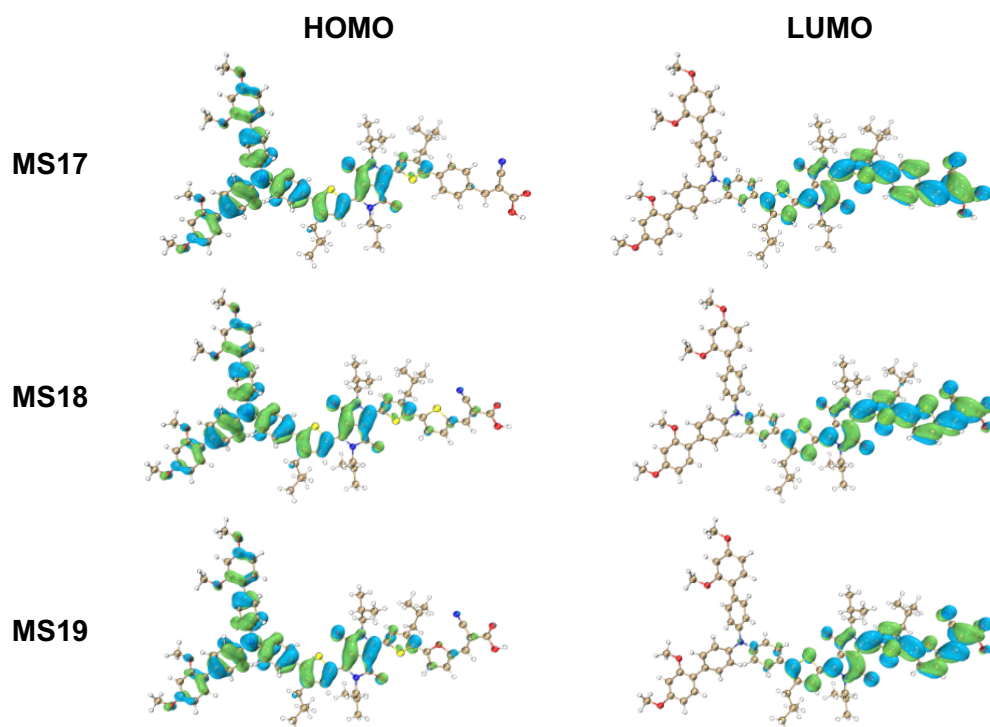


Figure 4.2. Distribution of the molecular orbitals obtained using the B3PW91 functional and 6-31G(d,p) basis sets.

More precisely, the HOMO wave functions were mainly localized on the N-(2',4'-bis (hexyloxy) - [1,1'-biphenyl]-4-yl) - 2',4'-bis (hexyloxy) -N-phenyl-[1,1'-biphenyl]-4-amine unit upon to the DPP.

The LUMO molecular orbitals were gradually spreading over the DPP- π -anchor segment of the dyes, with a pronounced feature on the cyanoacrylic acid unit. This latter feature should ensure a good electronic coupling between the dye and the TiO₂ substrate^{74,91}.

By comparing the HOMO/LUMO surfaces of Figure 4.2, it can be seen that both wave functions, overlap over the DPP-unit and are well spread over the whole dye backbone, which explains the high molar absorptivity and broad absorption onsets.

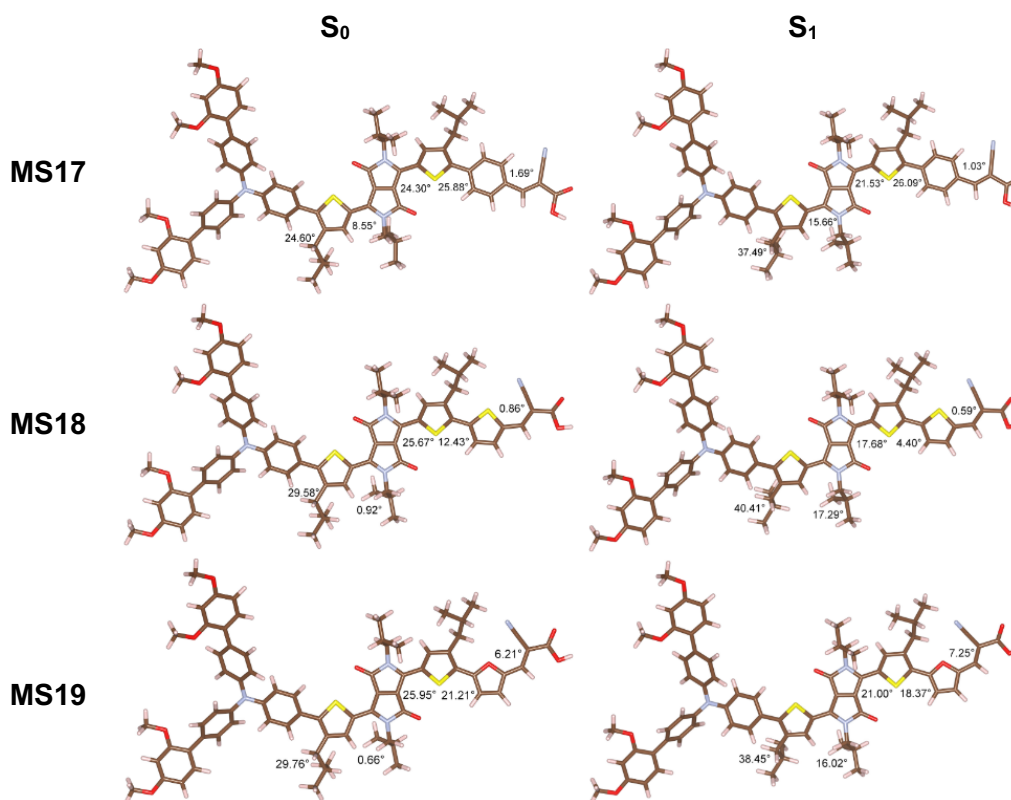


Figure 4.3. Geometry optimized structures of the ground state and the first excited state (S_1) of **MS17**, **MS18** and **MS19** with the corresponding dihedral angles between each plain using the CAM-B3LYP functional and 6-31G(d,p) basis sets.

The ground states (S_0) and the first excited states (S_1) geometries of the dyes were calculated using the CAM-B3LYP functional and 6-31G(d,p) basis sets (see Figure 4.3). The optimized geometries highlighted the structural difference of the 6 membered phenyl (**MS17**) versus the two 5 membered units (**MS18** and **MS19**).

By comparing the dihedral angles of the dyes' S_0 state a striking difference arose at the thiophene-DPP axis, on the donor side. For **MS18** and **MS19** it remains flat, whereas for **MS17** it showed a slight torsion of 8°. The thiophene- π -bridge axis also presented a clear trend, where it gradually decreased along the sequence: **MS17** (25.88°) > **MS19** (21.21°) > **MS18** (12.43°). The higher torsion of **MS17** was explained by, the bulkier size of the 6-membered phenyl ring, compared to the flatter five membered-rings. Interestingly, the furan containing dye (**MS19**) also showed a higher torsion that its thiophene analogue **MS18**.

It was speculated that the smaller size of the oxygen atom, compared to sulfur^{323,324}, yields a more constricted furan ring. Ultimately this would result in an increased steric clash between its neighbors.

This effect would also explain the unusually twisted furan-vinyl bond (6.25°) in **MS19** compared to its other two analogues that showed flat dihedral angles for the same axis. The excited state geometries showed less disparities.

However, the same trend as in S_0 was found in S_1 , with **MS17** and **MS18** being respectively the most and less twisted molecules, whereas the furan analogue (**MS19**) showed remaining torsion around the thiophene-furan-vinyl site.

The dyes' PV performances were evaluated with the copper based redox couple, $[\text{Cu}(\text{tmby})_2]^{+2/+1}$. Detailed photovoltaic parameters were reported in Table 4.2.

Table 4.2. Detailed PV performances measured under AM1.5G ($100 \text{ mW}\cdot\text{cm}^{-2}$).

	J_{sc} [$\text{mA}\cdot\text{cm}^{-2}$]	V_{oc} [mV]	FF [%]	PCE [%]
MS17	10.86	970.95	73	7.67
MS18	4.41	860.40	76	2.89
MS19	5.36	891.36	75	3.59

The best PCE was obtained by **MS17**, with a value of 7.67 %, which is to the best of our knowledge the highest for a sensitizer bearing a symmetrical DPP unit.

More specifically, the J_{sc} was close to $11 \text{ mA}\cdot\text{cm}^{-2}$ and the measured photo voltage was high with a value of 970.95 mV. This gratifying performance shows the compatibility of **MS17** with the copper redox couple. **MS19** comes second with a measured PCE of 3.59%, followed by the thiophene containing **MS18** with 2.89 %.

The most striking difference was found to be the J_{sc} with values more than two times lower than **MS17** (see Figure 4.4a), which could originate from either the low lying LUMO levels of **MS18** and **MS19** or their pronounced planarity.

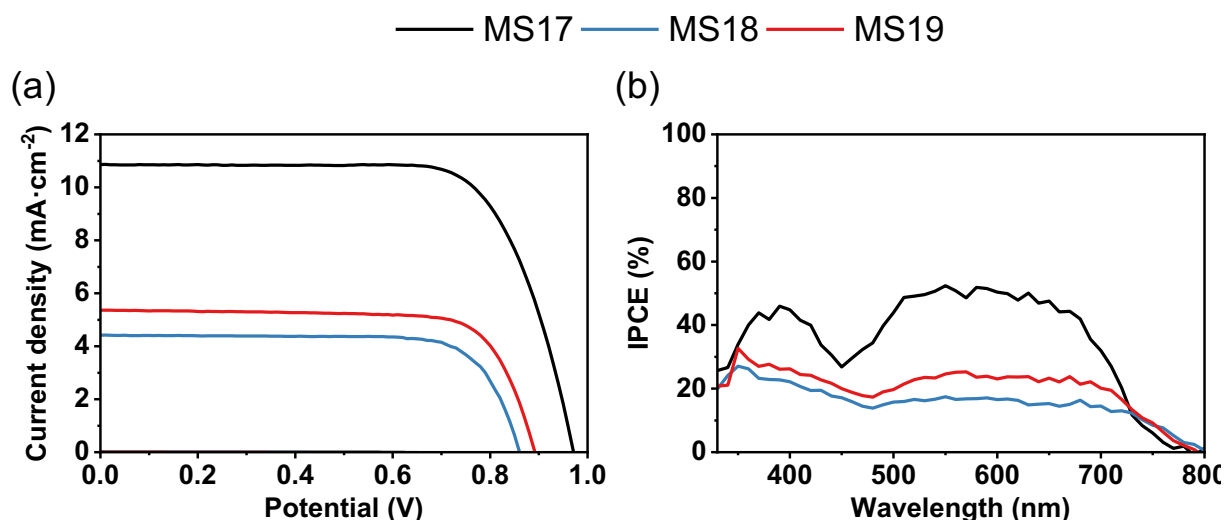


Figure 4.4. (a) J-V curves of cells measured under AM1.5G. (b) IPCE spectra of the cells.

The trends in short circuit current density, were consistent with the measured incident photo to current conversion efficiency (IPCE), showed in Figure 4.4b. Interestingly, **MS17** only managed to reach photon-conversion intensities of roughly 50% with an important valley around 450 nm, consistent with its film absorbance. **MS18** and **MS19** displayed lower conversion values below 30 %.

The results obtained from J-V and IPCE experiments highlighted clear disparities in the photo-current generation of these dyes. As explained in paragraph 1.4.3, the IPCE and J_{SC} are closely related through equations (1.31) and (1.33).

To gain more insight on the exact parameter causing the disparities in IPCE and by extent J_{SC} , time resolved spectroscopy and small modulation light experiments were performed, to estimate the collection, regeneration and injection efficiencies.

The light harvesting efficiency (LHE) was measured from 2.2 μm thick TiO_2 and plotted in Figure 0.59c. LHE values were found to be sufficiently high, as figures near unity were obtained within the 500 to 800 nm region.

The relative regeneration efficiencies (η_{reg}) of the dyes were determined via transient absorption spectroscopy (TAS). The decays of ΔA and corresponding lifetimes were presented on respectively Figure 4.5 (a-c) and Table 4.3.

The lifetimes of the **MS17** cation (37 μs) was found to not significantly higher than **MS18** (20 μs) and **MS19** (24 μs). The accelerated decays corresponds to reduction of D^+ by $[\text{Cu}(\text{tmby})_2]^{+1}$, which are considerably faster than the cations' profiles for all dyes (see Table 4.3). Especially for **MS18** that displayed a regeneration lifetime of 3.1 μs , significantly faster than **MS17** (6.4 μs) and **MS18** (6.1 μs).

Overall, the estimated dye regeneration efficiencies of the dyes were found to be relatively close to each other with values lying around 80%, indicating similar regeneration kinetics for all dyes.

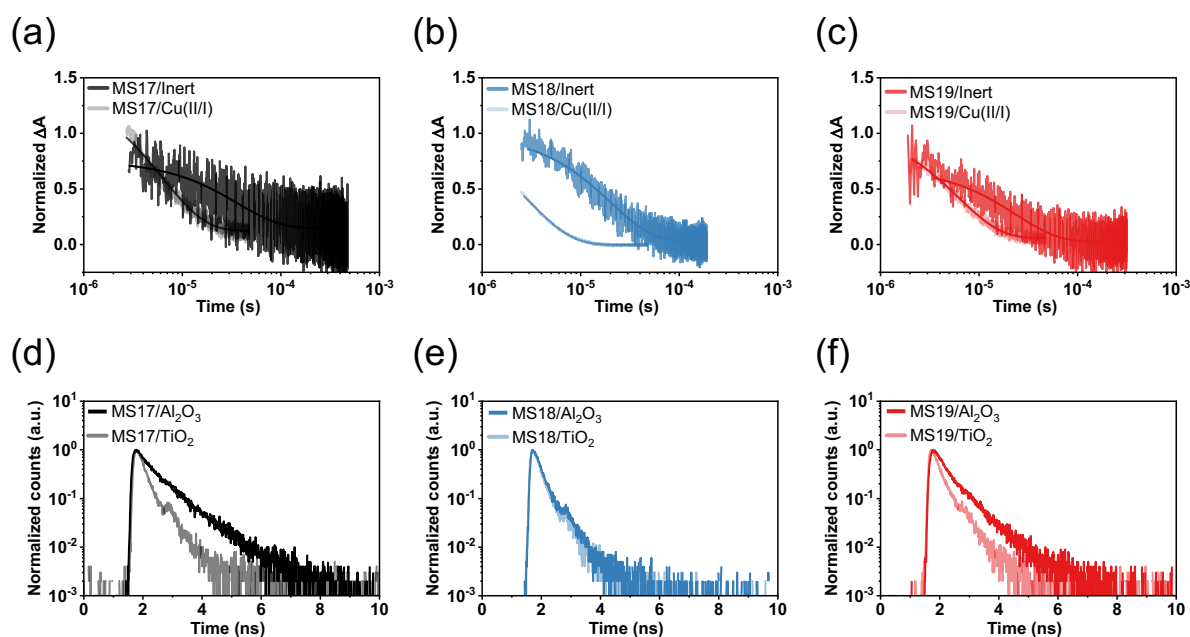


Figure 4.5. (a-c) Time-evolution of the dye oxidized state absorbance monitored at $\lambda_{Probe} = 820 \text{ nm}$ upon pulsed laser excitation at $\lambda_{Pump} = 500 \text{ nm}$ of half-devices composed of 4 μm thick TiO_2 layers sensitized with MS17 (a), MS18 (b) and MS19 (c), in contact with an inert electrolyte or a redox-active electrolyte containing the $[\text{Cu}(\text{tmby})_2]^{+2/+1}$ couple. The solid lines represent the monoexponential fittings. The laser fluence for the inert electrolyte samples was set to $2.2 \mu\text{J}\cdot\text{cm}^{-2}$ and subsequently increased to $0.6 \text{ mJ}\cdot\text{cm}^{-2}$ for the samples containing the copper electrolyte. (d-f) Time resolved photoluminescence decays of half-cells composed of 4 μm thick TiO_2 or Al_2O_3 layers dyed by MS17 (d), MS18 (e) or MS19 (f), in contact with an inert or a redox-active electrolyte based on the $[\text{Cu}(\text{tmby})_2]^{+2/+1}$ redox couple ($\lambda_{Pump}=520 \text{ nm}$, $\lambda_{Probe}=750 \text{ nm}$).

Table 4.3. Lifetimes and η_{reg} obtained from TAS.

	τ_{inert} [μ s]	$\tau_{Cu(II/I)}$ [μ s]	η_{reg}^a [%]
MS17	37	6.4	85.1
MS18	20	3.1	86.8
MS19	24	6.2	79.3

^aThe regeneration efficiency was calculated using: $\eta_{i,reg} = k_{i,Cu(II/I)} / (k_{i,inert} + k_{i,Cu(II/I)})$, with $k_{i,Cu(II/I)} = 1 / \tau_{i,Cu(II/I)}$, $k_{i,inert} = 1 / \tau_{i,inert}$, $i=MS17, MS18$ or $MS19$.

Time resolved photoluminescent decay (TRPL), was employed to estimate the relative electron injection efficiencies³⁰¹.

To mimic operating conditions, the sensitized films, of either TiO_2 or Al_2O_3 , were brought in contact with the same electrolyte composition as in devices^{265,302,325}. The decay profiles were plotted in Figure 4.5 (d-f) and the lifetimes extracted from the corresponding bi-exponential fittings summarized on Table 4.4.

Interestingly, samples fabricated with alumina sensitized with either **MS17** or **MS19** showed significantly higher lifetimes with $\tau_{av}(A) = 570$ ps (**MS18**) and $\tau_{av}(A) = 420$ ps (**MS19**), compared to **MS18** (160 ps). This strikingly short lifetime measured for **MS18** might originate from a more pronounced dye aggregation of this latter. As highlighted by DFT geometries optimizations **MS18** showed very planar structure.

Compared to the alumina samples, the decays measured from TiO_2 samples were accelerated by roughly 5 folds, for the phenyl (**MS17**, 170 ps) and furan (**MS19**, 170 ps) dyes, whereas it remained unchanged for thiophene sensitizer (**MS18**, 130 ps).

Overall, the estimated injection efficiencies (η_{inj}) revealed that **MS18** suffered from poor electron injection efficiency, with a value of $\eta_{inj} = 19$ %. The remaining two dyes, performed better than this latter, with values of 69 % (**MS17**) and 57 % (**MS19**).

Table 4.4. Averaged lifetimes on Al_2O_3 ($\tau(A)_{av}$), TiO_2 ($\tau(T)_{av}$) and η_{inj} obtained from TRPL.

	$\tau_{av}(A)$ [ps]	$\tau_{av}(T)$ [ps]	η_{inj}^a [%]
MS17	570	170	69
MS18	160	130	19
MS19	420	180	57

^aThe injection efficiency was estimated using: $\eta_{i,inj} = 1 - \tau(T)_{i,av} / \tau(A)_{i,av}$, with $i=MS17, MS18$ or $MS19$.

In the final stage, the devices were submitted to small light modulation techniques. Figure 4.6b shows the extracted charge at V_{OC} as function of the potential. This experiment revealed that **MS17** based devices possessed a high lying conduction band edge (CBE) compared to **MS18** and **MS19** devices.

Differences in conduction band edge (ΔCBE) are influenced by the amount of dye adsorbed on the titania surface (N), its dipole moment (μ) and the angle between the normal vector of the surface and the dye (θ), as described by equation (2.1) in Chapter 2^{304,305}.

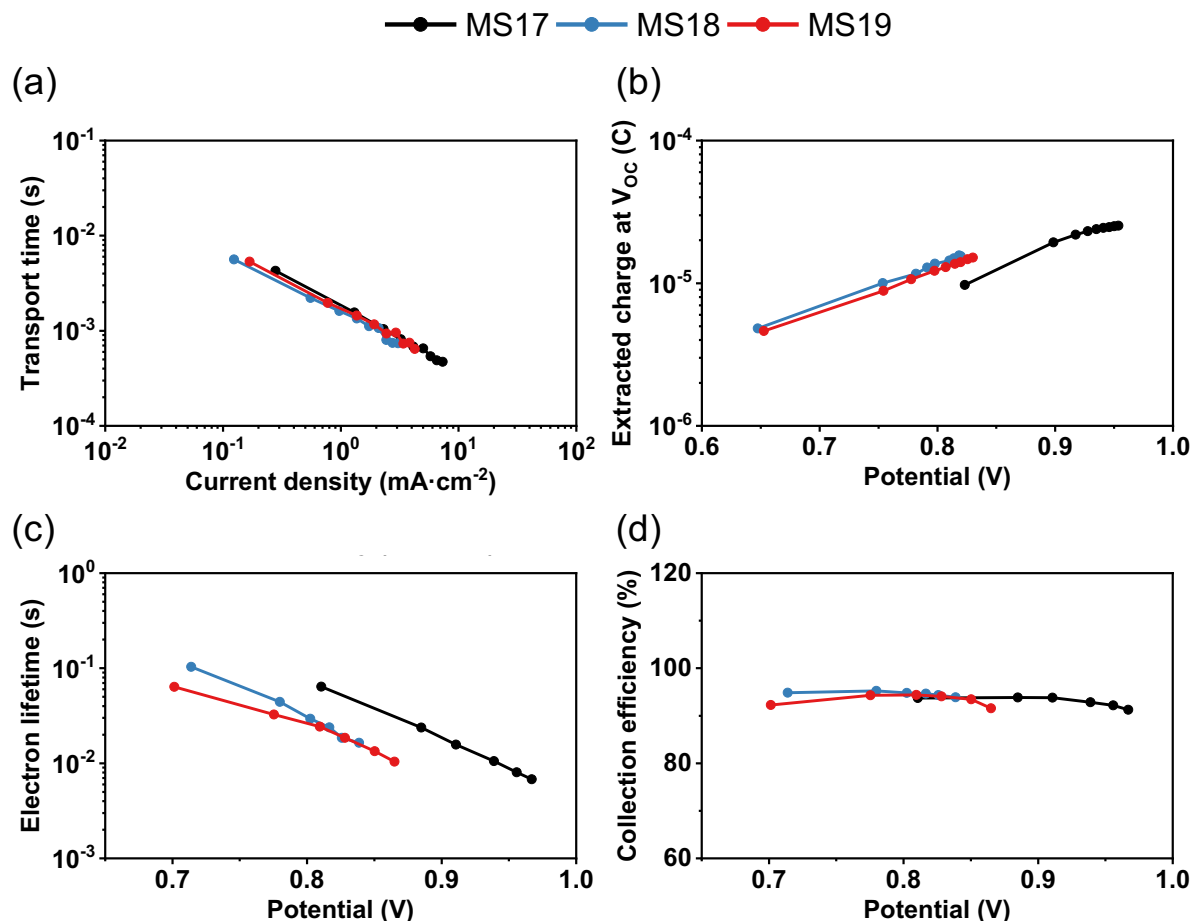


Figure 4.6. (a) Transport time as function of current density, (b) Extracted charge at open circuit potential, (c) Electron lifetime and open circuit potential and charge collection efficiency as function of the open circuit potential. The charge collection efficiency (η_{coll}) was estimated from the electron lifetime (τ_n) and the transport time (τ_{TR}) using the following equation: $\eta_{coll} = 1/(1 + \tau_{TR}/\tau_n)$.

To investigate the differences observed in Figure 4.6b, the dye loadings were estimated to be 16.34 (**MS17**), 14.27 (**MS18**) and 7.47 $\text{nmol}\cdot\text{cm}^{-2}\cdot\mu\text{m}^{-1}$ (**MS19**). This strikingly low **MS19** loading can be rationalized considering the optimized geometries obtained from DFT calculations, where it was found that **MS19** showed a rather distorted conformation. This peculiar conformation would ultimately render the formation of a dye layer more difficult for this latter. On the other hand, its phenyl counterpart (**MS17**), possess a twisted backbone but a rather linear structure, while the thiophene based dye (**MS18**) was found to be very planar. These two features, twisted linearity and planarity, could be facilitating the adsorption of **MS17** and **MS19** onto the TiO_2 surface.

The dyes' dipole moments (μ) were calculated with DFT and found to be 15.95 (**MS17**), 15.97 (**MS18**) and 14.92 D (**MS19**). Considering the Δ CBE equation, μ was determined to not explain the behaviors observed in Figure 4.6b, which leaves the adsorption angle (θ) and dye loading (N). More precisely, from the trends in Q_{oc} vs. V and dyes loadings it can be concluded that as they displayed close N values, **MS18** has a more tilted adsorption mode on the TiO_2 surface and probably suffer from more important dye aggregation than **MS17**. On the other hand, **MS19** sensitized films showed a dye coverage almost twice as low as **MS18**. Considering that **MS18** devices have a similar Δ CBE as **MS19**, compared to **MS17**, it would indicate the adsorption mode of **MS19** is somehow more perpendicular than **MS18**. The trend in θ would therefore be **MS17** < **MS19** < **MS18**, which is consistent with the tendency observed in the dyes' planarities.

The charge collection efficiency (η_{coll}) was estimated using the transport and electron times (Figure 4.6a and b). As seen in Figure 4.6a η_{coll} was found to be very similar for all dyes. This result confirms that the IPCEs of the devices were mainly limited by electron injection efficiencies.

The electron lifetimes (τ_n) were found to be higher for **MS17** based devices, which suggest a more efficient protection of the free electrons from the Cu(II). Interestingly, **MS18** and **MS19** displayed similar τ_n . This result can be explained by considering the measured dye loadings and approximated tilt angles. In the case of **MS18** a loading of $14.27 \text{ nmol}\cdot\text{cm}^{-2}\cdot\mu\text{m}^{-1}$ with an estimated higher θ than **MS19**, that showed a loading of $7.47 \text{ nmol}\cdot\text{cm}^{-2}\cdot\mu\text{m}^{-1}$. Similar to the shifts in CBE, the more tilted adsorption mode of **MS18** seems to be compensated by its higher loading, while the opposite occurs for **MS19**, thus explaining their similar τ_n .

Finally, considering the charge extraction and electron lifetime measurements, it can be concluded that the superior V_{oc} measured in **MS17** devices originate from a high lying CBE and long τ_n .

4.3 Conclusion

In summary, three new symmetrical DPP dyes were successfully synthesized. Three π -bridges were screened and the structural, optical properties as well as PV performances of corresponding dyes determined and compared. Impressive V_{oc} (970 mV) and PCE (7.67%) were measured for the dye coded **MS17**, synthesized with a phenyl spacer, under standard AM1.5G conditions.

The differences in photocurrents and voltages were investigated and it was found that the electron injection efficiency was the main discriminating factor. DFT calculations on the dyes ground and excited states showed that the 6-membered ring phenyl spacer would induce a more twisted conformation beneficial for its PV performances.

Interestingly, the furan based linker (**MS19**), also showed a non-negligible distorted geometry, compared to the readily flat thiophene (**MS18**). This trend in the geometries was found to be consistent with the injection efficiencies, which seems to indicate that the dyes adsorption mode on the TiO_2 plays an important role in limiting the performances. The phenyl spacer was found to be the best suited for achieved high efficiency DSSCs based on symmetrical DPP sensitizers.

Chapter 5 : From benzo-thiadiazole to benzo-oxadiazole: the effect of atom substitution on the photovoltaic performances of two D-A- π -A dyes containing a dithienopyrrole π -bridge.

Contributions:

In this chapter, I synthesized and characterized the dyes. Dr. Yameng Ren and I designed the dyes. Dr. Yameng Ren fabricated the devices, samples for TRPL and TAS, measured the small light modulation spectra as well as JV curves and IPCEs of the devices. Ma Wei and Jing Fu performed the computational calculations and Etienne Socie measured the TAS. Dr. Olivier Ouellette measured TRPL.

5.1 Introduction

Most recent advances in the DSSC research field, have been possible through development of new organic dyes^{2,326,327} and redox active coordination complexes^{224,328,329}. These improvements allowed to fabricate devices with power conversion efficiencies (PCEs) above 10%^{183,184} and corresponding photo-voltages higher than 1 V^{309,321} under standard AM1.5G conditions as well as 1000 lux, indoor light irradiation^{330,331}.

State of the art dyes are designed following the D-A- π -A pattern, where D is an electron donating unit, A, an electron accepting unit and π , a conjugated rigid linker that improves the charge transfer along the molecule. The π -bridge usually shows a strong aromatic character and can contain heteroatoms in order to broaden the dye spectral response. More specifically, fused 2'2'-bithiophenes linkers are often used, as they provide intense molar absorptivities and broad spectral responses^{322,332}.

Cyclopentadithiophene (CPDT) is an example of such a bridging unit, which proved to be beneficial for achieving highly efficient light absorbers^{206,209,333}. CPDT can be further improved by substituting the bridging C-sp³ unit for a nitrogen. The resulting dithienopyrrole (DTP), has showed promising performances in D- π -A dyes^{180,334}. Compared to CPDT, DTP narrows the band gap of the dye^{335,336} and has the attractive feature of being synthetically more accessible than CPDT. The standard procedure consists in a simple Pd-catalyzed cross coupling between an aliphatic amine and 3,3'-dibromo-2,2'-bithiophene³³⁷⁻³³⁹.

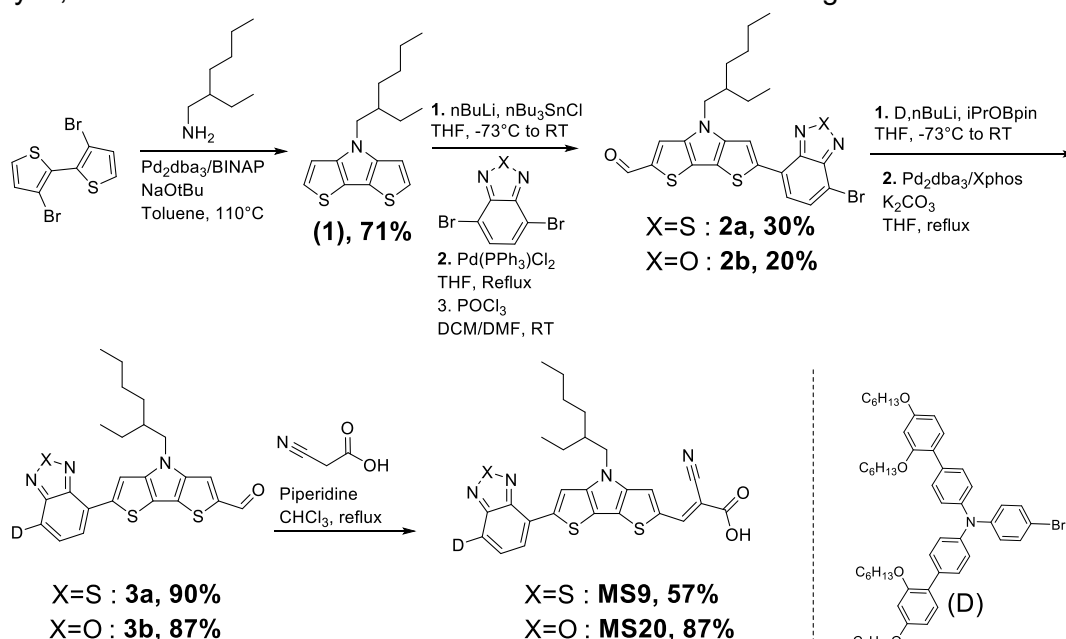
With these parameters in mind, two new dyes coded **MS9** and **MS20** (see Figure 5.1a) were synthesized using a N-(2-ethylhexyl)-dithienopyrrole bridging unit. To optimize the structure, two different auxiliary acceptors were probed: benzo-thiadiazole (**MS9**) and benzo-oxadiazole (**MS20**), while the donor and anchoring groups remained unchanged. The effect of the atom substitution was investigated by comparing the optical properties, structural conformation, energy levels as well as photovoltaic performances of DSSCs fabricated with [Cu(tmby)₂]^{+2/+1}. In a second stage, the difference in the PV parameters was furtherly investigated using time resolved spectroscopy and small light modulation techniques.

5.2 Results and discussion

The synthesis of **MS9** and **MS20** was performed following the procedure described on Scheme 5.1. Details can be found in the supporting information. The DTP core was obtained in 71 % yield via Pd-catalyzed C-N coupling of 2-ethyl-hexylamine and 3,3'-dibromo-2,2'-bithiophene. The auxiliary acceptors were installed by sequentially performing a Stille cross coupling and POCl₃ mediated formylation on the DPT-A core.

The donor was installed using a quick one-pot method, where the brominated donor was treated with butyl lithium (nBuLi) and subsequently quenched by iPrOBpin (2-Isopropoxy-4,4,5,5-tetramethyl-1,3,2-dioxaborolane), to generate the pinacol boronic ester in situ. Then **2a** or **2b** was added to the donor-boronic ester along with aqueous K₃PO₄ and the Pd-catalyst to perform the Suzuki coupling.

The dyes, **MS9** and **MS20** were finalized via the standard Knoevenagel condensation.



Scheme 5.1. Synthetic route to **MS9** and **MS20**.

The molar absorptivity of **MS9** and **MS20** was determined from diluted THF solutions of the dyes and plotted in Figure 5.1b. The absorption profile of **MS9** shows three distinct peaks, whereas only two can be observed for **MS20**. Both dye possess a similar peak at 330 nm, that corresponds to the π - π^* vibronic transition. The second intense transition corresponds to the intramolecular charge transfer (CT).

By comparing the values of the peak maxima ($\lambda_{\text{max,CT}}$), reported on Table 5.1, it can be noticed that the benzo-oxadiazole (**MS20**) acceptor induces a 20 nm red-shift of $\lambda_{\text{max,CT}}$ as well as an increase of $\epsilon(\lambda)$, compared to its benzo-thiadiazole (**MS9**) analogue.

The dyes Stokes shifts were estimated from their steady state emission spectrum in diluted THF solutions ($\lambda_{\text{PL,max}}$). **MS9** showed a higher value (149 nm) than **MS20** (130 nm), which indicates that the latter dye is less prone to conformational changes upon transition to the excited state.

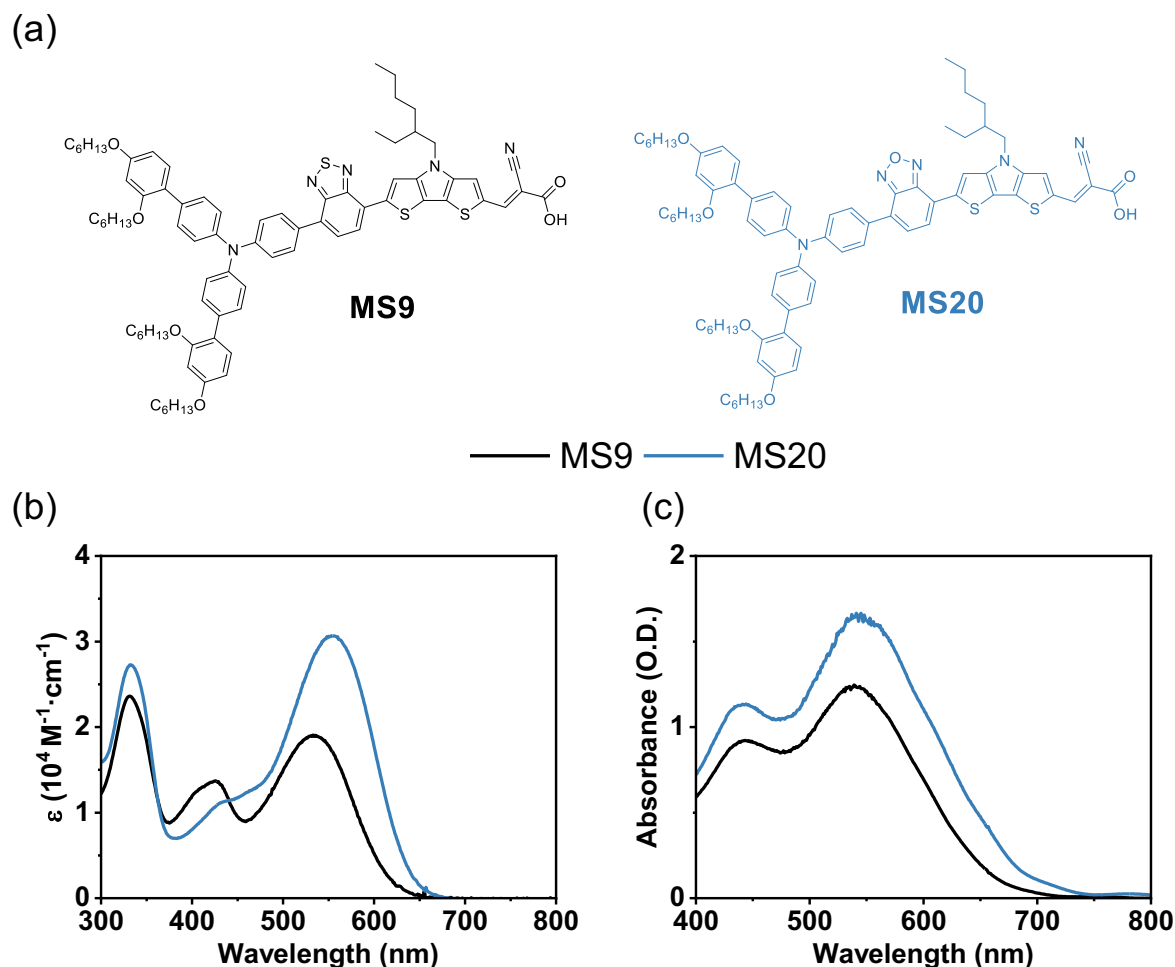


Figure 5.1. (a) Molecular structures of the sensitizers **MS9** and **MS20**. (b) Molar absorptivity of the three dyes dissolved in THF. (c) Absorbance of 2.2 μm thick TiO_2 films sensitized with the three dyes.

The dyes' E_{HOMO} were found to be very similar with values of 1.12 (**MS9**) and 1.15 V vs. NHE (**MS20**). Hence the shifts $\lambda_{\text{max,CT}}$ originated from differences in E_{LUMO} . **MS20** showed a E_{LUMO} roughly 100 mV lower than **MS9**. This effect might originate from the higher electronegativity of oxygen, compared to sulfur.

Table 5.1. Optical and electrochemical properties of **MS9** and **MS20**.

	λ_{onset}^a [nm]	$\lambda_{\text{max,CT}}(\epsilon)^a$ [nm($10^4 \text{ M}^{-1} \cdot \text{cm}^{-1}$)]	$\lambda_{\text{PL,max}}^{a,*}$ [nm]	$\lambda_{\text{abs,max}}^b$ [nm]	E_{HOMO}^c [V vs. NHE]	E_{LUMO}^d [V vs. NHE]	E_g^e [eV]
MS9	617	533(1.91)	682	539	1.12	-0.89	2.01
MS20	638	553(3.10)	692	545	1.15	-0.80	1.95

^aObtained from diluted THF solutions. ^bObtained from measurement 2.2 μm thick TiO_2 films sensitized with the dyes. ^cEstimated from the onset of the oxidation potential of the dyes adsorbed on TiO_2 measured using cyclic voltammetry, with Ferrocene as internal standard and subsequently converted to NHE by adding 0.624 V to the value²⁹⁹. ^dObtained from $E_{\text{HOMO}} - E_g$. ^eEstimated using: $E_g: 1242/\lambda_{\text{onset}}$. *Samples excited at 500 nm.

The optical and electronic properties of **MS9** and **MS20** were investigated using density functional theory (DFT).

The frontier orbitals wave functions (see Figure 5.2) showed that alteration of the auxiliary acceptor did not impact the distribution of the HOMO and LUMO of **MS9** and **MS20**.

More specifically, the dyes' HOMO wave functions were found to be mainly localized on the donor moiety and slightly extending up to the DTP linker. The **MS9** and **MS20** LUMO wave functions were from the auxiliary acceptor up to the anchoring unit, with a pronounced character on the cyanoacrylic acid anchor.

This latter should ensure a good orbital coupling between the dye and the TiO₂ substrate^{74,86,91}. By comparing the dyes' HOMO/LUMO distribution displayed in Figure 5.2, it can be seen that both wave functions, overlap over the DTP, which explains intense ICT transition.

In addition to that, it can be noticed that the presence of the auxiliary electron deficient units (BT or BO) was beneficial for the overlap of the HOMO and LUMO orbitals, by extending the LUMO wave functions distribution, almost up to the donor.

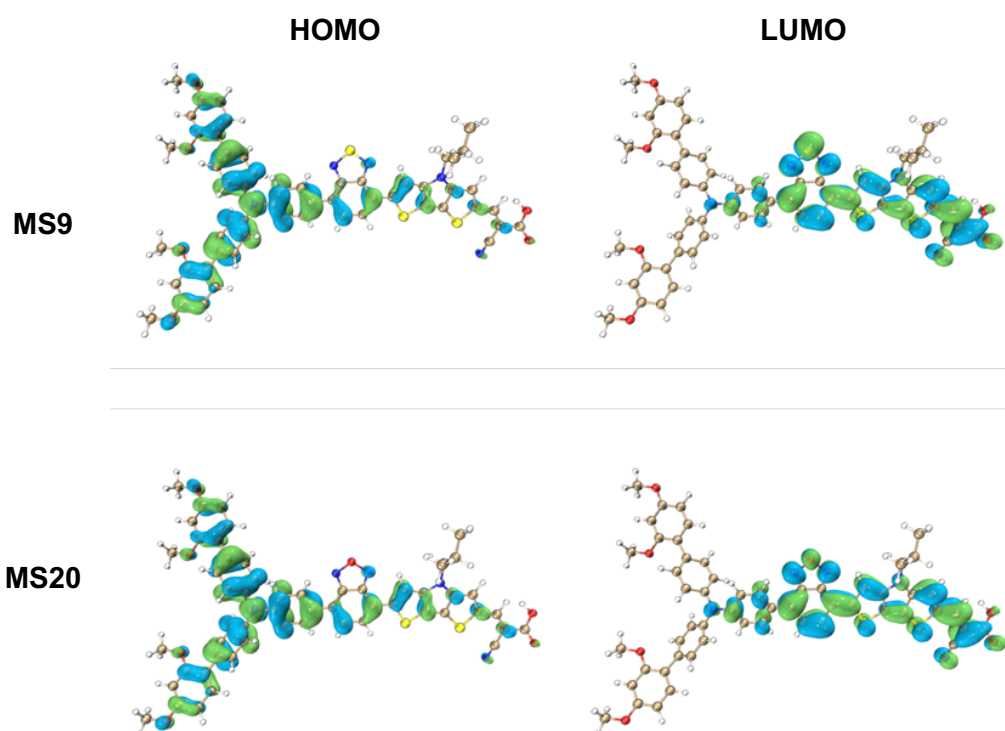


Figure 5.2. Distribution of the molecular orbitals obtained using the B3PW91 functional and 6-31G(d,p) basis sets.

The dyes' ground state (S_0) and the first excited state (S_1) geometries were calculated using the CAM-B3LYP functional and 6-31G(d,p) basis sets (see Figure 5.3). Interestingly, noticeable conformational changes were observed, especially around the Donor-acceptor-DTP axis.

By comparing the ground states geometries, it can be seen that the BT core induces more torsion of the Donor-BT bond in **MS9** (29.47°), compared to **MS20** (19.81°). This observation was conserved at the Acceptor-DTP axis, where **MS9** showed a dihedral angle of 11.71°, almost twice higher than **MS20** (4.48°). Upon transition to S_1 , the dihedral angles were reduced, synonym of a generalized planarization of the structure. Compared to S_0 , the acceptor-DTP axis torsion was drastically reduced for both **MS9** (0.41°) and **MS20** (0.14°). However, a difference was still noticed at the phenyl-acceptor axis where **MS9** (17.09°) showed a higher twist than **MS20** (9.02°).

These findings were explained by the difference of atomic radii between oxygen in sulfur^{323,324}. This latter, being more voluminous, might expand the five-membered ring and ultimately increase the steric clash between the adjacent units of the acceptor.

Additionally, the better optical performances of **MS20**, might be a combination of both electronic and geometric effects. As its higher planarity of this latter dye, could also improve its effective conjugation length. By comparing the geometries of the ground and excited state, it can be noticed that **MS20** sustained less conformational changes than **MS9**, as this former already displayed a rather flat structure in S_0 . This result was found to be consistent with the trend in Stoke shifts, found experimentally.

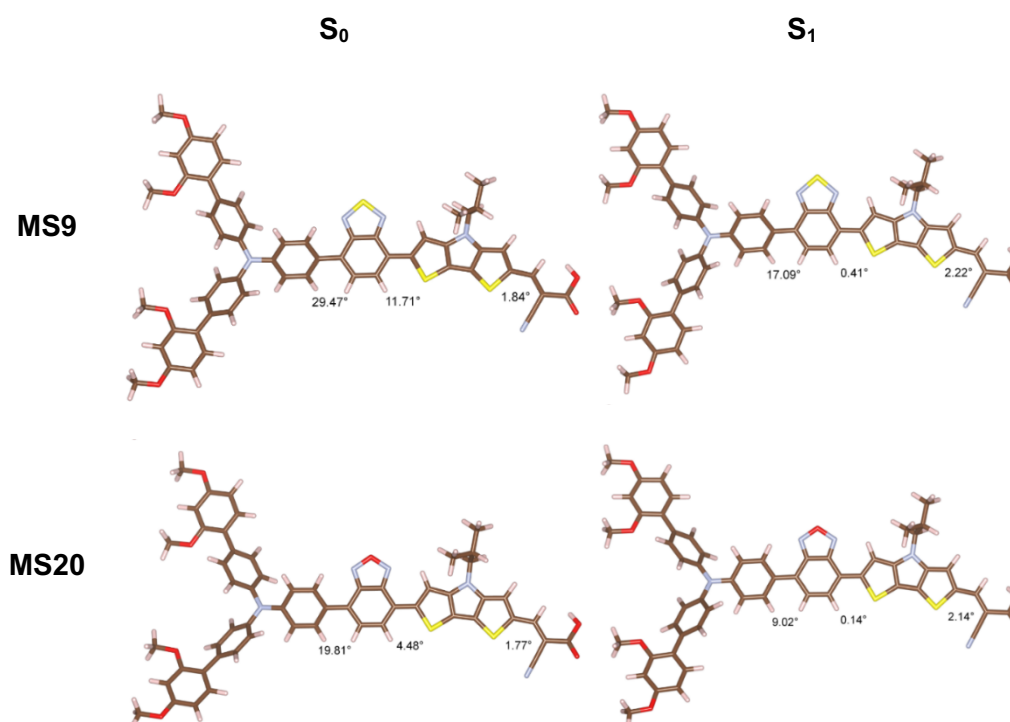


Figure 5.3. Geometry optimized structures of the ground state and the first excited state (S_1) of **MS9** and **MS20** with the corresponding dihedral angles between each plain using the CAM-B3LYP functional and 6-31G(d,p) basis sets.

MS9 and **MS20** were tested in devices fabricated with the $[\text{Cu}(\text{tmby})_2]^{+2/+1}$ redox couple. The photovoltaic parameters measured under AM1.5G were reported on Table 5.2 and the current-density potential (J-V) curves plotted in Figure 5.4a.

As seen from the J-V plot, **MS9** surpasses **MS20** despite the broader spectral response of this latter. As emphasized by Figure 5.4a, **MS9** managed to produce a higher short-circuit current densities (J_{sc}) and open circuit voltages (V_{oc}) than **MS20**.

Table 5.2. Detailed PV performances measured under AM1.5G ($100 \text{ mW}\cdot\text{cm}^{-2}$).

	J_{sc} [mA·cm ⁻²]	V_{oc} [mV]	FF [%]	PCE [%]
MS9	16.43	990	76	12.4
MS20	14.60	948	78	10.8

More specifically, the J_{SC} of $16.43 \text{ mA}\cdot\text{cm}^{-2}$ produced by **MS9**, outperformed **MS20** by almost $2 \text{ mA}\cdot\text{cm}^{-2}$ but also constitutes a record for $[\text{Cu}(\text{tmby})_2]^{+2/+1}$ based DSSCs. **MS9** produced a V_{OC} of 990 mV, only 42 mV lower than **MS20** (948 mV). The overall PCEs were readily high for **MS9** (12.4 %) and **MS20** (10.8 %), under standard AM1.5G conditions.

The incident photon to current conversion efficiency (IPCE) indicated that the disparities in J_{SC} originated from conversion efficiencies values lower by roughly 20%, within the 400 – 700 nm region, for **MS20** cells compared to **MS9** (see Figure 5.4b).

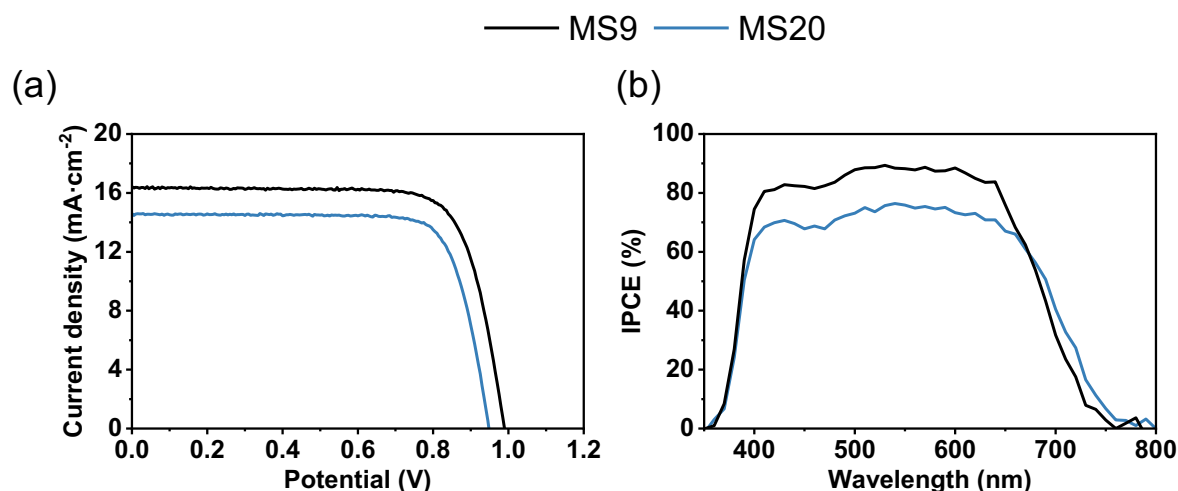


Figure 5.4. (a) J-V curves of cells measured under AM1.5G. (b) IPCE spectra of the cells.

As mentioned in the previous chapters, relative IPCE differences can be rationalized by determining the parameters influencing the photon conversion. More specifically, the extent of generated current will be influenced by the light harvesting (LHE), collection (η_{coll}), injection (η_{inj}) and regeneration (η_{reg}) efficiencies as explained in paragraph 1.4.3.2. The LHE was determined from the absorbance of sensitized TiO_2 films. As seen in Figure 0.59c, the LHEs were found similar, with values close to unity, for both dyes.

The second investigated parameters were the injection and regeneration efficiencies. They were determined using respectively time resolved spectroscopy (TRPL) and transient absorption spectroscopy (TAS).

The ΔA vs. $\log(t)$ profiles were displayed in Figure 5.5a (**MS9**) and Figure 5.5b (**MS20**) while the corresponding lifetimes were reported on Table 5.3. As it can be seen from the dye cation lifetimes, **MS20** displayed of slower electron recapture of $\tau_{inert} = 62 \mu\text{s}$ compared to **MS9** ($44 \mu\text{s}$). The rate of recombination between photo-injected electrons and D^+ , is mainly influenced by the distance between the free charge and the hole.

Table 5.3. Lifetimes and η_{reg} obtained from TAS.

	τ_{inert} [μs]	$\tau_{\text{Cu(II/I)}}$ [μs]	η_{reg}^a [%]
MS9	44	7.8	85
MS20	62	8.6	88

^aThe regeneration efficiency was calculated using: $\eta_{reg} = k_{i,\text{Cu(II/I)}} / (k_{i,\text{inert}} + k_{i,\text{Cu(II/I)}})$, with $k_{i,\text{Cu(II/I)}} = 1 / \tau_{i,\text{Cu(II/I)}}$, $k_{i,\text{inert}} = 1 / \tau_{i,\text{inert}}$, $i = \text{MS9 or MS20}$.

It is commonly accepted that for organic dyes, the holes are located on the HOMO level, i.e., the electron donating unit. Hence the differences in the dyes' τ_{inert} could be ascribed to disparities in the dyes' adsorption geometry on the TiO_2 surface. The addition of $[\text{Cu}(\text{tmby})_2]^{+2/+1}$ in the electrolyte solution results in a considerable acceleration of the decays.

No difference was observed for the corresponding lifetimes with $\tau_{\text{Cu(II/I)}}$ of 7.8 (**MS9**) and 8.6 μs (**MS20**). Overall, the regeneration efficiencies were found to be very similar for **MS9** (85%) and **MS20** (88%) synonym of similar dye regeneration kinetics, regardless of the acceptor properties.

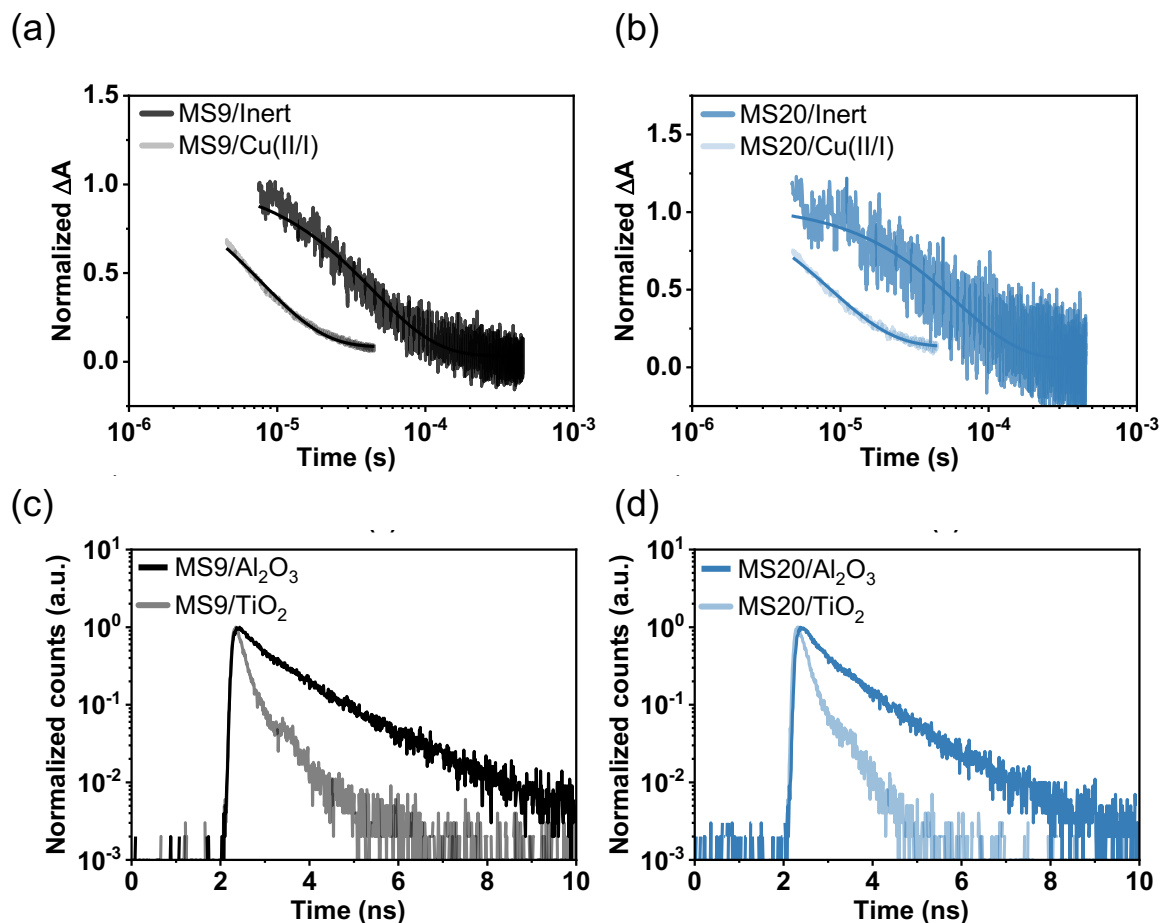


Figure 5.5. (a-b) Time-evolution of the dye oxidized state absorbance monitored at $\lambda_{\text{Probe}} = 820 \text{ nm}$ upon pulsed laser excitation at $\lambda_{\text{Pump}} = 500 \text{ nm}$ of half-devices composed of $4 \mu\text{m}$ thick TiO_2 layers sensitized with MS9 (a) and MS20 (b) in contact with an inert electrolyte or a redox-active electrolyte containing the $[\text{Cu}(\text{tmby})_2]^{+2/+1}$ couple. The solid lines represent the monoexponential fittings. The laser fluence for the inert electrolyte samples was set to $2.2 \mu\text{J}\cdot\text{cm}^{-2}$ and subsequently increased to $0.6 \text{ mJ}\cdot\text{cm}^{-2}$ for the samples containing the copper electrolyte. (c-d) Time resolved photoluminescence decays of half-cells composed of $4 \mu\text{m}$ thick TiO_2 or Al_2O_3 layers dyed by MS9 (c) and MS20 (d) in contact with an inert or a redox-active electrolyte based on the $[\text{Cu}(\text{tmby})_2]^{+2/+1}$ redox couple ($\lambda_{\text{Pump}}=520 \text{ nm}$, $\lambda_{\text{Probe}}=750 \text{ nm}$).

The electron injection efficiency was estimated by comparing the lifetimes of half cells fabricated with either Al_2O_3 or TiO_2 sensitized $4 \mu\text{m}$ thick films.

To mimic operating conditions, the cells were injected with the same electrolyte composition as in devices^{265,301,310,325,340}. The logarithmic plot of time resolved emission profiles as well as lifetimes extracted from bi-exponential fittings, are presented in Figure 5.5c and d as well as Table 5.4.

Table 5.4. Averaged lifetimes on Al_2O_3 ($\tau(A)_{av}$), TiO_2 ($\tau(T)_{av}$) and η_{inj} obtained from TRPL.

	$\tau_{av}(A)$ [ns]	$\tau_{av}(T)$ [ns]	η_{inj}^a [%]
MS9	1.05	0.21	79
MS20	0.80	0.19	75

^aThe injection efficiency was estimated using: $\eta_{i,inj} = 1 - \tau(T)_{i,av} / \tau(A)_{i,av}$, with $i=MS9$ and $MS20$.

A difference of roughly 200 ps can be observed between **MS9** (1.05 ns) and **MS20** (0.8 ns). The shorter $\tau_{av}(A)$ of **MS20** could be ascribed to either the presence of dye aggregates or the stronger electron withdrawing benzo-oxadiazole acceptor comprised in **MS20**. As highlighted by DFT calculations, this latter dye was found to possess a more planar structure in the S_0 state, which could facilitate inter-molecular stacking.

Upon swapping the metal-oxide substrate, the decays were considerably accelerated due to the injection of the photo-excited electron. The average lifetimes of these samples ($\tau_{av}(T)$) were found to be very similar for **MS9** (0.21 ns) and **MS20** (0.19 ns). The estimated charge injection efficiencies were found to be very close as well with values of 79 and 75% for respectively **MS9** and **MS20**. This result proves that η_{inj} is not the parameter limiting the IPCEs.

The charge collection efficiencies (η_{coll}) of **MS9** and **MS20** were estimated using small light modulation techniques.

As seen in Figure 5.6a and b, the transport times and extracted charges, were found to be very similar for both dyes, synonyms of similar electron transport timescales and conduction band edges.

However, electron lifetimes measurements (Figure 5.6c) revealed that **MS9** based devices possessed significantly longer τ_n . This striking difference was ultimately translated to lower collection efficiencies and V_{OC} for **MS20** based (Figure 5.6d). This final result ultimately explains the lower IPCE measured for **MS20** (see Figure 5.4b).

More precisely, electron lifetimes measurements reflect the degree of recombination between free electrons and the Cu(II) species in the electrolyte. In most cases, the rate of this recombination reaction will be influenced by the dye's behavior at the TiO_2 /electron interface. In this regard, the dye loading of **MS9** and **MS20** was measured, with values of respectively 30.1 and 25.7 nmol·cm⁻²· μ m⁻¹.

The slightly higher coverage achieved by **MS9** could be more efficiently protect free electrons from recombination with the $[Cu(tmby)_2]^{+2}$. More information can be obtained by considering, the geometrical differences exposed by the DFT calculations and the trend in τ_n .

More specifically, these findings suggest that the recombination between free electrons and $[Cu(tmby)_2]^{+2}$ is facilitated in the case of lesser steric hindrance around the donor, like it is the case in **MS20**. This effect is rationalized by the fact that a distorted donor could more efficiently repel the electrolyte, compared to a flatter configuration.

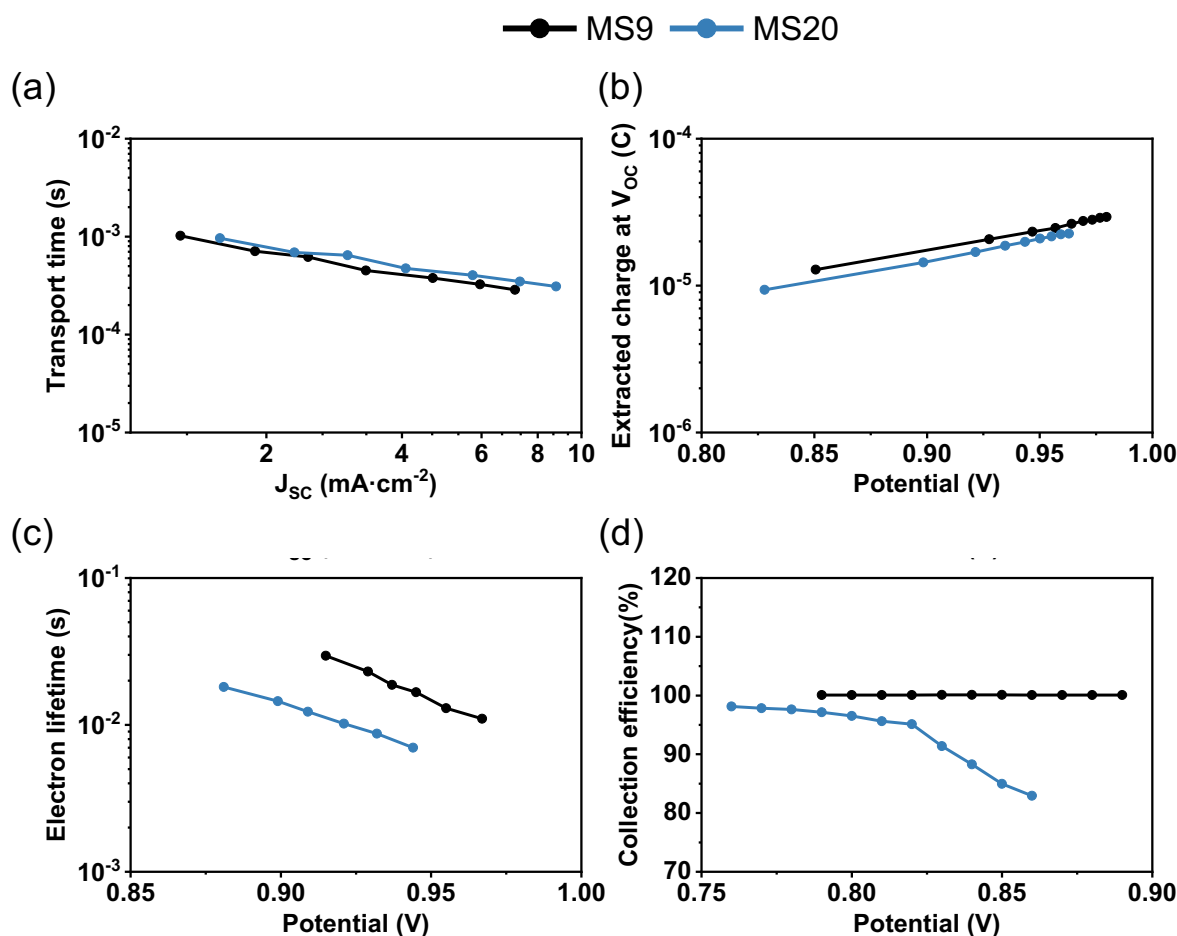


Figure 5.6. (a) Transport time as function of current density, Extracted charge at open circuit (b), Electron lifetime (c) and open circuit potential and charge collection efficiency as function of potential. The charge collection efficiency (η_{coll}) was estimated from the electron lifetime (τ_n) and the transport time (τ_{TR}) using the following equation: $\eta_{coll} = 1/(1 + \tau_{TR}/\tau_n)$.

5.3 Conclusion

In summary, two dyes coded **MS9** and **MS20** were successfully synthesized. Their auxiliary acceptor was varied from benzo-thiadiazole (**MS9**) to benzo-oxadiazole (**MS20**) and combined with a dithienopyrrole (DTP) π -linker. Investigation of their optical properties revealed that the benzo-oxadiazole acceptor induced a red-shift of the dye's spectral response by roughly 20 nm. In devices, **MS9** produced a J_{SC} of $16.43 \text{ mA}\cdot\text{cm}^{-2}$ which constitutes a record for $[\text{Cu}(\text{tmby})_2]^{+2/+1}$ based DSSCs.

The corresponding PCE was 12.4 %, while MS20 offered 10.8 % under similar conditions. DFT calculations revealed that this shift originates from both electronic and conformational contribution. The oxygen atom in the BO unit provides stronger electronegativity as well as smaller size, which indirectly increases the planarity of **MS20**.

This effect was also found to reduce, by extent, the repelling effect provided by the electron donating unit by diminishing its bulkiness. As a direct outcome, **MS20** based devices showed a lower electron lifetime, that was highlighted by the small light modulation techniques. The latter, was also found to be limiting in the devices' performances. This study highlights the importance of subtle dye design elements that needs to be thoroughly considered, from both electronic and geometric perspectives, as they can have significant deleterious impact on the PV performances of the sensitizers.

Chapter 6 : Simple D-A dyes synthesized in a one pot method enable high photo voltage.

Contributions:

In this chapter, I synthesized and characterized the dyes as well as measured the small light modulation spectra. Dr. Yameng Ren and Dan Zhang fabricated the devices and measured JV curves and IPCEs of the devices. Ma Wei and Jing Fu performed the computational calculations.

6.1 Introduction

Dye sensitized solar cells (DSSCs) consist of four main materials: a semi-conductor, a light absorbing dye, a redox active electrolyte and a counter electrode^{69,73,130,341}. Reducing the amount of steps required to access any of these latter is at the heart of lowering the production costs.

Nowadays, state of the art devices use organic dyes constructed according to the D-A- π -A or D- π -A pattern. Their main advantage lies in the dichotomy between the electron-donor and the electron-acceptor moieties^{2,342}. This class of dyes enabled power conversion efficiencies (PCE) above 10 % under standard AM1.5G conditions^{183,184,209,309}. However, they are produced via long and tedious synthetic routes, rendering up-scaling difficult and not cost-effective.

To circumvent this problem a new series of dyes following the simple donor-acceptor (D-A) pattern were developed, and discussed in this chapter. A short synthetic protocol, that allows the fabrication of the final dye in a one-pot method, was used. To study this class of D-A dyes in full DSSC, five new structures were synthesized with different electron acceptors, derived from benzo-diazoles. The central heteroatom of the acceptors' five-membered rings was modified from nitrogen (benzo-triazole) to sulfur (benzo-thiadiazole) and finally oxygen (benzo-oxadiazole).

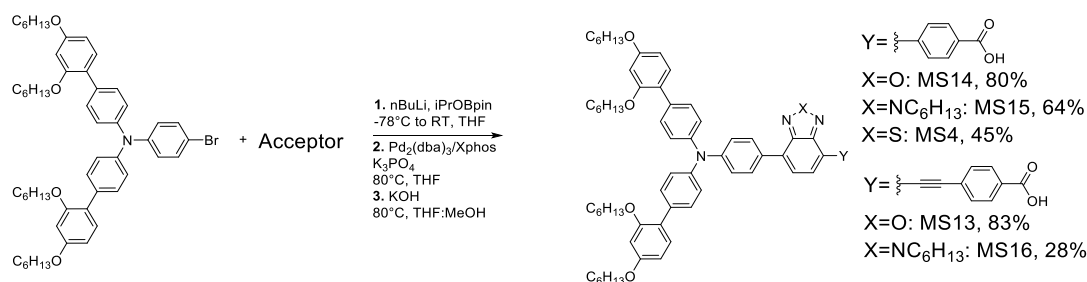
This systematic alteration probed the effect of an increased electronegativity, following the trend: N < S < O, with the aim to alter the excited state energy level and narrow the energy band gap of the dyes. Two sets of commercially available anchoring groups were used: benzoic acid (BA) and 4-ethynyl-benzoic acid (EBA).

6.2 Results and discussion

The dyes' synthesis was performed in one step, starting from N-(2',4'-bis(hexyloxy)-[1,1'-biphenyl]-4-yl)-N-(4-bromophenyl)-2',4'-bis(hexyloxy)-[1,1'-biphenyl]-4-amine obtained from a commercial source. The various electron accepting units were also synthesized in one step, from either a Suzuki or Sonogashira cross-coupling, as depicted in on Scheme 6.1. The procedure started by a Li-halogen exchange between the brominated electron donor and n-BuLi at -78°C.

The intermediate was subsequently quenched with an excess of 2-Isopropoxy-4,4,5,5-tetramethyl-1,3,2-dioxaborolane (iPrOBpin). In the next step, an aqueous solution of K₃PO₄ was added along with the acceptor-bromide and the Pd₂(dba)₃/Xphos catalytic system to perform a Suzuki coupling at 80°C.

Once the reaction completed, it was diluted with diethyl-ether as flashed through a pad of MgSO₄ to filter out metallic Palladium and inorganic salts. Finally, the crude was directly transferred into a second reaction vessel and submitted to hydrolysis under alkaline conditions to produce the final dye.



Scheme 6.1. Synthetic route to MS4, MS13, MS14, MS15 and MS16.

The dyes optical properties were investigated in diluted THF solution as well as adsorbed on 2.2 μm thick TiO₂ films. The results are displayed in Figure 6.1a and b. All dyes showed an intense peak below 350 nm, ascribed to a π-π* transition and a second one, corresponding to an intramolecular charge transfer (ICT) in the visible region.

Table 6.1. Optical and electrochemical properties of MS9 and MS20.

	λ_{onset}^a [nm]	$\lambda_{\text{max,CT}}(\epsilon)^a$ [nm(10 ⁴ M ⁻¹ ·cm ⁻¹)]	$\lambda_{\text{PL,max}}^{a,*}$ [nm]	$\lambda_{\text{abs,max}}^b$ [nm]	E_{HOMO}^c [V vs. NHE]	E_{LUMO}^d [V vs. NHE]	E_g^e [eV]
MS4	542	463(0.79)	603	468	1.05	-1.24	2.28
MS13	584	506(2.48)	704	502	1.18	-0.95	2.13
MS14	563	482(1.62)	685	486	1.13	-1.08	2.21
MS15	468	410(2.73)	553	410	1.08	-1.57	2.65
MS16	486	424(2.18)	531	424	1.10	-1.46	2.56

^aObtained from diluted THF solutions. ^bObtained from measurement 2.2 μm thick TiO₂ films sensitized with the dyes, ^cEstimated from the onset of the oxidation potential of the dyes adsorbed on TiO₂ measured using cyclic voltammetry, with Ferrocene as internal standard and subsequently converted to NHE by adding 0.624 V to the value²⁹⁹. ^dObtained from $E_{\text{HOMO}} - E_g$. ^eEstimated using: E_g : 1242/ λ_{onset} . *Samples excited at 500 nm.

As it can be seen on Table 6.1, the position of the ICT was greatly consistently affected by the electron deficiency of the acceptor.

More specifically, **MS15** and **MS16**, based on the weakest benzotriazole (BTz), showed the most blue shifted $\lambda_{\max,CT}$ values, whereas, the two dyes containing the stronger benzo-oxadiazole (BO) units, **MS13** and **MS14**, have the most red-shifted peaks. The absorption maxima of the benzothiadiazole (BT) dye (**MS4**) stands between the two other types of dyes. The effect of the supplementary ethynyl bond was found to induce a consistent 20 nm shift of $\lambda_{\max,CT}$, to the longer wavelengths, regardless of the acceptor's nature. The trend of the absorption maxima in solution was conserved upon adsorption of the sensitizers on TiO_2 films.

The dyes' Stokes shifts were determined from solution absorption and emission spectra (see Figure 0.77b). Interestingly, the two dyes containing the BTz acceptor (**MS15** and **MS16**) were found to have the smallest shifts along with **MS4** (BT), with values of respectively 143, 147 and 140 nm. These result indicate that **MS15**, **MS16** and **MS4**, seem to retain most of their conformation upon transition to the S_1 state. On the other hand, the two BO dyes (**MS13** and **MS14**), displayed greater shifts of respectively, 198 and 203 nm, synonym of stronger but similar conformation changes upon photo-excitation.

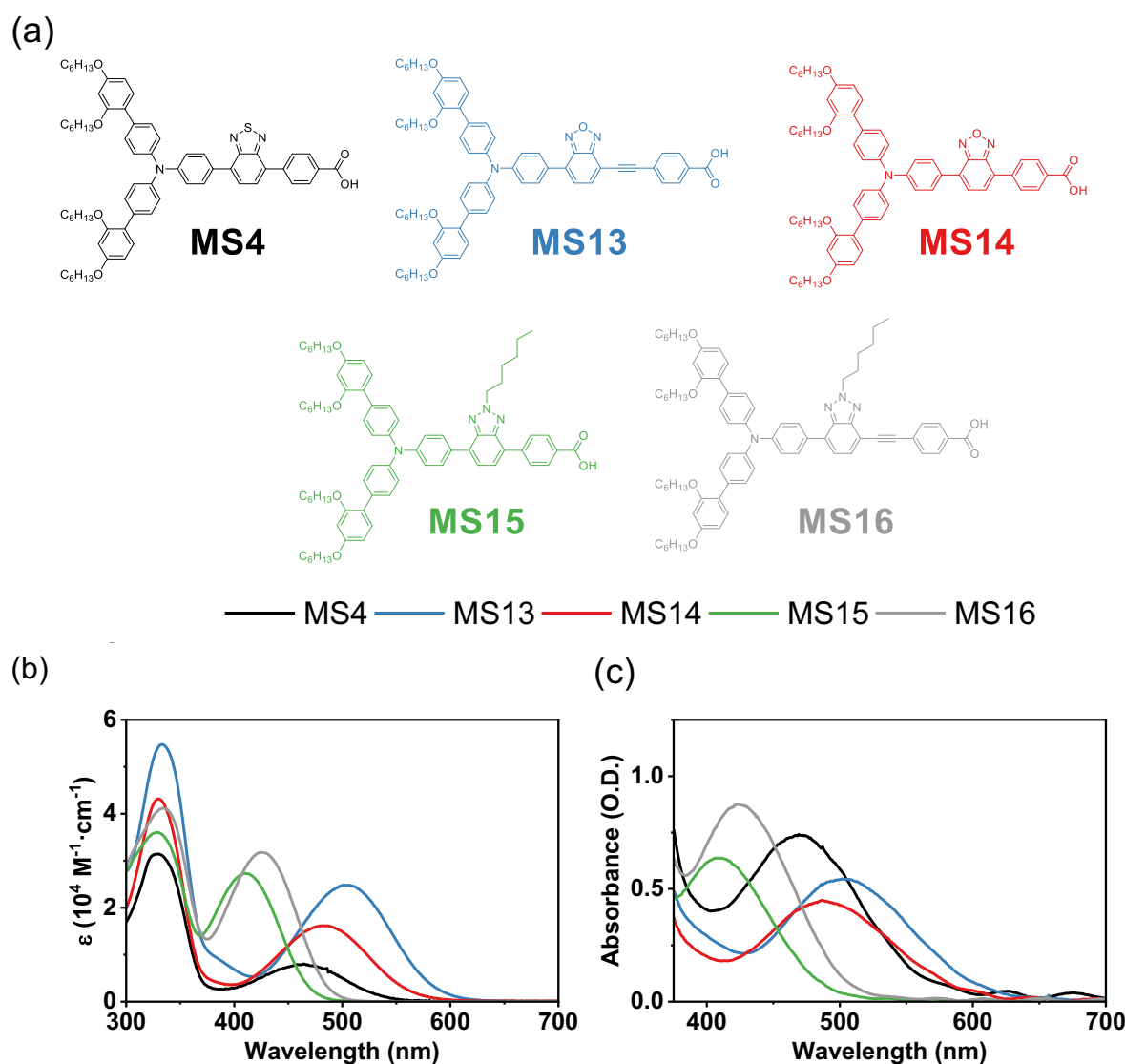


Figure 6.1. (a) Molecular structures of the sensitizers. (b) Molar absorptivity of the three dyes dissolved in THF. (c) Absorbance of 2.2 μm thick TiO_2 films sensitized with the three dyes.

Cyclic voltammetry (see Figure 0.16) was used to investigate the trend found in the dyes energy levels. As expected, the HOMO levels, were found to be similar with E_{HOMO} lying above 1 V vs. NHE for all dyes. These findings indicated that the shifts in absorption maxima originated from disparities in E_{LUMO} (Table 6.1). More specifically, the E_{LUMO} shifts were inversely proportional to the electronegativities of the acceptors' central atoms.

In addition to that, the triple bond linker was found to induce a subsequent stabilization of E_{LUMO} . Similar to the LUMO levels, the trend in energy band gaps (E_g) inversely follows the order of electronegativities according to N, BTz (3.04) < S, BT (2.58) < O, BO (3.44).

The apparent differences in optical properties were further investigated by means of density functional theory (DFT). The HOMO/LUMO wave functions of the dyes can be found in Figure 6.2.

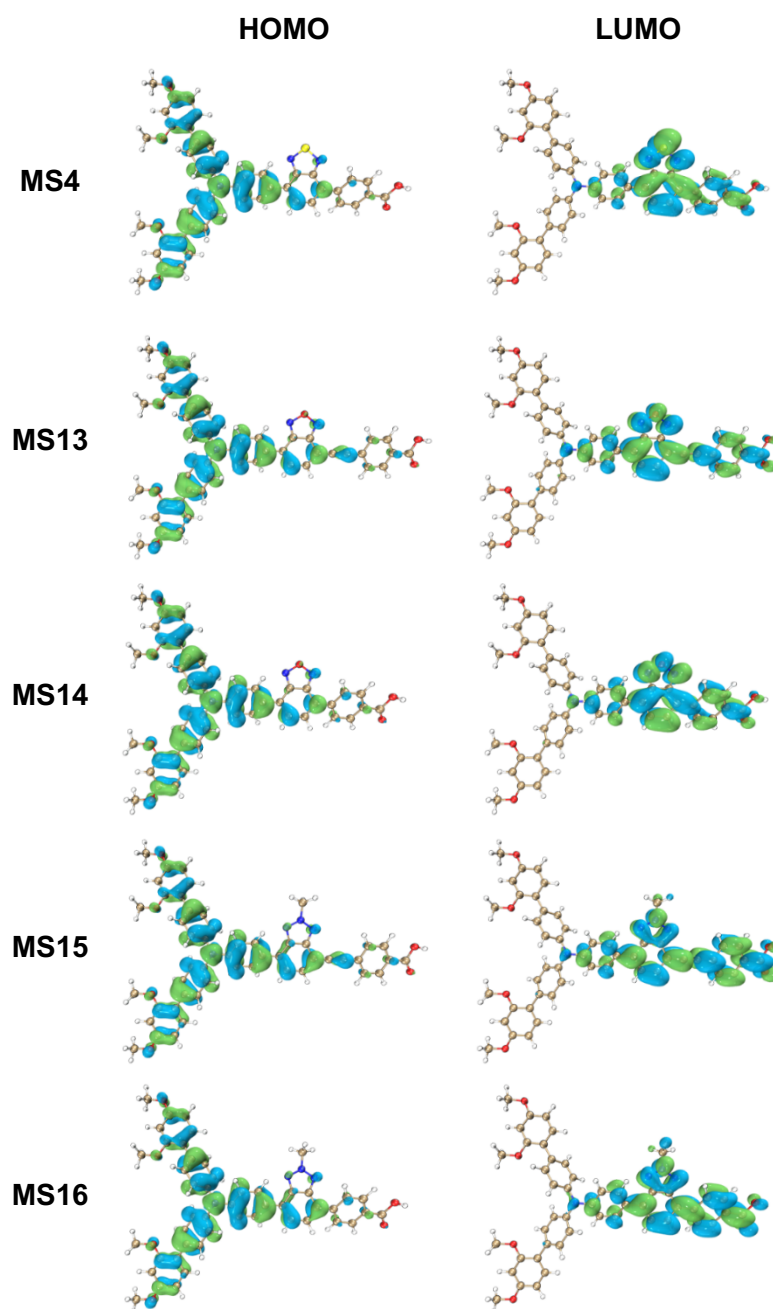


Figure 6.2. Distribution of the Molecular orbitals obtained using the B3PW91 functional and 6-31G(d,p) basis sets.

The ground states (S_0) and the first excited states (S_1) geometries of the dyes were calculated using the CAM-B3LYP functional and 6-31G(d,p) basis sets (see Figure 6.3). The effect of atom substitution can be investigated by comparing the ground state conformations of **MS4**, **MS13** and **MS15**.

The HOMO wave functions were all mainly located on the electron donating unit and slightly up to the six-membered ring of the electron acceptor.

The LUMO orbitals spread over the acceptor/anchor segment of the dyes, and more markedly on the BT, BTz and BO units. For all dyes, the LUMO wave functions were located adequately close to the TiO_2 surface which should ensure a good electronic coupling between the dye and the semi-conductor^{74,86}.

As seen in Figure 6.3, the main difference lies in the dihedral angles adjacent to the acceptor units. The torsion of these bond axes consistently increases with the atomic radius of the varied acceptor atoms: S (BT) > N (BTz) > O (BO). In a similar way to the findings in Chapter 5 it was speculated that, as the central atom shrinks, the ring contracts and reduces its steric interactions with the neighboring units. In addition to that effect, the insertion of a triple bond, was found to reduce the steric clash on both side of the acceptor while retaining the tendency in atomic radii.

In the S_1 state, the molecules showed flattened structures characterized by a general diminution of all dihedral angles. The heteroatoms' sizes had less impact on the dyes' geometries in the excited state, especially for the BTz (**MS15**, **MS16**) and BO (**MS13**, **MS14**) based dyes, where similar angles were observed at the phenyl-acceptor axes. By contrast, the BT dye (**MS4**) still retained a heavily distorted conformation, with a strikingly high value of 14.87° .

It is worth mentioning that the additional triple bond in **MS13** and **MS16** drastically improves their planarity in the S_1 state compared to their analogue compounds depleted of triple bond (**MS13** and **MS15**). Notably, the torsion along the acceptor-anchor was reduced from 13.17° (**MS13**) to 2.31° (**MS14**) for the BO dyes, as well as for the BTz based dyes from 11.11° (**MS15**) to 1.71° (**MS16**).

Generally, the stabilization of the dyes' energy levels can be achieved, either by altering the electronic properties of the building block, or increasing their planarity^{155,158}. The optical characterization of the D-A dyes presented in Table 5.1, show that the stabilization of the LUMO levels was increasing consistently with the acceptor central atom's electronegativity. This finding suggested that the variations of E_{LUMO} was solely influenced by the building block's electronic properties.

This hypothesis was further supported by the DFT calculations of the dyes' geometries, where the trend in planarity was found to be: **MS4** < **MS15** < **MS16** < **MS14** < **MS13**. Interestingly, the dyes' conformations seem to influence the molar absorptivity, as more planar molecules, based on the BO and Btz acceptors, displayed higher $\epsilon(\lambda)$ values than the less planar **MS4**.

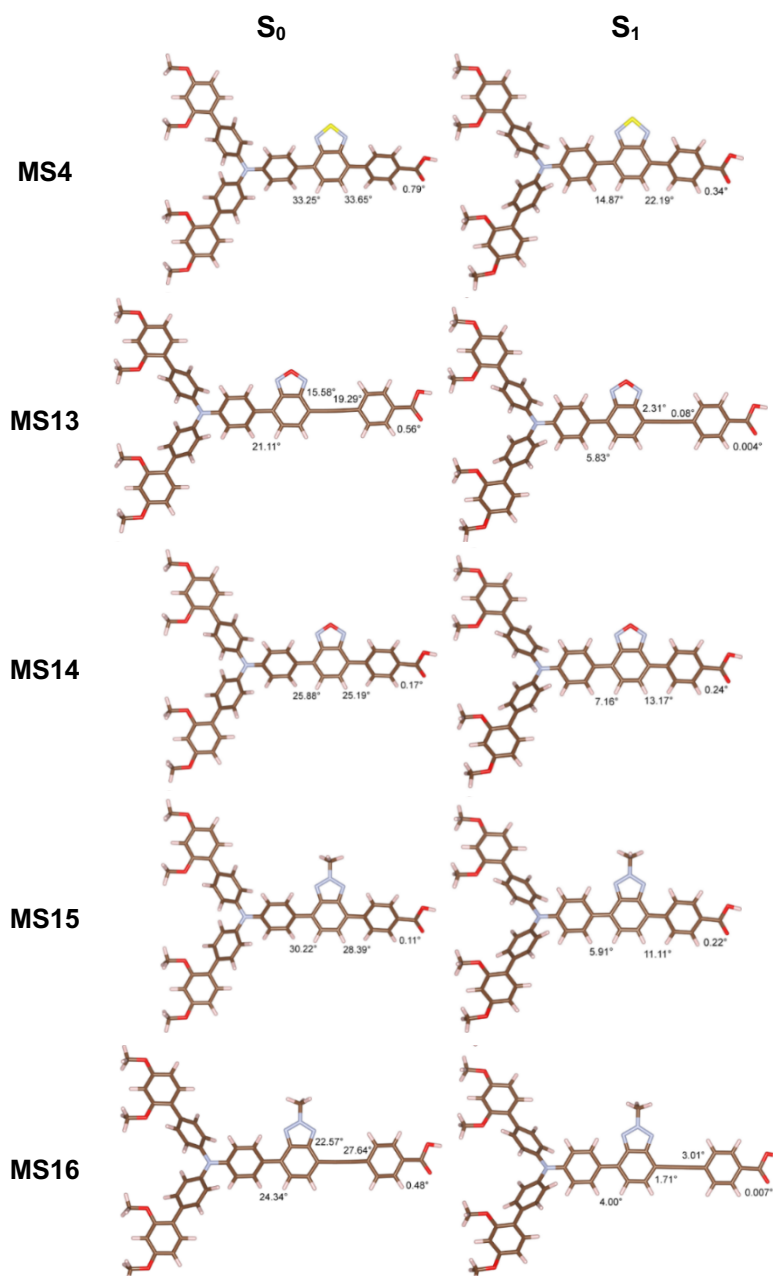


Figure 6.3. Geometry optimized structures of the ground state and the first excited state (S_1) of the dyes with the corresponding dihedral angles between each plain using the CAM-B3LYP functional and 6-31G(d,p) basis sets.

All dyes were tested in devices comprising the $[\text{Cu}(\text{tmby})_2]^{+2/+1}$ redox electrolyte. Current density-potential (J-V) plots and photovoltaic performances are summarized in Figure 6.4 and Table 6.2, respectively.

As expected, the short current density (J_{SC}) values were consistent with the band gap width: **MS14** > **MS13** > **MS4** > **MS16** > **MS15**.

The highest J_{SC} ($8.24 \text{ mA}\cdot\text{cm}^{-2}$) was achieved by **MS13**, the dye comprising a benzo-oxadiazole acceptor and triple bond linker.

Gratifyingly, all measured open circuit voltages (V_{OC}) were above 1 V, demonstrating the good compatibility of these simple sensitizers with the copper complex.

More specifically, devices fabricated with **MS13**, **MS14** and **MS15** produced photo-voltages of 1.10, 1.09 and 1.13 V, respectively. Overall the two dyes, based on the BO acceptor (**MS13** and **MS14**), produced equally high PCEs of 6.9%, under standard AM1.5G.

Table 6.2. Detailed PV performances measured under AM1.5G ($100 \text{ mW}\cdot\text{cm}^{-2}$).

	J_{sc} [$\text{mA}\cdot\text{cm}^{-2}$]	V_{oc} [V]	FF [%]	PCE [%]
MS4	7.19	1.06	69	5.6
MS13	8.24	1.10	72	6.9
MS14	8.96	1.10	70	6.9
MS15	4.41	1.13	72	3.8
MS16	5.32	1.06	72	4.4

The incident photon to current conversion efficiency (IPCE) of the devices was measured to further investigate the performances of the dyes. Figure 6.4b shows that the two highest values nearing 80 % were achieved with **MS15** and **MS16** (BTz). **MS4** and **MS14** showed IPCE values between 60 and 70%, whereas the lowest values around 50 %, were obtained by the most red-shifted dye **MS13**.

Furthermore, the IPCEs profiles indicated **MS15** and **MS16** suffered from their wide band gaps, that translated into very blue-shifted IPCE onsets (Figure 6.4b). The difference in J_{sc} between **MS4** and **MS14** was about $0.7 \text{ mA}\cdot\text{cm}^{-2}$ which seems to originate from the 25 nm red-shifted IPCE onset of **MS14** compared to **MS4**.

Despite its low photon conversion values of 50 % in the visible spectra, **MS13** managed to produce the highest J_{sc} ($8.24 \text{ mA}\cdot\text{cm}^{-2}$). As displayed in Figure 6.4b, this performance is attributed to its broader absorption onset, that compensates its lower conversions values.

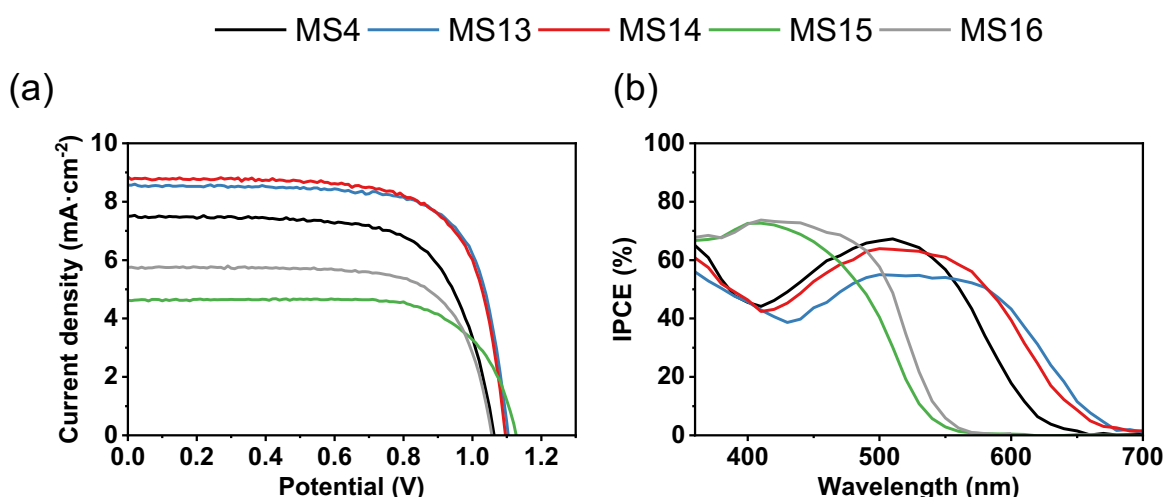


Figure 6.4. (a) J - V curves of cells measured under AM1.5G. (b) IPCE spectra of the cells.

Using a similar method than in the other chapters, the differences in IPCE plateau were investigated by estimating and comparing the harvesting (LHE), collection (η_{coll}), injection (η_{inj}) and regeneration (η_{reg}) of the devices. The light harvesting efficiency was measured for $2.2 \mu\text{m}$ thick TiO_2 films and plotted in Figure 0.77c.

It was found that all dyes possessed similar LHE values, ruling out this factor as discriminating element of the IPCE profiles.

The regeneration efficiency estimates the yield of dye cation (D^+) that is regenerated by the $[Cu(tmby)_2]^{+2/+1}$. It is known that only 0.1 eV driving force is good enough to efficiently regenerate D^+ with the copper complex³²⁰. Hence, the dye regeneration driving forces (ΔG_{reg}) were estimated, from the redox potential of $[Cu(tmby)_2]^{+2/+1}$ (0.871 V vs. NHE) and summarized on Table 6.3.

It was found that in all cases > 0.1 eV which should ensure a similar and sufficient for η_{reg} for all dyes. The charge injection efficiency evaluates the rate of interfacial electron transfer (IET) taking place between the dye excited state and its self-quenching rate. This IET is influenced by the dye LUMO level which dictates the driving force for electron injection and the electronic coupling between the LUMO level of the dye^{343,344}.

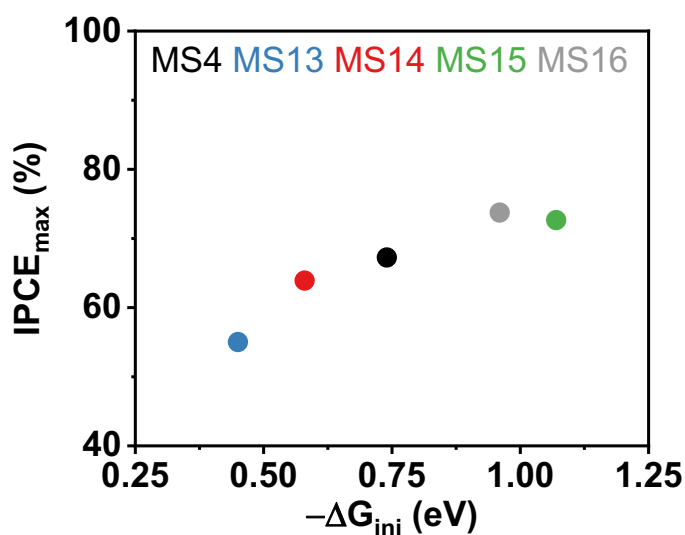


Figure 6.5. IPCE maximum of the devices vs. $-\Delta G_{inj}$.

The electronic coupling can be dismissed as a discriminating factor as DFT calculations showed that the dyes' LUMO wave functions had similar localizations. The injection driving force ($-\Delta G_{inj}$), is defined as the difference between E_{LUMO} and the conduction band edge of TiO_2 , located at -0.5 V vs. NHE^{73,86}. The estimated $-\Delta G_{inj}$ of each dye was collected in Table 6.3 and compared to the IPCE maxima in Figure 6.5. It was found that the IPCE maxima consistently decreases with $-\Delta G_{inj}$, indicating that the IPCEs might have been limited by insufficient driving force.

Table 6.3. ΔG_{reg} , $-\Delta G_{inj}$ and maximum IPCE estimated from Table 5.1.

	ΔG_{reg}^1 [eV]	$-\Delta G_{inj}^2$ [eV]	IPCE _{max} ³ [%]
MS4	0.179	0.74	67
MS13	0.309	0.45	55
MS14	0.259	0.58	64
MS15	0.209	1.07	73
MS16	0.229	0.96	74

¹Estimated from: $E_{HOMO}-0.871$, ²Estimated from: $E_{LUMO}+0.5$, ³Over the 400-700 nm window.

Finally, the electron lifetimes (τ_n), transport times (τ_{TR}) and η_{coll} were measured along with the charge extracted at V_{OC} (Q_{OC}). The results are plotted in Figure 6.6a to c. The devices were found to display similar transport times with no clear influence of the structural alteration (Figure 6.6a).

Combining τ_{TR} with the electron lifetimes allowed to estimate the charge collection efficiency. These values were found to lie around 95 % regardless of the dyes structure. This finding confirmed that the dyes performances were limited by the electron injection step.

The differences in V_{OC} obtained from the J-V experiments were rationalized by studying τ_n and Q_{OC} plotted in Figure 6.6c and b. The record device, fabricated with **MS15** (BTz), produced a photo voltage of 1.13 V showed long lifetime. This result indicates that **MS16** was able to slow down the reaction between the free electrons in the TiO_2 and $[Cu(tmby)_2]^{+2}$ species more effectively than the other sensitizers. One of the factors influencing the rate of electron recombination is the surface coverage. This latter was found to be 17.45 (**MS4**), 11.75 (**MS13**), 13.25 (**MS14**), 11.65 (**MS15**) and 13.75 $nmol \cdot cm^{-2} \cdot \mu m^{-1}$ (**MS16**). The dye with the highest V_{OC} (**MS15**) was found to be less adsorbed on TiO_2 , which suggests that in this case, the recombination rate is not influence by the dye coverage.

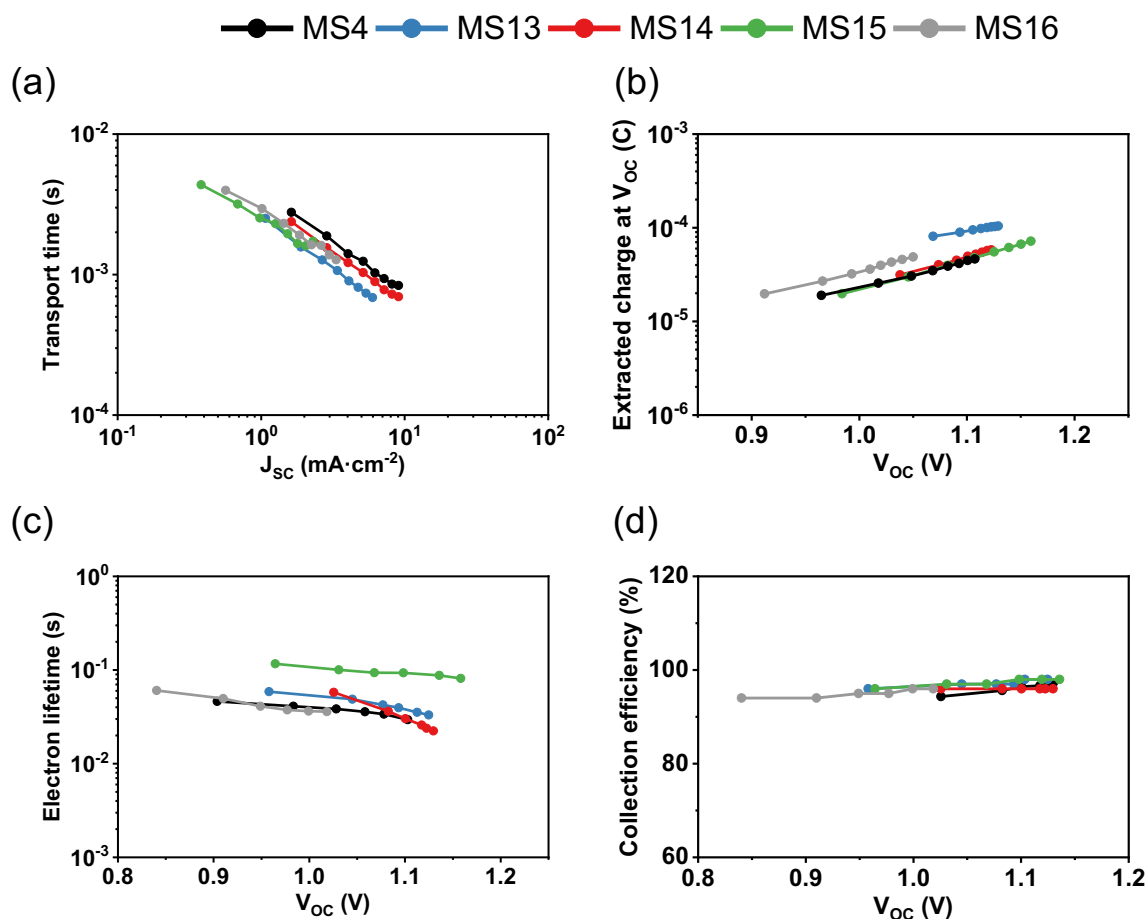


Figure 6.6. (a) Transport time as function of current density, (b) Extracted charge at open circuit potential, (c) Electron lifetime and open circuit potential and charge collection efficiency as function of the open circuit potential. The charge collection efficiency (η_{coll}) was estimated from the electron lifetime (τ_n) and the transport time (τ_{TR}) using the following equation: $\eta_{coll} = 1/(1 + \tau_{TR}/\tau_n)$.

More information on the interfacial configurations of the dyes can be obtained by comparing the relative shifts in the conduction band edge (ΔCBE) described by the charge extraction measurements in Figure 6.6c. From the logarithmic plot of Q_{OC} vs. V_{OC} , it can be seen that at similar Q_{OC} value, **MS14** and **MS16** possess a CBE shifted towards lower values than the other sensitizers.

As mentioned in the other chapters, shifts in CBE depend on variation of the dye loading (N), the dipole moment of the dyes (μ) and the angle between the dye and the normal vector of the TiO_2 surface (θ)^{304,305}. The dyes' dipole moments were found to be: 10.78 (**MS4**), 12.49 (**MS13**), 11.93 (**MS14**), 10.84 (**MS15**) and 11.53 D (**MS16**). These relatively similar values, indicate that the relative shifts in CBE can either be caused by variation in the dyes' loadings or adsorption geometries.

Hence, the ΔCBE experienced by **MS13** and **MS16** shift could originate from a more tilted adsorption geometry displayed by these two molecules, synonym of dye aggregation³⁴⁵. These dyes both feature an ethynyl linker, that was found reduce the general torsion of the dye, which by extent facilitate the dye inter-molecular stacking.

6.3 Conclusion

In summary, a series of small dyes, based on a simple D-A pattern, were synthesized using a one-pot method. Three electron accepting units were screened: benzothiazole (**MS4**), benzo-oxadiazole (**MS13** and **MS14**) and benzo-triazole (**MS15** and **MS16**) in combination with two linkers: 4-ethynyl benzoic acid and benzoic acid.

These new sensitizers were tested in devices fabricated with the high-redox potential couple $[\text{Cu}(\text{tmby})_2]^{+2/+1}$. They all produced photo-voltages lying around 1.1 V. The disparity in efficiencies originated from their photo-currents (J_{SC}). It was found that the devices IPCEs were limited by the dyes electron injection driving force ($-\Delta G_{\text{inj}}$), that depended on E_{LUMO} .

Paradoxically, the dye with the lowest IPCE value of 50% (**MS13**) was found to produce the highest photo-current of $8.24 \text{ mA}\cdot\text{cm}^{-2}$ and a high V_{OC} of 1.10 V, corresponding to a PCE of 6.9 % under AM1.5G. This dye benefited from its very red-shifted absorption onset of 584 nm. The small differences in photo-voltages were found to be mainly caused by discrepancies in the dyes' electron lifetimes.

By comparing the relative shifts in CBEs it was found that the two dyes bearing an ethynyl linker (**MS14** and **MS16**), might show more pronounced dye aggregation. DFT calculations explained that the triple was responsible for flattening the dyes' structure. Ultimately, this feature could favor inter-molecular stacking of the dyes. This study identified the benzo-oxadiazole building block as the most promising acceptor for such small D-A dye, despite its low lying LUMO.

Chapter 7 : Rational molecular design of a simple dye enables record photo-voltage and power conversion efficiencies, through alteration of electron recombination mechanism.

Contributions:

In this chapter, I synthesized, designed and characterized the dyes. Dr. Yameng Ren and Dan Zhang fabricated the devices and measured JV curves and IPCEs of the devices. Etienne Socie measured the TAS and processed the data.

7.1 Introduction

Improving the power output generated by a dye sensitized solar cell, implies boosting the photo-current density (J_{SC}) and photo-voltage (V_{OC}) of the devices. As explained in section 1.4, the J_{SC} , relies on the overlap between the incident photon to current conversion efficiency(IPCE) and the light source spectral photon flux(Φ) according to equation (1.31)⁷³: The V_{OC} will be defined by the position of the TiO_2 conduction band edge (E_{CBE}), the electrolyte redox potential (E_{redox}), the number of electrons in the $TiO_2(n_e)$, the conduction band states (N_{CB}) and a correction factor(β) (see equation (1.28))²¹⁵.

Most of the parameters described in the above paragraph, will depend on the molecular structure of the dye. More specifically, the strategy used to generate high photo-currents consists in using a narrow band gap dye that can harvest most wavelengths of the electromagnetic spectrum. However, a narrow band gap can lower the E_{CBE} , and by extent the V_{OC} . Hence, high photo-voltages are usually achieved by wide band gap dyes that will help lifting the conduction band edge, but at the cost of a limited the photo-current output.

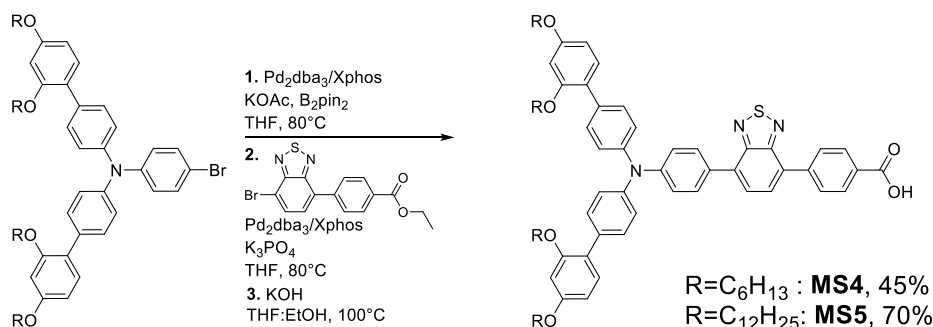
Co-sensitization is a method used to circumvent this particular conundrum. It consists in combining a dye who possesses a very broad spectral response with a secondary dye called a co-sensitizer. This latter usually possesses a wider band gap and smaller size than the former. The resulting co-sensitized device usually performs better than the single dye one, as the auxiliary sensitizer fills up the valley in the absorption spectra while improving the surface coverage of the TiO_2 ^{94,183,346,347}.

The pervious chapter highlighted the ability of simple D-A dyes to generate V_{OC} over 1.1 V with the $[Cu(tmby)_2]^{+2/+1}$ redox couple. To push the performances further, the dye coded **MS4** was modified by elongation of the alky chains located on the N-(2',4'-bis(hexyloxy)-[1,1'-biphenyl]-4-yl)-N-(4-bromophenyl)-2',4'-bis(alkoxy)-[1,1'-biphenyl]-4-amine donor, from hexyl to dodecyl, with the aim to reduce even further recombination rate between the electrons in the TiO_2 and the electrolyte.

7.2 Results and discussion

The dyes were synthesized according to Scheme 7.1. Briefly, it starts with a Miyaura borylation, to convert the two N-(2',4'-bis(hexyloxy)-[1,1'-biphenyl]-4-yl)-N-(4-bromophenyl)-2',4'-bis(alkoxy)-[1,1'-biphenyl]-4-amines into their pinacol-ester analogues.

The intermediate was subsequently reacted with ethyl 4-(7-bromobenzo[c][1,2,5]thiadiazol-4-yl)benzoate under the conditions of a Suzuki cross-coupling catalyzed by $\text{Pd}_2(\text{dba})_3$ and Xphos. The final dyes were obtained by hydrolysis of their ethyl-esters precursors with KOH.



Scheme 7.1. Synthetic route to **MS4** and **MS5**.

The dyes' molecular structures are illustrated in Figure 7.1a. Their optical and electrochemical properties were characterized and summarized on Table 7.1. As expected, the elongation of side chains on the donor moiety, does not induce any disparity in their opto-electrochemical properties.

Table 7.1. Optical and electrochemical properties of **MS4**, **MS5** and **XY1b**.

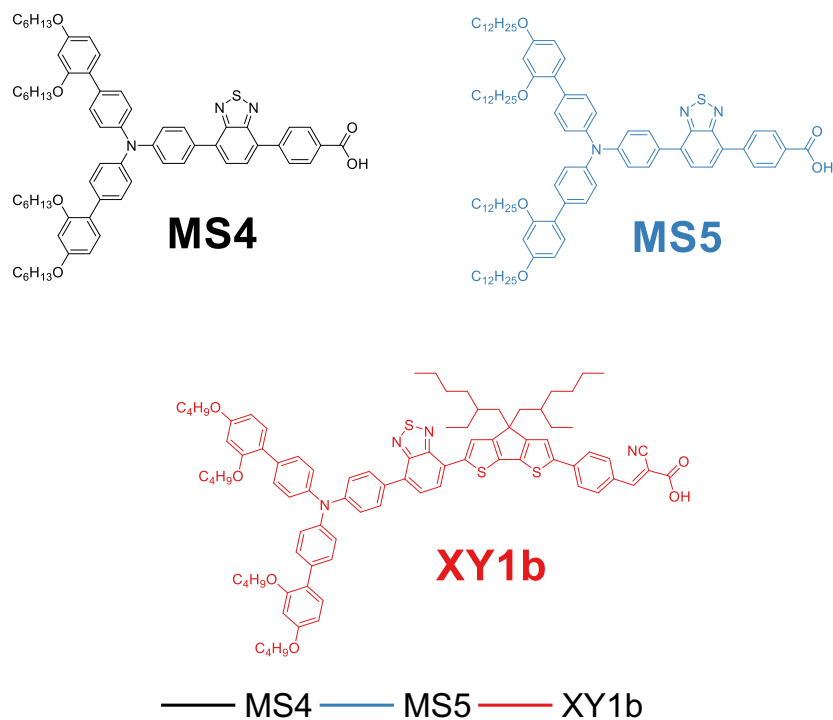
	λ_{onset}^a [nm]	$\lambda_{\text{max,CT}}(\epsilon)^a$ [nm($10^4 \text{ M}^{-1} \cdot \text{cm}^{-1}$)]	$\lambda_{\text{PL,max}}^{a,*}$ [nm]	$\lambda_{\text{abs,max}}^b$ [nm]	E_{HOMO}^c [V vs. NHE]	E_{LUMO}^d [V vs. NHE]	E_g^e [eV]
MS4	542	463(0.79)	603	468	1.05	-1.24	2.28
MS5	544	463(1.26)	603	468	1.08	-1.20	2.29
XY1b	619	542(3.60)	676	531	1.01	-1.00	2.01

^aObtained from diluted THF solutions. ^bObtained from measurement 2.2 μm thick TiO_2 films sensitized with the dyes, ^cEstimated from the onset of the oxidation potential of the dyes adsorbed on TiO_2 measured using cyclic voltammetry, with Ferrocene as internal standard and subsequently converted to NHE by adding 0.624 V to the value²⁹⁹. ^dObtained from $E_{\text{HOMO}} - E_g$. ^eEstimated using: E_g : $1242/\lambda_{\text{onset}}$. *Samples excited at 500 nm.

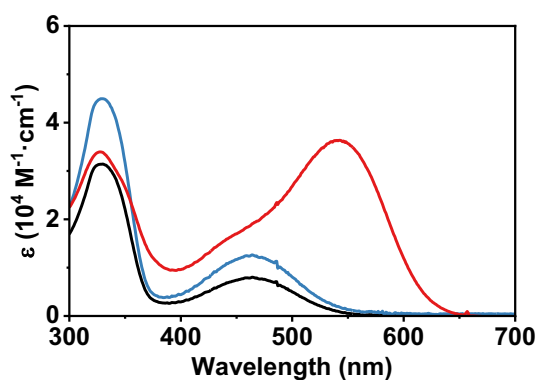
Both **MS4** and **MS5** present maxima located around 465 nm, in solution as well as adsorbed on TiO_2 films. Compared to the reference dye, **XY1b**, they both possess a much weaker molar absorptivity and blue shifted spectral response.

Benefiting from much stronger electron accepting unit and CPDT π -bridge, **XY1b**, showed a E_{LUMO} located at -1 V vs. NHE. On the other hand, **MS4** and **MS5** displayed LUMO levels of respectively -1.24 and -1.20 V vs. NHE while retaining similar E_{HOMO} as **XY1b**, around 1 V vs. NHE.

(a)



(b)



(c)

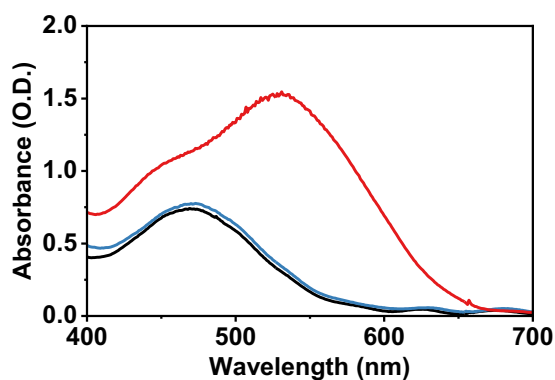


Figure 7.1. (a) Molecular structures of the sensitizers. (b) Molar absorptivity of the three dyes dissolved in THF. (c) Absorbance of 2.2 μm thick TiO_2 films sensitized with the three dyes.

In the next stage, devices sensitized with **MS4**, **MS5**, **XY1b** and a **MS5:XY1b** mixture, were fabricated with the $[\text{Cu}(\text{tmby})_2]^{+2/+1}$ redox couple.

The results are displayed in Figure 7.2a and detailed photovoltaic parameters were summarized on Table 7.2.

Table 7.2. Detailed PV performances measured under AM1.5G ($100 \text{ mW}\cdot\text{cm}^{-2}$).

	J_{sc} [$\text{mA}\cdot\text{cm}^{-2}$]	V_{oc} [V]	FF [%]	PCE [%]
MS4	8.8	1.17	73	7.6
MS5	8.8	1.24	73	8.0
XY1b	15.2	1.01	76	11.8
MS5:XY1b	15.8	1.05	81	13.5

As predicted by similar E_g of 2.28 eV, **MS4** and **MS5** produced similar short current densities (J_{SC}) of $8.8 \text{ mA}\cdot\text{cm}^{-2}$. On the other hand, **XY1b**, benefited from its broader absorption and achieved a J_{SC} of $15.2 \text{ mA}\cdot\text{cm}^{-2}$.

The open circuit voltages (V_{OC}) produced by the two small dyes, were both impressively high, with 1.17 and 1.24 V for respectively **MS4** and **MS5**. These two molecules only differ by the length of the aliphatic chains installed on the bis-alkoxy unit of the donor. More precisely, the length was doubled from hexyl to dodecyl, which enabled an impressive photo-voltage of 1.24 V. Compared to **XY1b**, these two very simple dyes offered open circuit potentials by almost 0.2 V higher.

Overall, **MS4** and **MS5**, obtained good power conversion efficiencies close to 8%, under AM1.5G conditions. The reference dye, **XY1b**, showed a PCE of 11.8% under the same conditions. The champion dye **MS5** was combined with **XY1b** in a co-sensitized system. The resulting device enabled J_{SC} and V_{OC} values of respectively $15.8 \text{ mA}\cdot\text{cm}^{-2}$ and 1.05 V. This DSSC delivered a record PCE of 13.5% under AM1.5G, which demonstrates the potential of **MS5** as a promising co-sensitizer.

The IPCEs showed high values of 80% for all devices (Figure 7.2b). The photon collection profile of **XY1b** effectively harvested light over a range of 400 to 700 nm. **MS4** and **MS5**, were found to have onsets above 600 nm, with a drop of 20 % to 60%, around 400 nm, consistent with their absorption profiles. The co-sensitized device, fabricated with **MS5:XY1b** possessed the same IPCE onset as **XY1b**, but with improved conversion efficiencies by roughly 10 %.

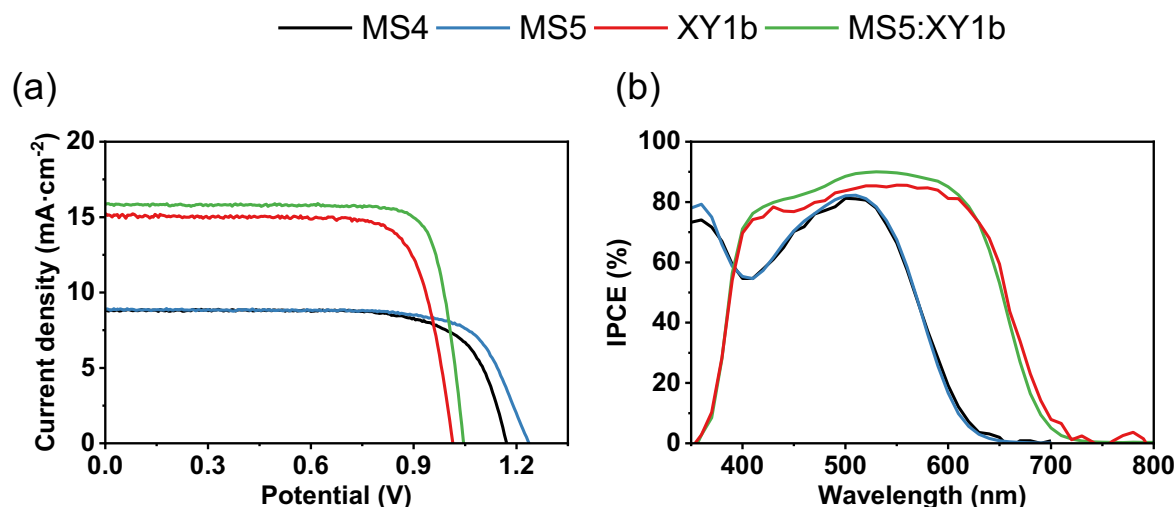


Figure 7.2. (a) J - V curves of cells measured under AM1.5G. (b) IPCE spectra of the cells.

The interfacial electron transfer (IET) between the photo-oxidized dye and the redox electrolyte was investigated by transient absorption spectroscopy (TAS). Figure 7.3a and b show the decays of samples fabricated with respectively **MS5** and **XY1b**.

The dye cation (D^+) of **MS5**, exhibited a high τ_{inert} of 345 μs , which was significantly higher than **XY1b** (49 μs). Interestingly, the co-sensitized sample showed a τ_{inert} closer to **XY1b**, with a value of 61 μs . The reduction of D^+ by $[\text{Cu}(\text{tmbpy})_2]^{+1}$ was found to occur at a similar rates for all samples (see Table 7.3).

Table 7.3. Lifetimes and η_{reg} obtained from TAS.

	τ_{inert} [μ s]	$\tau_{Cu(II/I)}$ [μ s]	η_{reg}^a [%]
MS5	345	5.9	98
XY1b	49	5.7	86
MS5:XY1b	61	6.0	91

^aThe regeneration efficiency was calculated using: $\eta_{i,reg} = k_{i,Cu(II/I)} / (k_{i,inert} + k_{i,Cu(II/I)})$, with $k_{i,Cu(II/I)} = 1 / \tau_{i,Cu(II/I)}$, $k_{i,inert} = 1 / \tau_{i,inert}$, $i = MS4, MS5$ or $MS5:XY1b$.

This finding indicates that the dodecyl chain does not impair the single electron transfer between the copper complex and the oxidized dye. Overall, the regeneration efficiencies (η_{reg}) were all found to be readily similar, with values close to 90 %.

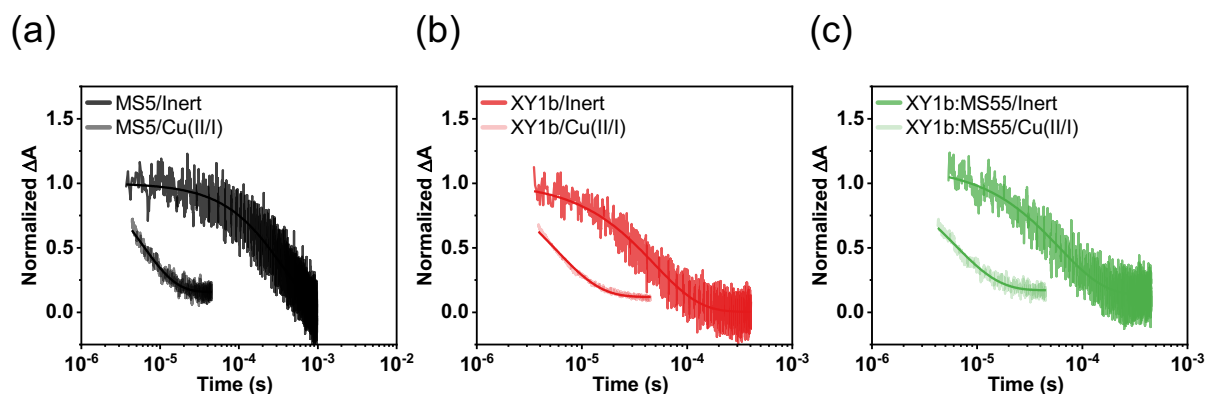


Figure 7.3. (a-c) Time-evolution of the dye oxidized state absorbance monitored at $\lambda_{Probe} = 820$ nm upon pulsed laser excitation at $\lambda_{Pump} = 500$ nm of half-devices composed of $4 \mu m$ thick TiO_2 layers sensitized with MS5 (a), XY1b (b) and MS5:XY1b (c), in contact with an inert electrolyte or a redox-active electrolyte containing the $[Cu(tmby)_2]^{+2/+1}$ couple. The solid lines represent the monoexponential fittings. The laser fluence for the inert electrolyte samples was set to $2.2 \mu J \cdot cm^{-2}$ and subsequently increased to $0.6 mJ \cdot cm^{-2}$ for the samples containing the copper electrolyte.

The PV performances were further investigated by comparing the electron lifetimes and charge extracted at V_{OC} of the single-dye devices, with the co-sensitized system (see Figure 7.4a and Figure 7.4b).

Charge extraction measurements, revealed that all devices possessed similar conduction band edge position. Electron lifetimes measurements (Figure 7.4b) showed that, **MS4** and **MS5** based devices had electron lifetimes (τ_n) much higher than the two **XY1b** based devices.

More precisely, the trend in τ_n was consistent with the photo voltages measured from the J-V plots, which indicated that the impressive open circuit voltages obtained by **MS4** (1.17 V) and **MS5** (1.24 V) were due to their particularly high electron lifetimes.

The increased performances of the co-sensitized device can therefore be explained by a reduced rate of electron recombination, which ultimately improves the J_{SC} and V_{OC} .

These findings demonstrated the beneficial effect of side-chain elongation. The stability under continuous light soaking at $45^\circ C$ under $100 mW \cdot cm^{-2}$ irradiation of the champion cell was measured of 1000 hours (Figure 7.4c). As it can be seen, the co-sensitized device managed to retain its PCE by roughly 90 % within this timeframe.

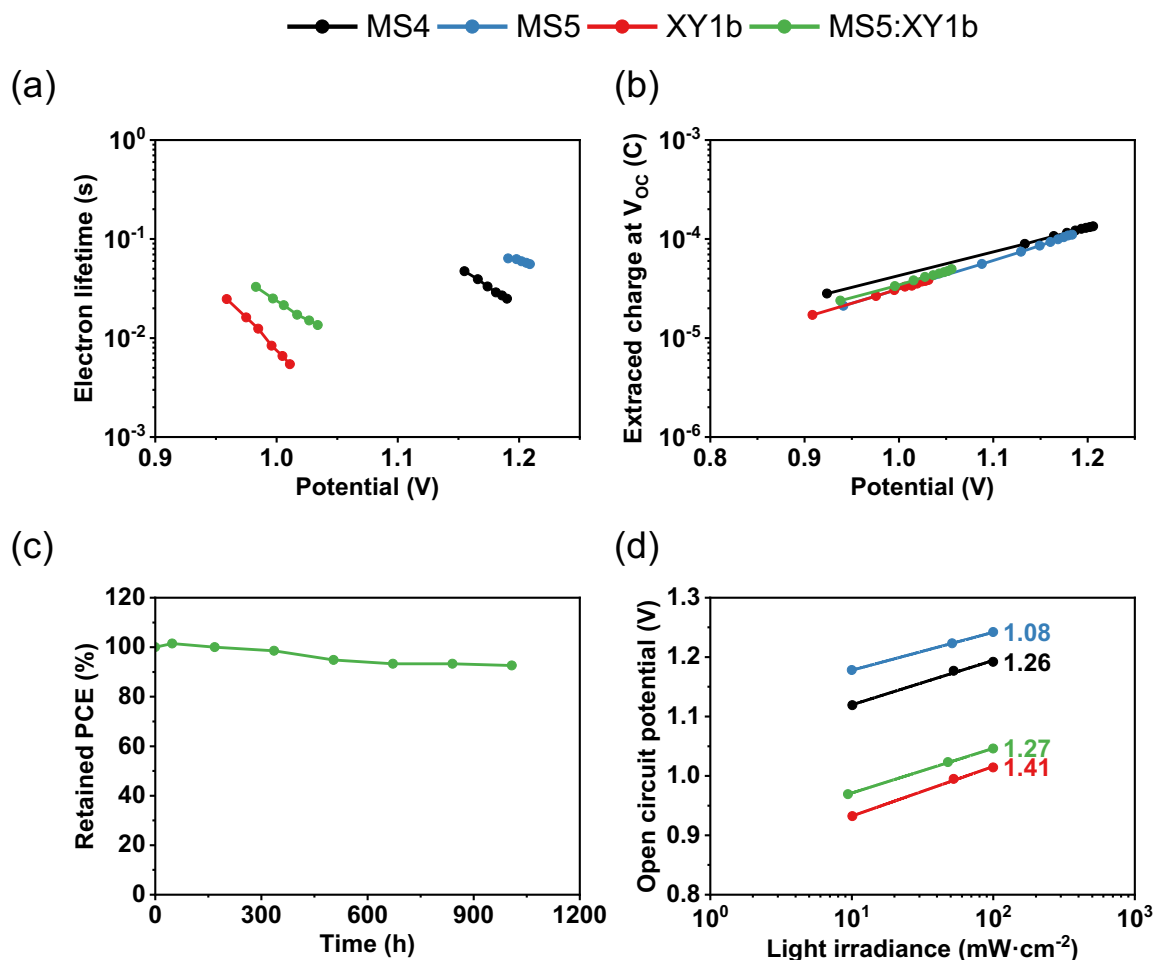


Figure 7.4. (a) Transport time as function of current density and (b) Extracted charge at open circuit potential, retained power conversion efficiency over 1000 hours under continuous $100 \text{ mW}\cdot\text{cm}^{-2}$ irradiation at 45°C and (d) logarithmic plot of the V_{OC} as function of light irradiance.

The ideality factors of the devices were estimated with the aim to investigate the electron recombination mechanism. These values were obtained from the linear fittings of the plots, displayed in Figure 7.4d. As mentioned in paragraph 1.3.1, it was established that ideality factors describe the deviation of a solar cell, from a band to band recombination observed in an ideal diode^{39,348}. In DSSCs, there are two main recombination pathways. The first consists in the reaction between a photo injected electron with the dye cation, D^+ . The second involves the oxidizing species present in the electrolyte, in this case $[\text{Cu}(\text{tmby})_2]^{+2}$, and free electrons.

TAS studies revealed that the dye cation quenching by $[\text{Cu}(\text{tmby})_2]^{+1}$ was fast enough compared to the recombination with D^+ , hence, this recombination route can be ignored.

A free electron can recombine with the electrolyte from three different sites: the conduction band, the sub-band trap states and pinholes on the TCO substrate^{349–351}. Usually this latter can be avoided by deposition of a compact TiO_2 blocking layer³⁵². Most DSSCs possess non-linear recombination kinetics occurring from the trap states, associated with ideality factors fluctuating between 1.5 and 2^{183,236,353,354}.

As mentioned before, **MS5** based devices achieved a particularly low ideality factor close to unity: 1.08 (Figure 7.4d). More precisely, the ideality factor gradually shifts from **XY1b** (1.41) to **MS4** (1.26) and finally to a value close to unity for **MS5** (1.08).

These values indicate that small dye structures with elongated aliphatic chains on the donor side, can affect the recombination mechanism of free electrons. The **MS5:XY1b** system showed a lowered ideality factor of 1.27, compared to the bare **XY1b**. This demonstrates that recombination pathways can also be altered by co-sensitization.

7.3 Conclusion

To conclude a new sensitizer based, on previously introduced donor-acceptor dyes, managed to produce a record V_{OC} of 1.24 V, associated with a good PCE of 8% with the $[Cu(tmby)_2]^{+2/+1}$ electrolyte under AM1.5G conditions. This dye, coded **MS5**, was used as co-sensitizer and combined with the broad spectral response dye **XY1b**, to yield a record PCE of 13.5% with the same electrolyte and irradiation conditions.

These exceptional performances were found to originate from the long n-dodecyl chains, located on the N-(2',4'-bis(hexyloxy)-[1,1'-biphenyl]-4-yl)-N-(4-bromophenyl)-2',4'-bis(alkoxy)-[1,1'-biphenyl]-4-amine donor, which drastically improved the electron lifetimes of **MS5** based devices. More specifically, this dye was able to induce a band to band like recombination mechanism, as it was indicated by its ideality factor of 1.08.

This study highlights the relevance of this class of simple dyes, in improving the performances of DSSCs. It was also demonstrated that these versatile dyes can operate alone and yield good PCEs or improve other dye system, in a co-sensitized system.

Conclusion

The work presented in this thesis managed to successfully highlight important design guidelines and understand their impact on both the dye properties as well as its PV performances.

In all studies, the geometry of the final dye proved to be a key factor in determining their final performances. More precisely, it was found that reducing the planarity of the molecule was beneficial for preventing dye aggregation. The choice of the bridging units, especially their ring size, was identified as an important step in the dye design. Notably, chapters 2 and 4 demonstrated that six-membered rings were a better choice over five membered rings.

To push the optimization to its limits, the heteroatoms embedded in either the bridging units or the electron acceptors were altered. The study presented in chapter 4 emphasized the importance of the heteroatoms' atomic radii. More specifically, when comparing furan and thiophene, the former was found to have a smaller ring size than the latter, which once embedded in a dye, would cause important distortion of the structure.

This effect was consistently observed in chapter 5, when comparing the benzo-oxadiazole versus benzo-thiadiazole. In this scenario, the size of the atomic radius altered the steric hindrance of the electron donor, toward the Cu(II) species. This latter study established once more the importance of the dye's geometrical features, at the atomic level.

Chapters 6 and 7 demonstrated that carefully engineered dyes developed with the simplest building blocks could deliver impressive performances. The final chapter described how the influence of aliphatic chains could drastically improve the PV performances and notably the photo-voltage. Furthermore, it was found that the recombination mechanism could be altered.

In addition to all the findings regarding the dyes' geometrical relevance towards the power output, Chapter 2 helped to understand a fundamental principle behind the design of D-A- π -A dye. Specifically, why it is necessary to use an auxiliary electron acceptor that has stronger electron withdrawing properties than the primary electron acceptor in order to impair an inadequate LUMO level localization. This result shows also the limits of the D-A- π -A model because of this internal electron accepting gradient that needs to be present.

Supporting information

Experimental details

Characterization of compounds

^1H and ^{13}C NMR spectra were recorded on Bruker AvanceIII-400 MHz NMR spectrometer with tetramethylsilane as the internal standard. Chemical shifts are reported in parts per million (ppm, δ). Mass spectra were collected on a HITACHI-80 mass spectrometer.

Optical characterization

UV-Vis spectrum were measured with a Hewlett Packard 8453 UV-Vis spectrometer. The measurements were performed with diluted solutions of the dyes in THF contained in 1 cm cuvettes or with 2.2 μm thick TiO_2 or Al_2O_3 films sensitized with the dyes. Emission spectrum were measured with a Fluorolog Horiba Jobin Yvon Model FL-1065.

Electrochemical characterization

Cyclic voltammograms were recorded by an Autolab Pgstat-30 potentiostat. A three electrode setup was used, comprising a reference $\text{Ag}/\text{AgCl}_{(\text{NaCl sat.})}$ electrode, a Pt wire counter electrode and a transparent 2.2 μm thick TiO_2 film sensitized with the dye, directly deposited on FTO as working electrode. The supporting electrolyte contained a 0.1 M LiTFSI in acetonitrile solution. The scan was performed under protected argon atmosphere at a rate of $20 \text{ mV}\cdot\text{s}^{-1}$. The ferrocene/ferrocenium redox couple was used as an internal standard with a formal potential of 0.391 V vs. $\text{Ag}/\text{AgCl}_{(\text{NaCl sat.})}$. The dye redox-potentials were firstly reported versus the ferrocene/ferrocenium couple and subsequently converted to the Normal Hydrogen Electrode (NHE) by addition of 0.624 V^{299} .

Density functional characterization

All calculations were performed with the Gaussian09[5] package based on the density functional theory (DFT). The long alkyl chains were simplified to methyl to reduce computational cost. Therefore, MS3 is not calculated separately. The ground-state energy levels and wave functions of the HOMO and LUMO orbitals of the dyes were calculated using the B3PW91 functional and 6-31G(d,p) basis sets. The structural optimizations of molecules in ground-state and the lowest energy singlet excited state (S1) are calculated using CAM-B3LYP hybrid functional and 6-31G(d,p) basis sets.

Solar cell fabrication and characterization

Chloroform (VWR), Ethanol (Fisher Chemical), chenodeoxycholic acid (Sigma), 1-methylbenzimidazole (TCI), chenodeoxycholic acid (TCI), and lithium bis(trifluoromethanesulfonyl)imide (LiTFSI) (TCI) were used without further purification. The organometallic complexes $[\text{Cu}(\text{tmby})_2][\text{TFSI}]$ and $[\text{Cu}(\text{tmby})_2][\text{TFSI}]_2$ were synthesized using a reported procedure²⁵⁴. The working electrodes were screen printed on cleaned FTO glasses (NSG-10, Nippon Sheet Glass). (The substrates were cleaned with a detergent (Deconex) in ultrasonic bath, and then treated with UV/O₃ (model no.256–220, Jelight Company, Inc.)). The TiO₂ underlayer was grown with a chemical bath deposition of TiCl₄ (40 mM) and heated at 60 °C for 30 mins. The mesoporous TiO₂ is obtained by screen printing the Dyesol 30 NRD (23 nm particle size) from Dyesol and WER2-0 scattering TiO₂ (400 nm particle size) pastes, as transparent (3 μm) and scattering layers (3 μm), respectively. The films were sintered with a ramped temperature profile, by keeping the substrates at 125, 250, 370, 450, and 500 °C for 5, 5, 5, 15, and 15 min, respectively, with a 5 min ramping duration between each temperature. Following a sintering process at 500 °C for 30 min, the working electrodes were dipped into 0.1 mM of dye solutions in a chloroform/ethanol (1:1 v/v) mixture containing 0.5 mM chenodeoxycholic acid for 16h. The PEDOT counter electrodes were prepared by electro-deposition on FTO glasses (TEC 6, Pilkington) following a reported procedure²⁴⁰. The two electrodes were then mechanically pressed together and sealed with a UV curing glue which was solidified using a UV curing unit (TEKLITE). The electrolyte solution consisted in 0.2 M $[\text{Cu}(\text{tmby})_2][\text{TFSI}]$ and 0.09 M $[\text{Cu}(\text{tmby})_2][\text{TFSI}]_2$, 0.1 M LiTFSI and 0.6 M NMB in acetonitrile. The electrolyte was injected into the device through a predrilled hole on the counter electrode side. The hole was subsequently sealed using the same UV light curing glue.

A black mask of with a 0.16 cm² aperture area was applied to the devices and the photovoltaic performances were measured using a 450W xenon light source (Oriel, U.S.A). A Schott K113 Tempax filter (Präzisions Glas & Optik GmbH) was used to reduce the spectral mismatches between AM 1.5G and the light source. The applied voltage was scanned a rate of 10 mV·s⁻¹ and Keithley model 2400 digital source meter (Keithley, U.S.A) was used to apply the external potential bias.

The incident photon to current conversion efficiency(IPCE) was measured using a computer controlled setup consisting of a 300W xenon light source (ILC Technology, USA), a monochromator (JobinYvon Ltd., UK), and a Keithley 2700 multimeter.

Transient absorption spectroscopy

A mesoporous TiO₂ layer was obtained by screen printing a 30 NRD (Dyesol) paste as transparent (4 μm) layer on microscope slides. The films were sintered with a ramped temperature profile, by keeping the substrates at 125, 250, 370, 450, and 500 °C for 5, 5, 5, 15, and 15 min, respectively, with a 5 min ramping duration between each temperature. Following a sintering process at 500 °C for 30 min, the working electrodes were dipped into 0.1 mM of dye solutions in a chloroform/ethanol (1:1 v/v) mixture containing 0.5 mM chenodeoxycholic acid for 16h. Then the working electrode was mechanically compressed over a bare counter electrode and sealed with UV curing glue and treatment in a UV curing unit(TEKLITE).

The inert electrolyte consisted 0.1 M LiTFSI and 0.6 M NMB in acetonitrile whereas the copper electrolyte contained 0.2 M $[\text{Cu}(\text{tmby})_2][\text{TFSI}]$ and 0.09 M $[\text{Cu}(\text{tmby})_2][\text{TFSI}]_2$, 0.1 M LiTFSI and 0.6 M NMB in acetonitrile. The electrolyte was injected through a predrilled hole on the counter electrode side and sealed with UV glue.

The samples were pumped by a ns laser beam centred at 500 nm obtained by tuning an optical parametric oscillator (GWU) pumped by a frequency-tripled (355 nm) Q-switched Nd:YAG laser (continuum Surelite, 20 Hz repetition rate). The laser power was set to a fluence of $0.6 \text{ mJ}\cdot\text{cm}^{-2}$ (for samples with the copper electrolyte) or $2.2 \text{ }\mu\text{J}\cdot\text{cm}^{-2}$ (samples with the inert electrolyte) with grey filters. The sample was then probed at 820 nm by a continuous Xenon arc lamp filtered by a monochromator with filters. The probe light was collected by a second monochromator and sent to a fast Silicon Avalanche Photodetector (APD410A/M, Thorlab), which converts photons into electrons. The induced transient voltage was recorded by a digital signal analyzer (DPO 7104C, Tektronix) and the signal acquisition averaged over 5000 laser shots.

Time resolved photo-luminescence

A mesoporous TiO_2 layer was obtained by screen printing a layer of 23 nm particle size 30 NRD (Dyesol) paste or 50 nm particle size Al_2O_3 (home-made) pastes transparent layers on microscope slides. The films were sintered with a ramped temperature profile, by keeping the substrates at 125, 250, 370, 450, and 500 °C for 5, 5, 5, 15, and 15 min, respectively, with a 5 min ramping duration between each temperature. Following a sintering process at 500 °C for 30 min, the working electrodes were dipped into 0.1 mM of dye solutions in a chloroform/ethanol (1:1 v/v) mixture containing 0.5 mM chenodeoxycholic acid for 16h. Then the working electrode was mechanically compressed over a bare counter electrode and sealed with UV curing glue and treatment in a UV curing unit (TEKLITE). The electrolyte consisted 0.1 M LiTFSI and 0.6 M NMB in acetonitrile whereas the copper electrolyte contained 0.2 M $[\text{Cu}(\text{tmby})_2][\text{TFSI}]$ and 0.09 M $[\text{Cu}(\text{tmby})_2][\text{TFSI}]_2$, 0.1 M LiTFSI and 0.6 M NMB in acetonitrile. The electrolyte was injected through a predrilled hole on the counter electrode side and sealed with UV glue. The decay curves were acquired using a LifeSpec II (Edinburgh Instruments) spectrometer with a 510 nm ps pulsed diode laser (EPL-510, Edinburgh Instruments) as light source and 85 ps pulse width. The decay was monitored at 750 nm. The instrument response function (IRF) was measured using a scatter substrate at 499 nm. The data was convoluted with the IRF and fitted with a bi exponential decay model.

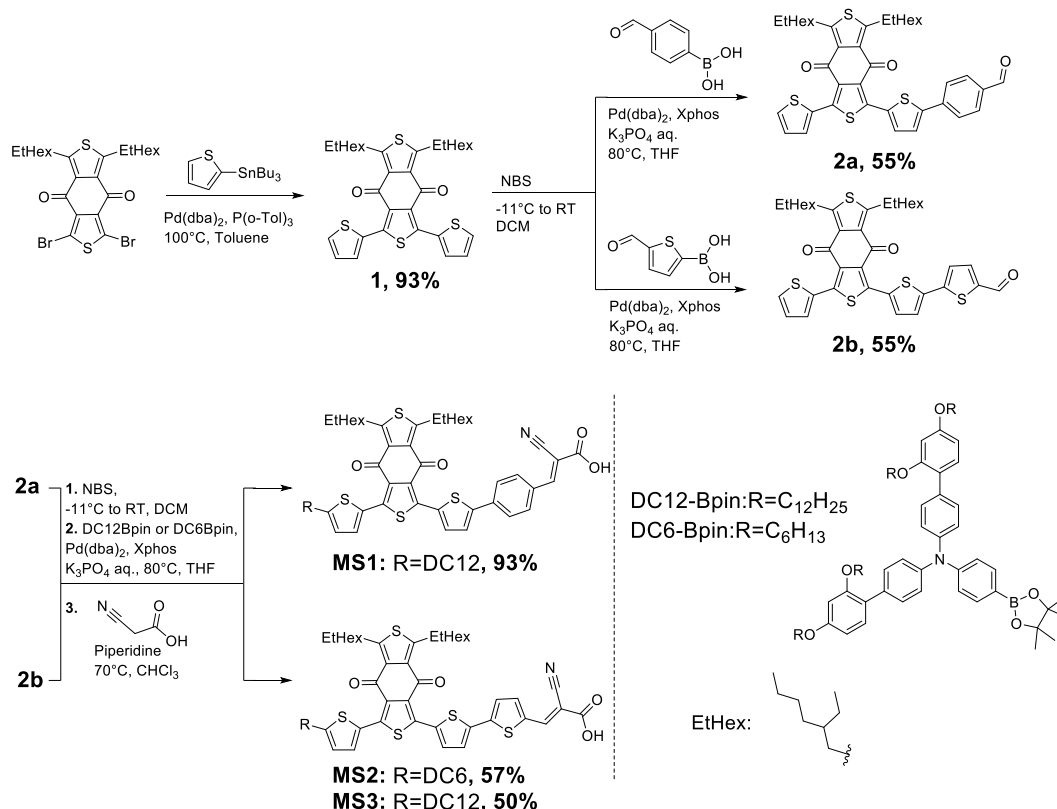
Small light modulation

The DYENAMO Toolbox System was used to record the electron lifetimes, transport time and charge extraction. It consists in a white LED light source (Seoul Semi- conductors), a 16-bit resolution digital acquisition board (National Instruments), and a current amplifier (Thorlabs PDA200C). To measure the extracted charge, the devices were kept under open-circuit conditions and illuminated by the LED source. After 1 s, the light source was turned off and the device short circuited. The total extracted charge was estimated by integration of the current over time. This procedure was repeated at different light intensities to yield the charge-voltage graph. The electron lifetime measurements, the light source modulated by superimposed current on the LED bias current before measuring the open-circuit voltage response. The lifetimes were estimated by a monoexponential fitting of open-circuit voltage decay curves.

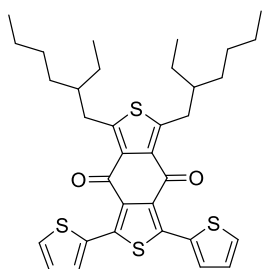
Supporting information to Chapter 2

Synthetic procedure

Chloroform (VWR), Methanol (Sigma), Ethanol (Fisher Chemical), dichloromethane (DCM, Thommen-Furler), hexanes (VWR International SA), diethyl ether (HUBERLAB AG), Acetic acid (VWR International SA), potassium phosphate tribasic (Acros), magnesium sulfate (Reactolab), N-bromosuccinimide (NBS, TCI), 2-(dicyclohexylphosphino)-2',4',6'-triisopropylbiphenyl (Fluorochem), and tris(dibenzylideneacetone)dipalladium(0) (Sigma), 2-(Tributylstannyl)thiophene (Sigma), bis(dibenzylideneacetone)palladium(0) (Fluorochem), tris(o-tolyl)phosphine (ABCR), Tetrabutylammonium fluoride solution 1.0 M in THF (Sigma), 4-formylphenylboronic acid (Fluorochem), 5-Formyl-2-thienylboronic acid (Fluorochem), piperidine (Acros), Cyanoacetic acid (ABCR) and 1,3-dibromo-5,7-bis(2-ethylhexyl)-4H,8H-benzo[1,2-c:4,5-c']dithiophene-4,8-dione (Suna. Tech Inc.) were used as received without further purification. Anhydrous THF and Toluene were purchased over molecular sieves from Acros Organics. N-(2',4'-bis(dodecyloxy)-[1,1'-biphenyl]-4-yl)-2',4'-bis(dodecyloxy)-N-(4-(4,4,5,5-tetramethyl-1,3,2-dioxaborolan-2-yl)phenyl)-[1,1'-biphenyl]-4-amine (**DC12-Bpin**) and N-(2',4'-bis(hexyloxy)-[1,1'-biphenyl]-4-yl)-2',4'-bis(hexyloxy)-N-(4-(4,4,5,5-tetramethyl-1,3,2-dioxaborolan-2-yl)phenyl)-[1,1'-biphenyl]-4-amine (**DC6-Bpin**) were synthesized following a reported procedure²⁰⁶. The solvents used for palladium catalyzed cross coupling reactions were degassed three times using the freeze-pump-thaw method and liquid nitrogen.

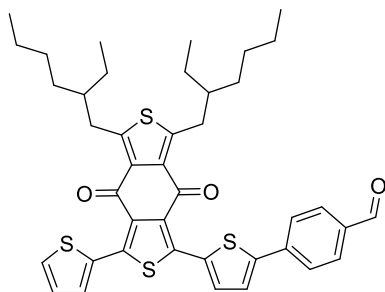


Scheme 0.1. Synthetic route to MS1, MS2 and MS3.

1,3-bis(2-ethylhexyl)-5,7-di(thiophen-2-yl)-4H,8H-benzo[1,2-c:4,5-c']dithiophene-4,8-dione(1)


1,3-dibromo-5,7-bis(2-ethylhexyl)-4H,8H-benzo[1,2-c:4,5-c']dithiophene-4,8-dione (0.5 g, 0.829 mmol, 1 eq.), tributyl(thiophen-2-yl)stannane (0.650 g, 1.743 mmol, 2.1 eq.) were charged in a schlenk tube and dissolved in 8 mL dry THF. The resulting solution was degassed three times using freeze-pump-thaw and liquid nitrogen. Then, bis(dibenzylideneacetone)palladium (23.9 mg, 41.5 μ mol, 0.05 eq.) and tri-*o*-tolylphosphine (15.2 mg, 49.8 μ mol, 0.06 eq.) were added to the reaction mixture before refluxing at 90°C for 16h. After cooling down to room temperature, Tetrabutylammonium fluoride was added before diluting twice with diethyl ether. The suspension was filtrated over a pad of Celite and washed with diethyl ether. The filtrate was evaporated using a rotary evaporator and methanol (100 mL) was added to induce precipitation of a yellow solid that was collected by filtration and dried under vacuum: 0.472 g (93%).

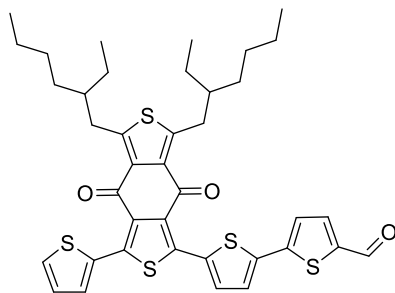
^1H NMR (400 MHz, Chloroform-*d*) δ 7.76 (d, *J* = 3.6 Hz, 2H), 7.53 (d, *J* = 5.0 Hz, 2H), 7.15 (t, *J* = 4.4 Hz, 2H), 3.34 (dd, *J* = 7.1, 2.1 Hz, 4H), 1.79 (p, *J* = 6.3 Hz, 2H), 1.50 – 1.20 (m, 16H), 0.92 (dq, *J* = 15.9, 9.2, 8.3 Hz, 12H). ^{13}C NMR (101 MHz, Chloroform-*d*) δ 177.70, 153.55, 142.41, 133.42, 133.14, 132.69, 130.51, 129.28, 127.19, 41.29, 33.65, 32.76, 28.83, 26.02, 23.02, 14.14, 10.90. HRMS (APPI/LTQ-Orbitrap) *m/z*: [*M*]⁺ Calcd for $\text{C}_{34}\text{H}_{40}\text{O}_2\text{S}_4$ 608.1906; Found 608.1927.

4-(5-(5,7-bis(2-ethylhexyl)-4,8-dioxo-3-(thiophen-2-yl)-4H,8H-benzo[1,2-c:4,5-c']dithiophen-1-yl)thiophen-2-yl)benzaldehyde(2a)


1,3-bis(2-ethylhexyl)-5,7-di(thiophen-2-yl)-4H,8H-benzo[1,2-c:4,5-c']dithiophene-4,8-dione(2) (0.465 g, 0.763 mmol, 1 eq.) was dissolved in dry DCM (15 mL), protected from light and placed under Argon in an ice/salt bath. *N*-bromosuccinimide (0.136 g, 0.763 mmol, 1 eq.) was added in one portion and the resulting reaction mixture was allowed to warm up to room temperature overnight. The solvent was removed and methanol (100 mL) was added to recover an orange solid. The solid (0.250 g, 0.36 mmol, 1 eq.), 4-formylphenylboronic acid (163 mg, 1.09 mmol, 3 eq.) and potassium phosphate tribasic (2M, 1 mL, 2 mmol, 5.5 eq.), were charged in a schlenk tube and dissolved in 4 mL THF. The resulting solution was degassed three times using freeze-pump-thaw and liquid nitrogen. Then, tris(dibenzylideneacetone)dipalladium(0) (16.6 mg, 18.2 μ mol, 0.05 eq.) and 2-dicyclohexylphosphino-2',6'-dimethoxybiphenyl (17.9 mg, 43.6 μ mol, 0.12 eq.) and the reaction mixture was refluxed at 70°C for 24 hours. After cooling down to room temperature, the mixture was diluted with 30 mL diethyl ether and flashed through a pad of MgSO_4 before evaporation to dryness. The crude was purified by flash chromatography on SiO_2 eluting from 100% hexanes to 20% DCM in hexanes by volume. The target product was obtained as an orange solid: 0.196 g (55%). ^1H NMR (400 MHz, Chloroform-*d*) δ 10.05 (s, 1H), 7.94 (d, *J* = 8.0 Hz, 2H), 7.86 (d, *J* = 8.0 Hz, 2H), 7.79 (t, *J* = 3.5 Hz, 2H), 7.54 (d, *J* = 5.1 Hz, 1H), 7.49 (d, *J* = 4.0 Hz, 1H), 7.20 – 7.12 (m, 1H), 3.35 (td, *J* = 6.0, 4.8, 2.3 Hz, 4H), 1.80 (h, *J* = 6.2 Hz, 2H), 1.50 – 1.16 (m, 16H), 0.92 (tq, *J* = 16.4, 7.1 Hz, 12H). ^{13}C NMR (101 MHz, Chloroform-*d*) δ 191.40, 177.74, 177.55, 153.77, 153.71, 131.72, 130.71, 130.49, 129.54, 127.26, 126.19,

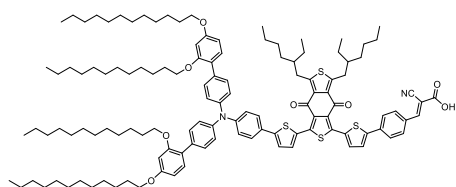
125.11, 41.29, 33.65, 32.76, 28.83, 26.02, 23.02, 14.14, 10.90. HRMS (APPI/LTQ-Orbitrap) m/z : $[M + H]^+$ Calcd for $C_{41}H_{45}O_3S_4^+$ 713.2246; Found 713.2258.

5'-(5,7-bis(2-ethylhexyl)-4,8-dioxo-3-(thiophen-2-yl)-4H,8H-benzo[1,2-c:4,5-c']dithiophen-1-yl)-[2,2'-bithiophene]-5-carbaldehyde(**2b**)



1,3-bis(2-ethylhexyl)-5,7-di(thiophen-2-yl)-4H,8H-benzo[1,2-c:4,5-c']dithiophene-4,8-dione(**2**) (0.465 g, 0.763 mmol, 1 eq.) was dissolved in dry DCM (15 mL), protected from light and placed under Argon in an ice/salt bath. N-bromosuccinimide (0.136 g, 0.763 mmol, 1 eq.) was added in one portion and the resulting reaction mixture was allowed to warm up to room temperature overnight. The solvent was removed and methanol (100 mL) was added to recover an orange solid. The solid (0.250 g, 0.36 mmol, 1 eq.), 5-formylthiophen-2-boronic acid (198 mg, 1.27 mmol, 3.5 eq.) and potassium phosphate tribasic (2M, 909 μ L, 1.82 mmol, 5 eq.) were charged in a schlenk tube along with 4 mL THF. The resulting solution was degassed three times using freeze-pump-thaw and liquid nitrogen. Then, tris(dibenzylideneacetone)dipalladium(0) (20 mg, 21.8 μ mol, 0.06 eq.) and 2-dicyclohexylphosphino-2',6'-dimethoxybiphenyl (17.9 mg, 43.6 μ mol, 0.12 eq.) were added before refluxing the mixture at 70°C for 24 hours. After cooling down to room temperature, the mixture was diluted with 30 mL diethyl ether and flashed through a pad of $MgSO_4$ before evaporation to dryness. The crude was purified by flash chromatography on SiO_2 eluting from 100% hexanes to 40% DCM in hexanes by volume. The target product was obtained as a red brick solid 0.144 g (55%). 1H NMR (400 MHz, Chloroform- d) δ 9.82 (s, 1H), 7.69 (dd, J = 3.7, 1.2 Hz, 1H), 7.63 (dd, J = 6.9, 4.0 Hz, 2H), 7.45 (dd, J = 5.2, 1.2 Hz, 1H), 7.30 (dd, J = 7.5, 4.0 Hz, 2H), 7.06 (dd, J = 5.2, 3.8 Hz, 1H), 3.30 – 3.18 (m, 4H), 1.70 (q, J = 6.3 Hz, 2H), 1.39 – 1.11 (m, 16H), 0.93 – 0.65 (m, 12H). ^{13}C NMR (101 MHz, Chloroform- d) δ 182.47, 177.45, 153.93, 153.78, 146.53, 142.29, 141.20, 139.13, 137.25, 135.04, 131.41, 130.80, 130.51, 129.66, 128.98, 128.41, 127.28, 125.95, 124.81, 41.29, 33.65, 32.76, 28.83, 26.02, 23.02, 14.14, 10.90. HRMS (APPI/LTQ-Orbitrap) m/z : $[M + H]^+$ Calcd for $C_{39}H_{43}O_3S_5^+$ 719.1810; Found 719.1812.

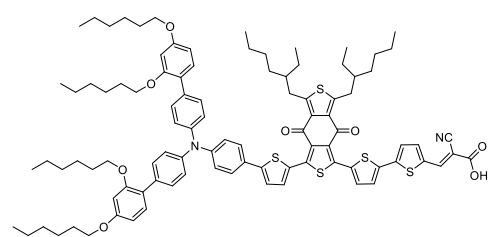
(E)-3-(4-(5-(3-(5-(4-((2',4'-bis(dodecyloxy)-[1,1'-biphenyl]-4-yl)(2'-(dodecyloxy)-4'-(undecyloxy)-[1,1'-biphenyl]-4-yl)amino)phenyl)thiophen-2-yl)-5,7-bis(2-ethylhexyl)-4,8-dioxo-4H,8H-benzo[1,2-c:4,5-c']dithiophen-1-yl)thiophen-2-yl)phenyl)-2-cyanoacrylic acid(**MS1**)



4-(5-(5,7-bis(2-ethylhexyl)-4,8-dioxo-3-(thiophen-2-yl)-4H,8H-benzo[1,2-c:4,5-c']dithiophen-1-yl)thiophen-2-yl)benzaldehyde(**2a**) (0.140 g, 0.196 mmol, 1 eq.) was dissolved in dry DCM (10 mL), protected from light and placed under Argon in an ice/salt bath. N-bromosuccinimide (37 mg, 0.202 mmol, 1.05 eq.) was added in one portion and the resulting reaction mixture was allowed to warm up to room temperature overnight. The solvent was removed and methanol (100 mL) was added to recover an orange solid. The solid (0.155 g, 0.195 mmol, 1.63 eq.), N-(2',4'-bis(dodecyloxy)-[1,1'-biphenyl]-4-yl)-2',4'-bis(dodecyloxy)-N-(4-(4,4,5,5-tetramethyl-1,3,2-dioxaborolan-2-yl)phenyl)-[1,1'-biphenyl]-4-amine (151 mg, 120 μ mol, 1 eq.) and potassium phosphate tribasic (2M, 200 μ L, 400 μ mol, 3.34 eq.) were charged

in a schlenk tube along with 5 mL THF. The resulting solution was degassed three times using freeze-pump-thaw and liquid nitrogen. Then, tris(dibenzylideneacetone)dipalladium(0) (11 mg, 12 μ mol, 0.1 eq.) and 2-(dicyclohexylphosphino)-2',4',6'-triisopropylbiphenyl (11.4 mg, 24 μ mol, 0.2 eq.) were added before refluxing the mixture at 70°C for 24 hours. After cooling down to room temperature, the mixture was diluted with 30 mL diethyl ether and flashed through a pad of MgSO₄ before evaporation to dryness. The crude was purified by flash chromatography on SiO₂ eluting from 100% hexanes to 50% DCM in hexanes by volume. The target product was obtained as a red orange solid. The aldehyde intermediate (205 mg, 111 μ mol, 1 eq.), cyanoacetic acid (94.5 mg, 1.11 mmoles, 10 eq.) and piperidine (110 μ L) were charged in a schlenk tube along with 4 mL distilled chloroform. The resulting solution was degassed three times using freeze-pump-thaw and liquid nitrogen. The mixture was refluxed for 2 days at 70°C. 30 mL HCl 1M was added to quench the reaction followed by extraction with dichloromethane (3x30 mL). The crude was evaporated to dryness and purified by flash chromatography on SiO₂ eluting from 100% dichloromethane to 8% methanol and 1% acetic acid in dichloromethane by volume. The target product was obtained as a red shiny solid 67 mg (31%). ¹H NMR (400 MHz, Chloroform-d) δ 8.19 (s, 1H), 7.97 (d, J = 8.0 Hz, 2H), 7.80 – 7.65 (m, 5H), 7.48 (d, J = 8.3 Hz, 2H), 7.38 (dd, J = 13.7, 6.1 Hz, 5H), 7.11 (d, J = 8.2 Hz, 6H), 6.47 (d, J = 6.7 Hz, 4H), 3.89 (q, J = 7.4 Hz, 8H), 3.26 (d, J = 7.1 Hz, 4H), 1.50 – 0.99 (m, 80H), 0.82 (ddq, J = 22.1, 14.6, 6.6 Hz, 24H). ¹³C NMR (101 MHz, CDCl₃) δ 176.70, 176.52, 158.58, 155.95, 151.37, 148.57, 148.30, 148.02, 144.38, 134.75, 134.50, 134.25, 132.47, 131.06, 130.74, 130.56, 129.82, 129.26, 125.75, 125.13, 123.86, 123.08, 122.45, 122.20, 122.11, 121.95, 121.87, 121.41, 104.32, 99.41, 67.37, 67.08, 40.20, 32.64, 31.78, 30.89, 28.68, 28.66, 28.65, 28.61, 28.59, 28.57, 28.40, 28.33, 28.28, 28.09, 27.85, 27.83, 25.07, 25.01, 22.00, 21.66, 13.12, 13.10, 9.87, 9.86. HRMS (MALDI/TOF) m/z: [M]⁺ Calcd for C₁₂₂H₁₆₂N₂O₈S₄⁺ 1911.1209; Found 1912.0729

(E)-3-(5'-(3-(5-(4-(bis(2',4'-bis(hexyloxy)-[1,1'-biphenyl]-4-yl)amino)phenyl)thiophen-2-yl)-5,7-bis(2-ethylhexyl)-4,8-dioxo-4H,8H-benzo[1,2-c:4,5-c']dithiophen-1-yl)-[2,2'-bithiophen]-5-yl)-2-cyanoacrylic acid (**MS2**)

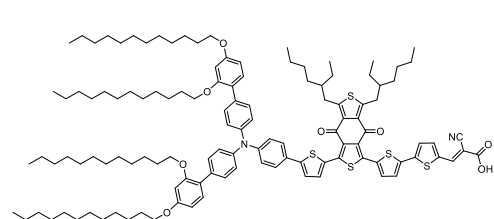


5'-(5,7-bis(2-ethylhexyl)-4,8-dioxo-3-(thiophen-2-yl)-4H,8H-benzo[1,2-c:4,5-c']dithiophen-1-yl)-[2,2'-bithiophene]-5-carbaldehyde(2b) (0.144 g, 0.2 mmoles, 1 eq.) was dissolved in dry DCM (10 mL), protected from light and placed under Argon in an ice/salt bath. N-bromosuccinimide (38 mg, 0.21 mmoles, 1.05 eq.) was added in one portion and the resulting reaction

mixture was allowed to warm up to room temperature overnight. The solvent was removed and methanol (100 mL) was added to recover an orange solid. The solid (66 mg, 83 μ mol, 1 eq.), N-(2',4'-bis(hexyloxy)-[1,1'-biphenyl]-4-yl)-2',4'-bis(hexyloxy)-N-(4-(4,4,5,5-tetramethyl-1,3,2-dioxaborolan-2-yl)phenyl)-[1,1'-biphenyl]-4-amine (126 mg, 136 μ mol, 1.64 eq.) and potassium phosphate tribasic (2M, 500 μ L, 1 mmoles, 12.1 eq.) were charged in a schlenk tube along with 5 mL THF. The resulting solution was degassed three times using freeze-pump-thaw and liquid nitrogen. Then, tris(dibenzylideneacetone)dipalladium(0) (7.57 mg, 8.27 μ mol, 0.1 eq.) and 2-(dicyclohexylphosphino)-2',4',6'-triisopropylbiphenyl (7.89 mg, 16.5 μ mol, 0.2 eq.) were added before refluxing the mixture at 70°C for 24 hours. After cooling down to room temperature, the mixture was diluted with 30 mL diethyl ether and flashed through a pad of MgSO₄ before evaporation to dryness. The crude was purified by flash chromatography on

SiO₂ eluting from 100% hexanes to 50% DCM in hexanes by volume. The target product was obtained as a red solid. The aldehyde intermediate (71 mg, 47 μ mol, 1 eq.), cyanoacetic acid (14 mg, 164 μ mol, 2.5 eq.) and piperidine (100 μ L) were charged in a schlenk tube along with 4 mL distilled chloroform. The resulting solution was degassed three times using freeze-pump-thaw and liquid nitrogen. The mixture was refluxed for 2 days at 70°C. 30 mL HCl 1M was added to quench the reaction followed by extraction with dichloromethane (3x30 mL). The crude was evaporated to dryness and purified by flash chromatography on SiO₂ eluting from 100% dichloromethane to 8% methanol and 1% acetic acid in dichloromethane by volume. The target product was obtained as a red shiny solid 21 mg (28 %). ¹H NMR (800 MHz, CDCl₃) δ 8.34 (s, 1H), 7.85 (d, J = 3.9 Hz, 1H), 7.75 (d, J = 3.9 Hz, 1H), 7.72 (d, J = 4.0 Hz, 1H), 7.60 – 7.56 (m, 2H), 7.51 – 7.48 (m, 4H), 7.21 (d, J = 8.6 Hz, 5H), 6.57 (dd, J = 6.0, 2.4 Hz, 4H), 4.00 (dt, J = 18.7, 6.5 Hz, 9H), 3.41 – 3.33 (m, 5H), 1.85 – 1.75 (m, 12H), 1.54 – 1.17 (m, 45H), 1.05 – 0.79 (m, 37H). ¹³C NMR (151 MHz, CD₂Cl₂) δ 159.72, 156.97, 145.35, 134.83, 133.70, 132.88, 132.69, 131.39, 130.77, 130.28, 126.67, 124.15, 122.91, 122.55, 105.35, 100.11, 68.35, 68.11, 53.82, 53.64, 53.46, 53.28, 53.10, 41.11, 33.58, 32.81, 32.76, 31.93, 31.63, 31.48, 29.70, 29.66, 29.37, 29.30, 29.09, 28.80, 26.10, 26.00, 25.77, 25.74, 23.06, 23.04, 22.70, 22.65, 22.61, 13.98, 13.95, 13.89, 13.87, 13.84, 10.74, 10.63, 0.76. HRMS (MALDI/TOF) m/z: [M]⁺ Calcd for C₉₆H₁₁₂N₂O₈S₅⁺ 1580.7017; Found 1581.5853.

(E)-3-(5'-(3-(5-(4-(bis(2',4'-bis(dodecyloxy)-[1,1'-biphenyl]-4-yl)amino)phenyl)thiophen-2-yl)-5,7-bis(2-ethylhexyl)-4,8-dioxo-4H,8H-benzo[1,2-c:4,5-c']dithiophen-1-yl)-[2,2'-bithiophen]-5-yl)-2-cyanoacrylic acid(**MS3**)



5'-(5,7-bis(2-ethylhexyl)-4,8-dioxo-3-(thiophen-2-yl)-4H,8H-benzo[1,2-c:4,5-c']dithiophen-1-yl)-[2,2'-bithiophene]-5-carbaldehyde(2b) (0.144 g, 0.2 mmol, 1 eq.) was dissolved in dry DCM (10 mL), protected from light and placed under Argon in an ice/salt bath. N-bromosuccinimide (38 mg, 0.21

mmol, 1.05 eq.) was added in one portion and the resulting reaction mixture was allowed to warm up to room temperature overnight. The solvent was removed and methanol (100 mL) was added to recover an orange solid. The solid (66 mg, 83 μ mol, 1 eq.), N-(2',4'-bis(dodecyloxy)-[1,1'-biphenyl]-4-yl)-2',4'-bis(dodecyloxy)-N-(4-(4,4,5,5-tetramethyl-1,3,2-dioxaborolan-2-yl)phenyl)-[1,1'-biphenyl]-4-amine (287 mg, 230 μ mol, 2.75 eq.) and potassium phosphate tribasic (2M, 500 μ L, 1 mmol, 12.1 eq.) were charged in a schlenk tube along with 5 mL THF. The resulting solution was degassed three times using freeze-pump-thaw and liquid nitrogen. Then, tris(dibenzylideneacetone)dipalladium(0) (7.57 mg, 8.27 μ mol, 0.1 eq.) and 2-(dicyclohexylphosphino)-2',4',6'-triisopropylbiphenyl (7.89 mg, 16.5 μ mol, 0.2 eq.) were added before refluxing the mixture at 70°C for 24 hours. After cooling down to room temperature, the mixture was diluted with 30 mL diethyl ether and flashed through a pad of MgSO₄ before evaporation to dryness. The crude was purified by flash chromatography on SiO₂ eluting from 100% hexanes to 30% DCM in hexanes by volume. The target product was obtained as a red solid 74 mg. The aldehyde intermediate (74 mg, 39 μ mol, 1 eq.), cyanoacetic acid (12 mg, 139 μ mol, 3.5 eq.) and piperidine (100 μ L) were charged in a schlenk tube along with 4 mL distilled chloroform. The resulting solution was degassed three times using freeze-pump-thaw and liquid nitrogen. The mixture was refluxed for 2 days at 70°C. 30 mL HCl 1M was added to quench the reaction followed by extraction with dichloromethane (3x30 mL). The crude was evaporated to dryness and purified by flash chromatography on SiO₂ eluting from 100%

dichloromethane to 8% methanol and 1% acetic acid in dichloromethane by volume. The target product was obtained as a red shiny solid 26 mg (34 %). ^1H NMR (400 MHz, Chloroform- d) δ 8.23 (s, 1H), 7.75 (s, 1H), 7.64 (s, 1H), 7.48 (d, J = 8.3 Hz, 2H), 7.40 (d, J = 8.3 Hz, 4H), 7.29 (s, 1H), 7.11 (d, J = 8.2 Hz, 5H), 6.56 – 6.41 (m, 4H), 3.90 (dt, J = 9.5, 6.6 Hz, 4H), 1.19 (q, J = 14.5, 14.1 Hz, 80H), 0.96 – 0.65 (m, 24H). ^{13}C NMR (101 MHz, CDCl_3) δ 158.58, 158.43, 155.95, 155.92, 147.10, 145.58, 145.11, 144.88, 144.36, 143.25, 142.35, 141.73, 141.21, 138.01, 136.87, 136.25, 133.46, 132.50, 132.04, 131.85, 131.64, 131.01, 130.36, 129.82, 129.78, 129.47, 129.27, 129.04, 127.91, 127.52, 127.40, 127.28, 126.83, 125.77, 125.34, 124.93, 123.74, 123.11, 122.91, 122.45, 122.07, 121.88, 104.30, 104.25, 99.43, 76.30, 75.99, 75.67, 67.38, 67.08, 58.52, 46.17, 44.82, 40.25, 37.13, 36.08, 35.63, 35.26, 33.10, 32.68, 32.21, 31.79, 31.25, 30.91, 30.90, 30.41, 30.22, 29.15, 29.03, 28.69, 28.66, 28.65, 28.63, 28.60, 28.58, 28.56, 28.41, 28.34, 28.30, 28.26, 28.10, 28.07, 27.84, 26.96, 26.07, 25.73, 25.08, 25.02, 24.18, 23.47, 22.16, 22.01, 21.68, 18.71, 18.21, 13.40, 13.16, 13.13, 13.10, 10.39, 9.89, 9.87, 0.75, 0.37, 0.12, 0.10, 0.08, 0.03. HRMS (MALDI/TOF) m/z : $[\text{M}]^+$ Calcd for $\text{C}_{120}\text{H}_{160}\text{N}_2\text{O}_8\text{S}_5^+$ 1917.0773; Found 1917.5767.

Optical characterization

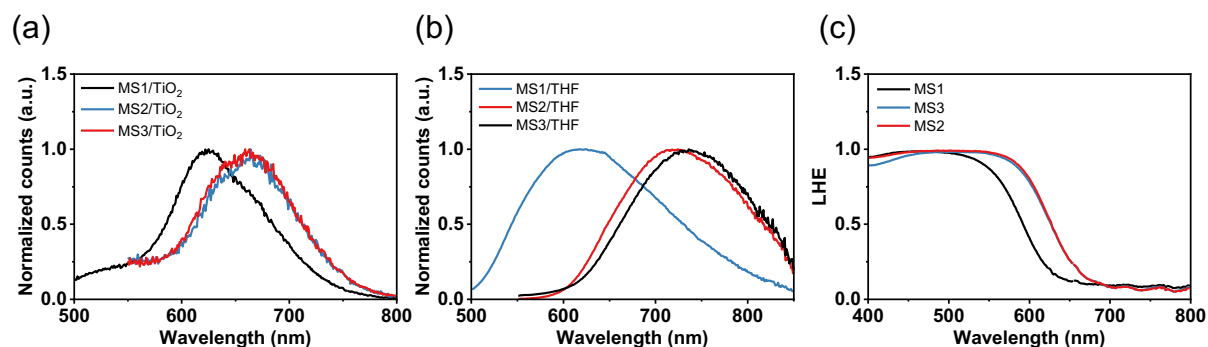


Figure 0.1. (a) Normalized emission spectra of the dyes adsorbed on 4 μm thick TiO_2 films. Normalized emission spectra of the dyes in diluted THF solutions (b). (c) Light harvesting efficiency (LHE) calculated using: $\text{LHE} = 1 - 10^{-A}$, with A being the absorbance of the sensitized films.

Electrochemical characterization

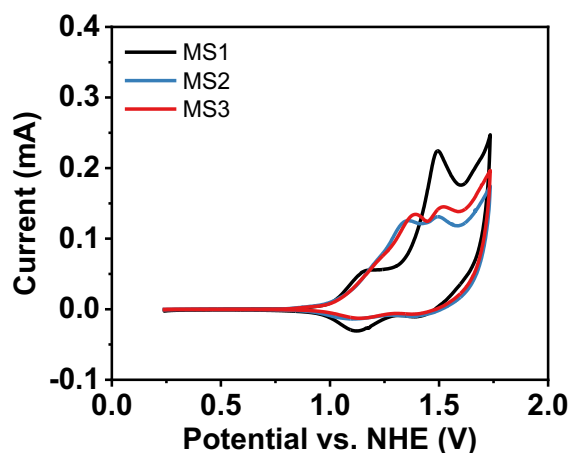


Figure 0.2. Cyclic voltammograms of the dyes adsorbed on a transparent TiO_2 film.

Computational calculations

Table 0.1. The calculated energy levels of HOMO and LUMO orbitals of MS dyes using Gaussian09 with B3PW91 functional and 6-31G(d,p) basis sets.

	HOMO [eV]	LUMO [eV]	E _g [eV]
MS1	-4.75	-2.90	1.85
MS2/MS3	-4.79	-3.01	1.78

Device fabrication and solar cell characterization

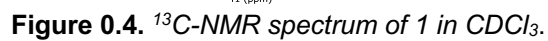
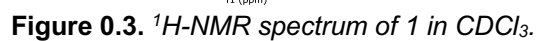
Table 0.2. Detailed statistical values of the devices at 10, 50 and 100% sun. The values were averaged over 4 cells.

MS1				
P_{in} [mW·cm ⁻²]	V_{oc} [mV]	J_{sc} [mA·cm ⁻²]	FF [%]	PCE [%]
98±2	880±31	8±1	69±3	5±1
51±1	850±30	3.9±0.6	72±3	5±1
10.1±0.2	790±33	0.7±0.1	73±8	4.2±0.9
MS2				
P_{in} [mW·cm ⁻²]	V_{oc} [mV]	J_{sc} [mA·cm ⁻²]	FF [%]	PCE [%]
99±2	890±12	9.2±0.3	66±4	5.5±0.6
52±1	870±10	4.8±0.2	71±3	5.8±0.5
10.1±0.2	807±9	0.91±0.03	75±3	5.5±0.3
MS3				
P_{in} [mW·cm ⁻²]	V_{oc} [mV]	J_{sc} [mA·cm ⁻²]	FF [%]	PCE [%]
99±2	860±23	7.4±0.3	69±4	4.4±0.5
52±1	840±20	3.8±0.1	73±4	4.6±0.4
10.1±0.2	780±20	0.73±0.03	75±7	4.2±0.5

Time resolved photo-luminescent decay

Table 0.3. Fitting parameters obtained from convolution of the TRPL decay curves with the IRF.

	A₁ [%]	τ₁ (A) [ps]	A₂ [%]	τ₂(A) [ps]	τ_{av}(A) [ps]	A₁ [%]	τ₁ (T) [ps]	A₂ [%]	τ₂(T) [ps]	τ_{av}(T) [ps]
MS1	49.7	180	50.3	710	450	60.3	40	39.7	210	105
MS2	36.7	100	63.3	510	360	59.0	32	40.9	180	94
MS3	36.4	140	63.6	570	410	52.3	27	47.7	198	109



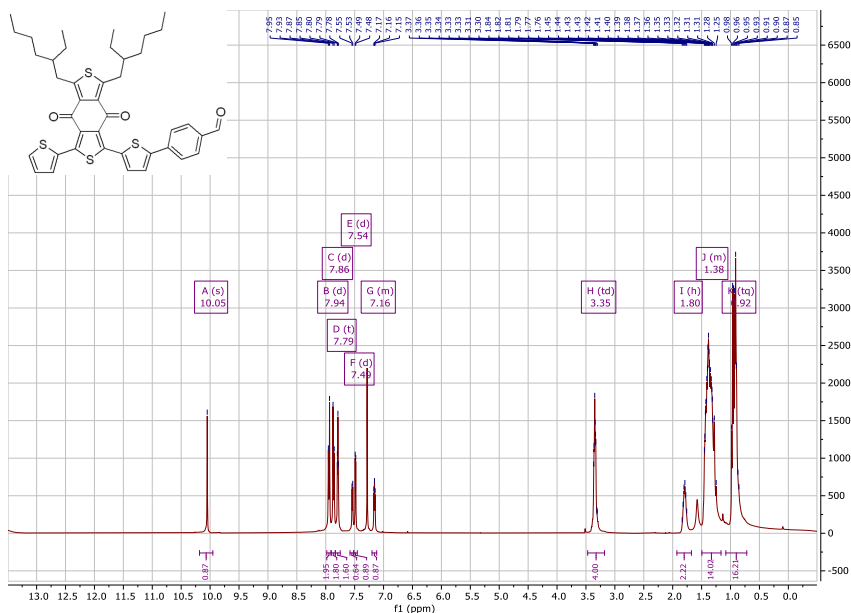


Figure 0.5. ^1H -NMR spectrum of 2a in CDCl_3 .

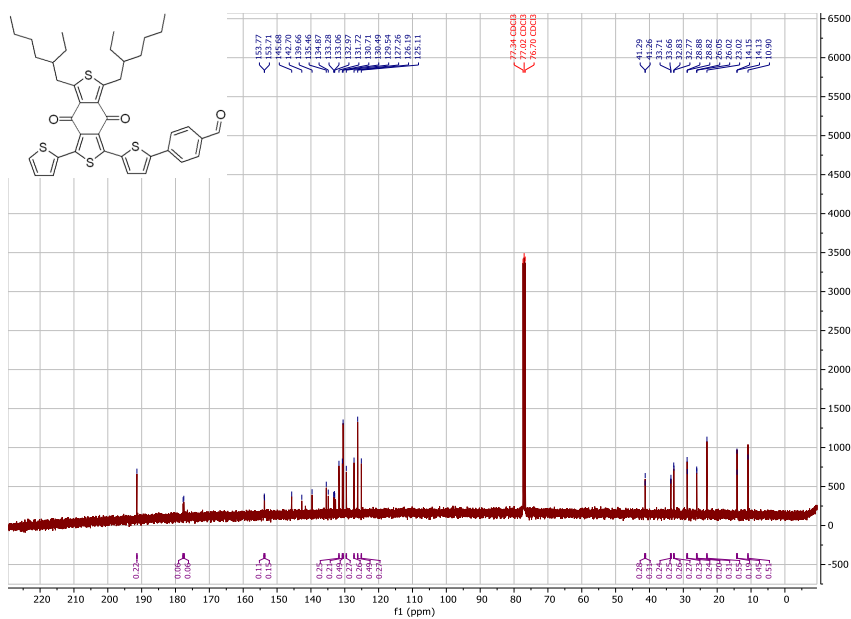


Figure 0.6. ^{13}C -NMR spectrum of 2a in CDCl_3 .

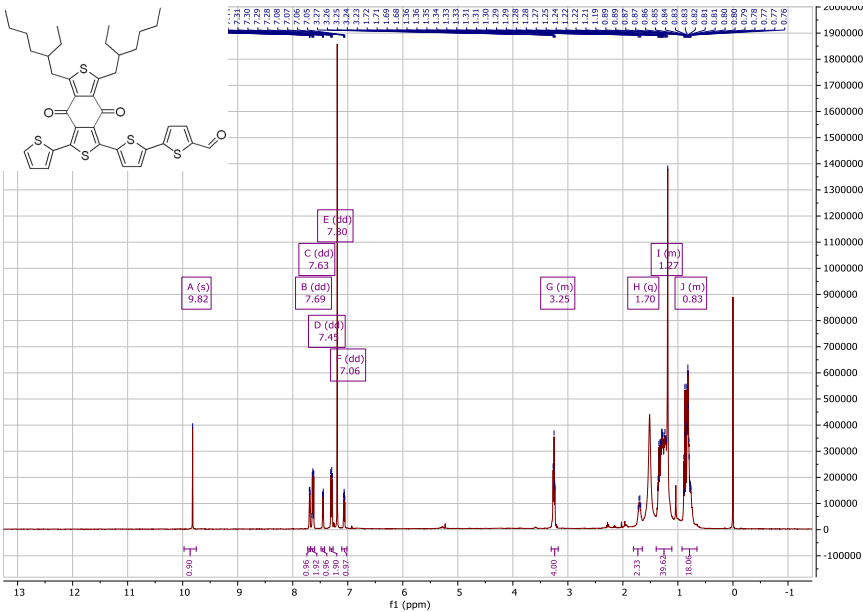


Figure 0.7. ^1H -NMR spectrum of **2b** in CDCl_3 .

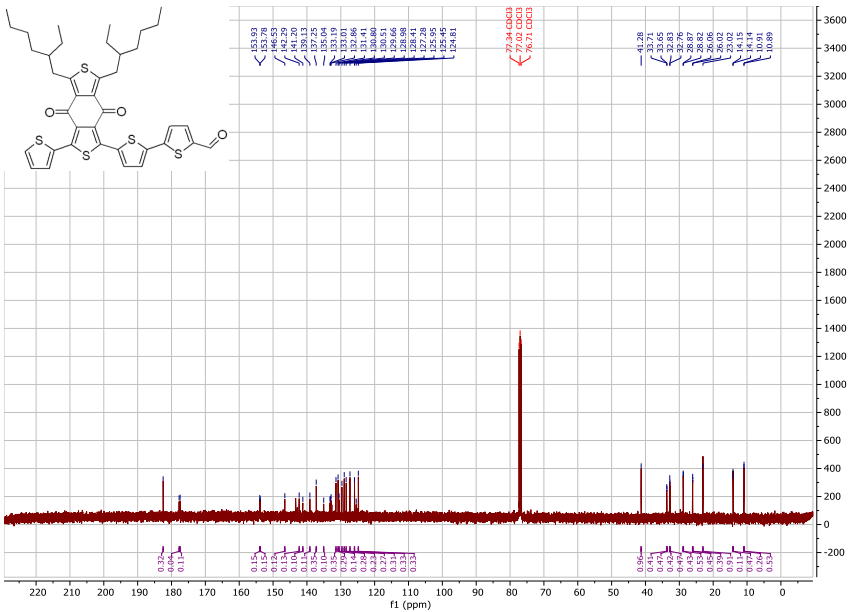


Figure 0.8. ^{13}C -NMR spectrum of **2b** in CDCl_3 .

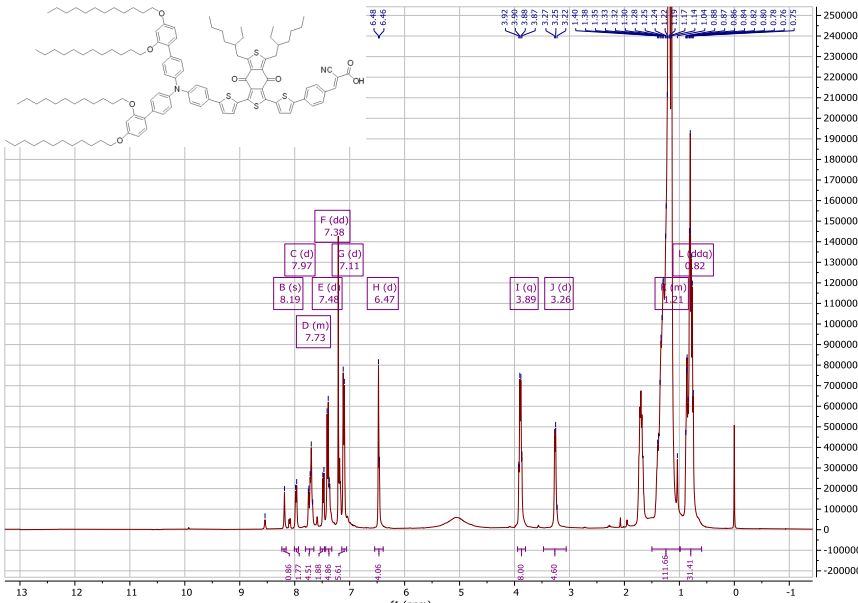


Figure 0.9. ^1H -NMR spectrum of MS1 in CDCl_3 .

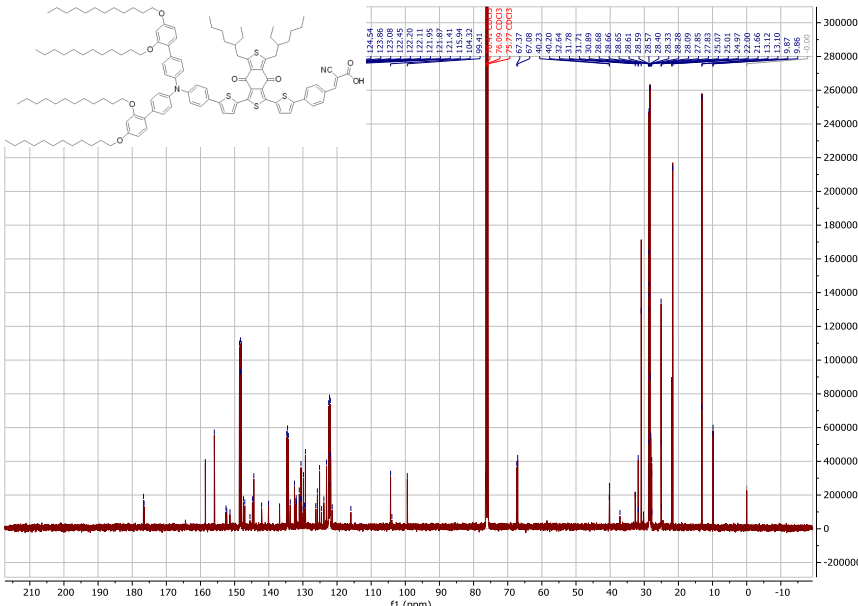


Figure 0.10. ^{13}C -NMR spectrum of MS1 in $\text{CDCl}_3/\text{Pyridine-}d_6$.

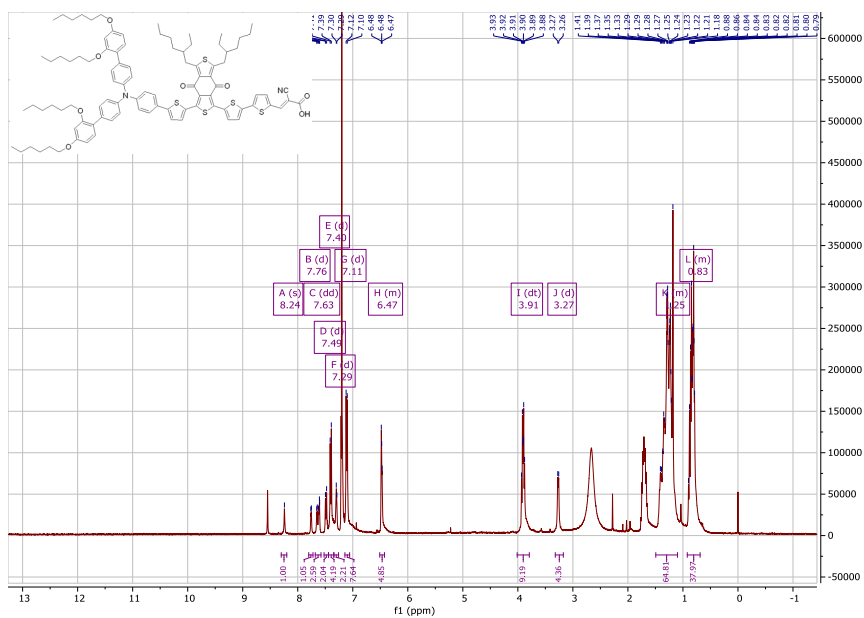


Figure 0.11. ^1H -NMR spectrum of MS2 in $\text{CDCl}_3/\text{Pyridine-}d_6$.

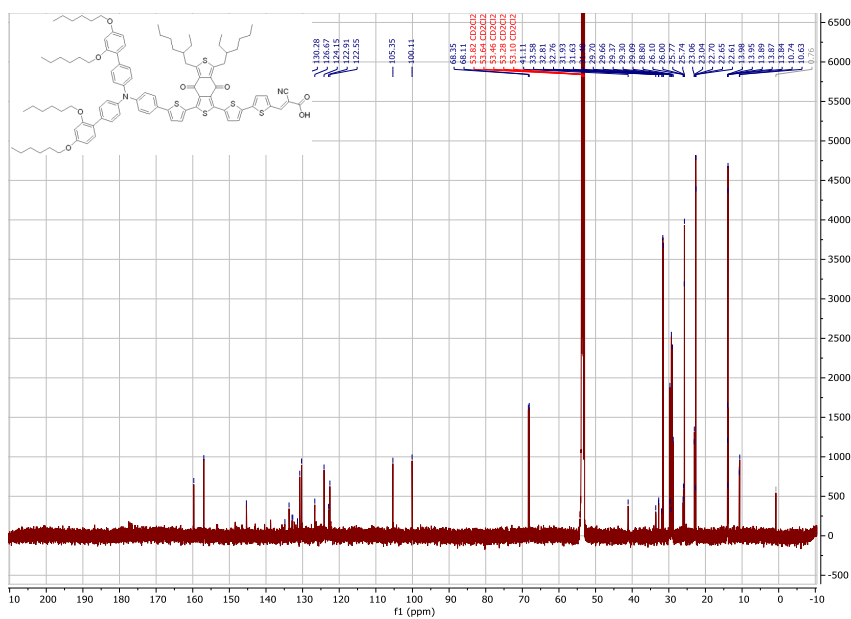


Figure 0.12. ^{13}C -NMR spectrum of MS2 in $\text{CDCl}_3/\text{Pyridine-}d_6$.

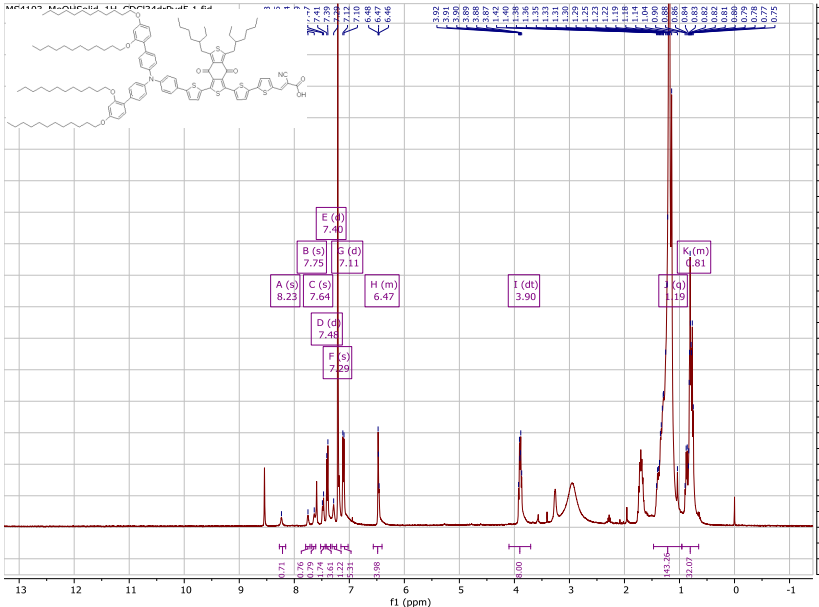


Figure 0.13. ^1H -NMR spectrum of MS3 in $\text{CDCl}_3/\text{Pyridine-}d_6$.

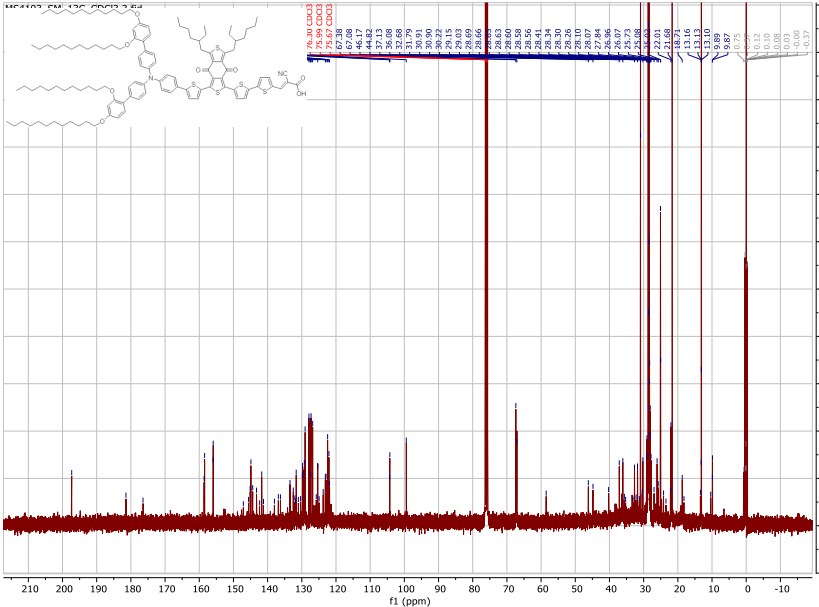
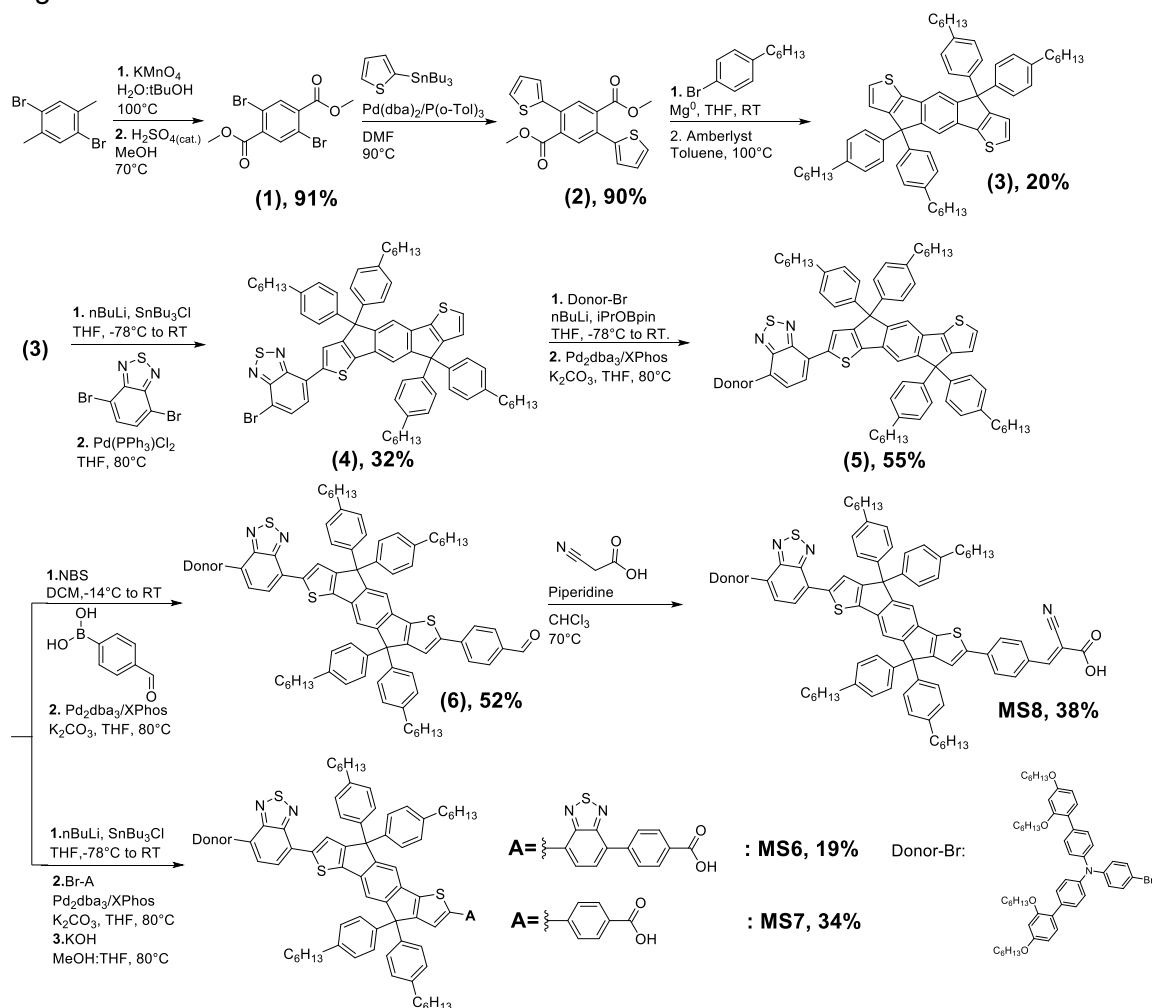


Figure 0.14. ^{13}C -NMR spectrum of MS3 in CDCl_3 .

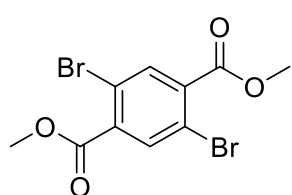
Supporting information to Chapter 3

Synthetic procedure

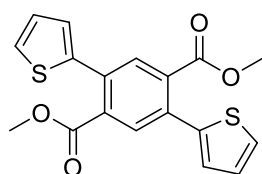
Chloroform (VWR), Methanol (Sigma), Ethanol (Fisher Chemical), dichloromethane (DCM, Thommen-Furler), hexanes (VWR International SA), diethyl ether (HUBERLAB AG), Acetic acid (VWR International SA), potassium phosphate tribasic (Acros), magnesium sulfate (Reactolab), N-bromosuccinimide (NBS, TCI), 1,4-dibromo-2,5-dimethylbenzene (Sigma), butyl lithium 1.6M in hexanes (Sigma), bis(dibenzylideneacetone)palladium(0)(Fluorochem), tris(o-tolyl)phosphine(ABCR), amberlyst (Sigma), 4,7-Dibromo-2,1,3-benzothiadiazole (Fluorochem), 2-(dicyclohexylphosphino)-2',4',6'-triisopropylbiphenyl (Fluorochem), and tris(dibenzylideneacetone)dipalladium(0), tri butyltinchloride (Sigma), 4-bromo-hexylbenzene (Fluorochem), Tetrabutylammonium fluoride solution 1.0 M in THF(Sigma), 4-formylphenylboronic acid(Fluorochem), 2-(Tributylstannyl)thiophene (Sigma), piperidine (Acros), Cyanoacetic acid(ABCR) and N-(2',4'-bis(hexyloxy)-[1,1'-biphenyl]-4-yl)-N-(4-bromophenyl)-2',4'-bis(hexyloxy)-[1,1'-biphenyl]-4-amine (**HDC6-Br**)(H.Glass SA) were used as received without further purification. Anhydrous THF and Toluene were purchased over molecular sieves from Acros Organics. The solvents used for palladium catalyzed cross coupling reactions were degassed three times using the freeze-pump-thaw method and liquid nitrogen.



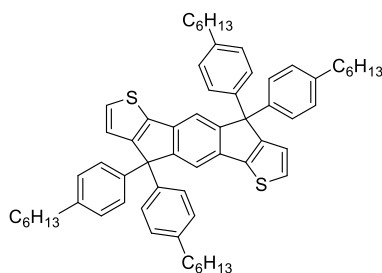
Scheme 0.2. Synthetic route to MS6, MS7 and MS8.

dimethyl 2,5-dibromoterephthalate(**1**)

1,4-dibromo-2,5-dimethylbenzene (5 g, 18.94 mmol, 1 eq.) was charged in the three necked round bottom flask equipped with a condenser and dissolved in 64 mL of a $\text{H}_2\text{O}:\text{tBuOH}(1:1, \text{v}:\text{v})$. Then, KMnO_4 (6.5.8 g, 41.5 mmol, 2.2 eq.) was added to the reaction mixture before being refluxed. After 1h30, a second portion of KMnO_4 (6.5.8 g, 41.5 mmol, 2.2 eq.) was added and the reaction was allowed to reflux overnight. After cooling down to room temperature, the crude was flashed through a pad of celite and acidified with 1M HCl, until pH=1 to afford the formation of a solid that was recovered by vacuum filtration. The intermediate was charged in a three necked round bottom flask equipped with a condenser and suspended in methanol (20 mL) and H_2SO_4 (0.5 mL) before being refluxed at 90°C overnight. The reaction was quenched by slow addition of Na_2CO_3 and diluted with diethylether (50 mL). The impurities were removed by filtration and the title product was obtained as a white solid: 5.61 g (91%). ^1H NMR (400 MHz, CDCl_3) δ 8.06 (s, 2H), 3.97 (s, 6H). ^{13}C NMR (101 MHz, CDCl_3) δ 163.59, 136.97, 135.61, 119.14, 52.98. HRMS (ESI/QTOF) m/z : $[\text{M} + \text{Na}]^+$ Calcd for $\text{C}_{10}\text{H}_8\text{Br}_2\text{NaO}_4^+$ 372.8682; Found 372.1663.

dimethyl 2,5-di(thiophen-2-yl)terephthalate(**2**)

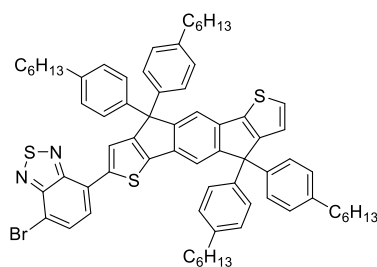
dimethyl 2,5-dibromoterephthalate(**1**) (1.74 g, 4.94 mmol, 1 eq.) and Tributyl(2-thienyl)stannane (3.87 g, 10.4 mmol, 2.1 eq.) were charged in a schlenk tube along with anhydrous DMF (20 mL) before being degassed three times using freeze-pump-thaw and liquid nitrogen. Then, Bis(dibenzylideneacetone)palladium (0.113 g, 0.198 mmol, 0.04 eq.) and Tri-*o*-tolylphosphine (90 mg, 0.297 mmol, 0.06 eq.) were added and the resulting reaction mixture was heated at 90°C for 24 hours. After cooling down to room temperature, saturated aqueous NaF was added to quench the reaction, and subsequently diluted with deionized water (180 mL). The organics were extracted with dichloromethane (4x60 mL). The solvent was concentrated under reduced pressure and methanol was added to afford the formation of a greenish solid that was washed with ethanol (2x30 mL) and hexanes (2x30 mL) before being dried. The target compound was obtained as a pale greenish solid: 1.59 g, (90%). ^1H NMR (400 MHz, CDCl_3) δ 7.75 (s, 2H), 7.32 (dd, $J = 5.0, 1.3$ Hz, 2H), 7.06 – 6.97 (m, 4H), 3.70 (s, 6H). ^{13}C NMR (101 MHz, CDCl_3) δ 167.04, 139.28, 132.58, 132.35, 131.12, 130.89, 126.44, 125.93, 125.64, 76.32, 76.00, 75.68, 51.53. HRMS (ESI/QTOF) m/z : $[\text{M} + \text{Na}]^+$ Calcd for $\text{C}_{18}\text{H}_{14}\text{NaO}_4\text{S}_2^+$ 381.0226; Found 381.0226.

4,4,9,9-tetrakis(4-hexylphenyl)-4,9-dihydro-s-indaceno[1,2-b:5,6-b']dithiophene(**3**)

Magnesium (0.7 g, 28.83 mmol, 6.5 eq.) and 1-(4-Bromophenyl)hexane (7.49 g, 31.052 mmol, 7 eq.) were charged in a two necked round bottom flask along with anhydrous THF (40 mL) and a catalytic amount of iodide before gently heating at 40°C until complete dissolution of the magnesium. After that, the reaction was cooled down to room temperature and dimethyl 2,5-di(thiophen-2-yl)terephthalate(**2**) (1.59 g, 4.45 mmol, 1 eq.) was added and the mixture was refluxed overnight. After cooling down to room temperature, the reaction was

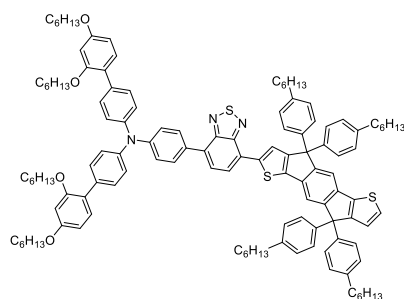
quenched with saturated aqueous ammonium chloride and the organics were washed with deionized water(100 mL), brine(100 mL) and dried over MgSO_4 . The crude was charged in a three necked round bottom flask along with toluene (10 mL) and 2 g amberlyst, before being refluxed at 120°C under argon overnight. The amberlyst was filtered off after cooling down to room temperature and toluene removed under reduced pressure. Hexanes was added to induce precipitation of the target product that was obtained as a greenish solid: 0.8 g(20%). ^1H NMR (400 MHz, CDCl_3) δ 7.35 (s, 2H), 7.16 (d, J = 4.9 Hz, 2H), 7.07 (d, J = 7.9 Hz, 8H), 6.97 (d, J = 8.0 Hz, 8H), 6.92 (d, J = 4.9 Hz, 2H), 2.47 (t, J = 7.8 Hz, 7H), 1.49 (q, J = 7.2 Hz, 9H), 1.34 – 1.14 (m, 24H), 0.83 – 0.76 (m, 12H). ^{13}C NMR (101 MHz, CDCl_3) δ 155.85, 153.40, 142.07, 141.36, 141.26, 135.09, 128.27, 127.89, 127.38, 126.81, 123.13, 117.48, 77.34, 77.02, 76.70, 62.65, 35.57, 31.73, 31.35, 29.72, 29.15, 27.02, 22.61, 14.10. HRMS (APPI/LTQ-Orbitrap) m/z : $[\text{M} + \text{H}]^+$ Calcd for $\text{C}_{64}\text{H}_{75}\text{S}_2^+$ 907.5305; Found 907.5324.

4-bromo-7-(4,4,9,9-tetrakis(4-hexylphenyl)-4,9-dihydro-s-indaceno[1,2-b:5,6-b']dithiophen-2-yl)benzo[c][1,2,5]thiadiazole (4)



4,4,9,9-tetrakis(4-hexylphenyl)-4,9-dihydro-s-indaceno[1,2-b:5,6-b']dithiophene(**3**)(0.747 g, 0.823 mmoles, 1 eq.) was charged in a two necked round bottom flask along with anhydrous THF(10 mL) before being degassed three times using freeze-pump-thaw and liquid nitrogen. The resulting solution was cooled down to -78°C using an acetone/dry-ice bath. Then, 1.6 M n-butyl lithium(0.5 mL, 0.8 mmoles, 1 eq.) was slowly added and the reaction mixture was subsequently stirred for 2 hours. Then, tri-n-butyltin chloride(0.3 mL, 1.06 mmoles, 1.3 eq.) was added and the reaction was allowed to warm up to room temperature overnight. After that, 5 mL of a 1 M tetrabutylammonium fluoride THF solution was added and the reaction mixture was diluted with diethylether(40 mL). The crude was flushed through a pad of celite, washed with deionized water (100 mL), brine (100 mL) before drying over MgSO_4 . The crude was charged in a schlenk tube along with 4,7-Dibromo-2,1,3-benzothiadiazole(0.5 g, 1.7 mmoles, 1.8 eq.) and anhydrous THF(10 mL) before being degassed three times using freeze-pump-thaw and liquid nitrogen. Then, bis(triphenylphosphine)palladium(II) chloride(59 mg, 83 μmoles , 0.09 eq.) was added and the resulting reaction was heated at 80°C overnight. After cooling down to room temperature, 3 mL of a 1 M tetrabutylammonium fluoride THF solution was added and the reaction mixture was diluted with diethylether(40 mL) before being flashed through a pad of celite. The solvent was removed under reduced pressure and the crude was purified by flash chromatography on SiO_2 eluting from 100% hexanes to 20% DCM in hexanes by volume. The target product was obtained as an red shinny solid: 0.288 g (32%). ^1H NMR (400 MHz, CDCl_3) δ 7.86 (s, 1H), 7.59 (d, J = 7.8 Hz, 1H), 7.44 (s, 1H), 7.41 (d, J = 7.8 Hz, 1H), 7.38 (s, 1H), 7.16 (dd, J = 8.3, 3.2 Hz, 5H), 7.09 (d, J = 8.1 Hz, 4H), 6.99 (t, J = 7.9 Hz, 7H), 6.93 (d, J = 4.9 Hz, 1H), 2.47 (t, J = 7.8 Hz, 8H), 1.53 – 1.41 (m, 8H), 1.30 – 1.14 (m, 25H), 0.77 (q, J = 6.4 Hz, 12H). ^{13}C NMR (101 MHz, CDCl_3) δ 156.50, 156.25, 153.77, 153.74, 153.55, 151.50, 143.94, 141.99, 141.84, 141.62, 141.49, 141.20, 140.74, 135.98, 134.73, 132.28, 128.45, 128.36, 128.00, 127.91, 127.62, 124.54, 123.67, 123.23, 117.98, 117.47, 111.54, 77.38, 77.06, 76.74, 63.39, 63.18, 63.04, 62.73, 62.51, 35.61, 31.76, 31.39, 31.38, 29.74, 29.19, 29.17, 26.96, 22.63, 14.14, 14.13. HRMS (nanochip-ESI/LTQ-Orbitrap) m/z : $[\text{M} + \text{H}]^+$ Calcd for $\text{C}_{70}\text{H}_{76}\text{BrN}_2\text{S}_3^+$ 1119.4349; Found 1119.4333.

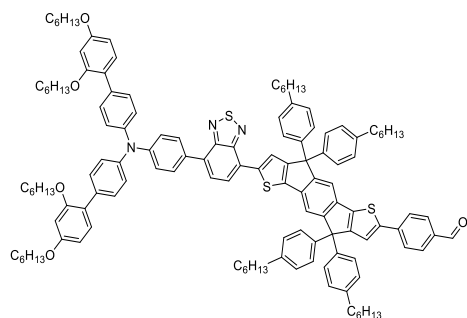
N-(2',4'-bis(hexyloxy)-[1,1'-biphenyl]-4-yl)-2',4'-bis(hexyloxy)-N-(4-(7-(4,4,9,9-tetrakis(4-hexylphenyl)-4,9-dihydro-s-indaceno[1,2-b:5,6-b']dithiophen-2-yl)benzo[c][1,2,5]thiadiazol-4-yl)phenyl)-[1,1'-biphenyl]-4-amine(**5**)



N-(2',4'-bis(hexyloxy)-[1,1'-biphenyl]-4-yl)-N-(4-bromophenyl)-2',4'-bis(hexyloxy)-[1,1'-biphenyl]-4-amine(**HDC6-Br**)(293 mg, 334 μ mol, 1.3 eq.) was charged in a schlenk tube and dissolved in anhydrous THF(3 mL) before being degassed three times using freeze-pump-thaw and liquid nitrogen. Then, n-butyl lithium 1.6M (0.5 mL, 0.745 mmoles, 2.9 eq.) was added dropwise to the reaction. The resulting solution was allowed to stir for 4 hours before

quenching with 2-Isopropoxy-4,4,5,5-tetramethyl-1,3,2-dioxaborolane (191 mg, 1.03 mmoles, 4 eq.). The reaction was allowed to warm up to room temperature overnight. Then, aqueous potassium carbonate 2M (0.6 mL, 1.29 mmoles, 5 eq.) and 4-bromo-7-(4,4,9,9-tetrakis(4-hexylphenyl)-4,9-dihydro-s-indaceno[1,2-b:5,6-b']dithiophen-2-yl)benzo[c][1,2,5]thiadiazole (**4**) were added to the reaction and the resulting mixture degassed three times using freeze-pump-thaw and liquid nitrogen. Then, tris(dibenzylideneacetone)dipalladium(0)(19 mg, 20.5 μ mol, 0.08 eq.) and 2-Dicyclohexylphosphino-2',4',6'-triisopropylbiphenyl(19 mg, 41.0 μ mol, 0.16 eq.) were added and the mixture heated at 85°C overnight. The reaction was allowed to cool down to room temperature before diluting with diethyl ether twice and flashing through a pad of MgSO₄. The solvent was removed and the crude purified using flash column chromatography on SiO₂, gradually eluting from 100% hexanes to 50% dichloromethane in hexanes by volume. The desired compound was obtained as a purple solid 260 mg (55%). ¹H NMR (400 MHz, CDCl₃) δ 7.95 (s, 1H), 7.82 (t, J = 6.5 Hz, 3H), 7.61 (d, J = 7.7 Hz, 1H), 7.50 – 7.32 (m, 6H), 7.21 – 7.05 (m, 15H), 6.99 (t, J = 8.6 Hz, 8H), 6.94 (d, J = 5.0 Hz, 1H), 6.47 (d, J = 6.1 Hz, 4H), 3.90 (q, J = 7.1 Hz, 7H), 2.48 (t, J = 7.8 Hz, 7H), 1.70 (dp, J = 14.6, 6.9 Hz, 8H), 1.50 (p, J = 7.5 Hz, 9H), 1.30 – 1.16 (m, 54H), 0.78 (d, J = 6.9 Hz, 21H). ¹³C NMR (101 MHz, CDCl₃) δ 158.59, 155.98, 155.44, 155.06, 152.96, 152.62, 152.49, 141.01, 140.96, 140.90, 140.45, 140.39, 140.22, 134.83, 134.59, 134.00, 129.84, 127.36, 127.30, 126.98, 126.86, 126.67, 124.49, 122.17, 121.95, 116.76, 116.38, 104.36, 99.40, 81.71, 76.45, 76.13, 75.81, 67.40, 67.08, 62.12, 61.67, 34.56, 34.55, 33.21, 30.91, 30.71, 30.60, 30.45, 30.34, 29.68, 29.49, 29.30, 29.10, 28.91, 28.72, 28.68, 28.64, 28.53, 28.35, 28.31, 28.14, 28.11, 28.08, 24.76, 24.00, 23.57, 21.67, 21.61, 21.57, 21.56, 20.15, 13.06, 13.02. HRMS (APPI/LTQ-Orbitrap) m/z: [M + H]⁺ Calcd for C₁₂₄H₁₄₆N₃O₄S₃⁺ 1837.0470; Found 1837.0482.

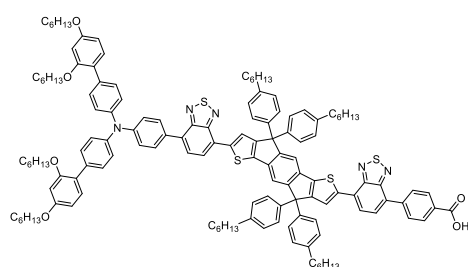
4-(7-(7-(4-(bis(2',4'-bis(hexyloxy)-[1,1'-biphenyl]-4-yl)amino)phenyl)benzo[c][1,2,5]thiadiazol-4-yl)-4,4,9,9-tetrakis(4-hexylphenyl)-4,9-dihydro-s-indaceno[1,2-b:5,6-b']dithiophen-2-yl)benzaldehyde(**6**)



N-(2',4'-bis(hexyloxy)-[1,1'-biphenyl]-4-yl)-2',4'-bis(hexyloxy)-N-(4-(7-(4,4,9,9-tetrakis(4-hexylphenyl)-4,9-dihydro-s-indaceno[1,2-b:5,6-b']dithiophen-2-yl)benzo[c][1,2,5]thiadiazol-4-yl)phenyl)-[1,1'-biphenyl]-4-amine(**5**)(0.208 g, 0.113 mmoles, 1 eq.) was charged in a round bottom flask and dissolved in 5 mL dichloromethane, protected from the dark and cooled down to -10°C with a water/NaCl bath. Then, N-

bromosuccinimide(20 mg, 0.113 mmoles, 1 eq.) was added and the reaction was allowed to warm up to room temperature overnight. After that, the solvent was removed and hexanes was added to precipitate the succinimide side product, which was filtered off. The solvent was removed to obtain the brominated intermediate. The crude was charged in a schlenk tube along with 4-Formylphenylboronic acid (34 mg), 2 M aqueous K₃PO₄(0.16 mL) and anhydrous THF (5mL) before being degassed three times using freeze-pump-thaw and liquid nitrogen. Then, tris(dibenzylideneacetone)dipalladium(0) (18 mg) and 2-(Dicyclohexylphosphino)-2',4',6'-triisopropylbiphenyl (18 mg) were added and the resulting reaction mixture was refluxed overnight. After cooling down to room temperature, the reaction mixture was diluted with diethylether (50 mL) and flashed through a pad of MgSO₄. The solvent was removed under reduced pressure and the crude was purified by flash chromatography on SiO₂ eluting from 100% hexanes to 100% dichloromethane. The desired product was obtained as a shiny red solid: 65 mg (52%). ¹H NMR (400 MHz, CDCl₃) δ 9.89 (s, 1H), 7.94 (s, 1H), 7.82 (t, J = 6.7 Hz, 3H), 7.76 (d, J = 8.2 Hz, 2H), 7.63 (d, J = 8.3 Hz, 2H), 7.42 (t, J = 11.1 Hz, 6H), 7.25 – 7.10 (m, 14H), 7.02 (dd, J = 8.2, 3.9 Hz, 9H), 6.50 – 6.44 (m, 4H), 3.90 (q, J = 6.8 Hz, 8H), 2.49 (t, J = 7.8 Hz, 9H), 1.70 (tt, J = 14.4, 6.7 Hz, 8H), 1.51 (h, J = 6.2, 5.5 Hz, 10H), 1.37 (dt, J = 24.5, 7.6 Hz, 3H), 1.25 (ddt, J = 20.6, 16.8, 7.4 Hz, 45H), 0.90 – 0.74 (m, 29H). ¹³C NMR (101 MHz, CDCl₃) δ 191.32, 157.14, 153.60, 145.00, 142.98, 141.81, 141.72, 141.62, 141.59, 140.76, 134.84, 130.49, 128.49, 128.44, 128.01, 127.89, 125.35, 122.94, 121.20, 117.70, 105.33, 100.44, 77.36, 77.04, 76.72, 68.44, 68.14, 63.18, 63.15, 35.61, 31.95, 31.74, 31.64, 31.55, 31.48, 31.37, 29.73, 29.39, 29.34, 29.19, 29.16, 29.11, 25.80, 25.79, 22.65, 22.62, 22.60, 14.12, 14.08, 1.05. HRMS (APPI/LTQ-Orbitrap) m/z: [M + H]⁺ Calcd for C₁₃₁H₁₅₀N₃O₅S₃⁺ 1941.0732; Found 1941.0826.

4-(7-(7-(7-(4-(bis(2',4'-bis(hexyloxy)-[1,1'-biphenyl]-4-yl)amino)phenyl)benzo[c][1,2,5]thiadiazol-4-yl)-4,4,9,9-tetrakis(4-hexylphenyl)-4,9-dihydro-s-indaceno[1,2-b:5,6-b']dithiophen-2-yl)benzo[c][1,2,5]thiadiazol-4-yl)benzoic acid(**MS6**)

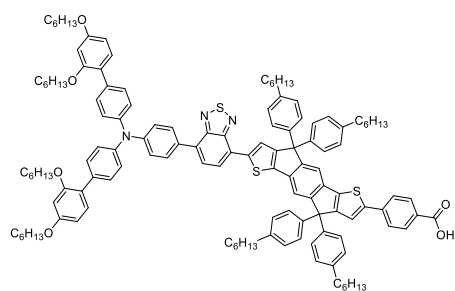


N-(2',4'-bis(hexyloxy)-[1,1'-biphenyl]-4-yl)-2',4'-bis(hexyloxy)-N-(4-(7-(4,4,9,9-tetrakis(4-hexylphenyl)-4,9-dihydro-s-indaceno[1,2-b:5,6-b']dithiophen-2-yl)benzo[c][1,2,5]thiadiazol-4-yl)phenyl)-[1,1'-biphenyl]-4-amine(**5**)(0.260 g, 0.141 mmoles, 1 eq.) was charged in a three necked round bottom flask and solubilized in anhydrous THF(5 mL) before being degassed three

times using freeze-pump-thaw and liquid nitrogen and subsequently cooled down to -78°C with an acetone/dry-ice bath. Then, 1M lithium diisopropylamide(0.16 mL, 0.156 mmoles, 1.1 eq.) in THF solution was added to the reaction and the resulting mixture was stirred at -78°C for 3hours. After that, tri-n-butyltin chloride(0.1 mL, 0.369 mmoles, 2.6 eq.) was added and the reaction was allowed to warm up to room temperature overnight. Saturated aqueous NaF(20 mL) was added to quench the reaction along with 100 mL deionized water. The crude was diluted with diethyl ether (50 mL) and the organic phase was washed with brine(100 mL) before drying over MgSO₄. Half of the crude was taken up in a schlenk tube along with Ethyl 4-(7-bromobenzo[c][1,2,5]thiadiazol-4-yl)benzoate(49 mg) and anhydrous THF(5 mL) before being degassed three times using freeze-pump-thaw and liquid nitrogen. Then bis(dibenzylideneacetone)palladium(7.7 mg) and tri-o-tolylphosphine(4.5 mg) were added and the resulting mixture was refluxed overnight. After cooling down to room temperature, 1M tetrabutylammonium fluoride (0.4 mL) was added along with diethyl ether(30 mL). The reaction

mixture was flashed over a pad of celite and the organics were removed. The intermediate was charged in a three necked round bottom flask equipped with a condenser along with 10 mL of a THF:EtOH(1:1, v:v) mixture and KOH(0.205 g). The reaction mixture was refluxed under argon overnight. After cooling down to room temperature, the reaction was acidified with 1M HCl (10 mL) and subsequently diluted with deionized water (50 mL). The organics were extracted with dichloromethane (3x30 mL) and the solvent removed under reduced pressure. The solvent was removed under reduced pressure and the crude was purified by flash chromatography on SiO₂ eluting from 100% DCM to 2% MeOH in DCM by volume. The target product was obtained as an purple shinny solid: 28 mg(19%)¹H NMR (600 MHz, CDCl₃) δ 8.30 (d, J = 7.9 Hz, 2H), 8.13 (s, 1H), 8.11 (d, J = 8.1 Hz, 2H), 8.07 (s, 1H), 7.98 (d, J = 7.4 Hz, 1H), 7.95 (d, J = 7.5 Hz, 1H), 7.93 – 7.90 (m, 2H), 7.81 (d, J = 7.5 Hz, 1H), 7.72 (d, J = 7.5 Hz, 1H), 7.58 (d, J = 5.0 Hz, 2H), 7.53 – 7.48 (m, 4H), 7.35 – 7.29 (m, 10H), 7.28 – 7.23 (m, 4H), 7.16 – 7.12 (m, 7H), 6.58 (dq, J = 5.6, 2.4 Hz, 4H), 4.01 (dt, J = 13.1, 6.5 Hz, 8H), 2.60 (t, J = 7.9 Hz, 8H), 1.87 – 1.75 (m, 7H), 1.62 (p, J = 7.7 Hz, 9H), 1.55 – 1.48 (m, 4H), 1.45 (tt, J = 9.2, 4.4 Hz, 4H), 1.42 – 1.21 (m, 39H), 0.99 – 0.92 (m, 6H), 0.89 (td, J = 7.0, 2.8 Hz, 23H). ¹³C NMR (151 MHz, CDCl₃) δ 159.58, 158.11, 156.98, 156.71, 156.69, 153.97, 153.77, 153.72, 152.66, 152.48, 148.20, 145.52, 143.95, 143.01, 142.37, 141.86, 141.81, 141.63, 141.59, 135.80, 135.28, 133.44, 132.12, 130.89, 130.82, 130.61, 130.40, 130.29, 129.79, 129.16, 128.82, 128.46, 128.45, 128.07, 128.00, 127.13, 126.18, 125.08, 124.49, 124.26, 123.76, 122.94, 122.85, 117.84, 117.74, 105.26, 100.38, 77.25, 77.04, 76.83, 68.40, 68.12, 65.90, 63.17, 63.15, 59.53, 38.16, 35.63, 33.71, 31.96, 31.94, 31.75, 31.64, 31.48, 31.40, 31.26, 29.74, 29.69, 29.58, 29.40, 29.34, 29.20, 29.09, 29.08, 28.98, 27.87, 26.88, 26.71, 26.40, 25.80, 25.78, 23.21, 22.73, 22.63, 22.61, 17.54, 15.30, 14.17, 14.14, 14.09, 13.61, 1.05. HRMS (MALDI/TOF) m/z: [M + H]⁺ Calcd for C₁₃₇H₁₅₂N₅O₆S₄⁺ 2091.0620; Found 2091.1779.

4-(7-(7-(4-(bis(2',4'-bis(hexyloxy)-[1,1'-biphenyl]-4-yl)amino)phenyl)benzo[c][1,2,5]thiadiazol-4-yl)-4,4,9,9-tetrakis(4-hexylphenyl)-4,9-dihydro-s-indaceno[1,2-b:5,6-b']dithiophen-2-yl)benzoic acid (**MS7**)



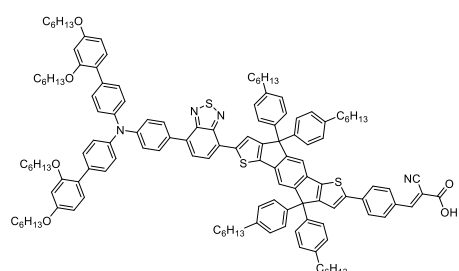
N-(2',4'-bis(hexyloxy)-[1,1'-biphenyl]-4-yl)-2',4'-bis(hexyloxy)-N-(4-(7-(4,4,9,9-tetrakis(4-hexylphenyl)-4,9-dihydro-s-indaceno[1,2-b:5,6-b']dithiophen-2-yl)benzo[c][1,2,5]thiadiazol-4-yl)phenyl)-[1,1'-biphenyl]-4-amine(**5**)(0.260 g, 0.141 mmoles, 1 eq.) was charged in a three necked round bottom flask and solubilized in anhydrous THF(5 mL) before being degassed three times using freeze-pump-thaw and liquid nitrogen and

subsequently cooled down to -78°C with an acetone/dry-ice bath. Then, 1M lithium diisopropylamide(0.16 mL, 0.156 mmoles, 1.1 eq.) in THF solution was added to the reaction and the resulting mixture was stirred at -78°C for 3hours. After that, tri-n-butyltin chloride(0.1 mL, 0.369 mmoles, 2.6 eq.) was added and the reaction was allowed to warm up to room temperature overnight. Saturated aqueous NaF(20 mL) was added to quench the reaction along with 100 mL deionized water. The crude was diluted with diethyl ether (50 mL) and the organic phase was washed with brine(100 mL) before drying over MgSO₄.

Half of the crude was taken up in a schlenk tube along with ethyl 4-bromobenzoate (31 mg) and anhydrous THF(5 mL) before being degassed three times using freeze-pump-thaw and liquid nitrogen. Then bis(dibenzylideneacetone)palladium(7.7 mg) and tri-o-tolylphosphine(4.5 mg) were added and the resulting mixture was refluxed overnight. After cooling down to room

temperature, 1M tetrabutylammonium fluoride (0.4 mL) was added along with diethyl ether (30 mL). The reaction mixture was flashed over a pad of celite and the organics were removed. The intermediate was charged in a three necked round bottom flask equipped with a condenser along with 10 mL of a THF:EtOH(1:1, v:v) mixture and KOH(0.205 g). The reaction mixture was refluxed under argon overnight. After cooling down to room temperature, the reaction was acidified with 1M HCl (10 mL) and subsequently diluted with deionized water (50 mL). The organics were extracted with dichloromethane (3x30 mL) and the solvent removed under reduced pressure. The solvent was removed under reduced pressure and the crude was purified by flash chromatography on SiO₂ eluting from 100% DCM to 2% MeOH in DCM by volume. The target product was obtained as an purple shinny solid: 47 mg(34%) ¹H NMR (600 MHz, CDCl₃) δ 8.09 (d, J = 8.2 Hz, 2H), 8.04 (s, 1H), 7.94 (d, J = 7.6 Hz, 1H), 7.93 – 7.90 (m, 2H), 7.71 (d, J = 7.6 Hz, 1H), 7.69 (d, J = 8.4 Hz, 1H), 7.55 (s, 1H), 7.52 – 7.48 (m, 4H), 7.42 (s, 1H), 7.34 – 7.29 (m, 5H), 7.27 – 7.21 (m, 7H), 7.12 (dd, J = 8.3, 5.8 Hz, 7H), 6.57 (dq, J = 5.4, 2.4 Hz, 4H), 4.00 (dt, J = 13.3, 6.5 Hz, 8H), 2.59 (t, J = 7.9 Hz, 8H), 1.87 – 1.75 (m, 8H), 1.67 – 1.57 (m, 9H), 1.51 (dq, J = 9.7, 7.2 Hz, 4H), 1.39 – 1.26 (m, 28H), 0.97 – 0.86 (m, 26H). ¹³C NMR (151 MHz, CDCl₃) δ 170.05, 159.58, 157.02, 156.98, 156.71, 153.96, 153.70, 153.51, 152.65, 148.20, 145.51, 145.24, 142.91, 142.53, 142.37, 141.83, 141.68, 141.64, 141.60, 140.05, 135.76, 135.14, 133.44, 132.13, 130.93, 130.89, 130.39, 130.29, 129.78, 128.47, 128.43, 128.38, 128.00, 127.89, 127.12, 126.16, 125.09, 124.92, 124.26, 122.94, 122.84, 120.87, 117.68, 117.63, 105.26, 100.38, 77.25, 77.04, 76.83, 68.40, 68.12, 65.90, 63.15, 63.12, 35.61, 31.95, 31.75, 31.64, 31.48, 31.39, 31.26, 29.74, 29.33, 29.20, 29.17, 29.14, 29.08, 27.87, 26.88, 25.79, 25.78, 22.62, 15.30, 14.13, 14.09, 13.65, 1.05. HRMS (MALDI/TOF) m/z: [M + H]⁺ Calcd for C₁₃₁H₁₅₀N₃O₆S₃⁺ 1957.0681; Found 1957.1367.

(E)-3-(4-(7-(7-(4-(bis(2',4'-bis(hexyloxy)-[1,1'-biphenyl]-4-yl)amino)phenyl)benzo[c][1,2,5]thiadiazol-4-yl)-4,4,9,9-tetrakis(4-hexylphenyl)-4,9-dihydro-s-indaceno[1,2-b:5,6-b']dithiophen-2-yl)phenyl)-2-cyanoacrylic acid (**MS8**)



4-(7-(7-(4-(bis(2',4'-bis(hexyloxy)-[1,1'-biphenyl]-4-yl)amino)phenyl)benzo[c][1,2,5]thiadiazol-4-yl)-4,4,9,9-tetrakis(4-hexylphenyl)-4,9-dihydro-s-indaceno[1,2-b:5,6-b']dithiophen-2-yl)benzaldehyde(**6**) (69 mg, 36 μmoles, 1 eq.), cyanoacetic acid(39 mg) and piperidine (0.1 mL) were charged in a schlenk tube along with anhydrous chloroform(5 mL) before being degassed

three times using freeze-pump-thaw and liquid nitrogen and subsequently refluxed overnight. After cooling down to room temperature, the reaction was acidified with acetic acid (20 mL). The solvents were removed under reduced pressure and the crude was purified by flash chromatography on SiO₂ eluting from 100% DCM to 2% MeOH in DCM by volume. The target product was obtained as an purple shinny solid: 27 mg(38%) ¹H NMR (600 MHz, CDCl₃) δ 8.26 (s, 1H), 8.10 (d, J = 8.4 Hz, 1H), 8.04 (s, 2H), 7.93 (dd, J = 17.3, 8.2 Hz, 3H), 7.73 (dt, J = 15.4, 7.8 Hz, 3H), 7.56 – 7.48 (m, 6H), 7.46 (s, 8H), 7.31 (dd, J = 13.0, 6.6 Hz, 3H), 7.27 – 7.17 (m, 7H), 7.12 (dq, J = 9.5, 4.3, 3.8 Hz, 9H), 6.57 (dq, J = 5.5, 2.3 Hz, 4H), 4.00 (dt, J = 13.4, 6.5 Hz, 8H), 2.59 (t, J = 7.5 Hz, 8H), 1.86 – 1.74 (m, 7H), 1.61 (h, J = 7.1, 6.6 Hz, 9H), 1.50 (h, J = 7.4 Hz, 4H), 1.46 – 1.42 (m, 5H), 1.41 – 1.21 (m, 87H), 0.95 – 0.91 (m, 6H), 0.89 (td, J = 6.7, 5.8, 3.5 Hz, 35H). ¹³C NMR (151 MHz, CDCl₃) δ 159.58, 157.26, 156.98, 153.96, 153.70, 152.64, 145.51, 141.76, 141.73, 141.64, 141.50, 141.43, 133.45, 133.01, 132.35,

130.89, 130.29, 129.78, 128.53, 128.51, 128.45, 127.99, 127.86, 125.44, 124.27, 122.93, 117.70, 105.25, 100.38, 77.25, 77.04, 76.82, 69.53, 68.40, 68.12, 63.16, 63.13, 59.53, 38.16, 35.61, 31.95, 31.74, 31.64, 31.55, 31.48, 31.39, 31.26, 30.19, 29.74, 29.39, 29.33, 29.19, 29.17, 29.08, 25.79, 25.78, 25.74, 25.67, 22.72, 22.65, 22.62, 22.60, 14.13, 14.09, 1.05. HRMS (MALDI/TOF) m/z : $[M + H]^+$ Calcd for $C_{134}H_{151}N_4O_6S_3^+$ 2008.0790; Found 2008.0474.

Optical characterization

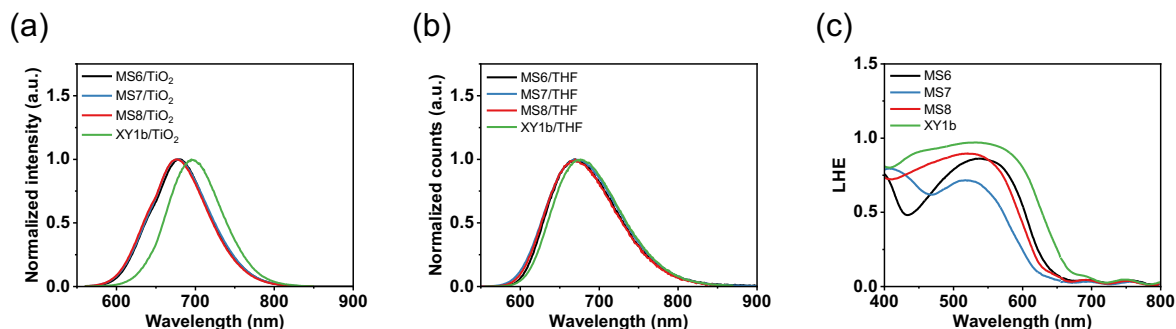


Figure 0.15. (a) Normalized emission spectra of the dyes adsorbed on 4 μm thick TiO_2 films. Normalized emission spectra of the dyes in diluted THF solutions (b). (c) Light harvesting efficiency (LHE) calculated using: $LHE=1-10^{-A}$, with A being the absorbance of the sensitized films.

Electrochemical characterization

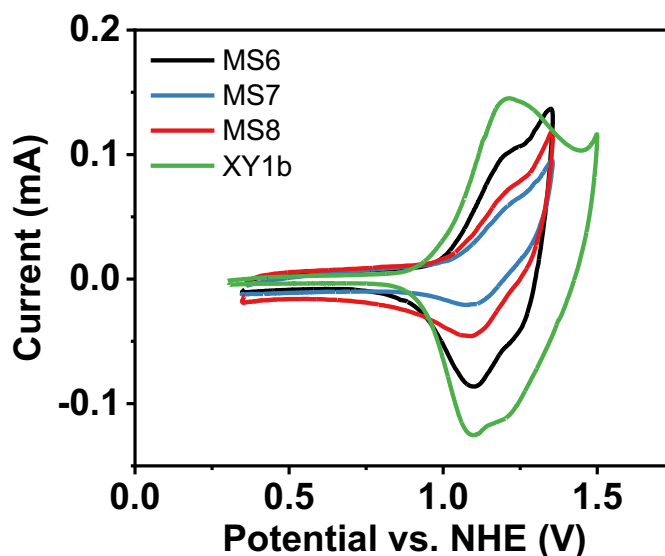


Figure 0.16. Cyclic voltammograms of the dyes adsorbed on a transparent TiO_2 film.

Computational calculations

Table 0.4. The calculated energy levels of HOMO and LUMO orbitals of MS dyes using Gaussian09 with B3PW91 functional and 6-31G(d,p) basis sets.

	HOMO [eV]	LUMO [eV]	E _g [eV]
MS6	-4.63	-2.75	1.88
MS7	-4.63	-2.52	2.11
MS8	-4.72	-2.90	1.82
XY1b	-5.62	-1.93	3.69

Time resolved photoluminescent decay

	A ₁ [%]	τ ₁ (A) [ns]	A ₂ [%]	τ ₂ (A) [ns]	A ₁ [%]	τ ₁ (T) [ns]	A ₂ [%]	τ ₂ (T) [ns]
MS6	48.2	0.63	51.8	1.5	57.5	0.4	42.5	0.78
MS7	49.1	0.6	51.9	1.57	39.6	0.43	60.4	0.9
MS8	45.9	1.06	54.1	2.05	55.8	0.43	44.2	0.95
XY1b	40.3	0.66	59.7	1.61	46.2	0.2	53.8	0.52

¹H and ¹³C NMR spectra

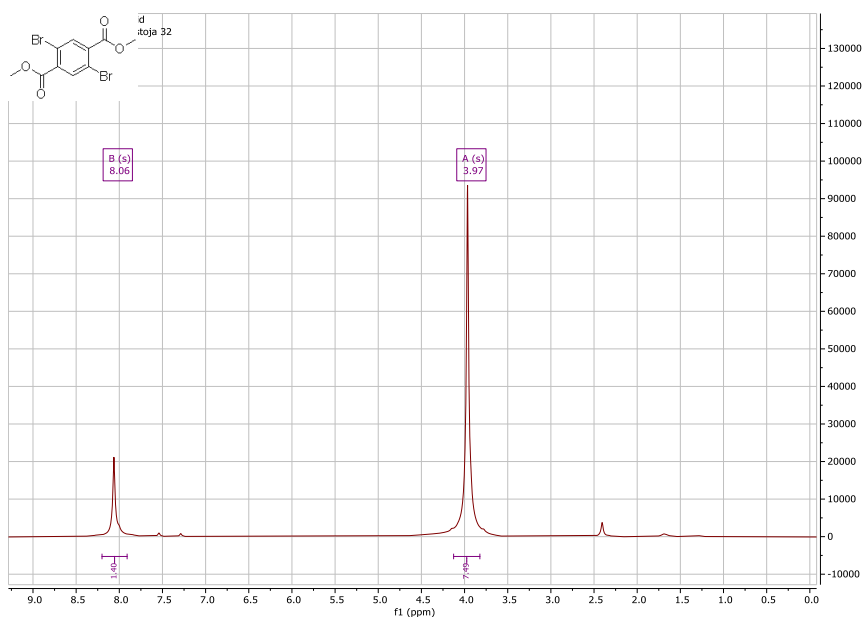
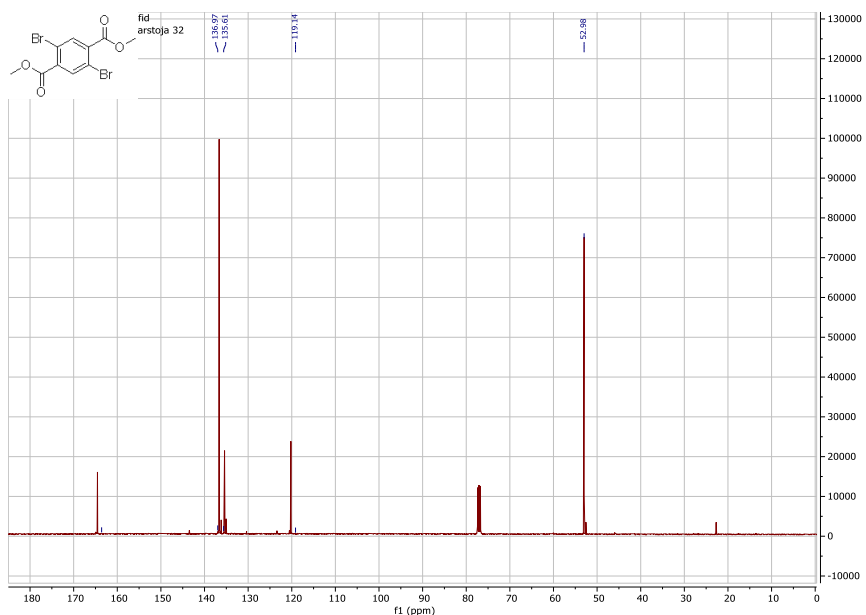
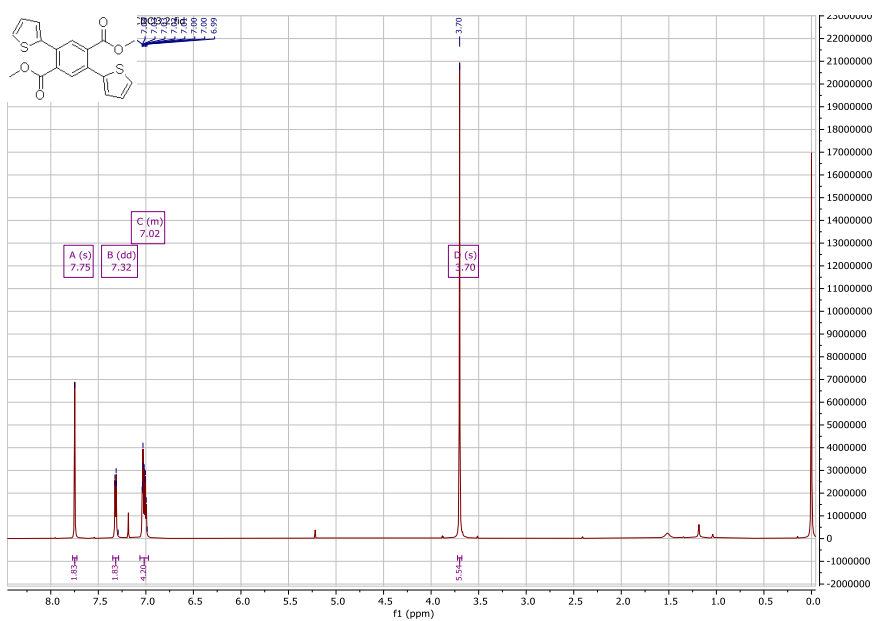
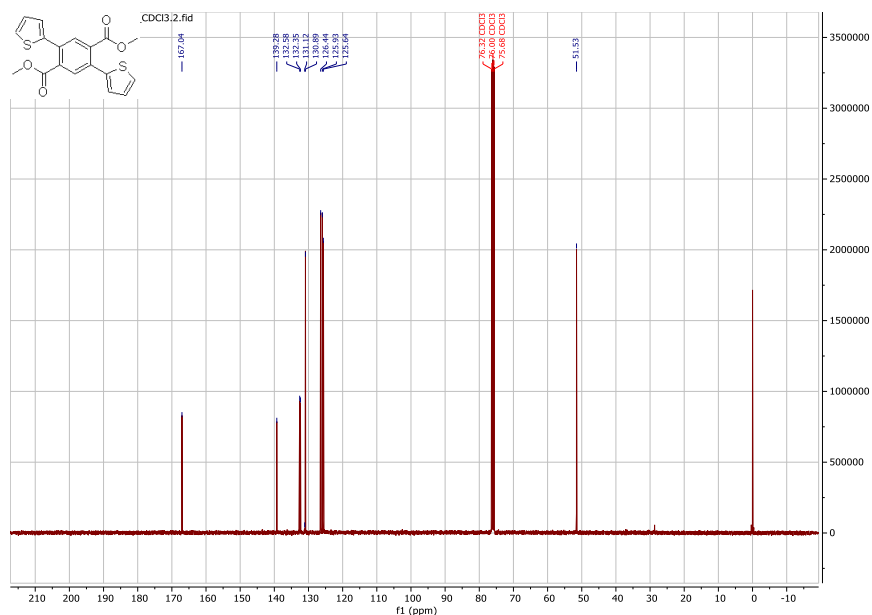
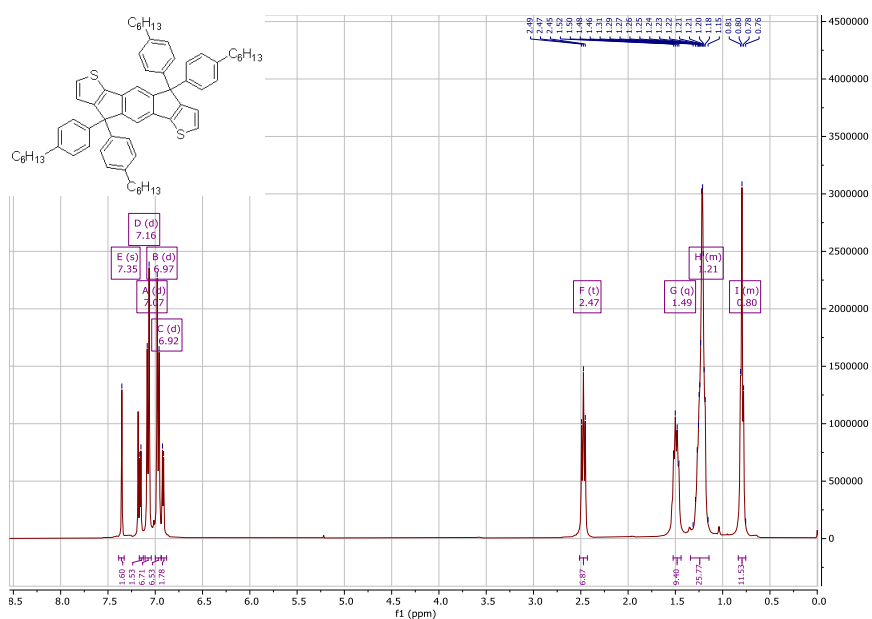
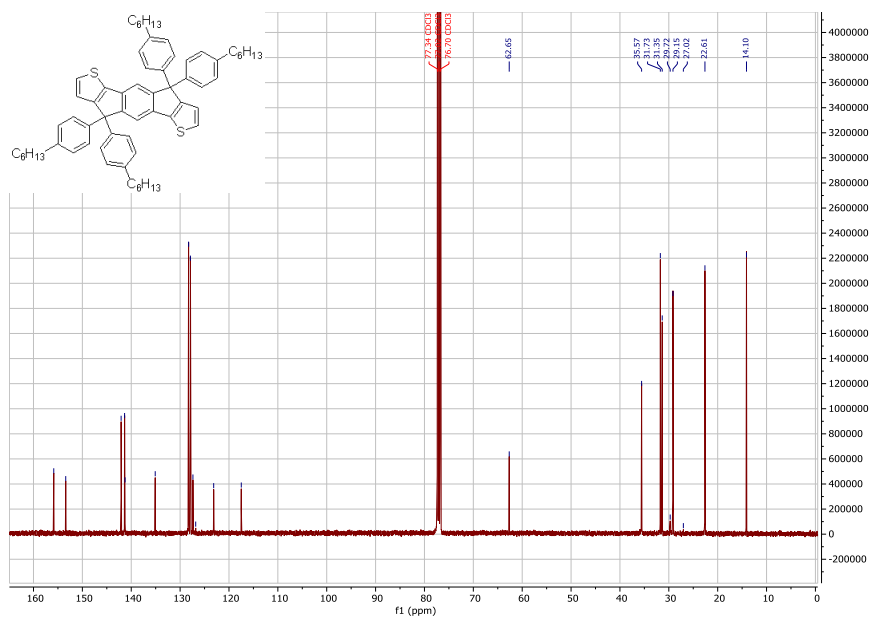
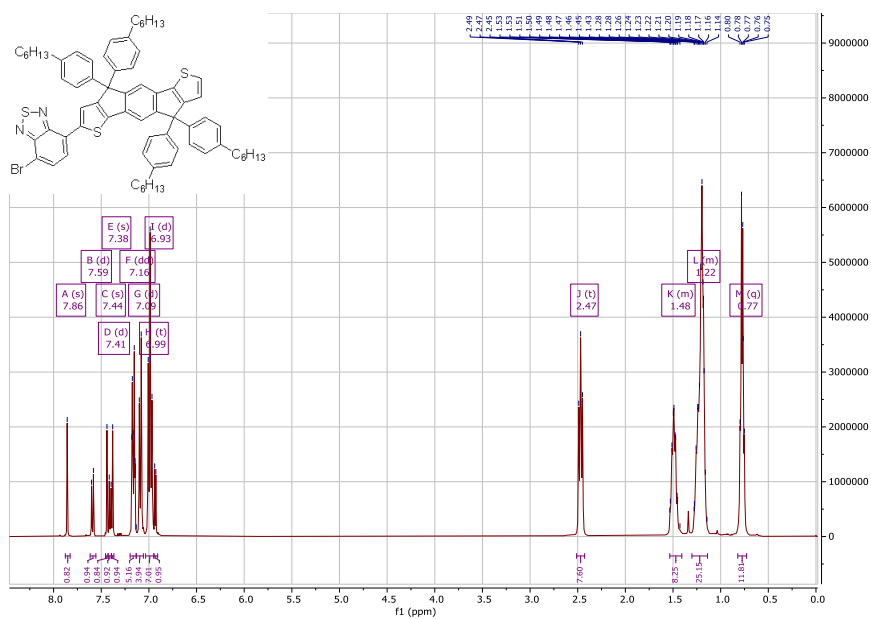
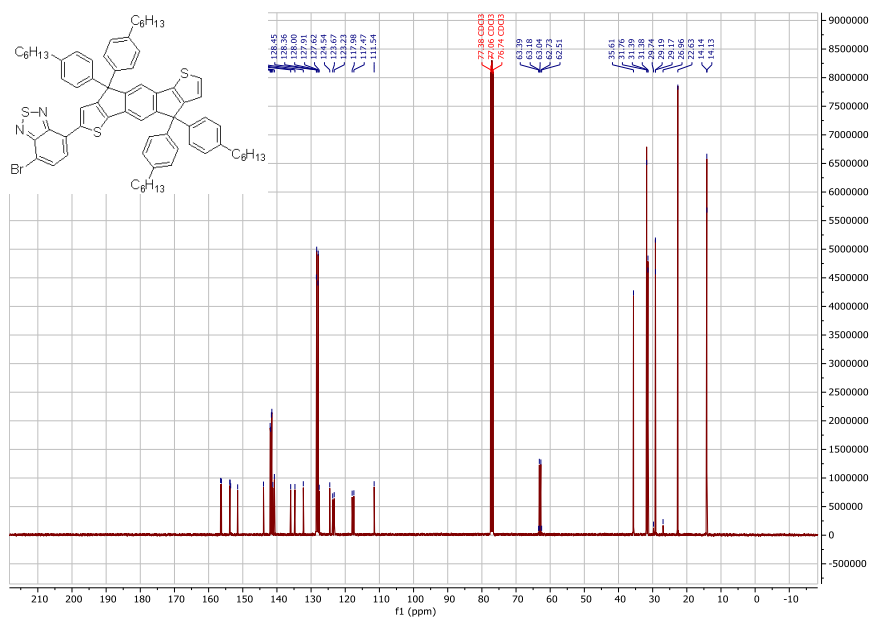
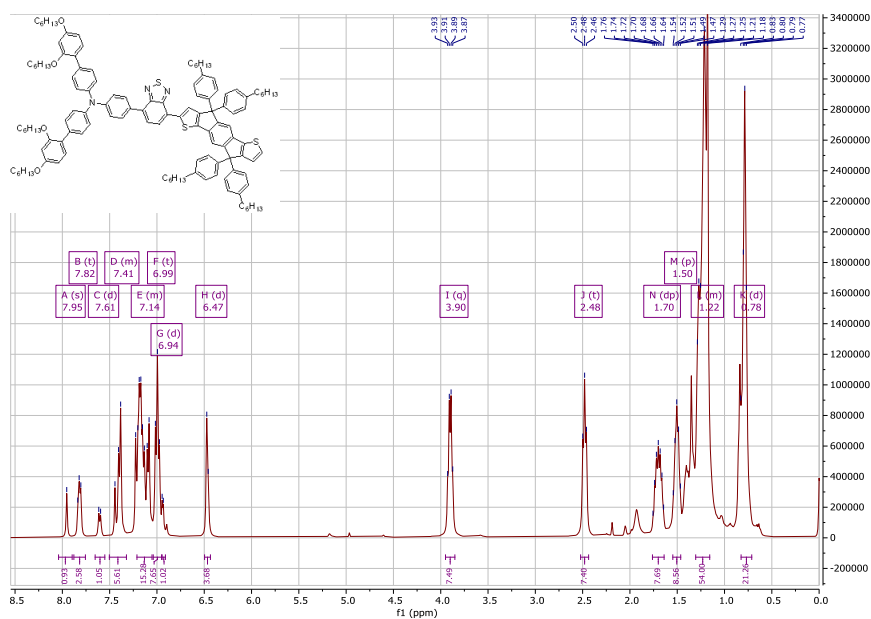


Figure 0.17. ¹H NMR of 1 in CDCl₃.

Figure 0.18. ^{13}C NMR of 1 in CDCl_3 .Figure 0.19. ^1H NMR of 2 in CDCl_3 .

Figure 0.20. ¹³C NMR of 2 in CDCl₃.Figure 0.21. ¹H NMR of 3 in CDCl₃.

Figure 0.22. ^{13}C NMR of 3 in CDCl_3 .Figure 0.23. ^1H NMR of 4 in CDCl_3 .

Figure 0.24. ^{13}C NMR of 4 in CDCl_3 .Figure 0.25. ^1H NMR of 5 in CDCl_3 .

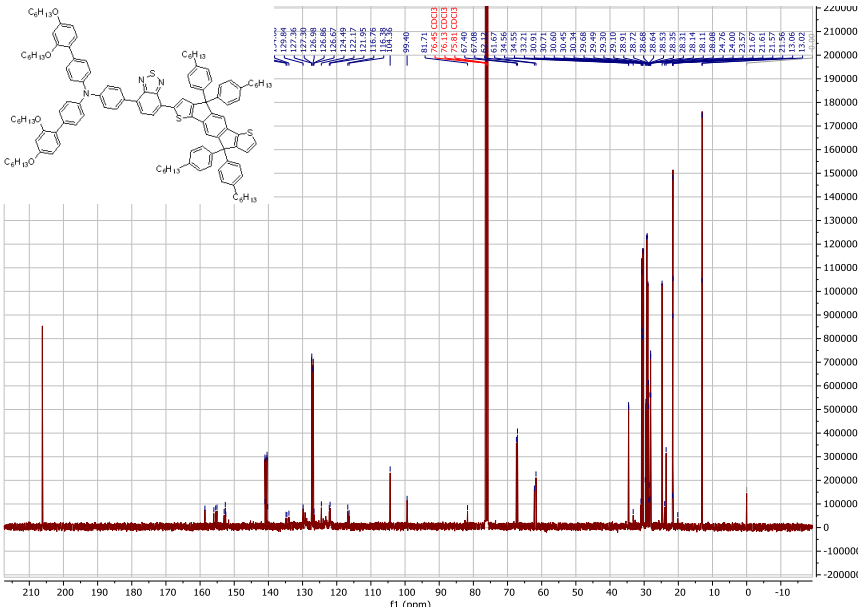


Figure 0.26. ^{13}C NMR of 5 in CDCl_3 .

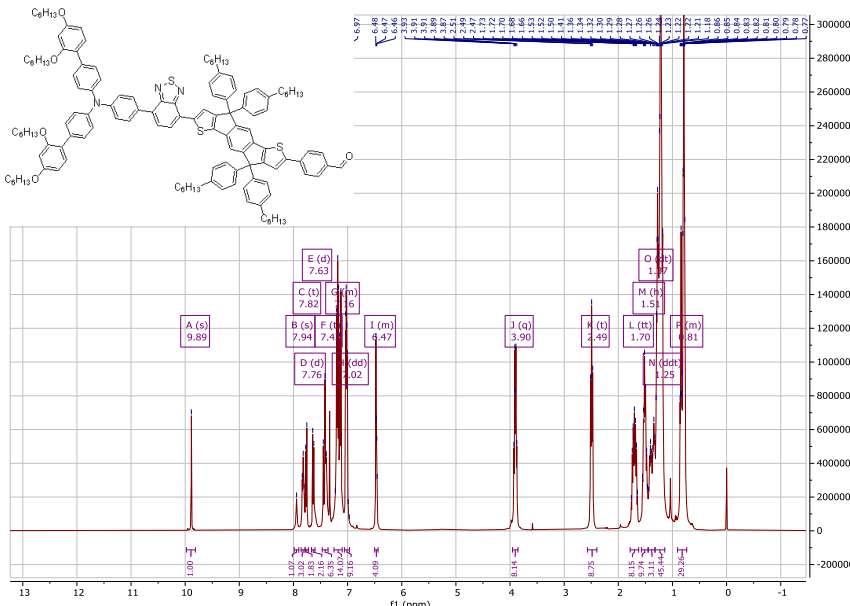


Figure 0.27. ^1H NMR of 6 in CDCl_3 .

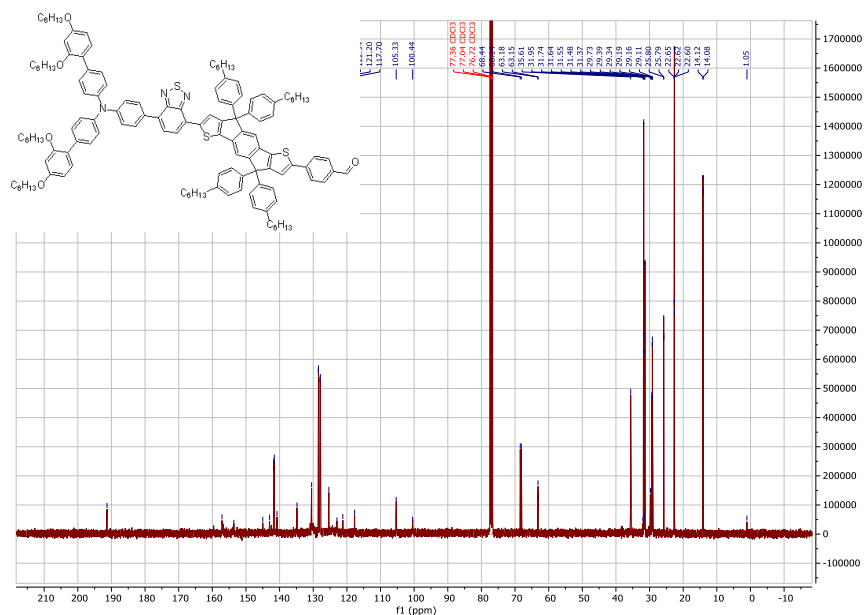


Figure 0.28. ^{13}C NMR of 6 in CDCl_3 .

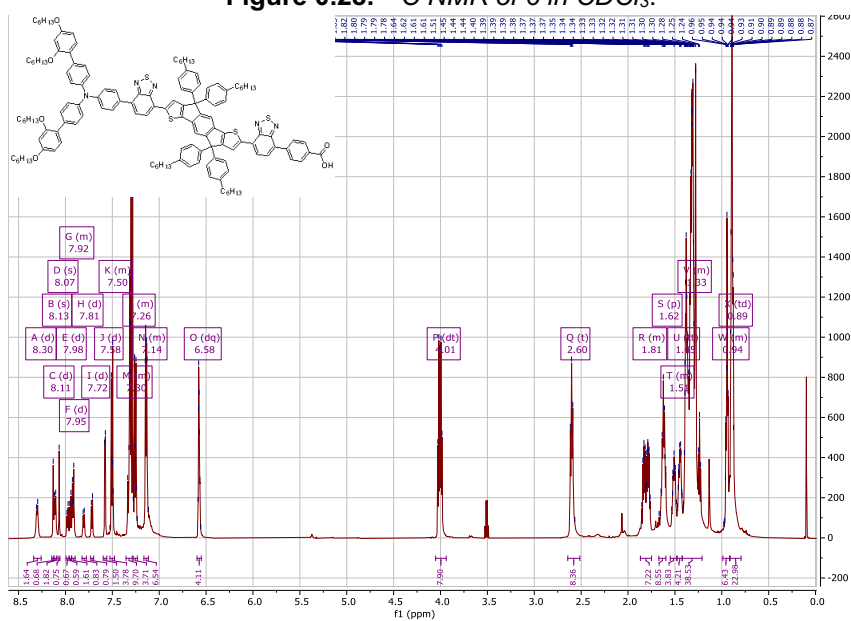
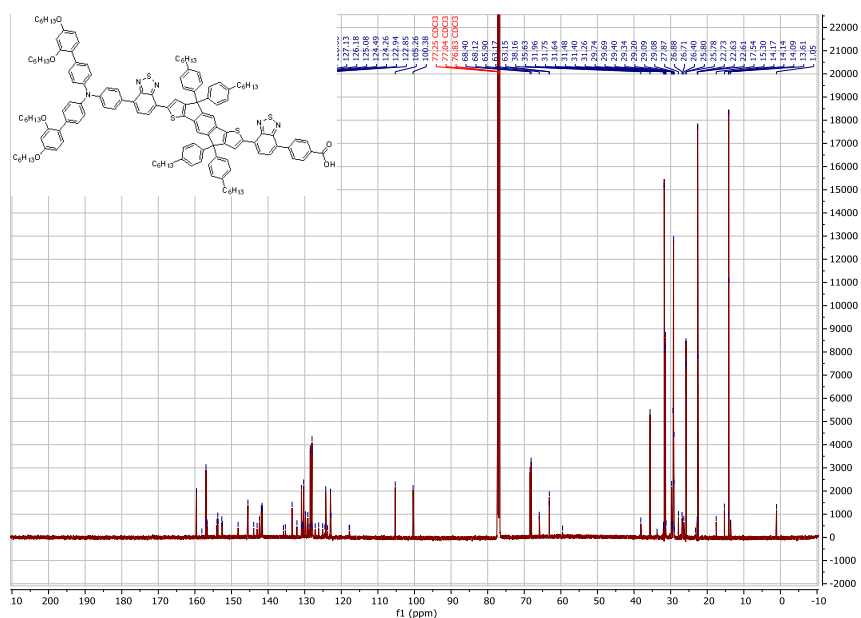
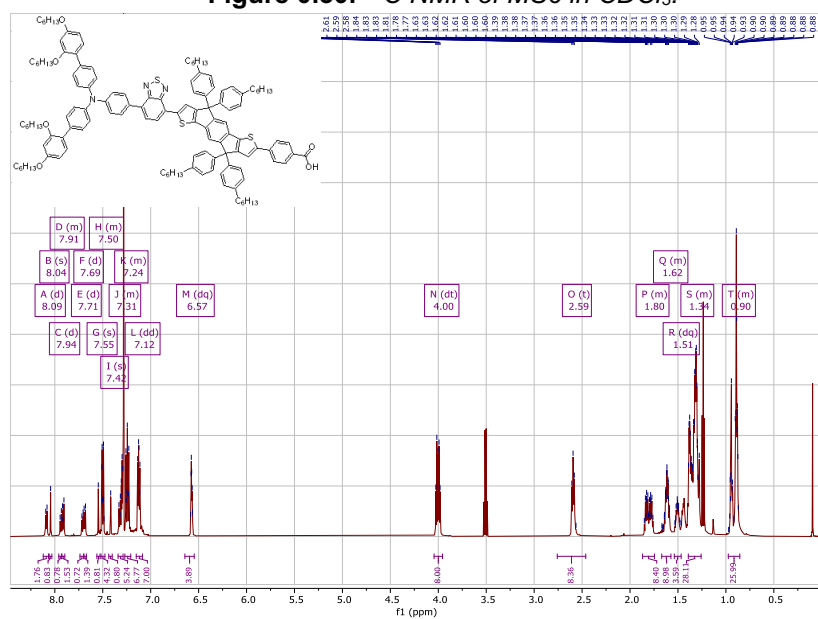
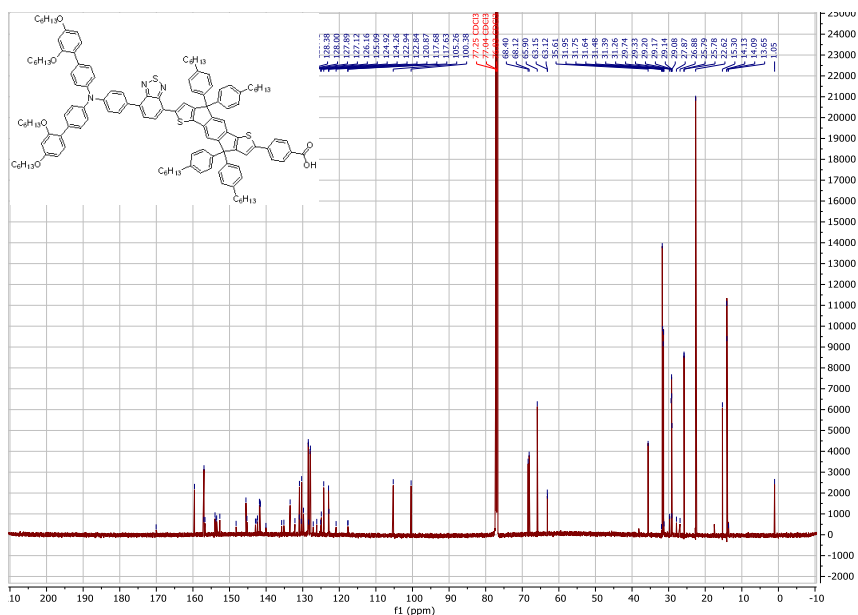
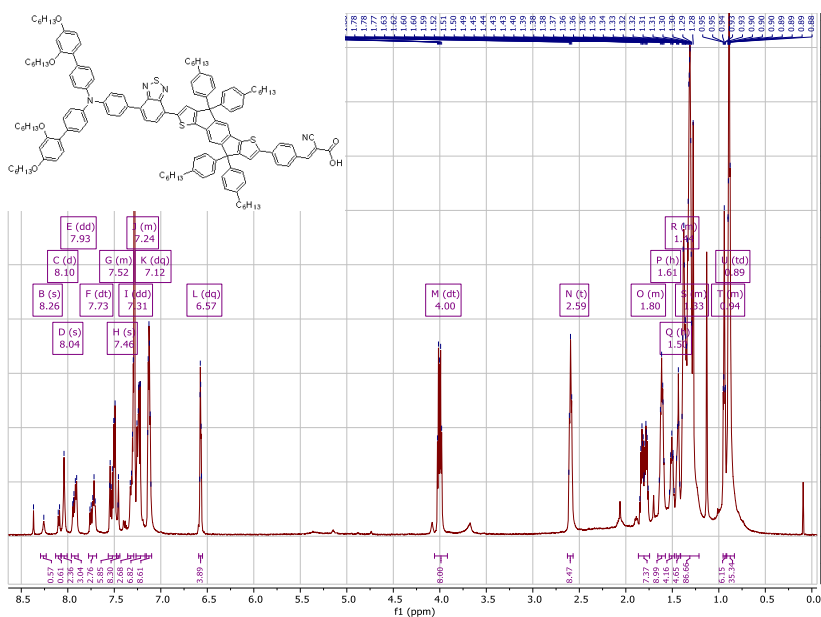


Figure 0.29. ^1H NMR of MS6 in CDCl_3 .

Figure 0.30. ^{13}C NMR of MS6 in CDCl_3 .Figure 0.31. ^1H NMR of MS7 in CDCl_3 .

Figure 0.32. ^{13}C NMR of MS7 in CDCl_3 .Figure 0.33. ^1H NMR of MS8 in CDCl_3 .

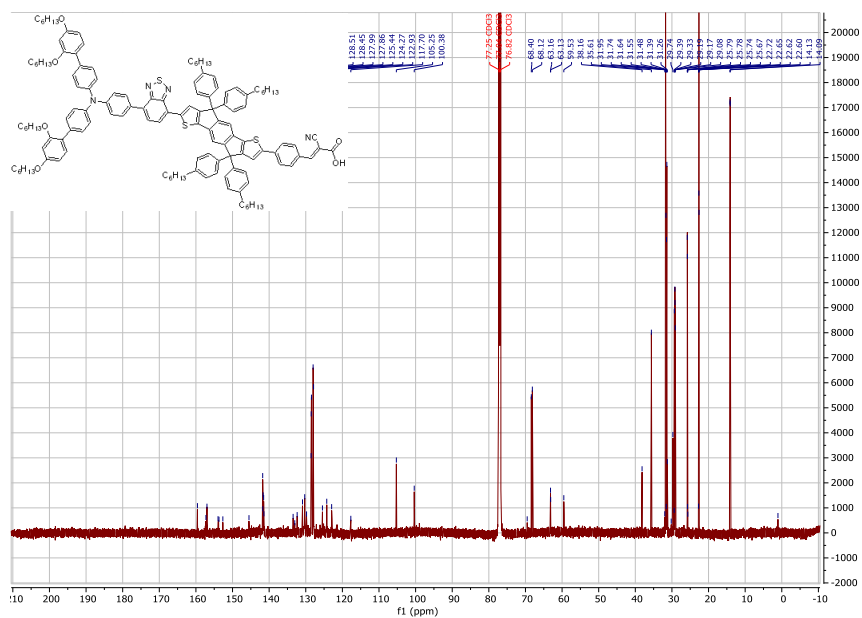
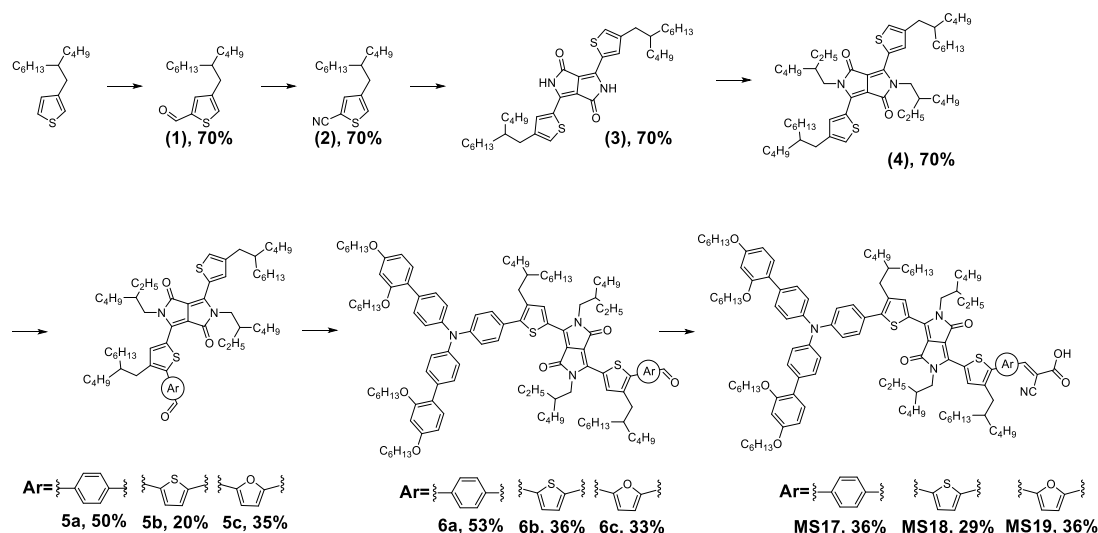


Figure 0.34. ^{13}C NMR of MS8 in CDCl_3 .

Supporting information to Chapter 4

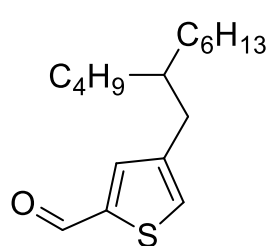
Synthetic procedure

Chloroform (VWR), Methanol (Sigma), Ethanol (Fisher Chemical), dichloromethane (DCM, Thommen-Furler), hexanes (VWR International SA), diethyl ether (HUBERLAB AG), Acetic acid (VWR International SA), potassium phosphate tribasic (Acros), magnesium sulfate (Reactolab), N-bromosuccinimide (NBS, TCI), 2-(dicyclohexylphosphino)-2',4',6'-triisopropylbiphenyl (Fluorochem), and tris(dibenzylideneacetone)dipalladium(0), 4-formylphenylboronic acid(Fluorochem), 5-Formyl-2-thienylboronic acid(Fluorochem), 5-Formyl-2-furanylboronic acid(Fluorochem), 2-Isopropoxy-4,4,5,5-tetramethyl-1,3,2-dioxaborolane (Sigma), piperidine (Acros), Cyanoacetic acid(ABCR) and N-(2',4'-bis(hexyloxy)-[1,1'-biphenyl]-4-yl)-N-(4-bromophenyl)-2',4'-bis(hexyloxy)-[1,1'-biphenyl]-4-amine (**HDC6-Br**)(H.Glass SA) were used as received without further purification. Anhydrous THF and Toluene were purchased over molecular sieves from Acros Organics. The solvents used for palladium catalyzed cross coupling reactions were degassed three times using the freeze-pump-thaw method and liquid nitrogen.



Scheme 0.3. Synthetic route to MS6014, MS6015 and MS6016.

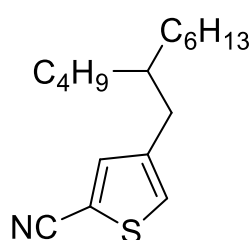
4-(2-butyloctyl)thiophene-2-carbaldehyde (**1**)



3-(2-butyloctyl)thiophene (9.6 g, 38 mmol, 1 eq.) was charged in a three necked round bottom flask and dissolved in anhydrous THF (60 mL) before being cooled down to -78°C with a dry-ice/acetone bath under argon. The 1M of lithium diisopropylamide (38 mL, 38 mmol, 1 eq.) was slowly added to the cold THF solution. The resulting mixture was stirred for 4 h at -78°C before adding anhydrous dimethylformamide (5 mL, 68 mmol, 5 eq.). The reaction was allowed to warm up to room temperature over night before quenching with saturated ammonium chloride solution (100 mL) and subsequently diluted with deionized water (200 mL). The organics were extracted with dichloromethane (3x60 mL) before drying with MgSO_4 . The solvent was removed under reduced pressure and the crude purified using flash column chromatography on SiO_2 eluting from 100% hexanes to 50% hexanes in dichloromethane by volume. The desired compound was obtained as a colorless oil: 8.32 g (78%). ^1H NMR (400

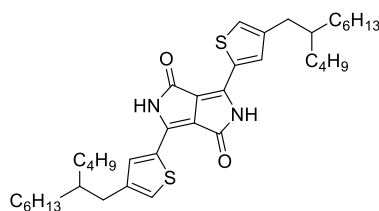
MHz, Chloroform-d) δ 9.90 (d, J = 1.3 Hz, 1H), 7.59 (d, J = 1.5 Hz, 1H), 7.37 (d, J = 1.4 Hz, 1H), 2.60 (d, J = 6.8 Hz, 2H), 1.69 – 1.56 (m, 2H), 1.41 – 1.12 (m, 18H), 1.00 – 0.78 (m, 6H). ^{13}C NMR (101 MHz, Chloroform-d) δ 183.03, 143.52 (d, J = 9.5 Hz), 137.67, 131.25, 38.95, 34.62, 33.22, 32.90, 31.87, 29.62, 28.83, 26.58, 22.99, 22.67, 14.11. HRMS (APPI/LTQ-Orbitrap) m/z : $[\text{M}]^+$ Calcd for $\text{C}_{17}\text{H}_{28}\text{OS}^+$ 280.1855; Found 280.1857

4-(2-butyloctyl)thiophene-2-carbonitrile (**2**)



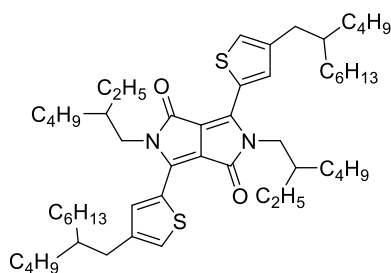
4-(2-butyloctyl)thiophene-2-carbaldehyde (**1**) (8.32 g, 29.67 mmol, 1 eq.) and hydroxylamine hydrochloride (3.09 g, 44.49 mmol, 1.5 eq.) were charged in a three necked round bottom flask equipped with a condenser and dissolved in a 100 mL EtOH: NEt_3 (1:1, v:v) mixture before being heated at 80°C overnight under argon. Upon cooling down to room temperature, the reaction mixture was evaporated. potassium acetate (0.4 g, 4.16 mmol, 0.14 eq.) and acetic anhydride (100 mL) were added and the resulting mixture was heated at 150°C overnight. The reaction was then poured over 200 g of NaOH in water/ice mixture and stirred until complete quenching. The organics were extracted using dichloromethane until the aqueous phase became colorless. The solvent was removed and the residue taken up with diethyl ether (150 mL) and washed with water (300 mL) and brine (300 mL) before drying over MgSO_4 . The crude was purified using flash column chromatography on SiO_2 , gradually eluting from hexanes to dichloromethane. The desired compound was obtained as a brown oil: 4.87 g (60%). ^1H NMR (400 MHz, Chloroform-d) δ 7.34 (d, J = 1.4 Hz, 1H), 7.08 (d, J = 1.4 Hz, 1H), 2.48 (d, J = 6.8 Hz, 2H), 1.51 (q, J = 6.0 Hz, 1H), 1.29 – 1.04 (m, 17H), 0.81 (t, J = 6.6 Hz, 6H). ^{13}C NMR (101 MHz, Chloroform-d) δ 142.92, 138.80, 128.23, 114.60, 109.27, 38.90, 34.42, 33.17, 32.85, 31.85, 29.60, 28.79, 26.92, 26.54, 22.97, 22.66, 14.10. HRMS (APPI/LTQ-Orbitrap) m/z : $[\text{M}]^+$ Calcd for $\text{C}_{17}\text{H}_{27}\text{NS}^+$ 277.1859; Found 277.1859.

3,6-bis(4-(2-butyloctyl)thiophen-2-yl)-2,5-dihydropyrrolo[3,4-c]pyrrole-1,4-dione (**3**)



4-(2-butyloctyl)thiophene-2-carbonitrile (**2**) (4.86 g, 17.52 mmol, 2.2 eq.) and KOtBu (2.68 g, 23.89 mmol, 3 eq.) were charged in a three necked round bottom flask equipped with a condenser and dissolved in 100 mL tert-amyl alcohol before being heated at 100°C for 2 hours under argon. Then, diisopropyl succinate (1.61 g, 7.96 mmol, 1 eq.) was added dropwise and the resulting mixture heated at 105°C overnight. After that, the reaction mixture was cooled down to 60°C and a 100 mL mixture of MeOH: AcOH (8:2, v:v) was added. The resulting mixture was heated at 120°C before cooling down to room temperature. The obtained red solid was filtrated and washed with additional methanol. The desired compound was obtained as a red brick solid: 2.46 g (49%). ^1H NMR (400 MHz, Chloroform-d) δ 8.00 (d, J = 1.3 Hz, 1H), 7.12 (s, 1H), 2.55 (d, J = 6.9 Hz, 2H), 1.61 (s, 2H), 1.20 (t, J = 6.0 Hz, 36H), 1.03 – 0.68 (m, 12H). HRMS (APPI/LTQ-Orbitrap) m/z : $[\text{M}]^+$ Calcd for $\text{C}_{38}\text{H}_{56}\text{N}_2\text{O}_2\text{S}_2^+$ 636.3778; Found 636.3775.

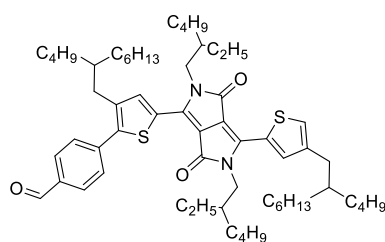
3,6-bis(4-(2-butyloctyl)thiophen-2-yl)-2,5-bis(2-ethylhexyl)-2,5-dihydropyrrolo[3,4-c]pyrrole-1,4-dione(4**)**



3,6-bis(4-(2-butyloctyl)thiophen-2-yl)-2,5-dihydropyrrolo[3,4-c]pyrrole-1,4-dione(**3**) (1.2 g, 1.88 mmoles, 1 eq.) and cesium carbonate (2.46 g, 7.54 mmoles, 4 eq.) were charged in a round bottom flask equipped with a condenser and heated at 100°C for 1 hour under vacuum to remove residual water. Then, anhydrous DMF(20 mL) was added and the mixture was heated at 100°C for 4 hours. After that, 2-ethylhexyl bromide (1.01 mL, 5.65 mmoles, 3 eq.) was added

dropwise and the reaction mixture was heated at 130°C overnight. The reaction was cooled down to room temperature before diluting 5 times with water. The organics were extracted using dichloromethane until the aqueous phase became colorless. The solvent was removed and the residue taken up with diethyl ether (200 mL) and washed with water(2x300 mL) and brine(2x300 mL). The crude was purified using flash column chromatography on SiO₂, gradually eluting from hexanes to dichloromethane. The desired compound was obtained as a red viscous oil 0.715 g (44%). ¹H NMR (400 MHz, Chloroform-d) δ 8.54 (s, 2H), 7.12 (s, 2H), 3.97 (dd, J = 6.0, 2.4 Hz, 3H), 3.93 (dd, J = 7.8, 4.0 Hz, 4H), 2.57 (d, J = 6.9 Hz, 4H), 1.79 (p, J = 6.6 Hz, 2H), 1.64 (d, J = 7.5 Hz, 2H), 1.34 – 1.08 (m, 48H), 0.80 (ddt, J = 13.7, 9.9, 7.1 Hz, 24H). ¹³C NMR (101 MHz, Chloroform-d) δ 143.52, 136.50, 126.47, 70.40, 45.79, 39.01, 38.86, 38.81, 34.81, 33.33, 33.30, 32.97, 32.94, 31.91, 30.23, 30.21, 30.13, 29.72, 28.89, 28.81, 28.38, 26.57, 26.55, 23.58, 23.50, 23.07, 22.96, 22.69, 14.14, 14.12, 14.04, 14.03, 10.90, 10.56. HRMS (APPI/LTQ-Orbitrap) m/z: [M]⁺ Calcd for C₅₄H₈₈N₂O₂S₂⁺ 860.6282; Found 860.6291.

4-(3-(2-butyloctyl)-5-(4-(4-(2-butyloctyl)thiophen-2-yl)-2,5-bis(2-ethylhexyl)-3,6-dioxo-2,3,5,6-tetrahydropyrrolo[3,4-c]pyrrol-1-yl)thiophen-2-yl)benzaldehyde(5a**)**

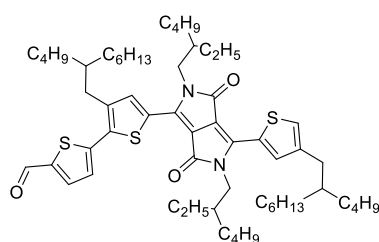


3,6-bis(4-(2-butyloctyl)thiophen-2-yl)-2,5-bis(2-ethylhexyl)-2,5-dihydropyrrolo[3,4-c]pyrrole-1,4-dione(**4**) (0.715 g, 0.83 mmoles, 1.05 eq.) was charged in a two necked round bottom flask dissolved in 8 mL dichloromethane and cooled down to -14°C under argon and protected from light. Then, N-bromosuccinimide(0.140 g, 0.79 mmoles, 1 eq.) was added and the reaction mixture was allowed to warm up to room

temperature overnight. Then, the solvent was removed and hexanes was added to precipitate unreacted N-bromosuccinimide and succinimide. The obtained suspension was filtered off and the filtrate evaporated to obtain the desired compound as a crude mixture between, mono, di and non-brominated (0.763 g). The obtained purple oil was used without further purification and 0.2 g were subsequently combined with 4-formylphenylboronic acid (80 mg, 0.532 mmoles, 2.5 eq.) and 2M aqueous potassium carbonate (0.3 mL, 0.638 mmoles, 3 eq.) in a schlenk tube along with 5 mL THF before being degassed three times using freeze-pump-thaw and liquid nitrogen. After that, tris(dibenzylideneacetone)dipalladium(0) (16 mg, 17 μmol, 0.08 eq.) and 2-dicyclohexylphosphino-2',4',6'-triisopropylbiphenyl (16 mg, 34 μmol, 0.16 eq.) were added and the mixture was heated at 70°C overnight. The reaction was cooled down to room temperature and diluted twice with diethyl ether before flashing through a pad of MgSO₄. The crude was evaporated to dryness and purified using flash column chromatography on SiO₂, gradually eluting from hexanes to 50% dichloromethane in hexanes by volume. The desired

compound was obtained as a purple solid 72 mg (50%). ^1H NMR (400 MHz, Chloroform- d) δ 9.99 (s, 1H), 8.58 (d, J = 3.9 Hz, 2H), 7.88 (d, J = 8.2 Hz, 2H), 7.59 (d, J = 8.1 Hz, 2H), 7.14 (s, 1H), 3.95 (dt, J = 7.2, 2.8 Hz, 4H), 2.66 (d, J = 7.2 Hz, 2H), 2.58 (d, J = 6.9 Hz, 2H), 1.81 (p, J = 6.6 Hz, 2H), 1.34 – 1.08 (m, 48H), 0.80 (ddt, J = 13.7, 9.9, 7.1 Hz, 24H). ^{13}C NMR (101 MHz, Chloroform- d) δ 191.49, 161.79, 161.66, 143.63, 142.11, 140.87, 140.73, 139.96, 139.23, 137.85, 136.85, 135.60, 130.02, 129.87, 129.36, 128.92, 126.85, 108.43, 107.80, 45.85, 39.21, 39.03, 39.02, 38.96, 38.83, 34.79, 33.34, 33.32, 33.03, 32.98, 32.95, 31.92, 31.86, 30.34, 30.32, 30.23, 30.21, 29.72, 29.64, 28.82, 28.79, 28.55, 28.37, 26.58, 26.56, 23.70, 23.59, 23.09, 23.07, 22.98, 22.70, 22.67, 14.14, 14.13, 14.11, 14.06, 14.03, 10.65, 10.57. HRMS (APPI/LTQ-Orbitrap) m/z : $[\text{M} + \text{H}]^+$ Calcd for $\text{C}_{61}\text{H}_{93}\text{N}_2\text{O}_3\text{S}_2^+$ 965.6622; Found 965.6613.

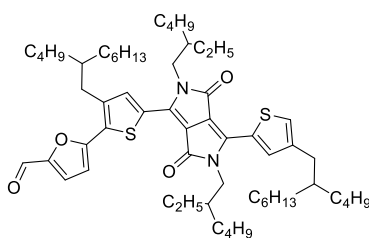
3'-(2-butyloctyl)-5'-(4-(4-(2-butyloctyl)thiophen-2-yl)-2,5-bis(2-ethylhexyl)-3,6-dioxo-2,3,5,6-tetrahydropyrrolo[3,4-c]pyrrol-1-yl)-[2,2'-bithiophene]-5-carbaldehyde(5b)



The desired compound (**5b**) was obtained using the same procedure as for compound (**5a**) and (5-formylthiophen-2-yl)boronic acid. The desired compound was obtained as a purple solid 39 mg (20%). ^1H NMR (400 MHz, Chloroform- d) δ 9.84 (s, 1H), 8.60 (d, J = 5.8 Hz, 2H), 7.67 (d, J = 4.0 Hz, 1H), 7.27 (s, 1H), 7.15 (s, 1H), 3.94 (dd, J = 7.8, 3.5 Hz, 4H), 2.77 (d, J = 7.3 Hz, 2H), 2.58 (d, J = 6.9 Hz, 2H), 1.79 (dq, J = 13.6,

6.3 Hz, 2H), 1.23 (dtd, J = 26.5, 14.1, 12.1, 6.4 Hz, 48H), 0.92 – 0.46 (m, 24H). ^{13}C NMR (101 MHz, Chloroform- d) δ 182.55, 161.73, 161.54, 144.90, 143.71, 143.39, 142.37, 138.32, 137.12, 136.59, 135.11, 134.84, 129.29, 129.08, 127.32, 127.14, 109.03, 107.83, 39.28, 39.02, 38.82, 38.60, 34.78, 34.29, 33.48, 33.44, 33.34, 33.31, 33.11, 32.97, 32.95, 31.91, 31.88, 30.34, 30.22, 30.20, 29.72, 29.69, 28.81, 28.79, 28.58, 28.53, 28.35, 26.58, 26.55, 26.42, 26.38, 23.73, 23.57, 23.10, 23.07, 23.04, 22.70, 22.68, 14.13, 14.10, 14.06, 14.03, 10.66, 10.56. HRMS (APPI/LTQ-Orbitrap) m/z : $[\text{M} + \text{H}]^+$ Calcd for $\text{C}_{59}\text{H}_{91}\text{N}_2\text{O}_3\text{S}_3^+$ 971.6186; Found 971.6170.

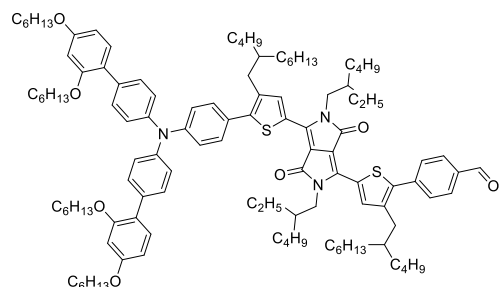
5-(3-(2-butyloctyl)-5-(4-(4-(2-butyloctyl)thiophen-2-yl)-2,5-bis(2-ethylhexyl)-3,6-dioxo-2,3,5,6-tetrahydropyrrolo[3,4-c]pyrrol-1-yl)thiophen-2-yl)furan-2-carbaldehyde(5c)



The desired compound (**5c**) was obtained using the same procedure as for compounds (**5a**) and (**5b**), and starting with (5-formylfuran-2-yl)boronic acid. The desired compound was obtained as a purple solid 72 mg (35%). ^1H NMR (400 MHz, Chloroform- d) δ 9.60 (s, 1H), 8.61 (d, J = 9.7 Hz, 2H), 7.26 (d, J = 3.8 Hz, 1H), 7.15 (s, 1H), 6.69 (d, J = 3.8 Hz, 1H), 3.94 (td, J = 7.1, 3.4 Hz, 4H), 2.80 (d, J = 7.2 Hz, 2H), 2.57 (d, J = 6.8

Hz, 2H), 1.91 (dq, J = 13.6, 6.3 Hz, 2H), 1.20 (dtd, J = 26.5, 14.1, 12.1, 6.4 Hz, 48H), 0.95 – 0.49 (m, 24H). ^{13}C NMR (101 MHz, Chloroform- d) δ 177.01, 161.72, 153.62, 151.84, 143.71, 143.31, 143.07, 138.40, 137.16, 134.81, 130.49, 130.36, 129.56, 129.29, 128.96, 128.39, 127.16, 125.42, 110.48, 109.17, 45.91, 45.87, 39.25, 39.02, 38.82, 38.42, 34.78, 34.58, 33.47, 33.34, 33.31, 33.12, 32.98, 32.95, 31.91, 31.88, 30.32, 30.29, 30.22, 30.20, 29.72, 28.82, 28.79, 28.59, 28.51, 28.36, 26.58, 26.56, 26.44, 26.39, 23.70, 23.58, 23.08, 22.70, 22.68, 14.14, 14.12, 14.10, 14.03, 10.61, 10.56, 10.55. HRMS (APPI/LTQ-Orbitrap) m/z : $[\text{M} + \text{H}]^+$ Calcd for $\text{C}_{59}\text{H}_{91}\text{N}_2\text{O}_4\text{S}_2^+$ 955.6415; Found 955.6405.

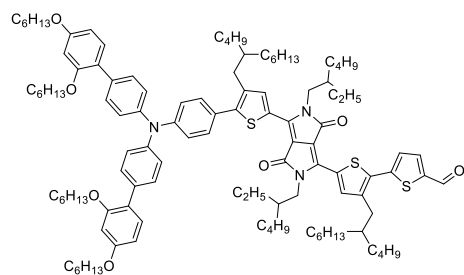
4-(5-(4-(5-(4-(bis(2',4'-bis(hexyloxy)-[1,1'-biphenyl]-4-yl)amino)phenyl)-4-(2-butylloctyl)thiophen-2-yl)-2,5-bis(2-ethylhexyl)-3,6-dioxo-2,3,5,6-tetrahydropyrrolo[3,4-c]pyrrol-1-yl)-3-(2-butylloctyl)thiophen-2-yl)benzaldehyde(**6a**)



4-(3-(2-butylloctyl)-5-(4-(4-(2-butylloctyl)thiophen-2-yl)-2,5-bis(2-ethylhexyl)-3,6-dioxo-2,3,5,6-tetrahydropyrrolo[3,4-c]pyrrol-1-yl)thiophen-2-yl)benzaldehyde(**5a**)(72 mg, 75 μ mol, 1 eq.) and N-bromosuccinimide (15 mg, 82 μ mol, 1.1 eq.) were charged in a two necked bottom flask and dissolved in dichloromethane(10 mL) before being allowed to react at room temperature overnight. The solvent was

removed under reduced pressure and hexanes was added to precipitate unreacted N-bromosuccinimide and succinimide. The resulting suspension was filtered off and evaporated to dryness to obtain the crude that was used for the next step without further purification. N-(2',4'-bis(hexyloxy)-[1,1'-biphenyl]-4-yl)-N-(4-bromophenyl)-2',4'-bis(hexyloxy)-[1,1'-biphenyl]-4-amine(102 mg, 117 μ mol, 1.3 eq.) was charged in a schlenk tube and dissolved in anhydrous THF(3 mL) before being degassed three times using freeze-pump-thaw and liquid nitrogen. Then, n-butyl lithium 1.6M (0.2 mL, 0.261 mmoles, 2.9 eq.) was added dropwise to the reaction. The resulting solution was allowed to stir for 4 hours before quenching with 2-Isopropoxy-4,4,5,5-tetramethyl-1,3,2-dioxaborolane (70 mg, 0.36 mmoles, 4 eq.). The reaction was allowed to warm up to room temperature overnight. Then, aqueous potassium carbonate 2M (0.3 mL, 0.45 mmoles, 5 eq.) and the crude obtained from the previous bromination reaction were added to the reaction and the resulting mixture degassed three times using freeze-pump-thaw and liquid nitrogen. Then, tris(dibenzylideneacetone)dipalladium(0)(7 mg, 7.2 μ mol, 0.08 eq.) and 2-Dicyclohexylphosphino-2',4',6'-triisopropylbiphenyl(7 mg, 14.4 μ mol, 0.16 eq.) were added and the mixture heated at 85°C overnight. The reaction was allowed to cool down to room temperature before diluting with diethyl ether twice and flashing through a pad of MgSO₄. The solvent was removed and the crude purified using flash column chromatography on SiO₂, gradually eluting from 100% hexanes to 100% dichloromethane. The desired compound was obtained as a purple solid 85 mg (53%). ¹H NMR (400 MHz, Chloroform-d) δ 9.99 (s, 1H), 8.70 (s, 1H), 8.55 (s, 1H), 7.87 (d, J = 8.1 Hz, 2H), 7.59 (d, J = 8.0 Hz, 2H), 7.46 – 7.37 (m, 4H), 7.28 (d, J = 8.6 Hz, 2H), 7.19 (d, J = 9.1 Hz, 2H), 7.12 (d, J = 8.5 Hz, 5H), 6.60 – 6.35 (m, 4H), 3.97 (d, J = 8.0 Hz, 4H), 3.90 (q, J = 6.8 Hz, 8H), 2.66 (d, J = 7.1 Hz, 4H), 1.85 (p, J = 6.3 Hz, 2H), 1.81 – 1.60 (m, 8H), 1.49 – 1.06 (m, 69H), 0.96 – 0.69 (m, 36H). ¹³C NMR (101 MHz, Chloroform-d) δ 191.51, 159.66, 157.01, 148.18, 145.68, 145.36, 140.85, 140.07, 139.20, 139.03, 137.56, 135.56, 133.73, 130.88, 130.36, 130.04, 129.97, 129.87, 129.14, 126.52, 124.36, 122.90, 122.38, 105.36, 100.44, 68.42, 68.14, 45.94, 45.87, 39.25, 39.14, 38.98, 38.85, 33.43, 33.37, 33.25, 33.10, 33.06, 31.93, 31.89, 31.65, 31.46, 30.34, 30.29, 29.73, 29.67, 29.35, 29.09, 28.61, 28.59, 28.51, 26.94, 26.39, 25.80, 25.76, 23.74, 23.71, 23.12, 23.07, 23.01, 22.72, 22.69, 22.65, 22.60, 14.16, 14.13, 14.09, 14.08, 14.06, 10.70, 10.68. HRMS (APPI/LTQ-Orbitrap) m/z: [M]⁺ Calcd for C₁₁₅H₁₆₁N₃O₇S₂⁺ 1760.1770; Found 1760.1704.

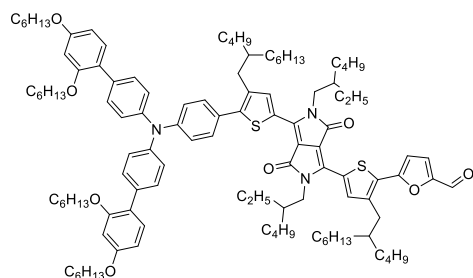
5'-(4-(5-(4-(bis(2',4'-bis(hexyloxy)-[1,1'-biphenyl]-4-yl)amino)phenyl)-4-(2-butyloctyl)thiophen-2-yl)-2,5-bis(2-ethylhexyl)-3,6-dioxo-2,3,5,6-tetrahydropyrrolo[3,4-c]pyrrol-1-yl)-3'-(2-butyloctyl)-[2,2'-bithiophene]-5-carbaldehyde(**6b**)



The desired compound (**6a**) was obtained using the same procedure as for compounds (**6b**) and starting with (**5b**). The desired compound was obtained as a blue solid 28 mg (36%). ¹H NMR (400 MHz, Chloroform-d) δ 9.84 (s, 1H), 8.73 (s, 1H), 8.63 – 8.59 (m, 1H), 8.58 (s, 1H), 7.67 (d, J = 3.9 Hz, 1H), 7.46 – 7.38 (m, 4H), 7.32 – 7.24 (m, 4H), 7.21 (s, 1H), 7.15 – 7.09 (m, 6H), 6.47 (dd, J = 5.8, 2.6 Hz, 4H), 3.92 (ddt, J = 12.9, 8.9,

5.0 Hz, 12H), 2.78 (d, J = 7.3 Hz, 3H), 2.67 (d, J = 7.1 Hz, 2H), 2.58 (d, J = 6.8 Hz, 4H), 1.91 – 1.59 (m, 10H), 1.49 – 0.99 (m, 69H), 0.92 – 0.68 (m, 36H). ¹³C NMR (101 MHz, Chloroform-d) δ 182.56, 161.47, 159.65, 156.99, 148.21, 145.33, 145.06, 143.29, 142.36, 139.32, 139.27, 138.32, 138.00, 137.66, 137.12, 136.61, 136.59, 134.50, 133.74, 130.87, 130.35, 129.94, 129.30, 127.32, 127.23, 126.42, 124.37, 122.88, 122.33, 109.29, 105.34, 100.43, 68.41, 68.14, 53.43, 39.30, 39.12, 39.03, 38.83, 38.61, 34.33, 33.45, 33.25, 33.12, 32.96, 31.91, 31.89, 31.63, 31.45, 30.35, 30.25, 29.72, 29.70, 29.33, 29.07, 28.80, 28.64, 28.59, 28.54, 28.47, 28.36, 26.43, 26.39, 25.79, 25.75, 23.74, 23.68, 23.58, 23.11, 23.08, 23.05, 22.71, 22.68, 22.64, 22.58, 14.15, 14.13, 14.10, 14.08, 14.06, 14.04, 10.69, 10.66. HRMS (APPI/LTQ-Orbitrap) m/z : [M]⁺ Calcd for C₁₁₃H₁₅₉N₃O₇S₃⁺ 1766.1335; Found 1766.1278.

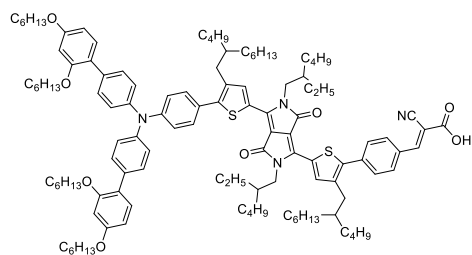
5-(5-(4-(5-(4-(bis(2',4'-bis(hexyloxy)-[1,1'-biphenyl]-4-yl)amino)phenyl)-4-(2-butyloctyl)thiophen-2-yl)-2,5-bis(2-ethylhexyl)-3,6-dioxo-2,3,5,6-tetrahydropyrrolo[3,4-c]pyrrol-1-yl)-3-(2-butyloctyl)thiophen-2-yl)furan-2-carbaldehyde(**6c**)



The desired compound (**6c**) was obtained using the same procedure as for compounds (**6a**) and (**6b**), and starting with (**5c**). The desired compound was obtained as a blue solid, 53 mg (33%). ¹H NMR (400 MHz, Chloroform-d) δ 9.61 (s, 1H), 8.74 (s, 1H), 8.57 (s, 1H), 7.45 – 7.37 (m, 4H), 7.32 – 7.26 (m, 3H), 7.23 – 7.18 (m, 2H), 7.17 – 7.10 (m, 6H), 6.69 (d, J = 3.8 Hz, 1H), 6.47 (dd, J = 5.8, 2.5 Hz, 4H), 3.97 (dd, J = 7.7, 4.4 Hz,

4H), 3.91 (dt, J = 8.6, 6.5 Hz, 8H), 2.81 (d, J = 7.3 Hz, 2H), 2.67 (d, J = 7.1 Hz, 2H), 1.98 – 1.78 (m, 2H), 1.78 – 1.59 (m, 8H), 1.47 – 1.03 (m, 42H), 1.00 – 0.54 (m, 36H). ¹³C NMR (101 MHz, Chloroform-d) δ 177.05, 159.65, 156.99, 153.75, 151.82, 145.33, 143.10, 139.36, 139.29, 138.07, 133.74, 130.88, 130.35, 129.95, 124.37, 122.88, 122.33, 110.40, 105.35, 100.43, 68.41, 68.14, 39.28, 39.12, 38.83, 38.45, 34.62, 33.25, 31.92, 31.89, 31.63, 31.45, 29.72, 29.33, 29.08, 28.65, 28.62, 28.53, 28.48, 26.45, 26.41, 25.79, 25.75, 23.71, 23.69, 23.10, 23.05, 22.71, 22.69, 22.64, 22.58, 14.15, 14.13, 14.11, 14.07, 14.05, 10.65. HRMS (APPI/LTQ-Orbitrap) m/z : [M]⁺ Calcd for C₁₁₃H₁₅₉N₃O₈S₂⁺ 1750.1563; Found 1750.1517.

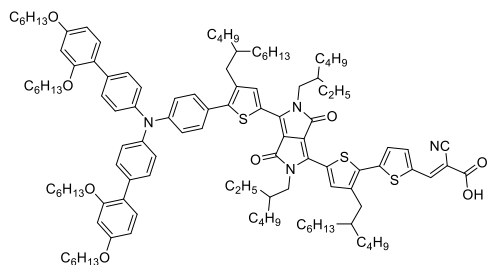
(E)-3-(4-(5-(4-(5-(4-(bis(2',4'-bis(hexyloxy)-[1,1'-biphenyl]-4-yl)amino)phenyl)-4-(2-butylloctyl)thiophen-2-yl)-2,5-bis(2-ethylhexyl)-3,6-dioxo-2,3,5,6-tetrahydropyrrolo[3,4-c]pyrrol-1-yl)-3-(2-butylloctyl)thiophen-2-yl)phenyl)-2-cyanoacrylic acid(**MS17**)



4-(5-(4-(5-(4-(bis(2',4'-bis(hexyloxy)-[1,1'-biphenyl]-4-yl)amino)phenyl)-4-(2-butylloctyl)thiophen-2-yl)-2,5-bis(2-ethylhexyl)-3,6-dioxo-2,3,5,6-tetrahydropyrrolo[3,4-c]pyrrol-1-yl)-3-(2-butylloctyl)thiophen-2-yl)benzaldehyde (**6a**) and 100 mg cyano acetic acid were charged in a schlenk tube and dissolved in anhydrous chloroform(5 mL) before being

degassed three times using freeze-pump-thaw and liquid nitrogen. Then, 0.4 mL piperidine was added to the reaction and the resulting mixture was heated at 70°C for 24h. Acetic acid was added and the solvents removed under reduced pressure before purification with flash column chromatography on SiO₂, gradually eluting from 100% dichloromethane to dichloromethane with 1% of Ethanol and 3 drops of acetic acid by volume. The target compound was obtained as a purple solid 30 mg (36%) ¹H NMR (400 MHz, THF-d₈) δ 10.82 (s, 1H), 9.13 (s, 1H), 9.03 (s, 1H), 8.37 (s, 1H), 7.89 (d, J = 4.1 Hz, 1H), 7.48 (d, J = 8.5 Hz, 5H), 7.45 – 7.35 (m, 2H), 7.22 (d, J = 8.3 Hz, 2H), 7.17 (dd, J = 8.5, 5.5 Hz, 6H), 6.58 (d, J = 2.4 Hz, 2H), 6.55 (d, J = 2.4 Hz, 1H), 6.53 (d, J = 2.3 Hz, 1H), 4.08 (d, J = 7.4 Hz, 4H), 3.97 (td, J = 6.4, 3.8 Hz, 8H), 2.93 (d, J = 7.1 Hz, 2H), 2.78 (d, J = 7.0 Hz, 2H), 1.55 – 1.14 (m, 69H), 1.04 – 0.75 (m, 36H). HRMS (MALDI/TOF) m/z: [M]⁺ Calcd for C₁₁₈H₁₆₂N₄O₈S₂⁺ 1827.1829; Found 1828.3346.

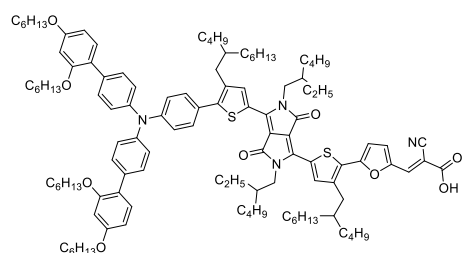
(E)-3-(5'-(4-(5-(4-(bis(2',4'-bis(hexyloxy)-[1,1'-biphenyl]-4-yl)amino)phenyl)-4-(2-butylloctyl)thiophen-2-yl)-2,5-bis(2-ethylhexyl)-3,6-dioxo-2,3,5,6-tetrahydropyrrolo[3,4-c]pyrrol-1-yl)-3'-(2-butylloctyl)-[2,2'-bithiophen]-5-yl)-2-cyanoacrylic acid(**MS18**)



The desired compound (**MS6018**) was obtained using the same procedure as for compounds (**MS6017**) and starting with (**6b**). The desired compound was obtained as a blue-green solid 8 mg (29%) solid, ¹H NMR (400 MHz, THF-d₈) δ 10.82 (s, 1H), 9.13 (s, 1H), 9.03 (s, 1H), 8.37 (s, 1H), 7.89 (d, J = 4.1 Hz, 1H), 7.48 (d, J = 8.5 Hz, 5H), 7.45 – 7.35 (m, 2H), 7.22 (d, J =

8.3 Hz, 2H), 7.17 (dd, J = 8.5, 5.5 Hz, 6H), 6.58 (d, J = 2.4 Hz, 2H), 6.55 (d, J = 2.4 Hz, 1H), 6.53 (d, J = 2.3 Hz, 1H), 4.08 (d, J = 7.4 Hz, 4H), 3.97 (td, J = 6.4, 3.8 Hz, 8H), 2.93 (d, J = 7.1 Hz, 2H), 2.78 (d, J = 7.0 Hz, 2H), 1.55 – 1.14 (m, 69H), 1.04 – 0.75 (m, 36H). HRMS (MALDI/TOF) m/z: [M]⁺ Calcd for C₁₁₆H₁₆₀N₄O₈S₃⁺ 1833.1393; Found 1834.1393.

(E)-3-(5-(5-(4-(5-(4-(bis(2',4'-bis(hexyloxy)-[1,1'-biphenyl]-4-yl)amino)phenyl)-4-(2-butylloctyl)thiophen-2-yl)-2,5-bis(2-ethylhexyl)-3,6-dioxo-2,3,5,6-tetrahydropyrrolo[3,4-c]pyrrol-1-yl)-3-(2-butylloctyl)thiophen-2-yl)furan-2-yl)-2-cyanoacrylic acid(**MS19**)



The desired compound (**MS19**) was obtained using the same procedure as for compounds (**MS17**) and (**MS18**), and starting with (**6c**). The desired compound was obtained as a green solid, 20 mg (36%). ^1H NMR (400 MHz, THF-d_8) δ 10.82 (s, 1H), 9.13 (s, 1H), 9.09 (s, 1H), 7.99 (s, 1H), 7.48 (d, J = 8.4 Hz, 4H), 7.42 (d, J = 8.4 Hz, 2H), 7.22 (d, J = 8.4 Hz, 2H), 7.17 (dd, J = 8.4, 5.3 Hz, 6H), 7.02 (d, J = 3.8 Hz, 1H), 6.58 (d, J = 2.3 Hz, 2H), 6.53 (dd, J = 8.4, 2.4 Hz, 2H), 4.09 (t, J = 8.5 Hz, 4H), 3.97 (td, J = 6.4, 3.9 Hz, 8H), 2.95 (d, J = 7.1 Hz, 2H), 2.78 (d, J = 6.9 Hz, 2H), 1.54 – 1.21 (m, 69H), 0.99 – 0.82 (m, 36H). HRMS (MALDI/TOF) m/z : $[\text{M}]^+$ Calcd for $\text{C}_{116}\text{H}_{160}\text{N}_4\text{O}_9\text{S}_2^+$ 1817.1621; Found 1818.1894.

Optical characterization

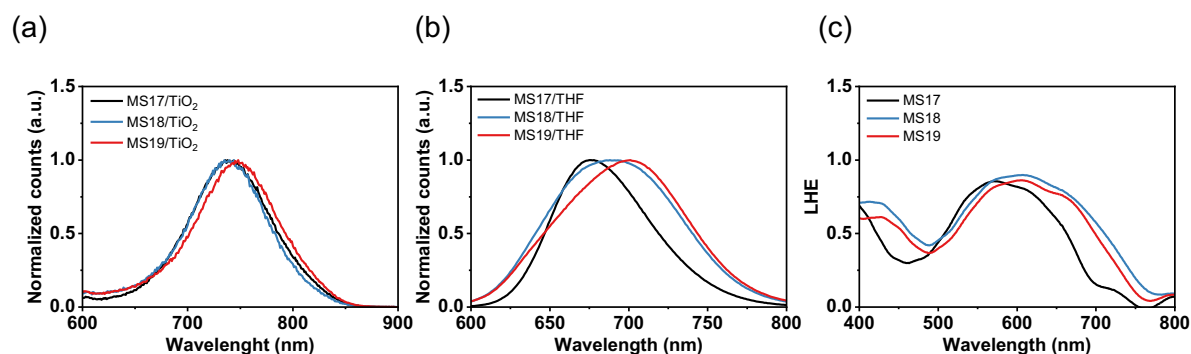


Figure 0.35. (a) Normalized emission spectra of the dyes adsorbed on 4 μm thick TiO_2 films. Normalized emission spectra of the dyes in diluted THF solutions (b). (c) Light harvesting efficiency (LHE) calculated using: $\text{LHE} = 1 - 10^{-A}$, with A being the absorbance of the sensitized films.

Electrochemical characterization

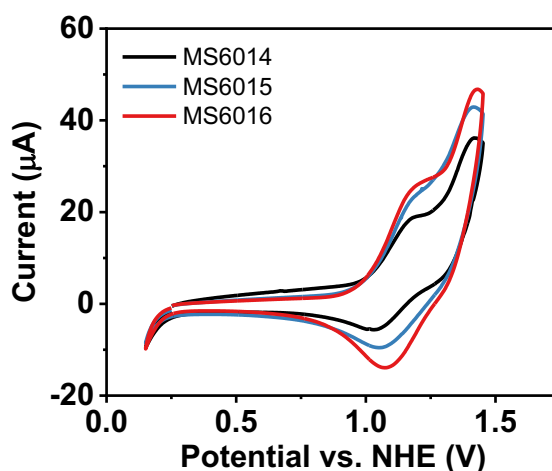


Figure 0.36. Cyclic voltammograms of the dyes adsorbed on a transparent TiO_2 film.

Computational calculations

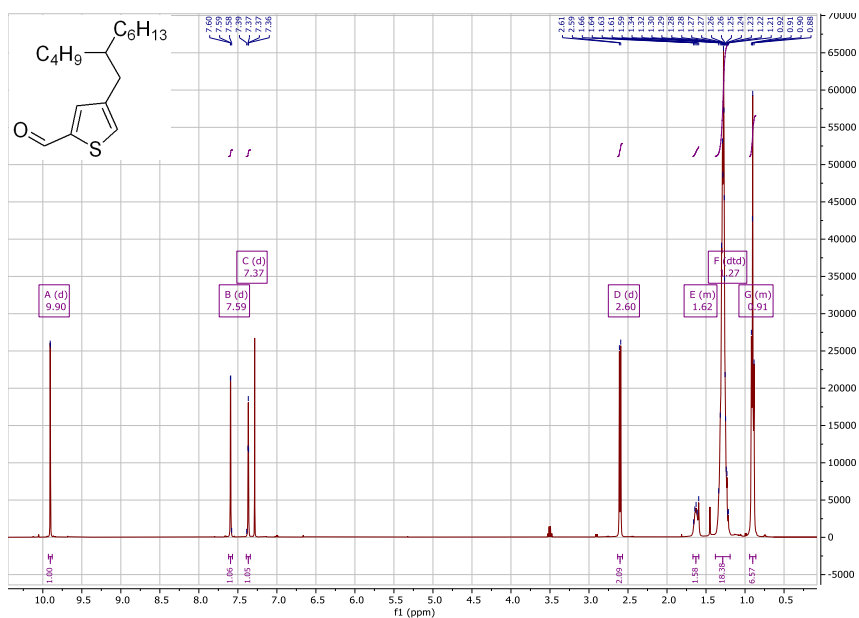
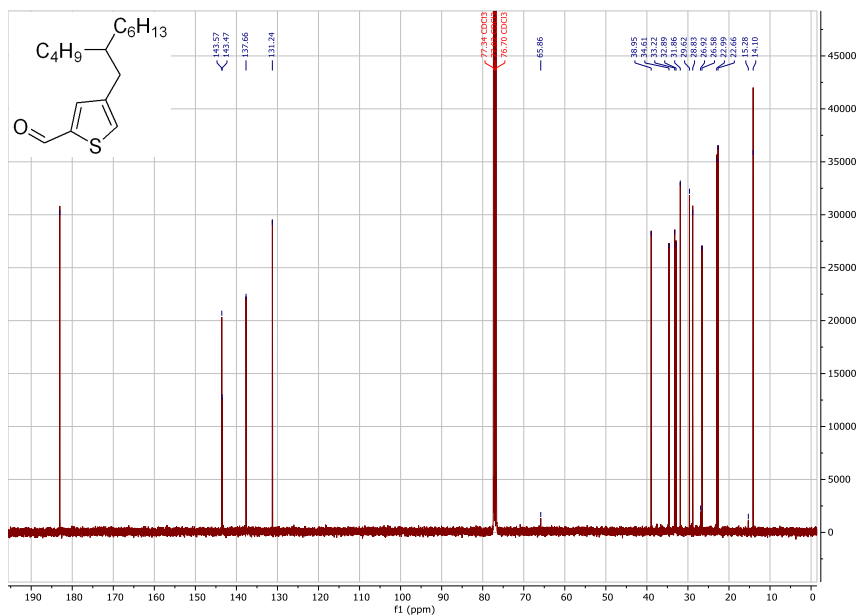
Table 0.5. The calculated energy levels of HOMO and LUMO orbitals of MS dyes using Gaussian09 with B3PW91 functional and 6-31G(d,p) basis sets.

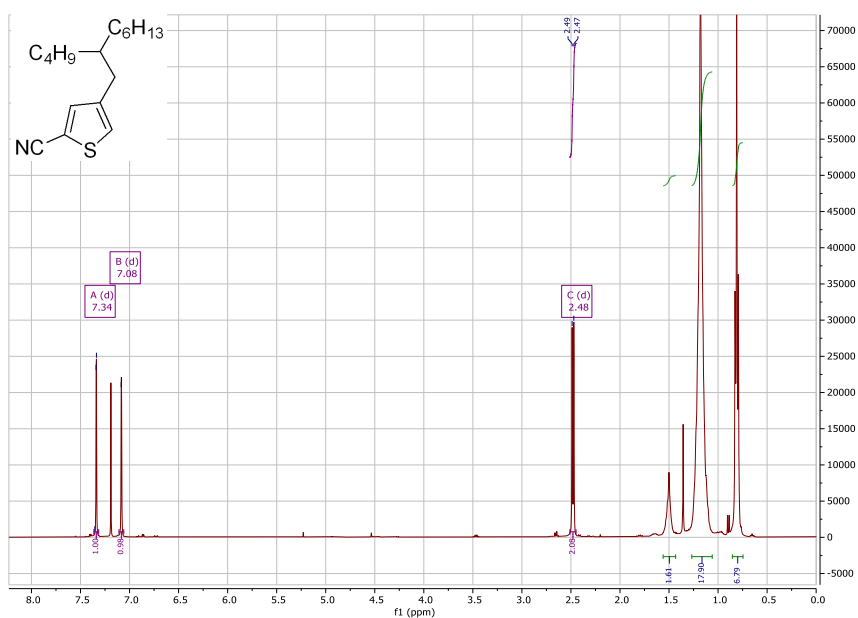
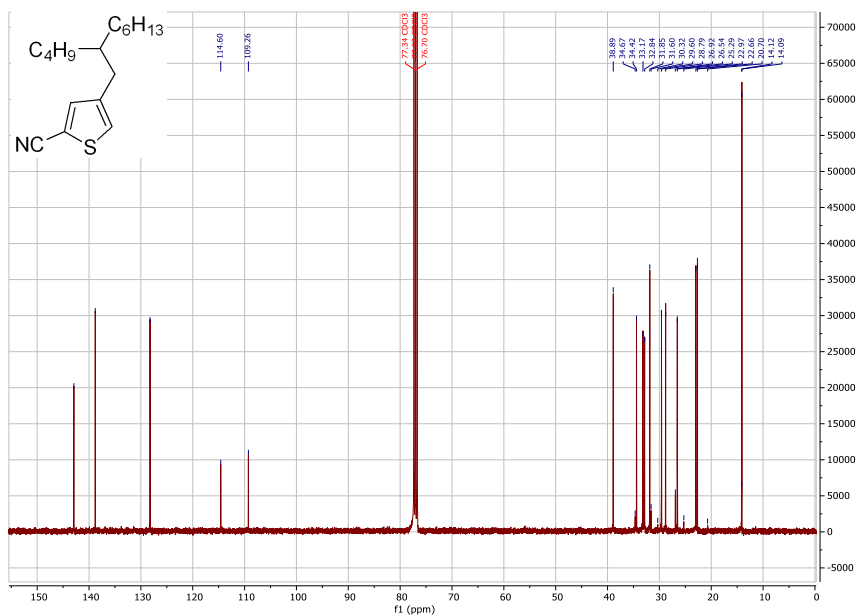
	HOMO [eV]	LUMO [eV]	E _g [eV]
MS17	-4.75	-2.95	1.79
MS18	-4.74	-3.03	1.72
MS19	-4.75	-2.97	1.77

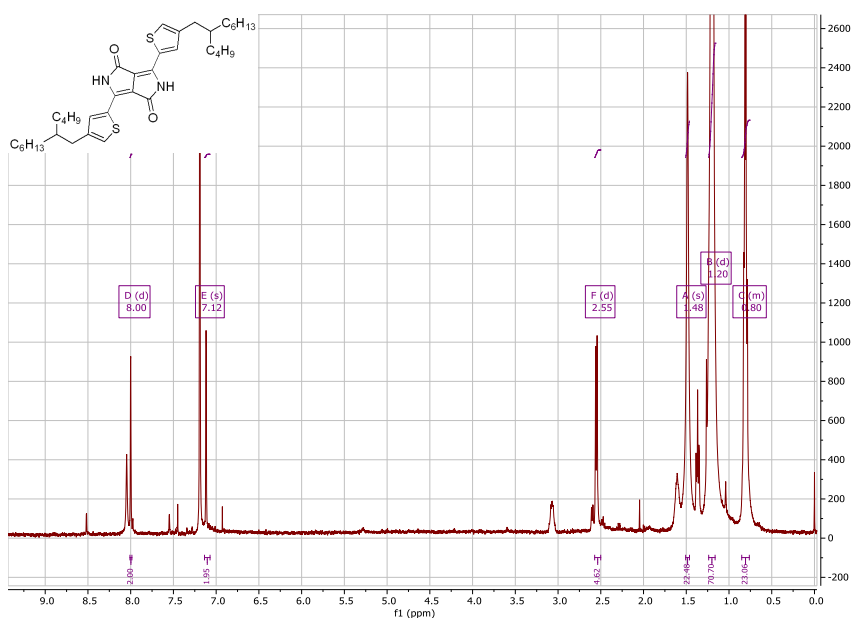
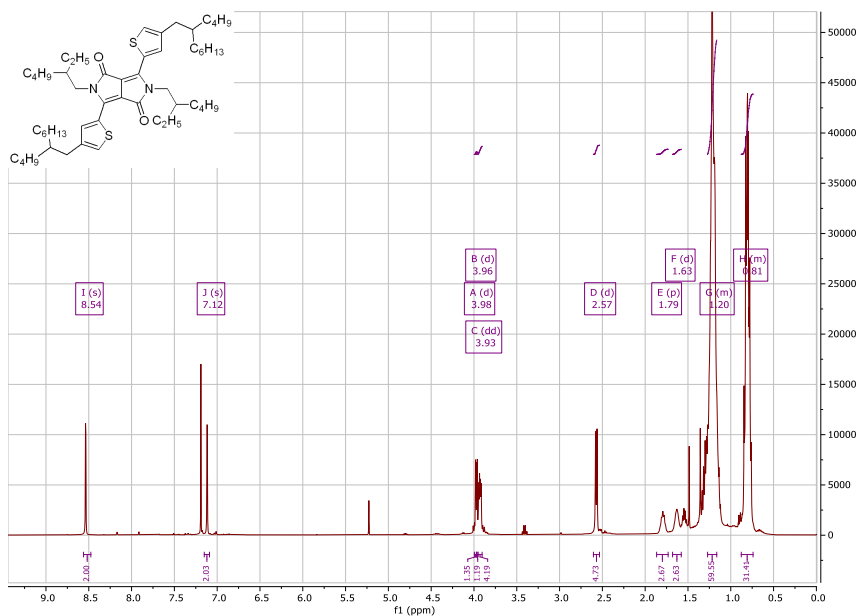
Device fabrication and solar cell characterization

Table 0.6. Detailed statistical values of the devices at 10, 50 and 100% sun.

MS17				
P _{in} [mW·cm ⁻²]	J _{sc} [mA·cm ⁻²]	V _{oc} [mV]	FF [%]	PCE [%]
100.13	10.86	970.95	73	7.67
53.87	5.86	950.15	77	8.00
10.84	1.17	883.93	78	7.46
MS18				
P _{in} [mW·cm ⁻²]	V _{oc} [mV]	J _{sc} [mA·cm ⁻²]	FF [%]	PCE [%]
100.05	4.41	860.40	76	2.89
53.83	2.43	844.38	78	2.97
10.83	0.49	782.09	76	2.73
MS19				
P _{in} [mW·cm ⁻²]	V _{oc} [mV]	J _{sc} [mA·cm ⁻²]	FF [%]	PCE [%]
100.28	5.36	891.36	75	3.59
53.91	2.95	865.87	76	3.61
10.86	0.58	788.62	72	3.03

^1H and ^{13}C NMR spectra**Figure 0.37.** ^1H NMR of **1** CDCl_3 .**Figure 0.38.** ^{13}C NMR of **1** in CDCl_3 .

Figure 0.39. ¹H NMR of 2 in CDCl₃.Figure 0.40. ¹³C NMR of 2 in CDCl₃.

Figure 0.41. ¹H NMR of 3 in CDCl₃.Figure 0.42. ¹H NMR of 4 in CDCl₃.

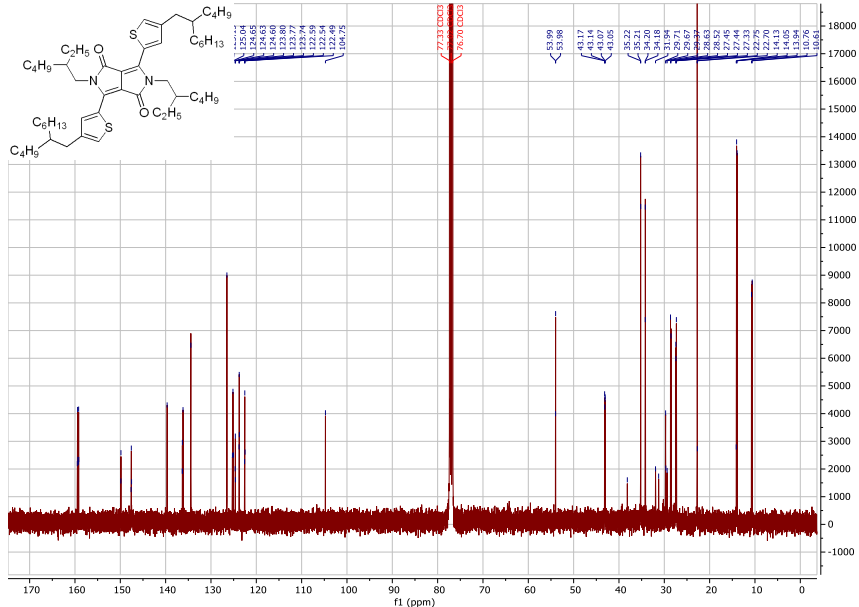


Figure 0.43. ^{13}C NMR of 4 in CDCl_3 .

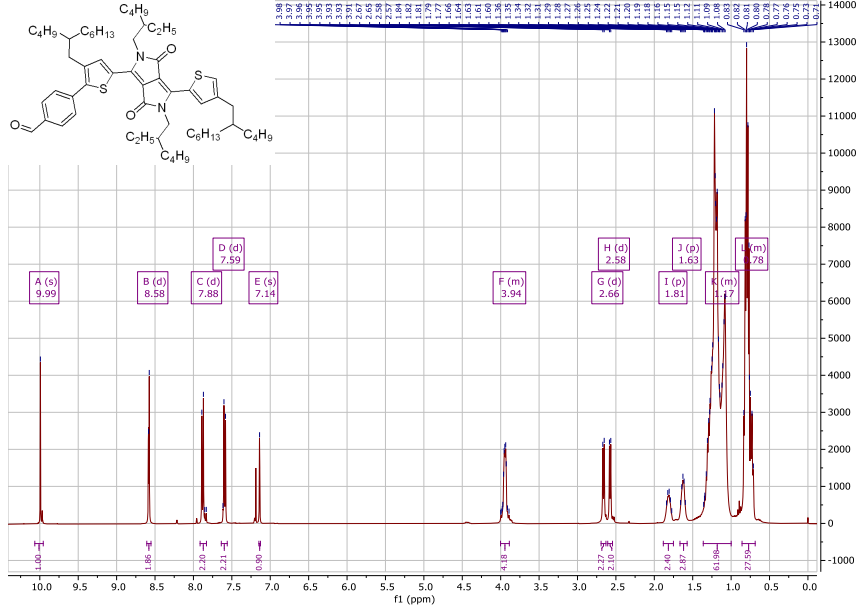


Figure 0.44. ^1H NMR of 5a in CDCl_3 .

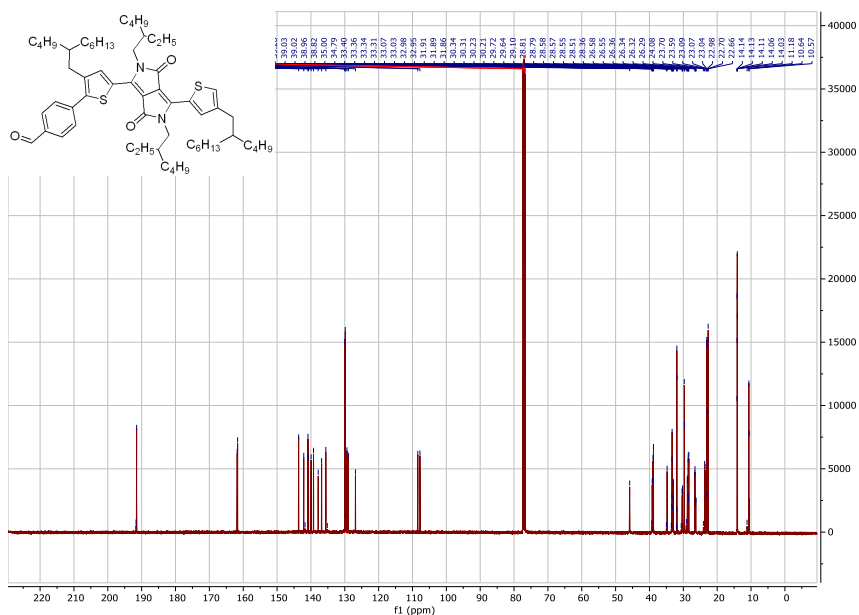


Figure 0.45. ^{13}C NMR of 5a in CDCl_3 .

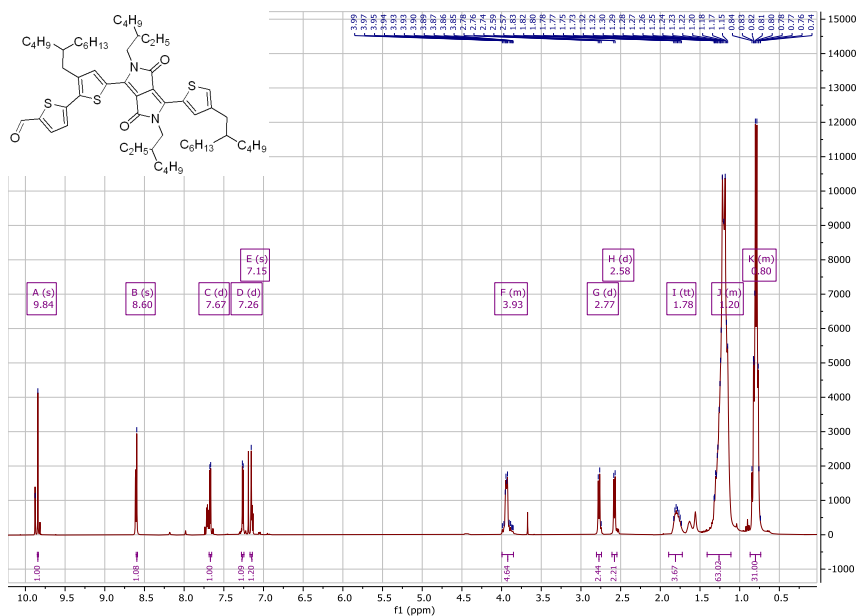


Figure 0.46. ^1H NMR of 5a in CDCl_3 .

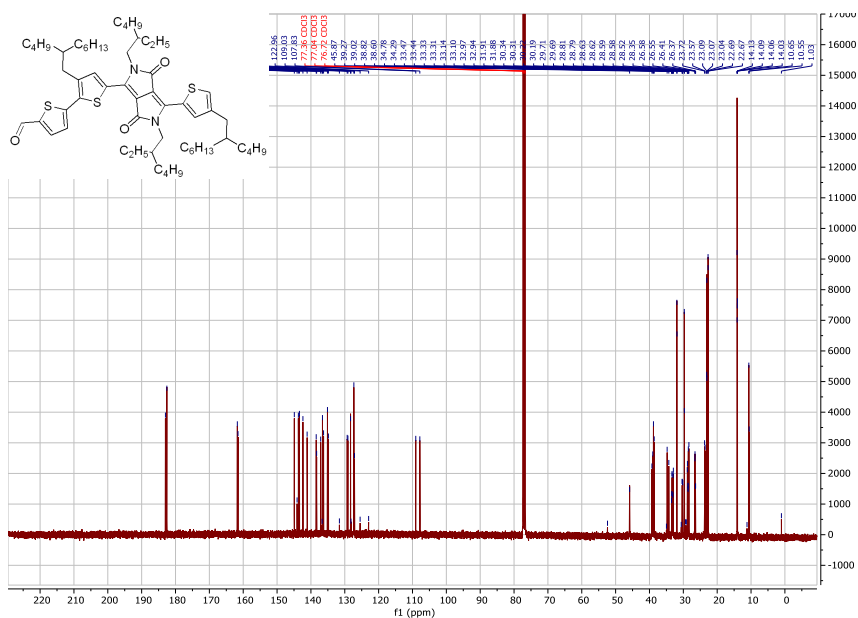


Figure 0.47. ^{13}C NMR of 5b in CDCl_3 .

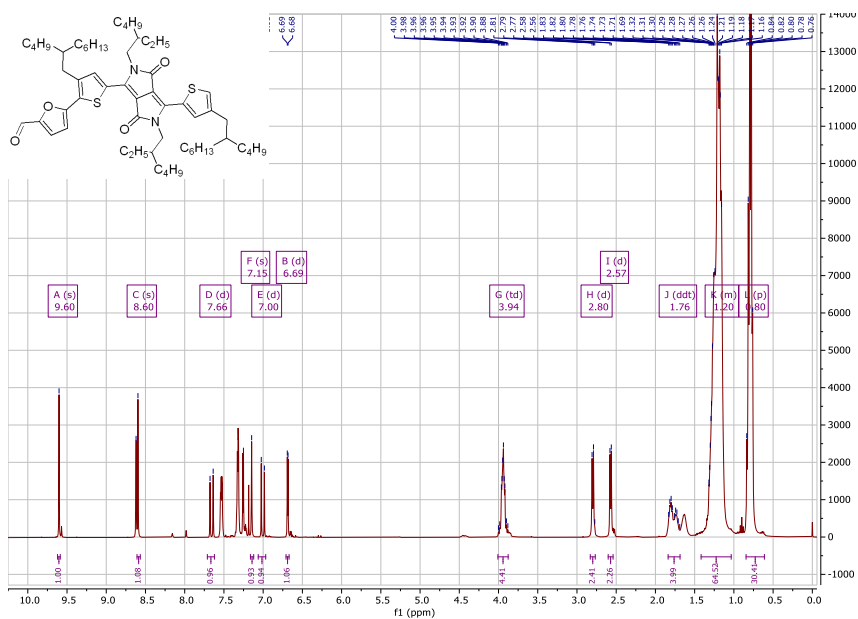


Figure 0.48. ^1H NMR of **5c** in CDCl_3 .

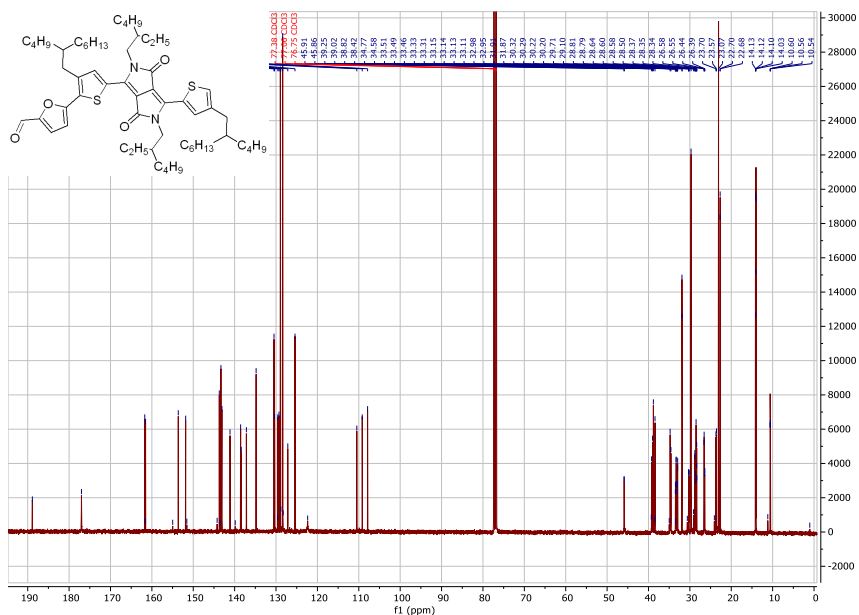


Figure 0.49. ^{13}C NMR of **5c** in CDCl_3 .

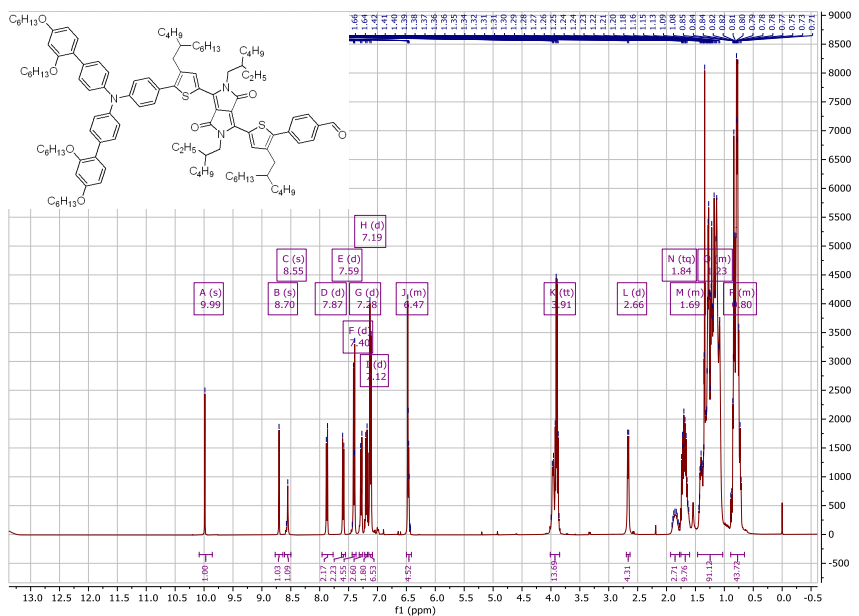


Figure 0.50. ^1H NMR of 6a in CDCl_3 .

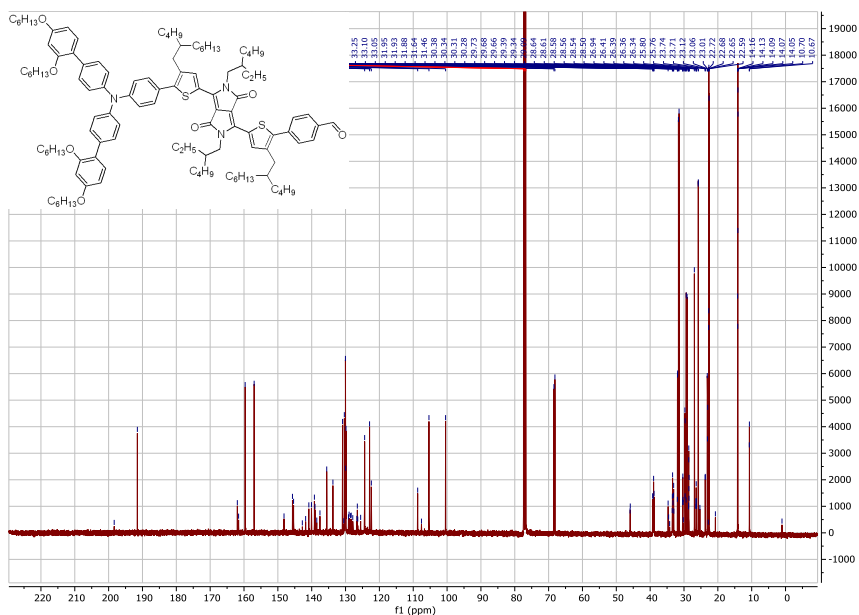


Figure 0.51. ^{13}C NMR of 6a in CDCl_3 .

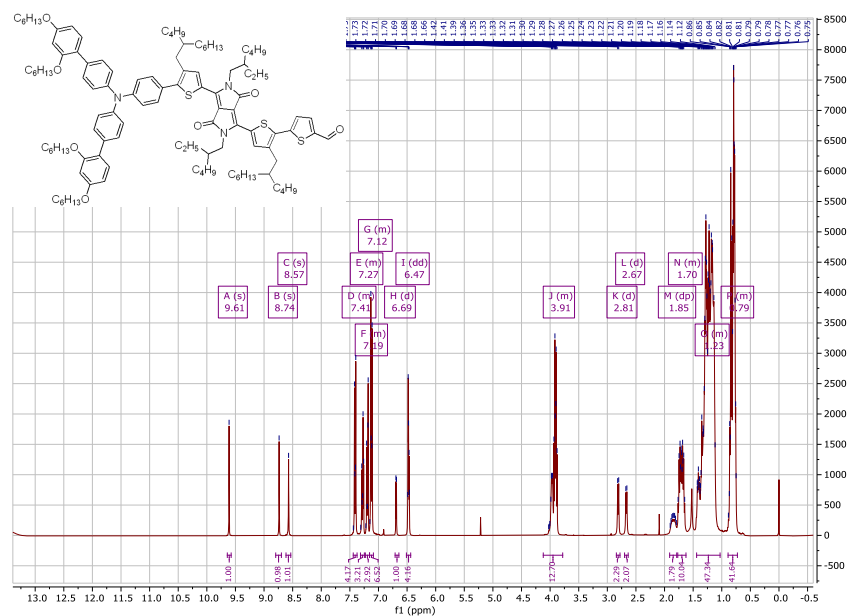


Figure 0.52. ^1H NMR of **6b** in CDCl_3 .

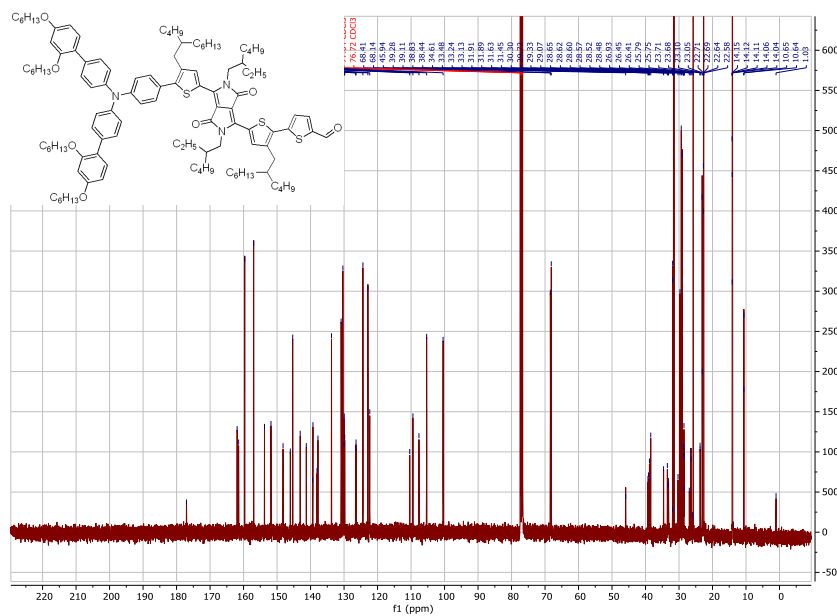


Figure 0.53. ^{13}C NMR of **6b** in CDCl_3 .

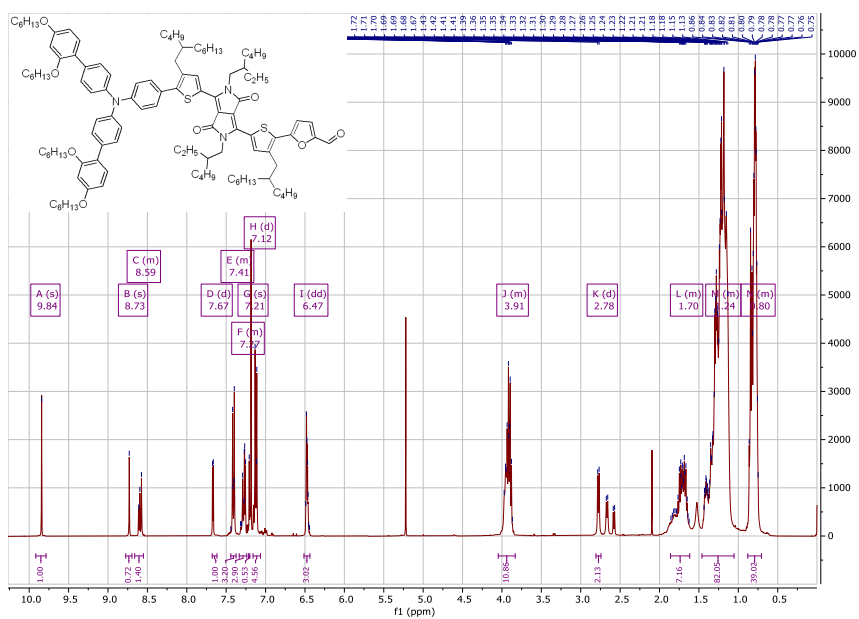
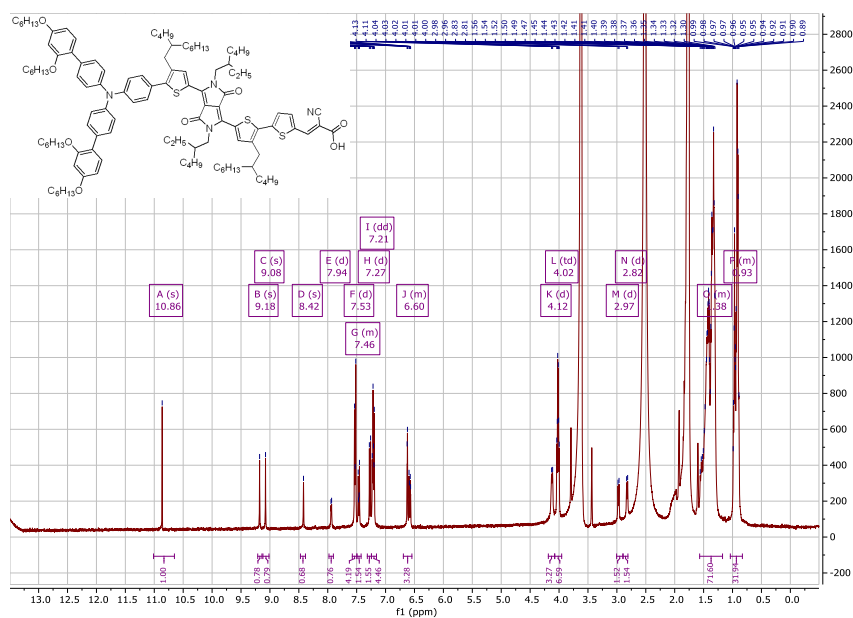
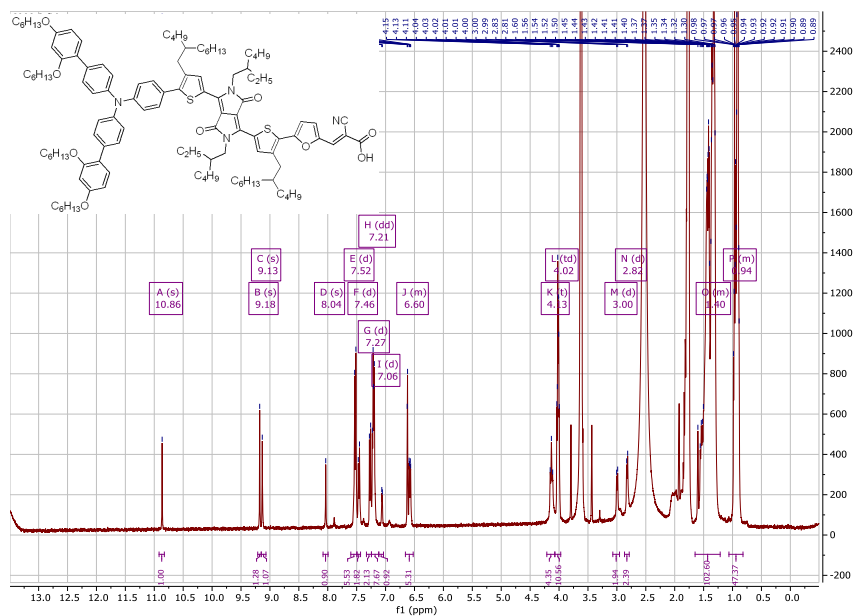


Figure 0.54. ^1H NMR of 6c in CDCl_3 .

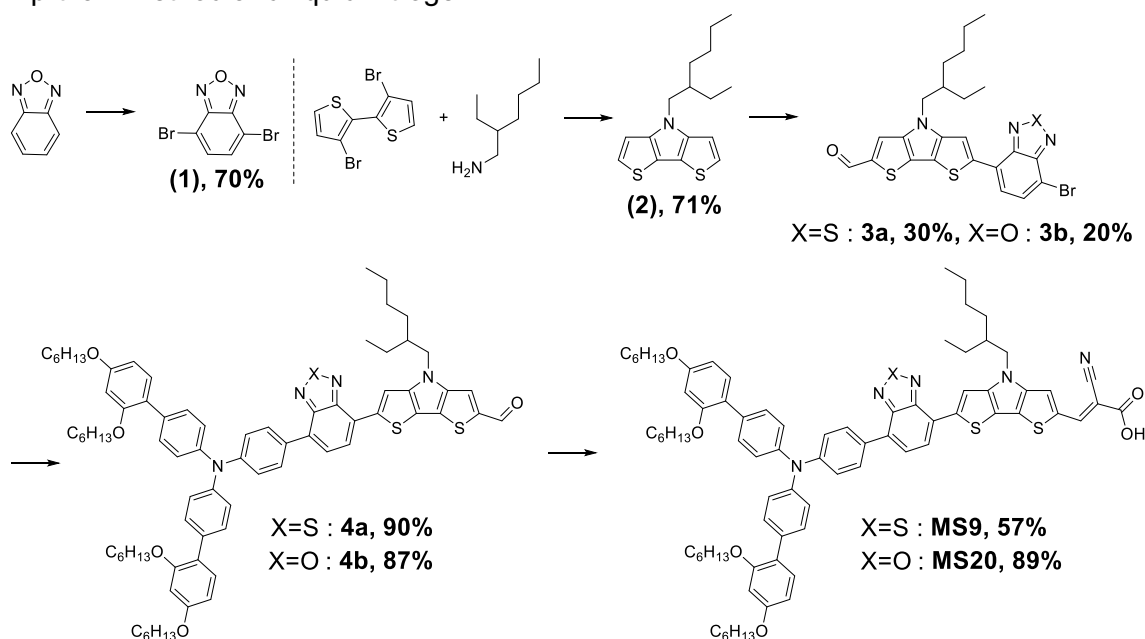


Figure 0.57. ^1H NMR of MS18 in CDCl₃.Figure 0.58. ^1H NMR of MS19 in CDCl₃.

Supporting information to Chapter 5

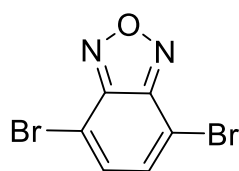
Synthetic procedure

Chloroform (VWR), Methanol (Sigma), Ethanol (Fisher Chemical), dichloromethane (DCM, Thommen-Furler), hexanes (VWR International SA), diethyl ether (HUBERLAB AG), Acetic acid (VWR International SA), potassium phosphate tribasic (Acros), magnesium sulfate (Reactolab), 3,3'-Dibromo-2,2'-bithiophene (Fluorochem), 2-(dicyclohexylphosphino)-2',4',6'-triisopropylbiphenyl (Fluorochem), and tris(dibenzylideneacetone)dipalladium(0) (Sigma), 2-Ethylhexylamine (ABCR), Tributyltin chloride (Sigma), 4,7-Dibromo-2,1,3-benzothiadiazole (Fluorochem), benzo[c][1,2,5]oxadiazole (Fluorochem), phosphoryl chloride (Sigma), bromide (Sigma), piperidine (Acros), Cyanoacetic acid (ABCR) and N-(2',4'-bis(hexyloxy)-[1,1'-biphenyl]-4-yl)-N-(4-bromophenyl)-2',4'-bis(hexyloxy)-[1,1'-biphenyl]-4-amine (**HDC6-Br**) (H.Glass SA) were used as received without further purification. Anhydrous THF and Toluene were purchased over molecular sieves from Acros Organics. The solvents used for palladium catalyzed cross coupling reactions were degassed three times using the freeze-pump-thaw method and liquid nitrogen.



Scheme 0.4. Synthetic route to MS9 and MS20.

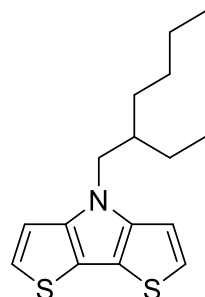
4,7-dibromobenzo[c][1,2,5]oxadiazole (**1**)



benzo[c][1,2,5]oxadiazole (1 g, 8.33 mmoles, 1 eq.), powdered iron (93 mg, 1.67 mmoles, 0.2 eq.) were charged in a two necked round bottom flask equipped with a condenser and heated at 90°C. Then bromide (1.28 mL, 24.98 mmoles, 3 eq.) was slowly added at 90°C and the resulting mixture was allowed to stir overnight. After cooling down to room temperature, the reaction was worked up with 2M Na₂S₂O₄ (50 mL) and 2M NaOH (50 mL) followed by dilution with 100 mL deionized water. The organics were extracted with dichloromethane (3x50 mL) and dried over MgSO₄ before evaporating the solvent under reduced pressure. The crude was purified by flash chromatography on SiO₂ eluting from 100% hexanes to 100% DCM in hexanes by volume. The target product was obtained as beige solid:

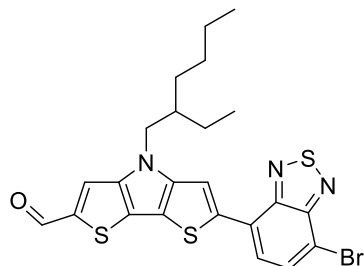
1.61 g (70%). ^1H NMR (400 MHz, CDCl_3) δ 7.54 (s, 2H). ^{13}C NMR (101 MHz, CDCl_3) δ 149.38, 134.23, 108.70. HRMS (APPI/LTQ-Orbitrap) m/z : $[\text{M} + \text{H}]^+$ Calcd for $\text{C}_6\text{H}_3\text{Br}_2\text{N}_2\text{O}^+$ 276.8607; Found 276.8618

4-(2-ethylhexyl)-4H-dithieno[3,2-b:2',3'-d]pyrrole(**2**)



2-ethylhexan-1-amine (0.199 g, 1.54 mmol, 1 eq.), 3,3'-dibromo-2,2'-bithiophene (0.5 g, 1.54 mmol, 1 eq.) and NaOtBu (0.445 g, 4.62 mmol, 3 eq.) were charged in a schlenk tube dissolved in dry Toluene (3 mL) and degassed three times using freeze-pump-thaw and liquid nitrogen. Then, tris(dibenzylideneacetone)dipalladium(0) (42 mg, 46 μmol , 0.03 eq.) and (-)-2,2'-Bis(diphenylphosphino)-1,1'-binaphthyl (115 mg, 185 μmol , 0.12 eq.) were added and the resulting reaction mixture was allowed to reflux at 110°C overnight. The reaction mixture was directly purified by flash chromatography on SiO_2 eluting from 100% hexanes to 50% DCM in hexanes by volume. The target product was obtained as yellowish thick oil: 0.319 g (71%). ^1H NMR (400 MHz, CDCl_3) δ 7.14 (d, J = 5.3 Hz, 2H), 7.01 (d, J = 5.2 Hz, 2H), 4.16 – 4.01 (m, 2H), 1.97 (p, J = 6.4 Hz, 1H), 1.44 – 1.25 (m, 8H), 0.93 (d, J = 7.4 Hz, 2H), 0.93 – 0.85 (m, 4H). ^{13}C NMR (101 MHz, CDCl_3) δ 145.31, 122.70, 114.55, 111.09, 51.35, 40.48, 30.67, 28.69, 24.05, 22.98, 14.03, 10.69. HRMS (APPI/LTQ-Orbitrap) m/z : $[\text{M}]^+$ Calcd for $\text{C}_{16}\text{H}_{21}\text{NS}_2^+$ 291.1110; Found 291.1107.

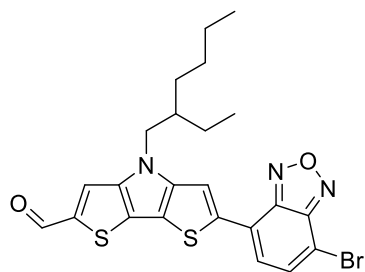
6-(7-bromobenzo[c][1,2,5]thiadiazol-4-yl)-4-(2-ethylhexyl)-4H-dithieno[3,2-b:2',3'-d]pyrrole-2-carbaldehyde(**3a**)



4-(2-ethylhexyl)-4H-dithieno[3,2-b:2',3'-d]pyrrole (**2**) (0.319 g, 1.09 mmol, 1.06 eq.) was charged in a schlenk tube along with dry THF (4 mL). The solution degassed three times with freeze-pump-thaw and liquid nitrogen before cooling down to -78°C with dry ice and acetone. Then, 1M Lithium diisopropylamide in THF (1 mL, 1.03 mmol, 1 eq.) was added and the resulting mixture was allowed to stir at -78°C for 3 hours before addition of Tri-*n*-butyltin chloride (0.5 mL, 1.63 mmol, 1.6 eq.). The reaction was then slowly warmed up to room temperature overnight. Then, a saturated aqueous solution of NaF (50 mL) was added and the organics were recovered with 40 mL diethylether. The organic phase was subsequently washed with deionized water, brine and dried over MgSO_4 before removing the solvent under reduced pressure. The obtained intermediate was charged in a schlenk tube along with 4,7-dibromobenzo[c][1,2,5]thiadiazole and dry Toluene (5 mL) before being degassed three times with freeze-pump-thaw and liquid nitrogen. Then, Bis(triphenylphosphine)palladium(II) chloride (50 mg, 72 μmol , 0.07 eq.) was added and the resulting reaction was refluxed at 110°C overnight. After that, a saturated aqueous solution of NaF (30 mL) was added and the organics were recovered with 40 mL diethylether. The organic phase was subsequently washed with deionized water, brine and dried over MgSO_4 before removing the solvent under reduced pressure. The crude was purified by flash chromatography on SiO_2 eluting from 100% hexanes to 50% DCM in hexanes by volume. The obtained product was dissolved in 10 mL of a mixture of dichloromethane:dimethylformamide (1:1, v:v) and cooled down to 0°C. Then POCl_3 (1.8 mL) was slowly added and the mixture was allowed to react at room temperature overnight. The reaction was carefully quenched with 6 M NaOH (20

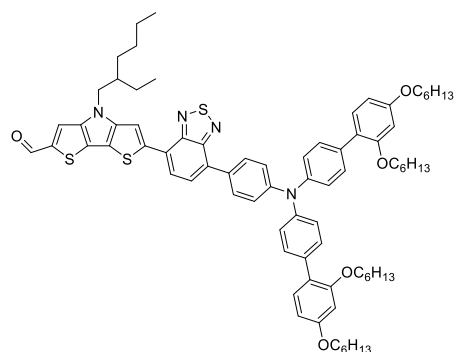
mL) at 0°C before diluted with deionized water (50 mL) and extracting the organics with dichloromethane before drying over MgSO₄. The solvent was removed under reduced pressure and the crude purified by flash chromatography on SiO₂ eluting from 100% hexanes to 100% DCM. The target product was obtained as a red solid 74 mg (30%, over two steps). ¹H NMR (400 MHz, CDCl₃) δ 9.83 (s, 1H), 8.21 (s, 1H), 7.80 (d, J = 7.7 Hz, 1H), 7.68 (d, J = 7.7 Hz, 1H), 7.56 (s, 1H), 4.11 (h, J = 7.5 Hz, 2H), 1.96 (p, J = 6.2 Hz, 1H), 1.37 – 1.19 (m, 8H), 0.86 (dt, J = 26.3, 7.1 Hz, 6H). ¹³C NMR (101 MHz, CDCl₃) δ 198.31, 182.98, 153.99, 151.59, 149.89, 145.24, 141.25, 140.90, 139.45, 132.32, 127.53, 125.65, 123.00, 115.41, 112.90, 112.70, 77.34, 77.02, 76.70, 51.45, 40.53, 30.65, 28.64, 24.15, 22.98, 14.08, 10.74. HRMS (APPI/LTQ-Orbitrap) m/z: [M + H]⁺ Calcd for C₂₃H₂₃BrN₃OS₃⁺ 532.0181; Found 532.0187.

6-(7-bromobenzo[c][1,2,5]oxadiazol-4-yl)-4-(2-ethylhexyl)-4H-dithieno[3,2-b:2',3'-d]pyrrole-2-carbaldehyde(**3b**)



The same procedure as for (**3a**) was used, with 4,7-dibromobenzo[c][1,2,5]oxadiazole (**1**) instead of 4,7-dibromobenzo[c][1,2,5]thiadiazole and starting with 0.436 g of (**2**). The target product was obtained as a red brick solid containing some 4,7-dibromobenzo[c][1,2,5]thiadiazole. The target product was obtained as a red solid 110 mg (20%, over 2 steps). ¹H NMR (400 MHz, CDCl₃) δ 9.84 (s, 1H), 8.10 (s, 1H), 7.61 – 7.54 (m, 2H), 7.40 (d, J = 7.5 Hz, 1H), 4.18 – 4.03 (m, 2H), 2.02 – 1.85 (m, 1H), 1.33 – 1.20 (m, 8H), 0.85 (dt, J = 26.7, 7.2 Hz, 6H). ¹³C NMR (101 MHz, CDCl₃) δ 183.07, 149.87, 149.63, 147.40, 145.61, 141.88, 138.84, 134.33, 125.75, 124.14, 122.66, 119.24, 115.45, 113.85, 106.83, 77.34, 77.02, 76.70, 51.55, 40.55, 30.64, 28.61, 24.13, 22.98, 14.01, 10.73. HRMS (APPI/LTQ-Orbitrap) m/z: [M + H]⁺ Calcd for C₂₃H₂₃BrN₃O₂S₂⁺ 516.0410; Found 516.0389.

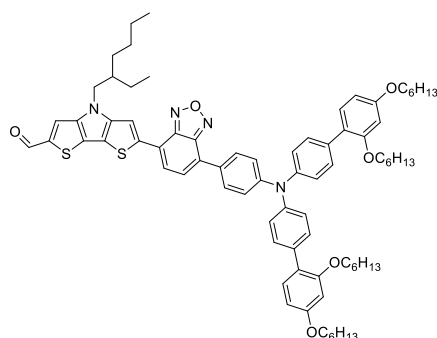
6-(7-(4-(bis(2',4'-bis(hexyloxy)-[1,1'-biphenyl]-4-yl)amino)phenyl)benzo[c][1,2,5]thiadiazol-4-yl)-4-(2-ethylhexyl)-4H-dithieno[3,2-b:2',3'-d]pyrrole-2-carbaldehyde(**4a**)



N-(2',4'-bis(hexyloxy)-[1,1'-biphenyl]-4-yl)-N-(4-bromophenyl)-2',4'-bis(hexyloxy)-[1,1'-biphenyl]-4-amine(**HDC6-Br**) (280 mg, 0.319 mmoles, 1.5 eq.) was charged in a schlenk tube, dissolved in dry THF (3 mL) and degassed three times with freeze-pump-thaw and liquid nitrogen before cooling down to -78°C with dry ice and acetone. Then, n-Butyllithium (0.4 mL, 0.618 mmoles, 2.9 eq.) 1.6M in hexanes was slowly added and the resulting solution was allowed to stir at -78°C for 4 hours before addition of 2-Isopropoxy-4,4,5,5-tetramethyl-1,3,2-dioxaborolane (0.160 g, 0.852 mmoles, 4 eq.). The reaction was allowed to warm up to room temperature overnight. The reaction was quenched with 2M aqueous K₂CO₃ (0.6 mL, 1.06 mmoles, 5 eq.) followed by addition of 6-(7-bromobenzo[c][1,2,5]thiadiazol-4-yl)-4-(2-ethylhexyl)-4H-dithieno[3,2-b:2',3'-d]pyrrole-2-carbaldehyde (**3a**) (0.110 g, 0.213 mmoles, 1 eq.). The resulting reaction mixture was degassed three times with freeze-pump-thaw and liquid nitrogen before adding Tris(dibenzylideneacetone)dipalladium(0) (16 mg, 17 μmol, 0.08

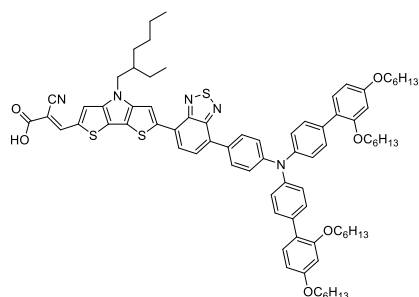
eq.), 2-(Dicyclohexylphosphino)-2',4',6'-triisopropylbiphenyl(16 mg, 34 μmol , 0.16 eq.) and subsequently heating at 80°C for 24 hours. piperidine (110 μL) were charged in a schlenk tube along with 4 mL distilled chloroform. The resulting solution was degassed three times using freeze-pump-thaw and liquid nitrogen. After cooling down to room temperature, the reaction was diluted with diethylether (20 mL) and flashed through a pad of MgSO_4 . The solvents were removed under reduced pressure and the crude was purified by flash chromatography on SiO_2 eluting from 100% hexanes to 100% dichloromethane. The target product was obtained as a red shiny solid 227 mg (87%). ^1H NMR (400 MHz, CDCl_3) δ 9.86 (d, J = 1.4 Hz, 1H), 8.13 (d, J = 2.2 Hz, 1H), 7.95 (d, J = 8.6 Hz, 2H), 7.61 (dd, J = 7.5, 3.1 Hz, 1H), 7.57 – 7.50 (m, 6H), 7.35 – 7.27 (m, 4H), 7.27 – 7.22 (m, 4H), 6.65 – 6.51 (m, 4H), 4.14 (t, J = 6.5 Hz, 2H), 4.01 (q, J = 6.8 Hz, 8H), 2.02 (hept, J = 6.2 Hz, 1H), 1.90 – 1.74 (m, 8H), 1.58 – 1.26 (m, 30H), 1.09 – 0.79 (m, 19H). ^{13}C NMR (101 MHz, CDCl_3) δ 182.86, 159.68, 157.01, 149.88, 149.06, 148.98, 147.94, 145.23, 145.13, 141.18, 140.34, 134.01, 130.93, 130.41, 128.95, 128.86, 128.15, 127.52, 126.57, 126.41, 124.63, 122.86, 122.80, 122.18, 121.63, 119.25, 114.68, 112.77, 105.36, 100.44, 68.44, 68.14, 51.40, 40.53, 31.67, 31.50, 30.66, 29.74, 29.37, 29.11, 28.64, 26.95, 25.82, 25.79, 24.15, 23.02, 22.67, 22.62, 14.10, 14.08, 14.05, 10.76. HRMS (APPI/LTQ-Orbitrap) m/z : $[\text{M} + \text{H}]^+$ Calcd for $\text{C}_{77}\text{H}_{93}\text{N}_4\text{O}_6\text{S}_2^+$ 1233.6531; Found 1233.6497.

6-(7-(4-(bis(2',4'-bis(hexyloxy)-[1,1'-biphenyl]-4-yl)amino)phenyl)benzo[c][1,2,5]oxadiazol-4-yl)-4-(2-ethylhexyl)-4H-dithieno[3,2-b:2',3'-d]pyrrole-2-carbaldehyde (**4b**)



The same procedure as for (**4a**) was used, with 0.136 g of 6-(7-bromobenzo[c][1,2,5]oxadiazol-4-yl)-4-(2-ethylhexyl)-4H-dithieno[3,2-b:2',3'-d]pyrrole-2-carbaldehyde(**3b**) instead of (**3a**). The target product was obtained as a red solid 0.361 mg (90%). ^1H NMR (400 MHz, CDCl_3) δ 9.78 (s, 1H), 8.20 (d, J = 1.8 Hz, 1H), 7.83 (td, J = 9.2, 8.5, 2.5 Hz, 3H), 7.63 (dd, J = 7.6, 2.9 Hz, 1H), 7.50 (s, 1H), 7.40 (d, J = 8.4 Hz, 4H), 7.31 – 7.07 (m, 10H), 6.49 – 6.31 (m, 4H), 4.06 (h, J = 7.6 Hz, 2H), 3.90 (q, J = 6.8 Hz, 8H), 2.01 – 1.86 (m, 1H), 1.85 – 1.62 (m, 8H), 1.47 – 1.09 (m, 29H), 0.83 (ddt, J = 18.6, 9.3, 7.0 Hz, 18H). ^{13}C NMR (101 MHz, CDCl_3) δ 182.87, 159.62, 157.01, 154.90, 154.07, 152.65, 150.15, 148.42, 145.45, 145.00, 142.36, 140.69, 133.62, 132.98, 130.90, 130.36, 130.33, 130.04, 129.86, 128.58, 127.67, 127.00, 126.94, 125.94, 125.83, 124.48, 124.38, 123.22, 122.95, 122.62, 122.57, 119.17, 114.93, 111.82, 105.34, 100.45, 68.85, 68.43, 68.14, 68.01, 65.42, 51.40, 40.53, 34.37, 31.65, 31.52, 31.49, 30.67, 30.09, 29.48, 29.35, 29.31, 29.11, 28.67, 26.09, 25.80, 25.79, 24.17, 23.01, 22.65, 22.61, 14.11, 14.09, 14.05, 10.77. HRMS (ESI/QTOF) m/z : $[\text{M}]^+$ Calcd for $\text{C}_{77}\text{H}_{92}\text{N}_4\text{O}_5\text{S}_3^+$ 1248.6224; Found 1248.6228.

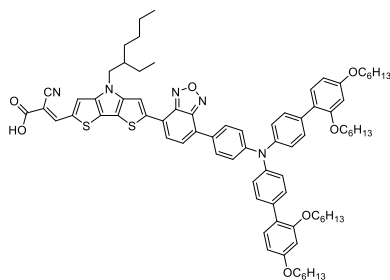
(E)-3-(6-(7-(4-(bis(2',4'-bis(hexyloxy)-[1,1'-biphenyl]-4-yl)amino)phenyl)benzo[c][1,2,5]thiadiazol-4-yl)-4-(2-ethylhexyl)-4H-dithieno[3,2-b:2',3'-d]pyrrol-2-yl)-2-cyanoacrylic acid(**MS9**)



6-(7-(4-(bis(2',4'-bis(hexyloxy)-[1,1'-biphenyl]-4-yl)amino)phenyl)benzo[c][1,2,5]thiadiazol-4-yl)-4-(2-ethylhexyl)-4H-dithieno[3,2-b:2',3'-d]pyrrole-2-carbaldehyde(**4a**) (0.227 g, 0.184 mmol, 1 eq.), cyanoacetic acid (0.227 g) and piperidine (0.5 mL) were charged in a schlenk tube along with dry chloroform (5 mL) and degassed three times using freeze-pump-thaw and liquid nitrogen. The resulting reaction was heated at 70°C for 24 hours. After cooling down to room temperature, acetic

acid (10 mL) was added along with dichloromethane (50 mL) before removing the solvents under reduced pressure. The residue was purified by flash chromatography on SiO₂ eluting from 100% dichloromethane to 5% ethanol and 1% acetic acid in dichloromethane by volume. The target product was obtained as a dark power after recrystallization from cold methanol 196 mg (82 %). ¹H NMR (400 MHz, CDCl₃ + 5 drops pyridine-d₅) δ 8.27 (s, 1H), 8.13 (s, 1H), 7.89 (d, J = 8.6 Hz, 2H), 7.67 – 7.60 (m, 2H), 7.50 (d, J = 7.5 Hz, 1H), 7.42 (d, J = 8.4 Hz, 4H), 7.15 (d, J = 8.3 Hz, 4H), 6.48 (d, J = 6.2 Hz, 4H), 4.10 (t, J = 6.2 Hz, 2H), 3.90 (q, J = 6.7 Hz, 8H), 1.69 (dq, J = 14.3, 6.9 Hz, 8H), 1.45 – 1.26 (m, 10H), 0.93 – 0.71 (m, 45H). HRMS (MALDI/TOF) m/z: [M]⁺ Calcd for C₈₀H₉₃N₅O₇S₂⁺ 1299.6511; Found 1299.5623.

(E)-3-(6-(7-(4-(bis(2',4'-bis(hexyloxy)-[1,1'-biphenyl]-4-yl)amino)phenyl)benzo[c][1,2,5]oxadiazol-4-yl)-4-(2-ethylhexyl)-4H-dithieno[3,2-b:2',3'-d]pyrrol-2-yl)-2-cyanoacrylic acid(**MS20**)



The same procedure as for (**MS9**) was used, with 0.361 g 6-(7-(4-(bis(2',4'-bis(hexyloxy)-[1,1'-biphenyl]-4-yl)amino)phenyl)benzo[c][1,2,5]oxadiazol-4-yl)-4-(2-ethylhexyl)-4H-dithieno[3,2-b:2',3'-d]pyrrole-2-carbaldehyde (**4b**) instead of (**4a**) and HCl 1M instead of acetic acid during the work-up. The target product was obtained as a dark red solid 0.217 mg (57%). ¹H NMR (600 MHz, Acetone) δ 8.43 (s, 2H), 8.06 – 7.99 (m, 3H), 7.57 – 7.52 (m, 4H), 7.33 – 7.25 (m,

2H), 7.25 – 7.17 (m, 5H), 6.65 (d, J = 2.3 Hz, 2H), 6.59 (dd, J = 8.5, 2.4 Hz, 2H), 4.37 (d, J = 7.5 Hz, 2H), 4.03 (q, J = 6.1 Hz, 8H), 1.84 – 1.72 (m, 8H), 1.54 – 1.45 (m, 3H), 1.43 (td, J = 14.6, 9.0 Hz, 7H), 1.39 (tt, J = 6.2, 2.9 Hz, 7H), 1.36 – 1.28 (m, 19H), 0.99 (t, J = 7.5 Hz, 3H), 0.97 – 0.89 (m, 7H), 0.90 – 0.85 (m, 11H). ¹³C NMR (151 MHz, CDCl₃) δ 159.60, 159.57, 156.97, 156.95, 154.86, 153.88, 152.45, 151.50, 148.28, 145.29, 144.27, 133.57, 130.92, 130.27, 129.88, 129.72, 126.62, 125.94, 125.25, 124.39, 122.87, 122.30, 114.93, 105.27, 105.24, 100.38, 100.36, 98.21, 77.26, 77.05, 76.83, 68.78, 68.40, 68.38, 68.12, 68.11, 67.98, 53.47, 40.51, 34.88, 34.54, 34.35, 31.95, 31.66, 31.64, 31.58, 31.51, 31.48, 30.68, 30.19, 30.07, 29.73, 29.69, 29.62, 29.48, 29.44, 29.39, 29.35, 29.34, 29.28, 29.07, 28.69, 28.66, 27.67, 26.09, 25.81, 25.80, 25.78, 25.76, 24.18, 23.06, 23.02, 22.72, 22.66, 22.61, 21.52, 14.18, 14.16, 14.10, 14.07, 10.82, 1.05. HRMS (MALDI/TOF) m/z: [M]⁺ Calcd for C₈₀H₉₃N₅O₆S₃⁺ 1315.6283; Found 1315.7170. HRMS (MALDI/TOF) m/z: [M]⁺ Calcd for C₈₀H₉₃N₅O₆S₃⁺ 1315.6283; Found 1315.7170.

Optical characterization

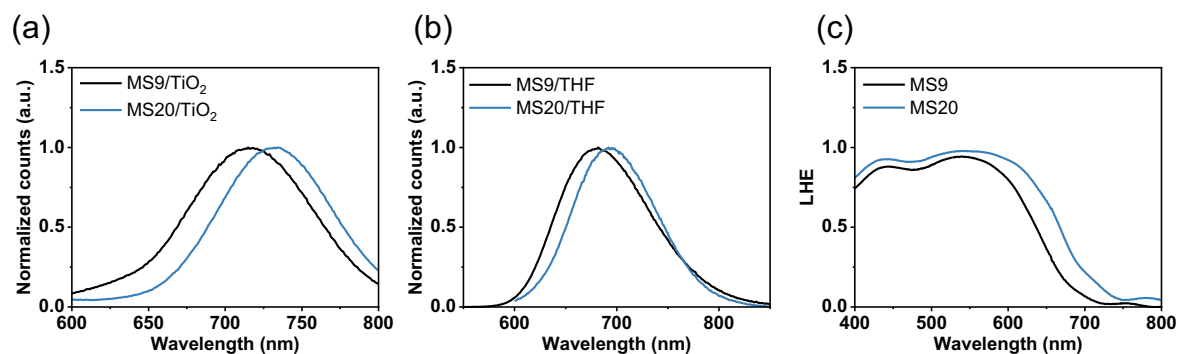


Figure 0.59. (a) Normalized emission spectra of the dyes adsorbed on 4 μm thick TiO_2 films. Normalized emission spectra of the dyes in diluted THF solutions (b). (c) Light harvesting efficiency (LHE) calculated using: $\text{LHE} = 1 - 10^{-A}$, with A being the absorbance of the sensitized films.

Electrochemical characterization

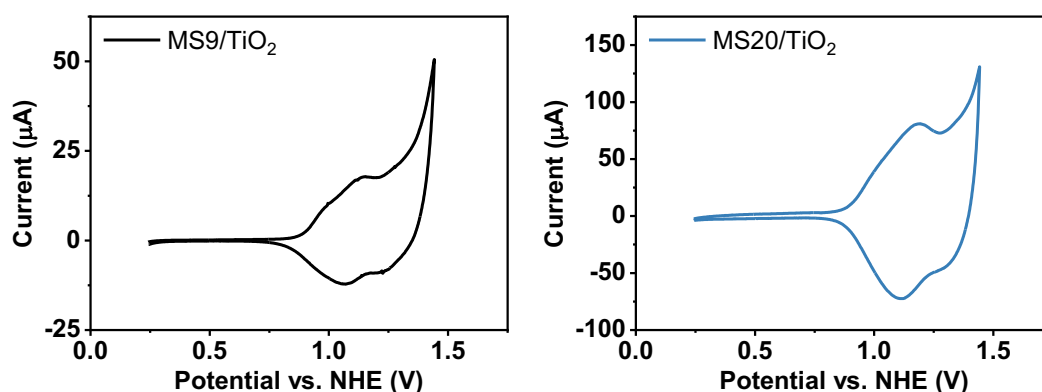


Figure 0.60. Cyclic voltammograms of the dyes adsorbed on a transparent TiO_2 film.

Computational calculations

Table 0.7. The calculated energy levels of HOMO and LUMO orbitals of MS dyes using Gaussian09 with B3PW91 functional and 6-31G(d,p) basis sets.

	HOMO [eV]	LUMO [eV]	E _g [eV]
MS9	-4.84	-2.97	1.87
MS20	-4.91	-3.09	1.82

Device fabrication and solar cell characterization

Table 0.8. Detailed PV performances of the devices at 2, 10, 50 and 100% sun.

MS9					
P_{In} [mW·cm ⁻²]	J_{sc} [mA·cm ⁻²]	V_{oc} [mV]	FF [%]	PCE [%]	
100	16.43	990	76.3	12.4	
51.1	8.33	971	78.0	12.3	
10	1.58	909	75.9	10.9	
2.1	0.31	809	75.4	9.1	

MS20					
P_{In} [mW·cm ⁻²]	J_{sc} [mA·cm ⁻²]	V_{oc} [mV]	FF [%]	PCE [%]	
100	14.60	948	78.3	10.8	
51.1	7.39	926	79.8	10.7	
10	1.38	857	79.4	9.4	
2.1	0.26	780	76.8	7.6	

Time resolved photoluminescent decay

	A_1 [%]	$\tau_1(A)$ [ps]	A_2 [%]	$\tau_2(A)$ [ns]	A_1 [%]	$\tau_1(T)$ [ps]	A_2 [%]	$\tau_2(T)$ [ps]
MS9	33.2	425.3	66.8	1.4	49.6	80.26	50.4	351.2
MS20	33.2	322.5	66.8	1.1	99.9	197.19	0.1	1978.2

¹H and ¹³C NMR spectra

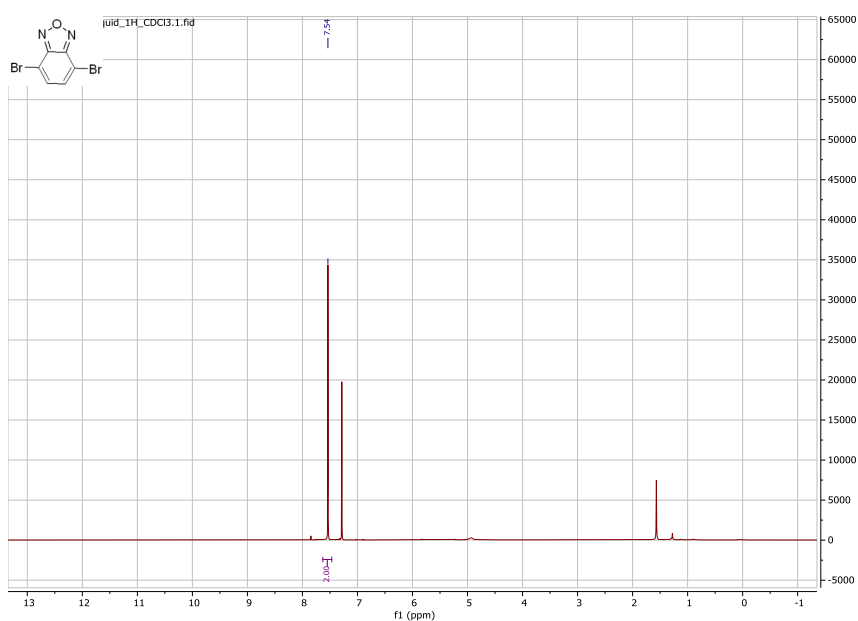
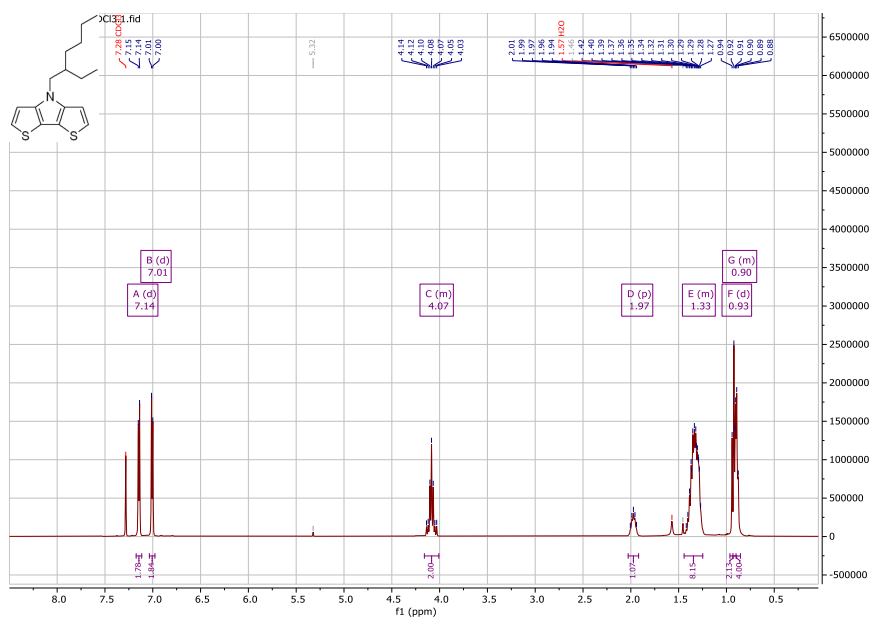
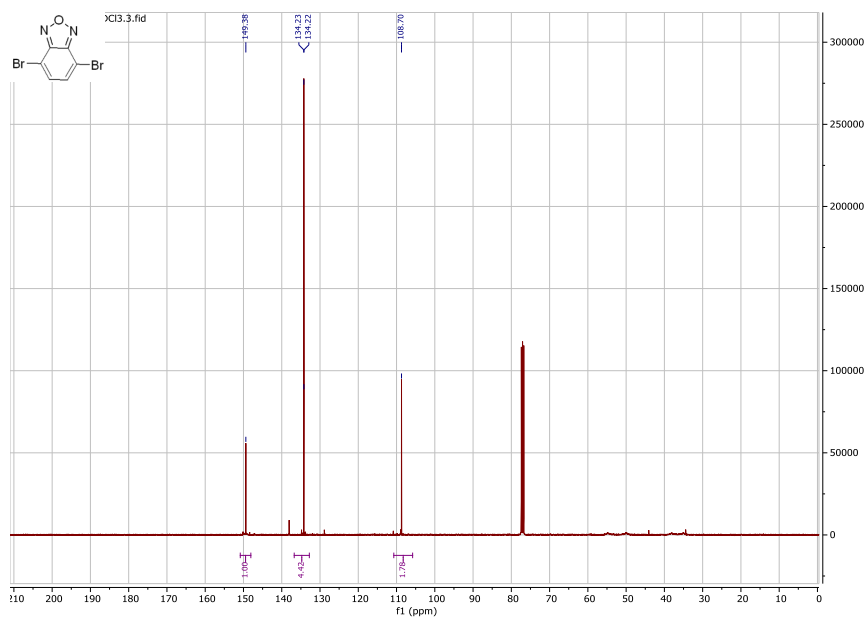
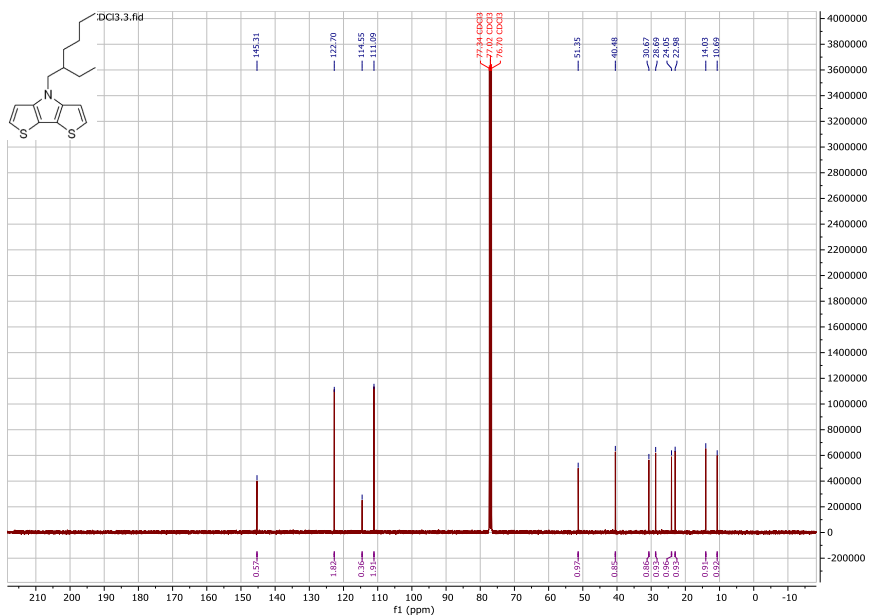
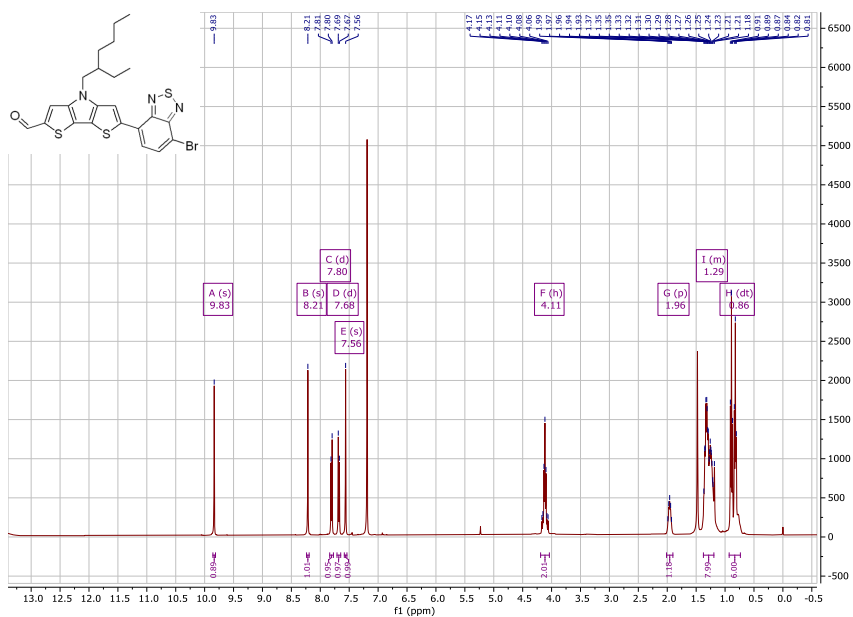
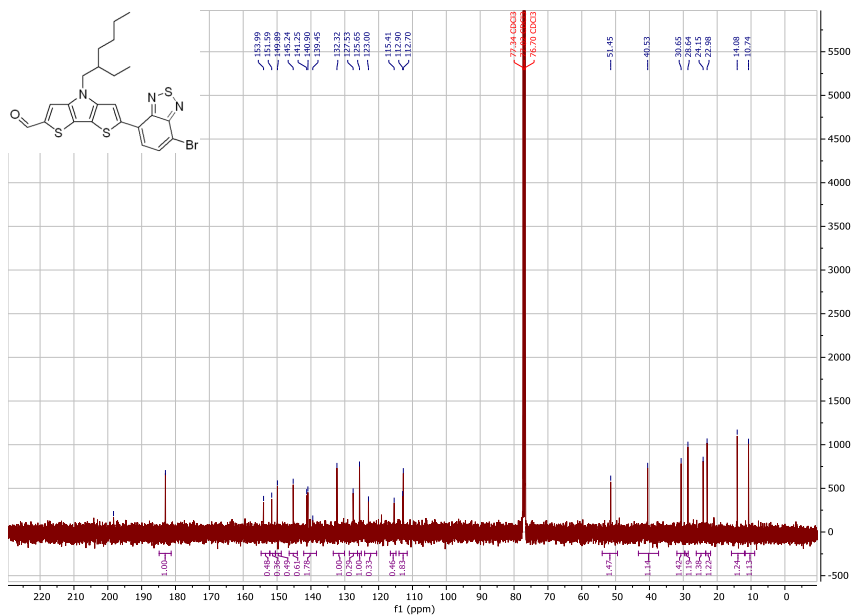
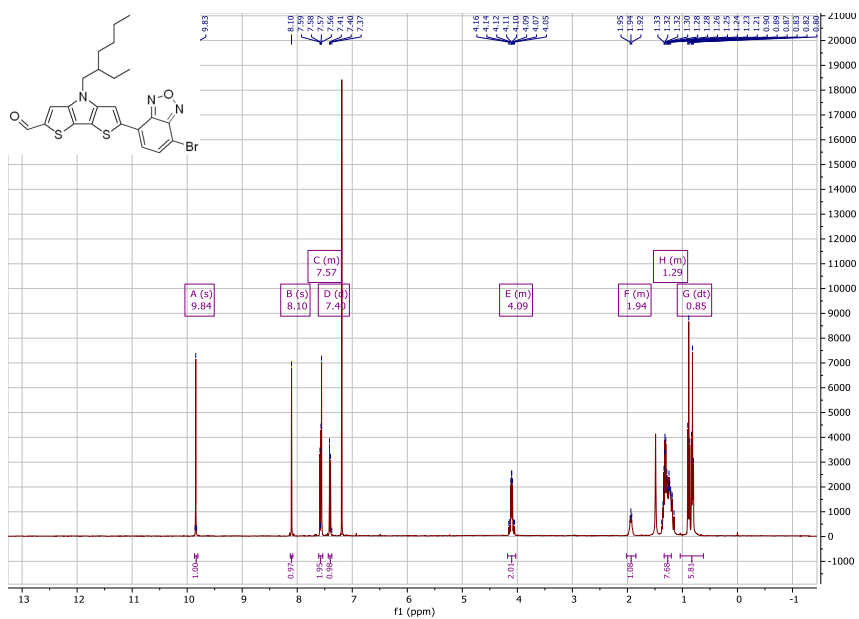


Figure 0.61. ¹H NMR of **1** in CDCl₃.



Figure 0.64. ¹³C NMR of 2 in CDCl₃.Figure 0.65. ¹H NMR of 3a in CDCl₃.

Figure 0.66. ^{13}C NMR of 3a in CDCl_3 .Figure 0.67. ^1H NMR of 3b in CDCl_3 .

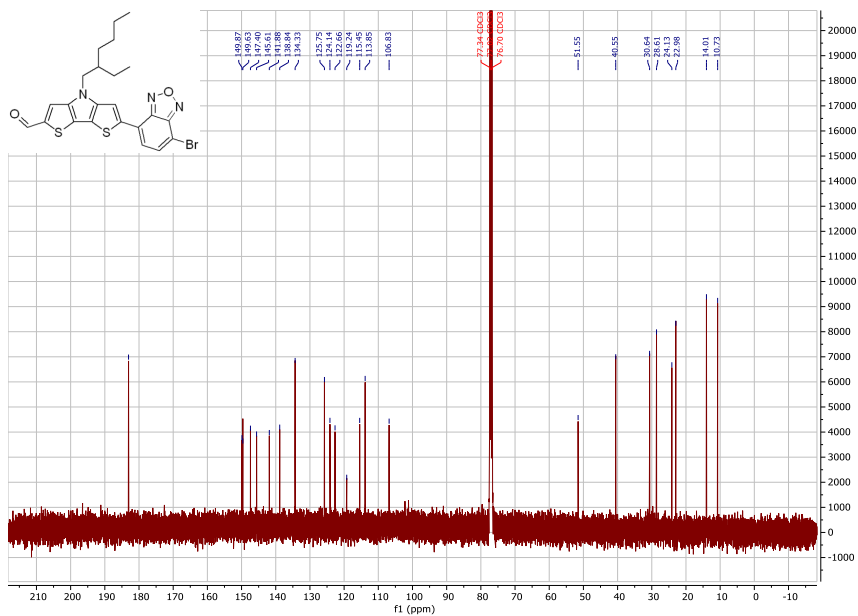


Figure 0.68. ^{13}C NMR of 3b in CDCl_3 .

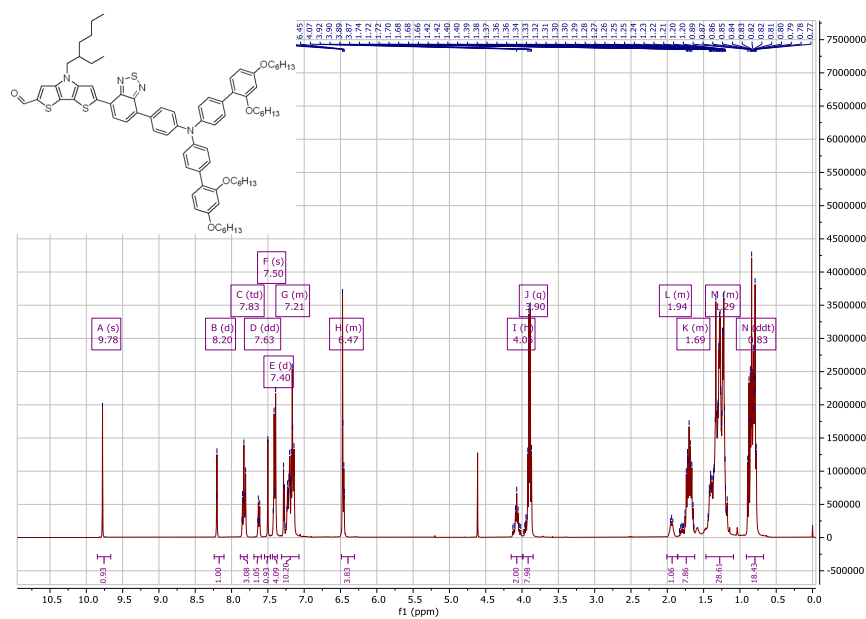
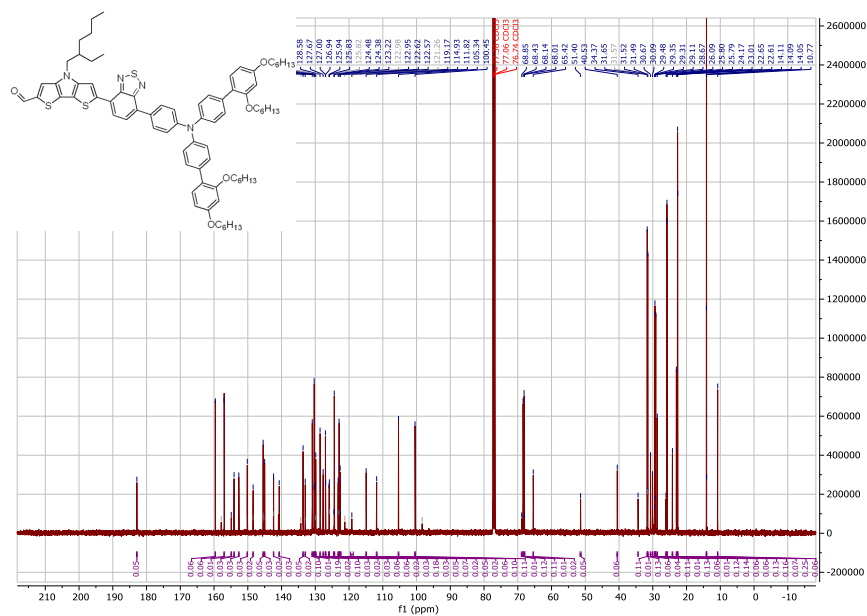


Figure 0.69. ^1H NMR of 4a in CDCl_3 .



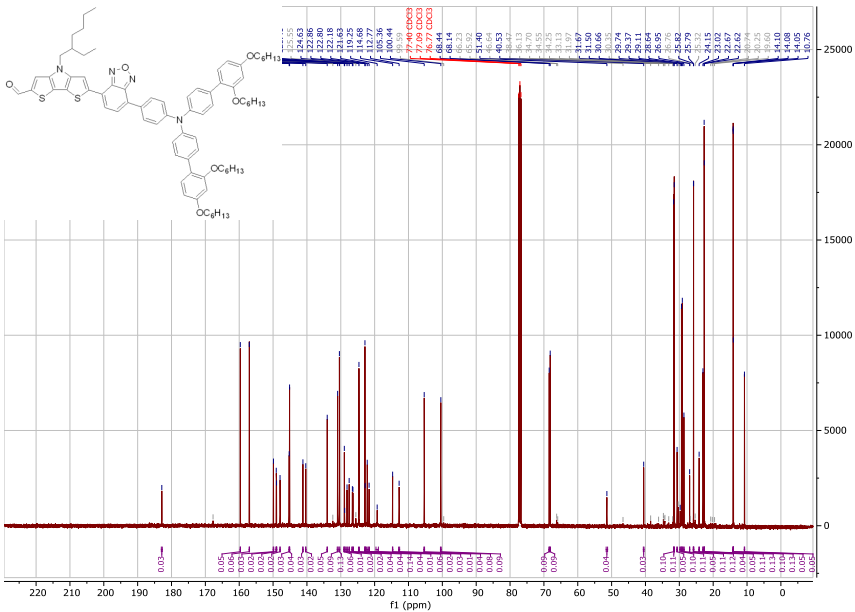


Figure 0.72. ^{13}C NMR of 4b in CDCl_3 .

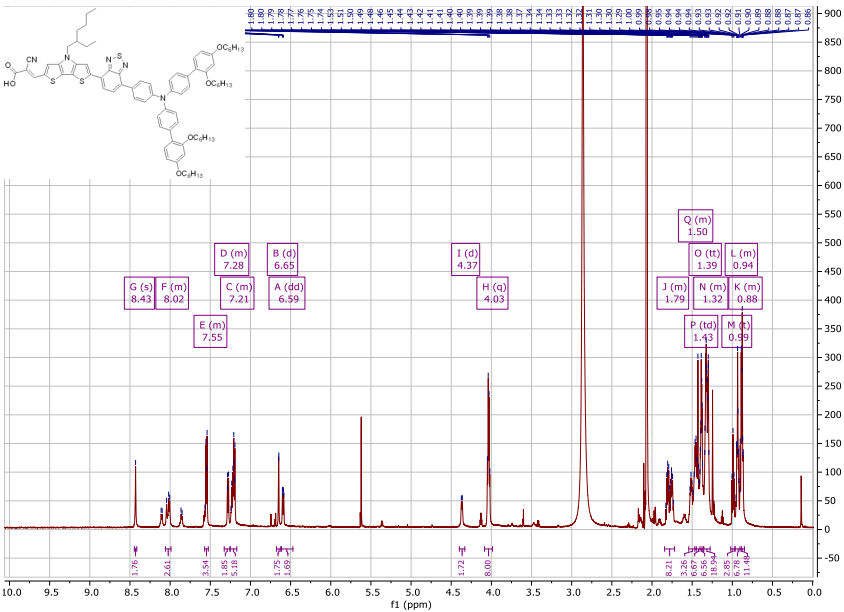
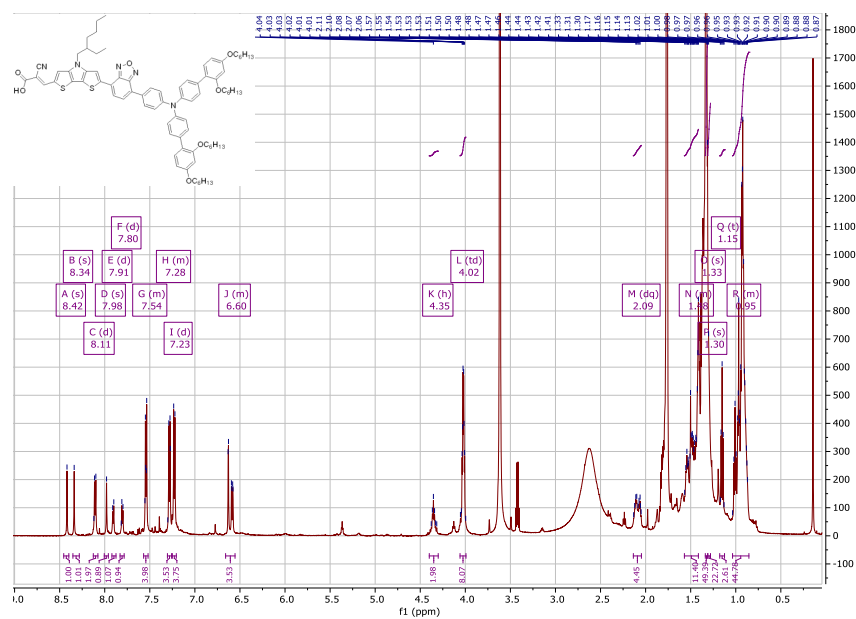
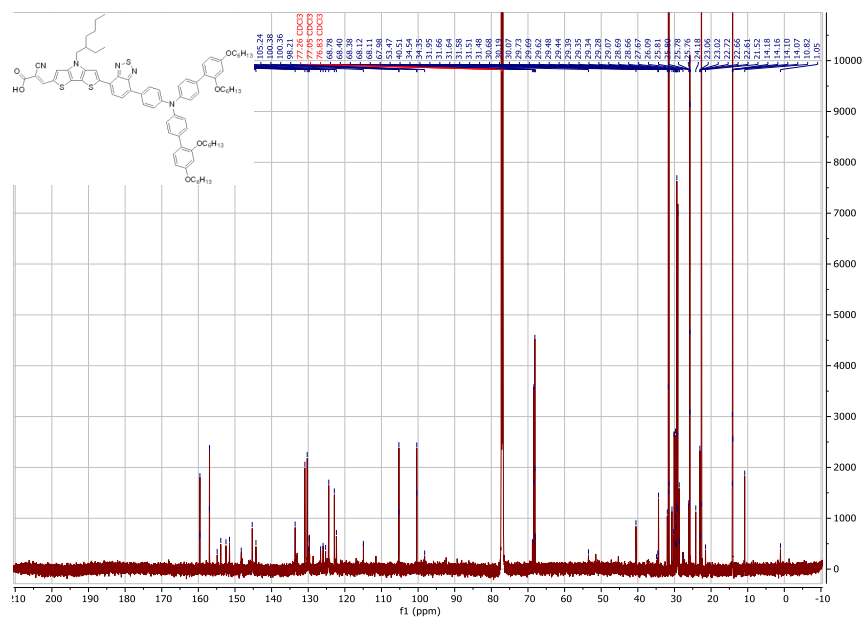


Figure 0.73. ^1H NMR of MS9 in Acetone- d_6 .



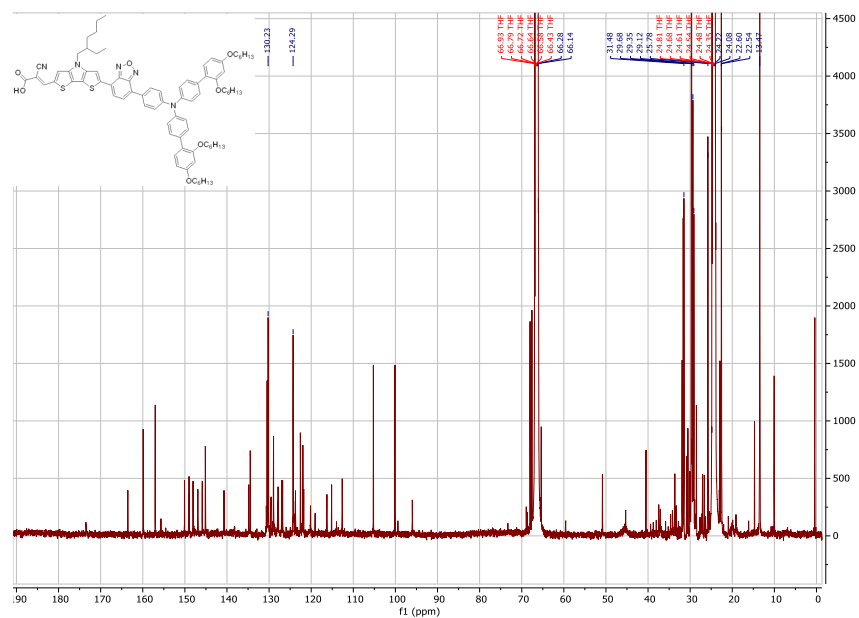
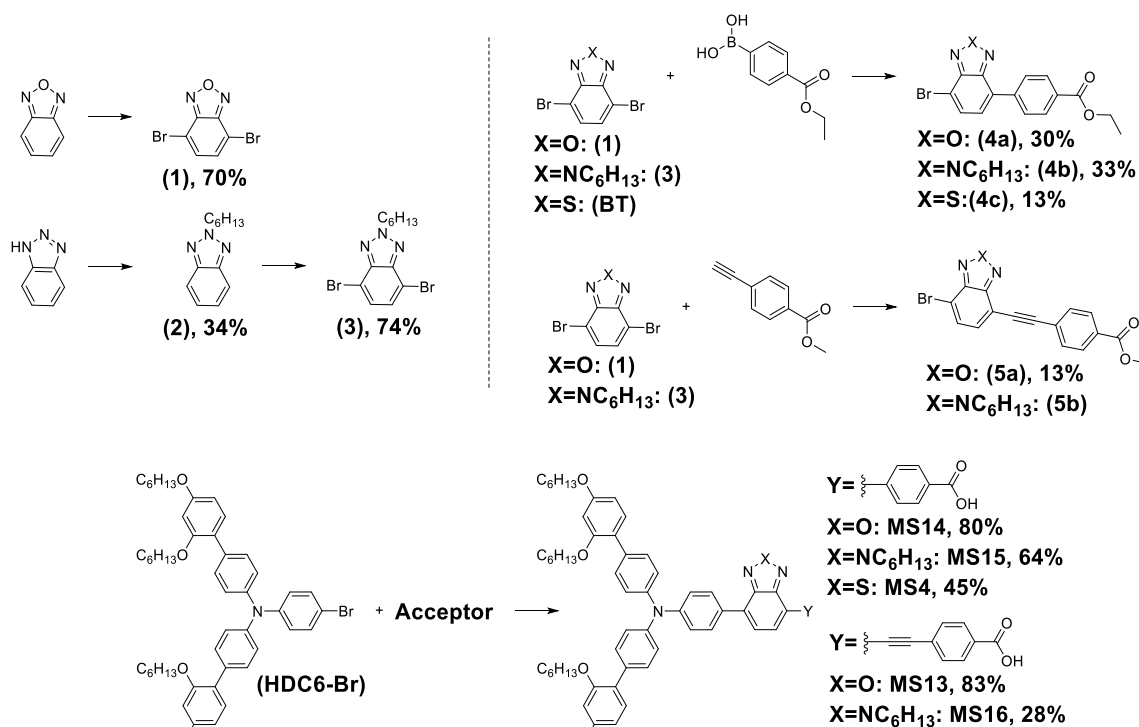


Figure 0.76. ^{13}C NMR of MS20 in THF-d_8 .

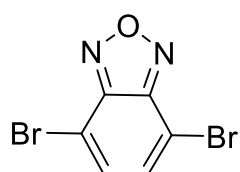
Supporting information to Chapter 6

Synthetic procedure

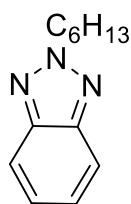


Scheme 0.5. Synthetic route to MS4, MS13, MS14, MS15 and MS16.

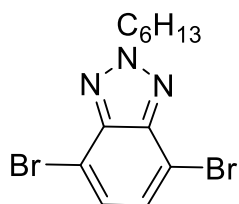
4,7-dibromobenzo[c][1,2,5]oxadiazole (1)



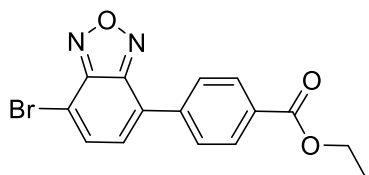
benzo[c][1,2,5]oxadiazole (1 g, 8.33 mmoles, 1 eq.), powdered iron(93 mg, 1.67 mmoles, 0.2 eq.) were charged in a two necked round bottom flask equipped with a condenser and heated at 90°C. Then bromide (1.28 mL, 24.98 mmolrd, 3 eq.) was slowly added at 90°C and the resutling mixture was allowed to stirr overnight. After cooling down to room temperature, the reaction was worked up with 2M Na₂S₂O₄ (50 mL) and 2M NaOH (50 mL) followed by dilution with 100 mL deionized water. The organics were extracted with dichloromethane (3x50 mL) and dried over MgSO₄ before evaporating the solvent under reduced pressure. The crude was purified by flash chromatography on SiO₂ eluting from 100% hexanes to 100% DCM in hexanes by volume. The target product was obtained as beige solid: 1.61 g (70%). ¹H NMR (400 MHz, CDCl₃) δ 7.54 (s, 2H). ¹³C NMR (101 MHz, CDCl₃) δ 149.38, 134.23, 108.70. HRMS (APPI/LTQ-Orbitrap) m/z: [M + H]⁺ Calcd for C₆H₃Br₂N₂O⁺ 276.8607; Found 276.8618.

2-hexyl-2H-benzo[d][1,2,3]triazole(**2**)

1H-benzo[d][1,2,3]triazole (5 g, 41.97 mmol, 1 eq.), KOtBu (4.7 g, 41.97 mmol, 1 eq.) and dry dimethylformamide (40 mL) were charged in a three necked round bottom flask equipped with a condenser and heated at 90°C under Argon, until dissolution of the solid. 1-bromohexanes (7.63 g, 46.17 mmol, 1.1 eq.) was then added and the resulting reaction mixture heated at 130°C overnight. The mixture was cooled down to room temperature and diluted with 100 mL hexanes. The resulting mixture was washed with saturated aqueous NH₄Cl (200 mL), brine (200 mL) and dried over MgSO₄. The solvent was removed under reduced pressure and the residues purified by flash chromatography on SiO₂ eluting from 100% hexanes to 100% DCM. The target product was obtained as colorless thick oil: 2.91 g (34 %). ¹H NMR (400 MHz, CDCl₃) δ 7.93 – 7.84 (m, 2H), 7.44 – 7.35 (m, 2H), 4.75 (t, J = 7.2 Hz, 2H), 2.20 – 2.08 (m, 2H), 1.47 – 1.24 (m, 7H), 0.93 – 0.85 (m, 2H). ¹³C NMR (101 MHz, CDCl₃) δ 144.28, 126.13, 117.95, 56.66, 31.21, 30.05, 26.24, 22.42, 13.95. HRMS (APPI/LTQ-Orbitrap) m/z: [M + H]⁺ Calcd for C₁₂H₁₈N₃⁺ 204.1495; Found 204.1488.

4,7-dibromo-2-hexyl-2H-benzo[d][1,2,3]triazole (**3**)

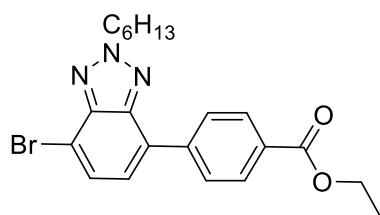
2-hexyl-2H-benzo[d][1,2,3]triazole(**2**) (2.10 g, 14.33 mmol, 1 eq.) and 8.5 mL HBr 48% wt in 8.5 mL water, were charged in a three necked round bottom flask equipped with a condenser and heated at 100°C before addition of bromide (1.62 mL, 31.52 mmol, 2.2 eq.) and the obtained reaction mixture was stirred at 135°C overnight. After cooling down to room temperature, the reaction was worked up with 2M Na₂S₂O₄ (50 mL) and 2M NaOH (50 mL) followed by dilution with 100 mL deionized water. The organics were extracted using dichloromethane (3x60 mL) and subsequently dried over MgSO₄. The crude was purified by flash chromatography on SiO₂ eluting from 100% hexanes to 50% DCM in hexanes by volume. The target product was obtained as a yellowish oil: 3.822 g (74%). ¹H NMR (400 MHz, CDCl₃) δ 7.46 (s, 2H), 4.80 (t, J = 7.4 Hz, 2H), 2.23 – 2.11 (m, 2H), 1.48 – 1.26 (m, 6H), 0.95 – 0.87 (m, 3H). ¹³C NMR (101 MHz, CDCl₃) δ 143.73, 129.52, 109.99, 57.48, 31.14, 30.19, 26.18, 26.03, 22.39, 13.93. HRMS (APPI/LTQ-Orbitrap) m/z: [M]⁺ Calcd for C₁₂H₁₅Br₂N₃⁺ 358.9627; Found 358.9640.

Ethyl 4-(7-bromobenzo[c][1,2,5]oxadiazol-4-yl)benzoate (**4a**)

4,7-dibromobenzo[c][1,2,5]oxadiazole(**1**) (0.6 g, 2.16 mmol, 1.1 eq.), (4-(ethoxycarbonyl)phenyl)boronic acid (0.381 g, 1.96 mmol, 1 eq.), 2M aqueous K₂CO₃ (1.96 mL, 3.93 mmol, 2 eq.) was charged in a schlenk tube, dissolved in dry THF (10 mL) and degassed three times with freeze-pump-thaw and liquid nitrogen. Then, Bis(triphenylphosphine)palladium(II) chloride (96 mg, 0.14 mmol, 0.07 eq.) was added and the mixture stirred at 80°C overnight. After cooling down to room temperature, the reaction was diluted with diethylether (20 mL), flashed through a pad of MgSO₄ and the solvents removed under reduced pressure. The crude was purified by flash chromatography on SiO₂ eluting from 100% hexanes to 100% DCM. The target product was obtained as a yellowish solid: 0.207 g (30%). ¹H NMR (400 MHz, CDCl₃) δ

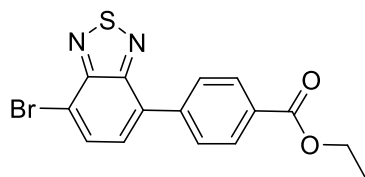
8.13 (d, $J = 8.5$ Hz, 2H), 7.98 (d, $J = 8.5$ Hz, 2H), 7.68 (d, $J = 7.4$ Hz, 1H), 7.46 (d, $J = 7.4$ Hz, 1H), 4.36 (q, $J = 7.1$ Hz, 2H), 1.36 (t, $J = 7.1$ Hz, 3H). ^{13}C NMR (101 MHz, CDCl_3) δ 165.00, 148.99, 147.39, 137.53, 133.12, 130.23, 129.47, 129.28, 129.20, 128.33, 127.70, 127.18, 107.86, 60.25, 28.68, 14.25, 13.32. HRMS (APPI/LTQ-Orbitrap) m/z : $[\text{M}]^+$ Calcd for $\text{C}_{15}\text{H}_{11}\text{BrN}_2\text{O}_3^+$ 345.9948; Found 345.9961.

Ethyl 4-(7-bromo-2-hexyl-2H-benzo[d][1,2,3]triazol-4-yl)benzoate (**4b**)



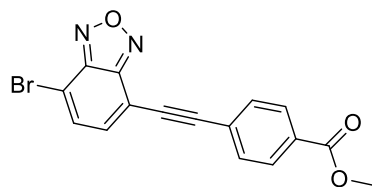
The same procedure as for (**4a**) was used, with 0.6 g of 4,7-dibromo-2-hexyl-2H-benzo[d][1,2,3]triazole (**4**) instead of (**1**) or (**3**). The target product was obtained as beige solid: 0.213 g (33%). ^1H NMR (400 MHz, CDCl_3) δ 8.11 (d, $J = 8.4$ Hz, 2H), 8.00 (d, $J = 8.4$ Hz, 2H), 7.59 (d, $J = 7.7$ Hz, 1H), 7.41 (d, $J = 7.7$ Hz, 1H), 4.72 (t, $J = 7.4$ Hz, 2H), 4.35 (q, $J = 7.1$ Hz, 2H), 2.08 (p, $J = 7.3$ Hz, 2H), 1.43 – 1.11 (m, 8H), 0.81 (t, $J = 6.9$ Hz, 4H). ^{13}C NMR (101 MHz, CDCl_3) δ 166.41, 144.46, 142.65, 140.91, 130.00, 129.96, 129.70, 129.19, 128.40, 125.41, 110.50, 61.04, 57.22, 31.17, 30.17, 26.22, 22.43, 14.37, 13.95. HRMS (APPI/LTQ-Orbitrap) m/z : $[\text{M}]^+$ Calcd for $\text{C}_{21}\text{H}_{24}\text{BrN}_3\text{O}_2^+$ 429.1046; Found 429.1064.

Ethyl 4-(7-bromobenzo[c][1,2,5]thiadiazol-4-yl)benzoate(**4c**)



The same procedure as for (**4a**) and (**4b**) was used, with 1g 4,7-dibromo-2,1,3-benzothiadiazole(**BT**) (1 g, 3.4 mmoles, 1.2 eq.). The desired product was obtained as a yellow fluffy solid (0.132 g, 13%). ^1H NMR (400 MHz, CDCl_3) δ 8.16 – 8.10 (m, 2H), 7.89 (dd, $J = 9.6, 7.9$ Hz, 3H), 7.56 (d, $J = 7.5$ Hz, 1H), 4.36 (q, $J = 7.1$ Hz, 2H), 1.36 (t, $J = 7.1$ Hz, 3H). ^{13}C NMR (101 MHz, CDCl_3) δ 166.27, 153.90, 152.90, 140.83, 132.89, 132.19, 130.50, 129.90, 129.12, 128.73, 114.20, 77.34, 77.23, 77.02, 76.71, 61.15, 29.71, 14.37, 1.03. HRMS (APPI/LTQ-Orbitrap) m/z : $[\text{M}]^+$ Calcd for $\text{C}_{15}\text{H}_{11}\text{BrN}_2\text{O}_2\text{S}^+$ 361.9719; Found 361.9724.

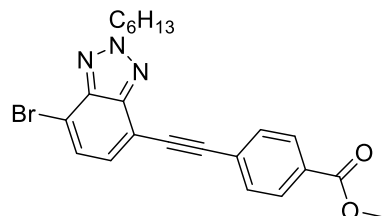
Methyl 4-((7-bromobenzo[c][1,2,5]oxadiazol-4-yl)ethynyl)benzoate (**5a**)



4,7-dibromobenzo[c][1,2,5]oxadiazole(**1**) (0.6 g, 2.16 mmoles, 1.1 eq.), methyl 4-ethynylbenzoate (0.287 g, 1.96 mmoles, 1eq.) were charged in a schlenk tube, dissolved in 10 mL of a dry THF:trimethylamine (1:1, v:v) and degassed three times with freeze-pump-thaw and liquid nitrogen. Then, Bis(triphenylphosphine)palladium(II) chloride (96 mg, 0.14 mmoles, 0.07 eq.) and copper iodide (11mg, 59 μmoles , 0.03 eq.) were added and the mixture stirred at 80°C overnight. After cooling down to room temperature, the reaction was diluted with diethylether (20 mL), flashed through a pad of celite and the solvents removed under reduced pressure. The crude was purified by flash chromatography on SiO_2 eluting from 100% hexanes to 100% DCM. The target product was obtained as a yellowish solid: 93 mg (13%). ^1H NMR (400 MHz, CDCl_3) δ 8.00 (d, $J = 7.9$ Hz, 2H), 7.61 (dd, $J = 13.9, 7.7$ Hz, 3H), 7.40 (d, $J = 7.3$ Hz, 1H), 3.88 (s, 3H). ^{13}C NMR (101 MHz, CDCl_3) δ 166.33, 149.36, 149.33, 134.86, 133.87, 131.93, 130.69, 129.67,

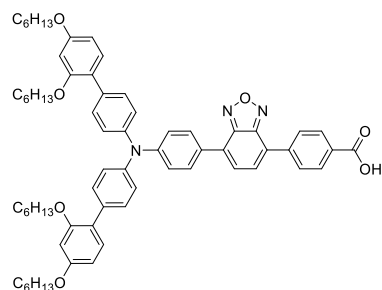
126.37, 111.98, 109.81, 97.39, 85.37, 52.38. HRMS (APPI/LTQ-Orbitrap) m/z : $[M]^+$ Calcd for $C_{16}H_9BrN_2O_3^+$ 355.9791; Found 355.9798.

Methyl 4-((7-bromo-2-hexyl-2H-benzo[d][1,2,3]triazol-4-yl)ethynyl)benzoate(**5b**)



The same procedure as for (**5a**) was used, with 0.6 g of 4,7-dibromo-2-hexyl-2H-benzo[d][1,2,3]triazole (**3**) instead of (**1**). The target product was obtained as a mixture with the biscoupled product: 0.146 g(22%).

4-(7-(4-(bis(2',4'-bis(hexyloxy)-[1,1'-biphenyl]-4-yl)amino)phenyl)benzo[c][1,2,5]oxadiazol-4-yl)benzoic acid (**MS514**)

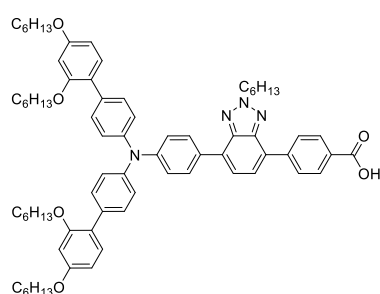


N-(2',4'-bis(hexyloxy)-[1,1'-biphenyl]-4-yl)-N-(4-bromophenyl)-2',4'-bis(hexyloxy)-[1,1'-biphenyl]-4-amine(**HDC6-Br**)(0.386 g, 0.419 mmoles, 1.5 eq.) was charged in a schlenk tube, dissolved in dry THF(3mL) and degassed three times with freeze-pump-thaw and liquid nitrogen before cooling down to -78°C with dry ice and acetone. Then, 1.6M n-Butyllithium in hexanes(0.55 mL, 0.866 mmoles, 3.1 eq.) was slowly added and the resulting solution was allowed to stir at -78°C for 4 hours before addition of 2-Isopropoxy-4,4,5,5-tetramethyl-1,3,2-dioxaborolane(0.220 g, 0.117 mmoles, 4.2 eq.). The resulting mixture was allowed to warm up to room temperature overnight. The reaction was quenched with 2M aqueous K_2CO_3 (0.75 mL, 1.45 mmoles, 5.2 eq.) followed by addition of Ethyl 4-(7-bromobenzo[c][1,2,5]oxadiazol-4-yl)benzoate (**4a**)(97 mg, 0.279 mmoles, 1 eq.). The resulting reaction mixture was degassed three times with freeze-pump-thaw and liquid nitrogen before adding Tris(dibenzylideneacetone)dipalladium(0)(20 mg, 22 μ mol, 0.08 eq.), 2-(Dicyclohexylphosphino)-2',4',6'-triisopropylbiphenyl(21 mg, 44 μ mol, 0.16 eq.) and subsequently heating at 80°C for 24hours. After cooling down to room temperature, the reaction was diluted with diethylether (20 mL) and flashed through a pad of $MgSO_4$. The solvents were removed under reduced pressure and the crude was purified by flash chromatography on SiO_2 eluting from 100% hexanes to 100% dichloromethane to recover the intermediate ester.

This latter was charged in a two necked round bottom flask equipped with a condenser along with 0.142 g of KOH and 10 mL of a THF:methanol (1:1, v:v) mixture. The reaction mixture was refluxed at 100°C under Argon for 24hours before addition of 1M H_3PO_4 (53 mL). The reaction mixture was diluted with water (50 mL) and the organics recovered by extraction with dichloromethane (3x30 mL) followed by drying over of $MgSO_4$. The crude was purified by flash chromatography on SiO_2 eluting from 100% DCM to 12% ethanol in DCM by volume. The target product was obtained after precipitation from cold methanol as a shiny red solid: 118 mg (80%). 1H NMR (400 MHz, Acetone) δ 8.21 – 8.02 (m, 4H), 8.02 – 7.91 (m, 2H), 7.88 (d, J = 7.4 Hz, 1H), 7.76 (d, J = 7.3 Hz, 1H), 7.51 – 7.33 (m, 4H), 7.22 – 7.01 (m, 8H), 6.53 – 6.38 (m, 4H), 3.89 (td, J = 6.4, 1.3 Hz, 8H), 1.71 – 1.55 (m, 9H), 1.34 (dtd, J = 15.3, 6.4, 5.4, 2.6 Hz, 5H), 1.23 (q, J = 3.5 Hz, 4H), 1.20 – 1.11 (m, 9H), 0.82 – 0.76 (m, 6H), 0.75 – 0.69 (m, 7H). ^{13}C NMR (101 MHz, Acetone) δ 205.40, 205.17, 166.32,

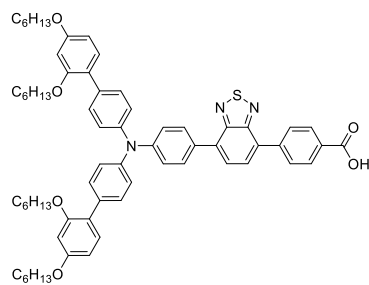
159.96, 157.09, 149.26, 149.16, 149.14, 145.12, 139.54, 134.49, 130.69, 130.67, 130.45, 130.08, 129.33, 128.96, 128.24, 127.76, 127.53, 125.90, 124.49, 122.45, 121.81, 105.83, 100.19, 68.11, 67.74, 31.47, 31.34, 25.68, 25.63, 22.41, 13.47, 13.43. HRMS (MALDI/TOF) m/z : $[M]^+$ Calcd for $C_{67}H_{77}N_3O_7^+$ 1035.5756; Found 1035.6650.

4-(7-(4-(bis(2',4'-bis(hexyloxy)-[1,1'-biphenyl]-4-yl)amino)phenyl)-2-hexyl-2H-benzo[d][1,2,3]triazol-4-yl)benzoic acid (**MS15**)



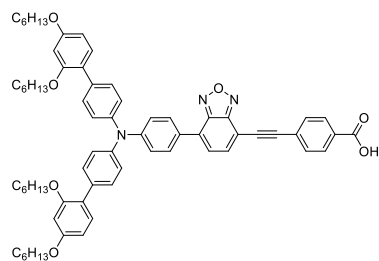
The same procedure as for (**MS14**) was used, with 0.120 g of Ethyl 4-(7-bromo-2-hexyl-2H-benzo[d][1,2,3]triazol-4-yl)benzoate (**4b**) instead of (**4a**). The target product was obtained as a green glassy solid: 0.052 g (64%). 1H NMR (400 MHz, Acetone) δ 8.33 – 8.22 (m, 2H), 8.18 (d, J = 8.2 Hz, 2H), 8.16 – 8.07 (m, 2H), 7.79 – 7.70 (m, 1H), 7.68 (d, J = 7.6 Hz, 1H), 7.52 – 7.45 (m, 4H), 7.26 – 7.08 (m, 8H), 6.60 (d, J = 2.4 Hz, 2H), 6.51 (dt, J = 8.9, 2.8 Hz, 2H), 4.78 (q, J = 6.3, 5.5 Hz, 2H), 3.97 (t, J = 6.1 Hz, 8H), 2.17 – 2.03 (m, 3H), 1.84 – 1.64 (m, 8H), 1.53 – 1.22 (m, 30H), 0.96 – 0.87 (m, 6H), 0.87 – 0.78 (m, 9H). ^{13}C NMR (101 MHz, Acetone) δ 205.31, 205.31, 205.29, 166.69, 159.81, 157.04, 147.94, 145.46, 143.33, 143.29, 141.60, 133.82, 133.80, 130.69, 130.52, 130.31, 129.83, 129.60, 129.42, 128.28, 127.52, 127.50, 125.28, 123.98, 123.34, 122.62, 122.55, 105.67, 100.20, 68.08, 67.71, 56.51, 31.52, 31.35, 31.17, 31.04, 29.84, 29.55, 29.35, 29.22, 29.16, 29.03, 28.97, 28.78, 28.58, 28.39, 26.08, 25.67, 22.44, 22.41, 22.27, 13.53, 13.49, 13.41. HRMS (MALDI/TOF) m/z : $[M]^+$ Calcd for $C_{73}H_{90}N_4O_6^+$ 1118.6855; Found 1118.7257.

4-(7-(4-(bis(2',4'-bis(hexyloxy)-[1,1'-biphenyl]-4-yl)amino)phenyl)benzo[c][1,2,5]thiadiazol-4-yl)benzoic acid (**MS4**)



The same procedure as for (**MS14**) was used, with 73 mg g of Ethyl 4-(7-bromobenzo[c][1,2,5]thiadiazol-4-yl)benzoate (**4c**) instead of (**4a**). The target product was obtained as a green glassy solid: 0.094 g (45%). 1H NMR (400 MHz, Acetone) δ 8.33 – 8.22 (m, 2H), 8.18 (d, J = 8.2 Hz, 2H), 8.16 – 8.07 (m, 2H), 7.79 – 7.70 (m, 1H), 7.68 (d, J = 7.6 Hz, 1H), 7.52 – 7.45 (m, 4H), 7.26 – 7.08 (m, 8H), 6.60 (d, J = 2.4 Hz, 2H), 6.51 (dt, J = 8.9, 2.8 Hz, 2H), 4.78 (q, J = 6.3, 5.5 Hz, 2H), 3.97 (t, J = 6.1 Hz, 8H), 2.17 – 2.03 (m, 3H), 1.84 – 1.64 (m, 8H), 1.53 – 1.22 (m, 30H), 0.96 – 0.87 (m, 6H), 0.87 – 0.78 (m, 9H). ^{13}C NMR (101 MHz, Acetone) δ 205.31, 205.31, 205.29, 166.69, 159.81, 157.04, 147.94, 145.46, 143.33, 143.29, 141.60, 133.82, 133.80, 130.69, 130.52, 130.31, 129.83, 129.60, 129.42, 128.28, 127.52, 127.50, 125.28, 123.98, 123.34, 122.62, 122.55, 105.67, 100.20, 68.08, 67.71, 56.51, 31.52, 31.35, 31.17, 31.04, 29.84, 29.55, 29.35, 29.22, 29.16, 29.03, 28.97, 28.78, 28.58, 28.39, 26.08, 25.67, 22.44, 22.41, 22.27, 13.53, 13.49, 13.41. HRMS (MALDI/TOF) m/z : $[M]^+$ Calcd for $C_{73}H_{90}N_4O_6^+$ 1118.6855; Found 1118.7257.

4-((7-(4-(bis(2',4'-bis(hexyloxy)-[1,1'-biphenyl]-4-yl)amino)phenyl)benzo[c][1,2,5]oxadiazol-4-yl)ethynyl)benzoic acid(**MS13**)

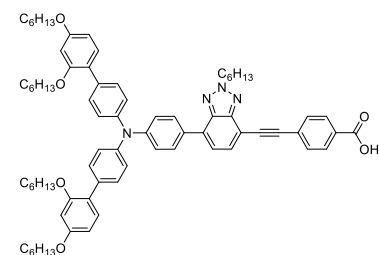


The same procedure as for (**MS14**) was used, with 93 mg of methyl 4-((7-bromobenzo[c][1,2,5]oxadiazol-4-

yl)ethynyl)benzoate (**5a**) instead of (**4a**). The target product was obtained as a green glassy solid: 117 mg (83%). ¹H NMR (400 MHz, Acetone) δ 7.99 (d, J = 8.3 Hz, 2H), 7.97 – 7.91 (m, 2H), 7.75 – 7.60 (m, 4H), 7.45 – 7.36 (m, 4H), 7.14 (d, J = 8.4 Hz, 2H), 7.07 (dd, J = 8.8, 2.6 Hz, 6H), 6.50 (d, J = 2.3 Hz, 2H),

6.46 (d, J = 2.4 Hz, 1H), 6.44 (d, J = 2.4 Hz, 1H), 3.96 – 3.81 (m, 8H), 1.69 – 1.54 (m, 7H), 1.41 – 1.27 (m, 10H), 1.23 (q, J = 3.4 Hz, 5H), 1.17 (dt, J = 6.7, 3.2 Hz, 9H), 0.82 – 0.75 (m, 7H), 0.72 (q, J = 5.4, 3.9 Hz, 7H). ¹³C NMR (101 MHz, Acetone) δ 206.17, 166.89, 160.87, 157.98, 151.19, 150.32, 149.38, 145.86, 137.39, 135.55, 132.64, 131.85, 131.60, 131.36, 130.83, 130.77, 130.27, 128.17, 127.71, 127.56, 125.53, 123.30, 122.40, 109.66, 106.71, 101.08, 96.46, 87.33, 69.01, 68.64, 32.38, 32.24, 30.42, 30.22, 30.03, 29.84, 29.65, 29.46, 29.26, 26.57, 26.52, 23.31, 14.36, 14.33. HRMS (MALDI/TOF) m/z: [M]⁺ Calcd for C₆₉H₇₇N₃O₇⁺ 1059.5756; Found 1059.6643.

4-((7-(4-(bis(2',4'-bis(hexyloxy)-[1,1'-biphenyl]-4-yl)amino)phenyl)-2-hexyl-2H-benzo[d][1,2,3]triazol-4-yl)ethynyl)benzoic acid(**MS16**)



The same procedure as for (**MS14**) was used, with 63 mg of Methyl 4-((7-bromo-2-hexyl-2H-benzo[d][1,2,3]triazol-4-

yl)ethynyl)benzoate(**5b**) instead of (**4a**). The target product was obtained as a green glassy solid: 31 mg (28%). ¹H NMR (400 MHz, Acetone) δ 8.17 – 8.09 (m, 5H), 7.76 (d, J = 8.3 Hz, 2H), 7.67 (q, J = 7.6 Hz, 2H), 7.55 – 7.48 (m, 5H), 7.24 (d, J = 8.4 Hz, 2H), 7.23 – 7.13 (m, 7H), 6.62 (d, J = 2.4 Hz, 2H), 6.55 (dd, J = 8.5, 2.3 Hz, 2H), 4.81 (t, J = 7.2 Hz, 2H), 4.04 – 3.96 (m, 9H), 2.13 (q, J = 7.2 Hz, 2H), 1.83 – 1.67 (m, 9H), 1.47 (ddd, J = 20.8, 9.8, 4.4 Hz, 4H), 1.45 – 1.31 (m, 9H), 1.30 (dp, J = 7.2, 3.4 Hz, 12H), 0.93 (d, J = 6.9 Hz, 5H), 0.92 – 0.78 (m, 11H). ¹³C NMR (101 MHz, Acetone) δ

205.50, 205.33, 205.32, 205.31, 205.30, 205.29, 205.28, 205.27, 205.27, 205.10, 166.13, 159.86, 157.06, 148.29, 145.36, 145.21, 142.31, 134.03, 131.69, 131.53, 131.01, 130.69, 130.35, 130.33, 129.82, 129.79, 129.46, 127.68, 124.14, 122.68, 122.53, 122.33, 110.52, 105.73, 100.20, 93.40, 88.79, 68.09, 67.73, 56.61, 31.51, 31.35, 31.05, 30.89, 30.81, 29.86, 29.72, 29.54, 29.35, 29.21, 29.15, 29.03, 28.96, 28.77, 28.58, 28.38, 26.07, 25.67, 25.65, 22.44, 22.41, 22.26, 13.51, 13.47, 13.40. HRMS (MALDI/TOF) m/z: [M]⁺ Calcd for C₇₅H₉₀N₄O₆⁺ 1142.6855; Found 1142.6753.

Optical characterization

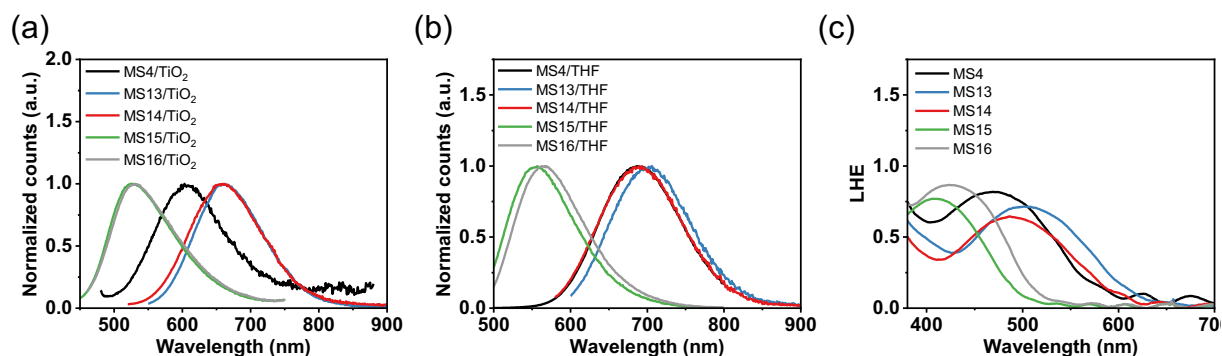


Figure 0.77. (a) Normalized emission spectra of the dyes adsorbed on 4 μm thick TiO_2 films. Normalized emission spectra of the dyes in diluted THF solutions (b). (c) Light harvesting efficiency (LHE) calculated using: $\text{LHE}=1-10^{-A}$, with A being the absorbance of the sensitized films.

Electrochemical characterization

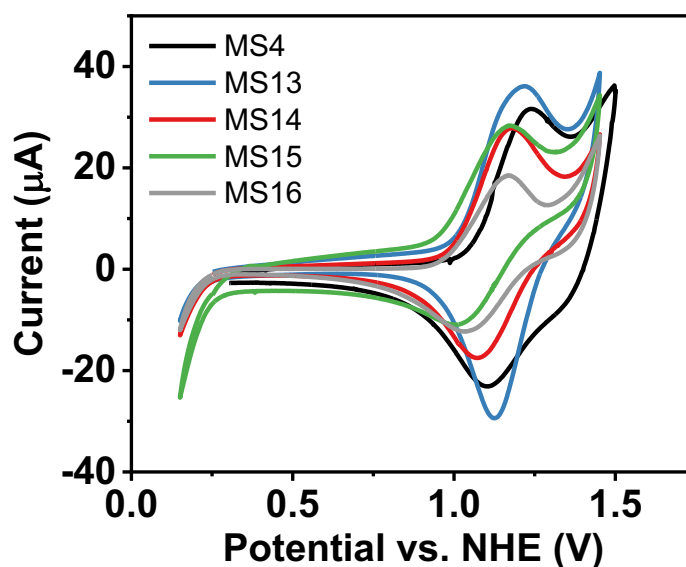
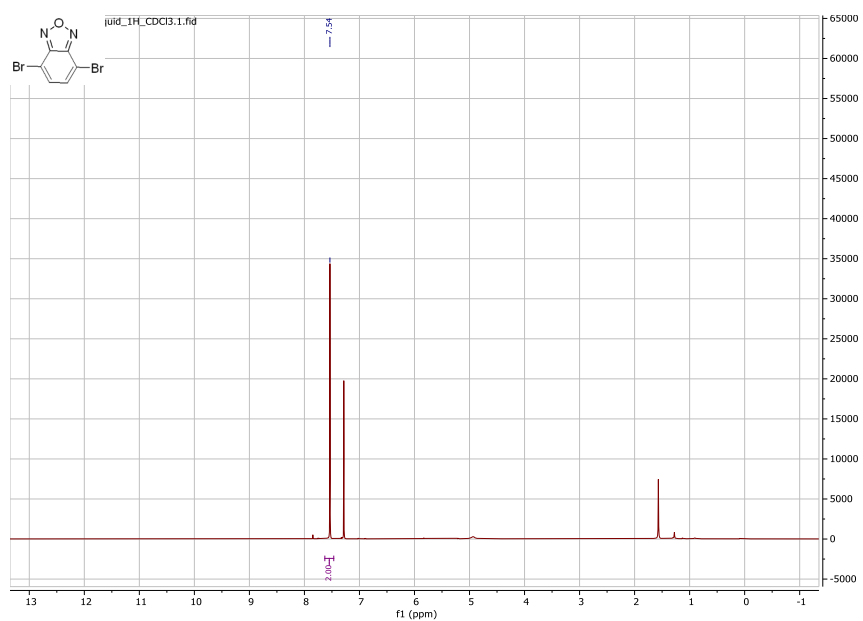
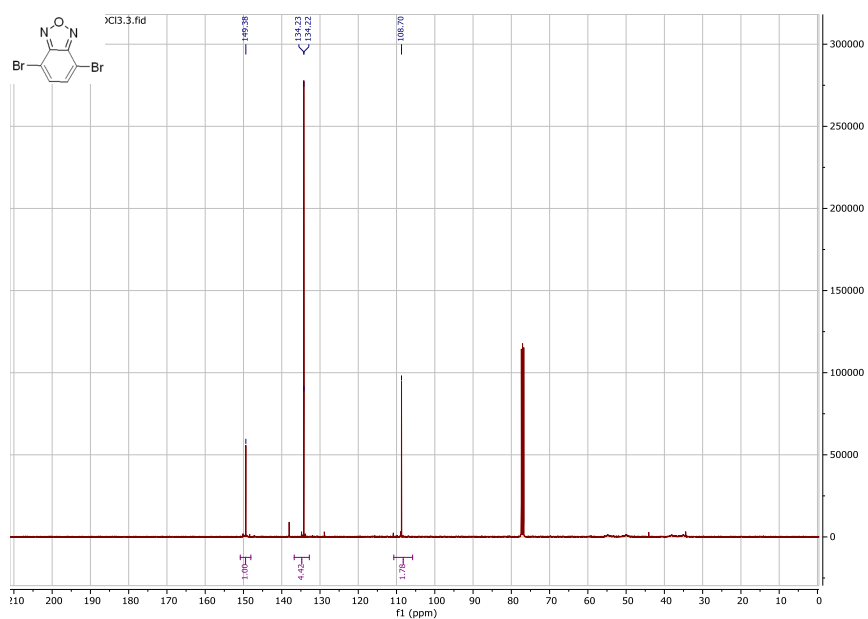


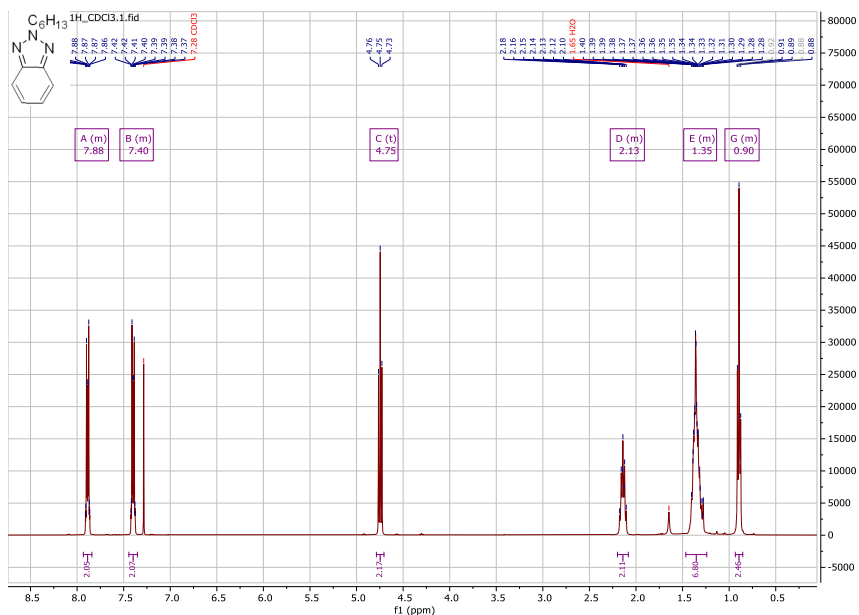
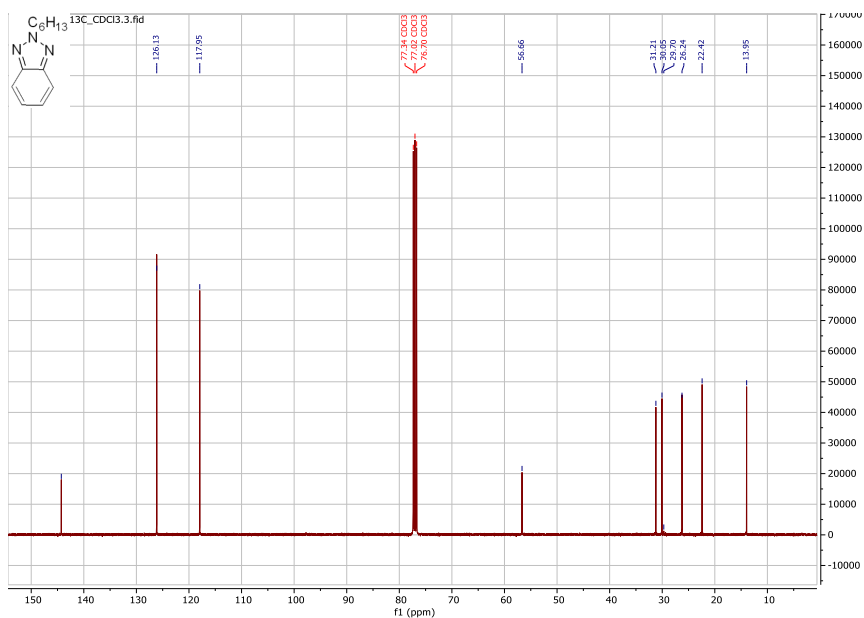
Figure 0.78. Cyclic voltammograms of the dyes adsorbed on a transparent TiO_2 film.

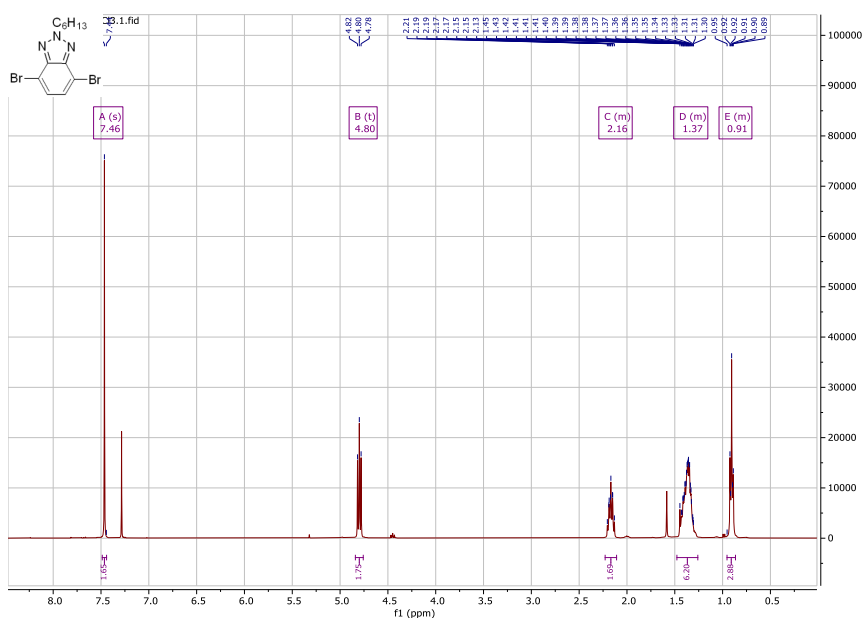
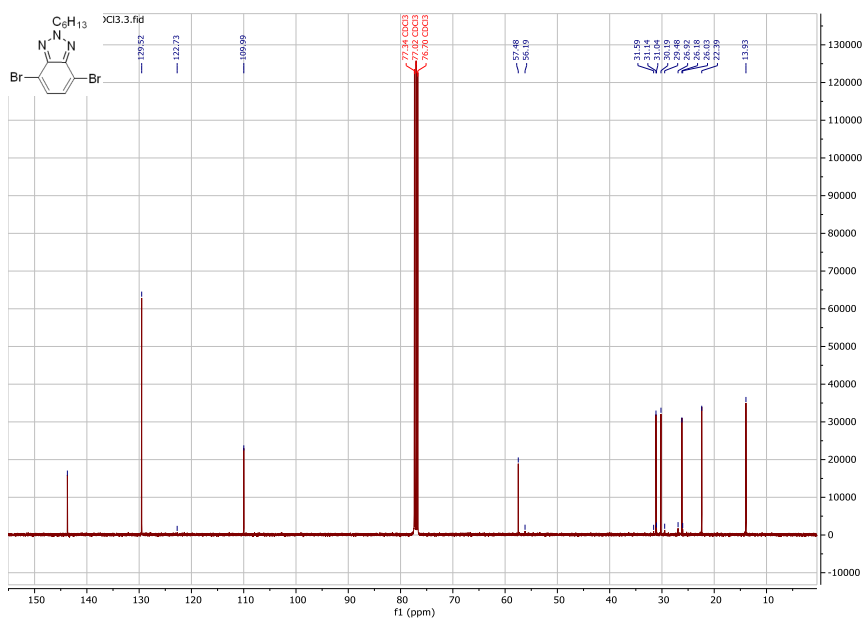
Computational calculations

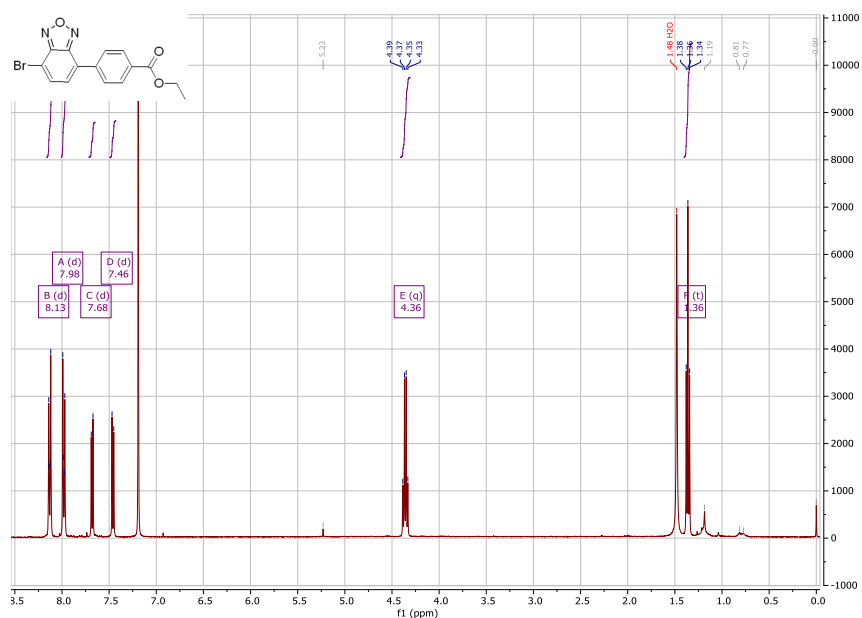
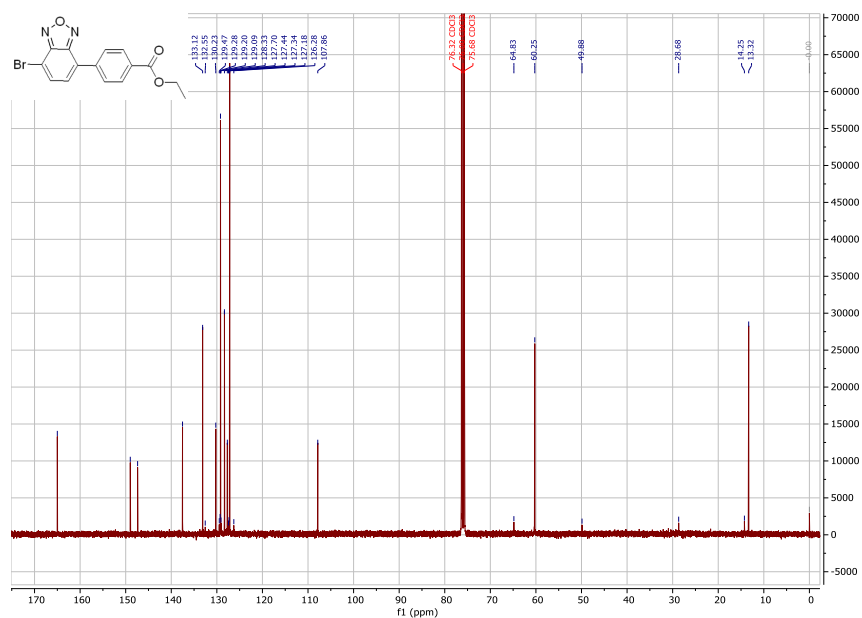
Table 0.9. The calculated energy levels of HOMO and LUMO orbitals of MS dyes using Gaussian09 with B3PW91 functional and 6-31G(d,p) basis sets.

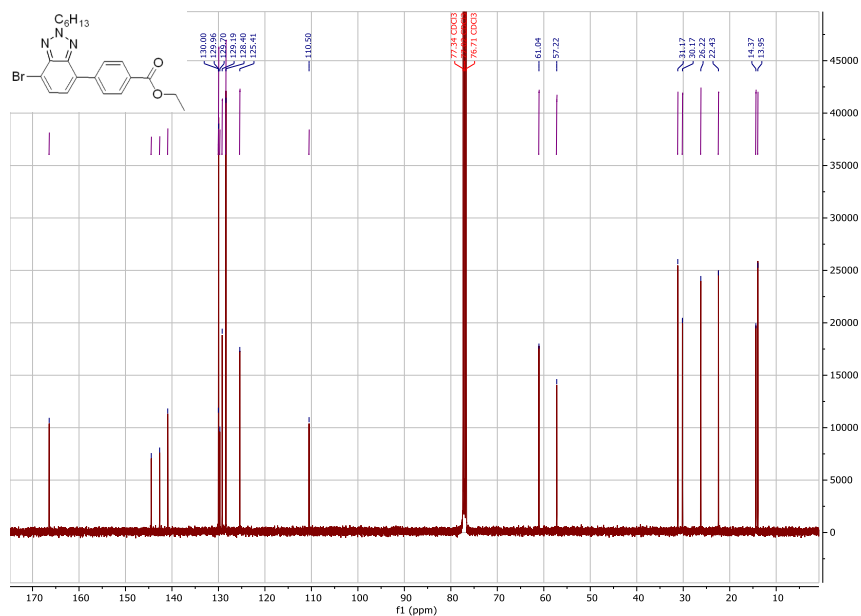
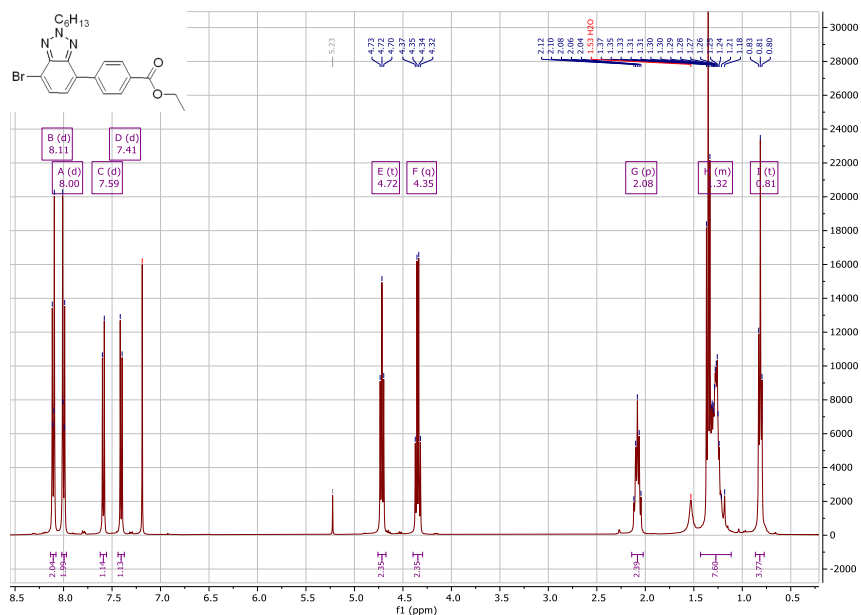
	HOMO [eV]	LUMO [eV]	E_g [eV]
MS4	-4.79	-2.50	2.29
MS13	-4.88	-2.79	2.09
MS14	-4.88	-2.68	2.20
MS15	-4.72	-2.21	2.51
MS16	-4.71	-1.96	2.75

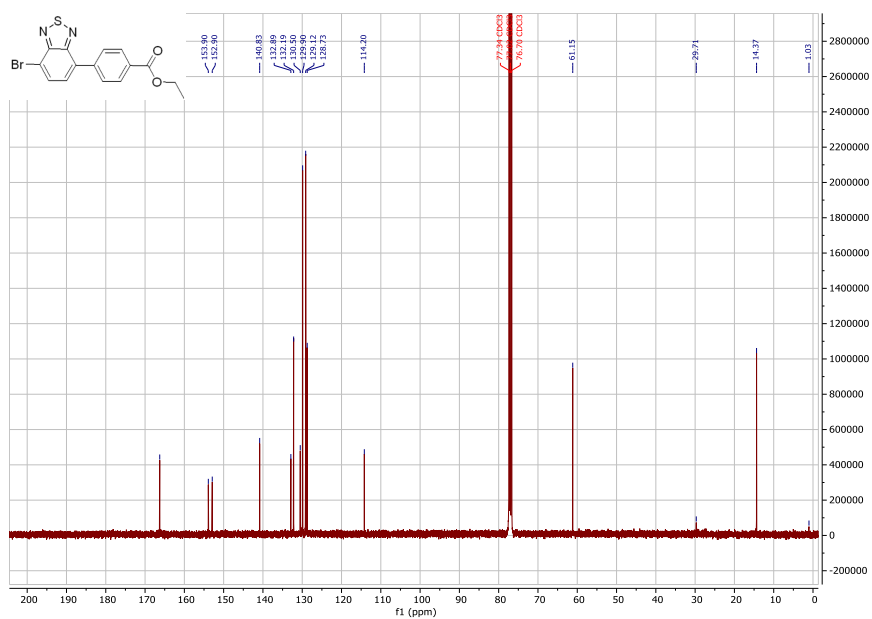
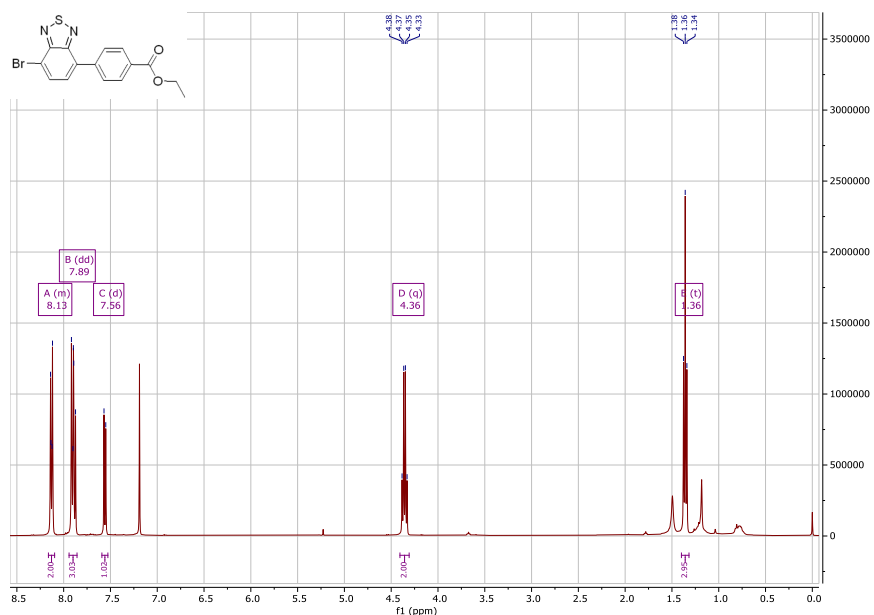
^1H and ^{13}C NMR spectra**Figure 0.79.** ^1H NMR of **1** in CDCl_3 .**Figure 0.80.** ^{13}C NMR of **1** in CDCl_3 .

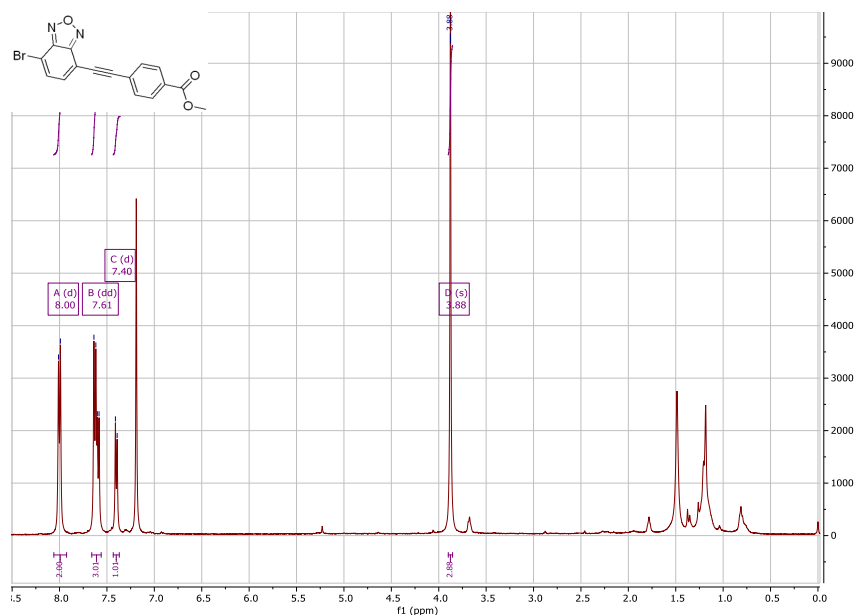
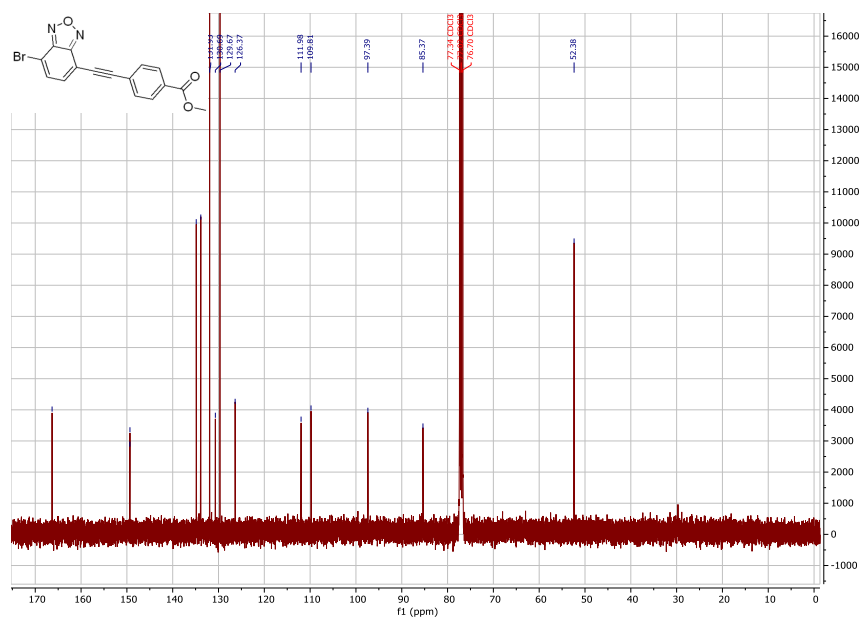
Figure 0.81. ¹H NMR of 2 in CDCl₃.Figure 0.82. ¹³C NMR of 2 in CDCl₃.

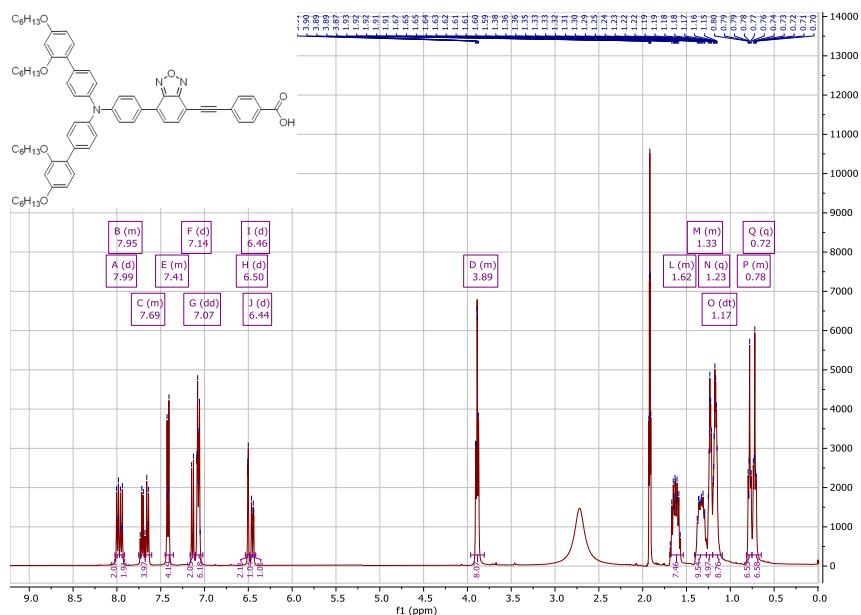
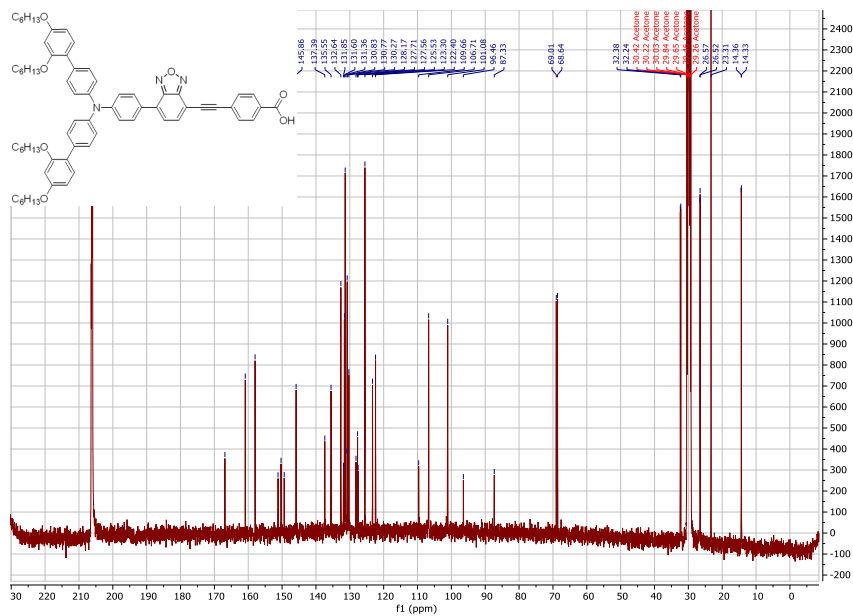
Figure 0.83. ¹H NMR of 3 in CDCl₃.Figure 0.84. ¹³C NMR of 3 in CDCl₃.

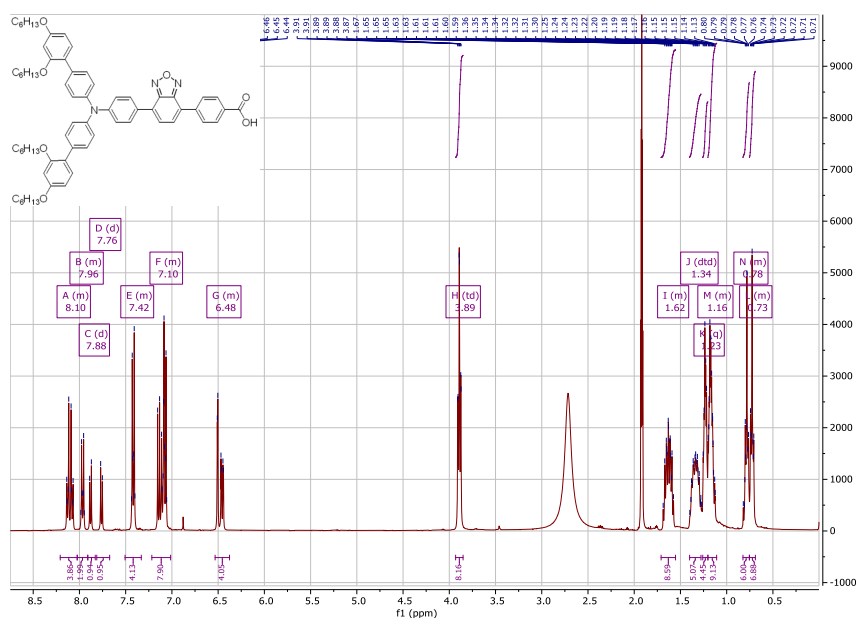
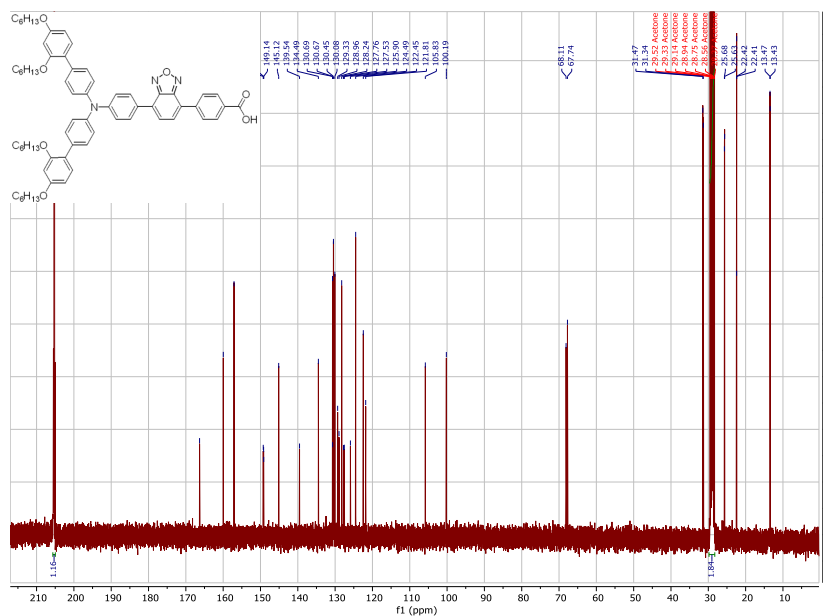
Figure 0.85. ¹H NMR of 4a in CDCl₃.Figure 0.86. ¹³C NMR of 4a in CDCl₃.





Figure 0.91. ¹H NMR of 5a in CDCl₃.Figure 0.92. ¹³C NMR of 5a in CDCl₃.

Figure 0.93. ¹H NMR of MS13 in Acetone-d₆.Figure 0.94. ¹³C NMR of MS13 in Acetone-d₆.

Figure 0.95. ^1H NMR of MS14 in Acetone- d_6 .Figure 0.96. ^{13}C NMR of MS14 in Acetone- d_6 .

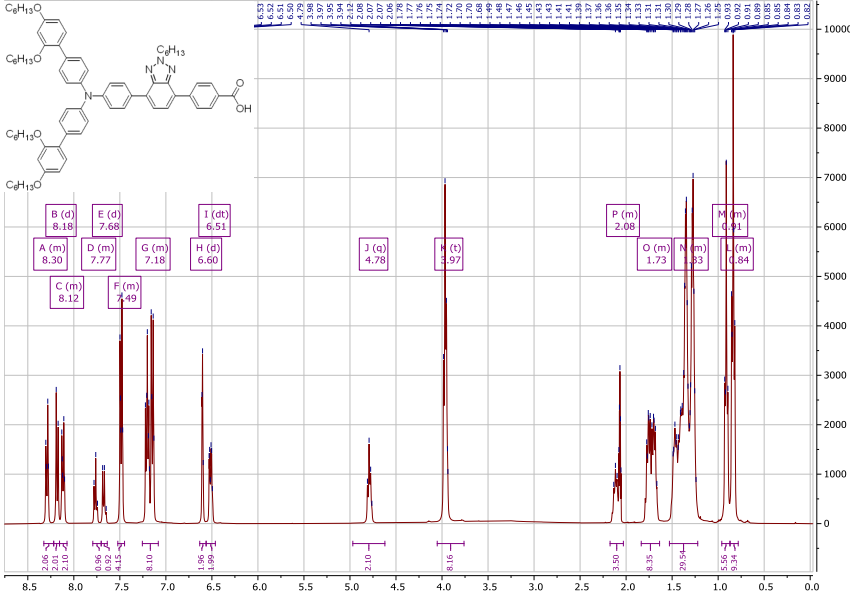


Figure 0.97. ^1H NMR of MS15 in Acetone- d_6 .

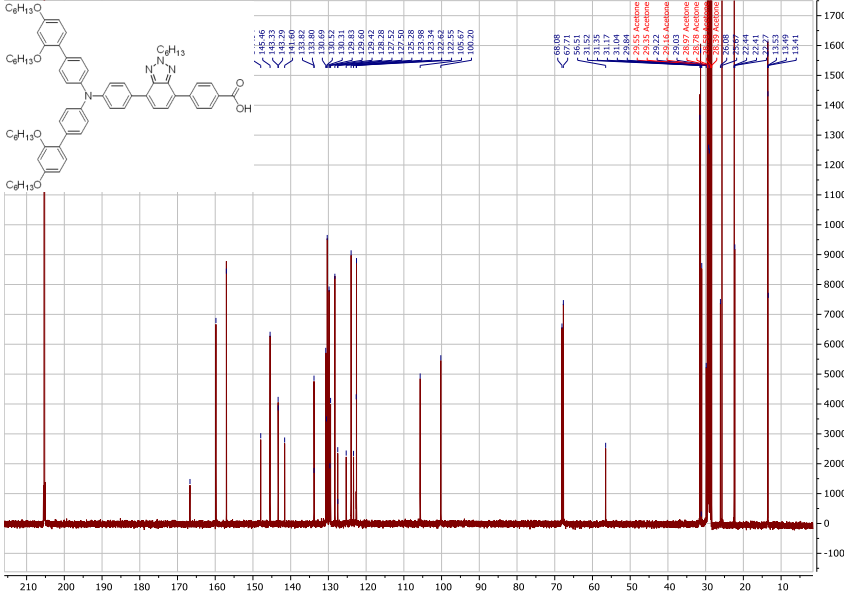
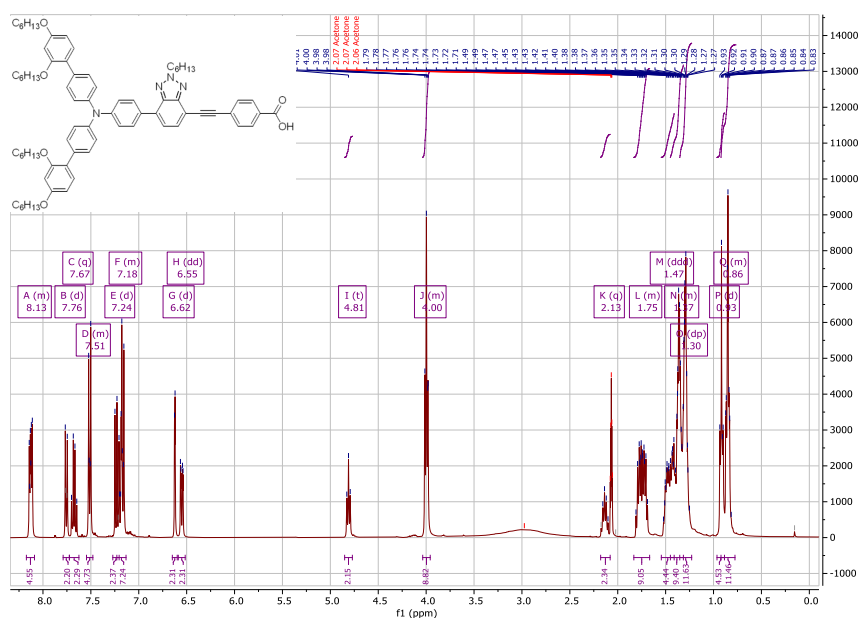
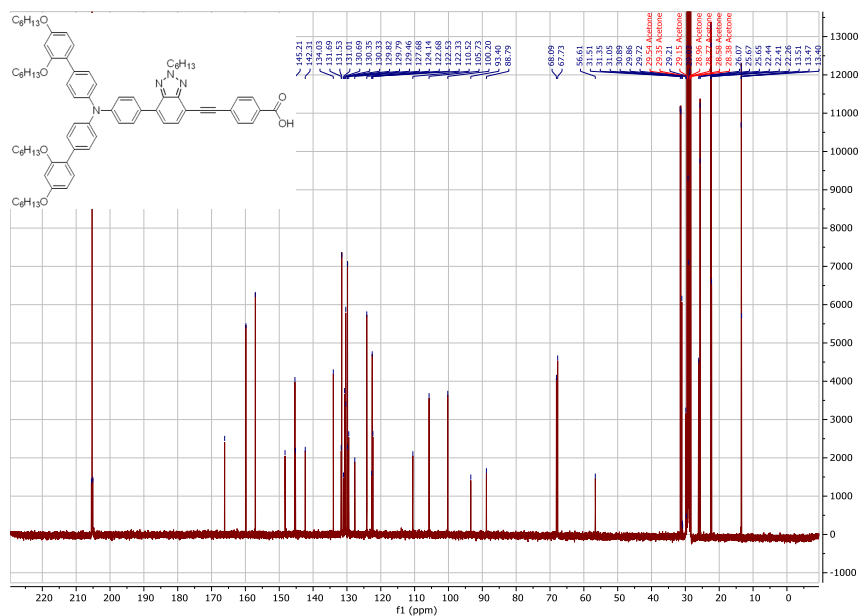


Figure 0.98. ^{13}C NMR of MS15 in Acetone- d_6 .

Figure 0.99. ¹H NMR of MS16 in Acetone-d₆.Figure 0.100. ¹³C NMR of MS16 in Acetone-d₆.

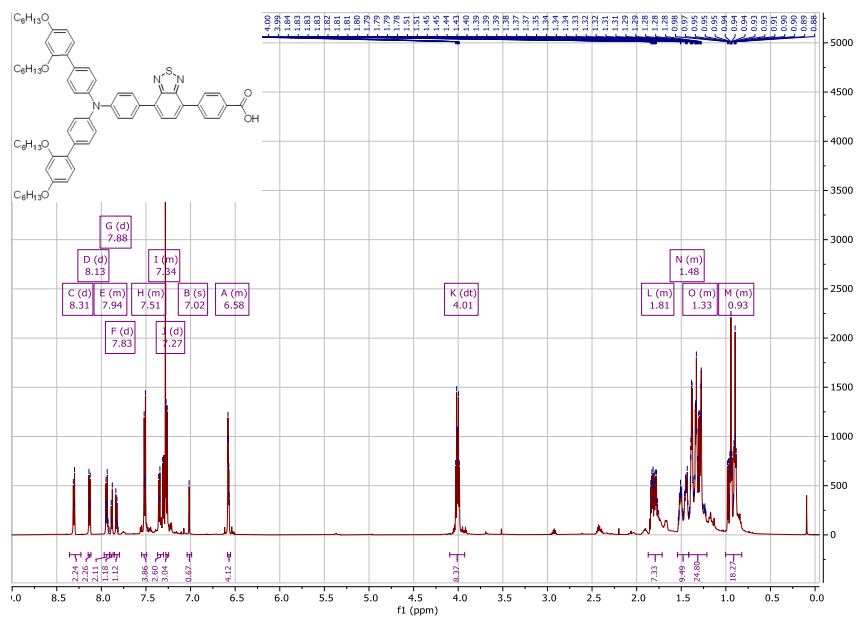


Figure 0.101. ^1H NMR of MS4 in Acetone- d_6 .

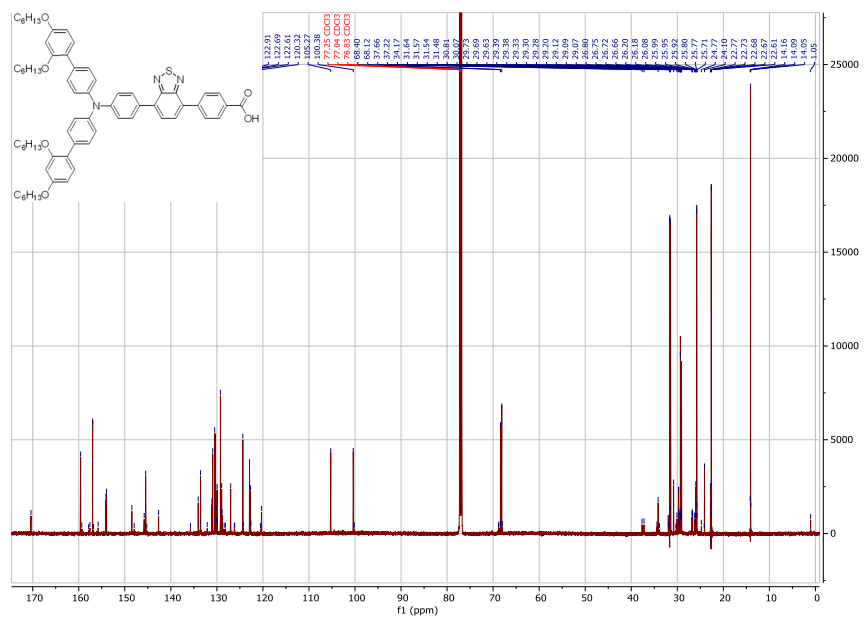
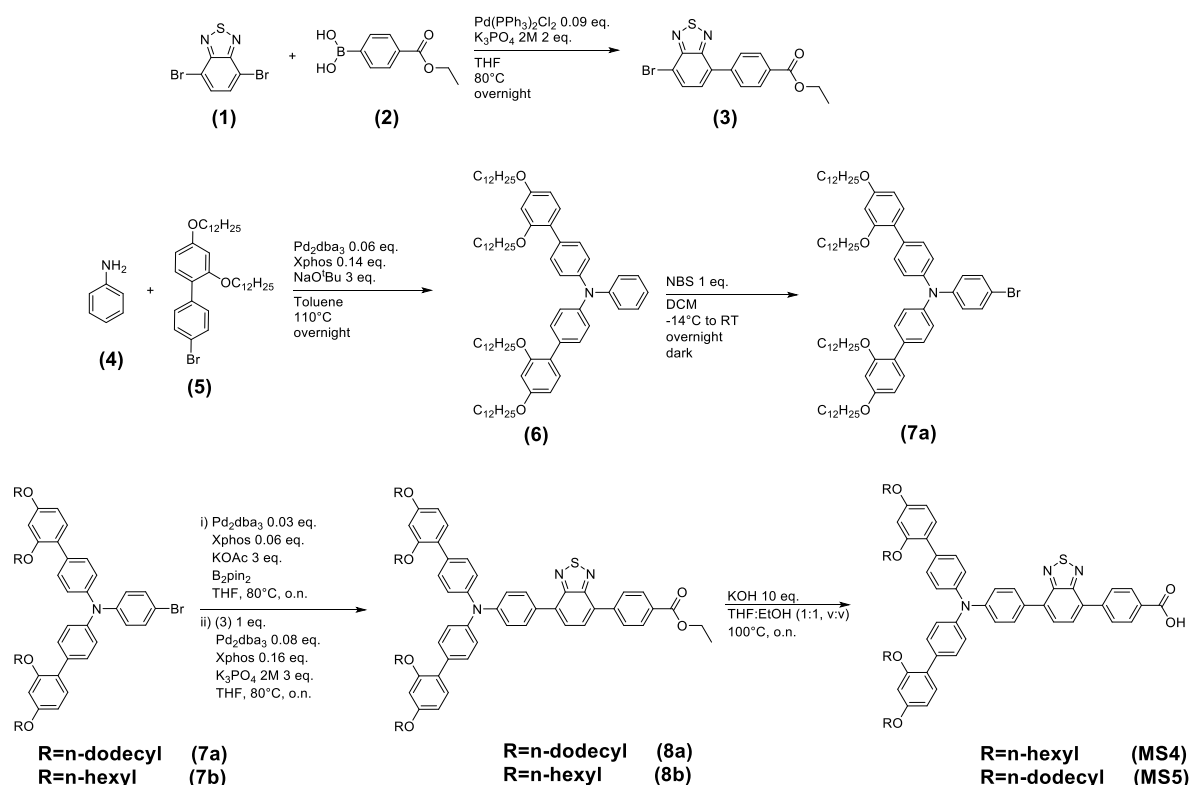


Figure 0.102. ^{13}C NMR of MS4 in Acetone- d_6 .

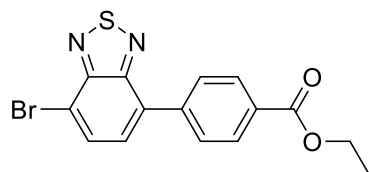
Supporting information to Chapter 7

Synthetic procedure

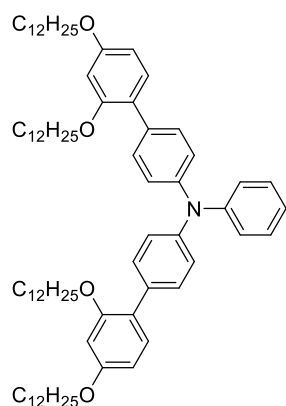
Acetonitrile (ABCR), tetrahydrofuran (THF) (ABCR), chloroform (CF) (ABCR), tert-butanol (Sigma-Aldrich), ethanol (EtOH) (Acros), 1-methylbenzimidazole (TCI), chenodeoxycholic acid (TCI), lithium bis(trifluoromethanesulfonyl)imide (LiTFSI) (TCI), methanol (Sigma), dichloromethane (DCM, Thommen-Furler), hexanes (VWR International SA), diethyl ether (HUBERLAB AG), hydrochloric acid (VWR International SA), potassium phosphate tribasic (Acros), magnesium sulfate (Reactolab), sodium tert-butoxide (ABCR), potassium hydroxide (MERCK), acetic acid/potassium salt (Sigma), bis(pinacolato)diboron (Fluorochem), Aniline (Sigma), N-bromosuccinimide (NBS, TCI), 4,7-dibromo-2,1,3-benzothiadiazole (Combi-Blocks, Inc.), 4-ethoxycarbonylphenylboronic acid (Fluorochem), 2-(dicyclohexylphosphino)-2',4',6'-triisopropylbiphenyl (Fluorochem), bis(triphenylphosphine)palladium(II) chloride (Fluorochem), tris(dibenzylideneacetone)dipalladium(0) (Sigma), and tris(dibenzylideneacetone)dipalladium(0) (Sigma) were used as received without further purification. Anhydrous THF and Toluene were purchased over molecular sieves from Acros Organics. The solvents used for palladium catalyzed cross coupling reactions were degassed three times using the freeze-pump-thaw method and liquid nitrogen.



Scheme 0.6. Synthetic route to MS4 and MS5.

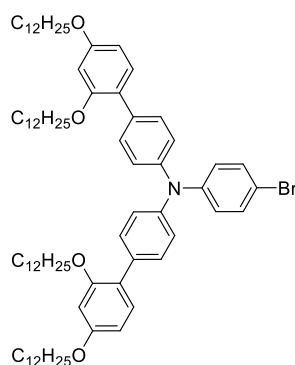
Ethyl 4-(7-bromobenzo[c][1,2,5]thiadiazol-4-yl)benzoate(**3**)

4-ethoxycarbonylphenylboronic acid(**1**) (550 mg, 2.83 mmoles, 1 eq.), 4,7-dibromo-2,1,3-benzothiadiazole(**2**) (1 g, 3.4 mmoles, 1.2 eq.) and potassium phosphate tribasic (2M, 2.83 mL, 5.67 mmoles, 2 eq.) were charged in a schlenk tube with 5 mL anhydrous THF and degassed three times. Then bis(triphenylphosphine)palladium(II) chloride (179 mg, 255 μ mol, 0.09 eq.) was added and the reaction mixture was refluxed at 80°C overnight under Argon atmosphere. After cooling down to room temperature, the solution was diluted twice with diethyl ether and flashed through a pad of magnesium sulfate. The solvents were removed, and the crude purified by Silica gel flash chromatography eluting with hexanes to 30% hexanes in DCM. The desired product was obtained as a yellow fluffy solid (0.132 g, 13%). ^1H NMR (400 MHz, CDCl_3) δ 8.16 – 8.10 (m, 2H), 7.89 (dd, J = 9.6, 7.9 Hz, 3H), 7.56 (d, J = 7.5 Hz, 1H), 4.36 (q, J = 7.1 Hz, 2H), 1.36 (t, J = 7.1 Hz, 3H). ^{13}C NMR (101 MHz, CDCl_3) δ 166.27, 153.90, 152.90, 140.83, 132.89, 132.19, 130.50, 129.90, 129.12, 128.73, 114.20, 77.34, 77.23, 77.02, 76.71, 61.15, 29.71, 14.37, 1.03. HRMS (APPI/LTQ-Orbitrap) m/z : $[\text{M}]^+$ Calcd for $\text{C}_{15}\text{H}_{11}\text{BrN}_2\text{O}_2\text{S}^+$ 361.9719; Found 361.9724.

N-(2',4'-bis(dodecyloxy)-[1,1'-biphenyl]-4-yl)-2',4'-bis(dodecyloxy)-N-phenyl-[1,1'-biphenyl]-4-amine(**6**)

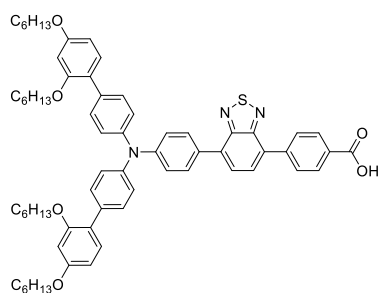
Aniline(**4**) (121 μ L, 1.33 mmoles, 1 eq.), 4'-bromo-2,4-bis(dodecyloxy)-1,1'-biphenyl (**2**) (2 g, 3.32 mmoles, 2.5 eq.) and sodium tert-butoxide (319 mg, 3.32 mmoles, 2.5 eq.) were charged in a schlenk tube along with 13 mL anhydrous Toluene and degassed three times. Then, tris(dibenzylideneacetone)dipalladium(0) (73 mg, 79.8 μ mol, 0.06 eq.) and 2-(dicyclohexylphosphino)-2',4',6'-triisopropylbiphenyl (88.7 mg, 186 μ mol, 0.14 eq.) were added before refluxing the mixture at 110°C overnight under Argon atmosphere. After cooling down to room temperature, the solution was diluted twice with diethyl ether and flashed through a pad of Celite. The solvents were removed and the residue purified with Silica gel chromatography eluting with hexanes to 50% dichloromethane in hexanes. The desired compound was obtained as a transparent wax (1.3 g, 86%). ^1H NMR (400 MHz, Acetone) δ 7.38 – 7.31 (m, 4H), 7.21 – 7.09 (m, 5H), 7.03 – 6.86 (m, 8H), 6.52 – 6.41 (m, 4H), 3.88 (q, J = 6.3 Hz, 8H), 1.71 – 1.55 (m, 8H), 1.44 – 1.05 (m, 23H), 0.73 (dt, J = 9.8, 6.8 Hz, 12H). ^{13}C NMR (101 MHz, Acetone) δ 205.39, 205.22, 205.21, 205.19, 205.17, 205.00, 159.81, 157.06, 147.96, 145.95, 133.27, 130.56, 130.18, 129.26, 123.97, 123.24, 122.67, 122.64, 105.80, 100.22, 68.07, 67.71, 31.76, 29.57, 29.55, 29.52, 29.49, 29.48, 29.46, 29.38, 29.32, 29.24, 29.22, 29.20, 29.18, 29.13, 29.10, 29.09, 28.99, 28.94, 28.88, 28.75, 28.55, 28.36, 26.05, 25.93, 22.46, 22.45, 13.51, 13.48. HRMS (nanochip-ESI/LTQ-Orbitrap) m/z : $[\text{M}]^+$ Calcd for $\text{C}_{78}\text{H}_{119}\text{NO}_4^+$ 1133.9134; Found 1133.9169.

N-(2',4'-bis(dodecyloxy)-[1,1'-biphenyl]-4-yl)-N-(4-bromophenyl)-2',4'-bis(dodecyloxy)-[1,1'-biphenyl]-4-amine(7)



N-(2',4'-bis(dodecyloxy)-[1,1'-biphenyl]-4-yl)-2',4'-bis(dodecyloxy)-N-phenyl-[1,1'-biphenyl]-4-amine(6) (1.26 g, 1.11 mmol, 1 eq.) was dissolved in 15 mL dichloromethane, protected from light and cooled down to -14°C . Then, NBS (198 mg, 1.11 mmol, 1 eq.) was added and the mixture allowed to warm up to room temperature overnight. The solvent was removed and hexanes was added to the crude to induce the formation of a white solid which was removed and discarded. Hexanes was removed and the desired product was obtained as a transparent wax and used for the next step without further purification.

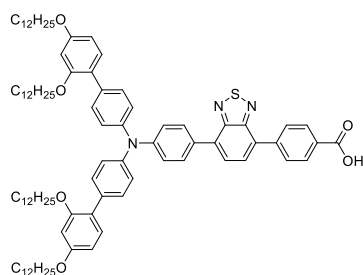
4-(7-(4-(bis(2',4'-bis(hexyloxy)-[1,1'-biphenyl]-4-yl)amino)phenyl)benzo[c][1,2,5]thiadiazol-4-yl)benzoic acid(MS4)



N-(2',4'-bis(hexyloxy)-[1,1'-biphenyl]-4-yl)-N-(4-bromophenyl)-2',4'-bis(hexyloxy)-[1,1'-biphenyl]-4-amine(7b) (450 mg, 513 μmol , 1 eq.), acetic acidpotassium salt (151 mg, 1.54 mmol, 3 eq.) and bis(pinacolato)diboron (261 mg, 1.03 mmol, 2 eq.) were charged in a schlenk tube with 5 mL anhydrous THF and degassed three times. Then tris(dibenzylideneacetone)dipalladium(0) (14.1 mg, 15.4 μmol , 0.03 eq.) and 2-(dicyclohexylphosphino)-2',4',6'-triisopropylbiphenyl (14.7 mg, 30.8 μmol , 0.06 eq.) were added and the reaction mixture refluxed at 80°C overnight under Argon atmosphere. After cooling down to room temperature, the solution was diluted twice with diethyl ether and flashed through a thin pad of Celite. The solvents were removed and 20 mL Ethanol was added to the residue to afford N-(2',4'-bis(hexyloxy)-[1,1'-biphenyl]-4-yl)-2',4'-bis(hexyloxy)-N-(4-(4,4,5,5-tetramethyl-1,3,2-dioxaborolan-2-yl)phenyl)-[1,1'-biphenyl]-4-amine as a beige wax, which was used for the next step without further purification. N-(2',4'-bis(hexyloxy)-[1,1'-biphenyl]-4-yl)-2',4'-bis(hexyloxy)-N-(4-(4,4,5,5-tetramethyl-1,3,2-dioxaborolan-2-yl)phenyl)-[1,1'-biphenyl]-4-amine (185 mg, 200 μmol , 1 eq.), ethyl 4-(7-bromobenzo[c][1,2,5]thiadiazol-4-yl)benzoate (72.7 mg, 200 μmol , 1 eq.) and potassium phosphate tribasic (2M, 413 μL , 826 μmol , 4.13 eq.) and 5 mL anhydrous THF were charged in a schlenk tube and degassed three times. Then tris(dibenzylideneacetone)dipalladium(0) (14.7 mg, 16 μmol , 0.08 eq.) and 2-(dicyclohexylphosphino)-2',4',6'-triisopropylbiphenyl (15.3 mg, 32 μmol , 0.16 eq.) were added and the reaction mixture was refluxed at 80°C overnight under Argon atmosphere. After cooling down to room temperature, the solution was diluted twice with diethyl ether and flashed through a pad of magnesium sulfate. The solvents were removed and the residue was taken to the next step without further purification. The crude was (216 mg, 200 μmol , 1 eq.) and potassium hydroxide (112 mg, 2 mmol, 10 eq.) were dissolved in 10 mL of a THF:Ethanol(1:1, v:v) mixture along with 5 drops of deionized water. The resulting reaction mixture was then refluxed at 100°C under Argon atmosphere overnight. After cooling down to room temperature, the reaction was quenched with 30 mL 1M hydrochloric acid and charged into a separation funnel. The organics were extracted using dichloromethane (3x10 mL) before drying over magnesium

sulfate and removing the solvent. The crude was purified using Silica gel flash chromatography eluting with dichloromethane and then 5% methanol in dichloromethane and 5 drops of acetic acid. The final product was finally washed with methanol and obtained as a shiny red solid (94 mg, 45%). ^1H NMR (600 MHz, CDCl_3) δ 8.31 (d, J = 8.3 Hz, 2H), 8.13 (d, J = 8.3 Hz, 2H), 7.97 – 7.91 (m, 2H), 7.88 (d, J = 7.4 Hz, 1H), 7.83 (d, J = 7.4 Hz, 1H), 7.53 – 7.48 (m, 4H), 7.37 – 7.32 (m, 2H), 7.31 (d, J = 9.0 Hz, 2H), 7.28 – 7.25 (m, 4H), 6.58 (dq, J = 5.6, 2.4 Hz, 4H), 4.01 (dt, J = 11.8, 6.6 Hz, 8H), 1.86 – 1.76 (m, 8H), 1.56 – 1.22 (m, 32H), 0.96 – 0.92 (m, 6H), 0.92 – 0.87 (m, 9H). ^{13}C NMR (151 MHz, CDCl_3) δ 170.49, 159.71, 159.44, 157.69, 157.10, 155.89, 154.20, 154.08, 148.59, 148.07, 145.90, 145.59, 142.78, 135.86, 134.17, 133.71, 133.67, 132.22, 131.20, 131.02, 130.60, 130.44, 130.26, 130.16, 130.08, 129.35, 129.09, 128.99, 127.12, 126.33, 126.25, 124.48, 124.40, 123.03, 122.81, 122.73, 120.66, 120.44, 105.39, 104.67, 100.50, 100.26, 77.37, 77.16, 76.95, 68.96, 68.86, 68.52, 68.46, 68.24, 68.14, 37.77, 37.35, 34.54, 34.48, 34.28, 33.98, 32.07, 31.76, 31.69, 31.66, 31.60, 30.93, 30.44, 30.31, 30.19, 29.85, 29.80, 29.75, 29.60, 29.51, 29.45, 29.41, 29.32, 29.21, 27.37, 26.92, 26.87, 26.84, 26.78, 26.32, 26.30, 26.21, 26.11, 26.04, 25.96, 25.91, 25.83, 24.89, 24.22, 22.89, 22.84, 22.78, 22.73, 14.28, 14.21, 14.17, 1.17. HRMS (APPI/LTQ-Orbitrap) m/z : $[\text{M} + \text{H}]^+$ Calcd for $\text{C}_{67}\text{H}_{78}\text{N}_3\text{O}_6\text{S}^+$ 1052.5606; Found 1052.5658.

4-(7-(4-(bis(2',4'-bis(dodecyloxy)-[1,1'-biphenyl]-4-yl)amino)phenyl)benzo[c][1,2,5]thiadiazol-4-yl)benzoic acid (**MS5**)



N - (2', 4'-bis (dodecyloxy) - [1, 1'- biphenyl] - 4-yl) - N - (4 - bromophenyl) - 2', 4'-bis (dodecyloxy)-[1,1'-biphenyl]-4-amine (**7a**) (450 mg, 593 μmol , 1 eq.), acetic acidpotassium salt (233 mg, 2.37 mmoles, 4 eq.) and bis(pinacolato)diboron (452 mg, 1.78 mmoles, 3 eq.) were charged in a schlenk tube along with 5 mL anhydrous THF and degassed three times. Then, tris (dibenzylideneacetone) dipalladium (0) (27.2 mg, 29.7 μmol , 0.05 eq.) and 2 - (dicyclohexylphosphino) - 2', 4', 6'-

triisopropylbiphenyl (31.1 mg, 65.3 μmol , 0.11 eq.) were added and the reaction mixture refluxed at 80°C overnight under Argon atmosphere. After cooling down to room temperature, the solution was diluted twice with diethyl ether and flashed through a thin pad of Celite. The solvents were removed and 20 mL Ethanol was added to the residue to afford N-(2',4'-bis(dodecyloxy)-[1,1'-biphenyl]-4-yl)-2',4'-bis(dodecyloxy)-N-(4-(4,4,5,5-tetramethyl-1,3,2-dioxaborolan-2-yl)phenyl)-[1,1'-biphenyl]-4-amine as a beige wax, which was used for the next step without further purification. N-(2',4'-bis(dodecyloxy)-[1,1'-biphenyl]-4-yl)-2',4'-bis(dodecyloxy)-N-(4-(4,4,5,5-tetramethyl-1,3,2-dioxaborolan-2-yl)phenyl)-[1,1'-biphenyl]-4-amine (392 mg, 311 μmol , 1 eq.), ethyl 4-(7-bromobenzo[c][1,2,5]thiadiazol-4-yl)benzoate (113 mg, 311 μmol , 1 eq.), potassium phosphate tribasic (2M, 642 μL , 1.28 mmoles, 4.13 eq.) were charged in a schlenk tube along with 5 mL of anhydrous THF and degassed three times. Then, tris (dibenzylideneacetone) dipalladium (0) (22.8 mg, 24.9 μmol , 0.08 eq.) and 2-(dicyclohexylphosphino)-2',4',6'-triisopropylbiphenyl (23.7 mg, 49.8 μmol , 0.16 eq.) were added and the reaction mixture was refluxed at 80°C overnight under Argon atmosphere. After cooling down to room temperature, the solution was diluted twice with diethyl ether and flashed through a pad of magnesium sulfate. The solvents were removed and the residue was taken to the next step without further purification. The crude and potassium hydroxide (174 mg, 3.1 mmoles, 10 eq.) were dissolved in 10 mL of a THF:Ethanol(1:1, v:v) mixture along with 5 drops of deionized water. The resulting reaction mixture was then refluxed at 100°C under Argon atmosphere overnight. After cooling down to room temperature, the reaction was quenched

with 30 mL 1M hydrochloric acid and charged into a separation funnel. The organics were extracted using dichloromethane (3x10 mL) before drying over magnesium sulfate and removing the solvent. The crude was purified using Silica gel flash chromatography eluting with dichloromethane and then 5% methanol in dichloromethane and 5 drops of acetic acid. The final product was finally washed with methanol and obtained as a shiny red solid (304 mg, 70%). ^1H NMR (600 MHz, CDCl_3) δ 8.33 (d, J = 8.3 Hz, 2H), 8.14 (d, J = 8.3 Hz, 2H), 7.97 – 7.93 (m, 2H), 7.89 (d, J = 7.4 Hz, 1H), 7.83 (d, J = 7.3 Hz, 1H), 7.56 – 7.49 (m, 4H), 7.36 (d, J = 8.6 Hz, 2H), 7.33 – 7.29 (m, 2H), 7.28 (d, J = 8.3 Hz, 5H), 6.58 (d, J = 6.9 Hz, 4H), 4.01 (dt, J = 11.7, 6.5 Hz, 8H), 1.86 – 1.72 (m, 8H), 1.56 – 1.09 (m, 46H), 0.91 (t, J = 7.0 Hz, 6H), 0.87 (t, J = 7.0 Hz, 6H). ^{13}C NMR (151 MHz, CDCl_3) δ 171.26, 159.60, 157.00, 156.98, 154.09, 153.97, 148.48, 148.10, 145.84, 145.48, 144.95, 142.76, 135.68, 134.07, 133.62, 133.56, 132.39, 131.05, 130.89, 130.71, 130.52, 130.32, 130.14, 129.97, 129.24, 128.97, 128.86, 126.99, 126.30, 126.22, 124.37, 122.91, 122.70, 120.39, 105.28, 100.41, 77.27, 77.05, 76.84, 68.42, 68.13, 37.55, 37.12, 34.21, 32.08, 32.05, 31.96, 31.94, 31.92, 31.90, 31.89, 31.88, 31.88, 31.87, 31.87, 31.85, 31.84, 31.83, 31.82, 31.82, 31.80, 31.80, 31.79, 31.78, 31.78, 31.77, 31.76, 31.75, 31.75, 31.74, 31.73, 31.73, 31.72, 31.71, 31.70, 31.69, 31.68, 31.47, 30.82, 29.87, 29.86, 29.84, 29.83, 29.82, 29.81, 29.80, 29.75, 29.74, 29.72, 29.69, 29.67, 29.66, 29.64, 29.62, 29.61, 29.60, 29.59, 29.58, 29.57, 29.57, 29.56, 29.55, 29.55, 29.54, 29.53, 29.53, 29.52, 29.51, 29.50, 29.49, 29.47, 29.47, 29.46, 29.45, 29.44, 29.43, 29.39, 29.36, 29.35, 29.33, 29.31, 29.29, 29.27, 29.26, 29.24, 29.15, 29.13, 29.08, 26.80, 26.75, 26.72, 26.66, 26.24, 26.22, 26.15, 26.13, 26.12, 26.04, 26.02, 25.94, 25.93, 25.90, 24.13, 22.85, 22.82, 22.76, 22.74, 22.71, 22.67, 22.62, 22.59, 14.41, 14.39, 14.38, 14.37, 14.37, 14.36, 14.35, 14.35, 14.34, 14.33, 14.33, 14.32, 14.31, 14.31, 14.30, 14.29, 14.28, 14.26, 14.25, 14.24, 14.18, 14.15, 14.10, 14.06, 14.04, 1.06. HRMS (APPI/LTQ-Orbitrap) m/z : $[\text{M} + \text{H}]^+$ Calcd for $\text{C}_{91}\text{H}_{126}\text{N}_3\text{O}_6\text{S}^+$ 1388.9362; Found 1388.9403.

^1H and ^{13}C NMR spectra

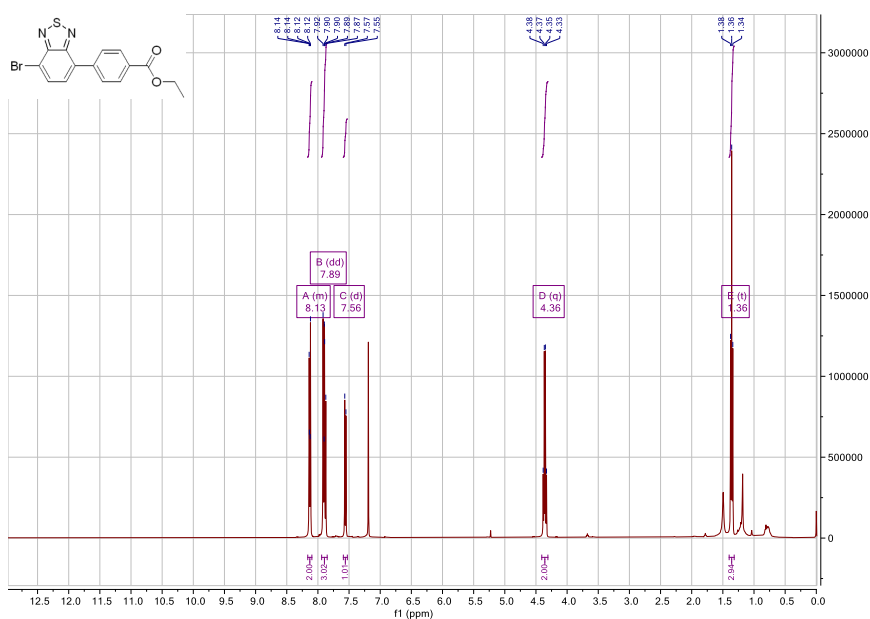
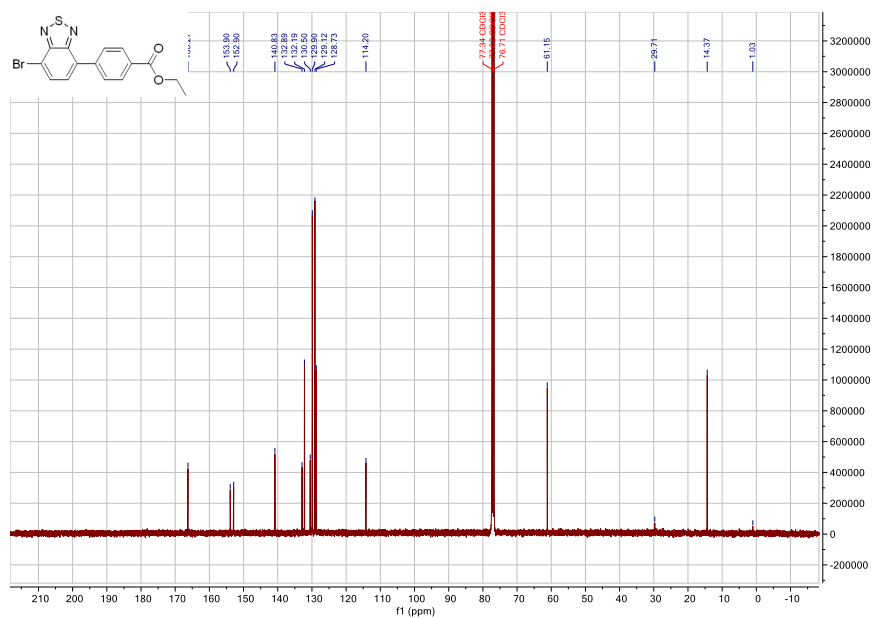
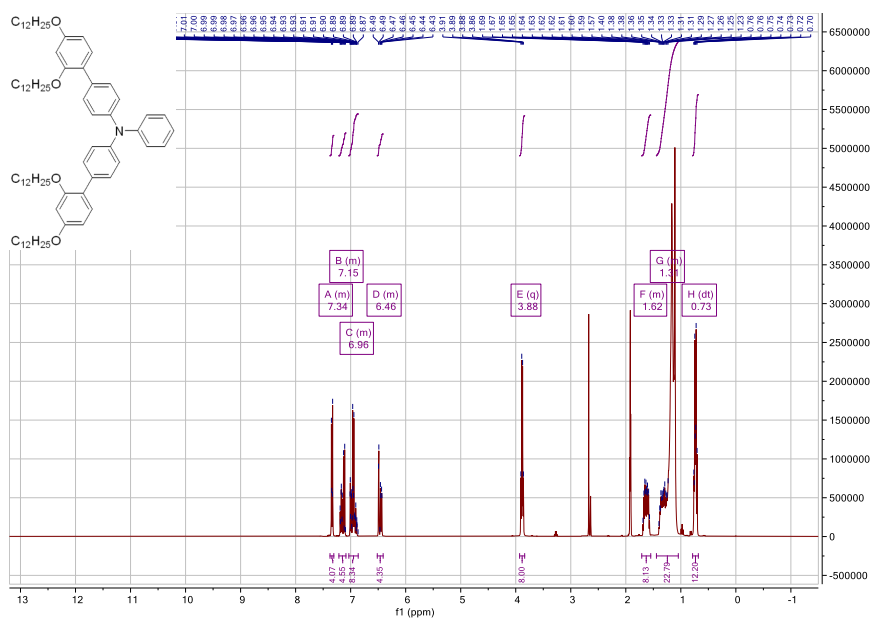
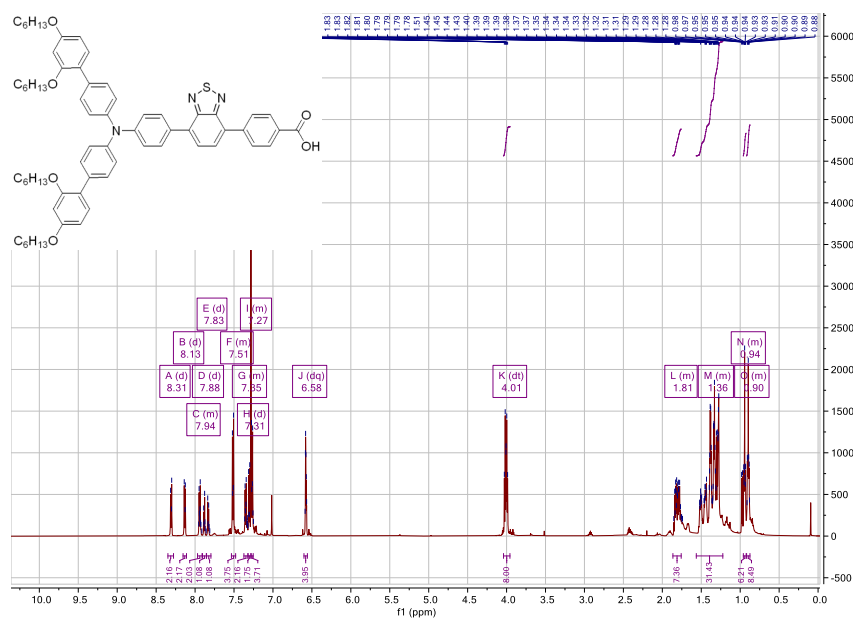
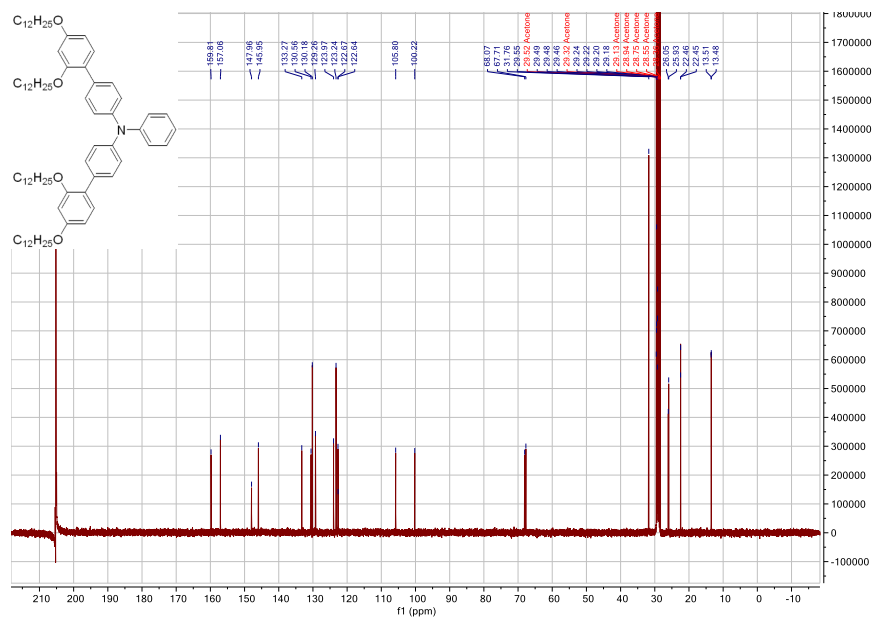


Figure 0.103. ^1H -NMR of 3 in CDCl_3 .

Figure 0.104. $^{13}\text{C-NMR}$ of 3 in CDCl_3 .Figure 0.105. $^1\text{H-NMR}$ of 6 in Acetone-d_6 .



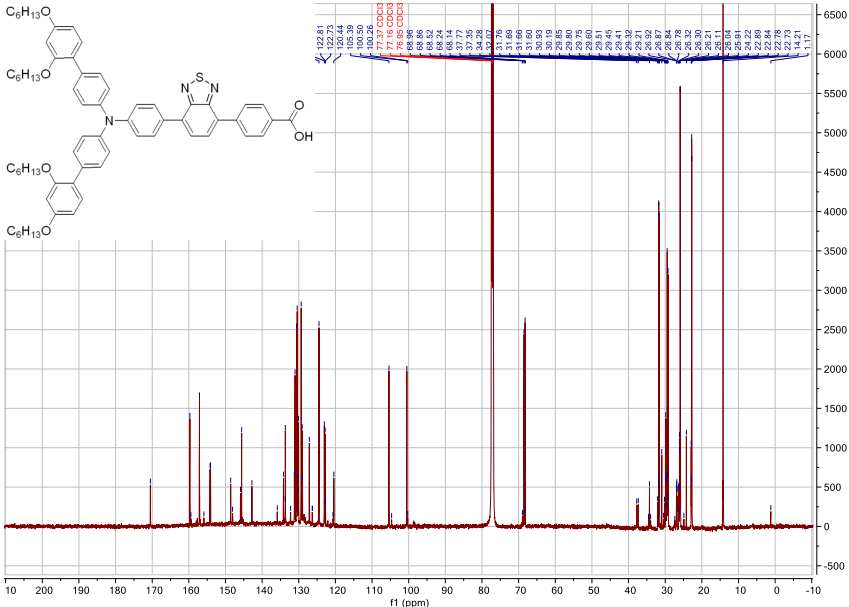


Figure 0.108. ^{13}C –NMR of MS4 in CDCl_3 .

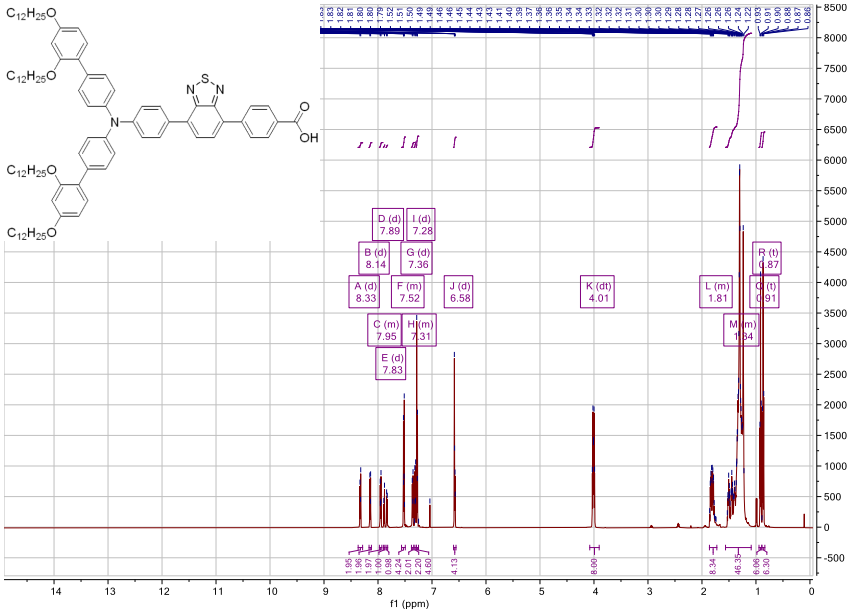


Figure 0.109. ^1H -NMR of MS5 in CDCl_3 .

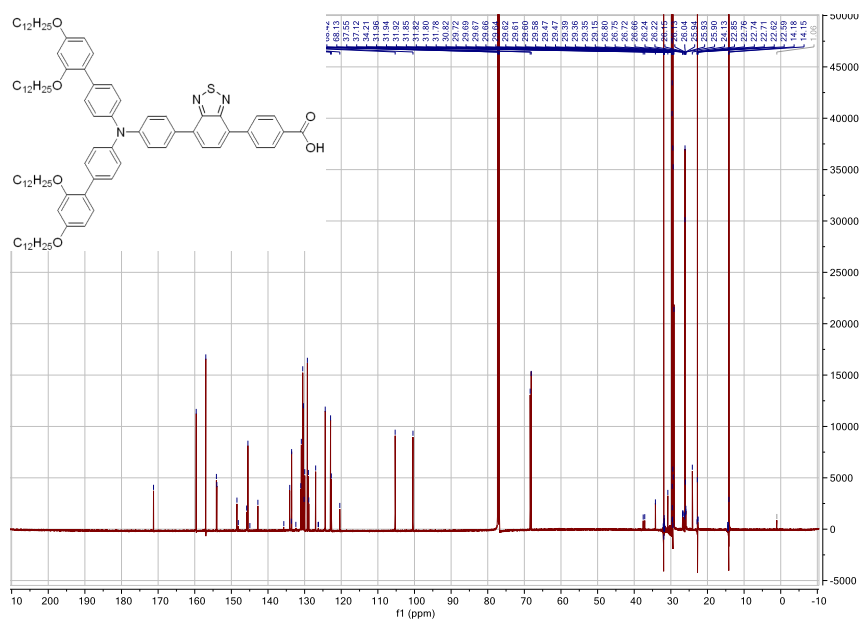


Figure 0.110. $^{13}\text{C-NMR}$ of MS5 in CDCl_3

References

- (1) Błaszczuk, A. *Dye. Pigment.* **2018**, 149, 707–718.
- (2) Wu, Y.; Zhu, W. *Chem. Soc. Rev.* **2013**, 42 (5), 2039–2058.
- (3) Zhu, W.; Wu, Y.; Wang, S.; Li, W.; Li, X.; Chen, J.; Wang, Z.; Tian, H. *Adv. Funct. Mater.* **2011**, 21 (4), 756–763.
- (4) Edwin Drake | American oil driller | Britannica
<https://www.britannica.com/biography/Edwin-Laurentine-Drake> (accessed May 1, 2020).
- (5) Daimler AG. Benz Patent Motor Car, the first automobile (1885-1886)
<https://www.daimler.com/company/tradition/company-history/1885-1886.html> (accessed May 1, 2020).
- (6) Ford Motor Company. Ford Motor Company Timeline | Ford.com
<https://corporate.ford.com/history.html> (accessed May 1, 2020).
- (7) Brunetti, M.; Prodi, F. *EPJ Web Conf.* **2015**, 98, 02001.
- (8) Kweku, D.; Bismark, O.; Maxwell, A.; Desmond, K.; Danso, K.; Oti-Mensah, E.; Quachie, A.; Adormaa, B. *J. Sci. Res. Reports* **2018**, 17 (6), 1–9.
- (9) Jones, D. A. *IEE Proc. A Phys. Sci. Meas. Instrumentation. Manag. Educ. Rev.* **1991**, 138 (1), 1–10.
- (10) Eriksson, O. *Sustain.* **2017**, 9 (6), 1063.
- (11) Verbruggen, A. *Energy Policy* **2008**, 36 (11), 4036–4047.
- (12) IEA. Data & Statistics - IEA [https://www.iea.org/data-and-statistics?country=WORLD&fuel=Energy consumption&indicator=Total final consumption \(TFC\) by sector](https://www.iea.org/data-and-statistics?country=WORLD&fuel=Energy%20consumption&indicator=Total%20final%20consumption%20(TFC)%20by%20sector) (accessed Apr 29, 2020).
- (13) Global electricity generation mix by scenario, 2018, Stated Policies and Sustainable Development Scenarios 2040 – Charts – Data & Statistics - IEA
<https://www.iea.org/data-and-statistics/charts/global-electricity-generation-mix-by-scenario-2018-stated-policies-and-sustainable-development-scenarios-2040> (accessed Apr 29, 2020).
- (14) International Energy Agency. Global Electricity Demand by Regions in the New Policies Scenario, 2000-2040 <https://www.iea.org/data-and-statistics/charts/global-electricity-demand-by-region-in-the-new-policies-scenario-2000-2040> (accessed Apr 29, 2020).
- (15) Parrott, J. E. *Sol. Energy* **1993**, 51 (3), 195.
- (16) DeVos, A. *Endoreversible thermodynamics of solar energy conversion*; Oxford University Press: Oxford ; New York, 1992.
- (17) Kopp, G.; Lean, J. L. *Geophys. Res. Lett.* **2011**, 38 (1).
- (18) Emilio, M.; Kuhn, J. R.; Bush, R. I.; Scholl, I. F. *Astrophys. J.* **2012**, 750 (2), 135.
- (19) ASTM. *Astm.* 2013, pp 1–21.
- (20) Hu, C.; White, R. M. *Sol. Cells* **1983**, 298.
- (21) Kasten, F.; Young, A. T. **2000**, 28 (22), 4735–4738.
- (22) Laue, E. G. *Sol. Energy* **1970**, 13 (1), 43–57.
- (23) National Renewable Energy Laboratory. Solar Spectral Irradiance: ASTM G-173
<http://rredc.nrel.gov/solar/spectra/am1.5/ASTMG173/ASTMG173.html> (accessed May 1, 2020).
- (24) Becquerel, A. E. *Comptes Rendus L'Academie des Sci.* **1839**, 9, 145.
- (25) Li, S. S.; Li, S. S. In *Semiconductor Physical Electronics*; Springer US: Boston, MA, 1993; pp 287–326.
- (26) Jones, E. D. In *Electronic Materials*; Miller, L. S., Mullin, J. B., Eds.; Springer US: Boston, MA, 1991; pp 155–171.
- (27) Zhang, Z.; Yates, J. T. *Chem. Rev.* **2012**, 112 (10), 5520–5551.
- (28) Wurfel, P. *J. Phys. C Solid State Phys.* **1982**, 15 (18), 3967.
- (29) Richard C. Dorf (University of California). *Systems, controls, Embedded, Energy and machines*; 2006; Vol. 1.

- (30) Bogart Jr, T. F. *Electronic Devices and Circuits*. Merrill Publishing Company 1968.
- (31) Dorf, R. C. *The Electrical Engineering Handbook Series*; CRC-Taylor & Francis., 1995.
- (32) Nelson, J. *The Physics of Solar Cells*; PUBLISHED BY IMPERIAL COLLEGE PRESS AND DISTRIBUTED BY WORLD SCIENTIFIC PUBLISHING CO., 2003.
- (33) Nielsen, L. D. *IEEE Trans. Electron Devices* **1982**, 29 (12), 1946.
- (34) Araújo, G. L.; Cuevas, A.; Ruiz, J. M. *IEEE Trans. Electron Devices* **1986**, 33 (3), 391–401.
- (35) Proctor, C. M.; Nguyen, T. Q. *Appl. Phys. Lett.* **2015**, 106 (8), 083301.
- (36) Lorenzo, E.; Araujo, G.; Cuevas, A.; Egido, M.; Minano, J.; Zilles, R. *Solar Electricity: Engineering of Photovoltaic Systems*; PROGENSA, 1994.
- (37) Charles, J. P.; Abdelkrim, M.; Muoy, Y. H.; Mialhe, P. *Sol. Cells* **1981**, 4 (2), 169–178.
- (38) Vishnoi, A.; Gopal, R.; Dwivedi, R.; Srivastava, S. K. *IEE Proceedings, Part G Circuits, Devices Syst.* **1993**, 140 (3), 155–164.
- (39) Green, M. A. *Solid State Electron.* **1977**, 20 (3), 265–266.
- (40) Green, M. A. *Solid State Electron.* **1981**, 24 (8), 788–789.
- (41) IECCE Standards [https://www.iecee.org/dyn/www/f?p=106:48:0::::](https://www.iecee.org/dyn/www/f?p=106:48:0::::(accessed May 6, 2020)) (accessed May 6, 2020).
- (42) Best Research-Cell Efficiency Chart | Photovoltaic Research | NREL <https://www.nrel.gov/pv/cell-efficiency.html> (accessed May 6, 2020).
- (43) Luceño-Sánchez, J. A.; Díez-Pascual, A. M.; Capilla, R. P. *Int. J. Mol. Sci.* **2019**, 20 (4).
- (44) Muteri, V.; Cellura, M.; Curto, D.; Franzitta, V.; Longo, S.; Mistretta, M.; Parisi, M. L. *Energies* **2020**, 13 (1).
- (45) Yoshikawa, K.; Kawasaki, H.; Yoshida, W.; Irie, T.; Konishi, K.; Nakano, K.; Uto, T.; Adachi, D.; Kanematsu, M.; Uzu, H.; Yamamoto, K. *Nat. Energy* **2017**, 2 (5), 1–8.
- (46) Kayes, B. M.; Nie, H.; Twist, R.; Spruytte, S. G.; Reinhardt, F.; Kizilyalli, I. C.; Higashi, G. S. In *2011 37th IEEE Photovoltaic Specialists Conference*; 2011; pp 4–8.
- (47) Badawy, W. A. *Journal of Advanced Research*. Elsevier B.V. March 1, 2015, pp 123–132.
- (48) Jackson, P.; Hariskos, D.; Wuerz, R.; Kiowski, O.; Bauer, A.; Friedlmeier, T. M.; Powalla, M. *Phys. Status Solidi - Rapid Res. Lett.* **2015**, 9 (1), 28–31.
- (49) K.K., S. F. *Solar Frontier Achieves World Record Thin-Film Solar Cell Efficiency: 22.3 %*; 2015.
- (50) Geisz, J. F.; Steiner, M. A.; García, I.; Kurtz, S. R.; Friedman, D. J. *Appl. Phys. Lett.* **2013**, 103 (4), 041118.
- (51) Matsui, T.; Sai, H.; Suezaki, T.; Matsumoto, M.; Saito, K.; Yoshida, I.; Kondo, M. *28th Eur. Photovolt. Sol. Energy Conf. Exhib.* **2013**, No. 1, 2213–2217.
- (52) Sai, H.; Matsui, T.; Kumagai, H.; Matsubara, K. *Appl. Phys. Express* **2018**, 11 (2).
- (53) Conibeer, G. *Materials Today*. Elsevier November 1, 2007, pp 42–50.
- (54) Green, M. A. *Prog. Photovoltaics Res. Appl.* **2001**, 9 (2), 123–135.
- (55) Conibeer, G.; Willoughby, A. *Solar Cell Materials: Developing Technologies*; John Wiley & Sons, 2014; Vol. 9780470065.
- (56) Green, M. A. *Prog. Photovoltaics Res. Appl.* **2020**, 28 (1), 3–15.
- (57) Jung, E. H.; Jeon, N. J.; Park, E. Y.; Moon, C. S.; Shin, T. J.; Yang, T. Y.; Noh, J. H.; Seo, J. *Nature* **2019**, 567 (7749), 511–515.
- (58) Liu, Q.; Jiang, Y.; Jin, K.; Qin, J.; Xu, J.; Li, W.; Xiong, J.; Liu, J.; Xiao, Z.; Sun, K.; Yang, S.; Zhang, X.; Ding, L. *Sci. Bull.* **2020**, 65 (4), 272–275.
- (59) Hirst, L. C.; Ekins-Daukes, N. J. *Prog. Photovoltaics Res. Appl.* **2011**, 19 (3), 286–293.
- (60) Wang, A.; Xuan, Y. *Energy* **2018**, 144, 490–500.
- (61) Alharbi, F. H.; Kais, S. *Renewable and Sustainable Energy Reviews*. Elsevier Ltd March 1, 2015, pp 1073–1089.
- (62) Kirchhoff, G. *Ann. Phys.* **1860**, 185 (2), 275–301.
- (63) Würfel, P.; Ruppel, W. *IEEE Trans. Electron Devices* **1980**, 27 (4), 745–750.
- (64) Dhankhar, M.; Pal Singh, O.; Singh, V. N. *Renewable and Sustainable Energy Reviews*. Elsevier Ltd December 1, 2014, pp 214–223.

- (65) Nelson, C. A.; Monahan, N. R.; Zhu, X. Y. *Energy Environ. Sci.* **2013**, 6 (12), 3508–3519.
- (66) Shockley, W.; Queisser, H. J. *J. Appl. Phys.* **1961**, 32 (3), 510–519.
- (67) Rühle, S. *Sol. Energy* **2016**, 130, 139–147.
- (68) Araújo, G. L.; Martí, A. *Sol. Energy Mater. Sol. Cells* **1994**, 33 (2), 213–240.
- (69) Polman, A.; Knight, M.; Garnett, E. C.; Ehrler, B.; Sinke, W. C. *Science (80-.)* **2016**, 352 (6283), aad4424–aad4424.
- (70) Nayak, P. K.; Mahesh, S.; Snaith, H. J.; Cahen, D. *Nat. Rev. Mater.* **2019**, 4 (4), 269–285.
- (71) Grätzel, M. *Acc. Chem. Res.* **2009**, 42 (11), 1788–1798.
- (72) Clifford, J. N.; Martínez-Ferrero, E.; Viterisi, A.; Palomares, E. *Chemical Society Reviews*. Royal Society of Chemistry February 22, 2011, pp 1635–1646.
- (73) Hagfeldt, A.; Boschloo, G.; Sun, L.; Kloo, L.; Pettersson, H. *Chem. Rev.* **2010**, 110 (11), 6595–6663.
- (74) Ardo, S.; Meyer, G. J. *Chem. Soc. Rev.* **2009**, 38 (1), 115–164.
- (75) Marcus, R. A. *J. Chem. Phys.* **1956**, 24 (5), 966–978.
- (76) Marcus, R. A. *Annu. Rev. Phys. Chem.* **1964**, 15 (1), 155–196.
- (77) Memming, R. *Semiconductor electrochemistry*; John Wiley & Sons, 2015.
- (78) Marcus, R. A.; Sutin, N. *BBA Reviews On Bioenergetics*. Elsevier August 1, 1985, pp 265–322.
- (79) Hush, N. S. *Trans. Faraday Soc.* **1961**, 57 (0), 557–580.
- (80) Hush, N. S. *J. Chem. Phys.* **1958**, 28 (5), 962–972.
- (81) Kuss-Petermann, M.; Wenger, O. S. *Phys. Chem. Chem. Phys.* **2016**, 18, 18657.
- (82) Clifford, J. N.; Palomares, E.; Nazeeruddin, M. K.; Grätzel, M.; Nelson, J.; Li, X.; Long, N. J.; Durrant, J. R. *J. Am. Chem. Soc.* **2004**, 126 (16), 5225–5233.
- (83) Gerischer, H. *Electrochimica Acta*. Pergamon November 1, 1990, pp 1677–1699.
- (84) Memming, R. *Progress in Surface Science*. Pergamon January 1, 1984, pp 7–73.
- (85) Watson, D. F.; Meyer, G. J. *Annu. Rev. Phys. Chem.* **2005**, 56 (1), 119–156.
- (86) Listorti, A.; O'Regan, B.; Durrant, J. R. *Chem. Mater.* **2011**, 23 (15), 3381–3399.
- (87) Gao, Y. Q.; Marcus, R. A. *Electrode React. J. Chem. Phys.* **2000**, 113, 679.
- (88) Rothenberger, G.; Fitzmaurice, D.; Grätzel, M. *J. Phys. Chem.* **1992**, 96 (14), 5983–5986.
- (89) Redmond, G.; Fitzmaurice, D. *J. Phys. Chem.* **1993**, 97 (7), 1426–1430.
- (90) Enright, B.; Redmond, G.; Fitzmaurice, D. *J. Phys. Chem.* **1994**, 98 (24), 6195–6200.
- (91) Katoh, R.; Furube, A. *J. Photochem. Photobiol. C Photochem. Rev.* **2014**, 20 (1), 1–16.
- (92) Matsuzaki, H.; Murakami, T. N.; Masaki, N.; Furube, A.; Kimura, M.; Mori, S. *J. Phys. Chem. C* **2014**, 118 (31), 17205–17212.
- (93) Ashokkumar, R.; Kathiravan, A.; Ramamurthy, P. *Phys. Chem. Chem. Phys.* **2014**, 16 (3), 1015–1021.
- (94) Pazoki, M.; Cappel, U. B.; Johansson, E. M. J.; Hagfeldt, A.; Boschloo, G. *Energy Environ. Sci.* **2017**, 10 (3), 672–709.
- (95) Koops, S. E.; Barnes, P. R. F.; O'Regan, B. C.; Durrant, J. R. *J. Phys. Chem. C* **2010**, 114 (17), 8054–8061.
- (96) Zhang, L.; Cole, J. M. *J. Mater. Chem. A* **2017**, 5 (37), 19541–19559.
- (97) Yum, J. H.; Jang, S. R.; Humphry-Baker, R.; Grätzel, M.; Cid, J. J.; Torres, T.; Nazeeruddin, M. K. *Langmuir* **2008**, 24 (10), 5636–5640.
- (98) Nelson, J.; Haque, S. A.; Klug, D. R.; Durrant, J. R. *Phys. Rev. B - Condens. Matter Mater. Phys.* **2001**, 63 (20).
- (99) Nelson, J. *Phys. Rev. B - Condens. Matter Mater. Phys.* **1999**, 59 (23), 15374–15380.
- (100) Van de Lagemaat, J.; Frank, A. J. *J. Phys. Chem. B* **2001**, 105 (45), 11194–11205.
- (101) Van De Lagemaat, J.; Park, N. G.; Frank, A. J. *J. Phys. Chem. B* **2000**, 104 (9), 2044–2052.
- (102) Van De Lagemaat, J.; Frank, A. J. *J. Phys. Chem. B* **2000**, 104 (18), 4292–4294.
- (103) Fisher, A. C.; Peter, L. M.; Ponomarev, E. A.; Walker, A. B.; Wijayantha, K. G. U. *J.*

- Phys. Chem. B* **2000**, *104* (5), 949–958.
- (104) Bisquert, J.; Fabregat-Santiago, F.; Mora-Seró, I.; Garcia-Belmonte, G.; Giménez, S. *J. Phys. Chem. C* **2009**, *113* (40), 17278–17290.
- (105) Boschloo, G.; Hagfeldt, A. *J. Phys. Chem. B* **2005**, *109* (24), 12093–12098.
- (106) Hagfeldt, A.; Boschloo, G.; Sun, L.; Kloo, L.; Pettersson, H. *Chem. Rev.* **2010**, *110* (11), 6595–6663.
- (107) Sun, Z.; Liang, M.; Chen, J. *Acc. Chem. Res.* **2015**, *48* (6), 1541–1550.
- (108) Listorti, A.; O'Regan, B.; Durrant, J. R. *Chem. Mater.* **2011**, *23* (15), 3381–3399.
- (109) Durrant, J. R.; Grätzel, M. *Imp. Coll. Press London* **2008**.
- (110) Cameron, P. J.; Peter, L. M. *J. Phys. Chem. B* **2005**, *109* (15), 7392–7398.
- (111) Hamann, T. W.; Jensen, R. A.; Martinson, A. B. F.; Van Ryswyk, H.; Hupp, J. T. *Energy Environ. Sci.* **2008**, *1* (1), 66–78.
- (112) Bel Hadj Tahar, R.; Ban, T.; Ohya, Y.; Takahashi, Y. *J. Appl. Phys.* **1998**, *83* (5), 2631–2645.
- (113) Sima, C.; Grigoriu, C.; Antohe, S. *Thin Solid Films* **2010**, *519* (2), 595–597.
- (114) Tang, H.; Prasad, K.; Sanjinès, R.; Schmid, P. E.; Lévy, F. *J. Appl. Phys.* **1994**, *75* (4), 2042–2047.
- (115) Park, N. G.; Van De Lagemaat, J.; Frank, A. J. *J. Phys. Chem. B* **2000**, *104* (38), 8989–8994.
- (116) Pagliaro, M.; Palmisano, G.; Ciriminna, R.; Loddo, V. *Energy Environ. Sci.* **2009**, *2* (8), 838–844.
- (117) Jose, R.; Thavasi, V.; Ramakrishna, S. *J. Am. Ceram. Soc.* **2009**, *92* (2), 289–301.
- (118) Boschloo, G. *Front. Chem.* **2019**, *7* (FEB), 77.
- (119) Gong, J.; Sumathy, K.; Qiao, Q.; Zhou, Z. *Renewable and Sustainable Energy Reviews*. Elsevier Ltd February 1, 2017, pp 234–246.
- (120) Hore, S.; Vetter, C.; Kern, R.; Smit, H.; Hinsch, A. *Sol. Energy Mater. Sol. Cells* **2006**, *90* (9), 1176–1188.
- (121) Fonstad, C. G.; Rediker, R. H. *J. Appl. Phys.* **1971**, *42* (7), 2911–2918.
- (122) Green, A. N. M.; Palomares, E.; Haque, S. A.; Kroon, J. M.; Durrant, J. R. *J. Phys. Chem. B* **2005**, *109* (25), 12525–12533.
- (123) Ramasamy, E.; Lee, J. *J. Phys. Chem. C* **2010**, *114* (50), 22032–22037.
- (124) Fukai, Y.; Kondo, Y.; Mori, S.; Suzuki, E. *Electrochem. commun.* **2007**, *9* (7), 1439–1443.
- (125) Zhang, Q.; Dandeneau, C. S.; Zhou, X.; Cao, C. *Adv. Mater.* **2009**, *21* (41), 4087–4108.
- (126) Solbrand, A.; Keis, K.; Södergren, S.; Lindström, H.; Lindquist, S. E.; Hagfeldt, A. *Sol. Energy Mater. Sol. Cells* **2000**, *60* (2), 181–193.
- (127) Matsumoto, Y. *J. Solid State Chem.* **1996**, *126* (2), 227–234.
- (128) Kim, B. G.; Chung, K.; Kim, J. *Chem. - A Eur. J.* **2013**, *19* (17), 5220–5230.
- (129) Gong, J.; Liang, J.; Sumathy, K. *Renewable and Sustainable Energy Reviews*. Pergamon October 1, 2012, pp 5848–5860.
- (130) O'Regan, B.; Grätzel, M. *Nature* **1991**, *353* (6346), 737–740.
- (131) Amadelli, R.; Argazzi, R.; Bignozzi, C. A.; Scandola, F. *J. Am. Chem. Soc.* **1990**, *112* (20), 7099–7103.
- (132) Nazeeruddin, M. K.; Liska, P.; Moser, J.; Vlachopoulos, N.; Grätzel, M. *Helv. Chim. Acta* **1990**, *73* (6), 1788–1803.
- (133) Nazeeruddin, M. K.; Bessho, T.; Cevey, L.; Ito, S.; Klein, C.; De Angelis, F.; Fantacci, S.; Comte, P.; Liska, P.; Imai, H.; Graetzel, M. *J. Photochem. Photobiol. A Chem.* **2007**, *185* (2–3), 331–337.
- (134) Nazeeruddin, M. K.; Kay, A.; Rodicio, I.; Humphry-Baker, R.; Mueller, E.; Liska, P.; Vlachopoulos, N.; Graetzel, M. *J. Am. Chem. Soc.* **1993**, *115* (14), 6382–6390.
- (135) Vougioukalakis, G. C.; Philippopoulos, A. I.; Stergiopoulos, T.; Falaras, P. *Coordination Chemistry Reviews*. Elsevier November 1, 2011, pp 2602–2621.
- (136) Nazeeruddin, M. K.; Péchy, P.; Renouard, T.; Zakeeruddin, S. M.; Humphry-Baker, R.; Cointe, P.; Liska, P.; Cevey, L.; Costa, E.; Shklover, V.; Spiccia, L.; Deacon, G. B.;

- Bignozzi, C. A.; Grätzel, M. *J. Am. Chem. Soc.* **2001**, *123* (8), 1613–1624.
- (137) Chiba, Y.; Islam, A.; Watanabe, Y.; Komiya, R.; Koide, N.; Han, L. *Japanese J. Appl. Physics, Part 2 Lett.* **2006**, *45* (24–28), L638.
- (138) Zakeeruddin, S. M.; Nazeeruddin, M. K.; Humphry-Baker, R.; Péchy, P.; Quagliotto, P.; Barolo, C.; Viscardi, G.; Grätzel, M. *Langmuir* **2002**, *18* (3), 952–954.
- (139) Wang, P.; Zakeeruddin, S. M.; Comte, P.; Charvet, R.; Humphry-Baker, R.; Grätzel, M. *J. Phys. Chem. B* **2003**, *107* (51), 14336–14341.
- (140) Shiu, J.-W.; Lan, Z.-J.; Chan, C.-Y.; Wu, H.-P.; Wei-Guang Diao, E. **2014**.
- (141) Aghazada, S.; Nazeeruddin, M. K. *Inorganics* **2018**, *6* (2), 52.
- (142) Gao, F.; Wang, Y.; Shi, D.; Zhang, J.; Wang, M.; Jing, X.; Humphry-Baker, R.; Wang, P.; Zakeeruddin, S. M.; Grätzel, M. *J. Am. Chem. Soc.* **2008**, *130* (32), 10720–10728.
- (143) Zhang, Q. T.; Tour, J. M. *J. Am. Chem. Soc.* **1998**, *120* (22), 5355.
- (144) Zhu, Y.; Champion, R. D.; Jenekhe, S. A. *Macromolecules* **2006**, *39* (25), 8712–8719.
- (145) Jenekhe, S. A.; Lu, L.; Alam, M. M. *Macromolecules* **2001**, *34* (21), 7315–7324.
- (146) Kleinhenz, N.; Yang, L.; Zhou, H.; Price, S. C.; You, W. *Macromolecules* **2011**, *44*, 872–877.
- (147) Yu, G.; Gao, J.; Hummelen, J. C.; Wudl, F.; Heeger, A. J. *Science* (80-.). **1995**, *270* (5243), 1789.
- (148) Brédas, J. L.; Norton, J. E.; Cornil, J.; Coropceanu, V. *Acc. Chem. Res.* **2009**, *42* (11), 1691–1699.
- (149) Bredas, J. L.; Street, G. B. *Polarons, Bipolarons, and Solitons in Conducting Polymers*; 1985; Vol. 18.
- (150) Liang, W. Y. *Phys. Educ.* **1970**, *5* (4), 226–228.
- (151) Gregg, B. A. *J. Phys. Chem. B* **2003**, *107* (20), 4688–4698.
- (152) May, V.; Kühn, O. *Charge and Energy Transfer Dynamics in Molecular Systems: Third Edition*; Wiley Online Library, 2011; Vol. 2.
- (153) Hummer, K.; Ambrosch-Draxl, C. *Phys. Rev. B - Condens. Matter Mater. Phys.* **2005**, *71* (8).
- (154) Karabunarliev, S.; Bittner, E. R. *J. Chem. Phys.* **2003**, *118* (9), 4291–4296.
- (155) Rissler, J. *Chem. Phys. Lett.* **2004**, *395* (1–3), 92–96.
- (156) Choi, H.; Baik, C.; Kang, S. O.; Ko, J.; Kang, M.-S.; Nazeeruddin, M. K.; Grätzel, M. *Angew. Chemie Int. Ed.* **2008**, *47* (2), 327–330.
- (157) Kim, B. G.; Zhen, C. G.; Jeong, E. J.; Kieffer, J.; Kim, J. *Adv. Funct. Mater.* **2012**, *22* (8), 1606–1612.
- (158) Meier, H.; Stalmach, U.; Kolshorn, H. *Acta Polym.* **1997**, *48* (9), 379–384.
- (159) Hong, S. Y.; Marynick, D. S. *Macromolecules* **1992**, *25* (18), 4652–4657.
- (160) Horiuchi, T.; Miura, H.; Sumioka, K.; Uchida, S. *J. Am. Chem. Soc.* **2004**, *126* (39), 12218–12219.
- (161) Kuang, D.; Uchida, S.; Humphry-Baker, R.; Zakeeruddin, S. M.; Grätzel, M. *Angew. Chemie Int. Ed.* **2008**, *47* (10), 1923–1927.
- (162) Ito, S.; Zakeeruddin, S. M.; Humphry-Baker, R.; Liska, P.; Charvet, R.; Comte, P.; Nazeeruddin, M. K.; Péchy, P.; Takata, M.; Miura, H.; Uchida, S.; Grätzel, M. *Adv. Mater.* **2006**, *18* (9), 1202–1205.
- (163) Uemura, Y.; Mori, S.; Hara, K.; Koumura, N. *Chem. Lett.* **2011**, *40* (8), 872–873.
- (164) Wang, Z. S.; Koumura, N.; Cui, Y.; Takahashi, M.; Sekiguchi, H.; Mori, A.; Kubo, T.; Furube, A.; Hara, K. *Chem. Mater.* **2008**, *20* (12), 3993–4003.
- (165) Koumura, N.; Wang, Z. S.; Miyashita, M.; Uemura, Y.; Sekiguchi, H.; Cui, Y.; Mori, A.; Mori, S.; Hara, K. *J. Mater. Chem.* **2009**, *19* (27), 4829–4836.
- (166) Lim, K.; Song, K.; Kang, Y.; Ko, J. *Dye. Pigment.* **2015**, *119*, 41–48.
- (167) Tang, Y.; Wang, Y.; Song, H.; Liu, Q.; Li, X.; Cai, Y.; Xie, Y. *Dye. Pigment.* **2019**, *171*, 107776.
- (168) Wang, J.; Liu, K.; Ma, L.; Zhan, X. *Chem. Rev.* **2016**, *116* (23), 14675–14725.
- (169) Hwang, S.; Lee, J. H.; Park, C.; Lee, H.; Kim, C.; Park, C.; Lee, M. H.; Lee, W.; Park, J.; Kim, K.; Park, N. G.; Kim, C. *Chem. Commun.* **2007**, *0* (46), 4887–4889.
- (170) Zeng, W.; Cao, Y.; Bai, Y.; Wang, Y.; Shi, Y.; Zhang, M.; Wang, F.; Pan, C.; Wang, P.

- Chem. Mater.* **2010**, 22 (5), 1915–1925.
- (171) Xu, M.; Wenger, S.; Bala, H.; Shi, D.; Li, R.; Zhou, Y.; Zakeeruddin, S. M.; Grätzel, M.; Wang, P. *J. Phys. Chem. C* **2009**, 113 (7), 2966–2973.
- (172) Li, X.; Zhang, X.; Hua, J.; Tian, H. *Mol. Syst. Des. Eng.* **2017**, 2 (2), 98–122.
- (173) Hagberg, D. P.; Jiang, X.; Gabrielsson, E.; Linder, M.; Marinado, T.; Brinck, T.; Hagfeldt, A.; Sun, L. *J. Mater. Chem.* **2009**, 19 (39), 7232–7238.
- (174) Gabrielsson, E.; Ellis, H.; Feldt, S.; Tian, H.; Boschloo, G.; Hagfeldt, A.; Sun, L. *Adv. Energy Mater.* **2013**, 3 (12), 1647–1656.
- (175) Tsao, H. N.; Yi, C.; Moehl, T.; Yum, J. H.; Zakeeruddin, S. M.; Nazeeruddin, M. K.; Grätzel, M. *ChemSusChem* **2011**, 4 (5), 591–594.
- (176) Peart, P. A.; Repka, L. M.; Tovar, J. D. *European J. Org. Chem.* **2008**, 2008 (13), 2193–2206.
- (177) Parker, T. C.; Marder, S. R. *Synthetic methods in organic electronic and photonic materials: A practical guide*; Royal Society of Chemistry, 2015.
- (178) Li, R.; Liu, J.; Cai, N.; Zhang, M.; Wang, P. .
- (179) Rasmussen, S. C.; Evenson, S. J.; McCausland, C. B. *Chem. Commun.* **2015**, 51 (22), 4528–4543.
- (180) Polander, L. E.; Yella, A.; Teuscher, J.; Humphry-Baker, R.; Curchod, B. F. E.; Ashari Astani, N.; Gao, P.; Moser, J. E.; Tavernelli, I.; Rothlisberger, U.; Grätzel, M.; Nazeeruddin, M. K.; Frey, J. *Chem. Mater.* **2013**, 25 (13), 2642–2648.
- (181) Imahori, H.; Umeyama, T.; Ito, S. *Acc. Chem. Res.* **2009**, 42 (11), 1809–1818.
- (182) Zeng, K.; Tong, Z.; Ma, L.; Zhu, W.-H.; Wu, W.; Xie, Y. *Energy Environ. Sci.* **2020**, No. December 2015.
- (183) Yella, A.; Lee, H. W.; Tsao, H. N.; Yi, C.; Chandiran, A. K.; Nazeeruddin, M. K.; Diau, E. W. G.; Yeh, C. Y.; Zakeeruddin, S. M.; Grätzel, M. *Science* (80-.). **2011**, 334 (6056), 629–634.
- (184) Mathew, S.; Yella, A.; Gao, P.; Humphry-Baker, R.; Curchod, B. F. E.; Ashari-Astani, N.; Tavernelli, I.; Rothlisberger, U.; Nazeeruddin, M. K.; Grätzel, M. *Nat. Chem.* **2014**, 6 (3), 242–247.
- (185) Grzybowski, M.; Gryko, D. T. *Adv. Opt. Mater.* **2015**, 3 (3), 280–320.
- (186) Li, Y.; Sonar, P.; Murphy, L.; Hong, W. *Energy Environ. Sci.* **2013**, 6 (6), 1684–1710.
- (187) Hao, Y.; Saygili, Y.; Cong, J.; Eriksson, A.; Yang, W.; Zhang, J.; Polanski, E.; Nonomura, K.; Zakeeruddin, S. M.; Grätzel, M.; Hagfeldt, A.; Boschloo, G. *ACS Appl. Mater. Interfaces* **2016**, 8 (48), 32797–32804.
- (188) Yum, J. H.; Holcombe, T. W.; Kim, Y.; Rakstys, K.; Moehl, T.; Teuscher, J.; Delcamp, J. H.; Nazeeruddin, M. K.; Grätzel, M. *Sci. Rep.* **2013**, 3 (1), 2446.
- (189) Yum, J. H.; Holcombe, T. W.; Kim, Y.; Yoon, J.; Rakstys, K.; Nazeeruddin, M. K.; Grätzel, M. *Chem. Commun.* **2012**, 48 (87), 10727–10729.
- (190) Holcombe, T. W.; Yum, J. H.; Yoon, J.; Gao, P.; Marszalek, M.; Censo, D. Di; Rakstys, K.; Nazeeruddin, M. K.; Graetzel, M. *Chem. Commun.* **2012**, 48 (87), 10724–10726.
- (191) Zhang, L.; Cole, J. M. *ACS Appl. Mater. Interfaces* **2015**, 7 (6), 3427–3455.
- (192) Yamamoto, T.; Zhou, Z.; Kanbara, T.; Shimura, M.; Kizu, K.; Maruyama, T.; Nakamura, Y.; Fukuda, T.; Lee, B.-L.; Ooba, N.; Tomaru, S.; Kurihara, T.; Kaino, T.; Kubota, K.; Sasaki, S. *J. Am. Chem. Soc.* **1996**, 118 (43), 10389–10399.
- (193) Newkome, G. R.; Paudler, W. W. *Contemporary Heterocyclic Chemistry: Syntheses, Reactions and Applications*; Wiley-Interscience, 1982.
- (194) Takimiya, K.; Osaka, I.; Nakano, M. **2013**.
- (195) Wang, Y.; Michinobu, T. *Journal of Materials Chemistry C*. Royal Society of Chemistry June 30, 2016, pp 6200–6214.
- (196) Behramand, B.; Molin, F.; Gallardo, H. *Dye. Pigment.* **2012**, 95 (3), 600–605.
- (197) Cameron, J.; Abed, M. M.; Chapman, S. J.; Findlay, N. J.; Skabara, P. J.; Horton, P. N.; Coles, S. J. *J. Mater. Chem. C* **2018**, 6 (14), 3709–3714.
- (198) Akkuratov, A. V.; Troshin, P. A. *Polym. Sci. - Ser. B* **2014**, 56 (4), 414–442.
- (199) Yang, G.; Tang, Y.; Li, X.; Ågren, H.; Xie, Y. *ACS Appl. Mater. Interfaces* **2017**, 9 (42), 36875–36885.

- (200) Liu, Y.; Cao, Y.; Zhang, W.; Stojanovic, M.; Dar, M. I.; Péchy, P.; Saygili, Y.; Hagfeldt, A.; Zakeeruddin, S. M.; Grätzel, M. *Angew. Chemie - Int. Ed.* **2018**, *57* (43), 14125–14128.
- (201) Haid, S.; Marszalek, M.; Mishra, A.; Wielopolski, M.; Teuscher, J.; Moser, J. E.; Humphry-Baker, R.; Zakeeruddin, S. M.; Grätzel, M.; Bäuerle, P. *Adv. Funct. Mater.* **2012**, *22* (6), 1291–1302.
- (202) Yella, A.; Mai, C. L.; Zakeeruddin, S. M.; Chang, S. N.; Hsieh, C. H.; Yeh, C. Y.; Grätzel, M. *Angew. Chemie - Int. Ed.* **2014**, *53* (11), 2973–2977.
- (203) Liyanage, N. P.; Yella, A.; Nazeeruddin, M.; Grätzel, M.; Delcamp, J. H. *ACS Appl. Mater. Interfaces* **2016**, *8* (8), 5376–5384.
- (204) Shen, Z.; Chen, J.; Li, X.; Li, X.; Zhou, Y.; Yu, Y.; Ding, H.; Li, J.; Zhu, L.; Hua, J. *ACS Sustain. Chem. Eng.* **2016**, *4* (6), 3518–3525.
- (205) Li, X.; Zheng, Z.; Jiang, W.; Wu, W.; Wang, Z.; Tian, H. *Chem. Commun.* **2015**, *51* (17), 3590–3592.
- (206) Zhang, X.; Xu, Y.; Giordano, F.; Schreier, M.; Pellet, N.; Hu, Y.; Yi, C.; Robertson, N.; Hua, J.; Zakeeruddin, S. M.; Tian, H.; Grätzel, M. *J. Am. Chem. Soc.* **2016**, *138* (34), 10742–10745.
- (207) Cao, Y.; Liu, Y.; Zakeeruddin, S. M.; Hagfeldt, A.; Grätzel, M. *Joule* **2018**, *2* (6), 1108–1117.
- (208) Freitag, M.; Teuscher, J.; Saygili, Y.; Zhang, X.; Giordano, F.; Liska, P.; Hua, J.; Zakeeruddin, S. M.; Moser, J. E.; Grätzel, M.; Hagfeldt, A. *Nat. Photonics* **2017**, *11* (6), 372–378.
- (209) Jiang, H.; Ren, Y.; Zhang, W.; Wu, Y.; Socie, E. C.; Carlsen, B. I.; Moser, J.-E.; Tian, H.; Zakeeruddin, S. M.; Zhu, W.-H.; Grätzel, M. *Angew. Chemie Int. Ed.* **2020**, anie.202000892.
- (210) Zhang, W.; Wu, Y.; Bahng, H. W.; Cao, Y.; Yi, C.; Saygili, Y.; Luo, J.; Liu, Y.; Kavan, L.; Moser, J. E.; Hagfeldt, A.; Tian, H.; Zakeeruddin, S. M.; Zhu, W. H.; Grätzel, M. *Energy Environ. Sci.* **2018**, *11* (7), 1779–1787.
- (211) Yella, A.; Humphry-Baker, R.; Curchod, B. F. E.; Ashari Astani, N.; Teuscher, J.; Polander, L. E.; Mathew, S.; Moser, J. E.; Tavernelli, I.; Rothlisberger, U.; Grätzel, M.; Nazeeruddin, M. K.; Frey, J. *Chem. Mater.* **2013**, *25* (13), 2733–2739.
- (212) Mathew, S.; Yella, A.; Gao, P.; Humphry-Baker, R.; Curchod, B. F. E.; Ashari-Astani, N.; Tavernelli, I.; Rothlisberger, U.; Nazeeruddin, M. K.; Grätzel, M. *Nat. Chem.* **2014**, *6* (3), 242–247.
- (213) Ahn, J.; Lee, K. C.; Kim, D.; Lee, C.; Lee, S.; Cho, D. W.; Kyung, S.; Im, C. *Mol. Cryst. Liq. Cryst.* **2013**, *581* (1), 45–51.
- (214) Tian, H.; Soto, A.; Xu, B.; Sun, L.; Hagfeldt, A.; Fabregat-Santiago, F.; Mora-Sero, I.; Kang, Y. S.; Bisquert, J.; Barea, E. M. *Nano* **2014**, *9* (5).
- (215) Marinado, T.; Nonomura, K.; Nissfolk, J.; Karlsson, M. K.; Hagberg, D. P.; Sun, L.; Mori, S.; Hagfeldt, A. *Langmuir* **2010**, *26* (4), 2592–2598.
- (216) Hardin, B. E.; Snaith, H. J.; McGehee, M. D. *Nat. Photonics* **2012**, *6* (3), 162–169.
- (217) Grätzel, M. *Inorg. Chem.* **2005**, *44* (20), 6841–6851.
- (218) Hagfeldt, A.; Graetzel, M. *Chem. Rev.* **1995**, *95* (1), 49–68.
- (219) Rowley, J. G.; Farnum, B. H.; Ardo, S.; Meyer, G. J. *J. Phys. Chem. Lett.* **2010**, *1* (20), 3132–3140.
- (220) Boschloo, G.; Hagfeldt, A. *Acc. Chem. Res.* **2009**, *42* (11), 1819–1826.
- (221) Clifford, J. N.; Palomares, E.; Md. Nazeeruddin, K.; Grätzel, M.; Durrant, J. R. *J. Phys. Chem. C* **2007**, *111* (17), 6561–6567.
- (222) Olsen, E.; Hagen, G.; Eric Lindquist, S. *Sol. Energy Mater. Sol. Cells* **2000**, *63* (3), 267–273.
- (223) Griffith, J. S.; Orgel, L. E. *Q. Rev. Chem. Soc.* **1957**, *11* (4), 381–393.
- (224) Saygili, Y.; Stojanovic, M.; Flores-Díaz, N.; Zakeeruddin, S. M.; Vlachopoulos, N.; Grätzel, M.; Hagfeldt, A. *Inorganics* **2019**, *7* (3), 30.
- (225) Hayami, S.; Komatsu, Y.; Shimizu, T.; Kamihata, H.; Lee, Y. H. *Coord. Chem. Rev.* **2011**, *255* (17–18), 1981–1990.

- (226) Krivokapic, I.; Zerara, M.; Daku, M. L.; Vargas, A.; Enachescu, C.; Ambrus, C.; Tregenna-Piggott, P.; Amstutz, N.; Krausz, E.; Hauser, A. *Coord. Chem. Rev.* **2007**, *251* (3–4), 364–378.
- (227) Endicott, J. F.; Brubaker, G. R.; Ramasami, T.; Kumar, K.; Dwarakanath, K.; Cassel, J.; Johnson, D. *Inorg. Chem.* **1983**, *22* (25), 3754–3762.
- (228) Li, X.; Reynal, A.; Barnes, P.; Humphry-Baker, R.; Zakeeruddin, S. M.; De Angelis, F.; O'Regan, B. C. *Phys. Chem. Chem. Phys.* **2012**, *14* (44), 15421–15428.
- (229) Sapp, S. A.; Elliott, C. M.; Contado, C.; Caramori, S.; Bignozzi, C. A. *J. Am. Chem. Soc.* **2002**, *124* (37), 11215–11222.
- (230) Cong, J.; Yang, X.; Kloo, L.; Sun, L. *Energy Environ. Sci.* **2012**, *5* (11), 9180–9194.
- (231) Cameron, P. J.; Peter, L. M.; Zakeeruddin, S. M.; Grätzel, M. *Coord. Chem. Rev.* **2004**, *248* (13–14), 1447–1453.
- (232) Mosconi, E.; Yum, J. H.; Kessler, F.; Gómez García, C. J.; Zuccaccia, C.; Cinti, A.; Nazeeruddin, M. K.; Grätzel, M.; De Angelis, F. *J. Am. Chem. Soc.* **2012**, *134* (47), 19438–19453.
- (233) Liu, Y.; Jennings, J. R.; Huang, Y.; Wang, Q.; Zakeeruddin, S. M.; Grätzel, M. *J. Phys. Chem. C* **2011**, *115* (38), 18847–18855.
- (234) Feldt, S. M.; Wang, G.; Boschloo, G.; Hagfeldt, A. *J. Phys. Chem. C* **2011**, *115* (43), 21500–21507.
- (235) Feldt, S. M.; Lohse, P. W.; Kessler, F.; Nazeeruddin, M. K.; Grätzel, M.; Boschloo, G.; Hagfeldt, A. *Phys. Chem. Chem. Phys.* **2013**, *15* (19), 7087–7097.
- (236) Feldt, S. M.; Gibson, E. A.; Gabrielsson, E.; Sun, L.; Boschloo, G.; Hagfeldt, A. *J. Am. Chem. Soc.* **2010**, *132* (46), 16714–16724.
- (237) Tsao, H. N.; Burschka, J.; Yi, C.; Kessler, F.; Nazeeruddin, M. K.; Grätzel, M. *Energy Environ. Sci.* **2011**, *4* (12), 4921–4924.
- (238) Kavan, L.; Yum, J. H.; Nazeeruddin, M. K.; Grätzel, M. *ACS Nano* **2011**, *5* (11), 9171–9178.
- (239) Carli, S.; Casarin, L.; Bergamini, G.; Caramori, S.; Bignozzi, C. A. *J. Phys. Chem. C* **2014**, *118* (30), 16782–16790.
- (240) Ellis, H.; Vlachopoulos, N.; Häggman, L.; Perruchot, C.; Jouini, M.; Boschloo, G.; Hagfeldt, A. *Electrochim. Acta* **2013**, *107*, 45–51.
- (241) Kakiage, K.; Aoyama, Y.; Yano, T.; Oya, K.; Fujisawa, J. I.; Hanaya, M. *Chem. Commun.* **2015**, *51* (88), 15894–15897.
- (242) Yum, J. H.; Baranoff, E.; Kessler, F.; Moehl, T.; Ahmad, S.; Bessho, T.; Marchioro, A.; Ghadiri, E.; Moser, J. E.; Yi, C.; Nazeeruddin, M. K.; Grätzel, M. *Nat. Commun.* **2012**, *3*, 631.
- (243) Hathaway, B. J.; Billing, D. E. *Coord. Chem. Rev.* **1970**, *5* (2), 143–207.
- (244) Bersuker, I. B. *Coord. Chem. Rev.* **1975**, *14* (4), 357–412.
- (245) Rorabacher, D. B. *Chem. Rev.* **2004**, *104* (2), 651–697.
- (246) Ambundo, E. A.; Deydier, M.-V.; Grall, A. J.; Agüera-Vega, N.; Dressel, L. T.; Cooper, T. H.; Heeg, M. J.; Ochrymowycz, L. A.; Rorabacher, D. B. *Inorg. Chem.* **1999**, *38* (19), 4233–4242.
- (247) Addison, A. W. *Inorganica Chim. Acta* **1989**, *162* (2), 217–220.
- (248) Cunningham, C. T.; Cunningham, K. L. H.; Michalec, J. F.; McMillin, D. R. *Inorg. Chem.* **1999**, *38* (20), 4388–4392.
- (249) Linnell, R. H.; Manfredi, D. *J. Phys. Chem.* **1960**, *64* (4), 497–499.
- (250) Burke, P. J.; Mcmillin, D. R.; Robinson, W. R. *Inorg. Chem.* **1980**, *19* (5), 1211–1214.
- (251) Burke, P. J.; Henrick, K.; McMillin, D. R. *Inorg. Chem.* **1982**, *21* (5), 1881–1886.
- (252) Bai, Y.; Yu, Q.; Cai, N.; Wang, Y.; Zhang, M.; Wang, P. *Chem. Commun.* **2011**, *47* (15), 4376–4378.
- (253) Li, J.; Yang, X.; Yu, Z.; Gurzadyan, G. G.; Cheng, M.; Zhang, F.; Cong, J.; Wang, W.; Wang, H.; Li, X.; Kloo, L.; Wang, M.; Sun, L. *RSC Adv.* **2017**, *7* (8), 4611–4615.
- (254) Saygili, Y.; Söderberg, M.; Pellet, N.; Giordano, F.; Cao, Y.; Munoz-García, A. B.; Zakeeruddin, S. M.; Vlachopoulos, N.; Pavone, M.; Boschloo, G.; Kavan, L.; Moser, J. E.; Grätzel, M.; Hagfeldt, A.; Freitag, M. *J. Am. Chem. Soc.* **2016**, *138* (45), 15087–

- 15096.
- (255) Freitag, M.; Giordano, F.; Yang, W.; Pazoki, M.; Hao, Y.; Zietz, B.; Grätzel, M.; Hagfeldt, A.; Boschloo, G. *J. Phys. Chem. C* **2016**, *120* (18), 9595–9603.
- (256) Cao, Y.; Liu, Y.; Zakeeruddin, S. M.; Hagfeldt, A.; Grätzel, M. *Joule* **2018**, *2* (6), 1108–1117.
- (257) Cao, Y.; Saygili, Y.; Ummadisingu, A.; Teuscher, J.; Luo, J.; Pellet, N.; Giordano, F.; Zakeeruddin, S. M.; Moser, J. E.; Freitag, M.; Hagfeldt, A.; Grätzel, M. *Nat. Commun.* **2017**, *8*, 15390.
- (258) Hoffeditz, W. L.; Katz, M. J.; Deria, P.; Cutsail, G. E.; Pellin, M. J.; Farha, O. K.; Hupp, J. T. *J. Phys. Chem. C* **2016**, *120* (7), 3731–3740.
- (259) Kavan, L.; Saygili, Y.; Freitag, M.; Zakeeruddin, S. M.; Hagfeldt, A.; Grätzel, M. *Electrochim. Acta* **2017**, *227*, 194–202.
- (260) Ferdowsi, P.; Saygili, Y.; Zakeeruddin, S. M.; Mokhtari, J.; Grätzel, M.; Hagfeldt, A.; Kavan, L. *Electrochim. Acta* **2018**, *265*, 194–201.
- (261) Bella, F.; Sacco, A.; Pugliese, D.; Laurenti, M.; Bianco, S. *J. Power Sources* **2014**, *264*, 333–343.
- (262) Duay, J.; Gillette, E.; Liu, R.; Lee, S. B. *Phys. Chem. Chem. Phys.* **2012**, *14* (10), 3329–3337.
- (263) Kelly, C. A.; Farzad, F.; Thompson, D. W.; Stipkala, J. M.; Meyer, G. J. *Langmuir* **1999**, *15* (20), 7047–7054.
- (264) Mengesha Tefashe, U.; Nonomura, K.; Vlachopoulos, N.; Hagfeldt, A.; Wittstock, G. *J. Phys. Chem. C* **2012**, *116* (6), 4316–4323.
- (265) Koops, S. E.; O'Regan, B. C.; Barnes, P. R. F.; Durrant, J. R. *J. Am. Chem. Soc.* **2009**, *131* (13), 4808–4818.
- (266) Wang, H.; Peter, L. M. *J. Phys. Chem. C* **2012**, *116* (19), 10468–10475.
- (267) Wu, J.; Lan, Z.; Hao, S.; Li, P.; Lin, J.; Huang, M.; Fang, L.; Huang, Y. *Pure Appl. Chem.* **2008**, *80* (11), 2241–2258.
- (268) Kusama, H.; Arakawa, H. *Sol. Energy Mater. Sol. Cells* **2005**, *85* (3), 333–344.
- (269) Yin, X.; Tan, W.; Zhang, J.; Weng, Y.; Xiao, X.; Zhou, X.; Li, X.; Lin, Y. *Colloids Surfaces A Physicochem. Eng. Asp.* **2008**, *326* (1–2), 42–47.
- (270) Kusama, H.; Konishi, Y.; Sugihara, H.; Arakawa, H. *Sol. Energy Mater. Sol. Cells* **2003**, *80* (2), 167–179.
- (271) Zhang, S.; Yanagida, M.; Yang, X.; Han, L. *Appl. Phys. Express* **2011**, *4* (4), 042301.
- (272) Boschloo, G.; Häggman, L.; Hagfeldt, A. *J. Phys. Chem. B* **2006**, *110* (26), 13144–13150.
- (273) Ziólek, M.; Martín, C.; Sun, L.; Douhal, A. *J. Phys. Chem. C* **2012**, *116* (50), 26227–26238.
- (274) Ryuzi, K.; Motohiro, K.; Kodate, S.; Furube, A.; Fuke, N.; Koide, N. *J. Phys. Chem. C* **2009**, *113* (48), 20738–20744.
- (275) Thomas, S.; Deepak, T. G.; Anjusree, G. S.; Arun, T. A.; Nair, S. V.; Nair, A. S. *Journal of Materials Chemistry A*. The Royal Society of Chemistry April 7, 2014, pp 4474–4490.
- (276) Wang, L.; Al-Mamun, M.; Liu, P.; Wang, Y.; Yang, H. G.; Wang, H. F.; Zhao, H. *NPG Asia Materials*. Nature Publishing Group November 13, 2015, pp e226–e226.
- (277) Hauch, A.; Georg, A. *Electrochim. Acta* **2001**, *46* (22), 3457–3466.
- (278) Papageorgiou, N.; Maier, W. F.; Grätzel, M. *J. Electrochem. Soc.* **1997**, *144* (3), 876.
- (279) Lee, Y. L.; Chen, C. L.; Chong, L. W.; Chen, C. H.; Liu, Y. F.; Chi, C. F. *Electrochem. commun.* **2010**, *12* (11), 1662–1665.
- (280) Kinoshita; K. John Wiley Sons, New York, NY January 1, 1988.
- (281) Murakami, T. N.; Ito, S.; Wang, Q.; Nazeeruddin, M. K.; Bessho, T.; Cesar, I.; Liska, P.; Humphry-Baker, R.; Comte, P.; Péchy, P.; Grätzel, M. *J. Electrochem. Soc.* **2006**, *153* (12), A2255.
- (282) Ramasamy, E.; Lee, W. J.; Lee, D. Y.; Song, J. S. *Appl. Phys. Lett.* **2007**, *90* (17), 173103.
- (283) Kay, A.; Grätzel, M. *Sol. Energy Mater. Sol. Cells* **1996**, *44* (1), 99–117.

- (284) Pringle, J. M.; Armel, V.; MacFarlane, D. R. *Chem. Commun.* **2010**, 46 (29), 5367–5369.
- (285) Han, L.; Koide, N.; Chiba, Y.; Mitate, T. *Appl. Phys. Lett.* **2004**, 84 (13), 2433–2435.
- (286) Seaman, C. H. *Sol. Energy* **1982**, 29 (4), 291–298.
- (287) Sommeling, P. M.; Rieffe, H. C.; Van Roosmalen, J. A. M.; Schönecker, A.; Kroon, J. M.; Wienke, J. A.; Hinsch, A. *Sol. Energy Mater. Sol. Cells* **2000**, 62 (4), 399–410.
- (288) Guo, X. Z.; Luo, Y. H.; Zhang, Y. D.; Huang, X. C.; Li, D. M.; Meng, Q. B. In *Review of Scientific Instruments*; American Institute of PhysicsAIP, 2010; Vol. 81, p 103106.
- (289) Jennings, J. R.; Liu, Y.; Wang, Q. *J. Phys. Chem. C* **2011**, 115 (30), 15109–15120.
- (290) Ardo, S.; Meyer, G. J. *J. Am. Chem. Soc.* **2011**, 133 (39), 15384–15396.
- (291) Qian, D.; Ma, W.; Li, Z.; Guo, X.; Zhang, S.; Ye, L.; Ade, H.; Tan, Z.; Hou, J. *J. Am. Chem. Soc.* **2013**, 135 (23), 8464–8467.
- (292) Meng, D.; Sun, D.; Zhong, C.; Liu, T.; Fan, B.; Huo, L.; Li, Y.; Jiang, W.; Choi, H.; Kim, T.; Kim, J. Y.; Sun, Y.; Wang, Z.; Heeger, A. J. *J. Am. Chem. Soc.* **2016**, 138 (1), 375–380.
- (293) Huang, X.; Weng, K.; Huo, L.; Fan, B.; Yang, C.; Sun, X.; Sun, Y. *J. Mater. Chem. C* **2016**, 4 (38), 9052–9059.
- (294) Zhang, S.; Qin, Y.; Uddin, M. A.; Jang, B.; Zhao, W.; Liu, D.; Woo, H. Y.; Hou, J. *Macromolecules* **2016**, 49 (8), 2993–3000.
- (295) Huo, L.; Liu, T.; Fan, B.; Zhao, Z.; Sun, X.; Wei, D.; Yu, M.; Liu, Y.; Sun, Y. *Adv. Mater.* **2015**, 27 (43), 6969–6975.
- (296) Hagberg, D. P.; Jiang, X.; Gabrielsson, E.; Linder, M.; Marinado, T.; Brinck, T.; Hagfeldt, A.; Sun, L. *J. Mater. Chem.* **2009**, 19 (39), 7232–7238.
- (297) Gao, P.; Tsao, H. N.; Grätzel, M.; Nazeeruddin, M. K. *Org. Lett.* **2012**, 14 (17), 4330–4333.
- (298) Roncali, J. *Chem. Rev.* **1997**, 97 (1), 173–205.
- (299) Pavlishchuk, V. V.; Addison, A. W. *Inorganica Chim. Acta* **2000**, 298 (1), 97–102.
- (300) Cao, Y.; Cai, N.; Wang, Y.; Li, R.; Yuan, Y.; Wang, P. *Phys. Chem. Chem. Phys* **2012**, 14, 8282–8286.
- (301) Kooops, S. E.; Durrant, J. R. *Inorganica Chim. Acta* **2008**, 361 (3), 663–670.
- (302) Haque, S. A.; Palomares, E.; Cho, B. M.; Green, A. N. M.; Hirata, N.; Klug, D. R.; Durrant, J. R. *J. Am. Chem. Soc.* **2005**, 127 (10), 3456–3462.
- (303) Barnes, P. R. F.; Miettunen, K.; Li, X.; Anderson, A. Y.; Bessho, T.; Gratzel, M.; O'Regan, B. C. *Adv. Mater.* **2013**, 25 (13), 1881–1922.
- (304) Ronca, E.; Pastore, M.; Belpassi, L.; Tarantelli, F.; De Angelis, F. *Energy Environ. Sci.* **2013**, 6 (1), 183–193.
- (305) Krüger, J.; Bach, U.; Grätzel, M. *Adv. Mater.* **2000**, 12 (6), 447–451.
- (306) Guo, Y.; Li, M.; Zhou, Y.; Song, J.; Bo, Z.; Wang, H. *Macromolecules* **2017**, 50 (20), 7984–7992.
- (307) Li, Y.; Gu, M.; Pan, Z.; Zhang, B.; Yang, X.; Gu, J.; Chen, Y. *J. Mater. Chem. A* **2017**, 5 (22), 10798–10814.
- (308) Cai, L.; Moehl, T.; Moon, S. J.; Decoppet, J. D.; Humphry-Baker, R.; Xue, Z.; Bin, L.; Zakeeruddin, S. M.; Grätzel, M. *Org. Lett.* **2014**, 16 (1), 106–109.
- (309) Liu, Y.; Cao, Y.; Zhang, W.; Stojanovic, M.; Dar, M. I.; Péchy, P.; Saygili, Y.; Hagfeldt, A.; Zakeeruddin, S. M.; Grätzel, M. *Angew. Chemie - Int. Ed.* **2018**, 57 (43), 14125–14128.
- (310) Haque, S. A.; Palomares, E.; Cho, B. M.; Green, A. N. M.; Hirata, N.; Klug, D. R.; Durrant, J. R. *J. Am. Chem. Soc.* **2005**, 127 (10), 3456–3462.
- (311) Yella, A.; Lee, H. W.; Tsao, H. N.; Yi, C.; Chandiran, A. K.; Nazeeruddin, M. K.; Diao, E. W. G.; Yeh, C. Y.; Zakeeruddin, S. M.; Grätzel, M. *Science (80-.)*. **2011**, 334 (6056), 629–634.
- (312) Hendriks, K. H.; Heintges, G. H. L.; Gevaerts, V. S.; Wienk, M. M.; Janssen, R. A. J. *Angew. Chemie - Int. Ed.* **2013**, 52 (32), 8341–8344.
- (313) Grzybowski, M.; Glodkowska-Mrowka, E.; Stoklosa, T.; Gryko, D. T. *Org. Lett.* **2012**, 14 (11), 2670–2673.

- (314) Zhang, J.; Vlachopoulos, N.; Hao, Y.; Holcombe, T. W.; Boschloo, G.; Johansson, E. M. J.; Grätzel, M.; Hagfeldt, A. *ChemPhysChem* **2016**, *17* (10), 1441–1445.
- (315) Holcombe, T. W.; Yum, J. H.; Kim, Y.; Rakstys, K.; Grätzel, M. *J. Mater. Chem. A* **2013**, *1* (44), 13978–13983.
- (316) Hao, Y.; Saygili, Y.; Cong, J.; Eriksson, A.; Yang, W.; Zhang, J.; Polanski, E.; Nonomura, K.; Zakeeruddin, S. M.; Grätzel, M.; Hagfeldt, A.; Boschloo, G. *ACS Appl. Mater. Interfaces* **2016**, *8* (48), 32797–32804.
- (317) Ganesan, P.; Yella, A.; Holcombe, T. W.; Gao, P.; Rajalingam, R.; Al-Muhtaseb, S. A.; Grätzel, M.; Nazeeruddin, M. K. *ACS Sustain. Chem. Eng.* **2015**, *3* (10), 2389–2396.
- (318) Lim, D. suk; Choi, K.; Hayati, D.; Park, D. H.; Ghifari, A.; Lee, K. M.; Ko, Y.; Jun, Y.; Suk, H. J.; Hong, J. *Dye. Pigment.* **2020**, *173*, 107840.
- (319) Qu, S.; Wu, W.; Hua, J.; Kong, C.; Long, Y.; Tian, H. *J. Phys. Chem. C* **2010**, *114* (2), 1343–1349.
- (320) Saygili, Y.; Söderberg, M.; Pellet, N.; Giordano, F.; Cao, Y.; Munoz-García, A. B.; Zakeeruddin, S. M.; Vlachopoulos, N.; Pavone, M.; Boschloo, G.; Kavan, L.; Moser, J. E.; Grätzel, M.; Hagfeldt, A.; Freitag, M. *J. Am. Chem. Soc.* **2016**, *138* (45), 15087–15096.
- (321) Zhang, W.; Wu, Y.; Bahng, H. W.; Cao, Y.; Yi, C.; Saygili, Y.; Luo, J.; Liu, Y.; Kavan, L.; Moser, J. E.; Hagfeldt, A.; Tian, H.; Zakeeruddin, S. M.; Zhu, W. H.; Grätzel, M. *Energy Environ. Sci.* **2018**, *11* (7), 1779–1787.
- (322) Roncali, J. *Macromol. Rapid Commun.* **2007**, *28* (17), 1761–1775.
- (323) Clementi, E.; Raimondi, D. L.; Reinhardt, W. P. *J. Chem. Phys.* **1967**, *47* (4), 1300–1307.
- (324) Slater, J. C. *J. Chem. Phys.* **1964**, *41* (10), 3199–3204.
- (325) Haque, S. A.; Tachibana, Y.; Willis, R. L.; Moser, J. E.; Grätzel, M.; Klug, D. R.; Durrant, J. R. *J. Phys. Chem. B* **2000**, *104* (3), 538–547.
- (326) Kim, B. G.; Chung, K.; Kim, J. *Chem. - A Eur. J.* **2013**, *19* (17), 5220–5230.
- (327) Yao, Z.; Zhang, M.; Wu, H.; Yang, L.; Li, R.; Wang, P. *J. Am. Chem. Soc.* **2015**, *137* (11), 3799–3802.
- (328) Saygili, Y.; Söderberg, M.; Pellet, N.; Giordano, F.; Cao, Y.; Munoz-García, A. B.; Zakeeruddin, S. M.; Vlachopoulos, N.; Pavone, M.; Boschloo, G.; Kavan, L.; Moser, J. E.; Grätzel, M.; Hagfeldt, A.; Freitag, M. *J. Am. Chem. Soc.* **2016**, *138* (45), 15087–15096.
- (329) Feldt, S. M.; Gibson, E. A.; Gabrielsson, E.; Sun, L.; Boschloo, G.; Hagfeldt, A. *J. Am. Chem. Soc.* **2010**, *132* (46), 16714–16724.
- (330) Michaels, H.; Rinderle, M.; Freitag, R.; Benesperi, I.; Edvinsson, T.; Socher, R.; Gagliardi, A.; Freitag, M. *Chem. Sci.* **2020**, *11* (11), 2895–2906.
- (331) Cao, Y.; Liu, Y.; Zakeeruddin, S. M.; Hagfeldt, A.; Grätzel, M. *Joule* **2018**, *2* (6), 1108–1117.
- (332) Xu, M.; Zhang, M.; Pastore, M.; Li, R.; De Angelis, F.; Wang, P. *Chem. Sci.* **2012**, *3* (4), 976–983.
- (333) Gabrielsson, E.; Ellis, H.; Feldt, S.; Tian, H.; Boschloo, G.; Hagfeldt, A.; Sun, L. *Adv. Energy Mater.* **2013**, *3* (12), 1647–1656.
- (334) Cai, N.; Zhang, J.; Xu, M.; Zhang, M.; Wang, P. *Adv. Funct. Mater.* **2013**, *23* (28), 3539–3547.
- (335) Odom, S. A.; Lancaster, K.; Beverina, L.; Lefler, K. M.; Thompson, N. J.; Coropceanu, V.; Bredas, J. L.; Marder, S. R.; Barlow, S. *Chem. - A Eur. J.* **2007**, *13* (34), 9637–9646.
- (336) Facchetti, A. *Chem. Mater.* **2011**, *23* (3), 733–758.
- (337) Chen, C. H.; Hsieh, C. H.; Dubosc, M.; Cheng, Y. J.; Hsu, C. S. *Macromolecules* **2010**, *43* (2), 697–708.
- (338) Coppo, P.; Cupertino, D. C.; Yeates, S. G.; Turner, M. L. *J. Mater. Chem.* **2002**, *12* (9), 2597–2599.
- (339) Ogawa, K.; Rasmussen, S. C. *J. Org. Chem.* **2003**, *68* (7), 2921–2928.
- (340) Tachibana, Y.; Rubtsov, I. V.; Montanari, I.; Yoshihara, K.; Klug, D. R.; Durrant, J. R.

- Transient luminescence studies of electron injection in dye sensitised nanocrystalline TiO₂ films*; 2001; Vol. 142.
- (341) Green, M. A. In *Physica E: Low-Dimensional Systems and Nanostructures*; North-Holland, 2002; Vol. 14, pp 65–70.
- (342) Mishra, A.; Fischer, M. K. R.; Büuerle, P. *Angewandte Chemie - International Edition*. March 23, 2009, pp 2474–2499.
- (343) Asbury, J. B.; Hao, E.; Wang, Y.; Ghosh, H. N.; Lian, T. *J. Phys. Chem. B* **2001**, 105 (20), 4545–4557.
- (344) Pastore, M.; De Angelis, F. *Phys. Chem. Chem. Phys.* **2012**, 14 (2), 920–928.
- (345) Zhang, L.; Cole, J. M. *J. Mater. Chem. A* **2017**, 5 (37), 19541–19559.
- (346) Freitag, M.; Teuscher, J.; Saygili, Y.; Zhang, X.; Giordano, F.; Liska, P.; Hua, J.; Zakeeruddin, S. M.; Moser, J. E.; Grätzel, M.; Hagfeldt, A. *Nat. Photonics* **2017**, 11 (6), 372–378.
- (347) Clifford, J. N.; Martínez-Ferrero, E.; Viterisi, A.; Palomares, E. *Chem. Soc. Rev.* **2011**, 40 (3), 1635–1646.
- (348) Qi, B.; Wang, J. *J. Mater. Chem.* **2012**, 22 (46), 24315–24325.
- (349) Huang, S. Y.; Schlichthörl, G.; Nozik, A. J.; Grätzel, M.; Frank, A. J. *J. Phys. Chem. B* **1997**, 101 (14), 2576–2582.
- (350) Halme, J.; Vahermaa, P.; Miettunen, K.; Lund, P. *Adv. Mater.* **2010**, 22 (35), E210–E234.
- (351) Cameron, P. J.; Peter, L. M. *J. Phys. Chem. B* **2005**, 109 (15), 7392–7398.
- (352) Ito, S.; Liska, P.; Comte, P.; Charvet, R.; Pechy, P.; Bach, U.; Schmidt-Mende, L.; Zakeeruddin, S. M.; Kay, A.; Nazeeruddin, M. K.; Grätzel, M. *Chem. Commun.* **2005**, 0 (34), 4351–4353.
- (353) Bisquert, J.; Mora-Seró, I. *J. Phys. Chem. Lett.* **2010**, 1 (1), 450–456.
- (354) Grätzel, M. *Journal of Photochemistry and Photobiology C: Photochemistry Reviews*. Elsevier October 31, 2003, pp 145–153.

Acknowledgements

First of all, I would like to express my gratitude to Dr. Shaik M. Zakeeruddin and Prof. Michael Graetzel, for giving me the opportunity to join the laboratory of photonics in interfaces and pursue a PhD. I am grateful for their guidance, help and the freedom I was provided throughout the completion of my thesis.

I thank Anne-Lene, Heidi and Carmen for their precious help regarding administrative matters and for answering to my e-mail in no time, but also the laughs and joyful atmosphere. I would like to thank the ISIC team, Jackie and the CH-BCH Magasin crew, Francesco and Daniel for their help regarding Mass spectrometry analysis as well as Aurélien for its assistance regarding NMR spectroscopy.

I am grateful to Dr. Anne-Sophie Chauvin, for accepting me in her teaching assistant team and allow me to help her in the education to general chemistry of hundreds of bachelor students. Along with that, I am grateful to my team-mates: Sunny, Ophélie, Julien, Bruno and Chloé for the fun they brought to the numerous exercise sessions and correction hours.

I would like to thank my office mates and all the LPI-LSPM members for their fruitful collaborations and good spirits: Anders, Natalie, Nick, Sandi, Algirdas, Vincent, Brian, Natalie, Jovana, Lukas, Olivier, Alexander, Marco, Hong, Hui-Seon, Esa, Anwar, Masaud and Félix.

I am thankful to Nadir, Luciano, Rory, Marta, Christophe, Xavier, Kevin, Marina, Florian, Wiktor, Mathieu for all the fun times, notably the many barbecues in the summer and the evenings at Sat'.

I would like give special thanks to Jean-David, Thomas, Amita, Wolfgang, Yuhang for the many good memories, meaningful discussion, coffees and hangouts. A special mention to Masoud for all the discussions and fights about football as well as FIFA games and generally, all the fun times. I thank my long-time friends, Vladimir and Selim for all the weekend activities and motivation.

Last but not the least, I am extremely grateful to my family: Liliana, Mirjana, Dario, Gabriel and Matteo and my girlfriend Alejandra, for their love, patience and support throughout my PhD.

Lausanne, March 2, 2021

Curriculum Vitae

STOJANOVIC MARKO

PERSONNAL INFORMATION

Born in Switzerland, 5 January 1992,
Adress 5 Rue des grand-portes 1213 Onex – Geneva,
E-mail marko.stojanovic.pro@gmail.com
Phone +41 76 376 97 68,

EDUCATION

2011-2014 – École polytechnique fédérale de Lausanne (EPFL), VD
EPFL Bachelor of Science BSc in Chemistry and Chemical Engineering

2014-2016 – École polytechnique fédérale de Lausanne (EPFL), VD
EPFL Master of Science MSc in Molecular and Biological Chemistry

2016-2021 – École polytechnique fédérale de Lausanne (EPFL), VD
EPFL PhD in Chemistry and Chemical Engineering

EXPERIENCE

August 2014 – Laboratory of catalysis and organic synthesis (LCSO) - EPFL, VD
Internship Synthesis and characterization of organic substrates for Platinum catalyzed Domino Reaction.

Supervised by Dr. Yifan Li and Prof. Jérôme Waser

August 2015 – Laboratory of photonics and interfaces (LPI) - EPFL, VD
Internship Synthesis and characterization of blue dyes for Dye Sensitized Solar cells.

Supervised by Dr. Chenyi Yi, Dr. Shaik M. Zakeeruddin and Prof. Michael Graetzel.

AWARDS

October 2015 – International Society of Electrochemistry Meeting
HKUST Best Poster Award for Investigation of Al/Air battery with application to electric vehicles.

December 2020 – Chemistry and chemical engineering section
EPFL Teaching excellency award.

PUBLICATIONS

- Seo, J.Y., Kim, H.S., Akin, S., **Stojanovic, M.**, Simon, E., Fleischer, M., Hagfeldt, A., Zakeeruddin, S.M. and Grätzel, M., 2018. Novel p-dopant toward highly efficient and stable perovskite solar cells. *Energy & Environmental Science*, 11(10), pp.2985-2992
- Liu, Y., Cao, Y., Zhang, W., **Stojanovic, M.**, Dar, M.I., Péchy, P., Saygili, Y., Hagfeldt, A., Zakeeruddin, S.M. and Grätzel, M., 2018. Electron-Affinity-Triggered Variations on the Optical and Electrical Properties of Dye Molecules Enabling Highly Efficient Dye-Sensitized Solar Cells. *Angewandte Chemie*, 130(43), pp.14321-14324
- Saygili, Y., **Stojanovic, M.**, Michaels, H., Tiepelt, J., Teuscher, J., Massaro, A., Pavone, M., Giordano, F., Zakeeruddin, S.M., Boschloo, G. and Moser, J.E., 2018. Effect of Coordination Sphere Geometry of Copper Redox Mediators on Regeneration and Recombination Behavior in Dye-Sensitized Solar Cell Applications. *ACS Applied Energy Materials*, 1(9), pp.4950-4962
- Di Franco, T., **Stojanovic, M.**, Keller, S.C., Scopelliti, R. and Hu, X., 2016. A Structure–Activity Study of Nickel NNN Pincer Complexes for Alkyl-Alkyl Kumada and Suzuki–Miyaura Coupling Reactions. *Helvetica Chimica Acta*, 99(11), pp.830-847.
- Saygili, Y., **Stojanovic, M.**, Kim, H.S., Teuscher, J., Scopelliti, R., Freitag, M., Zakeeruddin, S.M., Moser, J.E., Grätzel, M. and Hagfeldt, A., 2020. Liquid State and Zombie Dye Sensitized Solar Cells with Copper Bipyridine Complexes Functionalized with Alkoxy Groups. *The Journal of Physical Chemistry C*, 124(13), pp.7071-7081.
- Saygili, Y., **Stojanovic, M.**, Flores-Díaz, N., Zakeeruddin, S. M., Vlachopoulos, N., Grätzel, M., & Hagfeldt, A. (2019). Metal coordination complexes as redox mediators in regenerative dye-sensitized solar cells. *Inorganics*, 7(3), 30.
- Ummadisingu, A., Seo, J.Y., **Stojanovic, M.**, Zakeeruddin, S.M., Grätzel, M., Hagfeldt, A., Vlachopoulos, N. and Saliba, M., 2017. Additives, Hole Transporting Materials and Spectroscopic Methods to Characterize the Properties of Perovskite Films. *CHIMIA International Journal for Chemistry*, 71(11), pp.754-761.

COMPUTER SKILLS

Latex; Open Office, Windows, Macintosh, MATLAB, Igor pro, Origins pro

OTHER INFORMATION

Languages	French	Mother tongue
	Serbian	Mother tongue
	English	Fluent
Interests	Music – Cooking – Sports – Reading – film photography	

